CHEMICAL REVIEWS

pubs.acs.org/CR Review

Endohedrally Doped Cage Clusters

Jijun Zhao, Qiuying Du, Si Zhou,* and Vijay Kumar*

Cite This: *Chem. Rev.* 2020, 120, 9021–9163 Read Online

ACCESS | Metrics & More | Article Recommendations | Supporting Information

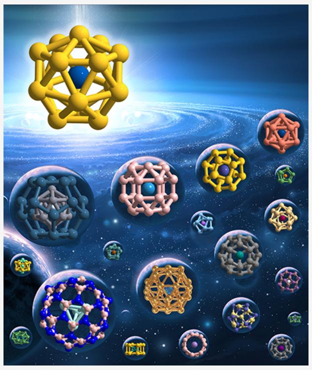

ABSTRACT: The discovery of carbon fullerene cages and their solids opened a new avenue to build materials from stable cage clusters as "artificial atoms" or "superatoms" instead of atoms. However, cage clusters of other elements are generally not stable. In 2001, *ab initio* calculations showed that endohedral doping of Zr and Ti atoms leads to highly stable Zr@Si_{16} fullerene and Ti@Si_{16} Frank–Kasper polyhedral clusters with large HOMO–LUMO gaps. In 2002, Zr@Ge_{16} was shown to form a Frank–Kasper polyhedron, suggesting the possibility of designing novel clusters by tuning endohedral and cage atoms. These results were subsequently confirmed from experiments. In the past nearly two decades, many experimental and theoretical studies have been carried out on different clusters, and many very stable cage clusters with possibly high abundance have been found by endohedral doping. Indeed in 2017, Ta@Si_{16} and Ti@Si_{16} cage clusters have been synthesized in bulk quantity of about 100 mg using a dry-chemistry method, giving rise to a new hope of developing cluster-based materials in macroscopic quantity besides the well-known C_{60} fullerene solid. Also, wet-chemistry methods have been used to synthesize endohedrally doped clusters as well as ligated clusters and their solids, which auger well for the development of novel nanostructured materials using atomically precise clusters with unique properties. In this comprehensive review, we present results of many such developments in this fast-growing field including (i) endohedrally doped Al, Ga, and In clusters, (ii) small endohedral carbon fullerene cages with ≤ 28 carbon atoms, (iii) metal doped boron cages, (iv) endohedrally doped cages of group 14 elements (Si, Ge, Sn, and Pb), (v) coinage metal (Cu, Ag, Au) cages doped with a transition metal atom as well as their ligated clusters and crystals, (vi) endohedrally doped cages of compound semiconductors, and (vii) multilayer Matryoshka cages and core–shell structures. In a large number of cases, we have performed *ab initio* calculations to present updated results of the most stable atomic structures and fundamental electronic properties of the endohedrally doped cage clusters. We discuss electronic, magnetic, optical, and catalytic properties in order to shed light on their potential applications. The stability of the doped cage clusters has been correlated to the concept of filling the electronic shells for superatoms such as within a spherical potential model and also using various electron counting rules including Wade–Mingos rules, systems with 18 and 32 electrons, and the spherical aromaticity rule. We also discuss cluster–cluster interaction in cluster dimers and assemblies of some of the promising doped cage clusters in different dimensions. Finally, we give a perspective of this field with a bright future.

CONTENTS

Received: October 14, 2019
Published: August 31, 2020

https://dx.doi.org/10.1021/acs.chemrev.9b00651
Chem. Rev. 2020, 120, 9021–9163

1. INTRODUCTION

Clusters are an intermediate state of matter between bulk materials and atoms or molecules. They are technologically very important for catalysis, crystal growth, optical and magnetic applications, environment and energy, biological systems, miniature devices, and designing novel cluster-assembled materials. In the past three decades, great efforts[1−9] have been made to understand their properties which depend in general on size and shape, while for multicomponent clusters the distribution of atoms could be quite different from what is known in bulk. Furthermore, periodicity, which is a well-known property of crystals, does not exist in clusters. Therefore, not only any rotational symmetry such as 5-fold and 10-fold is possible, but also practically there is an infinite number of structural possibilities that could lead to materials with diverse properties quite different from the corresponding bulk as the properties are closely correlated with atomic structure. Accordingly, clusters offer great opportunities to develop novel materials with desired properties[10−13]. However, it is generally difficult to determine the atomic structure of clusters experimentally, though this is done routinely for bulk materials by using an X-ray diffraction or neutron scattering method. Therefore, theoretical developments and calculations with predictive capabilities such as those based on DFT are generally necessary to determine the most stable atomic structures[14] and explore the physical and chemical properties of these finite systems.[15]

Experimental and theoretical progress during the past few decades has led to major strides in the understanding of the atomic structure, growth behavior as well as properties of clusters of a variety of materials. In a pioneering experiment by Knight *et al.*,[16] high abundance of sodium clusters with 2, 8, 18, 20, 34, 40, 58, 68, ... valence electrons was observed in the mass spectrum. These so called "*magic numbers*", which is a concept originally from the shell model of nuclei,[17] correspond to the complete filling of 1S, 1P, 1D, 2S, 1F, 2P, 1G, 2D, ... electronic shells in a simple spherical potential or a jellium model[1,18]. Here we use capital letters to represent the angular momentum character of the orbitals to distinguish them from atomic orbitals. These results have been later supported from atomistic calculations suggesting a weak dependence of electronic shells on the atomic structure of clusters of free electron-like systems.[19] For large sodium clusters containing more than 1500 atoms, Martin *et al.*[20] observed a transition of magic numbers from electronic shells to atomic shells associated with icosahedral or cuboctahedral packing. On the other hand, clusters of noble gas atoms such as Xe exhibit a series of magic numbers at 13, 19, 25, 55, 71, 87, and 147, ... out of which those with 13, 55, and 147 atoms can be related to the completion of MacKay icosahedra.[21] Generally speaking, these clusters with closed electronic and/or atomic shells exhibit high stability and usually high abundance (often referred to as *magic clusters*) in the mass spectrum,[7] while the abundance of clusters with one more atom is much lower.

Within the picture of the jellium model, doping has been used to change the number of valence electrons of a cluster to reach the closed electronic shell, for example, $[Al_{13}]^-$ and $Al_{12}Si$ are electronically equivalent. Experiments on anion aluminum clusters have shown high abundance of $[Al_{13}]^-$ and $[Al_{23}]^-$ clusters corresponding to the electronic shell closure at 40 and 70 valence electrons[22,23]. These clusters also have low reactivity with oxygen. In order to have a neutral cluster, the central Al atom in the icosahedral Al_{13} cluster can be replaced by a Si atom. Accordingly, $Al_{12}Si$ becomes a closed electronic shell cluster with a HOMO−LUMO gap of about 2 eV.[24] This cluster can be considered to be an endohedrally doped cluster $Si@Al_{12}$ (here the "@" symbol is used to denote that an atom or a group of atoms is encapsulated in a cage; similarly, exohedral doping is denoted by "&"). It satisfies the principle of developing endohedral clusters, although the idea of making stable cage clusters by endohedral doping started to attract wide attention after the predictions of silicon fullerenes and FK polyhedral clusters,[13] which will be discussed later.

Starting from an endohedrally doped cluster with closed electronic shell, e.g., $Si@Al_{12}$ having 40 valence electrons, it is possible to tailor the overall valence state and chemical behavior of the cluster as a superatom by changing the central dopant atom, e.g., $B@Al_{12}$ as a superhalogen, $P@Al_{12}$ as a super alkali metal, and $Ca@Al_{12}$ as a superchalcogen.[25] The term "*superatom*" has been coined to represent a group of atoms that behaves like an atom[12,26−29]. In principle, there are many possibilities for the rational design of endohedrally doped clusters (as superatoms) with stable cage-like configurations and tunable physical and chemical properties, which would be suitable for making new materials at the nanoscale.

In the 1980s, another very important milestone of cluster science has been the discovery of C_{60}, the carbon fullerene with icosahedral symmetry.[30] This is the highest-symmetry cage cluster and can be produced almost exclusively. Most interestingly, these fullerenes can be condensed to form solid C_{60}.[31] Doping of alkali atoms in this new crystalline phase of carbon (besides diamond and graphite) led to yet another exciting finding of superconductivity in doped solid C_{60}.[32] This discovery added another perspective to research on clusters that a group or aggregate of atoms rather than individual atoms could be the building blocks to make new phases of materials with the possibility of entirely different properties from the corresponding known bulk phases. Such aggregates of atoms can be also referred to as superatoms. These developments led to much interest in exploring similar possibilities for other elements/materials. In particular, there was much curiosity if similar structures could exist for silicon. But the weak π bonding in silicon compared to that in carbon species does not favor the fullerene-like empty cage structures. Moreover, unlike C_{60} fullerene, clusters of most other elements do not show such high abundance and therefore there has been slow progress in fulfilling the dream to produce cluster-assembled materials of other elements.

Another important factor that contributed to great efforts on understanding the silicon nanostructures and their properties has been the continuous downsizing of the silicon-based microelectronic devices. In an exciting work, Canham[33] reported the observation of visible light from a silicon wafer after being subject to electrochemical and chemical dissolution. Indeed, this so-called porous silicon was discovered earlier at Bell Lab in 1956[34] but did not attract much attention. Experiments by Canham and others ignited much interest in understanding this important phenomenon from porous silicon as bulk silicon is not a good material for optical applications due to its indirect band gap. Several studies on porous silicon and silicon clusters led to the understanding that the luminescence was due to nanoparticles of about 2 nm size as a result of quantum confinement effects.[35] This finding was also very important because nanostructures of compound semiconductors have been the focus of research for optical applications and it led to the hope that silicon may also be a useful optical material. However, unlike carbon, experimental studies on silicon clusters and nanoparticles did not show strong abundance of a particular size. But interestingly, in pioneering studies in 1987 and 1989, Beck[36,37] carried out experiments on metal doped silicon clusters to understand the Shottkey barrier at the nanoscale and found high abundance of clusters with 15 and 16 Si atoms doped with one Cr, Mo, or W atom, while the abundance of other species in this mass range was very little. He hypothesized that the silicon atoms might have formed a cage around the metal atom. But this finding remained unnoticed for quite some time as the understanding of the atomic structures of even the elemental silicon clusters was still evolving.

Around this time, research on fullerenes was thriving and many aspects of carbon fullerenes were being explored. One such direction was the doping of some atoms and other species in the cavity of carbon fullerenes.[38] Doping of fullerenes with an atom or a group of atoms inside the cage was a new idea and such species were named "endohedral fullerenes". For instance, $La@C_{82}$ means that a La atom is encapsulated in a C_{82} fullerene cage. A rich family of such endohedral fullerenes has been produced experimentally and investigated theoretically.[39−44] In these doped fullerenes, the endohedral dopant generally interacts weakly with the wall of the fullerene cage and the cage structure remains almost intact except for the possibility that the cage may transform to another isomer with different symmetry due to possible charge transfer from the endohedral species.

In 1992, T. Guo *et al.*[45] reported C_{28} cation to be the smallest fullerene that was produced in substantial abundance. Furthermore, it was shown that a tetravalent atom such as Ti and U inside the fullerene cage stabilizes C_{28} leading to endohedral C_{28}, i.e., Ti@C_{28} and U@C_{28} fullerenes. Interestingly, the mass abundance spectrum shows all doped fullerenes. No significant abundance of any undoped fullerene signifies that metal doping should be energetically favorable. They even attempted bulk synthesis of U@C_{28} and found the presence of U@C_{28} in the sublimed film, which was stable upon exposure to air and water.

Later in the year 1996, Jackson and Nellermoe[46] reported from *ab initio* calculations a Si_{20} fullerene structure similar to the smallest fullerene of carbon, namely C_{20}, and this Si_{20} cage was endohedrally doped with one Zr atom, leading to Zr@Si_{20}. They showed a large gain in energy (about 11 eV) due to the doping of a Zr atom. Following this work, in 2001 Hiura *et al.*[47] reported experiments in which silane gas was reacted with different metal ions. They obtained several metal doped silicon clusters containing some hydrogen atoms; but strikingly $Si_{12}W$ was reported to occur without any H atom. *Ab initio* calculations on this cluster predicted a hexagonal prism structure of silicon with the W atom inside, namely, W@Si_{12}.

Soon after, Kumar and Kawazoe[48,49] performed a pioneering *ab initio* study on Zr@Si_{20} fullerene and showed that this structure was not stable upon optimization. Following Smalley's work on wrap-shrinking of carbon fullerenes by removing carbon dimers with laser heating,[50] they removed excess Si atoms that protruded outward due to the shrinking of the structure. Then, they found that 16 silicon atoms were required to form a cage with a Zr atom inside. The predicted cage structure of Zr@Si_{16} has the features of a carbon fullerene in that each silicon atom on the cage is 3-fold connected, but the silicon cage is stabilized by endohedral doping of a Zr atom. They called it *silicon fullerene*; but it indeed has 8 pentagons and 2 rhombi unlike hexagons and pentagons in carbon fullerenes. It is noteworthy that carbon favors graphite structure which is composed of hexagons only, but 12 pentagons are needed to form a cage structure. However, for silicon there is no graphite-like bulk phase and the bond angles in pentagons are closer to the ones in the diamond structure. This exciting result attracted much attention as the elemental silicon cluster with 16 atoms has no high symmetry structure,[51,52] but doping of a metal atom does wonders to make a novel, symmetric and highly stable cage structure as the doping of a Zr atom leads to about 10 eV gain in energy, in contrast to generally weak dopant−cage interaction in endohedral carbon fullerenes.

Following this discovery, similar studies were done on Zr doping in a Ge_{16} fullerene cage and it transformed into a Z16 FK polyhedron of Ge, which is stabilized by the endohedral Zr atom.[53] Further, doping of Ti in Si_{16} also led to Z16 FK structure to be favorable over the fullerene structure.[48,49] Thus, even though we have a tetravalent metal atom from the same column in the periodic table, the structure and properties of an endohedrally doped cluster are very different when the metal atom is changed. These results showed the importance of the size of the metal dopant as it interacts with the cage very strongly so that a small change in its size alters the structure. Specifically, for a smaller Ti atom, a compact FK structure of Si_{16} is more favorable, while a slightly bigger Zr atom favors a more open fullerene cage of Si_{16}. Conversely, for a slightly bigger host cage made up of Ge atoms (about 4% bigger than Si atoms), a compact Z16-FK structure becomes favorable even for Zr dopant atom. Accordingly, a variety of endohedrally doped clusters with a suitable combination of the cage atoms and the metal atom have been studied. The results point to size selectivity of the cage depending upon the metal atom. These developments stimulated many theoretical and experimental works and led to the experimental realization of the Zr@Si_{16} fullerene, Ti@Si_{16} and Zr@Ge_{16} in FK structure as predicted and many other such species by doping of different atoms.[54−57]

During the past 15 years or so, besides C, Si, and Ge, endohedrally doped clusters of a wide variety of elements such as Sn, Pb, Au, Ag, Cu, and more recently B have been explored from both experimental and theoretical aspects. Many very stable clusters in neutral and charged states, such as Pt@Pb_{10},[58] $[AlPb_{12}]^+$,[59] Mo@B_{24},[60] W@Au_{12},[61,62] and $[Cu_{16}Sc]^+$,[63] have been found. Note that small clusters of Au and B are planar[64−66], but doping of metal atoms leads to the formation of endohedral cage structures. These developments have demonstrated that the concept of endohedral doping has wide applicability and that the atomic structure of the doped cluster is generally very different from that of the elemental cluster with high probability of enhanced stability and high abundance, leading to new opportunities in their practical use. As the atomic structure determines the properties, there is much hope that new functional materials with novel properties could be made.

In another interesting development, *magnetic superatoms* such as Mn@Sn_{12} have been theoretically predicted[67] and experimentally characterized[68,69]. We refer to a cluster as a magnetic superatom if it has partially occupied superatomic orbitals that are occupied following the Hund's rule of maximum spin. In clusters generally the magnetic moments are reduced by Jahn−Teller distortions but in some cases of (often) high symmetry clusters, Hund's rule wins due to favorable exchange splitting of up-spin and down-spin superatomic orbitals. Endohedral clusters are interesting because by having a transition metal or rare earth atom at the center, there is a possibility to increase the magnetic moments as well as exchange splitting that can help to stabilize magnetic superatoms and possibly lead to their high abundance in experiments and interesting magnetic cluster assembled materials.

Besides the high symmetry icosahedral magnetic superatom Mn@Sn_{12}, Khanna and co-workers have designed magnetic superatoms by placing a central transition metal atom with unpaired *d* electrons into an outer cage of alkali metal or alkaline-earth metal atoms. The *d* orbitals of the transition metal interact with the delocalized superatomic orbitals and stabilize the entire cluster. A fraction of the *d* electrons that interact with the cage remain unpaired and give rise to magnetic moments. Endohedral cage clusters with large magnetic moments of 4 or 5 μ_B as well as moderate HOMO−LUMO gaps of ca. 0.2−0.8 eV were predicted, such as for V@Li_8,[70] V@Na_8,[71] V@Cs_8,[71] Fe@Mg_8,[72] Tc@Mg_8,[73] and Fe@Ca_8[74] with transition metal-centered square antiprism configuration, Mn@Ca_9[75] and Mn@Sr_9[76] with Mn-centered capped square antiprism, and Sc@K_{12}, Sc@Cs_{12},[77] Y@K_{12}, Y@Rb_{12}, and Y@Cs_{12}[78] with transition metal centered icosahedron. Further, using anionic photoelectron spectroscopic experiments, X. Zhang *et al.*[79] showed evidences for the existence of magnetic superatoms in $[V@Na_n]^-$ (n = 7, 8, 9) clusters. More details about such magnetic superatoms and other related magnetic clusters can be found in an earlier review.[8]

Recently, using a dry-chemistry method, it has become possible to produce Ta@Si_{16} fullerenes and Ti@Si_{16} FK structures in large quantity (about 100 mg).[80] This very exciting development has opened up long awaited possibilities of assembling clusters of different materials and making use of their specific properties. There is hope that mass production of such clusters would be further increased in the near future. Also, there have been exciting developments in ligated clusters of Au and Ag, as well as other systems for which single crystal bulk structures have also been synthesized using wet-chemistry methods. Endohedral doping of these nanoclusters with other metal atoms has been possible.

Apart from the gas-phase clusters, research interest in endohedral cage clusters also comes from solid state chemistry. Many cage forms of homo-polyatomic and hetero-polyatomic clusters of group 13, 14, and 15 elements exist as soluble quasi-discrete units in salt-like intermetallic compounds, namely, the Zintl phases,[81−87] which can be isolated on preparative scale (10−1000 mg). Some salts of the polyhedral anions are also soluble in solvents. These clusters, usually having cage configurations and formally carrying certain number of negative charges according to the Zintl−Klemm concept,[88] are known as "*Zintl anions*" or "*Zintl clusters*", which are intriguing for not only the beauty of their polyhedral structures including icosahedron, but also the great synthetic potential as precursors for some novel materials. For example, $[Ge_9]^{4-}$ Zintl clusters have been used as soluble building blocks for a bottom-up fabrication of guest-free germanium clathrate[89] and germanium nanomorphologies with tunable composition.[90] Furthermore, the empty cage of the Zintl anion can be filled with one or even more guest atoms, forming the endohedral Zintl anion, also known as "intermetalloid cluster".[85] The 9-vertex cages are the smallest polyhedral skeleton to incorporate a transition metal atom, such as $[Ni@Ge_9]^{3-}$,[91] $[Co@Sn_9]^{5-}$,[92,93] $[Cu@Sn_9]^{3-}$, and $[Cu@Pb_9]^{3-}$,[94] while typical endohedral Zintl anions are based on 10-vertex and 12-vertex cages. Encapsulation of dual transition metal atoms leads to Zintl anions of prolate shape, such as $[Co_2@Ge_{16}]^{4-}$[95,96] and $[Pd_2@Sn_{18}]^{4-}$[97,98]. The pursuit of bigger Zintl anions has led to the discovery of an onion-like $[As@Ni_{12}@As_{20}]^{3-}$ Matryoshka cluster, which has an outer shell of As_{20} fullerene structure very similar to C_{20}, and an icosahedral $As@Ni_{12}$ core endohedrally doped inside the As_{20} cage.[99] The same idea has also been extended to some other Matryoshka clusters, such as $[Sn@Cu_{12}@Sn_{20}]^{12-}$[100] and $[Sb@Pd_{12}@Sb_{20}]^{3-}$[101,102].

In this review, we present not only an up-to-date account of these developments and concepts but also we have redone many calculations using state-of-the-art methods that may facilitate better comparison with experiments and propel further research. We hope that this would be a very helpful review for new entrants in this field and a valuable source for researchers in the broad area of nanoscience and novel materials. For some related topics that are not fully covered in this review, we recommend review articles on endohedral carbon fullerenes[8,39−44] and Zintl clusters.[81−87] It is also noteworthy to mention that there are much fewer experimental studies on endohedrally doped clusters than the theoretical ones. Accordingly, it is natural that many of the theoretical results have not been experimentally confirmed yet. In this review article, we aim to cover both classes of the works and present the current state of knowledge in this field.

The review is organized as follows. In Section 2, we start from a brief description of the methods used to calculate the structure and properties of clusters and an overview of different electron counting rules often used to understand the high stability of certain clusters. The early developments about electronic shell closing and the doped aluminum clusters as well as the underlying principles that are helpful to develop endohedral clusters and superatoms, are discussed in Section 3, along with studies on endohedrally doped clusters of Ga and In. Then, we discuss endohedrally doped cage clusters of carbon and boron (Section 4), silicon (Section 5), germanium, tin, and lead (Section 6), and gold, silver, and copper (Section 7). Endohedrally doped compound cages such as III−V BN, II−VI ZnS, and ZnO are discussed in Section 8. Section 9 describes unique species of multilayer core−shell (Matryoshka) clusters. To promote the materials applications of doped cage clusters, we present current progress on assemblies of these clusters from dimer to 1D, 2D, and 3D aggregates in Section 10. Finally, we end this review by giving a perspective about the current challenges and future directions of the endohedrally doped cage clusters in Section 11.

2. THEORETICAL METHODS AND MODELS

2.1. Methods of *ab Initio* Calculations on Clusters

In cluster science, state-of-the-art *ab initio* methods based on DFT and HF theory are essential tools to determine the equilibrium atomic structures and describe the electronic and other physical and chemical properties of atomic clusters. Particularly, a challenging and fundamental problem in the theoretical study of clusters is to determine their lowest-energy structures. In this regard, there are two critical considerations: (1) accurate description of the interatomic bonding and (2) global exploration of the potential energy surface to find the ground-state configuration.

Within the framework of DFT, the first issue relies on a proper choice of the exchange-correlation functional (assuming a sufficiently large basis set is used). As we will show later (e.g., see Tables 7 and 10), many earlier DFT calculations on the doped cage clusters were carried out with different functionals (e.g., LDA, PW91, B3LYP) and sometimes using relatively small basis sets. Thus, the results might vary with the computational scheme and could be even controversial to some extent. As shown in Table 1 and Tables S1 and S2 of the Supporting Information, the currently well accepted PBE0 hybrid functional[103] shows satisfactory performance for describing the bond lengths and vibrational frequencies of various dimers[104−111] and C_{60}[112,113], as well as lattice constants, cohesive energies, and bulk moduli of various elemental solids.

Table 1. Theoretical and Experimental (in Parentheses) Data for B, C, Al, Si, Ge, Au, Ag, and Cu Dimers: Equilibrium Bond Lengths l_0, Vibrational Frequencies ω_e, and Total Magnetic Moments M_t[a]

	l_0 (Å)	ω_e (cm^{-1})	M_t (μ_B)
B_2	1.62 (1.59)	1018.7 (1058)	2 (2)
C_2	1.31 (1.31)	1709.6 (1641.4)	2 (2)
Al_2	2.48 (2.49)	349.9 (345)	2 (2)
Si_2	2.15 (2.25)	562.4 (511)	2 (2)
Ge_2	2.38 (2.34)	293.5 (286)	2 (2)
Cu_2	2.24 (2.22)	261.5 (266.5)	0 (0)
Ag_2	2.58 (2.53)	185.7 (192)	0 (0)
Au_2	2.55 (2.47)	171.1 (190.9)	0 (0)

[a] The calculated values are based on the PBE0 functional accompanied with 6-311+G(d) basis sets for B, C, Al, Si, and Ge atoms and SDD basis sets for Au, Ag, and Cu atoms using the Gaussian09 package.

Previous benchmark studies have also demonstrated that the PBE0 functional is suitable for describing silicon clusters,[114] boron clusters[115,116], metal-organic I−III−VI semiconductor clusters,[117] and metal oxide clusters (ZrO_2, TiO_2, and Y_2O_3) interacting with H_2O_2, H_2O, and HO radicals.[118] Therefore, to present a unified yet accurate theoretical description of the endohedrally doped cage clusters, in this review we performed systematic *ab initio* calculations using the PBE0 functional combined with 6-311+G(d) basis sets (for light elements up to Kr) and SDD basis sets (for 3d transition metals and heavy elements beyond Kr) [abbreviated as PBE0/6-311+G(d), SDD thereafter] on endohedrally doped carbon, boron, silicon, germanium, gold, silver, and copper cages of different sizes, and the results are given in Tables S3−S22 of the Supporting Information. These results generally agree with experimental data where available, but it should be kept in mind that a different level of theory can lead to a different result such as ordering of isomers, vibrational frequencies, magnetic and optical properties, etc. and there could be temperature effects in experiments which are often not included in calculations.

It is further worth mentioning that the computed magnetic moments reported in Table 1 (and in most of the following contents) only involve the contribution from spin multiplicity of the clusters, namely, magnetic spin moments, while the contribution from orbital magnetism requiring consideration of the SOC effect has not been included. Sometimes orbital magnetic moment may have substantial impact on the total magnetic moment of a cluster containing heavy elements, and we will discuss a few such cases later.[119−121]

It is also worth pointing out that, in many of the early theoretical studies, cluster structures were determined by comparing the energies obtained by relaxing a few often presumed high-symmetry structures. This leaves the question open whether the lowest-energy structure determined this way is the true global minimum. In the past two decades or so, several global optimization algorithms, such as basin hopping,[122] minimum hopping,[123] genetic algorithm,[124−126] stochastic surface walking method,[127] and particle swarm optimization,[128] have been incorporated with *ab initio* calculations to determine the lowest-energy structures of a large variety of atomic and molecular clusters. Benefitting from the increasing computing power, these cutting-edge global search techniques have led to discovery of many novel endohedral cage clusters, as will be discussed in the following content.

Starting from the ground state structures of the neutral, cationic, and anionic clusters, we can define a series of key electronic properties as follows. AIP is the energy needed for the removal of an electron from a neutral cluster with the ground state configuration, while the resulting cationic cluster is allowed to relax. VIP is the energy needed for the removal of an electron from a neutral cluster with the ground state configuration, while the resulting cationic cluster still retains the geometry of the neutral state. AEA is the energy released by adding an electron to a neutral cluster with the ground state configuration, while the resulting anionic cluster is allowed to relax. VEA is the energy released by adding an electron to a neutral cluster with the ground state configuration, while the resulting anionic cluster still retains the geometry of the neutral state. These quantities can be computed from the differences of the total energies by *ab initio* calculations:

$$AIP = E^{+}(opt) - E^{0}(opt) \tag{1}$$

$$VIP = E^{+}(neu) - E^{0}(opt) \tag{2}$$

$$AEA = E^{0}(opt) - E^{-}(opt) \tag{3}$$

$$VEA = E^{0}(opt) - E^{-}(neu) \tag{4}$$

where $E^{+,0,-}(opt)$ are the energies of cation, neutral, and anion clusters with optimized geometry and $E^{+,-}(neu)$ are the energies of cationic and anionic clusters in the geometry of the corresponding neutral state, respectively.

Lastly, the interaction strength between the host cage X_n and the guest atom M in an endohedrally doped cage cluster M@X_n can be characterized by the embedding energy (E_{em}), which is defined as the energy gained by encapsulating the M atom to the pure cage X_n with the same structure as in the doped case:

$$E_{em} = E(X_n) + E(M) - E(M@X_n) \tag{5}$$

where $E(M@X_n)$ and $E(X_n)$ are the energies of the M-doped and empty X_n cage, respectively, both having the same structure as in the doped case; $E(M)$ is the energy of an individual M atom. By definition, a positive (negative) E_{em} value means that encapsulation of the guest atom is an exothermic (endothermic) process. Another important quantity to characterize the thermodynamic stability of a doped cage cluster M@X_n is the binding energy (E_b) defined as

$$E_b = n \times E(X) + E(M) - E(M@X_n) \tag{6}$$

where $E(X)$ is the energy of an individual X atom and n is the number of X atoms.

2.2. Electron Counting Rules for Endohedral Clusters

In a doped cluster, the dopant atom may have significant impact on the cluster geometry (e.g., formation of endohedral cage) by changing the total number of electrons and modulating the dopant−host interaction. For instance, small elemental clusters of B and Au are planar, while the most preferred cluster geometries become nearly spherical cage-like with the addition of an endohedral atom, as we will demonstrate in Sections 4.2 and 7.1, respectively. Generally speaking, the thermodynamic stability of a dopant atom in a host cage depends on not only the cavity space but also the type of dopant element (i.e., atomic radius of the dopant as well as the bonding character between the dopant atom and the host cage).

To account for the relative stability of atomic clusters in terms of electronic structure and to establish the correlation between geometric and electronic factors, various electron counting models have been introduced by chemists and physicists. Historically, these electron counting rules have played an important role in the advance of cluster science. While there are some conceptual overlaps in these rules, there have also been some controversies when the rules are applied to some systems, as they were developed from different disciplines based on different theoretical pictures or approximations.

To help our readers correlate the stability and electronic properties of an endohedral cluster with its atomic structure and total number of electrons (determined by the cluster size), here we give a brief overview of four commonly used electron counting rules: (1) 18-electron and 32-electron rules as extensions of the octet rule, (2) spherical aromaticity rule, (3) shell model within a spherical potential or jellium model, and (4) Wade−Mingos rules.

2.2.1. 18-Electron and 32-Electron Rules.

In his 1916 paper titled “The Atom and the Molecule”, Lewis[129] proposed the idea of the octet rule, which has become “a chemical rule of thumb". Without considering *d* or *f* electrons, the octet rule refers to the tendency of atoms to attain a fully filled valence shell s^2p^6 configuration as that of noble gases. Five years later, Langmuir[130] extended the octet rule to general cases and speculated that "The electrons in atoms tend to surround the nucleus in successive layers containing 2, 8, 8, 18, 18, and 32 electrons, respectively." This leads to the famous "18 electron principle" for metal complexes such as organometallic compounds with a transition metal atom having 9 orbitals (five *d*, one *s*, and three *p*), which can accommodate 18 electrons corresponding to a closed valence shell $d^{10}s^2p^6$. However, it should be noted that these 9 orbitals hybridize with the orbitals of the ligands forming bonding, anti-bonding, or nonbonding molecular orbitals. When 18 electrons occupy these orbitals, it is said to have achieved a closed electronic shell configuration as a noble gas atom. Typical examples are $Mo(CO)_6$, $Ni(CO)_4$, and $Fe(C_5H_5)_2$ compound molecules. In 2006, Pyykkö[131] rationalized the 18-electron principle by considering both the bonding contributions to the central metal atom as well as the successive occupations of ligand orbitals with increasing kinetic energy related to their nodal structures. An excellent example of an 18-electron endohedral cluster is icosahedral $W@Au_{12}$, as will be discussed in Section 7.1.1. In this case, 12 valence electrons (without counting the 5*d* electrons on Au atoms) on the Au_{12} icosahedral cage and 6 valence electrons on the W atom at the center constitute 18 electrons for electronic shell closing. This rule has been very effective in discovering many endohedral clusters. Beyond that, Dognon *et al.*[132] extended the octet and 18-electron rules to the "32-electron rule" by adding an *f*-like shell with 14 additional electrons. With this, an icosahedral caged cluster $Pu@Pb_{12}$ obeying the 32-electron rule was proposed, and it will be discussed in Section 6.3.2. In this case, 24 valence electrons from the Pb_{12} cage and 8 valence electrons from the Pu atom constitute 32 electrons corresponding to shell closing.

2.2.2. Spherical Aromaticity Rule.

Considering that the carbon fullerenes form a unique family of nearly spherical π-conjugated molecules, Hirsch and co-workers[133,134] put forward the $2(N + 1)^2$ rule for icosahedral fullerenes (such as C_{20}, C_{60}, and C_{80}), which is a spherical analogy to the famous Hückel rule[135] for the aromaticity of cyclic π-conjugated molecules, according to which annulenes with $4N + 2$ π electrons are aromatic. Within the picture of spherical aromaticity, the π-electron system of an icosahedral fullerene is approximated as a spherical electron gas surrounding the cage surface. The wave functions of such spherical electron gas can be characterized by the angular momentum quantum number ($l = 0, 1, 2, 3, \ldots$), analogous to the atomic *s*, *p*, *d*, *f*, ... orbitals, respectively. According to the Pauli principle, the maximum number of electrons to occupy an orbital with angular momentum quantum number l is $2(2l + 1)$, thereby giving rise to a series of magic number N_{el} for the total number of electrons to fully fill the π bonded shells:

$$N_{el} = \sum_{l=0}^{N} 2(2l + 1) = 2(N + 1)^2 \tag{7}$$

where N is indeed the angular momentum quantum number of the highest occupied molecular orbital. As a result, the spherical fullerenes with 18 ($N = 2$), 32 ($N = 3$), 50 ($N = 4$), and 72 ($N = 5$) π electrons are closed-shell systems. From DFT calculations at the GIAO-SCF/6-31G(d) level, a series of charged fullerenes with I_h symmetry possess large negative NICS values[136] at the cage center, i.e., −73.1 ppm for $[C_{20}]^{2+}$ ($N = 2$), −81.4 ppm for $[C_{60}]^{10+}$ ($N = 4$), and −82.9 ppm for $[C_{80}]^{8+}$ ($N = 5$), signifying strong aromaticity and also validating the $2(N + 1)^2$ rule.

Later, Hirsch *et al.* have extended the $2(N + 1)^2$ rule to inorganic caged clusters by considering double spherical aromaticity of both σ and π electrons.[137] For instance, the stability of Zintl anion $[E_9]^{4-}$ clusters (E = Si, Ge, Sn, Pb) with D_{3h} cage configuration and a total of 40 valence electrons was ascribed to their double spherically $2(N + 1)^2$ aromatic configuration with 32 σ electrons ($N_\sigma = 3$) and 8 π electrons ($N_\pi = 1$), whereas large negative NICS values (between −68.9 ppm and −87.7 ppm) at the cage centers were obtained.

2.2.3. Electronic Shell Model within a Spherical Potential or Jellium Model.

The pioneering work of Knight *et al.*[16] in 1984 on strong abundances of Na_n clusters with $n = 8$, 20, 40, 58, ... atoms and much weaker abundances of clusters with $n + 1$ atoms led to the concept of "magic number" in metal clusters. The stability of these clusters was interpreted with the filling of electronic shells within a spherical potential model following the nuclear shell model[17] and subsequently by using *ab initio* calculations within a spherical jellium model.[18] The essential idea of the electronic shell model is that electrons in metal clusters move in a spherically symmetric potential contributed by the metal ions (usually the background of positive ions is approximated by a jellium model) and the other electrons. Under spherical symmetry, solving the single-electron Schrödinger equation within an effective potential leads to the shell structure comprising a series of degenerate energy levels for the valence electrons.

As displayed in Figure 1, each electronic shell is characterized by the principal (radial) quantum number n_r and the

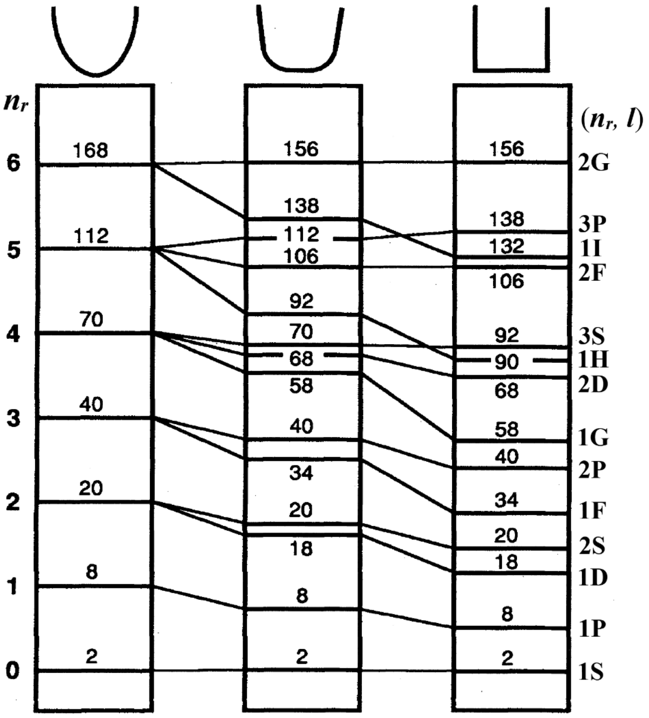

Figure 1. Energy-level occupations for 3D spherical harmonic (left), intermediate (middle), and square-well (right) potentials. The angular momentum l is denoted by capitals S, P, D, F, G, H, and I in order to differentiate from the atomic orbitals. The number near the electronic level indicates the total number of valence electrons. Adapted with permission from ref 1. Copyright 1993 The American Physical Society.

angular momentum quantum number *l*, where the quantum numbers follow the nuclear convention instead of the atomic one. It is noteworthy that changing the shape of the spherically symmetric potential well would affect both the spacing and ordering of these degenerate levels. Under the Woods−Saxon potential, which is an intermediate between harmonic and square-well potentials, there are electronic shells 1S, 1P, 1D, 2S, 1F, 2P, 1G, 2D, 3S, ... which are completely occupied with 2, 8, 18, 20, 34, 40, 58, 68, 70, ... electrons, respectively, giving rise to the magic numbers observed in experimental mass spectra. With the concept of superatom,[12,26−29] these electronic shells correspond to "superatomic orbitals". Furthermore, the open-shell clusters deformed from spherical shape can still be described by the ellipsoidal Clemenger−Nilsson shell model,[138] which yields a series of additional magic numbers due to the filling of electronic subshells. Although the shell model was originally developed for simple metal clusters with *s* and *p* valence electrons, it has been successfully extended to many other types of clusters and serves as an excellent guiding principle even today, as we will show in this review.

No doubt, there are certain similarities between the three kinds of electron counting rules discussed above, as they presume the same spherical symmetry and predict some common magic numbers such as 8 and 18. However, the fundamental physics behind them is distinctly different. The 18- and 32-electron rules count the total number of bonding electrons involved with the central metal atom, and the contributions from the ligand orbitals should be properly taken into account. The $2(N + 1)^2$ rule of spherical aromaticity mainly deals with spherical π-conjugated systems and has been extended to include the σ electrons. The shell model is a mean-field description for the delocalized valence electrons within a spherical potential of the entire metal cluster. All the above theoretical models ignore the detailed atomic structure of a cluster and are only able to derive the electronic shell structure under a symmetric effective potential. In order to correlate the polyhedral structure of a cage cluster with its number of valence electrons, one has to resort to the Wade−Mingos rules, also known as polyhedral skeletal electron pair theory.[139,140]

2.2.4. Wade−Mingos Rules. The Wade−Mingos rules were originally developed for rationalizing the structures of ligated clusters such as boranes, carboranes, and transition-metal carbonyl compounds and then extended to interpret the shape and stability of other clusters that are isoelectronic and isolobal with boranes.[141] According to Wade−Mingos rules, a complete polyhedron with all triangular faces (*closo*-deltahedron) with n_v vertices requires a total of $4n_v + 2$ valence electrons; among them, $2n_v + 2$ electrons are needed for the skeletal bonding molecular orbitals, and the rest $2n_v$ electrons either form radial covalent bonds with ligands (e.g., B−H bonds in boranes) or behave as lone-pair electrons (in the case of naked clusters). For those incomplete deltahedra with one (*nido*) and two (*arachno*) vertices missing, $4n_v + 4$ and $4n_v + 6$ valence electrons are required, respectively. Meanwhile, a total of $5n_v$ electrons are needed for a three-connected polyhedron. As a matter of fact, Wade−Mingos rules help understand the structures and stability of many Zintl anion clusters.[81,84−87,141] Some typical endohedral Zintl clusters will be discussed in Sections 3.2, 6.4, and 8.5.

It should be pointed out that, for a given cluster, more than one electron counting rule from different perspectives might all be applicable. Sometimes, the choice of the electron counting rule and the language of such theoretical analysis even depend on the background of the researcher. When applying these electron counting rules, how to define the number of "effective" valence electrons for a given metal element is also a delicate issue and relies on the specific situation. For example, only one *s* valence electron is usually counted for coinage metals (Cu, Ag, Au), leaving the filled d^{10} shell unaccounted, while for early transition metals such as Sc and Ti, all outer *s* and *d* electrons should be considered as valence electrons. In the following contents, we will adopt all these electron counting rules mainly following the original discussions in the literature, and will also add our own comments and understanding to give a more unified view.

3. ENDOHEDRAL CLUSTERS OF Al, Ga, AND In

3.1. Endohedral Clusters of Al—Development of Metal Clusters as Superatoms

Pure and doped Al clusters have been very extensively studied both experimentally and theoretically. In this direction, the development of a laser vaporization method[142] has been an important landmark in cluster science and it made the study of a variety of clusters possible. As early as 1986, Cox *et al.*[143] studied for the first time magnetic behavior of small aluminum clusters produced by a laser vaporization and condensation method. The mass spectrum showed the highest abundance of Al_{14} and almost no depletion in a magnetic field, suggesting zero magnetic moment on this cluster. Al_{14} has 42 valence electrons, which is 2 electrons more than the electronic shell closing at 40 electrons. In a capped icosahedron Al&Al_{13} structure of this cluster, the 3*s* valence electrons of the capping Al atom are localized and effectively it becomes a 40 valence electron cluster[144] similar to Na&Al_{13}. Accordingly, both Na&Al_{13} and Al&Al_{13} were shown to be magic. Leuchtner *et al.*[22,23] produced cation ($[Al_n]^+$, n = 1−33) and anion ($[Al_n]^-$, n = 5−37) clusters by laser vaporization and reacted them with oxygen. Strikingly, they found no reactivity for $[Al_7]^+$, $[Al_{13}]^-$, and $[Al_{23}]^-$. These clusters have 20, 40, and 70 valence electrons, respectively, which correspond to electronic shell closing in a spherical jellium model discussed in Section 2.2. Jarrold and Bower[145] also reported strong abundances of $[Al_7]^+$ and $[Al_{14}]^+$ in the mass spectrum of cation clusters, while Thomas *et al.*[146] reported high abundances of $[Al_{13}]^-$ and $[Al_{23}]^-$ as well as $[Al_{13}Cu]^-$. Clearly, the charge state of the cluster affects the abundances.

In general, the abundances of clusters in a mass spectrum depend on the nucleation conditions including temperature, kinetics, fragmentation of clusters, etc. In some cases, clusters with high ionization potential may not get ionized by the energy of the incident photon to create cationic clusters for detection while the mass range of the spectrometer may limit the detection of some clusters. In some experiments, exposure to reactant gases has been used to study the magic clusters. It has been generally observed that clusters with closed electronic shells and large HOMO−LUMO gaps survive under such exposure, such as $[Al_{13}]^-$ and $[Al_{23}]^-$ under exposure of oxygen. Strongly magic clusters have been reproduced in different laboratories, and also there has been support from theory as well as photoemission experiments in terms of large HOMO−LUMO gap, high AIP, and low AEA. In this review, we have referred to such magic clusters as stable or very stable clusters or superatoms.

The electronic spectra of anion aluminum clusters have been studied.[147,148] Taylor *et al.*[147] reported large electron affinities for Al_{13}, Al_{19}, and Al_{23}, all of which have one electron less for shell closing at 40, 58, and 70 electrons, respectively. Ma *et al.*[148] studied the atomic structures of Al clusters over a wide size range (13−75 atoms) by comparing the photoelectron spectra of anion clusters. Among these Al clusters, $[Al_{13}]^-$ has an icosahedral $Al@Al_{12}$ structure with the highest symmetry (I_h). There are 12 atoms on the surface, all forming a shell with triangular faces, and an atom at the center. It is one of the well-known platonic solids and referred to as a typical superatom, which has both the electronic and atomic shells completely closed. Electronic structure calculations on $[Al@Al_{12}]^-$ have shown a large HOMO−LUMO gap making it behave like an inert gas atom. On the other hand, neutral $Al@Al_{12}$ cluster has a slightly distorted icosahedral structure as obtained from *ab initio* calculations[144] because it is one electron short of the electronic shell closing at 40 electrons. Most strikingly, it has a high AEA of about 3.6 eV that is comparable to that of Cl, the highest for any element in the periodic table. Accordingly, a cluster of 13 Al atoms behaves like a Cl atom and $Na\&Al_{13}$ like a NaCl molecule. Bergeron *et al.*[149] also reported the formation of $[Al@Al_{12}I]^-$ as evidence for the superhalogen behavior of $Al@Al_{12}$. Recently, $[Al_{13}]^-$ superatom has been produced by a solution route using a dendrimer template.[150] This very interesting advance could facilitate assembly of such clusters to form novel materials.

Doping of aluminum clusters has been widely explored, and it offers the possibility of tailoring the properties of clusters and making new superatoms with atom-like properties. Doping with an alkali atom or a coinage metal atom has been studied from the point of view of having a closed electronic shell in order to form $Al_{13}X$ clusters with X, the dopant atom.[151] Also, Khanna and Jena[152] studied the $Si@Al_{12}$ cluster with the Si atom at the center of Al_{12} icosahedron using *ab initio* calculations. As Si has four valence electrons, $Si@Al_{12}$ has a closed electronic shell configuration with 40 electrons similar to $[Al@Al_{12}]^-$. Gong and Kumar[24] further studied $Si@Al_{12}$ and other icosahedral clusters with 40 valence electrons, such as $[B@Al_{12}]^-$, $Ge@Al_{12}$, $C@Al_{12}$, $[Ga@Al_{12}]^-$, $Ti@Al_{12}$, and $[As@Al_{12}]^+$ along with $[Al@Al_{12}]^-$, considering the dopant atom at the center of Al_{12} icosahedron using LDA calculation with symmetrized basis functions. Among these clusters, $[B@Al_{12}]^-$ was shown to be the most strongly bonded. This result is in agreement with the experimental observation[153] of strong abundance of $[Al_{12}B]^-$ among boron doped clusters as shown in Figure 2. The mass abundance spectra of $[Al_n]^-$ and $[Al_nB]^-$ clusters show the strongest peaks for $[Al_{13}]^-$ and $[Al_{12}B]^-$, respectively. The other prominent peak after which the intensity drops significantly is for $[Al_{23}]^-$ and $[Al_{22}B]^-$ clusters, respectively, both of which correspond to electronic shell closing at 70 electrons. Similar strong abundances have been obtained by Smith *et al.*[154] when $[Al_n]^-$ and $[Al_nB]^-$ clusters were exposed to oxygen. It is to be noted that in an icosahedron, the center to vertex distance is about 5% shorter than the nearest neighbor vertex to vertex distance. Accordingly, a smaller atom such as Si or B at the center of an Al_{12} icosahedral cage can provide better arrangement of atoms.

Generally speaking, for a doped $Al_{12}X$ cluster, the dopant atom X can sit at the center or replace one Al atom in the Al_{12} shell. To date, there have been numerous experimental and theoretical studies[24,144,146,150−194] on many dopants in aluminum clusters, in particular for $Al_{12}X$. In general, it has been found that an alkali atom caps[144,155,167−169,172,174] the Al_{13} icosahedron[144,151,167] or decahedron,[168] while a Cu atom occupies the center of Al_{12} and Al_{13} clusters.[146,155,165,170,171] This is striking as small clusters of sodium and copper have similar structures,[19] but Cu is a smaller atom and less electropositive compared with a sodium atom and has higher ionization potential (7.726 eV vs 5.139 eV). We have performed *ab initio* calculations on many clusters with 40 valence electrons such as $[Al_{13}]^-$, $Al_{12}Si$, $Al_{12}Ge$, $Al_{12}C$, $[Al_{12}B]^-$, $[Al_{12}N]^+$, $[Al_{12}P]^+$, $[Al_{12}As]^+$, and $[Al_{12}Ga]^-$, as well as $Al_{13}X$ with X = Cu, Li, Na, and K using PBE0/6-311+G(d) and the SDD method, as implemented in the Gaussian09 program.[195] These results are given in Table 2 and compared with available experimental data.[159,160,196,197] The atomic structures of some of the magic clusters and a few other cases are shown in Figure 3.

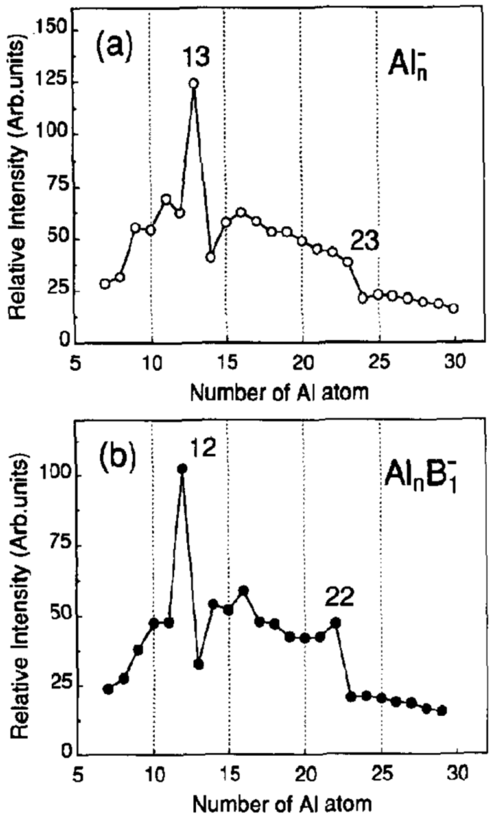

Figure 2. Relative abundances of (a) $[Al_n]^-$ and (b) $[Al_nB]^-$ clusters. In each case two magic numbers at (a) $n = 13$ and 23 and (b) $n = 12$ and 22 can be seen corresponding to electronic shell closing at 40 electrons and 70 electrons, respectively. Reproduced with permission from ref 153. Copyright 1991 Elsevier B.V.

First of all, the calculated AEA of $Al@Al_{12}$ is 3.425 eV, in good agreement with the experimental values of 3.62 eV,[196] 3.57 ± 0.05 eV in ref 160, and 3.40 eV in ref 197. The AEA of $B@Al_{12}$ is similarly large (3.218 eV), while for the closed electronic shell systems such as $C@Al_{12}$, $Si@Al_{12}$, and $Ge@Al_{12}$, with C, Si, and Ge occupying the center of the icosahedron, the AEA is 1.461, 1.873, and 1.869 eV, respectively. Our theoretical value for $Si@Al_{12}$ agrees well with the experimental result of 1.69 ± 0.07 eV.[159] These AEA values are quite small, while the AIP of $C@Al_{12}$, $Si@Al_{12}$, and $Ge@Al_{12}$ is as large as 6.491, 6.885, and 6.772 eV, respectively. The ionization potential of $Al_{12}Si$ was reported to be in the range of 6.42 and 7.90 eV from experiments,[159] and the calculated value lies in this range. Low AEA and high AIP are characteristics of magic clusters with closed electronic shell. Accordingly, these clusters are interesting superatoms.

Table 2. AIP, AEA, HOMO−LUMO Gap (E_{HL}), Position of X Atom (C for Center and V for Vertex in an Icosahedron), and the Binding Energy (E_b) of $Al_{12}X$ and $Al_{13}X$ Clusters[a]

Cluster, N_e	Position of dopant	E_b (eV/atom)	AIP (eV)	AEA (eV)	E_{HL} (eV)
$[Al@Al_{12}]^-$, 40		2.495*		3.425* (3.62* Expt. [196]), (3.57* ± 0.05 Expt. [160])	2.972
$[B@Al_{12}]^-$, 40	C	2.733*		3.218*	3.148
$[Ga@Al_{12}]^-$, 40	C	2.471*		3.438*	3.088
$C@Al_{12}$, 40	C	2.930	6.491	1.461	3.076
$Si@Al_{12}$, 40	C	2.796	6.885 (>6.42<7.90 Expt. [20])	1.873 (1.69 ± 0.07 Expt. [159])	3.170
$Ge@Al_{12}$, 40	C	2.720	6.772	1.869 (2.386 ± 0.008 Expt. [160])	3.167
$Al_{12}In$, 39	V	2.450	6.321	3.356	1.521
$Al_{12}Sn$, 40	V	2.661	6.743	2.387	2.704
$Al_{12}Sb$, 41	V	2.525	5.804	2.117	1.982
$Al_{12}Tl$, 39	V	2.415	6.209	3.232	1.484
$Al_{12}Pb$, 40	V	2.639	6.671	2.404	2.659
$Al_{12}Bi$, 41	V	2.514	5.789	2.070	2.014
$[N@Al_{12}]^+$, 40	C, V nearly degenerate	2.887*	6.355*		1.608
$[P@Al_{12}]^+$, 40	C	2.736*	5.118* (5.37* ± 0.04 Expt. [159])		3.306
$[Al_{12}As]^+$, 40	V, C nearly degenerate	2.695*	5.674*		3.214
$Cu@Al_{12}$, 37	C	2.436	6.551	2.984	1.684
$Al_{12}Ag$, 37	layer	2.392	6.312	2.867	1.443
$Al_{12}Au$, 37	C	2.455	6.253	2.933	1.389
$Cu@Al_{13}$, 40	C	2.571	6.594	2.137	2.817
$Al_{12}Sc$, 39	V	2.543	5.964	2.543 (2.53 Expt. [197])	1.550
$Al_{12}Ti$, 40	V	2.494	6.200	2.729	1.677
$Ag\&Al_{13}$, 40	Cap	2.528	7.168	2.028	2.893
$Au\&Al_{13}$, 40	Cap	2.585	6.601	2.059	2.822
$Li\&Al_{13}$, 40	Cap	2.519	6.719	1.940	2.895
$Na\&Al_{13}$, 40	Cap	2.491	6.351	1.794	2.931
$K\&Al_{13}$, 40	Cap	2.503	6.253	1.620	2.916
$Rb\&Al_{13}$, 40	Cap	2.493	6.110	1.515	2.936
$Cs\&Al_{13}$, 40	Cap	2.499	5.989	1.436	2.921
$Al@Al_{22}$, 69	C	2.667	5.988	3.168	1.229
$Si@Al_{22}$, 70	C	2.792	5.889	2.765	1.726
$[B@Al_{22}]^-$, 70	C	2.747*	5.884*	3.065*	1.888

[a] "Cap" denotes that the dopant atom caps an icosahedral Al_{13}, while "layer" means that the icosahedral structure transforms to a layered structure. Results for $X@Al_{22}$ (X = Al, B, and Si) are for a decahedral structure. * represents that the number is for a neutral cluster. The available experimental values (expt.) are given for comparison. For a magnetic cluster, the total spin magnetic moment is also given. N_e is the number of valence electrons.

Figure 4 shows the mass abundance[159] of Si doped aluminum anion clusters, in which a strong peak of $[Al_{13}]^-$ is seen but $[Al_{12}Si]^-$ is not much abundant. However, neutral Al_nSi clusters show a strong peak at $Al_{12}Si$. On the other hand, for cations, a strong peak is seen for $[Al_{11}Si_2]^+$ and $[Al_{12}P]^+$, both corresponding to the electronic shell closing at 40 electrons. X. Li *et al.*[160] have also studied doping of C, Ge, Sn, and Pb in Al_{12} and reported the AEA of $Ge@Al_{12}$ to be 2.386 ± 0.008 eV, which is slightly higher than the value (1.869 eV) obtained by us with the PBE0 functional. They concluded from the peaks in the photoelectron spectrum that the behavior of C in these clusters was different from that of Ge, Sn, and Pb. While Ge, Sn, and Pb were predicted to be at the center of Al_{12} icosahedron, C was not. However, several theoretical studies[161,162,170,175,192,193] and our own calculations using PAW[198] potentials with the PBE0 functional in VASP[199] as well as the PBE0/6-311+G(d) level of theory in the Gaussian09 program suggest C dopant having the lowest energy at the center of Al_{12}. It is to be noted that Zhao *et al.*[192] did not find strikingly high abundance of $[Al_{12}C]^-$ and the most abundant cluster was reported to be $[Al_7C]^-$. Leskiw and Castleman[200] also found $[Al_7C]^-$ to be strongly abundant but not $[Al_{12}C]^-$. $[Al_7C]^-$ continues to be strongly abundant even with oxygen exposure. Indeed, isoelectronic Al_7N has been found[181,201,202] to be a magic cluster with N inside an Al_7 capped octahedron. Averkiev *et al.*[203] have measured the photoelectron spectra of $[Al_7N]^-$ cluster and performed *ab initio* calculations of the structure and the electronic spectra. Zhao *et al.*[192] also reported C to be at the center of Al_{12} icosahedron anion. On the other hand, Li and Gong[179] reported C to be more favorable at a vertex site in $[Al_{12}C]^-$ distorted icosahedron, though for neutral cluster C is favorable at the center of Al_{12} icosahedron. They performed AIMD calculations and showed that the lowest-energy structure of $[Al_{12}C]^-$ differs from an icosahedron and the C atom caps on four Al atoms with a short bond length of about 2 Å, in contrast to about 2.45 Å in $C@Al_{12}$ icosahedron. The structure is shown in Figure 3d. Our calculations for $Al_{12}C$ anion further support the structure with C at the surface to be lower in energy than the isomer with C at the center of an icosahedron. A similar distorted structure was also reported[144,193] for Al_{14} to be nearly degenerate with a capped icosahedron. Interestingly, in the

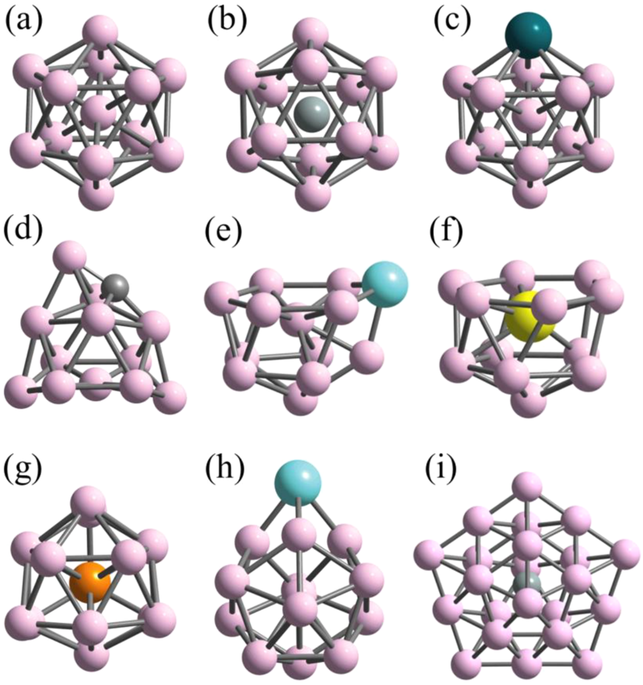

Figure 3. Atomic structures of (a) $[Al@Al_{12}]^-$ (I_h symmetry), (b) $Si@Al_{12}$ (I_h symmetry) and similarly also for $[B@Al_{12}]^-$, $[Ga@Al_{12}]^-$, $C@Al_{12}$, $[P@Al_{12}]^+$, $Ge@Al_{12}$, and $Cu@Al_{12}$, (c) $Al@Al_{11}In$ (also for $Al@Al_{11}Sn$, $Al@Al_{11}Sb$, $Al@Al_{11}Tl$, $Al@Al_{11}Pb$, $Al@Al_{11}Bi$, $Al@Al_{11}As^+$, $Al@Al_{11}Sc$, $Al@Al_{11}Ti$), (d) $[Al_{12}C]^-$, (e) $Al_{12}Ag$, (f) $Au@Al_{12}$, (g) $Cu@Al_{13}$, (h) $Ag\&Al_{13}$ (also for $Au\&Al_{13}$, $Li\&Al_{13}$, $Na\&Al_{13}$, $K\&Al_{13}$, $Rb\&Al_{13}$, and $Cs\&Al_{13}$), (i) $Si@Al_{22}$ (D_{5h} symmetry) (also for $[Al@Al_{22}]^-$ and $[B@Al_{22}]^-$) clusters obtained from PBE0/6-311+G(d), SDD calculations.

case of C at the surface of the distorted isomer, there is no imaginary frequency, but for $[C@Al_{12}]^-$, there are four imaginary frequencies. This also supports that C atom at the center of an icosahedron is dynamically unstable for the anion. However, for $[Al_{12}C]^+$, we find that the icosahedral structure with C at the center has the lowest energy. This differs from the results in ref 166 where C was reported to be favorable at the surface of a distorted icosahedron. $[Al_{12}C]^-$ and $Al_{12}P$ are isoelectronic, but the lowest-energy isomer of $[Al_{12}C]^-$ is not favored for $Al_{12}P$, which has an icosahedral structure with P at the center.

Further calculations[162,163] show that Sn and Pb favor a vertex site in an icosahedron due to their large size that leads to segregation[204,205] on the surface. The cation of these clusters also favors a vertex site[166] in an icosahedron. From PBE0 calculations, the AIP of icosahedral $P@Al_{12}$, which has one electron more than the electronic shell closing, is small (5.118 eV) similar to that of an alkali atom. This compares well with the experimental value of 5.37 ± 0.04 eV.[159] The formation of $Al_{12}PF$ is also supportive of the superalkali metal behavior of $P@Al_{12}$. $Al_{12}X$ clusters with a pentavalent atom (X = P, As, Sb, Bi) have also been studied by C. Wu *et al.*.[177] They reported P to be favorable at the center of the Al_{12} icosahedron for both neutral and cationic clusters, while As, Sb, and Bi occupy a vertex site due to their large size and form a C_{5v} structure for both neutral and cationic clusters. Our calculations for $[Al_{12}As]^+$ show that both the center and vertex sites for As are energetically nearly degenerate with the center site slightly lower in energy, although for the neural cluster the vertex site is 0.537 eV lower in energy than the center site. The calculated HOMO−LUMO gap of the magic cluster is 3.214 eV. On the other hand, Sb and Bi become favorable at a vertex site and the results are given in Table 2. Molina *et al.*[182] have studied endohedral doping of B, C, and N, as well as Al, Si, and P in Al_{12} with 39, 40, and 41 valence electrons, respectively, using the ADF package[206,207] with the PBE functional. They evaluated the nonadiabatic effects through Jahn−Teller distortions in clusters with an odd number of electrons and their effects on the electronic DOS. For the case of N doping, there are some studies[181] suggesting an N atom located at the center of the Al_{12} icosahedron while some other groups[202,208] have reported a different structure with N at the surface of a distorted structure. We have performed spin-polarized calculations with PBE functional in VASP for the $N@Al_{12}$ icosahedral isomer and by considering the lowest-energy structure of $[Al_{12}C]^-$. We find the latter to be about 0.13 eV lower in energy than the former isomer. In this respect, the behavior of the doping of N and P in aluminum clusters is different. However, for $[Al_{12}N]^+$, both the isomers become nearly degenerate. Castro *et al.*[191] have performed Jahn−Teller analysis of the electronic properties of $M@Al_{12}$ (M = B, Al, Ga)

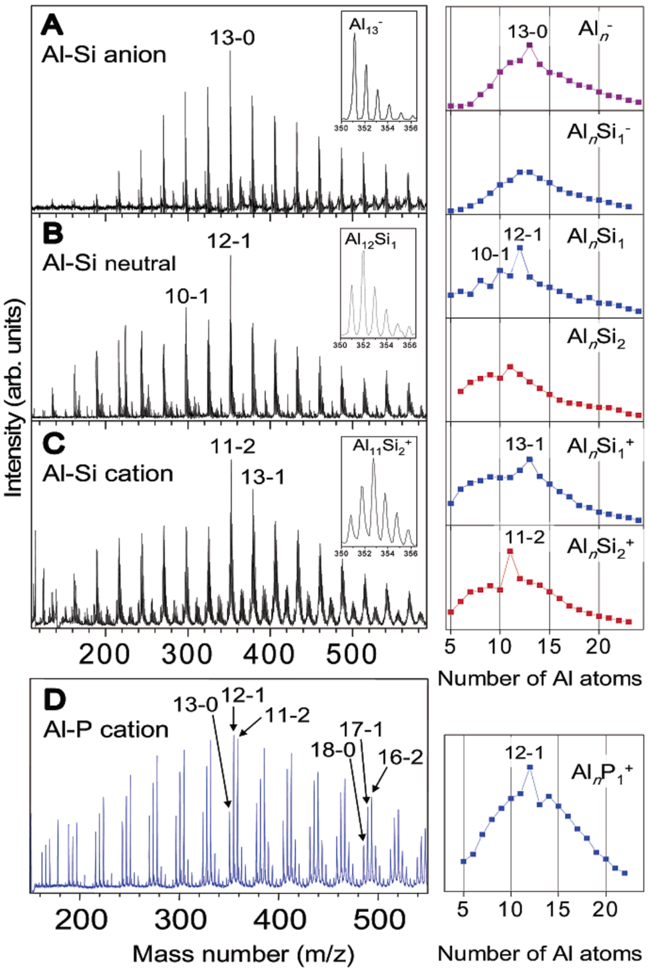

Figure 4. Mass spectra of (A) Al−Si anions, (B) Al−Si neutral clusters, (C) Al−Si cations, and (D) Al−P cations. On the right side of the figure, the intensity distributions obtained from the mass spectra are shown against the number of Al atoms, where they display distinctive peaks at the masses of the neutral $Al_{12}Si$ and the $[Al_{12}P]^+$ cation, as well as those of $[Al_{13}]^-$ and $[Al_{11}Si_2]^+$, all of which have 40 valence electrons corresponding to electronic shell closing. Note that $[Al_{12}Si]^-$ is not strongly abundant. Reproduced with permission from ref 159. Copyright 2006 American Chemical Society.

clusters with 39 valence electrons and have shown the lowering of the I_h symmetry to D_{2h} for B and D_{3d} for Al and Ga doping using all-electron fully relativistic DFT calculations. Lei[187] has studied mixed Al–B clusters and shown $Al_{12}B$ to be the most stable one. We have also studied the doping of Al_{12} with In and Tl. In both the cases, In and Tl are favorable at a vertex site in an icosahedron because of their large size. The results are given in Table 2.

3.1.1. Electronic Structure and Bonding Requirement for Endohedral Doping. It is generally believed that a molecule (or cluster) with a larger HOMO–LUMO gap typically possesses higher chemical stability or inertness.[209,210] But it should be pointed out that the correlation of HOMO–LUMO gap and stability is only a rule of thumb and should be used with caution. With the PBE0/6-311+G(d) level of theory, the calculated HOMO–LUMO gap (2.972 eV) of the magic cluster $[Al@Al_{12}]^-$ is smaller compared with 3.148, 3.076, 3.306, 3.170, and 3.167 eV for $[B@Al_{12}]^-$, $C@Al_{12}$, $[P@Al_{12}]^+$, $Si@Al_{12}$, and $Ge@Al_{12}$, respectively. Accordingly, all these doped clusters with 40 valence electrons (a magic number within the jellium picture) and closed electronic shell are even more stable than $[Al@Al_{12}]^-$. These results are supported from the strong abundances of $Al_{12}Si$, $[Al_{12}P]^+$, and $[Al_{12}B]^-$ found in the mass abundance spectra[153,154,158,159] of the doped Al clusters along with that of the undoped ones as discussed above. Besides the magic nature of neutral $Si@Al_{12}$, as well as $[P@Al_{12}]^+$ and $[Al_{11}Si_2]^+$ cations (Figure 4), Akutsu *et al.*[159] reported their inertness towards O_2 reactant similar to $[Al_{13}]^-$. Inertness toward oxygen was also reported for $[Al_{12}B]^-$.[154] Kumar[144] has shown low interaction energy of an Al atom on $Si@Al_{12}$. Meanwhile, interaction of a Li atom on Al_7, a sodium-like superatom, is quite different from the one on a halogen-like superatom Al_{13}.[193] In PES experiments, the electronic spectrum of $[Al_{12}Si]^-$ differs from that of $[Al_{13}]^-$ and $[Al_{12}B]^-$ as the detachment peak starts at higher energy,[159] because the added electron occupies an extra state above the electronic shell closing. The spectral features of $[Al_{12}Si]^-$ were found to be similar to those of $[Al_{13}Cs]^-$, while for $[B@Al_{12}]^-$ the features were similar to those of $[Al_{12}SiF]^-$, suggesting that they are isoelectronic.

The calculated atomic structures of several 40-electron clusters are given in Figure 3, while the energy levels for some cases are shown in Figure 5, along with the representative spectrum of Al_{12} that is obtained by removing Si atom from the center of $Si@Al_{12}$ cluster and keeping the positions of Al atoms fixed. The spin-polarized spectrum of this icosahedral cluster has the typical ordering of states, namely 1S, 1P, 1D, 2S, 1F, 2P, 1G, ... as one finds for a spherical jellium model. There are totally 36 valence electrons. Both up-spin and down-spin states up to 1F orbitals are fully occupied and can accommodate 34 electrons. The remaining two electrons occupy the up-spin 2P states, resulting in a net magnetic moment of 2 μ_B. When Al, Si, Ge, ... atoms occupy the center of the Al_{12} icosahedron, the *s* valence orbital of the center atom hybridizes with the 1S and 2S molecular orbitals of the cage and the bonding levels shift downward. Meanwhile, the *p* valence orbitals of the center atom hybridize predominantly with the 1P and 2P molecular orbitals of the cage and the bonding energy levels also shift downward, while the 1D and 1F states are not much affected. For the charged clusters, the spectrum shifts upward (downward) for anion (cation) cases. Accordingly, with the doping at the center, the ordering of the states of the doped clusters changes from the one in a spherical jellium model with the HOMO having the 1F instead of 2P character in all these cases. Thus, the angular momentum character of the dopant valence orbitals is very important in making endohedral species and the number of valence electrons alone is not sufficient. This aspect was also reported for endohedral doping of carbon fullerenes (see Section 4.1) that symmetry consideration dictates mixing of only those orbitals of the cage and the doping atom in a bonding state, which transform in the same irreducible representation of the point group of the whole cluster. This implies that orbitals of the dopant and the cage with the same angular momentum component will mix strongly.

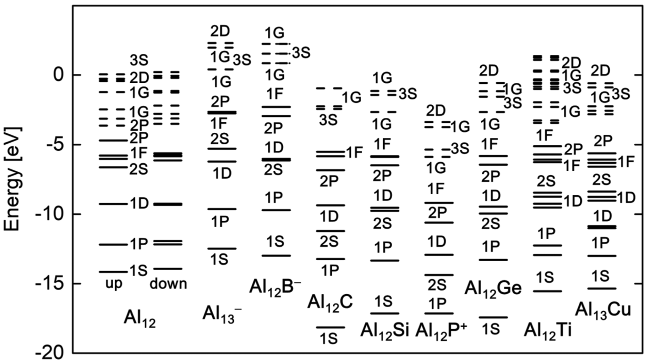

Figure 5. Electronic spectra of Al_{12} (obtained by removing Si atom in $Si@Al_{12}$ and keeping the Al atoms fixed), $[Al@Al_{12}]^-$, $[B@Al_{12}]^-$, $C@Al_{12}$, $Si@Al_{12}$, $Ge@Al_{12}$, $[P@Al_{12}]^+$, $Al@Al_{11}Ti$, and $Cu@Al_{13}$ obtained from PBE0/6-311+G(d), SDD calculations. The broken lines correspond to unoccupied states. The characters of the states are also given. For Al_{12}, "up" means up-spin orbitals and "down" means down-spin orbitals.

This argument is also clear from the results of Ti atom doping rather than a Si atom in Al_{12}. Both dopants have 4 valence electrons but titanium has partially occupied 3*d* valence orbitals. In the icosahedral structure, our calculations show that there are 6 μ_B magnetic moments and a small HOMO–LUMO gap. After optimization, the atomic structure becomes a bilayer structure with the Ti atom sitting at the center of one of the layers. However, an icosahedral isomer with Ti at a vertex has the lowest energy and a magnetic moment of 2 μ_B, as it was also reported in ref 197 while its anion has a 3 μ_B magnetic moment. The electronic spectrum of $Al@Al_{11}Ti$ is also shown in Figure 5 for comparison. A similar result has been obtained for $[Al@Al_{11}Sc]^-$, in agreement with a recent study,[197] but this anion is a singlet. The HOMO–LUMO gap in this icosahedral structure is 1.717 eV, which is much smaller than the value of 3.170 eV obtained for $Si@Al_{12}$. Clearly, the doping of Ti in Al_{12} has a significant difference from the case of $Si@Al_{12}$. A similar result has been obtained by Chauhan *et al.*,[211] who studied doping of Cr, Mn, Fe, Co, and Ni in Al_{12} and suggested the absence of electronic shell structure. Furthermore, Lang *et al.*[157] have measured physisorption of Ar on Ti, V, and Cr doped cation aluminum clusters and showed that Ti remains on the surface of the $Al_{12}Ti$ cluster, in agreement with the calculated results and that the critical size for endohedral doping in these clusters is 16 Al atoms for V or Cr doped clusters and 19–21 Al atoms for Ti doped clusters, respectively. Interestingly, recent experiments[197] on $[Al_{12}Sc]^-$ and $Al_{12}Ti$ as well as Ti, V, and Cr doping[157] did not find high abundance of these clusters as compared to some of the neighboring ones in the mass abundance spectra. Accordingly, in the case of Al_{12} icosahedral cage, it is important to have a dopant with *sp* valence orbitals.

Similar considerations also lead to the enhanced stability of cages of silicon and other group 14 members as well as coinage metals by doping of transition metals and rare earths. These systems will be discussed in the subsequent sections. Recently, Tam *et al.*[212] have studied the atomic and electronic structures of singly and doubly Si doped aluminum clusters in neutral and cationic states using B3LYP/6-311+G(d) and (U)CCSD(T)/cc-pvTZ calculations. They also found $Si@Al_{12}$ and $[Al_{11}Si_2]^+$ clusters to be magic. The simulated optical absorption spectra of these isoelectronic clusters have two pronounced bands corresponding to blue and violet lights. Note that a large HOMO−LUMO gap of 3.170 eV is obtained for $Si@Al_{12}$ (Table 2).

Chandrachud *et al.*[175] have simulated finite-temperature behavior of Al_{13} and $Al_{12}C$ clusters using AIMD and observed two important outcomes. Firstly, Al_{13} cluster undergoes isomerization at a much lower temperature than the melting temperature, while there is no isomerization in $Al_{12}C$. Secondly, the melting temperature of $Al_{12}C$ is much lower than the value for Al_{13} even though $Al_{12}C$ has a higher binding energy. This phenomenon is due to charge transfer from the Al cage to the central C atom that reduces the Al−Al bonding. Similar results were also obtained for $Ga_{12}C$, although the behavior of Ga_{13} is different from that of Al_{13} (see Section 3.2). These results showed that the finite-temperature properties of the endohedrally doped clusters are surprisingly different from our intuitions and should be explored in detail.

3.1.2. Open-Shell $Cu@Al_{12}$ and Closed-Shell $Cu@Al_{13}$ Superatoms. Kumar and Kawazoe[165] performed a detailed DFT study of doping of a Cu atom in Al_{12} and obtained a perfect icosahedral $Cu@Al_{12}$ cluster with 3 μ_B magnetic moment. It has a half-filled 2P shell within a jellium model as the HOMO and obeys Hund's rule of maximum spin at half-filling. The HOMO is triply degenerate with the spin-up 2P states fully occupied. Therefore, this cluster is an open electronic shell superatom resembling the characteristic of a P atom, unlike the closed-shell $Si@Al_{12}$. Accordingly, it can interact with a trivalent atom. Indeed, one finds $Cu@Al_{13}$ to be magic with a closed electronic shell at 40 electrons, analogous to an AlP molecule. However, the added Al atom was shown to be incorporated in the cage and there is a large HOMO−LUMO gap of 1.68 eV (2.817 eV)[165] with the PW91 (PBE0) functional. The configuration in which the added Al atom occupies the cage has lower energy than that of the configuration in which the added Al atom caps the $Cu@Al_{12}$ icosahedron with the Cu atom inside the cage. This agrees with the conclusions drawn from PES experiments[146,155] as well as other theoretical studies.[155,171] On the other hand, for the case of Ag and Au doping, Ag and Au atoms are favorable outside the Al_{13} cluster. Similar results have been obtained for the doping of alkali atoms (see Table 2). Therefore, Ag and Au behave like an alkali atom from the point of view of the atomic structure, and their important role is to contribute an electron to the electronic shell closing.

Comparing the energies of $Cu@Al_{12}$ and $Cu@Al_{13}$ clusters, there is a large gain of 4.35 eV in energy that leads to the higher stability of the $Cu@Al_{13}$ cluster. The mass abundance spectrum of Cu doped aluminum anion clusters is presented in Figure 6, showing strong abundance of $[Al_{13}Cu]^-$ even though it has 41 valence electrons (besides the ten 3*d* electrons on Cu). This is in contrast to the $[Al_{12}Si]^-$ cluster, which did not show high abundance as discussed above. The AEA of the $Al_{13}Cu$ cluster is low (2.137 eV) and the AIP is high (6.594 eV), making this cluster magic as observed. The observation of the high abundance of $[Al_{13}Cu]^-$ in spite of being a 41-electron species has been related to the high stability of the neutral cluster. Accordingly, the abundance may depend upon the nucleation conditions. We also find that the HOMO−LUMO gap of $Cu@Al_{13}{}^-$ is larger (1.730 eV) compared with the value of 1.522 eV for $Si@Al_{12}{}^-$ using the PBE0 functional. This could also have an impact on the abundance of clusters besides the nucleation conditions in experiments. For the case of Au doping, a disordered structure has been suggested for $Al_{12}Au$ from PES measurement with the Au atom occupying the central site in the Al_{12} cage.[155] However, our PBE0 calculations show an Al_6−Au−Al_5−Al layered structure of $Al_{12}Au$ (Figure 3) to be 0.417 eV lower in energy than the distorted decahedral cage with Au inside and 1 μ_B magnetic moment. Moreover, similar to $Ag\&Al_{13}$, an $Al@Al_{12}$ icosahedron with Au atom capping a triangular face also has the lowest energy for $Al_{13}Au$. The AEA and AIP of $Au\&Al_{13}$ are 2.059 and 6.601 eV, respectively, which are very similar to the case of $Cu@Al_{13}$, although Cu is inside the Al_{13} cage. These results suggest the importance of the total number of valence electrons in these two clusters, which is 40, a magic number, excluding the *d* electrons on Cu or Au.

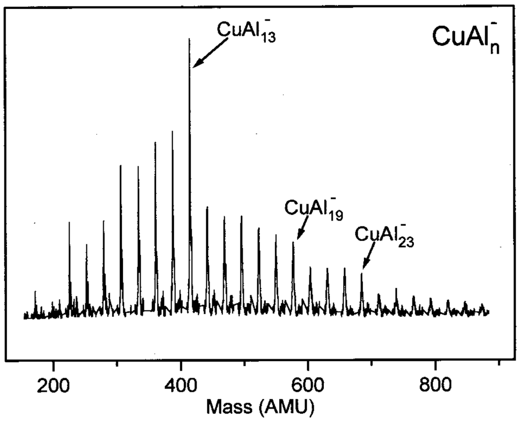

Figure 6. Mass abundance spectrum of Cu doped anion aluminum clusters $[CuAl_n]^-$. Reproduced with permission from ref 146. Copyright 2001 American Institute of Physics.

3.1.3. $X@Al_{12}$ with a Divalent Atom X—The Superchalcogens. Sun *et al.*[188] showed using *ab initio* calculations at the B3LYP/aug-cc-pVDZ level that $Al_{12}Be$ has an icosahedral structure with Be at the center and exhibits a superchalcogen character with two electrons less than the electronic shell closing at 40 electrons, thereby possessing a magnetic moment of 2 μ_B. They studied the first and second electron affinities and obtained a large HOMO−LUMO gap for $[Be@Al_{12}]^{2-}$. Also large binding energy and large HOMO−LUMO gap were obtained for $Be[Be@Al_{12}]$ and $Ca[Be@Al_{12}]$. The latter was shown to mimic CaO or CaS molecule. Similarly, $Li_2[Be@Al_{12}]$ mimics Li_2O. Interestingly, $[Be@Al_{12}]_2$ has characteristics of O_2 or S_2 molecule with a triplet state lower in energy than a singlet. They also studied interaction between $Al_{12}Be$ and FLi_3. The latter behaves like a super alkaline earth atom. The bonding between these two superatoms is ionic with Li interacting with $Al_{12}Be$. Dianion $[Al_{12}X]^{2-}$ clusters doped with divalent atoms X = Be, Mg, Ca, Sr, Ba, and Zn have been studied by Jimenez-Izal *et al.*[183] using gradient embedded GA. Small dopants such as Be and Zn were reported to occupy the center of Al_{12} icosahedron, while larger atoms Mg, Ca, Sr, and Ba were shown to occupy a vertex of an icosahedron.

3.1.4. Endohedrally Doped Aluminum Clusters and Hydrogen Storage. Q. Lu *et al.*[184] have investigated interaction of 12 and 14 H atoms with Mg@Al_{12} and Ca@Al_{12} clusters. It was shown that the doping of Mg and Ca atoms enhances the stability of aluminum clusters and that H atoms occupy the on-top sites along the surface of the clusters. In fact, similar to $[B_{12}H_{12}]^{2-}$ icosahedral cluster, there is a need to provide two electrons to $Al_{12}H_{12}$ icosahedral cluster to make it have an effective 26 electrons besides the electrons in the Al−H bonds, obeying the Wade−Mingos rule for $2n_v + 2$ skeleton bonding electrons as discussed in Section 2.2. This can be achieved by doping of a divalent atom, and that is why the doping of Mg and Ca enhances the stability. Such studies have attracted attention because of the interest in hydrogen storage for clean energy applications. Similar results have been reported for $[Li@Al_{12}H_{12}]^-$. Using the B3LYP/6-311+G* level of theory, Charkin *et al.*[186] have studied many 40-electron MAl_{12} neutral and charged clusters with M = Mg, Al, Si, P, Zn, Ga, As, Be, B, C, and N, and 50-electron $MAl_{12}H_{12}$ with M = Li, Na, Cu, Al, Be, Mg, and Ga, and reported relative energies of isomers, their IR-active vibrational frequencies, and ionization potentials.

Lu and Wan[213] have computationally studied hydrogen adsorption on the Sc-coated Si@Al_{12} cluster using the PBE functional and DNP basis set. In the $Al_{12}H_{12}$ cluster, hydrogen is covalently/ionically bonded with Al atoms and thus, high temperature is required to release it in such hydrides. For practical applications, it is important to have not only light weight but also fast kinetics and favorable thermodynamics at ambient conditions with high capacities to have an efficient reversible system to release and store hydrogen. In this regard, materials with about 20−40 kJ/mol (0.21−0.41 eV) binding energy of H_2 are considered to be ideal for hydrogen storage at ambient conditions.[214] Nanomaterials are attractive to store a large quantity of hydrogen due to their large surface area. Coating of metal atoms such as Li, Mg, Sc, Y, or Ti on some stable nanostructures such as C_{60}, graphene, and nanotubes has been the subject of many studies.[215−217] Adsorption of H_2 on Si@Al_{12} is very weak with the binding energy of less than 0.01 eV, as one would expect between two closed electronic shell systems. However, a Sc atom can bind on a hollow site of Si@Al_{12} with a gain in energy of about 1.84 eV. It has been shown from DFT calculations with the PBE functional that up to six H_2 molecules can be attached on each Sc atom with a desirable average binding energy of about 0.3 eV.[213] Adsorption of up to 4 Sc atoms on Si@Al_{12} was shown to not favor aggregation, unlike Ti on C_{60} in which case clustering of Ti atoms is inevitable.[218] Finally, a total of 19 H_2 molecules could be attached, reaching a maximum hydrogen content of 6.3 wt %.

3.1.5. $Al_{12}X$ with a Transition Metal Atom X. J. Zhang *et al.*[190] have performed a first-principles study of the $Al_{12}X$ (X = Sc−Zn) clusters using the DMol program[219] and PW91 functional considering four kinds of closed-packed geometries with high symmetry (I_h, D_{5h}, O_h, and D_{3h}). Besides determining the lowest-energy structures, they calculated the magnetic moments and also studied interaction with H, O, and N atoms. $Al_{12}Ni$ and $Al_{12}Cu$ were reported to favor icosahedral structures with Ni and Cu at the center and have 2 μ_B and 3 μ_B magnetic moments, respectively. The latter one is in agreement with the prediction of Kumar and Kawazoe[165] as discussed above. On the other hand, Sc, Ti, and V favor a vertex site in an icosahedron, as our calculations also showed in the case of Sc and Ti, while the lowest-energy structures with Cr, Mn, Fe, Co, and Zn are loose structures. A high magnetic moment of 5 μ_B was reported for Mn doping.

Gong and Kumar[220] studied doping of 3*d*, 4*d*, and a few 5*d* transition metal (M) atoms in Al_{12} icosahedron and explored the trends of bonding in these doped clusters to shed light on the structure and bonding of Al based quasicrystals. They also obtained about 5 μ_B magnetic moments for Mn and Cr doping and analyzed the changes in *sp*−*d* interaction as the dopant atom was changed in a *d* series. This is important in understanding the formation of quasicrystals as the transition metal atoms are well separated and interact via the Al atom. It was shown that the quasicrystal-forming elements, such as Mn, Fe, Co, Rh, and Pd, have large binding energies and strong *sp*−*d* interaction. Further, the M−Al bond length is shorter than the Al−Al bond length and this is expected to improve the binding between the M atom and the 12 vertex Al atoms and favor icosahedral packing. It was also suggested that Cr, Ru, and Cu may have a tendency to form binary quasicrystals, while Ni and Zn have weak *sp*−*d* interaction and may not form quasicrystals. This agreed with the experimental fact that Zn atoms are distributed randomly in the $(Al, Zn)_{49}Mg_{32}$ phase.[221]

3.1.6. Optical Absorption of X@Al_{12} Clusters and Derivatives. R. H. Xie *et al.*[178] have conducted TD-DFT calculations of the optical absorption spectra for a variety of icosahedral, dodecahedral, and tetrahedral clusters. Starting from an icosahedral Al@Al_{12} cluster, it has been shown that the optical gap can be tailored by substituting the central Al anion with a group 13 anion (B^-, Al^-, Ga^-, In^-), or a group 14 atom (C, Si, Ge, Sn), or a group 15 cation (N^+, P^+, As^+, Sb^+), by bonding with a hydrogen atom or an alkali metal atom (Li, Na, K) or a halogen atom (F, Cl, Br, I), or by attaching an organic functional group R [R = $C(C_2H_3)_3$, $C(CH_3)_3$, SCH_3, $C(C_6H_5)_3$]. The simulated optical adsorption spectra are given in Figure 7, in which one can see that the optical gaps and absorption spectra

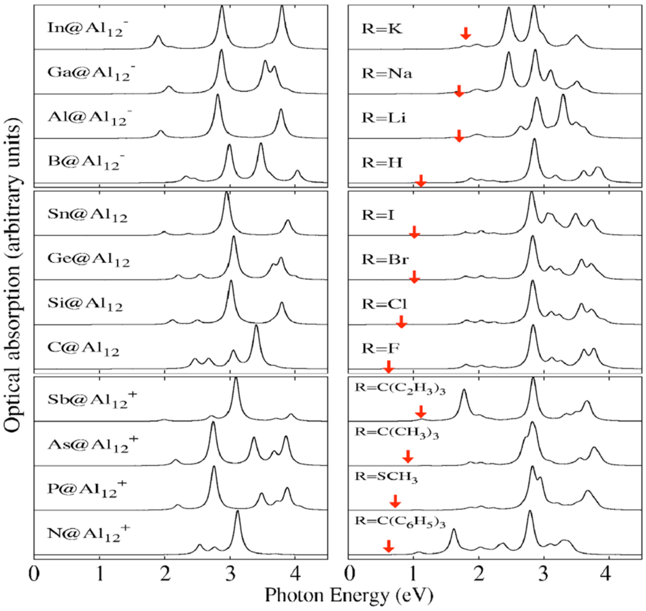

Figure 7. Calculated absorption spectra for $[Al@Al_{12}]^-$ by substitutional doping at the center and ionic and covalent bonding by attaching an R group. All spectra were broadened by 0.06 eV to simulate finite temperature. The arrows indicate the optical gaps not visible in the present scale. Reproduced with permission from ref 178. Copyright 2005 American Physical Society.

have been tailored over a wide wavelength range by varying the cluster species, i.e., from the ultraviolet to near infrared region.

3.1.7. Catalytic Behavior of X@Al_{12} Clusters.

L. Wang *et al.*[25] explored the chemisorption of H_2 molecule on the endohedrally doped icosahedral X@Al_{12} (X = B, Al, C, Si, P, Mg, Ca) clusters by DFT calculations using the PW91 functional and DNP basis set. They showed that the hydrogen dissociation behavior on these doped aluminum clusters can be tuned by the dopant atom. The computed reaction energies and activation barriers of the X@Al_{12} clusters are plotted in Figure 8. Interestingly, chemisorption of H_2 on Si@Al_{12} and C@Al_{12}, which are superatoms like noble gas atoms, is endothermic. For the other X@Al_{12} clusters, which are superhalogen (X = B, Al), superalkali metal atom (X = P), and superchalcogen (X = Mg, Ca) with respect to the 40-valence electron closed shell configuration, dissociative chemisorption of H_2 is exothermic with modest activation barriers. Ca@Al_{12} is the best candidate for dissociating an H_2 molecule with the largest reaction energy (−33.9 kcal/mol) and lowest activation barrier (10.9 kcal/mol). Therefore, the concept of superatom is still valid for understanding the catalytic behavior of the doped metal clusters and can serve as a guide for designing low-cost and efficient catalysts.

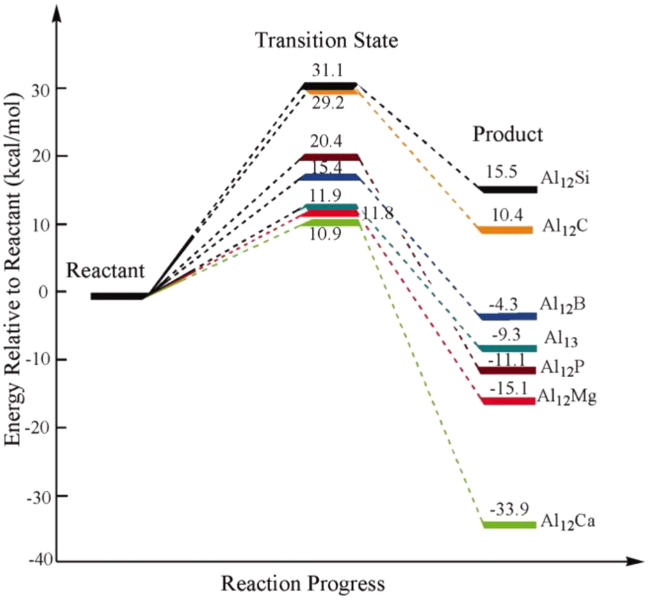

Figure 8. Reaction coordinate energy diagram for the transition from physisorbed H_2−Al_{12}X cluster (reactant) to the related chemisorbed form (product). Reproduced with permission from ref 25. Copyright 2009 Wiley Periodicals, Inc.

Following L. Wang's work, the interaction of X@Al_{12} clusters with various molecules and species, such as O_2, H_2O, and CO_2, has been investigated theoretically by different groups. Q. L. Lu *et al.*[222] found that X@Al_{12} (X = P^+, C, Si) superatoms (super-noble gas) are reluctant to react with the ground state O_2 molecule with high barriers and small adsorption energies, while on $[Al@Al_{12}]^-$, spin transformation of O_2 is much faster and dissociation depends on the spin state. J. Y. Zhao *et al.*[223] demonstrated that H_2O dissociation on X@Al_{12} (X = B, C, Si, P) clusters is difficult and involves low barriers for X = Mg, Zn, Ga, Ni, and Fe, with singlet $Al_{12}Fe$ having the lowest barrier. They also explored the adsorption behavior of CO_2 on the neutral and ionic X@Al_{12} clusters. Similar to H_2O molecule, CO_2 decomposition has relatively low barriers on the metal doped X@Al_{12} (X = Fe, Ni, Cu) clusters and requires large barriers for the non-metal doped systems (X = B, C, Si, P).[224] They further showed that the anionic $[X@Al_{12}]^-$ (X = Al, Be, Zn, Ni, Cu, B, P) clusters all have higher barriers for CO_2 chemisorption than those of the neutral counterparts. For the cationic analogues, physisorption to chemisorption of CO_2 only involves low barriers, and CO_2 chemisorption on $[Be@Al_{12}]^+$ has the lowest barrier.[225] Besides, P. Jin *et al.* suggested using X@Al_{12} (X = Al, C, N, P) clusters for DNA dysfunction owing to the strong binding and charge transfer between clusters and DNA nucleobases.[226]

3.1.8. Larger Doped Clusters of Aluminum.

Doping of larger Al clusters has also been studied but to a much lesser extent. Similar to Al@Al_{12} cluster, Kumar *et al.*[164] studied substitutional doping of a Si atom in Al_{19} and Al_{23} to form a double icosahedron of $Al_{18}Si$ and a decahedral Si@Al_{22} cluster with 58 and 70 valence electrons, respectively. As stated earlier, $[Al_{23}]^-$ has been found to be abundant in the mass spectrum of anionic aluminum clusters and it is non-reactive with oxygen. Accordingly, one expects Si@Al_{22} to be a magic cluster. Also, $[Al_{22}B]^-$ is abundant in the mass spectrum of B doped aluminum clusters as shown in Figure 2b. We have performed *ab initio* calculations on decahedral Si@Al_{22} as well as $[B@Al_{22}]^-$ clusters. The optimized structure has D_{5h} symmetry and is shown in Figure 3i for Si@Al_{22}, and a similar structure was obtained for $[B@Al_{22}]^-$. Substitutional doping of an Si atom enhances the binding energy of the Al@Al_{22} cluster (Table 2). Interestingly, Si@Al_{22} has a considerable HOMO−LUMO gap of 1.729 eV from our PBE0 calculations.

To conclude, it is remarkable that a variety of superatoms can be formed using Al@Al_{12} icosahedron as a mother cluster via appropriate doping. The above discussions show that besides Al_{13} itself a superhalogen, Be@Al_{12} (or Mg@Al_{12}, Ca@Al_{12}) is a superchalcogen, Cu@Al_{12} behaves like a superpnictogen, Si@Al_{12} and C@Al_{12} are closed-shell super-noble gases like Ar, and P@Al_{12} is a superalkali metal atom. Clearly, this demonstrates the versatility at the nanoscale, which can be exploited to build designer materials. The following sections will further cover a variety of superatoms based on endohedrally doped cage clusters of other elements and discuss their properties and potential applications.

3.2. Endohedrally Doped Clusters of Ga and In

Compared to doped Al clusters, there are only a few studies on endohedral doping of Ga and In clusters. Gallium is an interesting material from both fundamental and application points of view. Unlike aluminum, bulk gallium is a metallic molecular solid with a strong Ga_2 covalent bond and weaker intermolecular forces;[227] therefore, it has a low melting temperature. However, clusters of elemental Ga have covalent bonding and higher melting temperature than bulk Ga (302.9 K).[228] Also, Ga clusters exhibit a different behavior in comparison to those of Al. Similar to $[Al_{13}]^-$, $[Ga_{13}]^-$ has 40 valence electrons corresponding to electronic shell closing. However, as shown in Figure 9, Ga_{13} favors a decahedral Ga@Ga_{12} structure, as compared to an icosahedron for Al@Al_{12}.

Substitutional doping of B, C, N, Al, Si, P, Ge, and As in Ga_{13} has been studied by Henry,[229] and the optimized structures are shown in Figure 9. For $Ga_{12}B$ and $Ga_{12}C$, an icosahedral isomer is favorable with the B and C atoms endohedrally doped. These cages have D_{3d} and I_h symmetry, respectively. However, for $Ga_{12}N$, an isomer with N exohedrally bonded becomes lower in

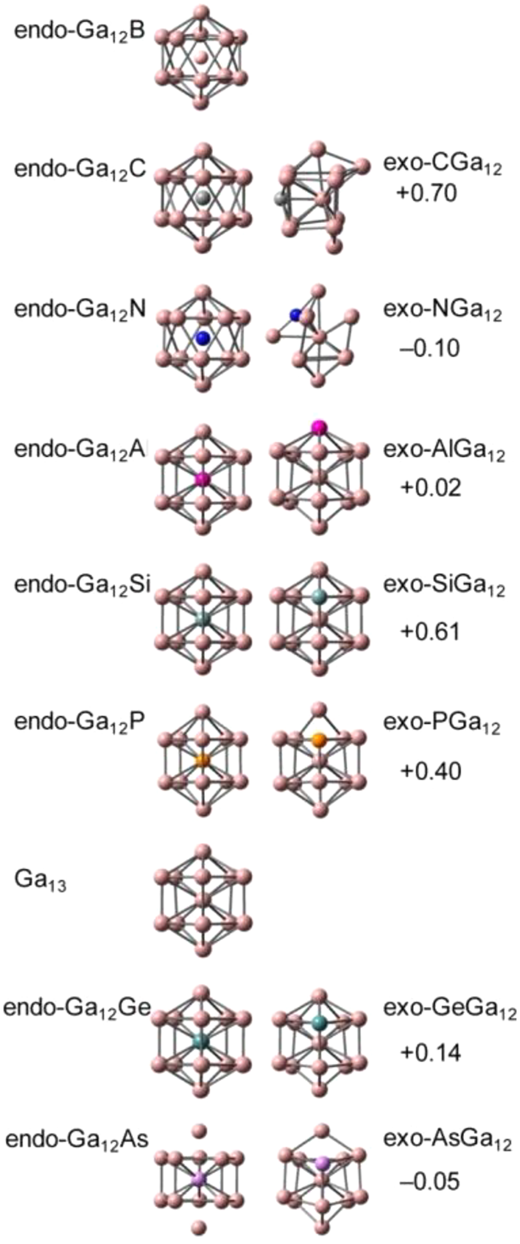

Figure 9. Lowest energy isomers of (left panel) X@Ga$_{12}$ (endo) and (right panel) exo-XGa$_{12}$ clusters. The energies of exohedral isomers are given relative to the corresponding endohedral isomers. Reproduced with permission from ref 229. Copyright 2012 American Chemical Society.

energy than an endohedral icosahedron. On the other hand, for Al, Si, P, and Ge doping, an endohedrally doped decahedron is favorable while for the case of As doping, exohedral doping in a decahedron is favorable. In all these cases except for Al, the cluster has D_{5h} symmetry. Henry has discussed changes in the bond lengths and bonding strength of the clusters with dopants. Similar to X@Al$_{12}$ with X = C, Si, and Ge, these X@Ga$_{12}$ clusters with 40 valence electrons adopt compact and symmetric structures, and are the most stable ones. In general, the *s*-*p* overlap in Ga$_{12}$X clusters is less developed compared with Al$_{12}$X clusters. L. Guo[230] has studied doping of an Al atom in Ga$_n$ clusters with n = 1−15 and has shown that for n up to 12, the Al atom lies on the surface while for n > 12, configurations with the endohedral Al atom are more favorable. This result differs from that obtained by Henry.[229] Thus, it would be desirable to explore these systems in more detail.

Chandrachud *et al.*[175] have investigated the thermodynamic behavior of C@Al$_{12}$ and C@Ga$_{12}$ clusters using AIMD simulation within GGA and found that the surface atoms in C@Ga$_{12}$ show significant motion around 325 K due to isomerization from icosahedron to decahedron. However, the mean square displacement in C@Ga$_{12}$ is much smaller than that for the elemental Ga@Ga$_{12}$ cluster. Therefore, the doping affects the melting dynamics of the cluster very significantly. G. Yuan *et al.*[231] have studied Ga$_{12}$X clusters with X = C, Si, Ge, Sn, and Pb using the DMol package with the BLYP functional. They obtained a D_{5h} decahedral cluster to have the lowest energy and a C_s symmetry isomer to be nearly degenerate for X = C. On the other hand, for the doping of Si and Ge, they found a D_{5h} symmetry decahedral isomer with Si and Ge inside to be most favorable, as also obtained by Henry.[229] In the case of Ga$_{12}$Sn and Ga$_{12}$Pb clusters, a C_s symmetry isomer with Sn and Pb on the surface was found to be most favorable. Further, for the anion of Ga$_{12}$C, a C_s isomer with C on the surface was found to have the lowest energy as in the case of $[Al_{12}C]^-$. On the other hand, anions of Si@Ga$_{12}$ and Ge@Ga$_{12}$ continue to favor the D_{5d} symmetry isomer with the dopant inside. Similarly, for the anions of Ga@Ga$_{11}$Sn and Ga@Ga$_{11}$Pb, a C_s symmetry isomer with Sn or Pb on the surface continues to be the most favorable one.

GaN is an important wide band gap semiconductor; thus it is interesting to study the behavior of N doped Ga clusters. B. Song *et al.*[232] have studied N doped gallium clusters having up to 15 Ga atoms using the DMol program and PBE functional. It was shown that for small clusters with up to 10 Ga atoms, N atom favors an inside position; but for larger clusters, the surface site becomes more favorable. Specifically, Ga$_{12}$N has a decahedral structure with N replacing a surface Ga atom. This is similar to the results obtained by Henry.[229]

Akutsu *et al.*[233] have studied indium clusters doped with Si and Ge. The mass abundance spectra showed higher abundances of In$_{12}$Si and In$_{12}$Ge clusters compared with the clusters with neighboring sizes. However, the magic behavior of these clusters is less prominent than that of Al$_{12}$Si or $[Al_{12}B]^-$. While indium is trivalent in bulk phase, in small clusters with less than 16 atoms, indium behaves like a monovalent atom, since the *s*-*p* overlap is not well developed due to larger separation between the valence *s* and *p* orbital energies going down in group 13 elements. This is supported from the fact that In$_8$ and In$_{18}$ clusters have a peak in the ionization potential, which can be understood if we consider indium monovalent so that these clusters will correspond to 1P and 1D electronic shell closing in a jellium model, respectively. Therefore, it seems reasonable to treat indium as monovalent in small clusters. Among the Si and Ge doped indium clusters, clusters with 10, 12, 14, and 16 In atoms show peaks in the curve of ionization potentials. The photoelectron spectra show a small hump in the cases of doped clusters with 10, 12, and 14 In atoms, which was interpreted as arising from a singly occupied molecular orbital of $[In_nX]^-$ clusters. It was also suggested that the doping of a Si or Ge atom in In$_n$ clusters might make the *s* to *p* excitation energies smaller and this may facilitate a trivalent In atom in such clusters because the geometric and electronic structures of an In$_n$ cluster change upon the doping of another atom, such as the formation of a cage structure. The trivalent character of In atoms has also been emphasized when oxygen atom interacts with In clusters. In an early study on In$_n$Na$_m$ clusters, Nakajima *et al.*[234] found higher ionization potential values for In_7Na and $In_{13}Na$ clusters, which were attributed to electronic shell closing at 8 and 40 valence electrons, respectively, meaning that In is monovalent in In_7Na, while it becomes trivalent in $In_{13}Na$.

Y. Liu *et al.*[235] have studied the atomic and electronic structures of neutral and anionic $In_{12}X$ (X = C, Si, Ge, Sn) clusters from *ab initio* calculations using the DMol package with the BLYP and B3LYP functional. They found that neutral and anionic $In_{12}C$ clusters have the C_s structure with the C atom at the surface of the cluster similar to the case of $[Al_{12}C]^-$. However, for the doping of Si, Ge, and Sn atoms, both neutral and anionic clusters have a D_{5h} symmetry structure with the dopant atom endohedrally doped in the In_{12} cage. As the size of the In atom is bigger, even the Sn atom becomes favorable at the center. The electron affinities of both Si@In_{12} and Ge@In_{12} were found to be similar with the values of 2.18 and 2.22 eV, respectively, from photoelectron spectroscopy experiments.[233] This was used to infer that both clusters have the same structure as indeed suggested from Liu's calculations.

In addition to gas-phase clusters, group 13 elements (except for Al) are able to form discrete endohedral cage clusters in the Zintl phase of intermetallic compounds. There have been only a few reports on Ga- and In-based Zintl anions, such as $[Ni@Ga_{10}]^{10-}$ anion in $Na_{10}Ga_{10}Ni$ crystal,[236] $[Zn@In_{10}]^{8-}$ anion in $K_8In_{10}Zn$ crystal,[237] and $[M@In_{10}]^{10-}$ anion in $Na_{10}Ga_{10}M$ (M = Ni, Pd, Pt) crystals.[238] All these crystals are constructed from close-packed layers of discrete metal-centered Ga_{10} or In_{10} cages separated by Na or K ions within and between the cluster layers. $[Zn@In_{10}]^{8-}$ anion has bicapped square antiprism structure with D_4 symmetry, while $[Ni@Ga_{10}]^{10-}$ and $[M@In_{10}]^{10-}$ (M = Ni, Pd, Pt) clusters adopt tetracapped trigonal prism structure with different extents of distortion. Due to the very high charge state, it is difficult to directly correlate these Zintl cluster anions to the doped Ga or In clusters of the gas phase, unlike the group 14 Zintl clusters that will be discussed in Section 6.4. However, it is interesting to note that in all these cases, the number of valence electrons is 40 (without counting the *d* electrons on transition metal atom and Zn atom), which correspond to the magic cluster in a spherical jellium model.

To summarize this section, doped aluminum clusters have played a very important role in developing different superatoms and gaining basic understanding of the *s-p* bonded clusters. Furthermore, Al, Ga, and In clusters behave differently; that is, Ga clusters show covalent bonding character and preference for decahedral structure while small In clusters tend to act like a monovalent atom and this behavior can be affected by doping. The finite-temperature behaviors of Al and Ga based clusters are also different. Therefore, these systems are very interesting and their further studies would shed more light on the nature of bonding, atomic structure, and finite temperature effects of these clusters. Lastly, it would be interesting to explore magnetism in Ga and In clusters doped with transition metal atoms.

4. ENDOHEDRALLY DOPED CARBON AND BORON FULLERENE CAGES

4.1. Metal Encapsulated Small Carbon Fullerenes M@C_n, n = 20−28

The discovery of C_{60} buckyball (also known as fullerene) in 1985 opened up a new territory of cage molecules or clusters,[30] which are ideal hosts for endohedral doping with different species. In the same year, Heath *et al.* have demonstrated the formation of a stable endohedral complex La@C_{60}, which was named as metallofullerene.[38] Thereafter, a rich variety of endohedral carbon fullerenes with different cage sizes and guest atoms have been generated, detected, and extensively investigated from many aspects.[8,39−44]

In the endohedral fullerenes, often with 60 or more carbon atoms, the doped atom does not interact strongly with the carbon cage. On the other hand, the small fullerene cages are relatively unstable owing to the increase in the curvature, resulting in strain in the cage and weakened π-conjugation.[39] The smallest fullerene C_{20} has all pentagonal faces and therefore the bonding tends to become sp^3 like in contrast to the predominant sp^2 bonding in large fullerenes. Indeed, from photoelectron spectroscopy experiments it has been suggested that $[C_n]^-$ cages are less stable than bicyclic rings for $n < 30$.[239] Also, O'Brien *et al.* performed photodissociation of C_{60} with a pulsed laser light and observed successive loss of C_2 until C_{32} fullerene was achieved. For smaller cage sizes, the strain energy becomes large and the fullerene explodes into open fragments.[50] An early DFT calculation at the B3LYP/cc-pVDZ level indicated that the T_d fullerene cage of C_{28} should be the smallest stable carbon fullerene.[240] These studies point to a limit of about 30 C atoms that one may produce a stable fullerene structure in experiments, even though smaller fullerenes such as C_{22} and C_{24} with one and two hexagons are in principle possible. Interestingly, metal doping has been used to stabilize smaller fullerenes down to C_{20}. In this review, we focus only on such small size metallofullerenes of carbon, i.e., M@C_n with $n \leq 28$, in which the endohedral metal atom plays a significant role in stabilizing the carbon fullerene cages, just like the silicon and germanium counterparts discussed in Section 5 and Section 6.1, respectively.

In 1987, Kroto[241] proposed that a C_{28} fullerene cage with T_d symmetry might be a candidate for the smallest fullerene. *Ab initio* calculations revealed that the T_d symmetry C_{28} fullerene possesses an open $^5A_2$ electronic ground state that lacks four electrons with regard to a closed electronic shell,[45,240] suggesting that it can be stabilized by trapping a tetravalent atom of suitable size inside the cage. Later, Z. Chen *et al.*[242] investigated a series of small fullerenes including neutral and quadruple charged C_{28} at the B3LYP/6-31G(d) level of theory. The computed NICS values at the cage center of C_{28} and $[C_{28}]^{4-}$ are 3.8 ppm and −34.3 ppm, respectively. The large negative NICS value of the latter corresponds to a 32-electron closed shell predicted by the spherical aromaticity model[133,136] (see Section 2.2) and suggests extra stability due to aromaticity.

Experimental observation of M@C_{28} was reported by T. Guo *et al.*[45] in 1992, who presented the mass spectral analysis of U@C_n clusters produced by laser vaporization of a graphite-UO_2 composite target. As shown in Figure 10, U@C_{28} is the most abundant species within the mass range of 200 to 500 amu. They further attempted bulk synthesis of U@C_{28} and confirmed that U@C_{28} was present in the sublimed film using XPS and photoemission spectroscopy analysis. Moreover, the 5*f* signature of uranium in photoemission spectra of the sublimed films was consistent with a formal 4+ valence state of U. However, two subsequent experiments on uranium endohedral metallofullerenes did not find any evidence for U@C_{28}.[243,244] It should be noted that the increase of curvature in small fullerenes makes the bonding develop sp^3 character with a dangling bond feature. This also makes the small fullerenes highly reactive and difficult to detect experimentally.

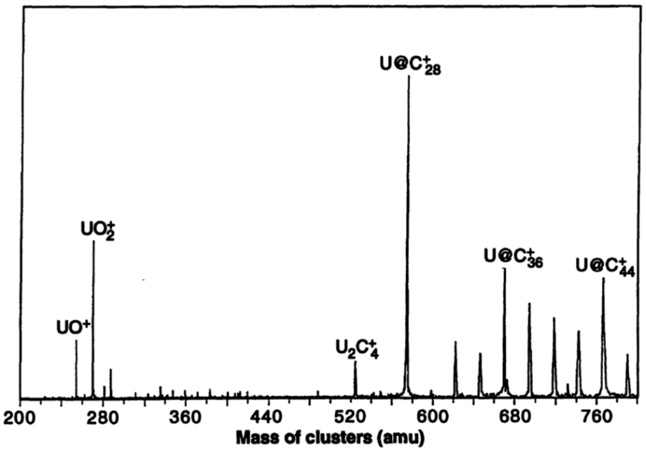

Figure 10. FT-ICR mass spectrum of positive carbon−uranium cluster ions produced by laser vaporization of a graphite-UO_2 composite disk, with conditions optimized to view the clusters in the mass range 200 to 500 amu. Note that $U@C_{28}$ cation is the most abundant cluster. Reproduced with permission from ref 45. Copyright 1992 American Association for the Advancement of Science.

The idea of stabilizing the C_{28} fullerene cage by a tetravalent guest metal (M) atom was further realized by T. Guo *et al.*[45] by considering M = Ti, Zr, and Hf. It was reported that the stabilization of the C_{28} cage with these metal atoms works to some extent with the relative abundance of cluster cations in the order $Ti@C_{28} \ll Zr@C_{28} < Hf@C_{28} < U@C_{28}$. Accordingly, among these M atoms, U doping produces the highest abundance. Indeed, one needs a metal atom with partially occupied f orbitals, which could hybridize strongly with the frontier orbitals of the C_{28} fullerene cage that also have f angular momentum character. The stability of this cage can be understood from the electronic shell closing with 32 valence electrons. For C_{28}, there are 28 π electrons and one needs a rare earth atom with four valence electrons such as Ce and Th, which is ideal and leads to a closed-shell symmetric tetrahedral cage with a large HOMO−LUMO gap of 2.41 and 2.37 eV (within GGA-PBE), respectively. Besides hybridization of the f-type cage molecular orbitals with f orbitals of the dopant atom, there is also hybridization between the d molecular orbitals of the carbon cage and the d orbitals of the metal atom such as for Ti, Zr, and Hf doping. While the interaction between (s, p) type hybrid orbitals of the cage with the (s, p) orbitals of the metal dopant in such a case is generally weak due to large separation in their energy levels, it has been found that the doping of U, Ti, Zr, and Hf leads to a large gain in energy that stabilizes the fullerene cage. The relative abundance of these metallofullerenes in experiments is in accordance with *ab initio* calculations, which predicted the highest binding energy for U doping and then for Hf, Zr, and Ti doping in descending order. For U doping, the U atom remains at the center of the symmetric cage which can be considered approximately spherical. Its 5f orbitals hybridize with the f-type molecular orbitals of the cage, leading to the stabilization and large gain in energy. For Zr and Hf, the C_{28} cage remains symmetric and the M atom locates at the center of the cage; but Ti atom drifts away from the center (see Figure 14 in the latter part). Note that Ti atom is smaller than Zr and Hf atoms. In all these cases, the strain due to doping in the C_{28} cage is small as most of the C−C bond lengths are about 1.45 Å. For these group 4 atoms, there is strong coupling of the d orbitals of the M atom with the d-type molecular orbitals of the carbon cage, leading to large gain in energy and sizeable HOMO−LUMO gap. With PBE functional, the theoretical gap values are 2.31, 2.31, and 1.94 eV for Hf, Zr, and Ti doping, respectively, while U doping leads to a magnetic cluster with a magnetic moment of 2 μ_B and a small HOMO−LUMO gap (0.45 eV).

Later, Dunk *et al.*[245] have used FT-ICR mass spectrometry and reported the smallest stable endohedral fullerene to be $M@C_{28}$ with M = Ti, Zr, Hf, and U as compared to C_{32} for the undoped case (see Figure 11). In their experiments, only $M@C_{28}$ cation species encapsulating group 4 metal atoms and U were found in relatively high abundance. These endohedral fullerene cages are formed by a bottom-up growth mechanism and act as precursors to larger metallofullerenes. In the family of endohedral C_{28} fullerene filled by a group 4 atom, they found that $Zr@C_{28}$ cation is not as favorable as $Ti@C_{28}$ cation, whereas $Hf@C_{28}$ cation was only weakly detected. This is in contrast to the results obtained by T. Guo *et al.*[45] as well as theoretical studies. A possible explanation for this behavior could be different nucleation conditions.

Stimulated by the experimental successes, there have been plenty of *ab initio* calculations on $M@C_{28}$ metallofullerenes endohedrally doped with various M atoms, including B,[246] C,[246−248] N and O,[246] Si, Ge, and Sn,[112,248−250] Mg, Al, S, and Ca,[249] Pb,[112] Sc,[112,246,249,251] Ti,[112,246,247,249−256] V, Cr, and Cu,[246,255] Mn and Co,[255] Fe,[246,251,255] Ni, Pd, and Pt,[112,255] Zr,[112,247−250,254,257] Hf,[112,254,257,258] U,[257,259,260] Pa,[259] Ce,[261] Th,[257,262] Pa^+, U^{2+}, and Pu^{4+},[262] and Ac (Ac = Th−Md).[263] Doping of an atom such as Mg, Ca, Al, S, C, Si, Ge, Sn, Cr, Cu, Pb, Pd, and Pt in C_{28} fullerene has been shown to be endothermic by *ab initio* calculations.[112,248−250,255] Note that none of these atoms has a partially occupied f orbital and also their d orbitals are either unoccupied or fully occupied such as for Cu, Pd, and Pt.

In order to address the primary concern for the stability of $M@C_{28}$ metallofullerenes and to elucidate whether and why a guest atom can be encapsulated stably inside the C_{28} cage, an early effort has been made by T. Guo *et al.*[249] who proposed using HF calculations that the elements with electronegativity smaller than 1.54 and suitably large ionic radius could be trapped inside C_{28} fullerene. Jackson and co-workers[248] found no covalent bonding between the C_{28} fullerene cage and the group 14 endohedral atoms (C, Si, Ge, and Sn) from LDA calculations, and the cage-atom interaction was shown to be a weakly ionic bond involving charge transfer from the endohedral atom to the cage. In contrast, $Zr@C_{28}$ exhibits strong covalent interaction between the Zr-4d orbitals and the C_{28} cage orbitals. Indeed, using a spherical potential model, it has been shown that the presence of partially occupied high-angular momentum valence states, namely, d and f orbitals in the endohedral atom, significantly enhances the energetic stability of the $Zr@C_{28}$ and $U@C_{28}$ complexes, respectively.[249] Miralrio and Sansores[112] have investigated the equilibrium geometries, binding energies, and electronic properties of selected $X@C_{28}$ fullerenes at the PBE/def2-TZVP level of theory. The binding energies are plotted against the atomic number of X in Figure 12. One can see that the endohedral fullerenes $X@C_{28}$ containing group 4 elements (X = Ti, Zr, Hf) possess exceptionally large binding energies of 8.072−13.759 eV in the sequence of $Ti@C_{28} < Zr@C_{28} < Hf@C_{28}$, consistent with their relative abundances observed in experiment.[45] Accordingly, these $X@C_{28}$ clusters exhibit large HOMO−LUMO gaps (1.943−2.312 eV), further suggesting their high chemical

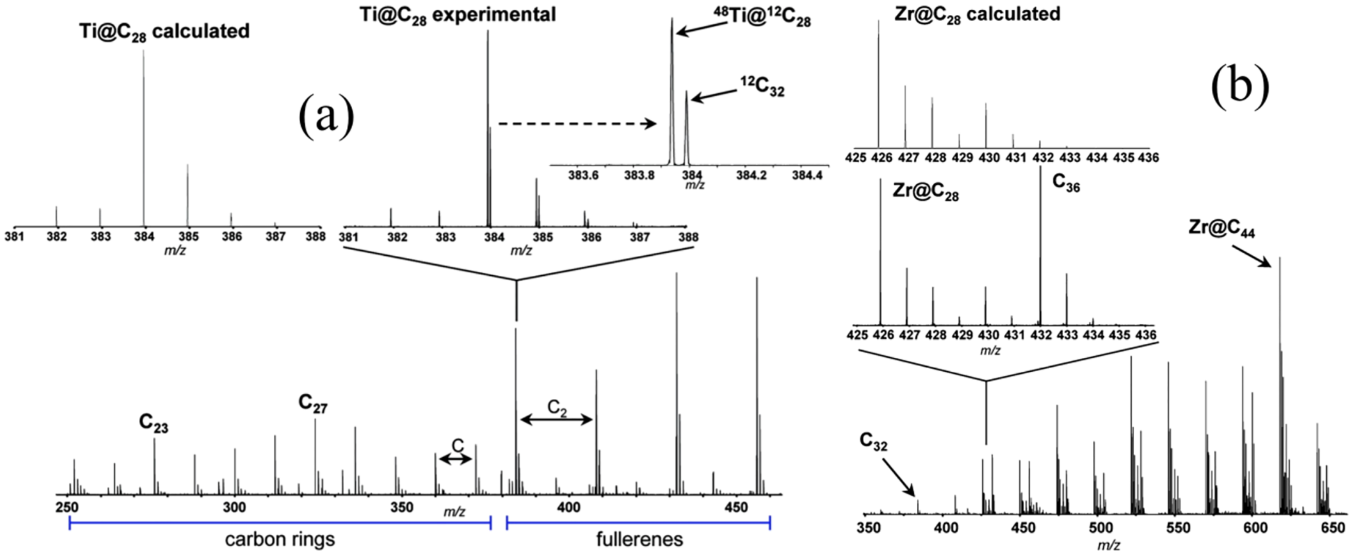

Figure 11. (a) FT-ICR mass spectrum (positive ions) resulting from laser vaporization of a titanium-containing graphite target under conditions that probe the ring-to-fullerene transition. Ti@C_{28} forms as the smallest fullerene. The approximate 52 mDa mass difference between the smallest empty cage (C_{32}) and Ti@C_{28} is clearly resolved. (b) Small endohedral fullerenes formed by vaporization of a Zr containing (0.8%) carbon rod. Zr@C_{28} is the smallest endohedral fullerene formed, whereas C_{32} is the smallest empty cage. Zr@C_{28} is not as favored as Ti@C_{28}. In the larger size range, high abundance of Zr@C_{44} is also seen. Reproduced with permission from ref 245. Copyright 2012 American Chemical Society.

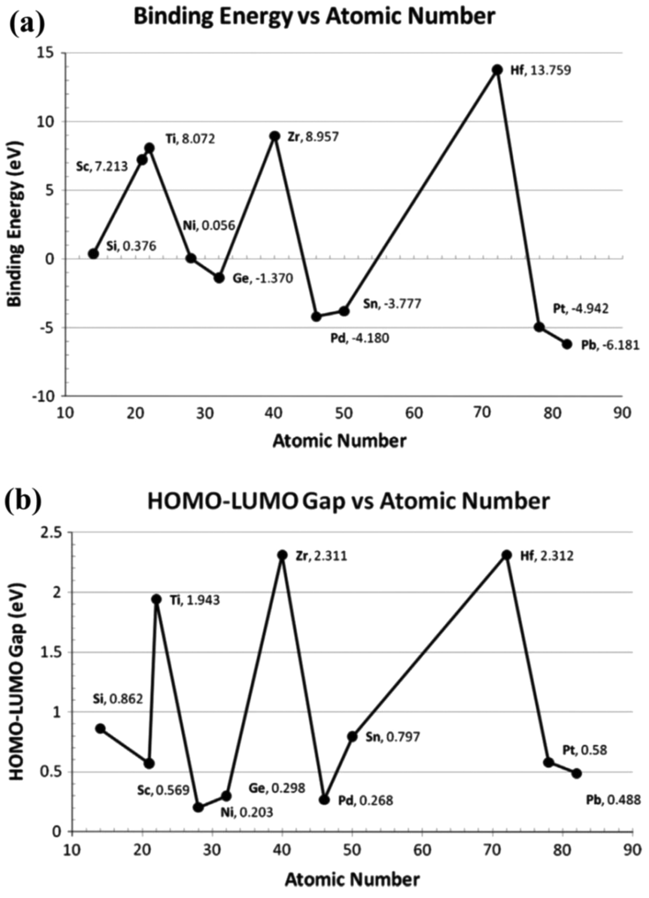

Figure 12. (a) Binding energy and (b) HOMO−LUMO gap of all X@C_{28} fullerenes versus the atomic number of X calculated with the PBE/def2-TZVP method. All the numbers are in eV. Reproduced with permission from ref 112. Copyright 2016 Elsevier B.V.

inertness. On the contrary, encapsulation of the endohedral atoms of group 10 and 14 is energetically unfavorable, with small binding energies and small HOMO-LUMO gaps of less than 1 eV. An exceptional case is Sc@C_{28}, which has a large binding energy of 7.213 eV that is comparable to Ti@C_{28}, but a rather small HOMO−LUMO gap of 0.569 eV due to an odd number of electrons.

The experimental realization of endohedral fullerenes M@C_{28} (M = Ti, Zr, Hf, U) as well as their high stability predicted by DFT calculations can be further interpreted by the 32-electron principle proposed by Dognon *et al.*,[132] which is discussed in Section 2.2. Following the first example of the endohedral clusters An@Pb_{12} (An = Pu, Am^+) fulfilling the 32-electron principle, Th@C_{28}, Pa^+@C_{28}, U^{2+}@C_{28}, and Pu^{4+}@C_{28} are qualified as a new family of 32-electron species using the bonding *s*-, *p*-, *d*-, and *f*-type molecular orbitals of the cage which interact with the atomic orbitals of the endohedral atom.[262] The sizeable HOMO−LUMO gaps of 2.4−2.9 eV (PBE) or 3.5−4.0 eV (B3LYP) suggest a closed electronic shell, and the large interaction energies of over 11 eV further signify their high thermodynamic stability. Similarly, a neutral U@C_{28} cluster with 34 valence electrons also obeys the 32-electron principle with the two extra electrons distributed on the C_{28} cage.[260]

The 32-electron rule is also applicable to Ti@C_{28}, Zr@C_{28}, and Hf@C_{28} due to the similarity of the electronic structures of these metallofullerenes and $[C_{28}]^{4-}$. Population analysis revealed a certain amount of charge transfer (0.5−3.4 electrons, depending on the methodology) from group 4 dopant to the C_{28} cage.[112,246,247,252] Therefore, the metallofullerenes can be formally viewed as an ionic complex of $[M]^{4+}@[C_{28}]^{4-}$ to some extent. Muñoz-Castro and King[254] computed the magnetic response properties of these endohedral clusters in terms of both global and local shielding tensors and found a homogeneous shielding region for the orientational averaged response, different from that observed for the hollow C_{28} cage. For a magnetic field oriented along a specific axis, a long-range shielding cone was observed, which supports the spherical aromaticity of the 32-electron systems and accords with the particular abundance of M@C_{28}. At the TZ2P/ZORA-PBE

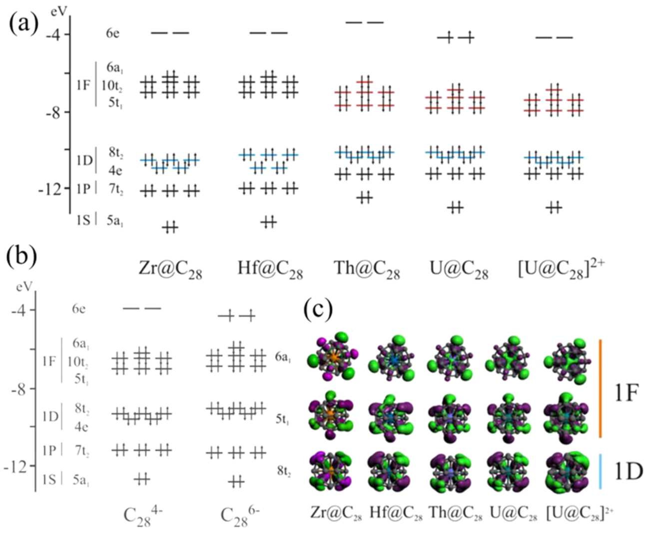

Figure 13. (a) Electronic structures involving the π-radial molecular orbitals of C_{28}, and the relevant levels resembling 1S, 1P, 1D, and 1F shells. The contributions from *d*- and *f*- orbitals of the endohedral dopant to the molecular orbitals of C_{28} are depicted in blue and red, respectively. (b) Electronic structure from the π-radial molecular orbitals of $[C_{28}]^{4-}$ and $[C_{28}]^{6-}$. Labels are related to (a) for comparison and demonstrate similarity though there are visible effects due to the presence of the metal atom. (c) Isosurface representations of selected molecular orbitals depicting *d*- and *f*-type bonding. Note that in both $Zr@C_{28}$ and $Hf@C_{28}$ no metal contribution is observed in the 1F molecular orbitals owing to the purely *d*-block element character of zirconium and hafnium. Reproduced with permission from ref 257. Copyright 2016 Wiley Periodicals, Inc.

level of theory, they also examined the bonding characters of $M@C_{28}$ cages encapsulating *f*-block element (U), *d*-block elements (Zr, Hf), and a borderline metal (Th) between these two blocks.[257] The molecular orbitals of the $M@C_{28}$ metallofullerene are depicted in Figure 13a and compared with those of $[C_{28}]^{4-}$ and $[C_{28}]^{6-}$ in Figure 13b. In the case of the *d*-block metal atoms such as Zr or Hf, the *d* orbitals of the metal atom hybridize with the 1D molecular orbitals of the C_{28} cage and the bonding states are shifted lower in energy compared with the states of $[C_{28}]^{4-}$ in which case there is no atom at the center, whereas the 1F orbitals originating from the C_{28} cage remain nearly at the same positions. However, for U (or U^{2+}) and Th encapsulation, *d*- and *f*-type orbitals of the metal atom hybridize with the 1D and 1F molecular orbitals of the C_{28} cage, respectively, and both shift to lower energies compared with the $[C_{28}]^{4-}$ case. Therefore, though one can see similarities of the molecular orbitals between $M@C_{28}$ (M = Zr, Hf, U^{2+}, and Th) and $[C_{28}]^{4-}$ as well as between $U@C_{28}$ and $[C_{28}]^{6-}$ due to their isoelectronic nature, there are differences induced by the presence of the central metal atom.

Note that previous calculations on $M@C_{28}$ metallofullerenes were performed at different levels of theory. To provide a unified overview of the geometric, energetic, and electronic properties of the representative $M@C_{28}$ metallofullerenes, herein we performed systematic *ab initio* calculations using the PBE0/6-311+G(d), SDD method. Our computational results are summarized in Table S3 and Figure 14. One can see that those systems fulfilling the 32-electron rule such as $Ti@C_{28}$, $Zr@C_{28}$, $Hf@C_{28}$, $Ce@C_{28}$, $Th@C_{28}$, and $[U@C_{28}]^{2+}$ possess relatively large binding energies and embedding energies (sometimes also referred to as interaction energies in the literature) as well as wider HOMO−LUMO gaps. All the 32-electron systems adopt T_d symmetry with endohedral metal atom located at the cage center, except for $Ti@C_{28}$ and $Zr@C_{28}$ having C_{3v} and C_{2v} symmetry in which the Ti and Zr atoms are displaced at the off-center position by 0.464 and 0.117 Å, respectively. As for the 3*d* transition metal doped C_{28} cages, the embedding energy decreases from Sc to Ni with the exception of Ti and Mn. For Ti atom doping, the embedding energy is large; while for Mn atom, it is small (see Table S3).

By extending the 32-electron endohedral $M@C_{28}$ metallofullerenes to cages of other sizes, Manna *et al.* have investigated a series of fullerene cages encapsulated with an actinide or lanthanide atom fulfilling the 32-electron principle, namely $M@C_{26}$ (M = Pr^-, Pa^-, Nd, U, Pm^+, Np^+, Sm^{2+}, Pu^{2+}, Eu^{3+}, Am^{3+}, Gd^{4+}, Cm^{4+})[264] and $M@C_{24}$ (M = Pu, Cm^{2+}, Sm, Gd^{2+}).[265] The most stable structures of $U@C_{26}$, $Pu@C_{24}$, and $Cf@C_{20}$ (corresponding to the 32-electron rule) are shown in Figure 15. In the ground state, bare C_{26} fullerene has a D_{3h} cage structure and an open-shell electronic configuration with a HOMO−LUMO gap of 1.62 eV at the B3LYP/def-TZVP level. After incorporating a rare earth metal atom/ion with 6 valence electrons, the resulting endohedral $M@C_{26}$ cage retains the same D_{3h} symmetry (Figure 15c), with the exception of M = Eu^{3+} or Gd^{3+} which yields a D_3 symmetry. The 6 valence electrons of the lanthanide or actinide atom/ion together with the 26 π electrons of the C_{26} cage result in a closed-shell 32-electron system with much enhanced HOMO−LUMO gap that lies in the range of 2.44 eV to 3.99 eV. According to the calculated Gibbs free energies and enthalpies of the reaction $M + C_{26} \rightarrow M@C_{26}$, encapsulation of Pr^-, Pa^-, U, Np^+, Pu^{2+}, Am^{3+}, Gd^{4+}, and Cm^{4+} atom/ion is thermodynamically favorable, while incorporation of Nd, Pm^+, Sm^{2+}, and Eu^{3+} inside C_{26} is endothermic.

Similar to the case of C_{26}, encapsulation of a metal atom/ion with eight valence electrons into a C_{24} fullerene cage may also lead to stable 32-electron systems. At the B3LYP/def-TZVP level of theory, Manna *et al.*[265] explored several endohedral metallofullerenes $M@C_{24}$ (M = Pu, Cm^{2+}, Sm, Gd^{2+}) and found that only Pu atom and Cm^{2+} cation can be stably filled into the C_{24} cage. The most stable species, $Pu@C_{24}$ has D_{6d} symmetry (Figure 15b) and a large HOMO−LUMO gap of 3.26 eV as compared to 1.83 eV for the bare C_{24} cage with C_2 symmetry. Moreover, the binding energy (6.77 eV/atom) for $Pu@C_{24}$ is even higher than the value (6.28 eV) theoretically predicted for $U@C_{26}$ and experimentally obtained (6.39 eV) for $U@C_{28}$, suggesting that one should be able to produce $Pu@C_{24}$ in large abundance.

Besides $Pu@C_{24}$, many other endohedral $M@C_{24}$ clusters have been explored by *ab initio* calculations, such as M = $Li^{0/+}$, $Na^{0/+}$, $K^{0/+}$, $Be^{0/2+}$, $Mg^{0/2+}$, $Ca^{0/2+}$,[266] M = Ti, Zr, Hf,[267] M = Sc, Y, La,[268] M = Cr, Mo, W,[269] and M = Mn, Fe, Co, Ni, Cu, Zn.[270] However, encapsulation of a large variety of metal atoms (M = Na, K, Mg, Ca, Mn, Co, Ni, Cu, Zn, Y, La) or ions (M = Li^+, Na^+, K^+, Ca^{2+}) into the C_{24} cage is actually energetically endothermic. Table 3 summarizes the geometrical parameters and key electronic properties of the $M@C_{24}$ metallofullerenes that are thermodynamically stable. Most of these metallofullerenes adopt low-spin states (singlet or doublet), except for $Fe@C_{24}$ which prefers a triplet state. Generally speaking, the HOMO−LUMO gaps for these endohedral complexes are in the range of 1.33 eV to 2.70 eV and are comparable to that of the bare C_{24} cage (1.78 eV).

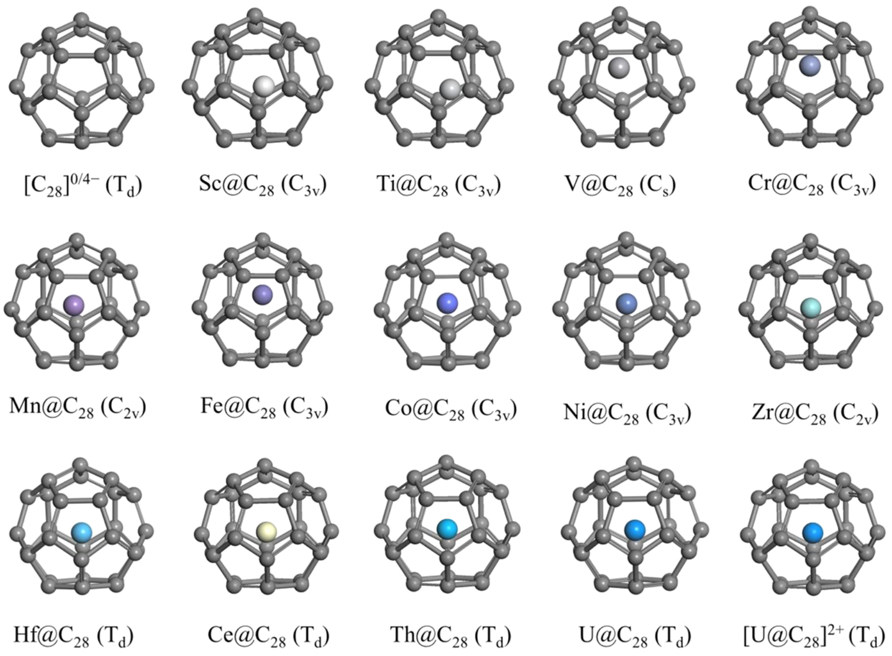
$[C_{28}]^{0/4-}$ (T_d) Sc@C_{28} (C_{3v}) Ti@C_{28} (C_{3v}) V@C_{28} (C_s) Cr@C_{28} (C_{3v})

Mn@C_{28} (C_{2v}) Fe@C_{28} (C_{3v}) Co@C_{28} (C_{3v}) Ni@C_{28} (C_{3v}) Zr@C_{28} (C_{2v})

Hf@C_{28} (T_d) Ce@C_{28} (T_d) Th@C_{28} (T_d) U@C_{28} (T_d) $[U@C_{28}]^{2+}$ (T_d)

Figure 14. Atomic structures of some representative M@C_{28} cage clusters from PBE0/6-311+G(d), SDD calculations. For each cluster, the symmetry is given in parentheses. In the cases where the symmetry is not T_d, the M atom is displaced from the center of the cage (see Table S3).

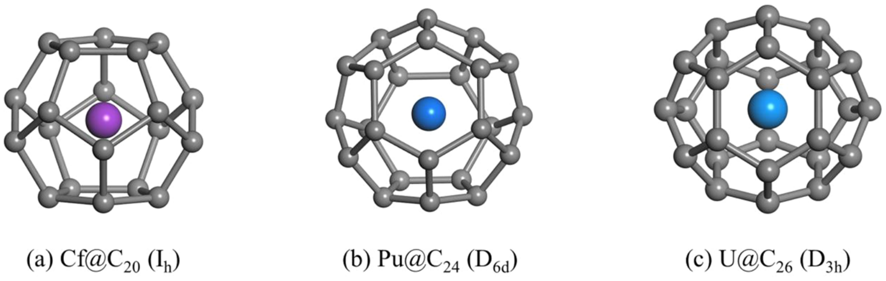
(a) Cf@C_{20} (I_h) (b) Pu@C_{24} (D_{6d}) (c) U@C_{26} (D_{3h})

Figure 15. Most stable structures of (a) Cf@C_{20}, (b) Pu@C_{24}, and (c) U@C_{26} clusters. The point group symmetry for each cluster is given in parentheses.

Table 3. Summary of the Previous Theoretical Results on Endohedrally Doped M@C_{24} Cages Using B3PW91 Hybrid Exchange-Correlation Functional and 6-31G(d) Basis Set Except for the 4*d* and 5*d* Transition Metal Atoms in Which Case LanL2DZ Basis Set Has Been Used[a]

Cluster	Method	Symmetry	M−C (Å)	ν (cm^{-1})	E_{em} (eV)	E_{HL} (eV)	Q (|e|)
Li@C_{24} [266]	B3PW91/6-31G(d)	C_2			1.65	1.33	−0.26
Be@C_{24} [266]	B3PW91/6-31G(d)	C_s			1.51	2.08	0.70
Sc@C_{24} [268]	B3PW91/6-31G(d)	D_{2d}	2.214	85.4	4.16	1.44	0.05
Ti@C_{24} [267]	B3PW91/6-31G(d)	C_s	2.027	121.3	5.18	1.73	0.39
Cr@C_{24} [269]	B3PW91/6-31G(d)	C_s	1.861	151.4	5.07	2.70	0.51
Fe@C_{24} [270]	B3PW91/6-31G(d)	C_s	1.828	174.1	1.25	1.81	0.89
Zr@C_{24} [267]	B3PW91/6-31G(d), LanL2DZ	S_4	2.236	76.5	3.22	1.47	1.63
Mo@C_{24} [269]	B3PW91/6-31G(d), LanL2DZ	C_s	1.994	74.7	2.40	2.36	0.64
Hf@C_{24} [267]	B3PW91/6-31G(d), LanL2DZ	S_4	2.228	80.0	4.02	1.47	1.79
W@C_{24} [269]	B3PW91/6-31G(d), LanL2DZ	C_s	2.021	39.8	3.54	2.44	1.37

[a] The shortest distance between M atom and C atom (M−C), lowest harmonic vibrational frequency (ν), embedding energy (E_{em}), HOMO−LUMO gap (E_{HL}), and on-site charge (Q) on M atom have been given. A positive value of Q means electrons are transferred from M atom to C_{24} cage.

Also, the embedding energy is smaller as compared to that in C_{28} because the doping leads to significantly increased C−C bond lengths in the C_{24} cage. Most of the M dopants except for Li and Sc donate a certain amount of charge (0.39−1.78 electrons) to the C_{24} host cage. Moreover, the infrared spectra of selected M@C_{24} fullerenes (M = Li, Be, Cr, Mo, W) have been simulated to help identification of these endohedral metallofullerenes in experiments.

Many *ab initio* calculations have been carried out on the smallest possible endohedral metallofullerene M@C_{20} to investigate its energetic stability, electronic structure, and magnetic properties using a variety of dopant atoms M, such as Fe, Co, and Ni,[271−274] V,[273,274] Na and K,[275,276] Li, Rb, and Cs,[276] Ce and Gd,[277] Nd and U,[278] Sc, Ti, Cr, and Mn,[274] Cu and Zn,[274] Dy and Cf,[279] Si, Ge, Sn, and Pb,[280] and Ag, Au, Cd, and Hg.[281] In addition to the gas-phase endohedral metallofullerenes, molecular electronic devices based on M@C_{20} metallofullerenes, e.g., Fe@C_{20} inside (8, 8) carbon nanotube,[272] Au(111)−Na@C_{20}−Au(111) and Au(111)−K@C_{20}−Au(111) junctions[275] have been proposed and their transport behaviors have been studied. However, it is questionable whether encapsulation of such a variety of M atoms inside a small C_{20} cage is exothermic. From PBE calculations with 6-31G(d) and LANL2DZ basis sets, it was revealed that doping of a 3*d* transition metal atom at the center of C_{20} fullerene is exothermic for Sc, Ti, V, Cr, Mn, and Fe and endothermic for Co, Ni, Cu, and Zn. However, Sc@C_{20}, Cr@C_{20}, and Fe@C_{20} metallofullerenes have imaginary frequency and thus are dynamically unstable.[274] The interaction energy between Nd/U dopant and C_{20} cage at the B3LYP/def-TZVP level of theory also signifies an endothermic process of encapsulation.[278] Moreover, Gonzalez *et al.*[281] have found that group 11 and group 12 atoms (Cu, Ag, Au, Zn, Cd, and Hg) prefer to form exohedral derivatives with C_{20} cage instead of endohedral ones. Using DFT calculations, Manna and Ghanty[278] have studied M@C_{20} with M = Pr^-, Pa^-, Nd, U, Pm^+, Np^+, Sm^{2+}, Pu^{2+}, Eu^{3+}, Am^{3+}, Gd^{4+}, and Cm^{4+}, all of which are 26 valence electron systems. They showed that the C_{20} fullerene with D_{3d} point group transforms to a highly symmetric I_h endohedral cage (Figure 15a) with the HOMO−LUMO gap in the range of 2.5−4.9 eV. The stability of these cages was attributed to the fulfillment of 26 valence electrons corresponding to the fully occupied *spd*-type levels of the cage and the partially occupied *f*-type molecular orbitals of the cage, which hybridize with the valence orbitals of the M atom. Using DFT calculations, F. Meng *et al.*[279] have also studied encapsulation of *f*-block metal atom/ion in C_{20} to enhance its stability. In order to make it a 32 valence electron system corresponding to a shell closing, one needs a metal atom that has 12 valence electrons since 20 π bonded electrons are contributed by the carbon cage. For M@C_{20} with M = Eu^{3-}, Am^{3-}, Gd^{2-}, Cm^{2-}, Tb^-, Bk^-, Dy, Cf, Ho^+, Es^+, Er^{2+}, Fm^{2+}, Tm^{3+}, Md^{3+}, Yb^{4+}, No^{4+}, Lu^{5+}, and Lr^{5+}, Meng *et al.* showed that the C_{20} cage could be stabilized to a highly symmetric I_h endohedral cage. The calculated HOMO−LUMO gap using B3LYP was found to lie in the range of 2.22−5.39 eV. These theoretical results demonstrate that the 32 valence electron rule applies to all of the small endohedral cages. However, it remains to be seen if the small-sized metallofullerenes below C_{28} (especially C_{20}) could be realized in experiments by endohedral doping of appropriate metal atoms.

4.2. Endohedrally Doped Cages of Boron

Boron lies just before carbon in the periodic table and has one valence electron less than carbon. This deficiency of an electron makes boron behave quite differently from carbon; thus boron favors three-center bonding leading to its very rich chemistry. Many boron compounds have empty B_{12} icosahedra (with all triangular faces) as their building blocks. However, B_{12} icosahedron is not stable as a free cluster itself owing to the presence of 36 valence electrons, while only 26 electrons are needed to form a cage. The lowest-energy structure of B_{12} cluster is planar.[66] But $[B_{12}H_{12}]^{2-}$ has 26 valence electrons leaving aside the 12 electrons bonded with 12 H atoms. Accordingly, it obeys the Wade−Mingos rule and the 12 boron atoms form an icosahedral cage structure. This cage is too small to encapsulate an atom. However, similar to carbon fullerenes, larger boron cages (also called borospherenes) have been studied. Considering three-center bonds, Szwacki *et al.*[282] placed a boron atom at the center of each of the 20 hexagonal faces of a C_{60} analogue of I_h-B_{60} and predicted a highly symmetric B_{80} cage. The 20 B atoms at the centers of hexagons contribute 60 valence electrons and make B_{80} an isoelectronic and isostructural analogue of the C_{60} buckyball. Later, this cage structure of B_{80} was shown to be dynamically unstable[283] and further DFT-based global searches[116,284,285] revealed core-shell structures with a central B_{12} icosahedron to be more stable than the hollow B_{80} cage. This type of structure is a precursor to bulk boron solid, and a few other large B_n clusters with $n \geq 68$ have also been shown to favor core-shell structures. However, it is yet to be understood when bulk behavior finally dominates the boron clusters, as in this size range other structures, namely quasi-planar structure of B_{84}[286] and quasi-planar or tubular structure of B_{70}[286,287] have been found to have very competitive energy.

Even though the hollow B_{80} cage is less stable than the more compact core-shell structures, endohedral doping of an atom or a group of atoms such as Sc_3 or Sc_3N inside the B_{80} cage improves its stability to energetically prevail over the core-shell structures.[288] There have been many DFT studies on endohedral doping of the B_{80} cage by a variety of guest species, such as Fe,[289] Co,[290] Ni,[291,292] and Be atoms,[293] La_2,[294] Y_2,[295] and Sc_2 dimers,[295] Sc_3 trimer,[288] Sc_3N,[288] Sc_2C_2, Sc_3C_2, Sc_3CN, and Sc_3C_2CN,[296] M_3N and M_2C_2 (M = Sc, La),[297] P_2N_2 and P_4N_4 clusters,[298] as well as B@Co_{12} and Co_{13} clusters.[299] Generally speaking, incorporation of most of these species into B_{80} borospherene is exothermic. For the case of a single atom encapsulated in a B_{80} cage, Fe and Be dopants have been reported to favor the cage center,[289,293] while Ni or Co atom prefers an off-center position near the inner center of a pentagon on the B_{80} cage.[290,291] The endohedral atom can affect the physical and chemical properties of the cage significantly. It has been found that encapsulating a Be atom in the B_{80} cage considerably enhances the adsorption energy of ozone on the cage to 5.188 eV, in comparison with 3.404 eV for the pristine B_{80}.[293] Interestingly, the magnetic moment of Ni@B_{80} cluster depends on the position of the Ni atom. It is 1.96 μ_B for the cage center position and zero for the off-center position, respectively. The energy difference between these two isomers is as small as 0.07 eV, thus providing an opportunity for single molecular magnetic switch.[291] A similar behavior has also been shown to occur in Sc_2@B_{80}, which exhibits a flexible location of the metal dopants and has two magnetic states (2 μ_B and 0 μ_B).[295] Considering that a multiply charged $[B_{80}]^{6-}$ cage is aromatic with a NICS value of −34.39 ppm, the doping of La_2 and Sc_3N clusters contributes six extra electrons into B_{80} fullerene in each case and results in highly stable endohedral complexes. This has been demonstrated by the high binding energy for La_2@B_{80} (6.713 eV) and Sc_3N@B_{80} (22.319 eV), appreciable HOMO−LUMO gap of 1.32 eV for La_2@B_{80} and 1.53 eV for Sc_3N@B_{80}, as well as high VIPs for La_2@B_{80} (6.14 eV) and Sc_3N@B_{80} (6.40 eV), computed at the B3LYP/6-31G(d), LanL2DZ level of theory.[294] For the guest clusters containing *p*-block elements such as Sc_3C_2CN[296] and P_4N_4,[298] strong bonding interaction between the encaged cluster and the boron cage has been found. To date, the largest clusters reported to be encapsulated in the B_{80} cage are Co_{13} and B@Co_{12}, which lead to trilayer Matryoshka clusters with large

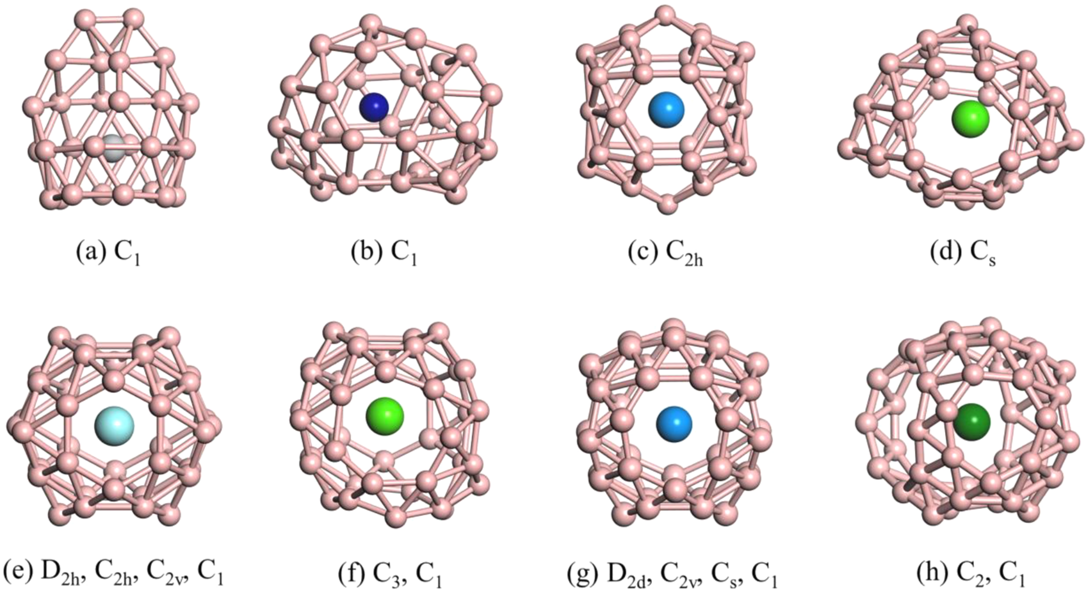

Figure 16. Atomic structures of (a) $Ti@B_{28}$, (b) $W@B_{32}$, (c) $U@B_{36}$, (d) $[Ca@B_{37}]^-$, (e) $M@B_{38}$, (f) $M@B_{39}$, (g) $M@B_{40}$, and (h) $M@B_{44}$. Here M denotes a variety of metal dopants (for details, see Tables 4 and 5).

magnetic moment and high stability[299] (see Section 9 for further discussion).

The above discussed large endohedral borospherenes are yet to be realized in a laboratory. On the other hand, B_{40} is the first boron fullerene or borospherene obtained in a laboratory.[300] By combining photoelectron spectroscopy and unbiased *ab initio* global search, a D_{2d} cage was reported as the ground state configuration of the neutral and anionic B_{40} clusters. Later an axially chiral borospherene (C_3) for $[B_{39}]^-$ has also been reported.[301] The smallest borospherene B_{28} was first theoretically predicted by J. Zhao *et al.*[115] and then experimentally confirmed by Y. J. Wang *et al.*[302] *Ab initio* global searches also suggested the existence of other neutral borospherenes, such as a D_{2h} cage for B_{38}[303] and a chiral C_2 cage for B_{44}.[304] However, quasi-planar isomers compete and the charge state of the boron cluster also affects its atomic structure in this size range of around 40 atoms, while smaller boron clusters are usually planar or quasi-planar or ring-shaped.[66] An interesting question is, whether the cage structures of B_{40} cluster and smaller ones can be stabilized by endohedral doping.

Intuitively, the borospherenes have suitable size (e.g., 6.2 Å diameter for B_{40}[300]) that should make them ideal hosts for enclosing various foreign atoms to form endohedral borospherene derivatives, just like the endohedral carbon fullerenes. Note that carbon fullerenes have only pentagons and hexagons but borospherenes can have triangles and higher polygons such as pentagons, hexagons, heptagons, and octagons. Q. Xu *et al.*[305] have reported that atoms with radius in the range of 1.60 Å (such as Sc) and 2.15 Å (such as Ba) could be candidates for endohedral doping in borospherene. This limits the choice of dopant atoms, but other factors besides size could be very important for the stability. After examining several dopants in B_{28} and B_{38}, $Ti@B_{28}$ as well as $M@B_{38}$ (M = Ca, La) were found to be excellent candidates to form metalloborospherenes. The geometric structures of previously reported $M@B_n$ metalloborospherenes (n = 28, 32−40, 44) are presented in Figure 16, in which $Ti@B_{28}$ and $M@B_{38}$ correspond to Figure 16a and Figure 16e, respectively.

To date, extensive DFT calculations have been carried out to explore the structure, stability, electronic properties, and potential applications of endohedral B_{40} cages doped with different atoms.[306−320] The essential theoretical results, including cluster symmetry, HOMO−LUMO gap, embedding energy, VIP, and VEA, are summarized in Table 4. For B_{40} cage encapsulating a single guest atom, the computed embedding energies are in the range of 1.479 eV (for Na[308]) to 8.22 eV (for U[315]), meaning that the encapsulation process is in general exothermic. For guest atoms of many transition metals or rare earth elements, the embedding energies in B_{40} are comparable to those of the experimentally synthesized endohedral $M@C_{82}$ (M = Sc, Y, La) metallofullerenes, e.g., 5.516 eV for $Sc@B_{40}$ versus 5.663 eV for $Sc@C_{82}$, 5.902 eV for $Y@B_{40}$ versus 5.941 eV for $Y@C_{82}$, 5.880 eV for $La@B_{40}$ versus 6.145 eV for $La@C_{82}$, computed at the same level of theory (PBE functional, 6-311+G(d) basis for boron or carbon and LanL2DZ basis for metal atoms).[307] Hence, from the thermodynamic point of view, all these proposed metalloborospherenes in Table 4 could possibly be synthesized in the laboratory.

As schematically shown in Figure 16g, upon relaxation most of the guest atoms (M = Ca, Sc, Y, La, Li, Na, K, Ti, Tl, Gd) prefer an off-center position inside the B_{40} cage, resulting in a lower point group symmetry of $M@B_{40}$ metalloborospherene (C_{2v}, C_s, or even C_1), whereas some metal atoms (M = Ba, Sr, U, Eu) stay at the cage center to preserve the original D_{2d} symmetry of the B_{40} cage. Note that there is an energetic competition between the endohedral and exohedral positions for an M atom interacting with the B_{40} cage. For example, it was found that Cu, Ag, and Au atoms can form both exohedral and endohedral derivatives with B_{40}, i.e., $M\&B_{40}$ and $M@B_{40}$ (M = Cu, Ag, Au). But the exohedral metalloborospherenes are energetically more favorable by 1 eV (for Cu), 1.19 eV (for Ag), and 2.5 eV (for Au).[311] Similarly, some alkali metal dopants such as Li and K prefer the exohedral adsorption site rather than the endohedral position.[308,310]

In addition to the single atom dopants, Chojecki *et al.*[316] examined the stability of endohedral and exohedral complexes of the B_{40} cage interacting with small molecules such as H_2, N_2, H_2O, and CO_2 using DFT calculations at the B97-D/cc-pVTZ level with dispersion correction. They found that none of the

Table 4. Summary of the Theoretical Results of the HOMO−LUMO Gap (E_{HL}), on-Site Charge (Q) on M, Embedding Energy (E_{em}), and VIP and VEA for Endohedrally Doped M@B_{40} Borospherenes Where M Denotes the Endohedral Atom or Cluster[a]

Cluster	Method	Symmetry	E_{HL} (eV)	Q (|e|)	E_{em} (eV)	VIP (eV)	VEA (eV)
Ca@B_{40} [306]	PBE0/6-311+G(d)	C_{2v}		1.60	3.565	5.94	
Sr@B_{40} [306]	PBE0/6-311+G(d)	D_{2d}		1.58	3.404	5.90	
Sc@B_{40} [307]	PBE/6-311+G(d), LanL2DZ	C_s	0.44		5.516	5.90	2.39
Y@B_{40} [307]	PBE/6-311+G(d), LanL2DZ	C_{2v}	0.40		5.902	5.74	2.38
La@B_{40} [307]	PBE/6-311+G(d), LanL2DZ	C_{2v}	0.32		5.880	5.67	2.38
Na@B_{40}[308]	PBE0/6-311+G(d)	C_{2v}	1.45	0.89	1.479	5.69	2.43
Ba@B_{40} [308]	PBE0/6-311+G(d), SDD	D_{2d}	1.63		3.768	6.19	2.39
Zn@B_{40} [320]	PBE/6-31G(d), LANL2DZ	C_{2v}	1.00		1.806		
Sc_3N@B_{40} [309]	B3LYP/6-31G(d,p)	C_{2v}	1.50			5.23	
Sc_2C_2@B_{40} [309]	B3LYP/6-31G(d,p)	C_1	1.13			5.08	
Ti@B_{40} [312]	PBE/6-311+G(d), SDD	C_1	0.74	0.37	5.112		
Ti_2@B_{40} [312]	PBE/6-311+G(d), SDD	C_s	0.86	1.17	9.319		
Eu@B_{40} [313]	PBE/6-311+G(d), CEP-31G	D_{2d}	0.72, 0.76	0.86	4.185	6.13	2.21
Gd@B_{40} [313]	PBE/6-311+G(d), CEP-31G	C_s	0.84, 0.36	0.88	4.883	5.79	2.38
Ba@B_{40} [314]	PBE+TS/DNP	D_{2d}	0.74		3.953		
U@B_{40} [315]	PBE/TZ2P	D_{2d}	0.76	0.53	8.22		

[a] For Eu@B_{40} and Gd@B_{40}, the molecular orbitals are spin polarized and two values of E_{HL} corresponding to spin-up and spin-down states are given. A positive value of Q means electrons are transferred from the M atom to the B_{40} cage.

resulting endohedral complexes was thermodynamically stable. Interestingly, the B_{40} cage is even able to accommodate a Ti_2 dimer with an appreciable embedding energy of 9.319 eV, but there is a noticeable deformation of the cage framework.[312] Also Sc_3N and Sc_2C_2 molecules have been embedded in B_{40} and the resulting endohedral cages have low VIP of 5.23 and 5.08 eV, respectively.[309] At present, no endohedral borospherene has been produced in the laboratory in this size range, though *ab initio* calculations do indicate the stability of such species. Also, it is quite possible that other metal dimers or aggregates or molecules can form stable endohedral complexes with B_{40} borospherene, which deserves further theoretical and experimental studies.

Population analyses of different M@B_{40} metalloborospherenes reveal that M atom or dimer donates some charge (between 0.37 electrons and 1.60 electrons) to the B_{40} host cage. But there is also back-donation from the negatively charged B_{40} cage to the unoccupied orbitals of the M dopant.[306,312,313] Therefore, the amount of the charge transfer is less than the formal charge of the M atom. Owing to the interaction between the dopant and boron cage, the HOMO−LUMO gap of M@B_{40} metalloborospherene is significantly reduced compared with that of the bare B_{40} cage (E_{HL} = 1.77 eV from PBE/6-311+G(d) calculation,[307] and E_{HL} = 3.13 eV from PBE0/6-311+G(d) calculation[300]). Also note that for all these M@B_{40} metalloborospherenes, the VEA is less than 2.5 eV, suggesting that they can accept electrons.[312,313]

The potential applications of the endohedral B_{40} cages have been explored by DFT calculations, such as gas sensor,[314,317] nonlinear optical material,[310] molecular electronics,[318] and spintronic devices.[319] It was predicted that acetone molecule can easily chemisorb on Ba@B_{40} from physisorption state with a small energy barrier of 0.116 eV and that the adsorption strength is moderate to ensure a short recovery time.[314] Using the nonequilibrium Green's function method, Y. An *et al.*[318] have computed the conductance of B_{40} cage to be about 130 μS. After endohedral doping, the central Sr atom acts as a bridge and provides more channels for the electron transmission, thus increasing the conductance to 200 μS. With the same theoretical technique, W. Wang *et al.*[319] explored spin-dependent transport properties of a series of M@B_{40} metalloborospherenes (M = Fe, Mn, Co, Ni) in contact with Au electrodes. For an individual Fe@B_{40} cluster, the on-site magnetic moment for Fe atom is reduced to about 2 μ_B, while for Mn@B_{40} the value is about 1.5 or 2.9 μ_B, depending on the location of the Mn dopant. The reduction in the magnetic moment is due to significant interaction between the metal atom and the boron cage. Furthermore, it has been shown that the transmission spectra of Fe@B_{40} and Mn@B_{40} metalloborospherenes are spin polarized, and those of Ni@B_{40} are spin-unpolarized. Interestingly, the transmission of Co-doped borospherenes could be either spin-polarized or unpolarized, depending on the encapsulation site of Co atom as well as the electrode−molecule distance, which can be ascribed to the screening effect of the Au electrodes.

In addition to the endohedral B_{40} cages discussed above, other medium-sized B_n cages (n = 28, 36, 37, 38, 39, 44) encapsulating various guest atoms, ions, or clusters have also been explored theoretically by many groups.[305,321−328] Their structures are shown in Figure 16, and the key results are summarized in Table 5. The general behavior of these endohedral boron cages is similar to that of the M@B_{40} metalloborospherenes. Briefly speaking, encapsulation of a foreign M atom (M = Ca, Sr, Ba, Sc, Ti, Y, La, Th, U) in these boron cages is exothermic with embedding energy in the range of 2.814 eV to 9.670 eV, further suggesting the existence of a large family of endohedral borospherene derivatives. By examining a number of endohedral and exohedral MB_n (n = 28, 38, 40) clusters, Q. Xu *et al.*[305] have discussed the effects of size match between the M atom and borospherene and found that the acceptable radius for a guest atom M to be incorporated in a boron cage is between 1.40 Å (Ti) and 1.95 Å (La) for B_{38} and between 1.60 Å (Sc) and 2.15 Å (Ba) for B_{40}, respectively. However, the relative stability of the endohedral and exohedral complexes of borospherenes depends on not only the size of the M atom but also the specific interaction between the dopant atom and the boron cage. For example, the atomic radius of Tl (1.90 Å) is close to that of Na (1.80 Å), Ca (1.80 Å), and Sr (2.00 Å); but Tl prefers to form an exohedral complex (Tl&B_{40}), while the endohedral M@B_{40} complexes are more

Table 5. Summary of Theoretical Results on Endohedrally Doped M@B_n Cages (n = 28, 36, 37, 38, 39, 44; and M Denotes the Endohedral Atom or Cluster)[a]

Cluster	Method	Symmetry	E_{HL} (eV)	Q (|e|)	E_{em} (eV)	VIP (eV)	VEA (eV)
Ti@B_{28} [305]	PBE/6-311+G(d), LanL2DZ	C_1	1.58		8.01	7.32	2.23
La@B_{38} [305]	PBE/6-311+G(d), LanL2DZ	D_{2h}	0.63, 0.68		4.08	5.93	2.38
U@B_{36} [321]	PBE0/6-311+G(d), ECP60MWB-SEG	C_{2h}	2.80	0.66	9.10	6.10	2.15[a]
$[Ca@B_{37}]^-$ [322]	CCSD(T)/6-311G(d)	C_s	1.94	1.71			
Gd@B_{38} [313]	PBE/6-311+G(d), CEP-31G	C_{2h}	0.58, 0.76	0.219	6.57	5.94	2.30
Th@B_{38} [321]	PBE0/6-311+G(d), ECP60MWB-SEG	D_{2h}	1.70	0.42	9.67	5.89	1.87[a]
Sc@B_{38} [323]	PBE/DNP	C_{2v}	0.58		5.22	6.05	2.47
Y@B_{38} [323]	PBE/DNP	C_{2v}	0.45		5.54	5.96	2.39
Ti@B_{38} [323]	PBE/DNP	C_{2v}	0.78		6.07	6.36	2.43
Ca@B_{38} [324]	PBE0/6-311G(d)	C_s	2.70	1.69	5.538	7.35	2.44[a]
$[Ca@B_{39}]^+$ [325]	PBE0/6-311+G(d)	C_3	3.06	1.58	5.18		
$FLi_2@B_{39}$ [326]	PBE0/6-311+G(2d)	C_1			1.99	7.34	2.20
Ca@B_{44} [327]	PBE/6-311+G(d)	C_2	0.77	0.739	4.48	6.52	2.74
Sr@B_{44} [327]	PBE/6-311+G(d), LanL2DZ	C_1	0.76	0.730	2.81	6.48	2.74
Ba@B_{44} [327]	PBE/6-311+G(d), LanL2DZ	C_1	0.73	0.756	2.93	6.50	2.77

[a]The values of the HOMO−LUMO gap (E_{HL}), on-site charge (Q) on M, embedding energy (E_{em}), VIP, and VEA are given. For Gd@B_{38}, the molecular orbitals are spin polarized and two values of E_{HL} corresponding to spin-up and spin-down states are given. A positive value of Q means electrons are transferred from the M atom to the B_n cage. [b]ADE instead of VEA as given in refs 321 and 324.

stable for M = Na, Ca, and Sr[306,308]. As for the B_{38} cage, Li (1.45 Å), Nb (1.45 Å), Mg (1.50 Å), Na (1.80 Å), and Fe (1.40 Å) all have atomic radii within the preferred range, but these atoms tend to stay outside the cage. Moreover, the number of delocalized electrons that contribute to the whole aromaticity ($\sigma + \pi$) should be taken into account for the stability and electronic properties of the endohedral cages. A good example is Ca@B_{38} (Figure 16e) with a sizeable HOMO−LUMO gap of 2.7 eV using the PBE0 functional (Table 5).[324] It has a large VIP of 7.35 eV and a small VEA (2.44 eV), suggesting chemical stability of this species. Note that doubly charged $[B_{38}]^{2-}$ is an aromatic cage with an NICS value of −37 ppm at the cage center. The encapsulated Ca atom donates two electrons to the B_{38} cage to satisfy the $\sigma + \pi$ double delocalization bonding requirement for a stable borospherene.[324] A similar picture of $\sigma + \pi$ double delocalization bonding is applicable to $[Ca@B_{39}]^+$ (Figure 16f),[325] leading to an exceptionally large HOMO−LUMO gap of 3.06 eV (PBE0) that is very close to the value for the bare B_{40} cage (3.13 eV[300]). Ti@B_{28} (Figure 16a) is also an interesting system as it has a large VIP and a small VEA. In this manner, endohedral doping is an effective way to provide excess valence electrons and thus to tailor the stability and electronic structure of borospherenes.

Among the endohedral borospherenes in Tables 4 and 5, several interesting magnetic species have been discovered, such as Gd@B_{38} (spin multiplicity = 9), Eu@B_{40} (spin multiplicity = 8), and Gd@B_{40} (spin multiplicity = 7)[313] with Gd (Eu) atom in the 3+ (2+) state and both Gd and Eu ions having f^7 spin-up states fully occupied. The Gd-doped boron cage can have spin multiplicity of 9 or 7 depending upon ferromagnetic or antiferromagnetic ordering between spins on Gd atom and the cage. The shortest distance between the M atom and these boron cages is 2.82 Å, 3.03 Å, and 2.75 Å, respectively, which are longer than the sum of the atomic radii of M and B atoms. The Gd (Eu) atom in Gd@B_{38} (Eu@B_{40}) resides at the cage center, whereas the Gd atom in Gd@B_{40} drifts from the cage center by about 0.46 Å, pointing to a hexagonal ring. These lanthanide-based endohedral metalloborospherenes, whose large magnetic moments stem mainly from the unpaired f electrons, are especially promising for applications in magnetic nanomaterials, biomedicines, and spintronics.

Similar to the previously reported 32-electron systems of metallofullerenes, namely, An@C_{28} (An = Th, Pa^+, U^{2+}, Pu^{4+}),[262] U@B_{36} (Figure 16c), Th@B_{38} (Figure 16e),[321] and U@B_{40}[315] can be regarded as novel 32-electron systems with fully occupied 1S, 1P, 1D, and 1F orbitals. Using the PBE0 functional, U@B_{36} has a large HOMO−LUMO gap of 2.80 eV and a large embedding energy of 9.10 eV, making it a very stable species. Th@B_{38} with large embedding energy (9.67 eV) as well as sizeable HOMO−LUMO gap (1.7 eV) is also an interesting species. As an example of 32-electron metalloborospherenes, the molecular orbital energy diagram and electron density difference map of U@B_{40} are shown in Figure 17. One can see strong participation of the atomic orbitals of U in the $1S^2 1P^6 1D^{10} 1F^{14}$ superatomic orbitals of U@B_{40} containing 32 electrons as well as characteristic of covalent bonding between the central U atom and the boron cage. The strong U−B_{40} interaction is further supported by the large embedding energy of 8.22 eV and the complete quenching of the quintet spin state for the encapsulated U atom. However, it is noteworthy that the HOMO-LUMO gap becomes smaller after doping, i.e., from 1.77 eV for bare B_{40} cage to 0.76 eV for U@B_{40} at the PBE/TZ2P level of theory.

For smaller B_n clusters with $n < 28$, cage configurations are no longer the ground states for bare boron clusters.[66] However, the electron deficiency and the tendency of boron to bind strongly with the metal dopant can modify the chemical bonding and electronic properties of pure boron clusters, as in the case of endohedrally doped silicon clusters that will be discussed in Section 5. It is therefore reasonable to anticipate that the potential energy surface of boron clusters would be modified significantly by encapsulation of some metal atoms, which in turn may lead to the stabilization of some cages or other unstable or metastable structures of the pure B clusters. In the past few years, many experimental and theoretical studies have been performed and novel wheel-shaped, drum-shaped, bowl-shaped, and cage structures have been discovered for the metal doped boron clusters.

At the PBE0/6-311G(d), SDD level of theory, Lv *et al.*[60] searched the potential energy surface of B_{24} clusters doped by a

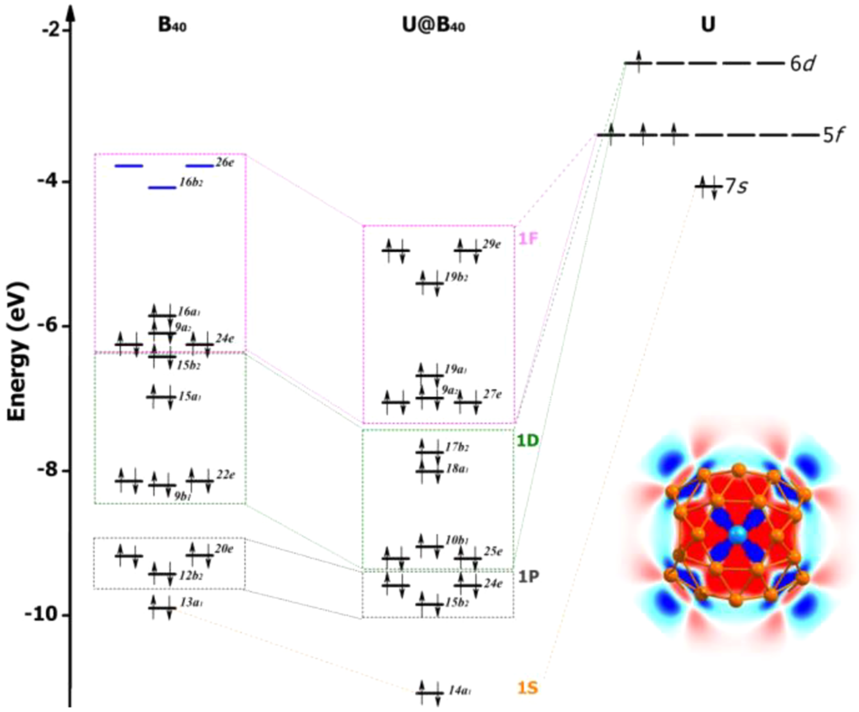

Figure 17. PBE/TZ2P-level molecular orbital energy diagrams of B_{40}, U, and U@B_{40}. The electron density difference map of U@B_{40} is shown in the lower right corner with regions of increased and decreased electron density indicated in red and blue, respectively (isovalue = 0.002). Reproduced with permission from ref 315. Copyright 2017 Springer Nature.

series of transition metal atoms (M = Ti, Zr, Hf, Cr, Mo, W, Fe, Ru, Os) using particle swarm optimization algorithm with DFT calculations. They found that the low-lying energy regime of these M-doped B_{24} clusters is generally dominated by endohedral cage-like isomers. In particular, a highly symmetric D_{3h} cage of B_{24} was reported to be stabilized by encapsulation of a Mo (W) atom, exhibiting a large binding energy of 5.37 eV/atom (5.43 eV/atom) and a sizeable HOMO−LUMO gap of 4.21 eV (4.18 eV) at the PBE0/6-311G(d) level of theory. As shown in Figure 18, there are six occupied π orbitals (1S, 1P, and two 1D orbitals namely $1D_{yz}$ and $1D_{xz}$) and three unoccupied π orbitals (remaining three 1D molecular orbitals) for the bare D_{3h} cage of B_{24}. Eight electrons in the four occupied π bonded orbitals (1S and 1P) interact relatively weakly with the atomic orbitals of the encapsulated Mo/W atom, whereas the *d* orbitals of Mo/W atom hybridize strongly with the 1D molecular orbitals of the boron cage. The bonding orbitals are fully occupied considering the six valence electrons of Mo (W) atom, thereby forming a stable 18-electron closed-shell configuration with a large HOMO−LUMO gap. In the case of Cr, though it belongs to the same group in the periodic table as Mo and W, its encapsulation leads to a different ground state structure of metalloborospherene due to its smaller atomic size and high spin state. The aforementioned endohedral D_{3h} cage was actually obtained for Cr@B_{24} cluster from AIMD simulation by L. Liu *et al.*,[329] which however is 0.33 eV higher in energy than the C_1 cage isomer, and has a total spin moment of 2 μ_B according to the *ab initio* calculation and global search by Lv *et al.*.[60]

Similar to Mo@B_{24} (or W@B_{24}), a highly stable endohedral metalloborospherene with D_2 symmetry was predicted for $[Ta@B_{22}]^-$,[330] which follows the bonding pattern of $\sigma + \pi$ double delocalization and conforms to the 18-electron rule. Such kind of 18-electron superatom with a universal $\sigma + \pi$ pattern can be further extended to a series of possibly multiply charged endohedral metalloborospherene with 23 to 28 B atoms, i.e., Ta@B_{23} (C_2), $[Ta@B_{24}]^+$ (C_2), $[Ta@B_{24}]^-$ (C_{2v}), Ta@B_{25} (C_1), $[Ta@B_{26}]^+$ (D_{2d}), $[Ta@B_{27}]^{2+}$ (C_2), and $[Ta@B_{28}]^{3+}$ (C_2).[331] Interestingly, the central Ta atom inside the $[Ta@B_{28}]^{3+}$ cage interacts with 28 B atoms, which is the highest coordination number in the spherical environment known in chemistry. A detailed *ab initio* study of Cr, Mo, and W doping has also been carried out for B_n clusters with n = 18, 20, 22, and 24 by Rahane *et al.*[332] It has been shown that a drum-shaped structure is favored for MB_{18} (M = Mo, W), while a bicapped drum is favored for CrB_{18} (B_{16} drum) and MB_{20} (M = Mo, W; B_{18} drum). Also, a cage structure has been obtained for Cr@B_{20}, M@B_{22}, and M@B_{24} for M = Cr, Mo, and W. Similar to the results by Lv *et al.*,[60] the Cr@B_{24} cage is distorted with some of the Cr−B bonds being elongated and the endohedral Cr atom does not interact with all the boron atoms strongly.

To gain insights into the structural evolution and formation of metalloborospherenes, extensive *ab initio* global searches have been conducted on metal doped boron clusters within certain size ranges, including FeB_n (n = 14, 16, 18, 20),[333] $[MnB_n]^{-/0/+}$ (n = 10−20),[334] MoB_n (n = 10, 12, 14, 16, 18, 20, 22, 24),[335] $[RuB_n]^{-/0}$ (n = 9−20),[336] CrB_n (n = 8, 10, 12, 14, 16, 18, 20, 22),[337] $[TaB_n]^{-/0}$ (n = 10−20),[338] and MB_n (M = 3*d*, 4*d*, 5*d* transition metal; n = 14, 16).[339] The structures for some representative M@B_n cage clusters (neutral or charged) with n = 18−24 are presented in Figure 19. In general, the M-encapsulated cage configuration appears as the doped boron cluster grows big enough. However, the critical size for the emergence of stable endohedral cage relies on the doping element M. For instance, cage formation occurs at n = 18 for Fe, n = 19 for Mn, n = 20 for Ru and Cr, and n = 22 for Mo, respectively. There is a delicate balance between the atomic

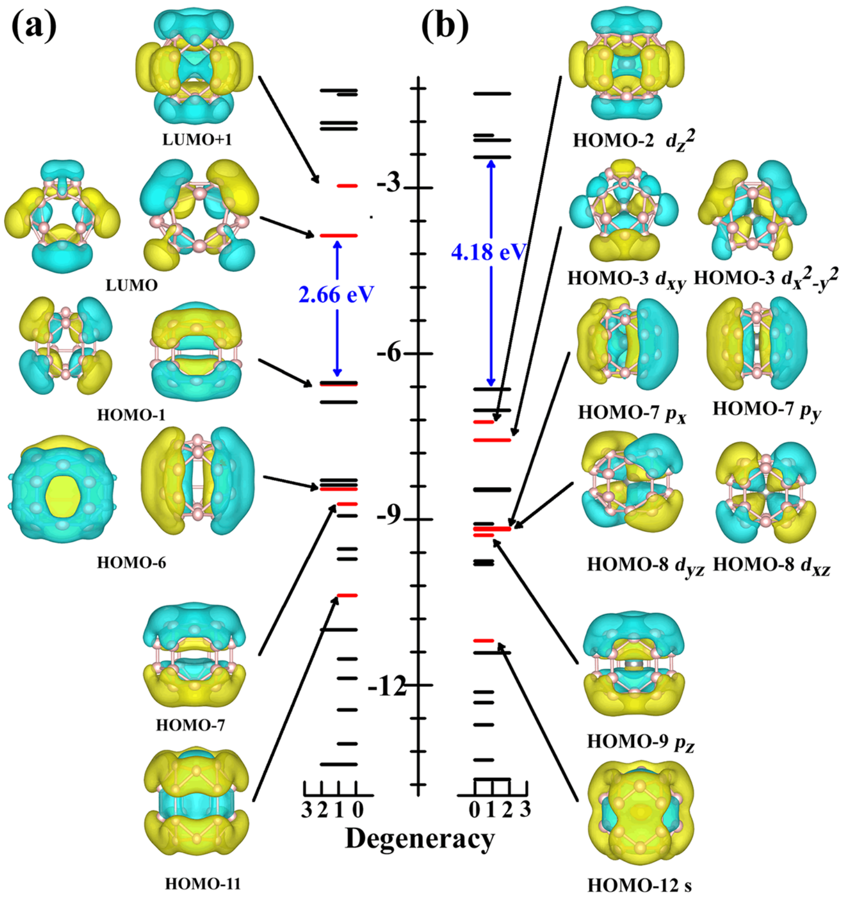

Figure 18. Eigenvalue spectra versus electronic state degeneracy of (a) bare D_{3h}-B_{24} cage and (b) D_{3h}-W@B_{24}. For each case, the HOMO−LUMO gap is indicated (in blue). The π-orbitals with energy levels shown by red lines for (a) and the orbitals involving 18-electron closed-shell configuration in (b) are shown. Reproduced with permission from ref 60. Copyright 2015 Royal Society of Chemistry.

size of the dopant M, M−B bonding strength, and electron count to fulfill the 18-electron rule. Indeed, Cr@B_{20}, [Mn@B_{20}]$^+$, and Mo@B_{22} belong to the 18-electron species, while Fe@B_{18} and Ru@B_{20} are not. This is quite similar to the cage formation by clusters of Si and Ge, as will be discussed in Sections 5 and 6.1 later.

The key theoretical results on endohedrally doped M@B_n cages (n = 18, 20, 22, 24) are summarized in Table 6. Except Zn@B_{20} which is not a closed-shell species, most neutral M@B_n cages possess a rather large HOMO−LUMO gap (3.29−4.28 eV) using the PBE0 or mPW3PBE functional, and there is a considerable amount of charge transfer (in the range of 0.76 and 2.75 electrons) from the boron cage to the encapsulated metal atom. Note that [Ta@B_{24}]$^-$ anion is isoelectronic to W@B_{24}, and [Mn@B_{20}]$^+$ cation is isoelectronic to Cr@B_{20}; thus, both of them have a sizeable HOMO−LUMO gap of around 4 eV.[331,334]

Besides the cage structures, a drum-like structure has been obtained for M@B_{14} for M = Cr, Mn, Fe, Co, and Ni.[339] This drum has two B_7 rings in an antiprism configuration, and the M atom is sandwiched between the rings, as depicted in Figure 20f. It was shown that the isoelectronic [Co@B_{14}]$^-$ and Ni@B_{14} clusters correspond to electronic shell closing at 24 valence electrons within the disk jellium model,[340] with 14 π bonded electrons coming from the two boron rings, one electron from each boron atom, and 10 electrons from the M atom. Both these clusters have a large HOMO−LUMO gap (with PBE functional) of 1.81 and 1.73 eV, respectively, and the M atom locates at the center. However, for Fe@B_{14}, the Fe atom is displaced from the center toward one of the B_7 rings and the singlet state has the lowest energy with a HOMO−LUMO gap of 1.3 eV using the PBE functional. Using the TPSSh/6-311+G(d) method, Minh Tam *et al.*[333] reported a triplet state with the structure similar to that of Ni@B_{14}, but our calculations confirmed that the singlet state is 0.26 eV lower in energy than the symmetric triplet isomer.

Furthermore, a metal-centered B_{16} drum with two B_8 rings in an antiprism configuration (Figure 20g) has been reported by Popov *et al.*[341] from a combined experimental and theoretical study on [Co@B_{16}]$^-$. In experiments, the clusters were produced using a laser vaporization cluster source and characterized by photoelectron spectroscopy. According to DFT calculations, the Co atom lies between the rings and has a magnetic moment of 2 μ_B, and there are two nearly degenerate drum-shaped structures for [CoB_{16}]$^-$. There are 26 valence electrons (16 from the two B_8 rings and 10 from Co$^-$) so that the two additional electrons beyond the electronic shell closing for a disk jellium model lead to a triplet state. On the contrary, [CoB_{16}]$^+$ cation is a closed-shell system with 24 valence electrons and a singlet spin state. Note that elemental boron clusters in this size range are generally planar;[66] thus, doping of a metal atom transforms the most stable structures into bowl or drum or cage structure. *Ab initio* calculations on 24 valence electron M@B_{16} clusters led to drum-shaped structures of [M@B_{16}]$^-$ (M = Mn, Tc, Re), M@B_{16} (M = Fe, Ru, Os), and [M@B_{16}]$^+$ (M = Co, Rh, Ir).[339] The anion of the Mn@B_{16} cluster has a large HOMO−LUMO

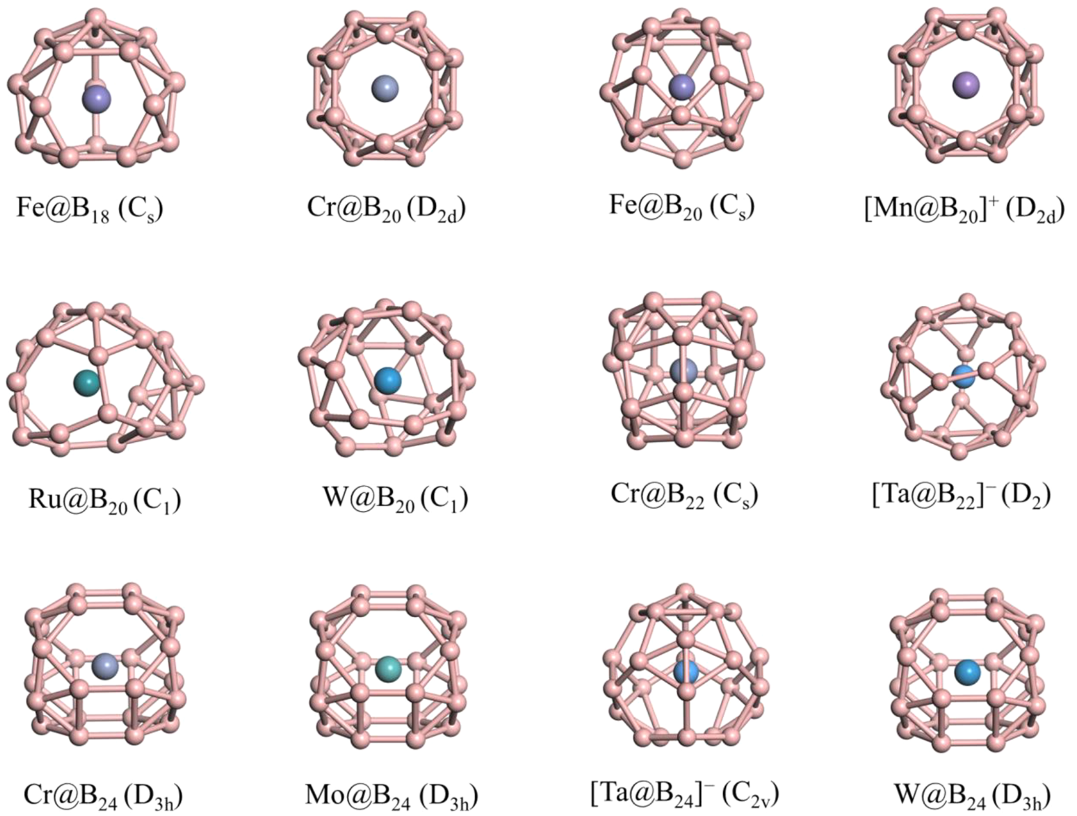

$Fe@B_{18}$ (C_s) $Cr@B_{20}$ (D_{2d}) $Fe@B_{20}$ (C_s) $[Mn@B_{20}]^+$ (D_{2d})

$Ru@B_{20}$ (C_1) $W@B_{20}$ (C_1) $Cr@B_{22}$ (C_s) $[Ta@B_{22}]^-$ (D_2)

$Cr@B_{24}$ (D_{3h}) $Mo@B_{24}$ (D_{3h}) $[Ta@B_{24}]^-$ (C_{2v}) $W@B_{24}$ (D_{3h})

Figure 19. Atomic structures of some representative $M@B_n$ cage clusters (neutral or charged) with $n = 18-24$ from PBE0/6-311+G(d), SDD calculations, showing the formation and evolution of the endohedral cage geometry. For each cluster, the symmetry is given in parentheses. The theoretical results are given in Table S4.

gap of 1.52 eV using the PBE0 functional, which supports the finding of this cluster in experiments.[342] B. Chen *et al.*[336] have also reported a drum-shaped structure for $[Ru@B_{18}]^{0/1-}$ and a similar drum structure for TaB_{18}. For TaB_{20}, a bicapped structure similar to MoB_{20} has been reported for neutral[338] and anionic[343] species. However, Fe and Ru dopants form an endohedral cage structure in the case of B_{20} with a large HOMO−LUMO gap of 2.1 and 2.20 eV (using PBE functional), respectively.

In Figure 19 and Table S4, we give an overview of the representative endohedral boron cages from our own PBE0 calculations. Clearly, endohedral doping with an appropriate transition metal atom can stabilize the B_n cages ($n = 18-24$) with radius of 2 Å to 2.5 Å, as evidenced by the substantial embedding energy of 6.265 eV to 17.995 eV. The largest value is obtained in the case of Ta doping and the smallest for Cr. The resulting metalloborospherenes have sizeable HOMO−LUMO gaps in the range of 3.188−4.534 eV and large binding energies of over 5 eV, suggesting their chemical and thermodynamic stabilities.

It is worth pointing out that the aforementioned endohedral metalloborospherenes are all from theoretical predictions. It remains a challenge to produce such clusters in the laboratory with a cluster beam apparatus as well as to characterize them using mass spectrometry, photoelectron spectroscopy, or infrared spectroscopy. However, many smaller metal-doped boron clusters with metal-centered monocyclic rings and metal-centered tubular structures have been produced in experiments by L. S. Wang's group[66,344,345] and characterized by photoelectron spectroscopy. The metal doped drum (or tubular) boron clusters have already been described above. In the following, we briefly discuss these metal-centered wheel-like boron clusters and anticipate that the endohedral metalloborospherenes would also be produced and confirmed from experiments in the near future.

The wheel-shaped doped boron clusters with a cyclic ring of boron and a metal atom at the center are endohedral species in two dimensions, and many such species have been studied from both experimental and theoretical aspects. First of all, it is interesting to note that the pure B_9^- cluster has a B_8 ring and a boron atom at the center[346] (Figure 20c). Saha *et al.*[340] have shown using the Laplacian of the electron density, bond critical points, bond ellipticity, and electron localization function that in such ring clusters, two electrons on each B atom on the ring can be considered to be covalently bonded with two neighboring atoms on the ring, leaving one electron delocalized. Accordingly, $[B_9]^-$ is a nice example of an all-boron wheel with effectively 12 delocalized valence electrons, corresponding to a magic number within a disk jellium model. It is also supported from the fact that this cluster has a large HOMO−LUMO gap of 4.12 eV using the PBE functional, suggesting its superior chemical stability. B_7 and B_8 are also boron-centered wheel-shaped clusters with 6-membered and 7-membered rings, respectively; but their HOMO−LUMO gaps (2.14 and 0.96 eV, respectively) are significantly smaller than that of $[B_9]^-$. These results suggest that in $[B_9]^-$ cluster the ring and center boron atoms behave differently. Again, $[B_8]^{2-}$ becomes special with a closed electronic shell.[346] Both $[B_8]^{2-}$ and $[B_9]^-$ have large NICS values[346] above the center of the cluster, suggesting the presence of σ and π aromaticity. Considering electronic equivalence of anion boron clusters and neutral boron clusters doped with a C atom, it was found that C doping is not favorable at the center in these boron clusters. However, P or

Table 6. Summary of Theoretical Results on Endohedrally Doped M@B_n Cages (n = 18, 20, 22, 24; and M Denotes the Endohedral Atom)[a]

Cluster	Method	Symmetry	E_{HL} (eV)	Q (|e|)	E_{em} (eV)	VIP (eV)	VEA (eV)
Fe@B_{18} [333]	TPSSh/6-311+G(d)	C_s		−1.00			
Fe@B_{20} [333]	TPSSh/6-311+G(d)	C_s					
Cr@B_{20} [337]	PBE0/6-311+G(d), Stuttgart	D_{2d}	4.28				
Cr@B_{22} [337]	PBE0/6-311+G(d), Stuttgart	C_s	3.92				
$[Mn@B_{20}]^+$ [334]	PBE0/6-311+G(d), Stuttgart	D_{2d}	4.53				
Zn@B_{20} [320]	PBE/6-31G, LanL2DZ	C_2	1.17	1.17	2.52		
Mo@B_{22} [335]	PBE0/6-311G(d), LanL2DZ	D_2	3.84	−0.76		8.26	1.61
Mo@B_{24} [335]	PBE0/6-311G(d), LanL2DZ	D_{3h}	3.75			8.33	1.30
Ru@B_{20} [336]	PBE0/6-311+G(d), Stuttgart	C_1	3.72	−1.95			
$[Ta@B_{24}]^-$ [331]	PBE0/6-311+G(d) , Stuttgart	C_{2v}	3.86	−1.27			
W@B_{20} [328]	mPW3PBE/6-31G, LanL2DZ	C_1	3.29	−1.52	8.05		
W@B_{24} [328]	mPW3PBE/6-31G, LanL2DZ	D_{3h}	4.02	−1.52	9.67		
Mo@B_{24} [60]	PBE0/6-311+G(d), Stuttgart	D_{3h}	4.21	−2.75		8.00	1.20
W@B_{24} [60]	PBE0/6-311+G(d), Stuttgart	D_{3h}	4.18	−2.59		8.03	1.26

[a] The values of the HOMO−LUMO gap (E_{HL}), on-site charge (Q) on M, embedding energy (E_{em}), VIP, and VEA are given. A negative value of Q means electrons are transferred from the B_n cage to the M atom.

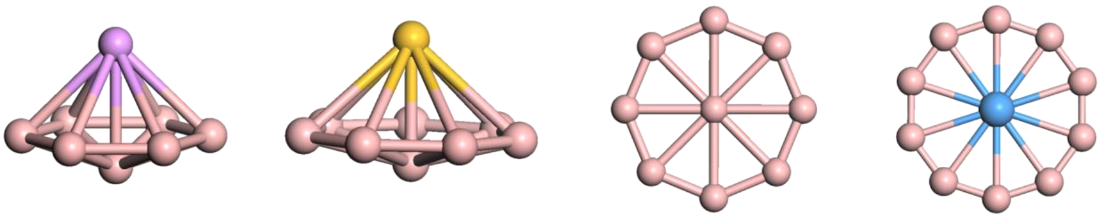

(a) B_7P (C_{6v}) (b) B_8Si (C_{7v}) (c) $[B_9]^-$ (D_{8h}) (d) $[TaB_{10}]^-$ (D_{10h})

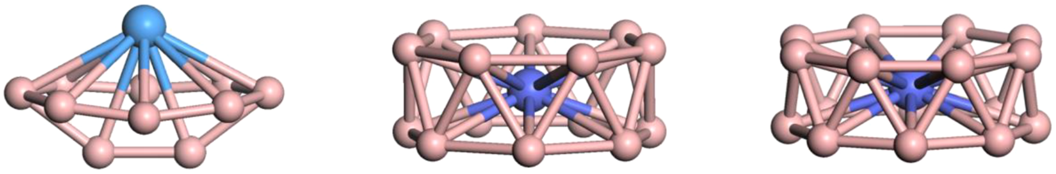

(e) $[TaB_{10}]^-$ (C_{2v}) (f) Co@B_{14} (D_{7d}) (g) Co@B_{16} (D_{8d})

Figure 20. Atomic structures of some representative small-sized MB_n clusters showing the evolution from umbrella-like (n = 7, 8, 10) to wheel-like (n = 10) and finally to drum-like structure (n = 14, 16). For each cluster, the symmetry is given in parentheses.

Si doping is very favorable and there are B_7P and B_8Si umbrella-shaped clusters (Figure 20a, b) with high stability and large HOMO−LUMO gaps of 3.29 and 4.3 eV (with PBE), respectively. Both clusters have closed electronic shells with 12 valence electrons and are magic. This is further supported by their very large ionization potentials (9.03 and 8.76 eV) and small vertical detachment energies (1.16 and 1.96 eV), respectively.

Ito *et al.*[347] have studied a series of doped planar cyclic clusters of boron, i.e., $[CoB_8]^-$ with D_{8h} symmetry, $[FeB_9]^-$, CoB_9, and $[NiB_9]^+$ with D_{9h} symmetry. Following the electron count given above, all these wheel-shaped clusters correspond to 18 valence electrons. We have performed a systematic DFT study (at the PBE0/6-311+G(d), SDD level) on ring (wheel) and bowl configurations for a large number of possible boron clusters with 8 to 10 atoms and doped them with different transition metal atoms so that we have the ring clusters with effectively 18 valence electrons. It was found that a wheel structure with the transition metal atom at the center is lower in energy than a bowl structure with the transition metal atom capping the bowl of B atoms (umbrella-shaped) for $[B_8Rh]^-$ (marginal), $[B_8Ir]^-$, B_8Pt (marginal), $[B_9Pt]^+$, $[B_9Ru]^-$, $[B_9Os]^-$, B_9Rh, B_9Ir, and $[B_{10}Re]^-$. Among them, $[B_8Rh]^-$, $[B_8Ir]^-$, and B_8Pt clusters have the metal atom lying slightly outside the ring, while the ring is deformed in the case of $[B_{10}Re]^-$. Interestingly, $[B_{10}Ta]^-$ is a Ta-centered wheel-shaped cluster without 18 valence electrons. This suggests that there may be other cases where wheel structure may be favorable without invoking 18 valence electrons. Recently, L. S. Wang and co-workers have reported wheel-shaped $[B_8Re]^-$ and $[B_9Re]^-$ clusters.[348] All the wheel structures are dynamically stable without imaginary frequency. In other cases, such as $[B_9Fe]^-$ and $[B_9Ni]^+$, we found that a bowl structure is lower in energy than the wheel structure. Galeev *et al.*[349] have reported a wheel configuration of $[TaB_{10}]^-$ and $[NbB_{10}]^-$, while W. L. Li *et al.*[350] have reported a wheel-like $[VB_{10}]^-$ cluster by comparing

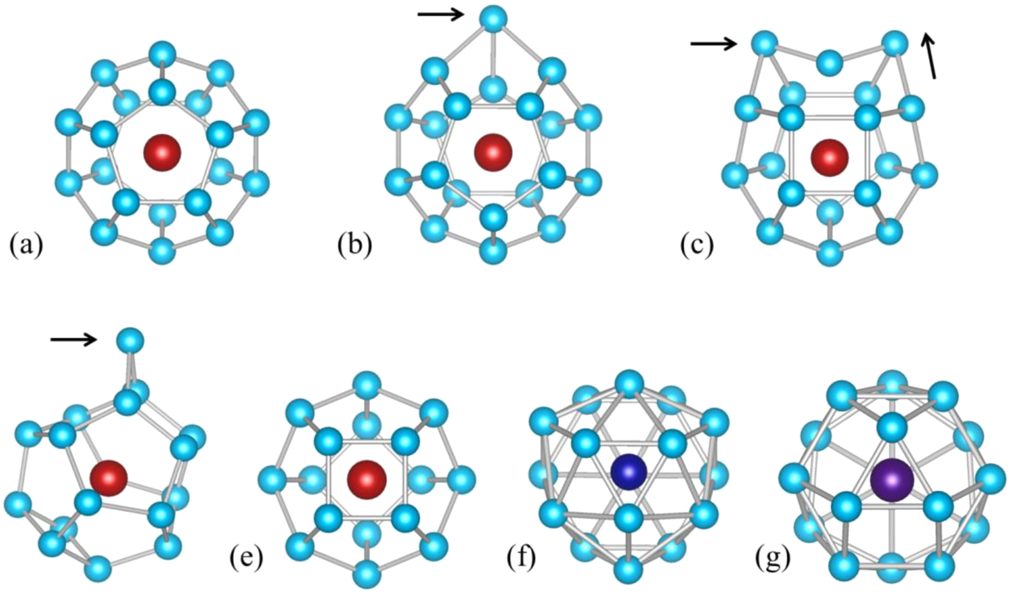

Figure 21. Shrinkage of the metal doped Si_{20} cage. (a) Dodecahedral Zr-encapsulated Zr@Si_{20}, (b−e) optimized structures of Zr@Si_{20}, Zr@Si_{19}, Zr@Si_{17}, and fullerene-like Zr@Si_{16}, respectively. The arrows indicate the atoms that were removed. The same structure (e) is obtained for Hf@Si_{16}. (f) The FK polyhedral structure of Ti@Si_{16}. (g) The deformed FK polyhedron of Hf@Si_{16}. Note that the FK isomer for Hf@Si_{16} is less stable than the fullerene-like structure in (e) by 0.006 eV/atom and in addition the triangle in the front showing 3-fold rotational symmetry rotates by 60° as shown in (g). The light blue balls represent Si atoms, and the central atom is M. For clarity, bonds connecting M to the cage atoms are not shown. Adapted with permission from ref 48. Copyright 2001 American Physical Society.

the photoelectron spectroscopic data with DFT calculations. We find that for $[TaB_{10}]^-$, the wheel structure is 0.189 eV lower in energy than a bowl structure and for Nb and V doping, the bowl-shaped structure becomes energetically favorable over a wheel structure. These two isomeric structures for $[TaB_{10}]^-$ are shown in Figure 20d, e. Pu *et al.*[351] have studied boron rings centered with hepta, octa-, nona-, and deca-coordinated 3*d* metal atoms and reported $[FeB_9]^-$ (D_{9h}) and $[VB_{10}]^-$ (D_{10h}) species. However, as discussed above, in both these cases, bowl structures are actually lower in energy than a wheel structure. Romanescu *et al.*[352] have reported $[Co@B_8]^-$ and $[Ru@B_9]^-$, both with 18 valence electrons, while $[MB_9]^-$ (M = Rh, Ir) have been studied by W. L. Li *et al.*.[353] Our results are consistent with these findings in the case of Rh doping; but for Co doping, a bowl structure is marginally lower in energy than a wheel structure. It is possible that the growth conditions in experiment may also affect the type of isomer present when more than one isomeric structure possesses comparable energies.

To summarize this section, *ab initio* calculations have led to exciting predictions of the stabilization of small carbon fullerenes with 20−28 carbon atoms by doping of a variety of transition metal and rare earth atoms. It is remarkable that M@C_{28} metallofullerenes with M = Ti, Zr, Hf, and U are endohedral species realized quite early in experiments. Hopefully, many successive theoretical predictions would stimulate more experiments. Also, in recent years great progress has been made in metal doped cage structures of boron. Similar to the cages of Si and many other elements discussed in subsequent sections, endohedral doping leads to transformation of small boron clusters into cages or rings or tubular structures. These new species could lead to new functionalization as well as derivatives of boron. Though experimental realization has succeeded in some cases, more efforts are desired to establish these new structures and explore their physical and chemical properties.

5. ENDOHEDRALLY DOPED SILICON CAGES

5.1. Theoretical Prediction of Doped Silicon Cages

Silicon is known as the backbone of modern microelectronics and the semiconductor industry. The miniaturization of electronic devices has motivated tremendous interest in silicon clusters and nanostructures.[354] *Ab initio* calculations and molecular beam electric deflection experiments revealed that the structures of very small Si_n clusters ($7 \leq n \leq 11$) are closed packed polyhedra or capped polyhedra[355,356]. In the size range of n = 12−20, the lowest-energy structures of Si_n clusters are mostly prolate in shape and built on two generic structural motifs: (1) the TTP Si_9 motif and (2) the Si_6/Si_6 (six-membered-puckered hexagonal ring Si_6 plus six-atom tetragonal bipyramid Si_6) motif.[51,52] For all the situations, there is a large portion of unsaturated Si atoms with dangling bonds on the cluster surface, which is undesirable for electronic device applications.

The discovery of carbon fullerenes[30] stimulated many efforts in searching for fullerene-like silicon cages.[354,357] However, unlike carbon that adopts both sp^3 and sp^2 bonding, silicon favors sp^3 bonding, as π bonding is much weaker than that in carbon. As a result, silicon solid does not exist in the graphite phase, and the hollow cage structures for silicon clusters are usually unstable. In 2001, Kumar and Kawazoe[48] performed *ab initio* calculations on the stabilization of a Si_{20} dodecahedron by encapsulating a Zr atom. As shown in Figure 21, the Zr@Si_{20} dodecahedral fullerene structure is deformed upon optimization. Shrinking the Si_{20} cage by removing Si atoms eventually led to an optimally bonded and highly symmetric Zr@Si_{16} cluster (D_{4h}). This Si_{16} fullerene-like cage is composed of eight pentagonal and two quadrilateral faces, and each silicon atom on the cage is three-fold coordinated as that in carbon fullerenes. Note that the Si_{16} fullerene cage is completely different from the ground state structure of pristine Si_{16}

Table 7. Summary of Previous Theoretical Studies on Doped Silicon Clusters $[\mathrm{M}_x\mathrm{Si}_n]^{q}$[a]

Method	System
HF/6-31G(d)	CuSi_n ($n = 4, 6, 8, 10, 12, 14$) [477]
MP2/6-31G(2df, p)	CuSi_n ($n = 4{-}10$) [445]
Quantum Monte Carlo	$\mathrm{Cr@Si}_{12}$ [368]
LDA/Gaussian orbital basis set	$\mathrm{Zr@Si}_{20}$ [46]
LDA/TZP	$[\mathrm{TaSi}_n]^+$ ($n = 1{-}13, 16$) [388]
GGA/TZ2P	MSi_n ($n = 1{-}14$; M = Cr, Mo, W, Mn, Tc, Re, Fe, Ru, Os, Co, Rh, Ir) [375]
BP86/TZP	TaSi_n ($n = 1{-}13$) [382]; YSi_n ($n = 1{-}16$) [407]; $\mathrm{M@Si}_{12}$ (M = Ti, V, Cr, Mn, Fe, Co, Ni, Cu, Zn) [448]
BP86/6-311+G(d)	$[\mathrm{Mn@Si}_{14}]^+$ [474]
B3P86/6-311+G(d)	$\mathrm{M@Si}_{12}$ (M = Sc, Ti, V, Cr, Mn, Fe, Co, Ni) [451]
PW91/planewave	MSi_n ($n = 14{-}17$; M = Cr, Mo, W) [358]; MSi_n ($n = 8{-}12, 14$; M = Be, Mg, Zn, Cd, Sn, Mn) [67]; YSi_n ($n = 4{-}20$) [370]; $\mathrm{M@Si}_{10}$ (M = Ni, Pd, Pt) [58]; CrSi_n ($n = 8{-}17$) [362]; MSi_n ($n = 8{-}16$; M = Ti, Cr) [364]; MSi_n ($n = 8{-}16$; M = Ti, Zr, Hf) [365]; $\mathrm{Th@Si}_{20}$ [366]; MSi_{20} (M = Y, La, Sm, Gd, Tm, Ac) [367]; $\mathrm{W@Si}_{12}$, $\mathrm{Ti@Si}_{15}$, $\mathrm{Ti@Si}_{16}$ [395]; $\mathrm{M@Si}_{12}$ (M = Ti, Cr, Zr, Mo, Ru, Pd, Hf, Os) [435]
PW91/DNP	CoSi_n ($n = 2{-}13$) [387]; FeSi_n ($n = 2{-}14$) [389]; CoSi_n ($n = 2{-}14$) [399]; LaSi_n ($n = 1{-}21$) [408]; EuSi_n ($n = 1{-}13$) [413]; NiSi_n ($n = 1{-}17$) [416]; MnSi_n ($n = 1{-}15$) [420]; $\mathrm{Eu@Si}_{20}$ [422]; GdSi_n ($n = 1{-}17$) [428]; HoSi_n ($n = 1{-}12, 20$) [437]
PW91/TZP	MSi_n ($n = 1{-}14$; M = Ti, Zr, Hf, V, Nb, Ta, Ni, Pd, Pt, Cu, Ag, Au) [394]
PW91/LanL2DZ	MSi_n ($n = 9{-}20$; M = Ti, Zr, Hf) [410]; MSi_n ($n = 14{-}20$; M = Ti, Zr, Hf) [411]; MSi_n ($n = 8{-}20$; M = Ti, Zr, Hf) [412]
B3PW91/LanL2DZ	$\mathrm{M@Si}_{16}$ (M = Ti, Zr, Hf) [359]; $\mathrm{M@Si}_{12}$ (M=Hf, Ta, W, Re, Os, Ir, Pt, Au) [390]; $\mathrm{M_2@Si}_{20}$ (M = V, Cr, Co, Zr, Mo, Hf, Re, Fe, Os, Ni, Pd, Pt, Cu, Ag) [415]; AuSi_n ($n = 1{-}16$) [423]
B3PW91/6-311G(d,p)	$\mathrm{M@Si}_{16}$ (M = Ti, Zr, Hf) [359]
B3PW91/6-311+G(d, p)	$\mathrm{M@Si}_{16}$ (M = Ti, Zr) [361]; $\mathrm{M@Si}_n$ ($n = 15, 16$; M = Sc, Ti, V, Cr, Mn, Fe, Co, Ni) [418]
PBE/NRLMOL basis[a]	CrSi_n ($n = 11{-}14$) [371]; FeSi_n ($n = 9{-}11$) [377]; FeSi_n ($n = 1{-}14$) [434]
PBE/planewave	$\mathrm{W@Si}_n$ ($n = 12, 14, 16$) [374]; MSi_n ($n = 10, 12, 14$; M = Nb, Ta, W) [378]; $\mathrm{Ti@Si}_{16}$ [396]; $\mathrm{M@Si}_{16}$ (M = Ti, Zr, Hf) [421]; $\mathrm{M@Si}_{16}$ (M = La, Ce, Pr, Nd, Sm, Eu, Gd, Tm, Yb, Lu) [119]; $\mathrm{M@Si}_{10}$ (M = Ni, Cu, Ag, Au) [436]; $\mathrm{M@Si}_{12}$ (M = V, Nb, Ta, Cr, Mo, W) [436]
PBE/DNP	$[\mathrm{V}_n\mathrm{Si}_{12}]^-$ ($n = 1{-}3$) [443]; $[\mathrm{V_3Si}_n]^-$ ($n = 3{-}14$) [444]
PBE/DZVP	$\mathrm{M@Si}_{12}$ (M = Sc, Ti, V, Cr, Mn, Fe, Co, Ni) [385]; $[\mathrm{M@Si}_n]^{-/0/+}$ ($n = 15{-}17$; M = Sc, Ti, V) [391]
PBE/DZP	$[\mathrm{ScSi}_n]^-$ ($n = 14{-}18$) [400]; MSi_n ($n = 14{-}18$; M = Sc^-, Ti, V^+) [401]; $[\mathrm{Ta@Si}_n]^+$ ($n = 14{-}18$) [426]
PBE/TZ2P	CrSi_n ($n = 6{-}16$) [440]; WSi_n ($n = 6{-}16$) [446]; FeSi_n ($n = 6{-}16$) [447]; $[\mathrm{Fe_2Si}_n]^{-/0/+}$ ($n = 2{-}12$) [459]
PBE/tier2	$[\mathrm{M@Si}_{16}]^+$ (M = Ti, Zr, Hf) [425]
PBE/6-311+G(d)	$[\mathrm{Cr}_n\mathrm{Si}_{15-n}]^{-/0}$ ($n = 1{-}3$) [460]; $[\mathrm{CoSi}_n]^{-/0}$ ($n = 3{-}12$) [466]
BLYP/DNP	NiSi_n ($n = 2{-}14$) [398]; MSi_n ($n = 8{-}16$; M = Sc, Ti, V, Cr, Mn, Fe, Co, Ni, Cu, Zn) [405]; LaSi_n ($n = 1{-}21$) [408]; $\mathrm{Eu@Si}_{20}$ [422]
B3LYP/cc-pVDZ	HoSi_n ($n = 12{-}20$) [452]; $[\mathrm{AuSi}_n]^-$ ($n = 4{-}12$) [454]
B3LYP/aug-cc-pVDZ	$[\mathrm{Ti_2Si}_{20}]^{-/0}$ [462]; $[\mathrm{Fe_2@Si}_{20}]^{-/0/+}$ [465]
B3LYP/DGDZVP	$[\mathrm{YSi}_n]^-$ ($n = 6{-}17$) [472]
B3LYP/TZP	$\mathrm{Cr@Si}_{12}$, $\mathrm{Mn^+@Si}_{12}$ [449]
B3LYP/TZVP	$\mathrm{Ni@Si}_{12}$ [393]; $\mathrm{M@Si}_n$ ($n = 10, 12$; M = Zn, Cu, Ni) [397]; $\mathrm{Ni@Si}_{12}$, $\mathrm{Cu@Si}_{12}$ [419]; $\mathrm{M@Si}_{20}$ (M = U^{6-}, Np^{5-}, Pu^{4-}, Am^{3-}, Cm^{2-}) [430]
B3LYP/aug-cc-pVTZ	$\mathrm{M@Si}_n$ ($n = 6{-}10$; M = Be, B^+, C^{2+}) [470]
B3LYP/aug-cc-pVTZ-PP	$[\mathrm{AuSi}_n]^-$ ($n = 4{-}12$) [454]
B3LYP/LanL2DZ	WSi_n ($n = 1{-}6; 12$) [373]; $\mathrm{M@Si}_{20}$ (M = Ba, Sr, Ca, Zr, Pb) [363]; MSi_n ($8 \leq n \leq 20$; M = W, Zr, Os, Pt, Co) [376]; $\mathrm{M@Si}_{12}$ (M = Cu, Mo, W) [379]; FeSi_n ($n = 1, 2, 5, 6, 10, 12, 14$) [380]; MSi_n ($n < 15$, M = V, Fe, Ni) [383]; ReSi_n ($n = 1{-}12$) [384]; ZrSi_n ($n = 1{-}16$) [386]; $\mathrm{M@Si}_{12}$ (M=Hf, Ta, W, Re, Os, Ir, Pt, Au) [390]; $\mathrm{M@Si}_{10}$ (M=Ni, Pd, Pt) [392]; $\mathrm{Mo_2Si}_n$ ($n = 9{-}16$) [402]; TiSi_n ($n = 2{-}15$) [403]; $\mathrm{Zr_2Si}_n$ ($n = 16{-}24$) [409]; $\mathrm{M_2@Si}_{20}$ (M = V, Cr, Co, Zr, Mo, Hf, Re, Fe, Os, Ni, Pd, Pt, Cu, Ag) [415]; $[\mathrm{AgSi}_n]^-$ ($n = 3{-}12$) [433]; $\mathrm{Pd_2Si}_n$ ($n = 10{-}20$) [438]; $[\mathrm{V_2Si}_{20}]^{-/0}$ [442]; $[\mathrm{NbSi}_n]^{-/0/+}$ ($n = 2{-}20$) [450]; $[\mathrm{NbSi}_n]^{-/0}$ ($n = 3{-}12$) [453]; $\mathrm{Pt_2Si}_n$ ($n = 10{-}20$) [457]; $[\mathrm{Nb_2Si}_n]^{-/0}$ ($n = 13{-}20$) [463]; $[\mathrm{Nb_2Si}_{20}]^{-/0}$ [464]; MSi_n ($n = 10, 12, 14$; M = Ag, Au) [473]
B3LYP/ECP28MWB	HoSi_n ($n = 12{-}20$) [452]
B3LYP/3-21G*(6d, 7f)	AgSi_n ($n = 1{-}15$) [429]
B3LYP/6-31G(d)	MSi_{10} (M = Li, Be, B, C, Na, Mg, Al, Si) [467]

Table 7. continued

Method	System
B3LYP/6-31+G(d)	Cu@Si$_n$ (n = 9–15) [406]; Cu@Si$_n$ (n = 9–14) [414]; MSi$_{14}$ (M = Sc, Ti, V, Cr, Mn, Fe, Co, Ni) [417]; CuSi$_n$ (n = 6, 8, 10, 12) [427]
B3LYP/6-311G(d)	MSi$_{12}$ (M = Sc, Ti, V, Cr, Mn, Fe, Co, Ni, Cu, Zr, Mo, W, Re, Os, Pt, Au) [381]
B3LYP/6-311+G(d)	CuSi$_n$ (n = 4, 6, 8, 10, 12) [372]; [CuSi$_n$]$^-$ (n = 4–18) [431]; [CrSi$_n$]$^-$ (n = 3–12) [432]; AgSi$_n$$^-$ (n = 3–12) [433]; [ScSi$_n$]$^-$ (n = 6–20) [439]; [NbSi$_n$]$^{-/0/+}$ (n = 2–20) [450]; [NbSi$_n$]$^{-/0}$ (n = 3–12) [453]; [Nb$_2$Si$_n$]$^{-/0}$ (n = 13–20) [463]; [Nb$_2$Si$_{20}$]$^{-/0}$ [464]
B3LYP/6-311+G(2d)	MSi$_{14}$ (M = Sc, Ti, V, Cr, Mn, Fe, Co, Ni) [417]
B3LYP/6-311+G(d, p)	M@Si$_n$ (n = 15, 16; M = Sc, Ti, V, Cr, Mn, Fe, Co, Ni) [418]
X3LYP/ECP56MHF	HoSi$_n$ (n = 12–20) [441]
X3LYP/6-31G	HoSi$_n$ (n = 12–20) [441]
HSE06/aug-cc-pVDZ, LanL2DZ	M@Si$_{16}$ (M = Ti, Zr, Hf) [461]
mPW2PLYP/aug-cc-pVTZ	[ScSi$_n$]$^{-/0}$ (n = 4–16) [458]
LDA, PBE, PBE0, B3LYP/planewave	M@Si$_{20}$ (M = Ba, Ca, Cr, Cu, K, Na, Pb, Rb, Sr, Ti, V, Zr) [424]
PBE, BLYP, B3LYP/DZP, TZP	M@Si$_{14}$ (M = V, Cr, Mn, Fe) [456]

[a] Here M denotes the dopant atom, x is the number of M atoms, n is the number of Si atoms, and q is the charge on the cluster. [b] NRLMOL basis sets are Gaussian-type basis functions supplemented by a diffuse Gaussian with a six s, five p, and three d basis set for silicon and seven s, five p, and four d basis set for transition metal atoms, as implemented in the NRLMOL code.[478,479]

cluster based on the "six/six motif".[51,52] Such structural transformation after encapsulating a metal atom can be ascribed to strong metal–silicon interaction, as evidenced by the large embedding energy of about 14 eV for Zr@Si$_{16}$. With the PW91 functional, the calculated HOMO–LUMO gap for Zr@Si$_{16}$ is about 1.58 eV, compared to 1.11 eV for the elemental Si$_{16}$ cluster. Therefore, the structural and chemical stabilities of metal encapsulated silicon clusters are largely enhanced with regard to the pristine silicon clusters. In this manner, symmetric fullerene-like cage structures of silicon can be stabilized by encapsulation of a metal atom, opening a new avenue toward novel silicon nanostructures.

For metal encapsulated silicon cages, Kumar and Kawazoe[48,49] further found a dependence of the cage geometry on the size of the metal atom. Encapsulation of a Ti atom that is isoelectronic with Zr but has a slightly smaller atomic radius leads to a more compact tetrahedral FK polyhedron for the Si$_{16}$ cage (Figure 21f), which is lower in energy than the fullerene isomer by 0.781 eV. Furthermore, incorporation of smaller atoms such as Mo and Fe is optimal in Si$_{15}$[358] and Si$_{14}$[48,49] cages, respectively. Therefore, it is possible to design novel silicon cage clusters with desired size and to tailor their electronic properties by encapsulating an appropriate metal dopant. For example, the HOMO–LUMO gap of Ti@Si$_{16}$ is 2.35 eV as predicted by PW91 calculation, which is notably larger than that of Zr@Si$_{16}$ (1.58 eV). In the case of Hf doping which lies in the same column as Ti and Zr in the periodic table, both the fullerene and the FK isomers becomes nearly degenerate, and a triangle of Si$_3$ (see the front triangle showing 3-fold symmetry of the FK isomer in Figure 21) rotates by 60° and we call this isomer as FK1.

Subsequently, extensive *ab initio* calculations by Kumar and co-workers[58,67,358−370] and many other groups[119,371−477] have been conducted on the endohedrally doped Si$_n$ cages with various metal dopants in different size range. Most of these theoretical calculations are briefly summarized in Table 7. Generally speaking, doping of most transition metal, lanthanide, and actinide atoms (except Ag) allows the formation of stable endohedral silicon cages. For AgSi$_n$ clusters up to n = 15, *ab initio* calculations[404,429] combined with anionic photoelectron spectroscopic data[433] revealed that their ground state structures are dominated by exohedral configurations with Ag atom occupying the surface sites, whereas endohedral cage configurations are metastable isomers and lie higher in energy (e.g., E_{em} = 3.221 eV for Ag@Si$_{10}$ with Ag-centered pentagonal prism structure[429]). Many other elements in the periodic table, such as He, Li, Be, B, C, F, Ne, Na, Mg, Al, Cl, K, Ca, Sr, Ba, Zn, Cd, Sn, and Pb, have also been explored as the dopant atoms or ions in silicon cages.[67,363,467−471]. But most of them are unable to form endohedral silicon cages as the ground states; instead, the dopants tend to adsorb on the cage surface or participate in the cage framework. The preference of encapsulating a transition metal or lanthanide atom to stabilize the silicon cage is attributed to the presence of partially occupied d (f) orbitals on the metal atom as well as the D (F) type molecular frontier orbitals of the silicon cage, leading to strong coupling between them. Also by varying the size of the guest atom, cages with different number of Si atoms can be stabilized, and similar stabilization of the cages of Ge, Sn, and Pb atoms has been achieved. These guest metal atoms are capable of forming strong multicenter bonds with the silicon atoms on the host cage. In the small size range such as Si$_{10}$, it is possible to encapsulate an atom with s-p valence electrons as is the case for Be@Si$_{10}$, which has a bicapped tetragonal antiprism of Si$_{10}$

encapsulating one Be atom at the center. This has been confirmed as the lowest-energy structure by two independent DFT-based structural searches[467,470] and will be further discussed later in Section 5.3.1.

In addition to the singly metal doped Si_n cages, stable endohedral Si_n cages ($n \leq 20$) doped with multiple metal atoms (up to three) have also been considered. For smaller cages with no more than 14 vertices, one metal dopant occupies the cage center, while the other one or two metal atoms stay on the surface sites and participate in the cage framework to form a silicon−metal polyhedron.[443,459,460,463,475] On the contrary, large Si_n clusters with $n \geq 16$ are able to accommodate two metal (M) atoms in the cage,[376,402,409,438,442,457,462−465] forming a variety of $M_2@Si_n$ endohedral complexes usually with ellipsoid or fused-cage shape. Beyond the Si_{20} host cage, Gao and Zeng[476] proposed that a tetrahedral fullerene cage Si_{28}, which is indeed the silicon counterpart of T_d-C_{28} fullerene, can be fully stabilized by encapsulating a tetrahedral 4-atom metal cluster, i.e., Al_4 or Ga_4. At the PBE/6-31G(d) level of theory, the resulting endohedral silicon fullerenes $Al_4@Si_{28}$ and $Ga_4@Si_{28}$ possess large embedding energies of 12.1 and 15.0 eV, substantial HOMO−LUMO gaps of 0.95 and 0.90 eV, and large negative NICS values of −36.4 ppm and −43.4 ppm, respectively, suggesting their satisfactory chemical and energetic stabilities.

5.2. Experimental Characterizations of Doped Silicon Clusters

The relative stability, adsorption reactivity, and vibrational, electronic, and magnetic properties of doped silicon clusters have been extensively investigated by different experimental techniques, including mass spectrometry,[36,37,47,54,55,57,480−486] anion photoelectron spectroscopy,[54,55,57,431−433,442−444,453,454,460,466,485−493] X-ray absorption spectroscopy,[56] XMCD spectroscopy,[493] valence band and core-level photoionization spectroscopy,[494] IR-MPD spectroscopy,[475,495−498] and tunable IR-UV2CI spectroscopy.[499] In the following subsections, we will present an overview of the most essential findings from these experiments, paying particular attention to the discovery and identification of endohedral silicon cages enclosing a metal atom.

5.2.1. Mass Spectra and Adsorption Reactivity.

Prior to the theoretical predictions, Beck[36,37] generated metal doped silicon clusters using a reaction between metal and silicon atoms in a supersonic jet and detected these clusters by laser photoionization time-of-flight mass spectrometry. As shown in Figure 22, there are strikingly high abundances of $Si_{15}M$ and $Si_{16}M$ clusters with M = Cr, Mo, and W and low abundances of clusters with other sizes. On the contrary, $CuSi_{10}$ is the dominant species in the mass spectrum of Cu-doped silicon clusters. Based on the observed abundance spectra, Beck hypothesized a possible scenario where the metal atom might have acted as a seed and the silicon atoms formed a cage structure with a certain number of atoms around it.

Later in 2006, Jaeger *et al.*[480] studied photodissociation of $[MSi_n]^+$ clusters (M = Cu, Ag, Cr). For Cu and Ag, photodissociation proceeds with the loss of metal atom, suggesting weaker metal−silicon bonds. While for $[Cr@Si_{15}]^+$ and $[Cr@Si_{16}]^+$, the dissociation occurs via the loss of silicon atoms, suggesting stronger metal−silicon bonding and more stable metal encapsulated structures. In the same year, Neukermans *et al.*[483] experimentally demonstrated the effects of the relative atomic sizes of the metal (M = Cr, Mn, Cu, Zn) and group 14 host (X = Si, Ge, Sn, Pb) atoms on the abundance of the metal encapsulated cage clusters. The results are summarized in Table 8. The peculiarly abundant sizes for $[MSi_n]^+$ are n = 15, 16 for Cr and Mn, n = 10 for Cu, and none for Zn, respectively. The doped cages of other group 14 elements will be discussed in Section 6. Besides metal encapsulation, Kaneko *et al.*[482] observed the formation of Ar-encapsulated Si cage clusters, among which $Ar@Si_{15}$ and $Ar@Si_{16}$ emerge as the magic clusters in the mass spectra.

In 2001, Hiura *et al.*[47] used an ion trap to produce $[MSi_nH_x]^+$ cluster ions from reaction of transition metal ions M^+ (M = Hf, Ta, W, Re, Ir, etc.) with silane SiH_4. Figure 23 shows the time-resolved quadrupole mass spectra of $[WSi_nH_x]^+$ cluster ions. One can clearly see that a sequential growth starts from W^+ and ends up with $[WSi_{12}H_x]^+$. For each type of metal atom, there is such a specific cluster size m where further reaction almost ceases, i.e., m = 14 for Hf, m = 13 for Ta, m = 12 for W, m = 11 for Re, and m = 9 for Ir. As n reaches m, the $[WSi_nH_x]^+$ cluster tends to lose all of the H atoms and the dehydrogenated $[MSi_n]^+$ dominates. By assuming that the metal atom is encapsulated in the Si_n cage and each Si atom on the cage contributes one electron to the central metal atom, Hiura *et al.* proposed an 18-electron rule to explain the high stability of WSi_{12} and other metal doped clusters (i.e., $HfSi_{14}$, $TaSi_{13}$, $ReSi_{11}$, $IrSi_9$). With a total of 18 electrons, the central W atom attains Rn-like closed electronic shell configuration ($[Xe]5d^{10}6s^26p^6$). Later, the same group further examined the reactions of small tungsten $[W_x]^+$ clusters (x = 1−5) with silane and their sequential reactions using mass spectrometry.[481] For each metal cluster size x, the Si or SiH_2 addition stops at some particular number of silicon atoms, i.e., n = 12 for x = 1, n = 17 and 18 for x = 2, n = 22 for x = 3, n = 25 and 26 for x = 4, and n = 29 for x = 5, suggesting that the small tungsten clusters are coated with silicon atoms.

Nakajima and co-workers[54,55,57,80,485−489] have carried out a series of experiments on transition metal and rare earth metal doped silicon clusters. They used a chemical probe method to deduce the molecular structure of $[TbSi_n]^-$ clusters by measuring their adsorption reactivity toward H_2O vapor.[485] In the size range of n = 10−16, they obtained low reactivity of clusters from the abundance in mass spectra and this suggested the encapsulation of Tb atom in silicon cages. Similarly, they measured the mass abundance spectra and H_2O adsorption reactivity of $[MSi_n]^-$ (M = Ti, Hf, Mo, W) cluster anions and concluded that $[MSi_n]^-$ is considerably stabilized by the metal encapsulated cage geometry at n = 15−16.[54] To confirm the theoretically predicted high stability of $Ti@Si_{16}$ cluster,[48] they measured the mass spectra of neutral $Ti@Si_n$ clusters and its isoelectronic counterparts, i.e., anionic $[Sc@Si_n]^-$ clusters and cationic $[V@Si_n]^+$ clusters.[55] As shown in Figure 24, MSi_{16} clusters were produced in high abundance exhibiting their magic behavior. These results were further supported by their nonreactivity toward H_2O adsorption, suggesting that the metal atom is well encapsulated in the silicon cage. Later, they examined the mass spectra of $M@Si_n$ clusters (M = Sc, Ti, V, Y, Zr, Nb, Lu, Hf) with different charge states. In addition to the known "magic clusters" of $[Sc@Si_{16}]^-$, $Ti@Si_{16}$, and $[V@Si_{16}]^+$, prominent peaks were observed for $Zr@Si_{16}$, $[Nb@Si_{16}]^+$, and $[Ta@Si_{16}]^+$.[486] Further measurement of the adsorption reactivity of MSi_n clusters toward H_2O vapor revealed a "threshold size" of nonreactivity for each type of these clusters, as summarized in Table 9. Above the threshold size, the metal atom is likely to be encapsulated within a silicon cage. The reactivity is, however, recovered upon the doping of a second metal atom. For a given series of transition metal

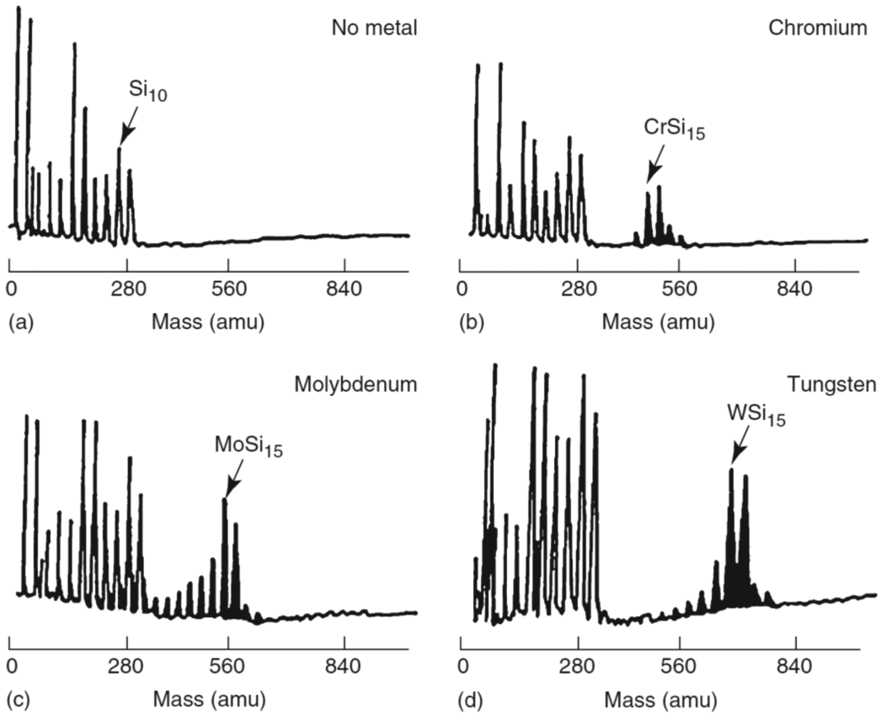

Figure 22. 193 nm photoionization mass spectra showing (a) bare silicon clusters formed by 532 nm laser vaporization of a silicon wafer. (b) Reaction products formed in a supersonic nozzle between chromium and silicon to form $CrSi_n$ clusters. (c and d) Results for $MoSi_n$ and WSi_n, respectively. The mixed metal−silicon peaks are darkened for emphasis while the undarkened peaks are due to bare silicon clusters. Reproduced with permission from ref 37. Copyright 1989 American Institute of Physics.

Table 8. Summary of the Particularly Abundant Sizes (n) for the 16 Different MX_n (M = Cr, Mn, Cu, Zn; X = Si, Ge, Sn, Pb) Combinations Studied[a]

M	Si_n	Ge_n	Sn_n	Pb_n
Cr	$(15, 16)^+$	$(14, 15, 16)^+$	$(10\text{-}16)^+$, $(10)^0$	$(10, 12)^{+,0}$
Mn	$(15, 16)^{(+)}$	$(14, 15, 16)^{(+)}$	$(13, 16)^+$, $(12)^{0,+}$	$(12)^{+,0}$
Cu	$(10)^+$	$(7, 10)^+$	$(10)^{+,0}$	$(10, 12)^{+,0}$
Zn			$(10, 12)^0$	$(12)^0$

[a] The charge state is indicated in the superscript. Reproduced with permission from ref 483. Copyright 2006 Elsevier B.V.

elements (3*d*, 4*d*, or 5*d*), the threshold cage size generally decreases from group 3 to group 5, conforming to the reduction of the atomic radius. Nakajima *et al.* further investigated the H_2O adsorption reactivity of $[M_{1,2}Si_n]^-$ (n = 6−20; M = Sc, Y, Tb, Ho, Lu) clusters,[487] and it was found to generally decrease with increasing number of Si atoms. The reactivity showed local minima at n = 12 and 16, implying the encapsulation of the metal atom in a silicon cage. Moreover, the lower reactivity at n = 16 with respect to that at n = 12 implies that the metal atom is completely enclosed by the silicon cage at n = 16.

On the basis of mass spectrometry, Janssens *et al.*[484] demonstrated that the molecular structures of transition metal doped silicon clusters can be probed by argon physisorption, based on the fact that argon atom does not attach to elemental silicon clusters but only to the metal doped clusters below a certain critical size. The critical sizes for Ar attachment, i.e., $[Si_{12}Ti]^+$, $[Si_{11}V]^+$, $[Si_{10}Cr]^+$, $[Si_7Co]^+$, $[Si_{11}Cu]^+$, may be related to the formation of endohedral singly metal doped silicon cages. In particular, the results of encapsulation at 13 and 12 Si atoms for Ti and V agree with those obtained from adsorption of H_2O as shown in Table 9.

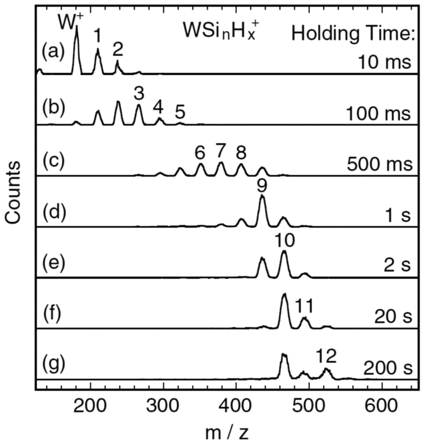

Figure 23. Time-resolved mass spectra of $[WSi_nH_x]^+$ cluster ions produced in the external quadrupole static attraction ion trap. Each spectrum was observed after a given holding time: (a) 10 ms, (b) 100 ms, (c) 500 ms, (d) 1 s, (e) 2 s, (f) 20 s, and (g) 200 s. The numbers shown above the peaks represent the number of Si atoms, n, in $[WSi_nH_x]^+$. Reproduced with permission from ref 47. Copyright 2001 American Physical Society.

5.2.2. Infrared Spectra.

During the past decade, IR-MPD combined with DFT calculations has been a powerful tool to identify the atomic structures of transition metal doped silicon cluster cations, including $[CuSi_n]^+$ (n = 6−11),[495] $[VSi_n]^+$ (n = 4−16),[495,496] $[MnSi_n]^+$ (n = 6−16),[497] $[NbSi_n]^+$ (n = 4−12),[498] $[CoSi_n]^+$ (n = 5−8), and $[Co_2Si_n]^+$ (n = 8−12).[475] Generally speaking, the IR spectra are dominated by modes related to Si_n moieties. For a given cationic cluster, the simulated IR spectrum of the lowest-energy structure from DFT calculations can usually explain the experimental one; however,

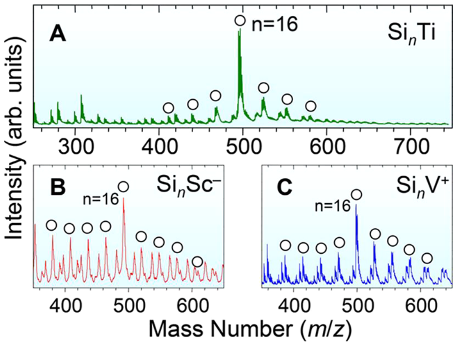

Figure 24. Mass spectra showing size-selective formation of (A) $TiSi_{16}$ neutral clusters, (B) $[ScSi_{16}]^-$ anions, and (C) $[VSi_{16}]^+$ cations. Reproduced with permission from ref 55. Copyright 2005 American Chemical Society.

sometimes higher energy isomers may exist in the molecular beam and therefore contribute to the experimental IR spectrum. According to the IR-MPD results, smaller $[MSi_n]^+$ clusters ($n \leq 8$ for Co, $n \leq 10$ for Mn, $n \leq 11$ for Cu and V, $n \leq 12$ for Nb) prefer exohedral structures, while endohedral cage structures are found for larger clusters such as $[VSi_n]^+$ and $[MnSi_n]^+$ ($n = 12$–16). As a representative, Figure 25 shows the experimental IR-MPD spectra of $[VSi_n]^+$ with $n = 12$–15 together with the simulated IR spectra of the lowest-energy isomers within harmonic approximation at the BP86/6-311+G(d) level of theory.[496] One can see that the experimental IR-MPD spectra are well reproduced by the harmonic vibrational spectra from DFT calculations. In particular, $[V@Si_{16}]^+$ was shown to be a fluxional cluster oscillating around a symmetric FK polyhedron. The doubly doped $[Co_2Si_n]^+$ clusters ($n = 9$–11) also form endohedral cage structures, with one Co atom encapsulated in the cage interior and another Co atom located on the surface.[475]

Apart from the aforementioned IR-MPD studies of cationic binary clusters, Y. Li *et al.* obtained the IR spectra of neutral $CoSi_n$ ($n = 10$–12) clusters using the IR-UV2CI technique.[499] Combined with DFT calculations at the B3P86/6-311+G(d) level of theory, it has been shown that these $CoSi_n$ clusters have endohedral cages with double-layered structure of silicon framework encapsulating a Co atom.

5.2.3. Photoelectron Spectra.

The photoelectron spectra of anionic silicon clusters have been studied experimentally since 1987,[500−502] while extensive measurements of the photoelectron spectra of a rich variety of metal doped silicon clusters have been carried out by Nakajima's group,[54,55,485−487] Bowen's group,[490−492] and Zheng's group.[431−433,442−444,453,454,460,466] These include the photoelectron spectra of anionic $[MSi_n]^-$ clusters in a wide size range, including $[TbSi_n]^-$ ($n = 6$–16),[485] $[TiSi_n]^-$ ($n = 8$–18),[54] $[HfSi_n]^-$ ($n = 12$–18),[54] $[MoSi_n]^-$ ($n = 8$–17),[54] $[WSi_n]^-$ ($n = 8$–17),[54] $[MSi_n]^-$ ($n = 6$–20; M = Sc, Ti, V, Y, Zr, Nb, Lu, Tb, Ho, Hf, Ta),[487] $[CrSi_n]^-$ ($n = 8$–12),[490] $[EuSi_n]^-$ ($n = 3$–17),[491] $[LnSi_n]^-$ ($n = 3$–13; Ln = Ho, Gd, Pr, Sm, Eu, Yb),[492] $[CuSi_n]^-$ ($n = 4$–18),[431] $[CrSi_n]^-$ ($n = 3$–12),[432] $[AgSi_n]^-$ ($n = 3$–12),[433] $[NbSi_n]^-$ ($n = 3$–12),[453] $[AuSi_n]^-$ ($n = 4$–12),[454] and $[CoSi_n]^-$ ($n = 3$–12).[466] From such experiments on anionic clusters, one can determine the threshold energy of electron detachment, which gives the AEA of the corresponding neutral cluster. In general, a minimum on the size dependent curve of AEA indicates that the neutral cluster is relatively more stable than its neighboring sizes.

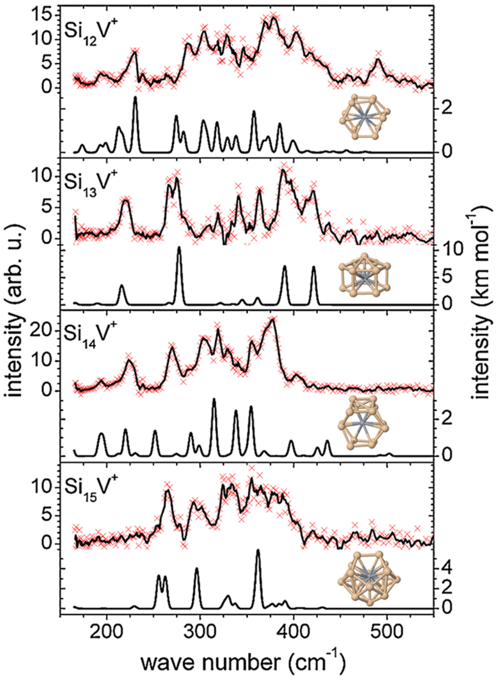

Figure 25. IR-MPD spectra (upper traces) of $[VSi_n]^+ \cdot Xe$ complexes ($n = 12$–15) and the corresponding computed harmonic vibrational spectra and geometries of the lowest-energy isomers of $[VSi_n]^+$ (lower traces). The experimental data points (red crosses) are overlaid with a three-point running average. Reproduced with permission from ref 496. Copyright 2011 American Physical Society.

As a representative, the photoelectron spectra of the anionic silicon clusters doped with a single metal atom of group 3 (Sc, Y, Tb, Ho, Lu), group 4 (Ti, Zr, Hf), and group 5 (V, Nb, Ta) in the size range of $n = 6$–20[487] are given in Figure 26. For group 3 dopants, local maxima in the threshold energy of electron detachment have been found at $n = 10$ and 16, implying that the excess electron on the cluster anion completes the closure of an electronic shell at $n = 10$ and 16, respectively. In the case of group 4 elements, the measured AEA exhibits a local minimum at $n = 16$, suggesting that an electronic shell is completed at this size. As for group 5 metal doped silicon clusters, the size dependence of the threshold energy of

Table 9. Threshold Sizes for Low Adsorption Reactivity of H_2O on Cationic/Neutral/Anionic MSi_n Clusters: (a) $ScSi_n$, (b) $TiSi_n$, (c) VSi_n, (d) YSi_n, (e) $ZrSi_n$, (f) $NbSi_n$, (g) $LuSi_n$, (h) $HfSi_n$, and (i) $TaSi_n$[a]

	Group 3			Group 4			Group 5		
	cation	neutral	anion	cation	neutral	anion	cation	neutral	anion
3*d*	Sc: 17	15	15	Ti: 13	13	11	V: 12	10	9
4*d*	Y: 21	20	20	Zr: 15	14	12	Nb: 13	12	11
5*d*	Lu: 21	16	18	Hf: 14	14	12	Ta: 13	10	11

[a] Reproduced with permission from ref 486. Copyright 2007 American Chemical Society.

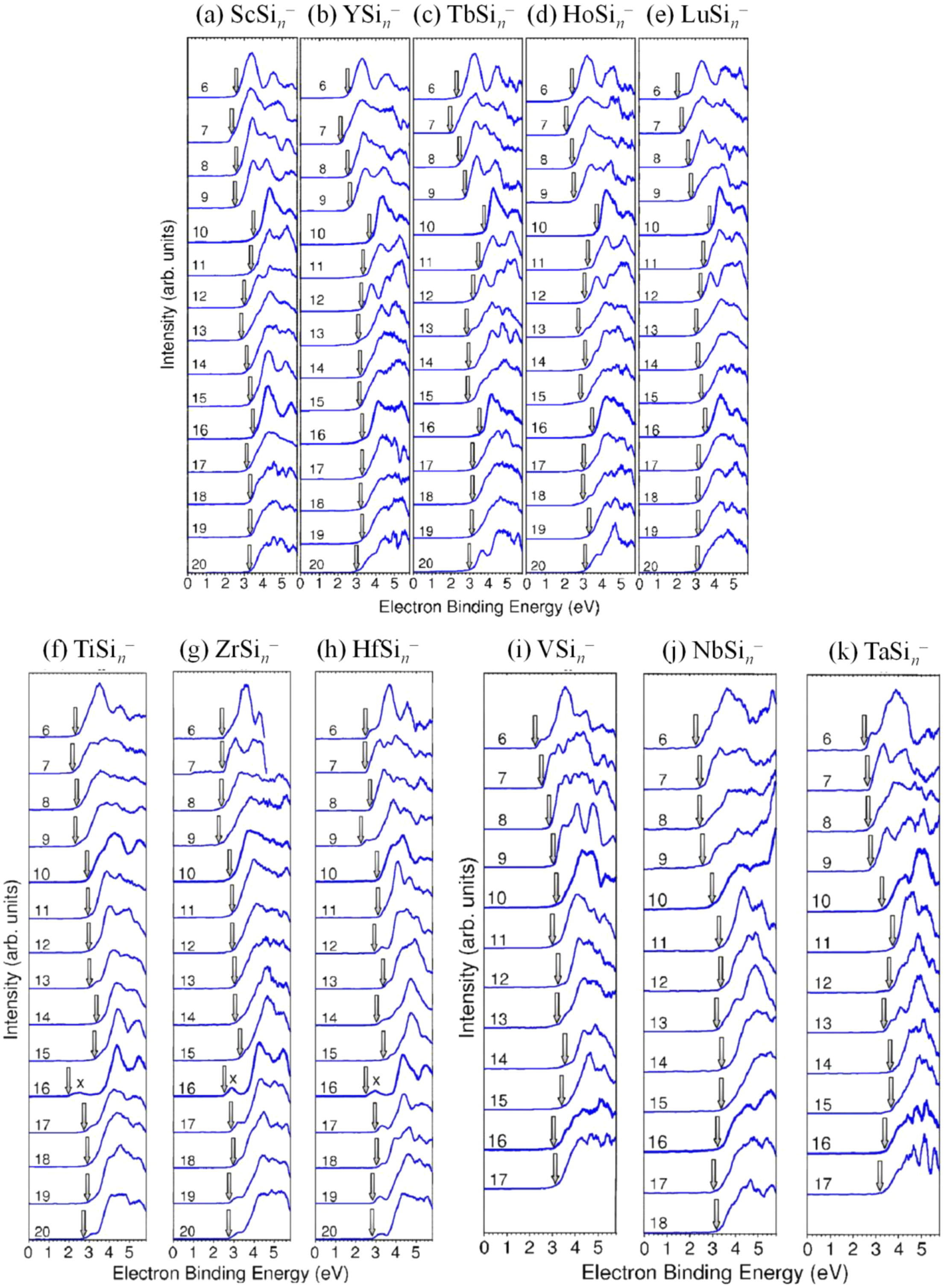

Figure 26. Photoelectron spectra of (a) $[ScSi_n]^-$, (b) $[YSi_n]^-$, (c) $[TbSi_n]^-$, (d) $[HoSi_n]^-$, (e) $[LuSi_n]^-$, (f) $[TiSi_n]^-$, (g) $[ZrSi_n]^-$, (h) $[HfSi_n]^-$, (i) $[VSi_n]^-$, (j) $[NbSi_n]^-$, and (k) $[TaSi_n]^-$ for $n = 6-20$ at 213 nm. Arrows indicate the threshold energy of electron detachment. Reproduced with permission from ref 487. Copyright 2008 American Institute of Physics.

electron detachment is relatively smooth, while a local maximum at $n = 14$ or 15 can still be seen.

During the study of metal doped silicon clusters, particular attention has been paid to the magic size at $n = 16$. Nakajima and co-workers[55,57,486,487] reported the photoelectron spectra of $[MSi_{16}]^-$ (M = Sc, Y, Lu, Ti, Zr, Hf, V, Nb, Ta), which are shown in Figure 27. $[MSi_{16}]^-$ clusters doped with group 4 elements (M = Ti, Zr, Hf) exhibit common spectral features, namely, a small bump around 2.5−3.0 eV (labeled as X), followed by a large energy separation and more discrete transitions at higher binding energies (A and B peaks), suggesting that the neutral clusters are closed-shell species with a large HOMO-LUMO gap, the largest for $Ti@Si_{16}$ in agreement with the theoretical predictions of Kumar and Kawazoe.[48] Also the

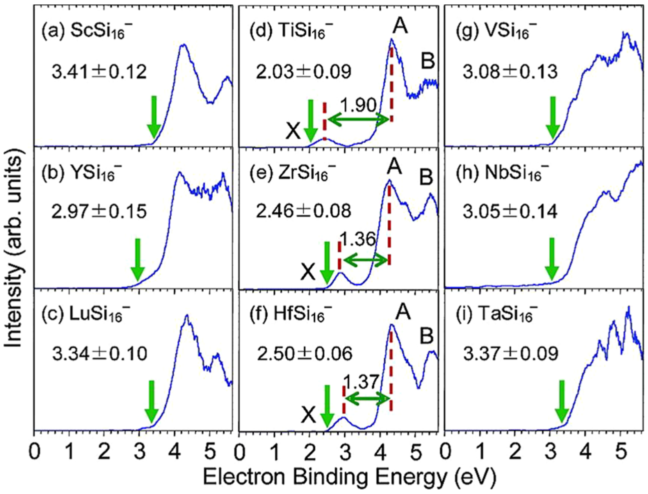

Figure 27. Photoelectron spectra and threshold energies of (a) $[ScSi_{16}]^-$, (b) $[YSi_{16}]^-$, (c) $[LuSi_{16}]^-$, (d) $[TiSi_{16}]^-$, (e) $[ZrSi_{16}]^-$, (f) $[HfSi_{16}]^-$, (g) $[VSi_{16}]^-$, (h) $[NbSi_{16}]^-$, and (i) $[TaSi_{16}]^-$ at 213 nm. Among these, the HOMO-LUMO gaps for the spectra of (d) $[TiSi_{16}]^-$, (e) $[ZrSi_{16}]^-$, and (f) $[HfSi_{16}]^-$ are shown by arrows between dashed vertical lines. $TiSi_{16}$ has the largest gap and smallest threshold energy, indicating that it is most stable among Ti, Zr, and Hf doped clusters. The anions of these clusters have the excess electron in a singly occupied MO marked by X. Vertical arrows indicate the adiabatic detachment energy, and the values are shown in eV. Reproduced with permission from ref 486. Copyright 2007 American Chemical Society.

HOMO−LUMO gap is smaller for the cases of Zr@Si_{16} and Hf@Si_{16}, suggesting their structure is different from the Ti@Si_{16} case, as also predicted by Kumar and Kawazoe.[48] In contrast, for $[MSi_{16}]^-$ clusters doped with group 3 and 5 elements, the detachment peaks start in the higher energy region above 3 eV without a separate peak (as peak X for $[TiSi_{16}]^-$). Further experiment of halogen atom addition suggests that V@Si_{16} is a super alkali metal species (one electron more than the electronic shell closing) and Ti@Si_{16} is a closed-shell cluster. On the other hand, Sc@Si_{16} anion has a high adiabatic detachment energy of 3.41 eV, and accordingly Sc@Si_{16} can be viewed as a superhalogen like Al_{13}. Moreover, Ti@Si_{16} and Ta@Si_{16} superatomic clusters have been deposited on a substrate to make 2D cluster-assemblies,[488,489] which will be discussed in Section 10.3.

Grubisic *et al.*[492] recorded the photoelectron spectra of $[LnSi_n]^-$ (Ln = Ho, Gd, Pr, Sm, Eu, Yb) clusters with $n = 3-13$ and found that the electronic structures (spectral patterns) of these clusters fall into two categories: (i) $[YbSi_n]^-$, $[EuSi_n]^-$, and $[SmSi_n]^-$ ($n \geq 10$) clusters with Ln atom in a nominal 2+ oxidation state; and (ii) $[HoSi_n]^-$, $[PrSi_n]^-$, $[GdSi_n]^-$, and $[SmSi_n]^-$ ($n \leq 7$) clusters with Ln atom in a nominal 3+ oxidation state. The observed limited effect of the identity of the lanthanide (Ln) atom on the chemical properties of the $[LnSi_n]^-$ clusters implies that the *f* electrons may not contribute significantly to the bonding with the neighboring silicon atoms. Therefore, the magnetism of the isolated lanthanide atom arising from the unpaired *f* electrons might be retained, rendering Ln@Si_n clusters promising candidates as building blocks of silicon-based magnetic nanomaterials. Kumar *et al.*[367] studied doping of different rare earth metal atoms in dodecahedral Si_{20} anion and indeed showed the existence of magnetic moments, with the largest being 7 μ_B for $[Gd@Si_{20}]^-$, suggesting that the *f* electrons remain unpaired after doping. On the other hand, Th@Si_{20} was shown to be nonmagnetic,[366] while La@Si_{20} is a superhalogen. These metal doped Si_{20} clusters will be further discussed in Section 5.3.8.

Zheng and co-workers measured the photoelectron spectra of several kinds of silicon clusters doped with one metal atom and carried out global search based *ab initio* calculations to determine the most stable structures of these anionic clusters.[431−433,453,454,466] Within the generalized Koopmans' theorem,[503] the photoelectron spectrum of a cluster anion can be calculated from its electronic DOS by DFT calculations and compared with the experimental photoelectron spectrum to identify its ground state structure. In addition to the singly doped silicon clusters, the same group also reported the photoelectron spectra of anionic silicon clusters doped with two or three transition metal atoms, such as $[V_2Si_{20}]^-$,[442] $[V_xSi_{12}]^-$ ($x = 1-3$),[443] $[V_3Si_n]^-$ ($n = 3-14$),[444] and $[Cr_xSi_{15-x}]^-$ ($x = 1-3$).[460] The essential information about the atomic and electronic structures of these clusters from the combined photoelectron spectroscopy and DFT studies will be discussed in Section 5.3.

5.2.4. X-ray Absorption Spectra and XMCD Spectra.

Lau *et al.*[56] employed X-ray absorption spectroscopy at the transition-metal $L_{2,3}$ edges to probe the local electronic structure of the dopant atoms in size-selected transition metal doped silicon cluster cations. The measured X-ray absorption spectra are shown in Figure 28. Among $[VSi_n]^+$ clusters ($n = 14-18$), $[VSi_{16}]^+$ exhibits the best resolved electronic structure with sharp lines, reflecting high degeneracy of electronic levels as well as high symmetry of the cluster geometry. $[VSi_{16}]^+$ is isoelectronic with Ti@Si_{16}, which was shown to have a tetrahedrally symmetric FK polyhedron structure.[48,49] Despite different number of valence electrons, $[TiSi_{16}]^+$ and $[CrSi_{16}]^+$ cluster cations show somewhat similar spectral features as those of $[VSi_{16}]^+$, suggesting their nearly identical local electronic density of states at the transition metal atoms and a similar geometric environment. Note that for $CrSi_{16}$ a capped Cr@Si_{15} cage has been shown to have the lowest energy.[358] Later, the same group used a combination of direct and resonant core-level photoionization spectroscopy with valence band photoionization curves to determine the HOMO−LUMO gaps of size-selected clusters, which are 0.8 ± 0.2 eV for $[VSi_{15}]^+$, 2.1 ± 0.2 eV for $[VSi_{16}]^+$, and 0.5 ± 0.2 eV for $[VSi_{17}]^+$, respectively.[494] A large HOMO−LUMO gap for $[VSi_{16}]^+$ supports the FK polyhedral structure for the isoelectronic Ti@Si_{16}, which was shown to have a large gap.[48,49]

Later, Zamudio-Bayer *et al.*[493] investigated the magnetic properties of $[MnSi_n]^+$ ($n = 7-14$) clusters using X-ray absorption and XMCD spectroscopy combined with DFT calculations. As shown in Figure 29, a sharp transition from high-spin state to low-spin state occurs at $n = 11$. Such quenching of magnetism on Mn atom is a consequence of 3*d* electron delocalization due to the strong interaction with the silicon cage, which can be related to the transition of the cluster from an exohedral to endohedral structure as revealed by the IR-MPD spectra.[497]

5.2.5. Large-Scale Production of Ti@Si_{16} and Ta@Si_{16} Superatoms.

In order to be able to use the tailor-made properties of clusters and superatoms, it is important to produce them in large quantity and find ways for high-yield synthesis. The commonly used laser vaporization method for gas-phase clusters is not appropriate for large-scale production though a great amount of research has been carried out in the laboratory and much fundamental progress has been achieved. The wet

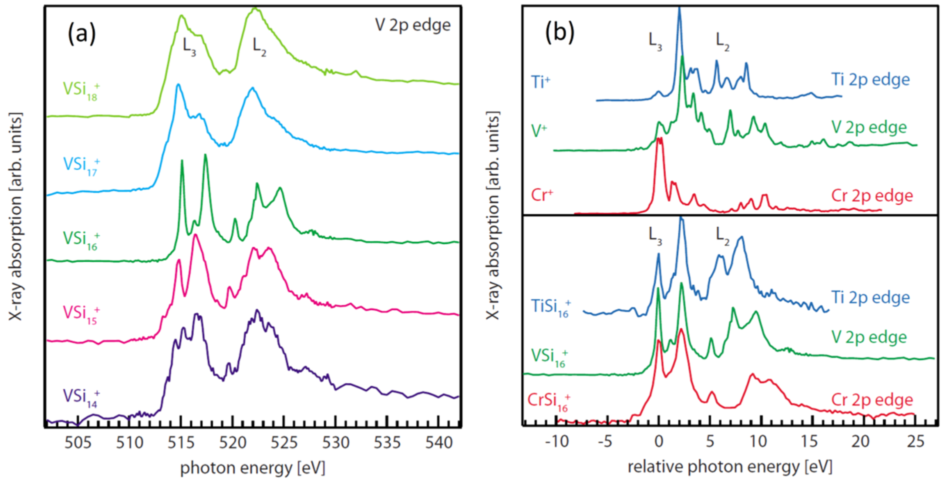

Figure 28. (a) $L_{2,3}$ X-ray absorption spectra of size-selected $[VSi_n]^+$ clusters (n = 14−18). The $[VSi_{16}]^+$ spectrum is characterized by the sharpest lines, indicating a highly symmetric structure with high degeneracy of the electronic levels. The double peak structure can be linked to the electronic DOS in tetrahedral symmetry. (b) Transition-metal $L_{2,3}$ X-ray absorption spectra of $[TiSi_{16}]^+$, $[VSi_{16}]^+$, and $[CrSi_{16}]^+$ clusters in the lower panel and of bare Ti^+, V^+, and Cr^+ ions in the upper panel. The spectra are aligned at the first peak position. While bare ions show differing spectra, the relative excitation energy in doped silicon clusters is nearly identical. This surprising fact indicates almost identical local electronic structure at the dopant atom site. Relative positions of the L_2 edge shift because of decreasing 2p spin-orbit splitting from Cr to Ti. In the titanium spectrum, the 5 eV feature of the L_3 line is partially masked by overlapping L_2 intensity. Reproduced with permission from ref 56. Copyright 2009 American Physical Society.

chemistry methods have been used to produce various endohedral clusters; many of them have been discussed in this review.

Recently, Tsunoyama *et al.*[80,488] have reported a large-scale clean dry process with high-power impulse magnetron sputtering to scale up the production of superatoms. Using this method, they could produce 100 mg scale of Ti@Si_{16} and Ta@Si_{16} superatoms. This is an important breakthrough as one would be able to use several experimental techniques to study the molecular structure and other properties of such clusters and also produce their assemblies. They used PEG-DME to stabilize such superatoms and characterize their properties with different methods such as mass spectrometry, X-ray photoemission spectroscopy, Raman spectroscopy, and ^{29}Si NMR. From these, it was concluded that the charge state of Ti@Si_{16} is neutral, while Ta@Si_{16} cluster carries a positive charge. Hence, both Ti@Si_{16} and $[Ta@Si_{16}]^+$ species are closed-electronic shell superatoms (Ta@Si_{16} being an alkali metal type superatom with one excess electron), as earlier predicted from calculations[361,369] and also confirmed from experiments by Lau *et al.*[56]

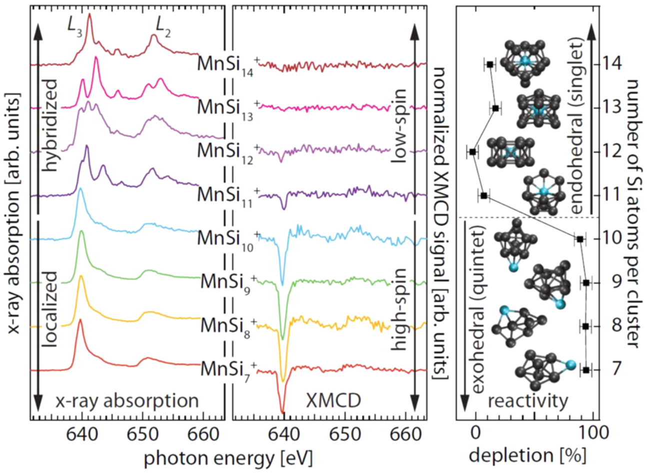

Figure 29. Manganese 2p X-ray absorption (left) and XMCD (center) spectra of $[MnSi_n]^+$ clusters (n = 7−14), indicating quenched magnetic moments for $n \geq 11$. Corresponding ground state structures of $[MnSi_n]^+$ and the depletion of singly doped clusters in the presence of oxygen as a measure of the exohedral-to-endohedral transition (right). Reproduced with permission from ref 493. Copyright 2013 American Physical Society.

For surface enhanced Raman spectroscopy, Ti@Si_{16} and Ta@Si_{16} superatoms were soft-landed on an Ag/$SrTiO_3$ substrate with a coverage of 10−15 monolayers. Two strong broad peaks were commonly obtained at 300 and 620 cm^{-1} in the spectra. The latter was considered to arise from the overtone at the fundamental mode. Two strong peaks were observed at 470 cm^{-1} and 140 cm^{-1} for Ti@Si_{16}, which were slightly red shifted to 450 cm^{-1} and 125 cm^{-1} in the case of Ta@Si_{16}. Earlier Kumar *et al.*[361] calculated the IR spectra and Raman activities for the fullerene and FK polyhedral isomers of M@Si_{16} (M = Ti and Zr). They obtained the strongest Raman active peak at 318.1 cm^{-1} for Ti and 312 cm^{-1} for the Zr doped FK polyhedron, respectively. However, in the fullerene isomer, the lower symmetry splits this peak and the first and second most intense peaks were obtained at 316.9 (313.4) cm^{-1} and 380.7 (373.4) cm^{-1}, respectively, for Ti (Zr) cases using the B3PW91/6-311+G(d,p) scheme with Zr treated by the SDD basis set. Tsunoyama *et al.*[80] also obtained similar results using DFT calculations at the PBE/def-TZVP level. The mode at around 316 cm^{-1} arises from the ring atoms in the fullerene isomer, and the peak in the FK isomer corresponding to the breathing mode of the cage has a similar value. On the other hand, the mode at around 380 cm^{-1} arises from the square atoms in the fullerene cage. It is noteworthy that the bond lengths in the ring connecting pentagons are longer (2.38 Å) than those in the square (2.30 Å) for Zr@Si_{16} and are weaker than the bonds in the square in the fullerene isomer.[361] Accordingly, they have lower vibrational frequency. The bond lengths in the FK isomer of Ti@Si_{16} are also longer (2.26−2.37 Å), and therefore, the frequency of the breathing mode is similar. From these results, we can say that the peak emanating from Si atoms is expected to be weakly dependent on the type of metal atom. The observed broad peak at around 300 cm^{-1} agrees well with the calculated strong mode for the FK-Ti@Si$_{16}$, but the strong peaks at 470 cm^{-1} and 140 cm^{-1} differ from the calculated intensities of the modes in these regions. However, it should be noted that the samples containing Ti@Si$_{16}$ as well as Ta@Si$_{16}$ superatoms were contaminated with pure silicon clusters (Si$_6$, Si$_7$, and Si$_{10}$ being significantly abundant in the mass spectra of the samples).[80] The Raman spectra of size-selected Si clusters (Si$_6$) in a matrix of Ar, Kr, or N$_2$ interestingly showed a broad peak at 470 cm^{-1} and also a rising edge below 200 cm^{-1}.[504] The other reason for the difference could be the presence of PEG-DME ligands and superatom−superatom interactions.

The 100 mg scale quantity of the samples also made NMR experiments possible, and a similar electronic distribution for both Ti@Si$_{16}$:PEG-DME and Ta@Si$_{16}$:PEG-DME samples was concluded to be consistent with the XPS results. However, it should be noted that for Ta@Si$_{16}$, calculations show (see later discussions in Section 5.3.7 on theoretical results) fullerene isomer to be lowest in energy while for Ti@Si$_{16}$, a FK polyhedron is favored. These results suggest that the PEG-DME ligands interact with the Ta@Si$_{16}$ superatom via changing electron distribution and cause rearrangements of the polyhedral Si scaffold.[80]

5.2.6. Halide Ions as Template for Large-Scale Production of Silafullerans. Besides the endohedral silicon cages discussed above, it was shown that exohedral capping with hydrogen can lead to stable empty silicon cages such as Si$_{20}$H$_{20}$ fullerene,[360] which has the highest I$_h$ symmetry similar to C$_{20}$H$_{20}$. Functionalization of such hydrogenated silicon fullerenes does not affect much the HOMO−LUMO gap, and these clusters could be interesting for diverse applications including tagging, biosensors, and other related optical properties.[505]

To produce such silicon fullerenes in large quantity using a wet-chemistry route, Pichierri *et al.*[506] suggested using anions as nucleation center in an anion-templated synthesis method, so that the useful properties of the silicon nanoparticles can be retained to a large extent. They came up with the idea of using halogen anions, namely encapsulation of anions of F, Cl, Br, and I in a Si$_{20}$H$_{20}$ cage since their size fits well in this cage. It was shown that endohedral doping of F$^-$ and Cl$^-$ leads to slight shrinkage of the Si$_{20}$H$_{20}$ cage while I$^-$ leads to slight expansion. However, Br$^-$ does not make any significant structural change. The endohedral doping was shown to increase the HOMO-LUMO gap of the empty Si$_{20}$H$_{20}$ cage by about 0.5 eV.

Following this idea, Tillman *et al.*[507] reported one-step synthesis of the [20]silafullerane with an endohedral chlorine ion and obtained [nBu$_4$N][Si$_{32}$Cl$_{45}$] in 27% yield. X-ray analysis showed silafullerane cage as part of the [nBu$_4$N]-[Si$_{32}$Cl$_{45}$] lattice. As shown in Figure 30, the [Si$_{32}$Cl$_{45}$]$^-$ cluster has a dodecahedral Si$_{20}$ core with an endohedral Cl$^-$ ion. It carries optimally eight chloro and 12 Cl$_3$Si groups so that each silicon atom fulfills tetravalent bonding. The Cl$_3$Si groups can be transformed into Cl with the removal of SiCl$_2$. One can then carry out Si−Cl and Si−H exchange to obtain the[20] silafullerane with the endohedral Cl$^-$ ion. These developments pave the way for further progress in making derivatives, functionalized molecules, and 3D networks.

5.3. Endohedrally Doped Silicon Cages by Size from Calculations

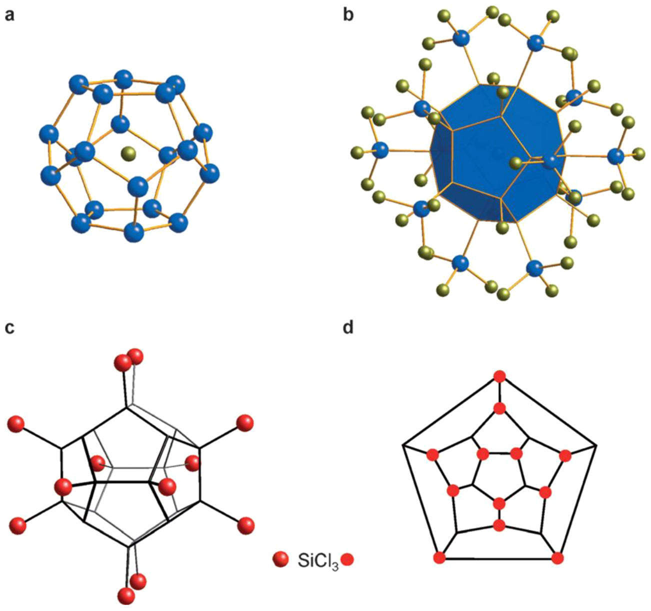

Figure 30. (a) Dodecahedral Si$_{20}$ core with an endohedral Cl$^-$ ion, (b) full structure of the silafullerane [Si$_{32}$Cl$_{45}$]$^-$, (c) pairwise octahedral arrangement of 12 Cl$_3$Si groups, and (d) Schlegel diagram illustrating the equivalence of all 12 five-membered rings (each of the red filled circles represents one Cl$_3$Si substituent attached to a Si^0 cluster atom). Reproduced with permission from ref 507. Copyright 2015 Wiley-VCH Verlag GmbH & Co. KGaA, Weinheim.

In the literature, there have been extensive DFT calculations on doped silicon cage clusters using many different theoretical schemes (see Table 7). Accordingly, the results might vary with the computational scheme depending on e.g. the choice of the exchange-correlation functional and the basis set. In order to present a unified overview, we have performed systematic *ab initio* calculations on the atomic structures, energetic stability, and electronic and magnetic properties of these endohedral M@Si$_n$ cages of different sizes (n = 10, 11, 12, 13, 14, 15, 16, 18, 20) at the level of PBE0/6-311+G(d), SDD. For each cluster size, we considered several different isomeric configurations. Among these, two growth behaviors[48,49,354,369] are noteworthy to mention: (i) a fullerene-like growth in which all the atoms on the cage are tricoordinated similar to carbon fullerenes; and (ii) a FK polyhedral type growth behavior. However, unlike carbon fullerenes where hexagons are most favorable and pentagons exist as defects, fullerene-like silicon structures have sp^3 bonding, and thus favor pentagons instead of hexagon, while squares/rhombuses are present as defects. Similar to the isolated pentagon rule in carbon fullerenes, there is an isolated rhombus rule in silicon fullerenes.[369] We can go from an 8-atom cube (all the faces being square) to a 20-atom dodecahedral cage (all pentagonal faces) by successively adding more pentagons. Thus, a 10-atom pentagonal prism has two pentagons and five rhombi; a 12-atom fullerene-like structure has four pentagons and four rhombi but the rhombi are not isolated; a 14-atom fullerene structure has three isolated rhombi and six pentagons; a 16-atom fullerene cage has two isolated rhombi and eight pentagons; an 18-atom fullerene cage has one rhombus and ten pentagons (as we shall show later, there is an exception in this case with one rhombus, one hexagon, and nine pentagons); and finally, a 20-atom dodecahedron has all 12 pentagonal faces and no rhombus. FK phases, also known as topologically close packed phases, are well known in complex alloys and often have 12-fold, 14-fold, 15-fold, and 16-fold coordination polyhedra with all triangular

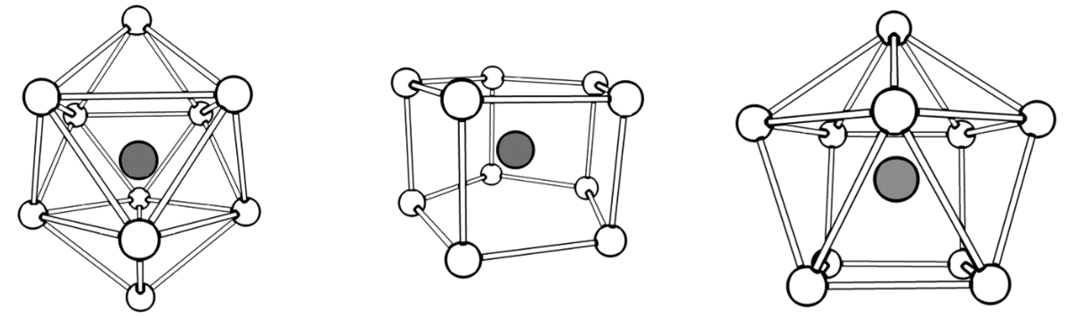

(a) Bicapped Tetragonal Antiprism (D_{4d})

(b) Pentagonal Prism (D_{5h}, C_s)

(c) Capped Tetragonal-pentagonal mixed Antiprism (C_{2v}, C_s, C_1)

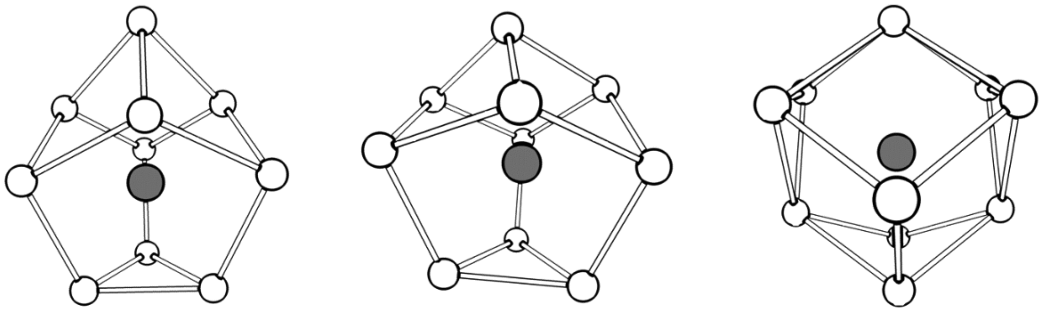

(d) Fullerene-like Cage (C_{3v})

(e) Distorted Fullerene-like Cage (C_s)

(f) Capped Crown-like Structure (C_{3v})

Figure 31. Schematic structures of isomers for $M@Si_{10}$ cage clusters with the dopant atom M (highlighted by dark grey filled circle). Si atoms are shown by empty circles. The symmetry is given in parentheses for the lowest energy isomer of different M atoms as given in Table S5.

faces, such as 12-atom icosahedron with 20 faces, 14-atom bicapped hexagonal antiprism, capped three hexagons, and a 16-atom polyhedron with T_d symmetry. In the same spirit, we can say a 10-atom bicapped tetragonal antiprism and the higher polyhedra with 18 and 20 atoms are in the same class. In many cases, these two types of growth behaviors are either most favorable or low-lying structures. The FK structures are more compact due to triangular faces, while the fullerene structures are more open. Depending upon the relative sizes of the dopant and the cage atoms, one or the other type of isomer may be favored. But some clusters also prefer other polyhedral cages as their lowest-energy structures, in which different types of polygonal faces may exist. We shall present many such cases below.

Here we focus mainly on the endohedral cage clusters. There are cluster structures obtained by further capping Si atoms or hydrogenation on an existing endohedral $M@Si_n$ cage. These will be mentioned only briefly since the endohedral atom does not play an important role in the stabilization of the silicon cage in these situations. In the following, we describe these endohedral $M@Si_n$ clusters by cage size n, including our theoretical results, earlier calculations available in the literature as well as the relevant experimental facts, whereas some doubly or triply metal-doped silicon cage clusters are also briefly discussed.

5.3.1. Endohedrally Doped Si_{10} Cages. We start the discussion of endohedral $M@Si_n$ cages from $n = 10$, since many calculations indicated that Si_{10} is the smallest cage to completely enclose a guest atom.[58,67,372,375,377,380,389,394,399,405,414,445] As shown in Figure 31, six possible structural isomers for the endohedral $M@Si_{10}$ cages have been considered: (a) a bicapped tetragonal antiprism, (b) fullerene type, (c) an isomer with triangular and (distorted) rhombi faces, (d and e) fullerene-like with all atoms having three neighbors on the cage but having a triangle in addition to pentagons and rhombi, and (f) an isomer having a hexagon instead of a pentagon. In an early study, Kumar *et al.*[58] considered several isomers, including isomers (a), (c), and (f) in Figure 31. Other theoretical studies have explored a number of guest atoms, including Be,[67,467] V,[394] Ti,[394] Mn,[420] Fe,[375,376,380,383,389,405,434] Co,[375,399,405] Ni,[58,392,394,397,405,436] Cu,[397,406,414,436,445] Zn,[397] Pd,[58,392,394] Pt,[58,392,394] and Au.[394,436] We have considered cage isomers in Figure 31 for each dopant and also allowable spin states in our own PBE0 calculations to determine the most stable structure. Upon relaxation, Ti, Cr, Zn, or Au dopant atom escapes from the interior of the Si_{10} cage, as it is too small to accommodate these guest atoms. For Cu, Zn, Pd, and Pt dopants, the previously proposed endohedral $M@Si_{10}$ cage configuration (Figure 31a) is only metastable and higher in energy than the exohedral isomer with pentacapped trigonal prism,[372] at the PBE0/6-311+G(d), SDD level.

As summarized in Table S5, the remaining stable $M@Si_{10}$ endohedral cages (M = Be, Mn, Fe, Co, Ni) from our *ab initio* calculations are bicapped tetragonal antiprism (Figure 31a) for Be,[67,467,470] (distorted) pentagonal prism (Figure 31b) for Mn[420] and Fe,[383,389,405,434] and capped tetragonal−pentagonal mixed antiprism (Figure 31c) for Co[375,405] and Ni.[394,405] These theoretical results can be compared with available experiments. First, the formation of endohedral cage $Cr@Si_{10}$ was supported by the critical size for Ar attachment.[484] The measured IR spectra indicated isomer (c) in Figure 31 to be the most probable structure for neutral $Co@Si_{10}$.[499] The photoelectron spectrum combined with DFT calculation suggested an endohedral cage configuration (Figure 31d) for $[Co@Si_{10}]^-$.[466] This structure was also obtained for the isoelectronic Ni@Si_{10}.[58] However, the proposed structure for the neutral Co@Si_{10} (Figure 31d) in ref 466 is higher in energy by 0.258 eV than the current ground state (Figure 31c).

For all these endohedral complexes, there is appreciable bonding between the M dopant and Si_{10} cage, as signified by the computed embedding energy in the range of 3.828 and 6.575 eV. There is charge transfer between the cage and the M atom, but the direction of charge depends upon the M atom. Note that the charge transfer analysis should be taken as indicative only but not quantitative since it generally depends on the computational methodology. Our NBO charge analysis shows that there is a significant electronic charge transfer from the silicon cage to the metal atom[380,389,399,405,420] (i.e., about 3.6 to 4.0 electrons) as shown in Table S5, except that Be atom donates nearly one electron to the surrounding Si atoms. Besides the interatomic charge transfer, there is also internal electronic configuration change (charge transfer) from the 4*s* to 3*d* state in the 3*d* transition metal atoms.[389,405,420]

Note that undoped Si_{10} itself is a very stable tetracapped trigonal prismatic cluster with 40 valence electrons and has a large HOMO−LUMO gap of 3.345 eV using the PBE0 functional, and it is more abundant than neighboring clusters in the mass spectrum of pure silicon clusters (Figure 22). The doping of Co anion or Ni atom with 10 valence electrons stabilizes it further and changes the atomic structure with a large HOMO−LUMO gap. Indeed, among the M@Si_{10} clusters explored in Table S5, Ni@Si_{10} possesses the largest HOMO−LUMO gap of 3.299 eV using the PBE0 functional. Furthermore, the HOMO−LUMO gap for the hollow cage structure of Si_{10} in Figure 31c without endohedral Ni atom is also large (2.204 eV). Therefore, Ni atom enhances the stability of the Si_{10} cluster and increases the HOMO−LUMO gap of the Si_{10} cage due to interaction of the Ni valence orbitals with the orbitals of the cage. There is about 3.6 electrons transferred from the Si_{10} cage to Ni dopant from our NBO analysis.

Table S5 also shows that compared to the large magnetic moments of free transition metal atoms,[389] the magnetic moment of the transition metal dopant is either largely reduced or completely quenched by the silicon cage, due to the interaction between silicon *s*, *p* orbitals and metal *d* orbitals as well as the concomitant charge transfer. As a consequence, the computed total magnetic moment for Mn@Si_{10}, Fe@Si_{10}, Co@Si_{10}, and Ni@Si_{10} is 3 μ_B, 2 μ_B, 1 μ_B, and 0 μ_B, respectively. A similar effect of quenching of magnetic moments on the transition metal dopant was reported earlier for 10-atom clusters of group 14 elements[58] and in other studies,[48,49,380,383,389,420,434] but the values of the magnetic spin moments for the endohedral cage clusters might be different, depending on the choice of the computational method and the specific cage geometry. According to the electron counts by the Wade−Mingos rules, the bicapped tetragonal antiprism as a 10-vertex *closo*-deltahedron for Be@Si_{10} requires a total of $4n_v + 2 = 42$ valence electrons which it has, while the pentagonal prism as a three-connected 10-vertex polyhedron for Mn@Si_{10} and Fe@Si_{10} requires $5 \times n_v = 50$ valence electrons for achieving a closed electronic shell. For the latter case, the total number of electrons is only 47 and 48 for Mn@Si_{10} and Fe@Si_{10}, respectively, thereby leading to a magnetic moment of 3 μ_B and 2 μ_B.

Early studies on the Fe@Si_{10} cluster suggested it to be an 18-electron closed-shell species.[377] From our calculations, however, Fe@Si_{10} adopts a triplet spin state as also obtained earlier[376] and has a moderate HOMO−LUMO gap of 1.275 eV, showing no signature of magic cluster. The limited applicability of the 18-electron rule for the endohedral silicon cage clusters was ascribed to geometric and electronic factors, such as crystal field effect on *d* states of the transition metal atom, *p-d* hybridization, size of transition metal atom, and the distribution of dangling bonds of the silicon atoms.[394,405] The applicability of the electron counting rule with electronic shell completion in the endohedral silicon cages of other sizes will be further discussed in the subsequent subsections.

There have also been some studies on silicon cages doped with more than one metal atom. As an example, replacing the top Si atom by Fe on the structure in Figure 31a leads to a stable endohedral cage cluster of Fe@$FeSi_9$, which has a total magnetic moment of 2 μ_B and a moderate HOMO−LUMO gap of 0.68 eV using the PBE functional.[459] Some examples of other sizes will be discussed later.

5.3.2. Endohedrally Doped Si_{11} Cages. Intermediate to the well-studied Si_{10} and Si_{12} cages, few studies have been made on Si_{11} cages, which have lower symmetry but are able to accommodate 3*d* transition metal dopants with relatively smaller atomic size, e.g., Cr,[371,440] Mn,[405] Fe,[377] Co,[387,399] Ni,[398] and Cu.[406,414] Several possible cage configurations of Si_{11} are schematically plotted in Figure 32. Considering these isomeric structures and the above six 3*d* transition metal dopants, we performed *ab initio* calculations at the PBE0/6-311+G(d), SDD level of theory. Even though endohedral cage structures were proposed for $MnSi_{11}$[405] and $CuSi_{11}$,[406,414] our geometry optimizations found their true ground state configurations to be capped open cage and capped cage, respectively. Our results for the remaining four endohedral M@Si_{11} cage clusters (M = Cr, Fe, Co, Ni) are summarized in Table S6. The most stable geometries of Cr@Si_{11} (Figure 32f) and Ni@Si_{11} (Figure 32e) are the same as those reported in the literature.[371,398,440] The present structure of Cr@Si_{11} is also supported by the photoelectron spectrum of its anion measured by Zheng and co-workers.[432] The calculated ground state (Figure 32a) for Fe@Si_{11} is 0.175 eV lower in energy compared with the structure reported in ref 377. The favorable spin state of Fe@Si_{11} is triplet, similar to the cases of Fe@Si_{10} and Fe@Si_{12}. According to our calculations, the most favorable structure of Co@Si_{11} (Figure 32a) is in line with previous reports,[387,399] which is further supported by the agreement between the measured and simulated infrared spectra of the neutral Co@Si_{11} cluster with this structure.[499] The binding energy is the largest for Ni@Si_{11}, and its HOMO−LUMO gap is also large, which makes it a very stable cluster.

5.3.3. Endohedrally Doped Si_{12} Cages. Endohedral M@Si_{12} cages have been widely investigated.[362,364,368,371−376,378−385,387−390,393−395,397−399,403,405,406,410,412−414,416,420,423,427,434−436,440,447−451,453,466,473] Generally speaking, most 3*d*, 4*d*, and 5*d* transition metal atoms can stabilize the Si_{12} cage by endohedral doping.[381] However, our geometry optimizations at the PBE0/6-311+G(d), SDD level found open cage structures for $ScSi_{12}$ and YSi_{12} clusters, in agreement with the previous finding for $ScSi_{12}$,[451] while the endohedral cage isomers for Zr@Si_{12} and Hf@Si_{12} are less stable than the exohedral configurations by over 0.5 eV. For the remaining 3*d*, 4*d*, and 5*d* transition metal atoms, we have explored many possible Si_{12} frameworks, and the lowest-energy configurations

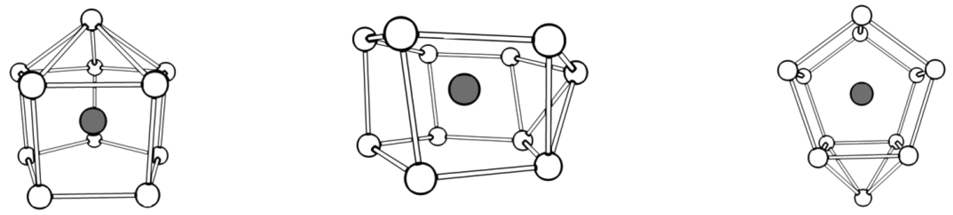

(a) Top Capped Pentagonal Prism (C_{5v}, C_1)

(b) Pentagonal-hexagonal Mixed Prism (C_s)

(c) Side Capped Pentagonal Prism (C_{2v})

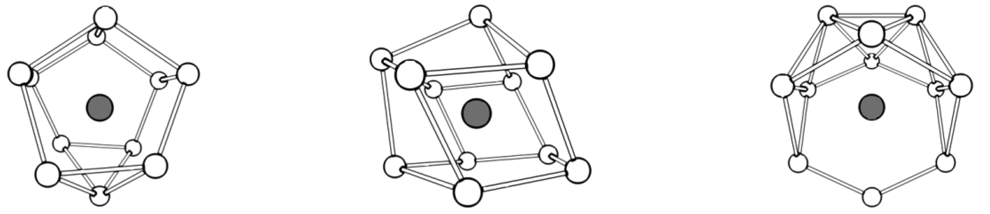

(d) Distorted Side Capped Pentagonal Prism (C_1)

(e) Distorted Top Capped Pentagonal Prism (C_{2v})

(f) Tricapped Two Interpenetrating Capped Pentagons (C_{2v})

Figure 32. Schematic structures of isomers for M@Si_{11} cage clusters with the dopant atom M as given in Table S6. Other details are as in Figure 31.

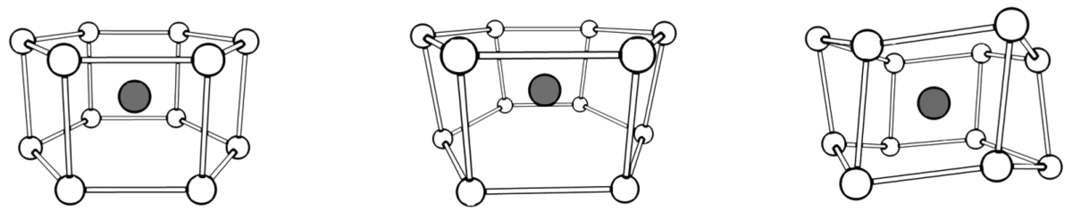

(a) Hexagonal Prism (D_{6h})

(b) Distorted Hexagonal Prism (C_{2h}, C_i, C_1)

(c) Puckered Hexagonal Prism (D_{3d}, C_{2h}, C_s)

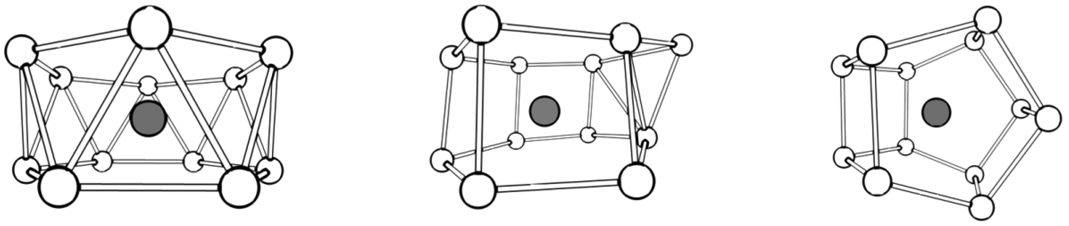

(d) Hexagonal Antiprism (D_{6d})

(e) Face Capped Pentagonal-hexagonal Mixed Prism (C_s)

(f) Distorted Dimer Capped Pentagonal Prism (D_{2d})

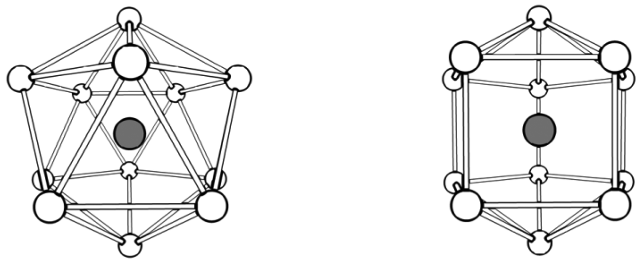

(g) Perfect Icosahedron (I_h)

(h) Bicapped Pentagonal Prism (D_{5h})

Figure 33. Schematic structures of isomers for M@Si_{12} cage clusters with M the endohedral dopant as given in Table S7. Other details are as in Figure 31.

of M@Si_{12} clusters are generally based on metal-centered hexagonal prism with different extents of distortion, that is, perfect hexagonal prism (Figure 33a) for Mn,[420,448] Nb,[381,394,450,453] Mo,[379,435,436] Ru,[375,435] Ta,[388] W,[373,374,376,378,379,390,436] Re,[384,390] and Os,[375,376,390,435] distorted hexagonal prism (Figure 33b) for Ti[403,435,448] and V,[405,448,451] puckered hexagonal prism (Figure 33c) for Cr,[362,451] Fe,[380,389,434,447,448,451] Co,[451] Cu,[372,379,405,406,414,419,448] and Zn,[448] and face-capped pentagonal-hexagonal mixed prism (Figure 33e) for Ni,[393,397,419,451] Pd, Pt, and Au. Note that the isomeric structure in Figure 33e can also be viewed as a severely deformed hexagonal prism. The structural and electronic properties of the most stable cage structures of endohedral M@Si_{12} clusters obtained from our calculations are summarized in Table S7.

It should be pointed out that the most stable endohedral cage structure for each metal dopant reported in the literature might be different, depending on the computational methodology and the considered isomeric structures. For instance, the D_{2d} cage (Figure 33f), a fullerene-like structure with four pentagons and four rhombi, which was predicted as the ground state for Au@Si_{12}, is more stable than the isomeric configuration in Figure 33e by 0.069 eV at the B3PW91/LanL2DZ level[423] but less stable than the structure in Figure 33e by 0.016 eV at the current PBE0/6-311+G(d), SDD level. Similarly, a perfect hexagonal prism was predicted as the ground state for Pd@Si_{12};[394] but a severely deformed hexagonal prism (Figure 33e) prevails in energy by 0.389 eV according to our PBE0 calculations. As for Pt@Si_{12}, a puckered hexagonal prism (Figure 33c)[394] was considered as the lowest-energy configuration, which is less stable than our predicted ground state (Figure 33e) by 0.288 eV.

As described in Section 5.2, there is plenty of experimental information about the atomic structures of M@Si_{12} clusters and their anions/cations, which mostly conform to the theoretical results in Table S7. First, the formation of endohedral cages in Ti@Si_{12} was indicated by argon physisorption on $[\mathrm{Ti@Si}_n]^+$ clusters as a structural probe.[484] Also, the reactivity of $[\mathrm{TiSi_n}]^+$ clusters with H_2O decreases for $n = 12$ and beyond and becomes very small for $n = 15$ and 16, suggesting that the metal atom is not available for adsorption.[54] Furthermore, the threshold size of nonreactivity toward H_2O vapor (corresponding to the emergence of an endohedral silicon cage) was $n = 12$ for neutral NbSi_n clusters.[486] More specifically, IR-MPD results suggested a distorted hexagonal prism for both $[\mathrm{V@Si_{12}}]^+$[496] and $[\mathrm{Mn@Si_{12}}]^+$.[497] The former is isoelectronic to $\mathrm{TiSi_{12}}$ and the latter to neutral Cr@Si_{12}. Photoelectron spectroscopic data combined with DFT calculations led to a perfect hexagonal prism for $[\mathrm{Nb@Si_{12}}]^-$[453] (which is isoelectronic with neutral Mo@Si_{12}), a slightly distorted hexagonal prism for $[\mathrm{Cr@Si_{12}}]^-$,[432] and a puckered hexagonal prism for $[\mathrm{Cu@Si_{12}}]^-$,[431] respectively. However, the experimental IR-UV2CI spectrum of Co@Si_{12}[499] could be better resolved by assuming a bicapped pentagonal prism rather than the puckered hexagonal prism from the present calculations.

Similar to the aforementioned metal doped Si_{10} clusters, there is a substantial amount of charge transfer from the Si_{12} cage to the metal dopant (see Table S7), which was also observed in previous *ab initio* calculations.[373,376,380,384,389,390,398,399,403,412,416,420,423,435,450,466] As we have shown for the M@Si_n cages of other sizes, the electron donation from the silicon cage to the transition metal (or rare earth metal) dopant is a universal phenomenon, and the amount of charge transfer is in the range of 1.8 to 3.7 electrons, with an exception of Cu@Si_{12} for which the charge transfer is lower (about 0.9 electrons). In contrast, there is barely any charge transfer between the Zn dopant and the Si_{12} host cage, thereby resulting in a small embedding energy of 3.067 eV only for Zn.

Among the endohedral M@Si_{12} clusters in Table S7, only Fe@Si_{12} adopts the high-spin triplet state, whereas the most favorable spin state for all the other clusters is either singlet or doublet depending upon even or odd number of electrons. L. J. Guo *et al.*[405] also found that the magnetic properties of Fe@Si_n clusters are somewhat unique among the 3*d* transition metal doped silicon clusters. It is worth pointing out that the lowest-energy spin state of Fe@Si_{12} sensitively depends on the choice of the exchange-correlation functional. Earlier DFT calculations with the PBE or PW91 functional predicted that the magnetic moment of 4 μ_B for the free Fe atom is completely quenched inside the Si_{12} cage due to significant charge transfer from Si to Fe,[385,389,434,447] while other DFT calculations with a hybrid functional such as B3LYP predicted a triplet spin state.[380,383] Nevertheless, state-of-the-art measurement on the magnetic depletion using the XMCD technique is desirable.

Unlike the spin-polarized Fe@Si_{12} cluster, the doping of Ru and Os (also belonging to group 8 elements) in Si_{12} leads to no magnetic moment in Ru@Si_{12} and Os@Si_{12}, which have hexagonal prism structure with D_{6h} symmetry (Figure 33a) and seem to satisfy the 20-electron rule corresponding to $1S^21P^61D^{10}2S^2$ orbitals.[385] Our PBE0 calculations show sizeable HOMO−LUMO gap and large embedding energy for Ru@Si_{12} (E_{HL} = 2.789 eV, E_{em} = 11.806 eV) and Os@Si_{12} (E_{HL} = 2.598 eV, E_{em} = 13.244 eV), signifying their high stability. Uchida *et al.*[390] have argued that the 18- and 20-electron rules are more applicable to M@Si_{12} clusters encapsulating a 5*d* transition metal atom than in the case of 3*d* and 4*d* transition metal atoms.

The utility and limitation of the 18-electron rule in transition metal doped silicon cages have been intensely debated by many authors[371,377,381,385,390,391,405,417,440,446,448,451] since the early stage of studies. If one assumes that each Si atom contributes one electron to the π bonded valence manifold, Cr@Si_{12}, Mo@Si_{12}, and W@Si_{12} belong to the 18-electron species. Among M@Si_{12} clusters, W@Si_{12} possesses the second largest embedding energy of 13.004 eV and the second highest HOMO−LUMO gap of 3.094 eV (see Table S7). These values are comparable to the previously reported embedding energy of 12.17 or 9.96 eV and HOMO−LUMO gap of about 2.6 eV (with B3LYP functional).[379,390] The notably high stability from theoretical calculations can be related to the experimental observation of W@Si_{12} cluster as a magic species with high stability.[481] Similar to W@Si_{12}, Mo@Si_{12} possesses substantial embedding energy (10.693 eV) and HOMO−LUMO gap (2.832 eV) from the present PBE0 calculations, which are also comparable to the previously reported values of 7.8 and 2.19 eV at the B3LYP/LanL2DZ level.[379] Cr@Si_{12} also has a notably large HOMO−LUMO gap as obtained from different calculations: 3.360 eV (using PBE0 from present calculations), 2.939 eV (B3PW91),[362] 3.04 eV (B3LYP),[381] 3.97 eV (GW_0),[435] and 2.88 eV (B3P86).[451] Under the Wigner−Witmer rule,[508] which requires that the products in a reaction have the same spin multiplicity as reactants, the embedding energy of Cr@Si_{12} can be significantly amplified from 5.44 to 10.81 eV,[385] which is comparable to the values for W@Si_{12} and Mo@Si_{12} (13.004 and 10.693 eV, respectively, from our own PBE0 calculations). In other words, these three clusters exhibit high stability in terms of HOMO−LUMO gap and dopant−cage interaction energy from DFT calculations with various hybrid functionals. Therefore, it was argued that the stability and electronic properties of endohedral Si_{12} clusters doped with transition metal atoms can be rationalized within the 18-electron rule.[385,390] Uchida and co-workers[390] have studied doping of 5*d* transition metal atoms (M = Hf, Ta, W, Re, Os, Ir, Pt, Au) using DFT calculations. They found hexagonal prism (Figure 33a) and bicapped pentagonal prism (Figure 33f) as two favorable structures—the former for M = Ta, W, Re, and Os with the total number of valence electrons being 53 to 56, while the latter for Re, Os, Ir, Pt, and Au with 55−59 valence electrons. The hexagonal prism is particularly favored for clusters with 54 valence electrons, and the structure is maintained for 53, 55, and 56 valence electron systems due to the covalent bonding between M atom and Si cage as well as charge transfer to the M atom. A similar behavior was obtained for the bicapped pentagonal prism structure. Accordingly, they suggested the rigidness of these structures against variation of the number of electrons. It is noteworthy that the icosahedral isomer (Figure 33g) is not favored by any of the dopants (see Table S7), which was also found by Goicoechea and McGrady.[448]

A detailed analysis of the molecular orbitals of Cr@Si_{12} by Abreu *et al.*[440] revealed that this cluster should be viewed as a "16-electron" system instead of an "18-electron" one as the $3d_z^2$ orbital of Cr acts as the LUMO of the entire cluster. They associated these electrons with the metal atom. However, the orbitals are hybridized, and therefore, the charge is likely to be shared with the Si cage. The appreciable HOMO−LUMO gap of Cr@Si_{12} has been attributed to the crystal field splitting of the 3*d* orbitals with the $3d_z^2$ orbital being pushed up in energy, which is a geometric consequence of the hexagonal prism structure. Later, the same group[446] also analyzed the molecular orbitals of the W@Si_{12} cluster and suggested that the 18-electron rule does not apply to W@Si_{12} either, since the $5d_z^2$ orbital (as the LUMO) is unoccupied due to crystal-field splitting. Accordingly, the enhanced stability of $[W@Si_{12}]^+$ observed as a magic species in experiment by reacting transition metal ions with silane[481] might be interpreted by the onset of completely encapsulated structure that stops further growth through silane interaction.

However, the above model cannot explain the relative stability of $FeSi_n$ (n = 9−16) since the 3*d* shell of Fe dopant is fully occupied in all these clusters.[447] Regarding this issue, Phi *et al.*[451] argued that the number of delocalized electrons over the entire cluster should be used for the electron counting rules, as indeed it was done by Kumar[369] and supported from experiments[56] for Ti doped silicon clusters. They further proposed a consistent way to count the number of electrons in order to explain the relative stability of the M@Si_{12} (M = Sc−Ni) clusters. Within the picture of the shell model, the delocalized valence electrons move in an average confining potential related to the cluster geometry. In turn, the energy ordering and the degeneracy of the orbitals are affected by both the shape and charge of the clusters. In these M@Si_{12} clusters, the superatomic orbitals of P, D, F, G, ... shells, which are degenerate in a spherical confining potential, split due to the (distorted) hexagonal prismatic shape. The electronic total and partial densities of states of Cr@Si_{12} obtained by Gaussian broadening of the electronic levels along with the superatomic orbitals are plotted in Figure 34. The shell sequence derived from the orbital shapes is $1S^21P^41P_z^21D^81F^82S^21D^2_{z^2}1F^42P^41G^22D^82P_z^21G^62D^0_{z^2}$. Note that the electrons in the shell orbitals with n_r = 1 are localized on the Si−Si bonds, while those in n_r = 2 shell orbitals are more delocalized and are responsible for the dopant-cage interactions. Due to the orbital splitting by the hexagonal prismatic shape of the cluster, the P_z and Dz^2subshells are much higher in energy than the other P and D subshells. As a result, the n_r = 2 orbitals are filled to the $2D^8$ subshell, leaving the LUMO−$2Dz^2$ empty. Therefore, the Cr@Si_{12} cluster has 16 delocalized electrons in the filled $2S^22P^62D^8$ shells.

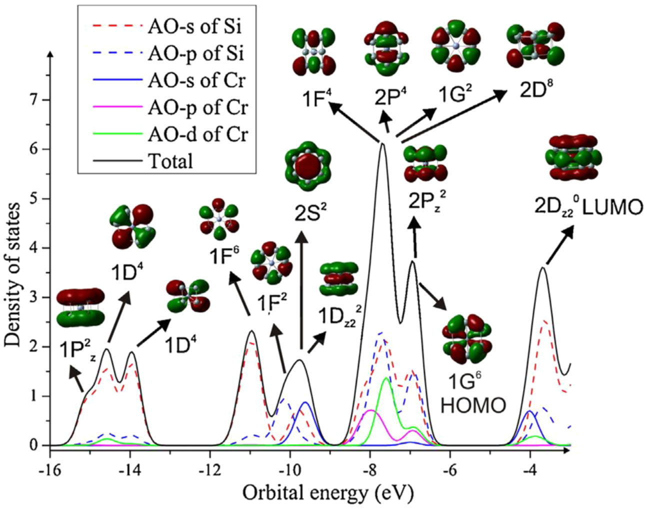

Figure 34. Total and partial densities of states of the D_{3d} ground state structure of Cr@Si_{12}. Orbital energies are calculated at the B3P86/6-311+G(d) level of theory. Molecular orbitals are shown and assigned based on comparison with shell orbitals. Reproduced with permission from ref 451. Copyright 2015 Elsevier B.V.

It is also noteworthy that many M@Si_{12} clusters (M = Ti, V, Cr, Mn, Fe, Co, Cu, Zn, Nb, Mn, Ru, Ta, W, Re) adopt rigorous, distorted, and puckered hexagonal prism structures (Figure 33a, b, c), which can be considered as 3-connected 12-vertex cages. Except for Zn@Si_{12} with 60 electrons that attains the electron-precise count required by the Wade−Mingos rules (5 × n_v = 60), most of the aforementioned M@Si_{12} clusters have 54−56 electrons. In the latter case, the encapsulated metal atom attains a 16-electron configuration, while the entire cluster is electron deficient.[448]

Even though Si_{12} is a relatively small host cage, doping of two dopant atoms may also lead to stable endohedral Si_{12} cage, e.g., B_2@Si_{12} having a tetracapped tetragonal prism with a B_2 unit inside the cage.[471] On the other hand, Fe_2Si_{11} is a Fe-centered distorted icosahedron with 11 Si atoms and one Fe atom on the surface.[459]

5.3.4. Endohedrally Doped Si_{13} Cages. Compared to the neighboring sizes n = 12 and 14, there have been relatively less theoretical studies on endohedrally doped Si_{13} cages. The previously explored metal dopants include Ti,[364,365,403,410,412] Cr,[362,364,371,440] V,[496] Mn,[420,497] Fe,[369,434] Zr,[365,386,410] Nb,[450] Hf,[365,410] Ta,[382,388] and W.[446] By considering the isomeric structures in Figure 35, our PBE0 calculations have determined the ground states of these M@Si_{13} clusters, and the essential results are summarized in Table S8. Although an endohedral cage structure in Figure 35c was previously proposed for Cr@Si_{13}[362,364,440] and Mn@Si_{13},[397] our calculations suggest a capped cage configuration (Figure 35e) lower in energy by 0.060 and 0.165 eV, respectively, consistent with other reports.[371,420] Among the remaining nine endohedral cage clusters, Fe@Si_{13} adopts a high spin state with a total magnetic moment of 2 μ_B. Except for Fe@Si_{13} that has top-capped puckered hexagonal prism structure (Figure 35c), all M@Si_{13} clusters adopt top-capped hexagonal prism (Figure 35b), in agreement with previous theoretical results for V@Si_{13},[364,365,496] Zr@Si_{13},[365] Hf@Si_{13},[365] and Ta@Si_{13}.[382,388] Note that top-capped hexagonal antiprism with C_{6v} symmetry (Figure 35a) was considered as the ground state structure for Ti@Si_{13}[412] and W@Si_{13},[446] but it is higher in energy by 0.524 and 0.421 eV, respectively, according to our calculation at the PBE0/6-311+G(d), SDD level. Similarly, side-capped hexagonal prism (Figure 35d) was previously proposed for Ti@

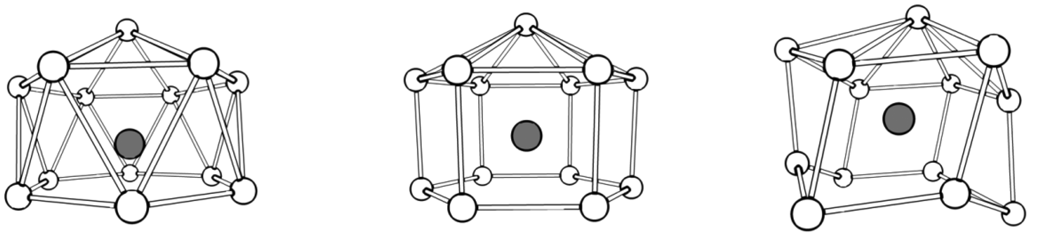

(a) Top Capped Hexagonal Antiprism (C_{6v})

(b) Top Capped Hexagonal Prism (C_{6v})

(c) Top Capped Puckered Hexagonal Prism (C_{3v})

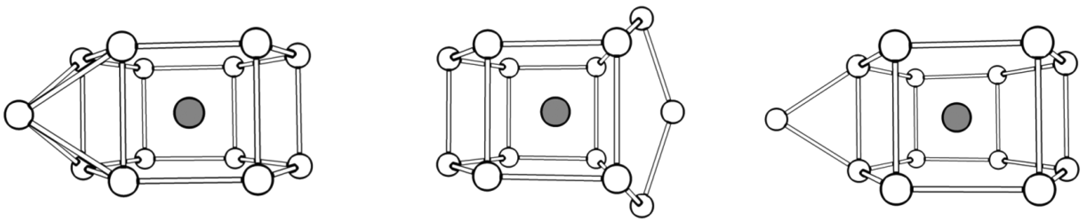

(d) Side Capped Hexagonal Prism (C_2)

(e) Distorted Side Capped Hexagonal Prism (C_{2v}, C_s)

(f) Side Capped Hexagonal Prism (C_1)

Figure 35. Schematic structures of isomers for M@Si$_{13}$ cage clusters with M the endohedral dopant as given in Table S8. Other details are as in Figure 31.

Si$_{13}$,[410] Fe@Si$_{13}$,[447] Zr@Si$_{13}$, and Hf@Si$_{13}$[410] but is less stable by 0.690, 0.266, 0.613, and 0.595 eV, respectively, compared with the lowest energy structures we have obtained. It is interesting to mention that, Si$_{13}$ cages encapsulating a group 4 transition metal atom have sizeable HOMO−LUMO gap and large embedding energy: E_{HL} = 2.922 eV and E_{em} = 10.231 eV for Ti@Si$_{13}$, E_{HL} = 2.865 eV and E_{em} = 12.606 eV for Zr@Si$_{13}$, E_{HL} = 2.823 eV and E_{em} = 11.127 eV for Hf@Si$_{13}$. The high stability of these endohedral cage clusters can be rationalized by the Wade−Mingos rules with $4n_v$ + 4 electrons if one considers the enclosed Ti/Zr/Hf atom contributing all of the four valence electrons to skeletal bonding and the top-capped hexagonal prism structure as a 13-vetex (*nido*)-deltahedron.

5.3.5. Endohedrally Doped Si$_{14}$ Cages.

As schematically shown in Figure 36, we explored many possible Si$_{14}$ cages for endohedral doping of a guest atom M. The previously explored dopant elements include Sc,[391,405,458] Ti,[364,365,391,403,410−412] V,[391,417,456] Cr,[358,362,364,417,440,456,460] Mn,[456] Fe,[380,389,434,447,456] Zn,[405] Nb,[378,450] Mo,[358] Zr,[365,376,386,410−412] Hf,[365,410−412] Ta,[378] W,[358,374,376,378] Os,[376] and Au.[473] Note that n = 14 is the threshold size of nonreactivity toward H$_2$O vapor for neutral ZrSi$_n$ and HfSi$_n$ clusters in experiments.[486] Again, we have carried out PBE0 calculations by considering a few possible cage isomers with different spin multiplicities. From our optimization and earlier results of Jaiswal *et al.*,[370] an initial endohedral configuration of Y@Si$_{14}$ would transform into an open cage structure after relaxation suggesting that 14 Si atoms are not sufficient to form a cage with Y in agreement with experiments (Table 9), while the most stable structure for Cu@Si$_{14}$ is a bicapped 12-vertex cage. Meanwhile, the ground state configurations for both Fe@Si$_{14}$ and Mn@Si$_{14}$ clusters are based on face-capping on a 13-vertex cage.[417] Thus, these four clusters will not be discussed further.

The results for the most stable endohedral M@Si$_{14}$ cages are summarized in Table S9. Five kinds of endohedral cage configurations emerge as the lowest-energy isomers for different transition metal dopants: (i) fullerene-like structure composed of six pentagons and three quadrilaterals (Figure 36a) for V,[417] W,[374,378] and Ta,[378] (ii) another fullerene-like cage (Figure 36b) for Zr[386] and Nb,[450] (iii) *arachno*-architecture (Figure 36c) for Cr[440,460] and Mo, (iv) cubic cage (Figure 36h) for Ru and Os,[48,49] and (v) bicapped hexagonal prism (Figure 36d) for Sc, Ti,[364,365] and Hf.[365] Since we have considered up to 12 cage geometries, the present lowest-energy structures may differ from the previously reported ones, but usually the present ones are more stable. For instance, the fullerene-like cage (Figure 36a) was believed to be the most stable structure for Ti@Si$_{14}$[403,410−412] and Hf@Si$_{14}$;[410−412] but it is higher in energy than isomer (d) by 0.372 eV for Ti and 0.372 eV for Hf, respectively. The previously predicted isomer (Figure 36i) for Sc@Si$_{14}$[458] is less stable than the lowest-energy isomer in Figure 36d by 0.084 eV from our calculations. The isomeric structure in Figure 36g was previously proposed for Mo@Si$_{14}$ and W@Si$_{14}$[358] as the ground state. In our calculations, however, it would transform into the isomeric structure shown in Figure 36c upon optimization. This is the ground state for Mo@Si$_{14}$ but is a high-energy isomer for W@Si$_{14}$ lying 0.731 eV higher than that in Figure 36a. Among the endohedral M@Si$_{14}$ clusters, those with fullerene-like cage structures (Figure 36a, b) usually possess relatively smaller HOMO−LUMO gap (less than 2 eV with PBE0 functional). This can be understood by the Wade−Mingos rules for these 14-vertex three-connected polyhedra that require a total of 70 valence electrons. But all the clusters in this structure have less number of valence electrons and are electron deficient since each transition metal dopant (M = V, W, Ta, Zr, Nb) can contribute up to 6 electrons and the Si$_{14}$ cage has 56 electrons.

In contrast, Cr@Si$_{14}$ and Mo@Si$_{14}$ clusters both with *arachno*-architecture in Figure 36c possess sizeable HOMO−LUMO gap of over 3 eV (see Table S9) and satisfy the Wade−Mingos rules with $4n_v$ + 6 = 62 valence electrons. The electronic states and molecular orbitals of Cr@Si$_{14}$ have also been discussed within the picture of the 18-electron rule, as

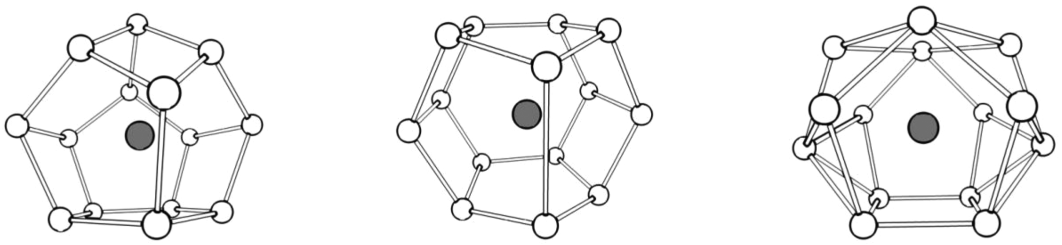

(a) Fullerene-like Cage (D_{3h}, C_{2v}, C_s)

(b) Fullerene-like Cage (C_{2v}, C_s)

(c) Arachno Architecture (C_{2v})

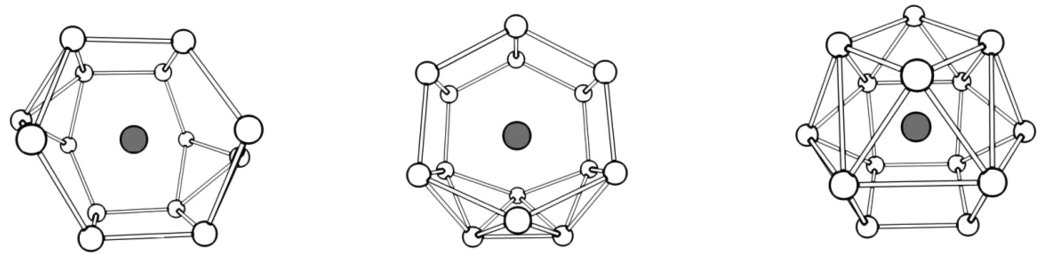

(d) Bicapped Hexagonal Prism (C_{2h})

(e) Dimer Capped Hexagonal Prism (C_{2v})

(f) Tetracapped Pentagonal Prism (C_{2v})

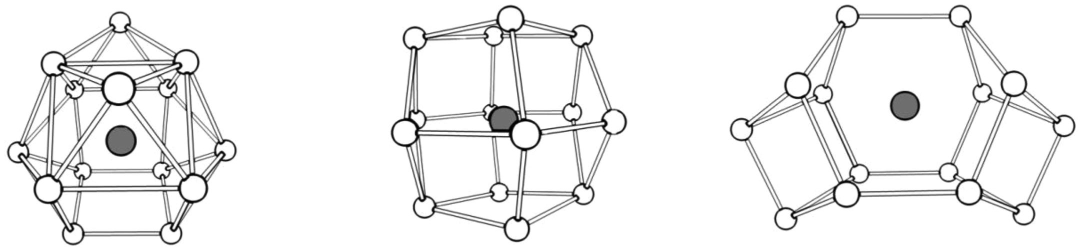

(g) Tetracapped Pentagonal Prism (C_{2v})

(h) Cubic Cage (O_h, D_{4h})

(i) Basket-like Cage (C_{2v})

Figure 36. Schematic structures of isomers for M@Si_{14} cage clusters with M the endohedral dopant as given in Table S9. Other details are as in Figure 31.

shown in Figure 37.[440] It was suggested that the central Cr atom possesses an electronic configuration of $4s^2 4p^6 3d^{10}$ with five 3*d* orbitals being fully occupied. However, it should be kept in mind that these are hybrid orbitals arising from interaction of Cr orbitals with those of the Si cage. Owing to the nearly spherical shape of the cage, there is no significant crystal field splitting and all the 3*d* orbitals are located within an energy range of 0.8 eV. One can also see notable hybridization between the $3d_{xz}$ and the $4p_x$ orbitals, resulting in two mixed orbitals, while the $3d_{xy}$ and $3d_{yz}$ orbitals of Cr hybridize with those of the Si_{14} cage to produce two sets of orbitals each. In this manner, Cr@Si_{14} has 18 effective valence electrons and exhibits the highest stability among the examined $CrSi_n$ clusters (n = 6−16), satisfying the 18-electron rule.

The high stability of Cr@Si_{14} and its isoelectronic counterpart $[Mn@Si_{14}]^+$ has also been discussed by several other groups.[417,456,474] In $[Mn@Si_{14}]^+$, there is a strong hybridization between the 3*d* orbitals of Mn and the 2D shell orbitals of the Si_{14} cage along with a large amount of charge transfer from the Si_{14} cage to the Mn dopant.[474] Consequently, the 3*d* shell of Mn is filled and its magnetic moment is completely quenched, as observed in the XMCD experiment.[493] The 18 delocalized electrons distributed on nine molecular orbitals are mainly responsible for the interaction between the Mn dopant and the Si_{14} cage and confer spherical aromaticity to the cationic $[Mn@Si_{14}]^+$ cluster.

In an earlier theoretical study, X. Jin *et al.*[456] discussed the structural landscape in M@Si_{14} clusters (M = V, Cr, Mn, Fe) by considering three candidate structures—a fullerene-like D_{3h} cage (Figure 36a), a C_{2v} *arachno*-polyhedron (Figure 36c), and an octahedral cage (Figure 36h) and using three functionals (PBE, BLYP, and B3LYP). It was found that the global minimum structure for a given cluster is rather sensitive to the choice of computational method. The key picture is that these apparently very different structures make use of the limited electron density available from the endohedral metal atom in very different ways. An early transition metal dopant favors the structure that maximizes charge transfer from the electropositive metal to the silicon cage, while for later transition metal dopants, the preferred cage geometry minimizes repulsions with the increasingly core-like *d* electrons.

Combining anion photoelectron spectroscopy and DFT-based global search, Zheng and co-workers revealed a bicapped hexagonal antiprism structure with D_{6d} symmetry for triply metal doped silicon cluster anions of $[V_3Si_{12}]^-$[443] and $[Cr_3Si_{12}]^-$[460] as well as their neutral counterparts. In this unique wheel-like structure, three metal atoms form a central axis with one in the cage interior and two on the surface. Replacing one surface Cr atom by Si in the Cr_3Si_{12} cluster leads to the lowest-energy structure of Cr_2Si_{13}. Interestingly, these cluster anions possess sizeable magnetic moment, e.g., 4 μ_B for

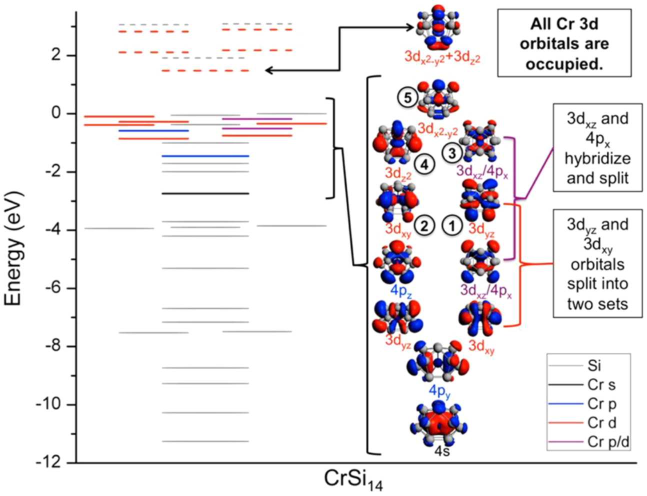

Figure 37. $Cr@Si_{14}$ energy levels and selected orbitals. The orbital energy levels of $Cr@Si_{14}$ are shown and are assigned based on orbital composition as predominantly silicon, shown in gray, or having chromium *s*, *p*, *d*, or *p-d* hybrid character, shown in black, blue, red, and purple, respectively. Occupied orbital energy levels are shown with solid lines, and unoccupied orbital energy levels are shown with dashed lines. The selected orbitals are those with high Cr character, and the contributing Cr orbitals are noted. Numbers 1 to 5 denote the hybrid orbitals that have strong 3*d* character of Cr. Reproduced with permission from ref 440. Copyright 2014 American Chemical Society.

$[V_3Si_{12}]^-$ and 7 μ_B for $[Cr_3Si_{12}]^-$. The four unpaired electrons in the 14-vertex deltahedron of $[V_3Si_{12}]^-$ can be interpreted by the Wade−Mingos rules with $4n_v + 2 = 58$ valence electrons and the remaining 4 electrons leading to 4 μ_B magnetic moment on $[V_3Si_{12}]^-$. In a similar manner we can understand $[Cr_3Si_{12}]^-$. The on-site magnetic moments of $[V_3Si_{12}]^-$ align in a ferrimagnetic manner, that is, 2.4 μ_B on each of the surface V atoms and −0.6 μ_B on the interior V atom. There are also negligibly small induced moments on Si atoms (−0.018 μ_B per atom).[443]

5.3.6. Endohedrally Doped Si_{15} Cages. In experimental mass spectra of various metal doped silicon clusters,[36,37,480,483] $M@Si_{15}$ was seen as the "magic number" peak for M = Cr, Mo, W, and Mn, suggesting the existence of endohedral cages with 15 Si atoms. Kumar and Kawazoe[48,49] studied Mo and W doped silicon clusters with 15 and 16 atoms and explained the long-standing observations by Beck.[36,37] Subsequent theoretical studies have explored Si_{15} cages encapsulating a variety of guest atoms, including Sc,[391,418,458] V,[391,418] Ti,[364,365,391,395,401,410−412,418] Cr,[358,362,364,418,440] Fe,[418] Y,[370,407] Zr,[365,376,386,410−412] Hf,[365,410−412] Ta,[426] and W.[358,376] The previously considered Si_{15} cage geometries for endohedral doping are schematically plotted in Figure 38, and our PBE0 results for the aforementioned dopants are summarized in Table S10. Note that our geometry optimization obtained capped cage structures for $Fe@Si_{15}$, $Mn@Si_{15}$, and $Y@Si_{15}$ clusters, and thus, they will not be discussed further.

Generally speaking, the lowest-energy structures obtained for $M@Si_{15}$ agree with most of the reported structures. The ground state structure of $Sc@Si_{15}$ (Figure 38a) is consistent with that found in refs 391 and 458 and prevails the one reported in ref 418 by 0.14 eV. The most stable structure of $Ti@Si_{15}$ (Figure 38b) is identical to that reported in the literature,[364,365,391,395,401,410−412] and the same structure is also found for $Hf@Si_{15}$ here, in agreement with the previous finding.[365] The ground state structure of $V@Si_{15}$ (Figure 38c) is in line with the previous reports.[391,418] As for $Cr@Si_{15}$, the previously proposed ground state structures in Figure 38g[362,418,440] and Figure 38f[358] are slightly higher in energy than the present ground state structure in Figure 38c by 0.04 and 0.06 eV, respectively. The lowest-energy structure of $Zr@Si_{15}$ (Figure 38h) is more stable than the isomer (Figure 38b) in ref 365 and the isomer of Figure 38i in ref 386 by 0.09 and 0.334 eV, respectively. The same ground state configuration (Figure 38f) has been obtained for $Mo@Si_{15}$ and $W@Si_{15}$ by present calculations and Kumar's previous one.[358] For $Ta@Si_{15}$, the isomeric structure in Figure 38d is energetically more favorable than that in Figure 38b predicted in ref 426 by 0.043 eV.

Among the ten $M@Si_{15}$ clusters in Table S10, the HOMO−LUMO gaps for the dopants of group 4 (Ti, Zr, Hf) and group 6 (Cr, Mo, W) elements are relatively large, ranging from 1.94 to 3.03 eV. These are also comparable to the previously reported values for $M@Si_{15}$ clusters (M = Cr, Ti, Zr, Hf) using different hybrid functionals.[362,410−412,418] In contrast, the HOMO−LUMO gaps for the dopant of group 3 (Sc) and group 5 elements (V, Nb, Ta) with odd number of valence electrons are less than 1 eV. The embedding energies for most of the dopants except for Sc and Cr atoms, are substantial and lie in the range of 10 eV to 14 eV. Neither the 18-electron nor 20-electron rule seems to be applicable to account for the stability and electronic structure of these $M@Si_{15}$ clusters.

Previously, Kumar and Kawazoe[358] found that a 15-atom silicon cage is the optimal host for encapsulating Cr, Mo, and W atoms. Abreu *et al.*[446] ascribed the high stability of $[WSi_{15}]^+$ observed in Beck's early experiment to a combination of geometric and electronic features, as evidenced by its highest silicon removal energy and tungsten embedding energy as well as the second highest HOMO−LUMO gap among $[WSi_n]^+$ clusters (n = 6−16).

In addition to the singly doped silicon cages, the lowest-energy structure of Nb_2 doped Si_{14} cluster is an endohedral 15-vertex cage with a central Nb atom,[463] similar to the geometry in Figure 38b. Furthermore, doping two Mo atoms into Si_{15} cluster results in a tubular structure filled with a Mo_2 dimer,[402] instead of a metal-centered endohedral cage.

5.3.7. Endohedrally Doped Si_{16} Cages. Following the pioneering work by Kumar and Kawazoe,[48,49] transition metal doped Si_{16} cage clusters have attracted particular interest during the last two decades. They showed fullerene-like and FK polyhedron structures to be particularly stable. Subsequently a large number of studies have been made and possible suitable metal atom dopants to match the size of 16-atom silicon cage have been found to be early transition metals of 3*d*, 4*d*, and 5*d* series, as well as some rare earth metals including Sc,[391,400,401,418,439] Ti,[359,361,364,365,391,395,396,401,410−412,418,421,435,461] V,[391,401,425] Cr,[358,364,425] Y,[370,407,472] Zr,[359,361,365,376,386,410−412,421,435,461] Nb,[450] Mo,[358] Hf,[359,365,376,410−412,421,435,461] Ta,[388,426] W,[358,376] La,[408] Gd,[428] Ho,[441,452] and Ln[119] (Ln = La, Ce, Pr, Nd, Sm, Eu, Gd, Tm, Yb, Lu). For the dopants of group 6 elements (Cr, Mo, W), endohedral $M@Si_{16}$ cage configurations were found to be less stable than the Si-capped $M@Si_{15}$ cage.[358] Furthermore, the most stable structures of neutral $V@Si_{16}$ and $Nb@Si_{16}$ are also capped cage structures from our calculations. Hence these five doped silicon clusters will not be further discussed. It is worth mentioning that the cations of these V and Nb doped clusters become isoelectronic, respectively, with neutral Ti and Zr doped clusters which form 16 Si atom cages. As we have

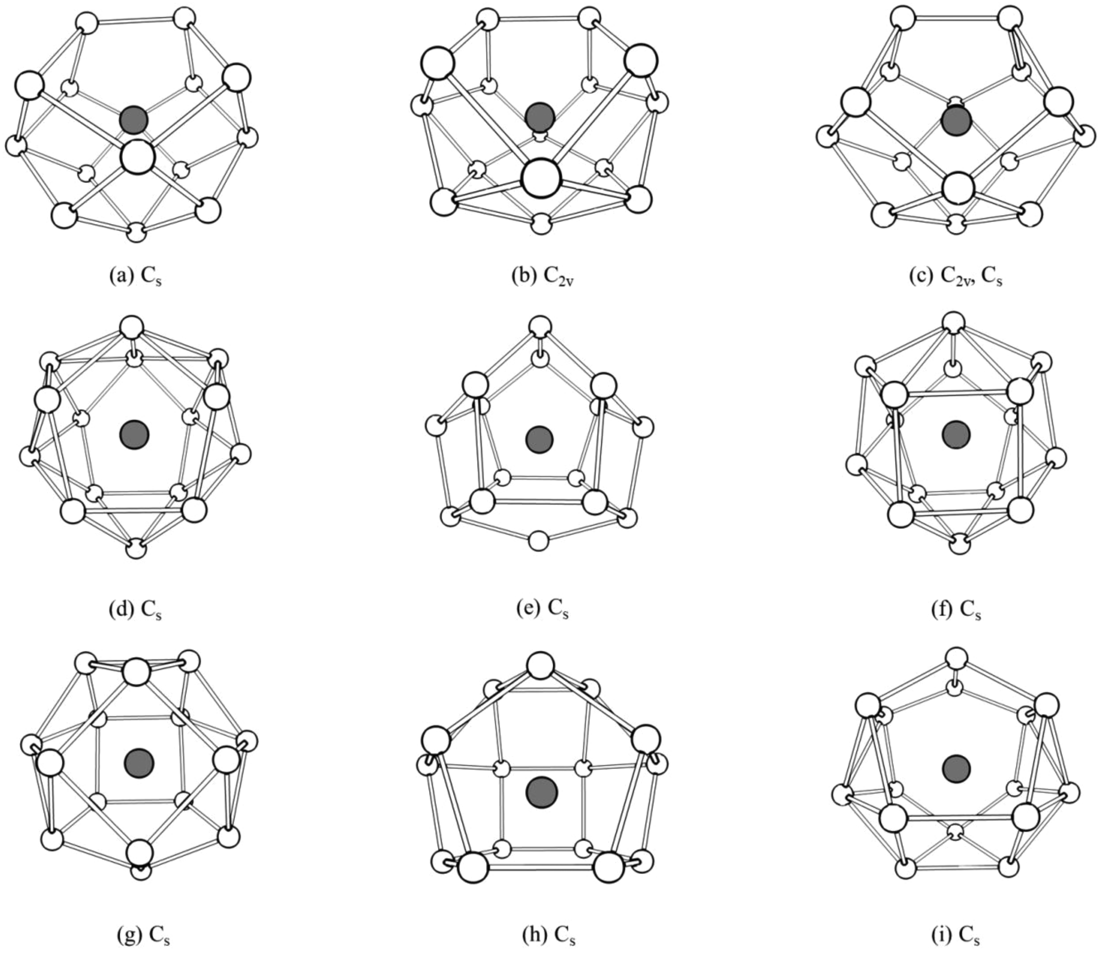

Figure 38. Schematic structures of isomers for M@Si_{15} cage clusters with M the endohedral dopant as given in Table S10. All isomers can be viewed to have mixed fullerene-like cage and FK polyhedron features; thus, they are not specifically named on the plot. Other details are as in Figure 31.

discussed above, there are strong experimental indications for the FK polyhedral structure of $[Si_{16}V]^+$ with high symmetry using X-ray absorption spectroscopy[56] and IR-MPD spectroscopy.[340]

In order to explore different endohedrally doped cages, we considered six possible topologies for 16-vertex polyhedron in our *ab initio* calculations at the PBE0/6-311+G(d), SDD level of theory. The atomic structures of these polyhedron structures are shown in Figure 39, and other results are given in Table S11. Generally speaking, there are three types of endohedral Si_{16} cages: (i) a fullerene-like cage formed by three-coordinated silicon atoms only (isomer a), (ii) FK polyhedron with triangular facets only (Figure 39b) as *closo*-deltahedron, and (iii) mixed fullerene-FK-like polyhedra with triangular, quadrilateral, pentagonal, or hexagonal facets (Figure 39c, d, e, f). Our calculations confirm the finding from most previous theoretical calculations that fullerene-like cage is energetically favorable for Y,[370,407,472] Zr,[359,361,365,386,410−412,461] La,[408] Hf,[359,365,410−412,461] Ta,[388] and Ho[441,452] dopants. On the other hand, FK polyhedron is the ground state for Sc@Si_{16}[391] and Ti@Si_{16}.[48,359,361,364,365,391,395,396,421,461] It is to be noted that in some cases such as Hf doping, the energy difference between the fullerene-like and FK polyhedral isomers is small and the lowest-energy structure may depend on the exchange-correlation functional used. In particular, using PW91 functional, a deformed FK polyhedron (Figure 21g) was found[48,49] to be lower in energy than the FK isomer but slightly higher in energy than the fullerene isomer. Also, in cases such as Ti@Si_{16}, Zr@Si_{16}, Hf@Si_{16}, and V@Si_{16}^+, the 16-atom cage is structurally optimal and that leads to their high abundance.

Starting from an initial fullerene-like cage, Gd@Si_{16} cluster relaxes into a unique FK-like polyhedron (Figure 39f) with C_{2v} symmetry. More interestingly, it is a magnetic species with a rather high spin moment of 6 μ_B, which mainly originates from the unpaired 4*f* electrons.[428] As seen in Table S11, in this case the smallest embedding energy of 7.360 eV indicates relatively weaker dopant−cage interaction or strain in the structure due to slightly larger size of Gd compared with Zr, but the magnetic moment on Gd is not quenched as *f* electrons are very localized. By analyzing the on-site charge and magnetic moment of the Gd@Si_{16} cluster, T. G. Liu *et al.*[428] suggested that the highly localized 4*f* electrons of Gd do not interact with the silicon cage to a large extent. The valence electron configuration of Gd atom is $4f^7 5d^1 6s^2$ with a total of ten valence electrons. If we assume that the Gd atom contributes four electrons and each Si atom on the Si_{16} cage has four valence electrons, there would be a total of 68 electrons, which is a magic number within the spherical jellium model. The remaining six unpaired 4*f* electrons on Gd account for the total magnetic moment of 6 μ_B for Gd@Si_{16}. Similarly, Ho@Si_{16} with a fullerene-like cage structure carries a magnetic spin moment of 5 μ_B, which is derived mainly from the 4*f* states of

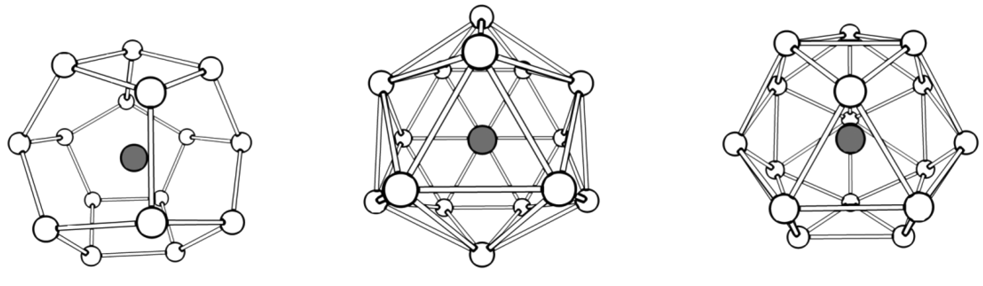

(a) Fullerene-like Cage
(D_{4d}, C_{4v}, C_{2v}, C_2, C_s)

(b) Frank-Kasper Polyhedron
(T_d, D_{2d})

(c) Frank-Kasper-like Polyhedron 1
(C_{3v})

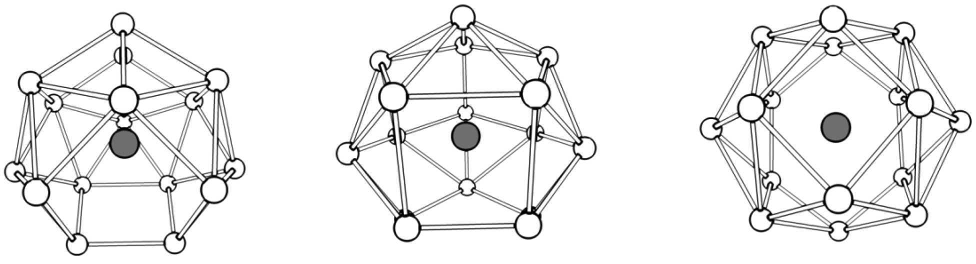

(d) Frank-Kasper-like Polyhedron 2
(C_{2v})

(e) Frank-Kasper-like Polyhedron 3
(C_s)

(f) Frank-Kasper-like Polyhedron 4
(C_{2v})

Figure 39. Schematic structures of isomers for M@Si_{16} cage clusters with M the endohedral dopant as given in Table S11. Here c−f are mixed type and have triangular, quadrilateral, pentagonal, or hexagonal facets. Other details are as in Figure 31.

Ho (about 4 μ_B).[452] The observation of appreciable magnetic spin moments in lanthanide doped silicon clusters fulfills the early expectation from calculations by Kumar *et al.*[366] and also from experiments by Grubisic *et al.*[492] based on photoelectron spectra of these clusters. By taking into account the SOC effect, Zeng and co-workers[119] further examined the magnetic properties of the lanthanides doped silicon cage clusters Ln@Si_{16} and found that late lanthanides doped clusters maintain large magnetic moments, especially for Eu (5.85 μ_B) and Gd (6.81 μ_B). When the 4*f* shell is less than half-filled, the directions of orbital moments of Ln atoms are opposite to the spin moments, and vice versa. In particular, some Ln atoms like Pr, Nd, Sm, and Tm possess large orbital moments of up to 2.71 μ_B.

In the case of Ti, Zr, and Hf doped Si_{16} clusters, there are 4 valence electrons on the transition metal atom and 64 electrons on the silicon cage. Therefore, the total number of valence electrons is 68 and this was suggested[361] as the reason for the excellent stability of these clusters because 68 electrons correspond to a magic number in the spherical shell model. This viewpoint was supported also from photoelectron spectroscopic experiments.[56] Figure 40 shows the energy level of f-Zr@Si_{16} and FK-Ti@Si_{16} clusters. For FK-Ti@Si_{16}, one can see the superatomic orbitals in the sequence of $1S^2 1P^6 1D^{10} 1F^{14} 2S^2 1G^{18} 2P^6 2D^{10}$.

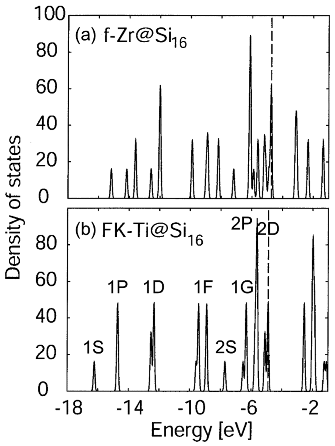

Figure 40. Kohn−Sham energy spectra of fullerene type f-Zr@Si_{16} and FK-Ti@Si_{16} clusters with Gaussian broadening (half width 0.05 eV) calculated with PW91 functional and planewave basis. Broken line shows the HOMO. Reproduced with permission from ref 395. Copyright EDP Sciences, Springer-Verlag 2003.

In another interpretation, the stability of Ti@Si_{16}, Zr@Si_{16}, and Hf@Si_{16} clusters was associated with the 20-electron rule, i.e., 16 bonding electrons contributed by Si atoms coordinating with the tetravalent metal atom.[391] This viewpoint could be considered particularly for the fullerene isomer. Around each Si atom, we can construct sp^3 hybrid orbitals, out of which one would point outward of the cage and have one electron, giving rise to 16 π bonded electrons. This together with the 4 valence electrons of the encapsulated M atom leads to a 20-electron system. Interestingly, the $[Si_{16}]^{4-}$ cage was also shown to be aromatic with NICS value of −40.9 ppm for fullerene-like structure and −22.9 ppm for the FK polyhedron, respectively.[392] Further studies on a tetravalent metal atom (or ion) M doped endohedral M@Si_{16} cages have shown them to have 18 electrons in π states and 50 electrons in σ states, fulfilling the $2(N + 1)^2$ rule of spherical aromaticity.[133] Nevertheless, such a unique coincidence for the closing of electronic shells within different electron counting models results in a large HOMO−LUMO gap of 2.095−2.966 eV (using HSE06 functional) and sizeable embedding energy in the range of 10.658 eV to 14.812 eV in these three clusters. The high stability of these magic clusters with totally 68 valence electrons is directly evidenced by the strong peaks in experimental mass spectra of Ti@Si_{16}, Zr@Si_{16}, and Hf@Si_{16} clusters and their isoelectronic counterparts of cluster anions/cations.[55,486] The calculated HOMO−LUMO gaps are comparable to previous DFT results using different functionals, such as 2.34 eV (PBE)[391] and 3.468 eV (B3PW91)[365] for Ti@Si_{16}, 1.58 eV (PW91)[365] and 2.117 eV (B3LYP)[386] for Zr@Si_{16}, and 1.576 eV (PW91)[365] for Hf@Si_{16}. For comparison, the HOMO−LUMO gaps of Ti@Si_{16}, Zr@Si_{16}, and Hf@Si_{16} determined from experimental photoelectron spectra of their anionic species (Figure 27) were 1.90, 1.36, and 1.37 eV, respectively.[486] It should be noted that the anionic clusters become slightly deformed and have lower HOMO−LUMO gaps than the neutral clusters.[361] Moreover, valence band and core-level photoionization spectroscopic measurement yields a HOMO−LUMO gap of 2.1 ± 0.2 eV for $[VSi_{16}]^+$ (isoelectronic to Ti@Si_{16}).[494]

Combining global search with GA incorporated with DFT relaxation, high-level CCSD(T) calculations, and comparison between the simulated photoelectron spectra and experimental data, X. Wu *et al.*[461] recently revisited the neutral and anionic M@Si_{16} clusters (M = Ti, Zr, Hf). For neutral Ti@Si_{16}, the FK deltahedron (Figure 39b) with T_d symmetry and distorted FK polyhedron (Figure 39c) with C_{3v} symmetry are nearly degenerate as the ground state as it was found earlier,[48,49] while the latter one is the most probable structure for $[Ti@Si_{16}]^-$ anion. For neutral/anionic Zr@Si_{16} and Hf@Si_{16} clusters, their ground states at finite temperatures up to 300 K are the fullerene-like cage (Figure 39a), based on which the experimental photoelectron spectra can be well reproduced.

In addition to single transition metal atom doping, 16 Si atoms are able to form a fused dual-cage configuration to enclose two metal atoms like Pd[438] and Pt[457] or to form an elongated cage to accommodate two Mo atoms.[402] In the former structure, the two metal atoms are well separated and individually encapsulated by a Si_{10} pentagonal prism, and the two pentagonal prisms share a quadrilateral face. For the latter situation, a Mo_2 dimer with Mo−Mo distance of 2.484 Å is encapsulated by a cage-like D_{4d} Si_{16} frame with slight distortion. At the B3LYP/LanL2DZ level, the theoretical HOMO−LUMO gap is 1.593 eV for Pd_2Si_{16}, 1.52 eV for Pt_2Si_{16}, and 1.556 eV for Mo_2Si_{16}, respectively.

5.3.8. Endohedrally Doped Si_{18} and Si_{20} Cages. As an intermediate size between Si_{16} and Si_{20}, endohedral Si_{18} cages have received less attention, and only a few transition metal atom (Ti, Zr, Hf[412]) or rare earth metal atom (La[408] and Ho[441,452]) have been considered as dopant. We optimized the initial endohedral M@Si_{18} cage structures for M = Ti, Zr, Hf, La, and Ho at the PBE0/6-311+G(d), SDD level of theory. Upon optimization, the cage configurations of Hf@Si_{18} and Zr@Si_{18} are broken, while the Ti@Si_{18} (Ho@Si_{18}) transforms into a bicapped 16-vertex cage encapsulating a Ti(Ho) atom. Hence, only the computational results on La@Si_{18} are given in Table S12. As shown in Figure 41a, the 18-vertex cage of La@Si_{18} is composed of one hexagon, eight pentagons, and two quadrilaterals, which can be derived from the dodecahedral cage of La@Si_{20} by removing two Si atoms.[408]

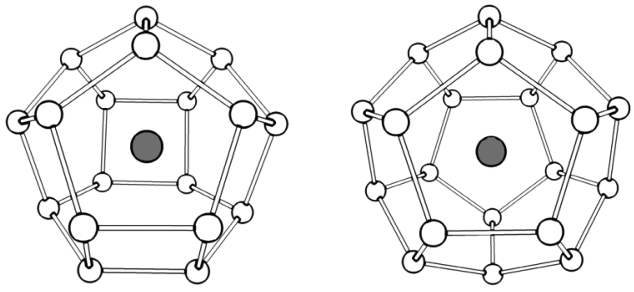

(a) Fullerene-like Cage (C_2, C_1) (b) Fullerene Cage (I_h)

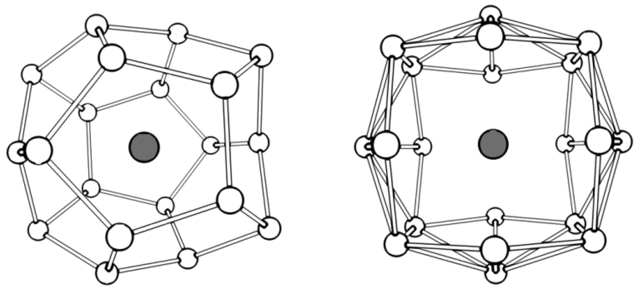

(c) Distorted Fullerence Cage (T_h, D_{5d}, D_{2h}, C_{2h}, C_i) (d) Frank-Kasper Deltahedron (D_{4h})

Figure 41. Schematic structures of isomers for M@Si_{18} (a) and M@Si_{20} (b, c, d) cage clusters with M the endohedral dopant as given in Table S12. Other details are as in Figure 31.

Among the fullerene-like silicon cages, Si_{20} dodecahedron is the largest one to accommodate a transition metal, lanthanide or actinide atom. Owing to the large radius of a pristine Si_{20} cage, only a heavy metal atom can be encapsulated in Si_{20} dodecahedron.[365,366,368] Previously explored endohedral metal atoms in Si_{20} cage include Cs,[422] Rb,[422] Ca,[363] Sr,[363] Ba,[363] Zr,[363] Pb,[363] Y,[367] La,[367,408] Pa,[367] Pr,[455] Sm,[367] Eu,[422] Gd,[367,422] Ho,[441,452], Tm,[367] Ac,[367] and Th.[366] However, using minima hopping method combined with DFT calculations, Willand *et al.*[424] re-examined the structure of Si_{20} cages singly doped with a wide range of simple and transition metal atoms (M = Ba, Ca, Cr, Cu, K, Na, Pb, Rb, Sr, Ti, V, Zr). After unbiased structural search, either exohedral compact configurations or endohedral smaller cages with excess Si atoms forming an apical bud are more stable by 0.58−4.74 eV than the presumed endohedral M@Si_{20} cage structures. According to our calculations and previous study,[428] Gd@Si_n clusters adopt capped endohedral cage structures starting from $n = 17$. J. Wang *et al.*[422] also found that the endohedral cage structures of Cs@Si_{20} and Rb@Si_{20} are high-lying isomers with energy difference larger than 4−6 eV compared with the ground states. Therefore, we only computed the geometric, electronic, and magnetic properties of M@Si_{20} clusters with M = Y, La, Pr, Sm, Eu, Ho, Tm, Yb, Ac, Th, and U, and the results are summarized in Table S12. Note that there are silicon clathrate compounds[509] such as M_xSi_{46} (type-I with x typically 8) and M_xSi_{136} (Type-II, $x \sim 24$) with M an alkali metal or alkaline earth metal, in which the M atoms lie inside Si_{20}, Si_{24}, and Si_{28} fullerene-like cages as building units of clathrates. Accordingly, the behavior of silicon with doping of such atoms is different in the form of clusters. Similar clathrates exist for Ge and Sn also.

In general, the lowest-energy structures of M@Si_{20} clusters from our optimization at the PBE0/6-311+G(d), SDD level of theory agree with most previous reports for Y@Si_{20},[367] La@Si_{20},[367,408] Eu@Si_{20},[422] Ho@Si_{20},[452] and Th@Si_{20}.[366] After enclosing a metal atom, the dodecahedral Si_{20} cage with original I_h symmetry usually undergoes Jahn−Teller distortion and its symmetry reduces to D_{5d} (Y@Si_{20} and La@Si_{20}), C_{2h} (Sm@Si_{20}, Yb@Si_{20}, and Ac@Si_{20}), D_{2h} (Eu@Si_{20}), C_i (Ho@

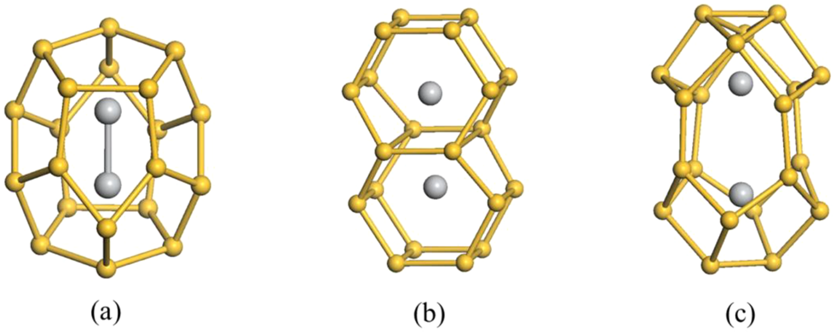

Figure 42. Schematic structures of three isomers for endohedral $M_2@Si_{20}$ clusters. M (Si) atom is shown by grey (yellow) ball.

Si_{20} and Tm@Si_{20}), and T_h (U@Si_{20}), respectively. As an exception, Th@Si_{20} still retains I_h symmetry and possesses the highest embedding energy of 15.423 eV (13.9 eV reported in ref 366 using planewave method with PW91 functional), which can be attributed to the large atomic radius of Th. Indeed, it was suggested that Th is the only atom which stabilizes the neutral Si_{20} fullerene with icosahedral symmetry.[366] This is because Th can exist in 4+ state, and in the dodecahedral structure of Si_{20}, we need four electrons to fill F subshell in the spherical potential model. This also accounts for why the computed HOMO−LUMO gaps are comparatively small (1.336 eV using PBE0, see Table S12).

Noticeably, doping a lanthanide atom with open *f* shell (e.g., Sm, Eu, Ho, Tm) into the Si_{20} fullerene cage induces a substantial magnetic moment of 3−5 μ_B (see Table S12). Previous DFT calculations also predicted consistently large magnetic spin moments in these endohedrally doped M@Si_{20} clusters, namely, 3 μ_B for Tm@Si_{20},[367] 4 μ_B for Sm@Si_{20},[367] 5 μ_B for Ho@Si_{20},[452] 7 μ_B for Eu@Si_{20},[422] as well as Gd@Si_{20} anion.[367] The magnetism of these endohedral cage clusters mainly stems from the partially filled 4*f* states of the central metal atom.[367,452,455] Furthermore, the strongly localized 4*f* electrons induce significant orbital magnetic moments in these endohedral clusters, e.g., −0.37 μ_B, −1.41 μ_B, and 2.41 μ_B for Pa, Sm, and Tm, respectively.[367] Also note that even with the same D_{2h} cage geometry, the total magnetic spin moment from the present PBE0 calculations is 2 μ_B less than that in ref 422 using the PW91/DNP method. Nevertheless, these lanthanide metal doped silicon cages with large magnetic moment and appreciable embedding energy (6.574 eV to 15.423 eV) are ideal building blocks for future spintronics and high-density magnetic storage.

Following the 32-electron rule firstly demonstrated for an icosahedral Pu@Pb_{12} cluster and its isoelectronic counterparts,[132] Dognon *et al.*[430] derived a new family of highly stable 32-electron compounds by encapsulating an actinide anion (U^{6-}, Np^{5-}, Pu^{4-}, Am^{3-}, Cm^{2-}) in the dodecahedral cage of Si_{20}, having HOMO−LUMO gap in the range of 1.5 eV to 2.0 eV (at the B3LYP/TZ2P level) and total binding energy in the range of 84.26 and 113.43 eV. In the case of Si_{20} dodecahedral fullerene cage, the bonding becomes closer to sp^3 type and accordingly 20 lobs point outward of the cage and contribute 20 π bonded valence electrons. This together with 12 electrons coming from the suitably charged actinide atom give rise to a 32-electron system with 1S, 1P, 1D, and 1F states fully occupied in the spherical potential model. Similar 32-electron systems have been proposed for endohedrally doped carbon fullerenes and discussed in Section 4.1 before.

Beyond single metal dopant, there have been early theoretical studies on $Si_{18}M_2$ (M = Cr, Mo, W) clusters[360] due to their observation in experiments.[47] These clusters were shown to have a hexagonal double prism tubular structure with M atoms between the hexagons. Further continuation of this tubular structure was shown to get deformed. The large interior space of Si_{20} cage might be able to accommodate two transition metal atoms. Experimentally, it was conjectured that more than 20 Si atoms are required to encapsulate two metal atoms completely.[487] On the theoretical side, the lowest-energy geometries and energetic stabilities of dual transition metal doped Si_{20} clusters (i.e., $M_2@Si_{20}$) have been explored by several groups. Depending on the size and number of *d* electrons of the metal atom, as well as the M−M bond strength, there are three types of Si_{20} framework structures for endohedral doping, i.e., elongated dodecahedron cage (Figure 42a) for W_2,[376] Zr_2,[409] V_2,[442] and Nb_2,[463,464] double hexagonal prisms stacked structure (Figure 42b) for Ti_2,[462] and FK structure as the combination of two M@Si_{10} endohedral structural units (Figure 42c) for Fe_2.[465] In an early DFT study,[415] a rich class of $M_2@Si_{20}$ clusters possessing perfect, stacked, or deformed double hexagonal prisms have been predicted for M = V, Cr, Mo, Hf, Fe, Co, Re, and Os. However, *ab initio* based global search is still needed to locate the true lowest-energy structures of these doped clusters.

5.3.9. Cage Size vs Atomic Radius of Dopant Element.

According to the above discussions, for each transition metal, rare earth, or actinide metal atom, there is a suitable size range for the silicon cage to enclose a metal dopant. Beyond that, too small a silicon cage cannot completely encapsulate the metal atom leading to basket-like open structures, while too many silicon atoms usually lead to capped cage configurations. To present a complete picture about this effect, Figure 43 displays the correlation between the atomic radius of the doping atom[510] and the possible number of silicon atoms in the cage. In general, one can see that the suitable cage size range generally increases with the radius of the dopant metal atom. However, the atomic size of the dopant atom M is not the only factor determining the formation and thermodynamic stability of an endohedral M@Si_n cage. Many other electronic and geometric factors, such as the electron affinity and occupancy of *d* valence orbitals of the metal atom, symmetry of silicon cage, coordination number of the endohedral metal atom, and the bonding properties and the orbital hybridization between metal and silicon atoms[369,390,405] may also play some roles in determining the allowable size range of the silicon cage. To gain more sophisticated insights, electron counting rules (such as Wade−Mingos rules and the spherical potential model) are necessary to understand the precise correlation between the geometry of

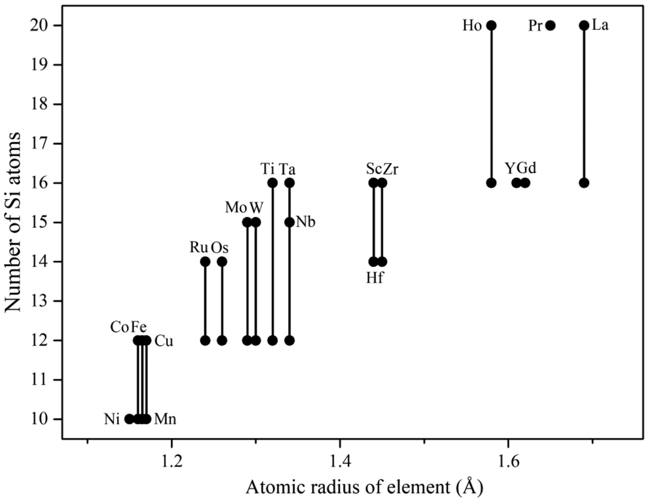

Figure 43. Covalent atomic radius of the dopant element[510] versus the allowable size (number of atoms) range of the silicon cages.

a particular endohedrally doped Si cluster and its electronic structure.

5.4. Physical and Chemical Properties of Doped Silicon Cages

The endohedrally doped silicon cages with enhanced stability and tunable electronic properties provide new opportunities for many potential applications in cluster-based materials and devices. Here we give an overview of the optical and transport properties of the singly metal atom-doped silicon clusters, as well as their gas adsorption and catalytic behaviors. The cluster-assembled materials with doped silicon cages will be discussed in Section 10.

Since silicon nanomaterials play an important role in opto-electronics, the optical properties of endohedrally doped silicon clusters have attracted much attention. Based on the equilibrium structures, the infrared and Raman spectra of doped M@Si$_n$ clusters (M = Ti, Zr, Hf) in the size range of n = 14−20 were simulated by DFT calculations.[361,410,411] For different structural isomers, their infrared intensities and Raman activities showed distinct features, which is helpful for identifying the atomic structures of these clusters in experiments. Also, the calculated optical absorption spectra of Zr@Si$_{16}$ fullerene and Ti@Si$_{16}$ FK isomers showed emission in red and deep blue regions using B3PW91 hybrid functional implemented in the Gaussian program, suggesting possibilities of their identification as well as usefulness in optoelectronics.[361] It would be very interesting to elucidate how doping of different elements in the same group could lead to different structures and properties of silicon clusters. This is what is exciting about these systems with the possibility of making them in high abundances. However, the polarizabilities of these different isomers were shown to have similar values.[361] Within the framework of DFT, the static dipole polarizabilities of FeSi$_n$ (n = 1−14) have been computed by Ma *et al.*.[434] Compared with the pristine Si$_n$ clusters, the polarizabilities of Si atoms are enhanced by Fe doping. Overall, the total cluster polarizability per atom decreases as the cluster grows bigger.

TD-DFT and RPA have been used to calculate the absorption spectra (or dynamic polarizabilities) of a variety of doped silicon clusters, including Ti@Si$_{16}$ and Zr@Si$_{16}$,[361] Cu@Si$_n$ (n = 9−14),[414] M@Si$_{16}$ (M = Ti, Zr, Hf),[435] M@Si$_{12}$ (M = Ti, Cr, Zr, Mo, Ru, Pd, Hf, Os),[435] M@Si$_{12}$ (M = Ti, V, Cr, Ni, Zr, Nb, Mo, Pd, Hf, Ta, W, Pt),[436] M@Si$_{10}$ (M = Ni, Cu, Ag, Au),[436] and M@Si$_{12}$ (M = Sc−Zn).[511] Oliveira *et al.*[435] calculated the polarizabilities and absorption spectra for several Si$_{12}$M and Si$_{16}$M clusters using RPA and GW methods. Figure 44 shows the optical absorption spectra of selected M@Si$_n$ clusters calculated from the Kohn−Sham electronic states within the RPA in the energy range of 0−10 eV.[435] Here the structures of M@Si$_{12}$ clusters were obtained by optimizing a hexagonal prism structure while for M@Si$_{16}$, a FK isomer was considered. One can see that the absorption spectra sensitively rely on the dopant element as well as size of the silicon cage, though for the case of M@Si$_{16}$ (M = Ti, Zr, Hf), the spectra look similar because of their nearly identical structure, but for M@Si$_{12}$, the structure depends on the M atom. However, it should be noted that the structure of Zr@Si$_{16}$ and Hf@Si$_{16}$ is fullerene-like and has lower HOMO−LUMO gap. Accordingly, their absorption properties differ from that of the Ti@Si$_{16}$ cluster.[361] In other words, these doped silicon clusters possess tunable optical adsorption properties, making them suitable as building blocks for the next generation of opto-electronic devices.

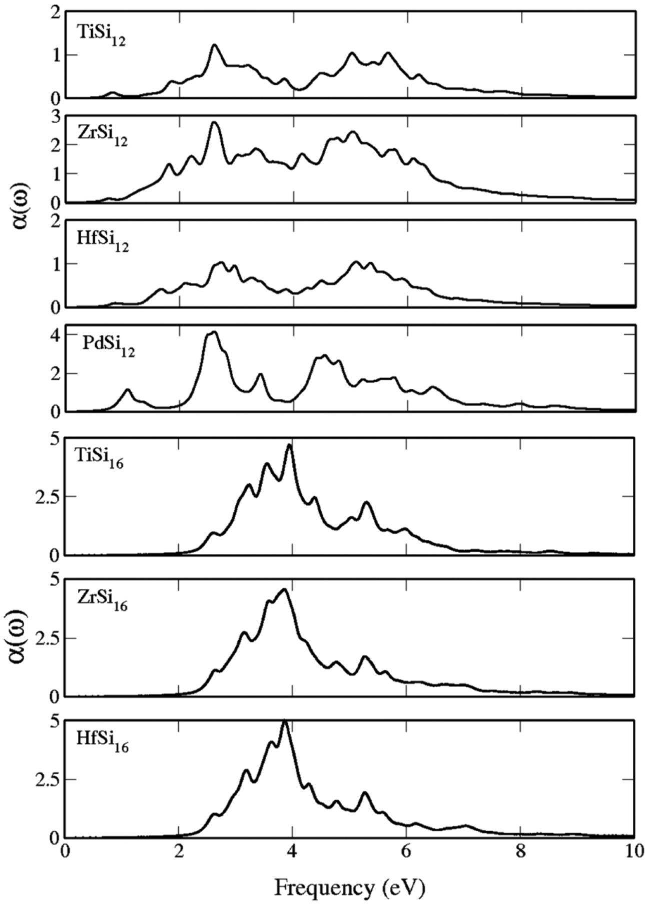

Figure 44. Dynamic polarizabilities (in arbitrary units) of Ti@Si$_{12}$, Zr@Si$_{12}$, Hf@Si$_{12}$, Pd@Si$_{12}$, Ti@Si$_{16}$, Zr@Si$_{16}$, and Hf@Si$_{16}$ calculated within RPA. Reproduced with permission from ref 435. Copyright 2014 American Chemical Society.

Kong and co-workers carried out DFT pseudopotential calculations on the spin-dependent transport through a M@Si$_{12}$ (M = Mn, Fe, Co) cluster using two jellium model leads.[512] Interestingly, the Mn- and Fe-doped systems exhibit highly spin-polarized transmission that could be potentially

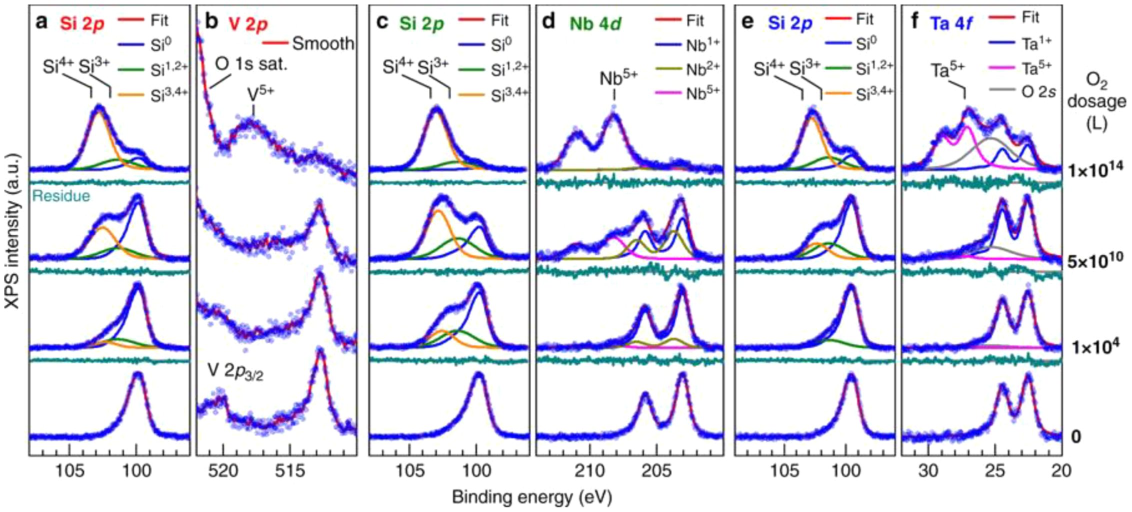

Figure 45. XPS spectra for M@Si_{16} deposited on a C_{60} substrate measured after different O_2 exposures. The XPS spectra obtained before and after O_2 exposures for (a) Si 2*p* and (b) V 2*p* of V@Si_{16}, (c) Si 2*p* and (d) Nb 4*d* of Nb@Si_{16}, and (e) Si 2*p* and (f) Ta 4*f* of Ta@Si_{16}, where the amounts of O_2 exposures are defined as Langmuir (L). Reproduced with permission from ref 514. Copyright 2018 Springer Nature.

useful as the ballistic spin filters in Si based spintronics. In contrast, the Co doped system has very small magnetic moment. Owing to the charge transfer from silicon atoms to the localized *d* orbitals of the metal atom, the conductance (especially in the minority channels) is reduced with respect to the pure Si cages.

The chemical reactivity of MSi_n cage clusters has also been explored from both experimental and theoretical aspects. Ohara *et al.* measured the mass spectra of cationic $[TiSi_n]^+$ clusters before and after exposure to H_2O. They observed a decrease in the abundance of $[TiSi_n]^+$ clusters with $n = 7-11$ upon reaction with H_2O, while the intensities of clusters with $n = 13-17$ remained unchanged.[54] To understand these results, Kawamura *et al.* performed *ab initio* calculations using ultrasoft pseudopotential and PW91 functional.[513] They confirmed that Ti@Si_n clusters with $n \geq 13$ all have cage structures with the metal atom embedded in the silicon cage and thus are inert toward H_2O adsorption with interaction energies smaller than 0.204 eV. For $n < 13$, the Ti@Si_n clusters have basket-like structures with the metal atom partially covered by Si atoms and available for reaction with H_2O. Consequently, these small-sized clusters strongly adsorb H_2O molecule with interaction energies of 0.989−1.188 eV, consistent with the experimental results by Ohara et al.[54]

Nakajima and co-workers have carried out a series of experiments on the oxidative reactivity of M@Si_n clusters based on XPS spectra. In early studies, they found that the Ta@Si_{16} clusters immobilized on HOPG or C_{60} substrate remain stable upon exposure to 10^4 Langmuir oxygen.[488,489] Recently, they explored the oxidation process of M@Si_{16} (M = V, Nb, Ta) clusters deposited on a C_{60} covered surface.[514] As shown in Figure 45, at 1×10^4 L oxygen exposure, the original peak components of XPS spectra for Si and M atoms are mostly retained. At 5×10^{10} L exposure, some changes in the Si 2*p* signal are evident, but the spectra of central metal M mostly keep their original profiles, suggesting that the metal atom is still protected against oxidation by the partially oxidized Si_{16} cage. By an extreme exposure of 1×10^{14} L, the main Si 2*p* and metal core peaks completely shift toward higher binding energies, whose charge states are Si^{3+} or Si^{4+} and M^{5+}, respectively, which indicates that the deposited M@Si_{16} clusters are finally oxidized into SiO_2 and M_2O_5. Compared to a crystalline surface of silicon, the stability of M@Si_{16} on the C_{60} substrate toward oxygen is enhanced by a factor of 10^4, due to the charge transfer between the cluster and substrate that satisfies the 68-electron shell closure as $[M@Si_{16}]^+$. The chemical robustness depends on superatomic "periodicity" (Ta@Si_{16} > V@Si_{16} > Nb@Si_{16}), which can be explained by the degree of electron density spreading outside the silicon cage according to DFT calculations.

Nakajima and co-workers[515] also explored the reaction kinetics of Ta@Si_{16} clusters deposited on the C_{60} based substrate upon exposure to NO. XPS clearly showed two oxidation stages including dissociative chemisorption of NO on the cage surface, and then under extreme reaction conditions, the collapse of silicon cage and NO oxidation of the central Ta atom. Further DFT calculations revealed that dissociation of NO on the supported Ta@Si_{16} cluster is strongly suppressed by the weakened molecular physisorption and larger dissociation barrier compared to that on the bare Si(111) surface. The chemical stability of Ta@Si_{16} is greatly enhanced by the superatomic nature of shell closure with valence electrons coupled with metal encapsulation.

Kumar and Kawazoe[360] studied interaction of hydrogen with $Si_{12}M$, $Si_{18}M_2$ (M = Cr, Mo, W), and also Zr@Si_{16} fullerene clusters in order to understand the experimental observation of no hydrogen on $Si_{12}W$ and $Si_{18}W_2$ clusters.[47] It is important to mention that two different experiments produced very different results. In one experiment,[47] interaction of silane gas with metal monomers was observed to lead to $Si_{12}W$ and $Si_{18}W_2$ clusters that did not have any H attached, but in other experiments[36,37] laser vaporization of Si and the addition of $M(CO)_6$ to the He carrier gas led to high abundance of $Si_{15}W$ and $Si_{16}W$. Therefore, the growth behavior of these clusters depends on the nucleation conditions. It was found theoretically that H interacts with these clusters relatively weakly,[360] in agreement with the experimental findings. Furthermore, interaction with H enhances the *sp*^{3} bonding between the silicon atoms and weakens the Si−M interactions. This leads to distortion in the cage and appearance of magnetism. $Si_{12}CrH_{12}$ was shown to have a magnetic moment of 4 μ_B, mostly localized on Cr atom. Further removal of M atom was shown to lead to the empty cages $Si_{12}H_{12}$, $Si_{16}H_{16}$, and $Si_{20}H_{20}$ with large HOMO-LUMO gap ranging from 2.5 to 3 eV, which is attractive for optoelectronic applications. Note that experiments on $Si_{29}H_{24}$ clusters have shown emission of visible light.[516]

S. Li *et al.* have investigated the reactivity of W@Si_{12} cluster with O_2 molecule by planewave DFT calculations using PBE functional.[517] They suggested that O_2 only weakly adsorbs on the W@Si_{12} hexagonal prism cage with binding energies smaller than 0.027 eV. Dissociation of O_2 on the cluster involves an energy barrier of 0.593 eV and is a spin-forbidden process. Therefore, W@Si_{12} cluster may exhibit high inertness toward O_2 in ambient conditions, in close agreement with the experimental observations of magic number of W@Si_{12}. A subsequent DFT study exploited the W@Si_{12} cluster as a gas sensor for CO and NO molecules, which show exothermic adsorption energies of 0.248 eV to 1.212 eV on different sites of the cluster.[518] Finite charge transfer by molecular adsorption induces dramatic changes to the electronic properties of W@Si_{12}. The other gas molecules such as HCN, CO_2, N_2, O_2, and H_2O are only weakly physisorbed on W@Si_{12} cluster.

Ona *et al.*[427] compared the reactivity of endohedral and exohedral isomers of $CuSi_n$ clusters at the B3LYP/6-31+G(d) level of theory. They showed that the exohedral isomers of $CuSi_6$, $CuSi_8$, $CuSi_{10}$, and $CuSi_{12}$ carry positive charge on Cu and negative charge on Si atoms and thus are more reactive to adsorb an H^+ proton. On the contrary, the endohedral isomers of $CuSi_{10}$ and $CuSi_{12}$ with cage-like structures have very little negative charge or even positive charge on the silicon cage. Consequently, these endohedral doped clusters exhibit lower reactivity than those with the metal atom in the periphery.

Recently, S. Zhou *et al.* proposed to utilize V@Si_n (n = 12−15) clusters as highly active photocatalysts for CO_2 hydrogenation.[519] By comprehensive DFT calculations, they showed that these clusters can favorably chemisorb CO_2 and dissociate H_2 molecules due to the unsaturated states of the silicon cage, which are mediated by *sp-d* hybridization and charge transfer between V and Si atoms. The CO_2 adsorption strength is correlated to the *p* orbital center of Si atoms, conforming to a recently established "*p* band theory" for non-metal catalysts.[520,521] Hydrogenation of CO_2 on V@Si_n is energetically and kinetically favorable with barriers down to 0.67−1.53 eV for the formation of CO, formic acid, formaldehyde, methanol, and methane, and product selectivity is uniquely determined by the cluster size and geometry (Figure 46). Moreover, these clusters have suitable energy gap and can absorb sunlight from the visible to ultraviolet region to drive the catalysis. Their theoretical results shine light to utilize the stable and experimentally accessible metal doped silicon cage clusters for energy conversion, and to control their catalytic activity and selectivity at atomic precision.

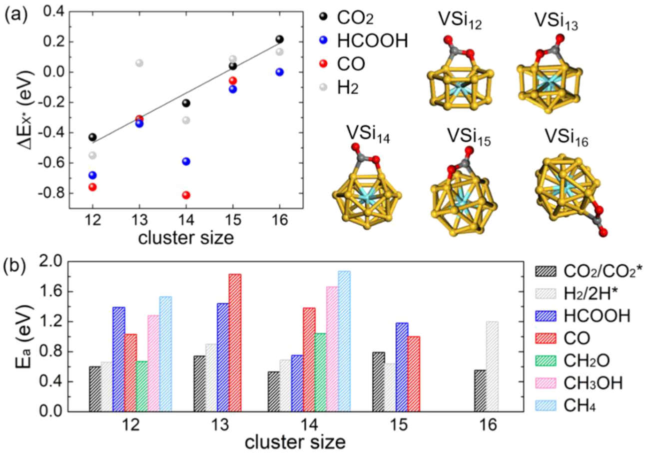

Figure 46. (a) Adsorption energy (ΔE_{X*}) of CO_2, CO, HCOOH, and H_2 on VSi_n (n = 12−16) clusters. The black line is a linear fitting of ΔE_{CO2*}. The structures of VSi_n clusters chemisorbed with a CO_2 molecule are shown on the right. The C, O, Si, and V atoms are represented in gray, red, yellow, and cyan colors, respectively. (b) Kinetic barrier (E_a) for chemisorption of CO_2 and dissociation of the H_2 molecule, and the barrier of the rate-limiting step for CO_2 hydrogenation to various products on the VSi_n clusters. Reproduced with permission from ref 519. Copyright 2019 American Chemical Society.

To summarize, among doped cage clusters, endohedral silicon clusters have attracted the maximum attention with extensive experimental as well as theoretical research ever since the 16 atom silicon clusters FK Ti@Si_{16} and fullerene-like Zr@Si_{16} were predicted from *ab initio* calculations. While prior to these findings, elemental silicon clusters have attracted much attention due to interest in miniature devices of silicon, a major problem has been that pure silicon clusters do not exhibit high abundance at a particular size. The prominent advantages of endohedral doping are the size selectivity and the possibility to produce such species in high abundance coupled with the advantage of tailoring their properties with suitable combination of the cage and the dopant atoms. This research has been dominated with many theoretical predictions of highly stable clusters of sizes ranging from 10 to 20 silicon atoms and endohedrally doped with one metal or rare earth atom, but experiments have helped with establishing endohedral doping as well as structures. To date, some progress has been achieved in encapsulating more than one atom, but more research is needed to develop further ideas and principles for making such species. A very desirable outcome has been the production of 100 milligram scale quantity of such species that has allowed us to do further research on assemblies of these clusters. This could open up new directions in making low-dimensional devices using designer clusters with desired properties. For example, many of these cluster species have interesting optical and magnetic properties and it may one day be possible to make interesting atomistic devices based on silicon, an earth abundant element and the backbone material of the modern semiconductor industry. While assemblies of such species are being studied, this is still in its infancy as we need to overcome the difficulty of possible agglomeration. Perhaps extensive research on nanoparticles of compound semiconductors, also discussed in this review, may provide some helpful clues. On the other hand, small silicon clusters doped with partially or fully covered metal atom could be potential catalysts as the control is likely to be much better than that for pure metal clusters. We hope to see much further progress in these directions.

6. ENDOHEDRALLY DOPED CAGES OF Ge, Sn, AND Pb

6.1. Doped Germanium Cages

In group 14 of the periodic table, germanium lies just below silicon, and its structural and electronic properties resemble those of silicon in many ways. However, at the nanoscale, doping can make Ge clusters behave quite differently from those of Si. The evolution of atomic structures and electronic properties of pure germanium clusters as a function of cluster size has been well investigated both experimentally[500,522−525] and theoretically.[526,527] Generally speaking, the growth behavior of pure germanium clusters is similar to but slightly different from that of silicon clusters. It was found that small Ge_n clusters with 8 ≤ n ≤ 11 have spherical-like compact structures, while medium-sized Ge_n clusters (n = 12−20) adopt structures based on a TTP motif and are all prolate in geometry.[527] Therefore, it can be expected that similar to silicon, fullerene-like germanium cages can be achieved by properly doping with metal atoms. However, slightly bigger size of Ge atom (about 4%) makes the doped Ge clusters to have quite different properties from the Si counterparts.

Soon after the theoretical prediction of metal-encapsulated silicon cages, Kumar and Kawazoe performed a series of DFT calculations to explore the possible germanium cages stabilized by metal doping.[53,58,67,528,529] Analogous to $M@Si_n$ clusters, they explored $M@Ge_n$ (n = 14−16; M = Ti, Zr, Hf, Fe, Ru, Os) clusters with various possible cage configurations such as FK polyhedron, capped decahedron, fullerene-like cage, and cubic cage.[528] In particular, when Zr atom was doped in a fullerene structure of Ge following the results for $Zr@Si_{16}$, it was found that the fullerene cage transformed to a compact FK structure with all triangular faces (see Figure 39). Surprisingly, it has a larger HOMO−LUMO gap than that for $Zr@Si_{16}$ fullerene. Moreover, FK isomer has higher symmetry (T_d) than the fullerene isomer (D_{4d}). The strong interaction of the Ge cage with the Zr atom as well as the larger size of the Ge atom compared with Si leads to a more compact structure. The same behavior has been obtained for Th doping in the Ge_{20} cage,[529] which favors a more compact structure as compared to the $Th@Si_{20}$ fullerene structure. Furthermore, a Zn-doped Ge_{12} icosahedral cage could be stabilized and it has a large HOMO−LUMO gap of 2.212 eV using the PW91 functional. This is in contrast to Si for which such a cage cannot be stabilized. The interaction of Zn with the Ge cage leads to a moderate embedding energy of 3.388 eV.[53] In general, a large HOMO−LUMO gap of up to about 2 eV and appreciable embedding energy of up to about 12.8 eV were obtained for the endohedrally doped Ge clusters. The growth behavior of $M@Ge_n$ is distinct from that of $M@Si_n$ also due to the more extended nature of the Ge valence orbitals, which enhances the metallic nature in the bonding and results in higher coordination of Ge atoms. Furthermore, about 4% larger size of the Ge atom enlarges the size of the cage if the number of Ge atoms is the same as in the Si cage. Accordingly, for a given metal atom, Ge is likely to favor a more compact packing compared to Si or to form a cage with less number of Ge atoms; otherwise, one may need to endohedrally dope a larger guest atom than for the same cage of Si.

As compared to the metal doped silicon clusters, fewer experiments have been carried out on gas-phase metal doped germanium clusters.[57,483,530−539] In an early experiment by X. Zhang *et al.*,[530] a prominent peak in the mass spectrum of Co−Ge binary clusters was observed and assigned to $[CoGe_{10}]^-$. Its high stability was explained by the 18-electron rule and an endohedral structure was proposed, where the Co atom is encapsulated in the bicapped tetragonal antiprism structure of Ge_{10}. Neukermans *et al.*[483] performed a mass spectrometric stability investigation of neutral and cationic MX_n clusters (X = Si, Ge, Sn, Pb; M = Cr, Mn, Cu, Zn; $n \leq 20$). The "magic number" sizes with enhanced abundance for these binary compositions are summarized in Table 8. The doped silicon, tin, and lead clusters are discussed in Sections 5.2, 6.2, and 6.3, respectively. In the case of Mn, Cr, and Cu doped germanium clusters, the magic number sizes are n = 14, 15, and 16 for $[MnGe_n]^+$ and $[CrGe_n]^+$ and n = 7 and 10 for $[CuGe_n]^+$ clusters, respectively.

Similar to the experimental studies of doped silicon clusters discussed in Section 5.2, Nakajima's group[57,531] also employed mass spectrometry and anion photoelectron spectroscopy to investigate the relative stability and electronic properties of MGe_n clusters (n = 8−20; M = Sc, Ti, V, Y, Zr, Nb, Lu, Hf, Ta) in different charge states. Prominent peaks corresponding to $TiGe_{16}$, $[VGe_{16}]^+$, $[YGe_{16}]^-$, $ZrGe_{16}$, $[NbGe_{16}]^+$, $[LuGe_{16}]^-$, $HfGe_{16}$, and $[TaGe_{16}]^+$ clusters were observed in the mass spectra of anionic, neutral, and cationic clusters. To deduce the molecular structures of these clusters, the adsorption reactivity toward H_2O vapor was measured. Roughly speaking, the threshold size for the suppressed reactivity of MGe_n clusters indicates the occurrence of endohedral germanium cage with metal encapsulation. The reactivities of MGe_n clusters in anionic, neutral, and cationic states toward water vapors are plotted in Figure 47. One can see a correlation between the threshold size and the metallic bond radius of the encapsulated metal element. The threshold size of metal doped germanium clusters is always smaller than that of metal doped silicon clusters, owing to the larger covalent radius of Ge atom and longer Ge−Ge bond length with regard to the Si counterparts.

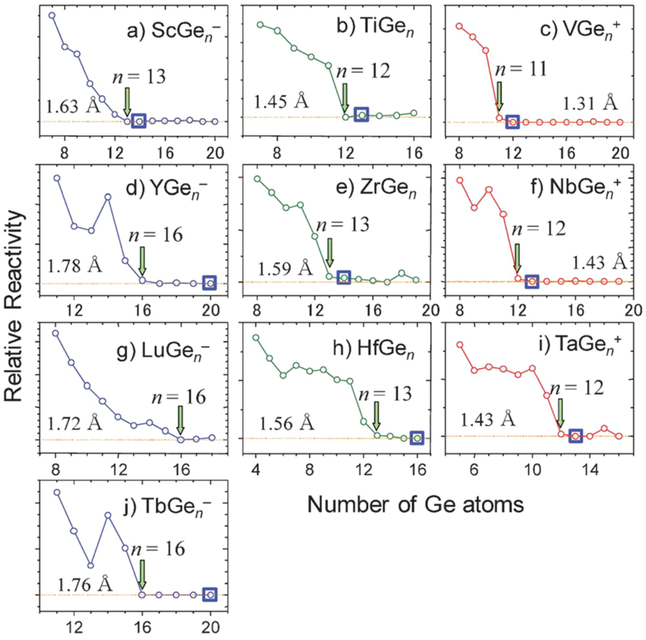

Figure 47. Relative reactivity of anionic/neutral/cationic $[MGe_n]^{-/0/+}$ clusters towards H_2O vapor; (a) $[ScGe_n]^-$, (b) $TiGe_n^0$, (c) $[VGe_n]^+$, (d) $[YGe_n]^-$, (e) $ZrGe_n^0$, (f) $[NbGe_n]^+$, (g) $[LuGe_n]^-$, (h) $HfGe_n^0$, (i) $[TaGe_n]^+$, and (j) $[TbGe_n]^-$. Vertical arrows show the threshold size of $[MGe_n]^{-/0/+}$ where the relative reactivity is lost. A metallic bond radius (in Å) is given in each plot, the threshold sizes of metal-atom doped Si_n are also shown by a square for comparison. The threshold size of $[MGe_n]^{-/0/+}$ is always smaller than that for $[MSi_n]^{-/0/+}$. The change in the threshold size can be reasonably explained by metal encapsulation in a Ge-cage. Reproduced with permission from ref 531. Copyright 2012 Royal Society of Chemistry.

As a representative, the size-dependent photoelectron spectra of $[TiGe_n]^-$, $[ZrGe_n]^-$, and $[HfGe_n]^-$ clusters are shown in Figure 48. For all these three cluster anions, the threshold energy for electron detachment (corresponding to electron affinity of the neutral cluster) exhibits a local minimum at n = 16 associated with the presence of a small bump around 2.8−3.0 eV (labeled as X), followed by a large energy

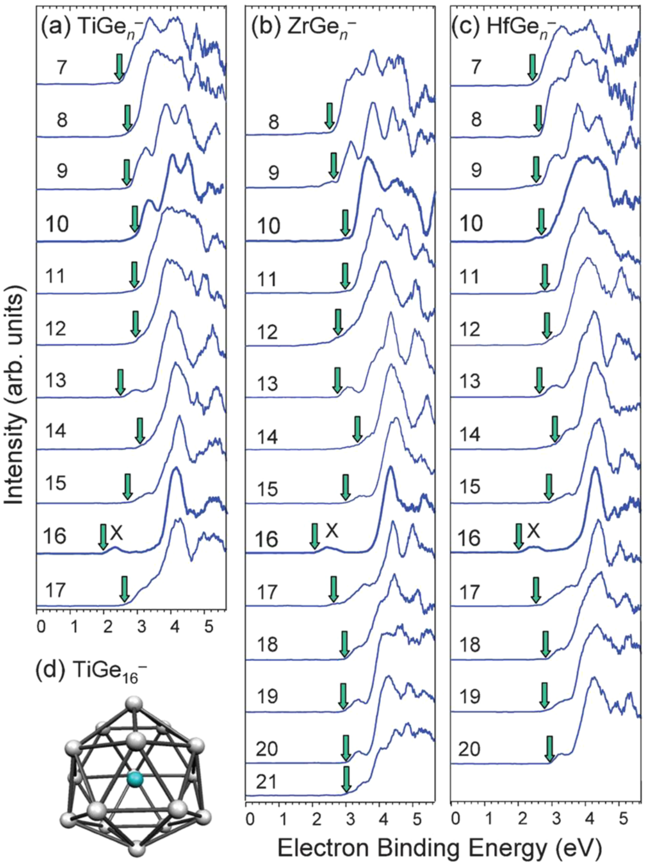

Figure 48. Photoelectron spectra of (a) $[TiGe_n]^-$ (n = 7−17), (b) $[ZrGe_n]^-$ (n = 8−21), and (c) $[HfGe_n]^-$ (n = 7−20) at 213 nm. In (d), the FK structure of $[TiGe_{16}]^-$ is shown, which was obtained from DFT calculation using the B3PW91 functional. The threshold energy in each case exhibits a local minimum at n = 16, and a small bump labeled X appears for n = 16, implying that the excess electron occupies a singly occupied molecular orbital. Reproduced with permission from ref 531. Copyright 2012 Royal Society of Chemistry.

gap and more discrete transitions at higher binding energies. Hence, particular attention has been paid to the endohedral $[M@Ge_{16}]^-$ clusters, and their photoelectron spectra are shown in Figure 49. The HOMO−LUMO gaps determined from the spectra are 1.77 eV for Ti@Ge$_{16}$, 1.90 eV for Zr@Ge$_{16}$, and 1.83 eV for Hf@Ge$_{16}$, suggesting their superatomic character with closed electronic shell. We will further discuss this in Section 6.1.7. On the other hand, the photoelectron spectra for the doping of trivalent atoms Sc, Y, Lu, and Tb are similar and correspond to a closed electronic shell. However, the doping of pentavalent atoms V, Nb, and Ta does not show the presence of any large HOMO−LUMO gap.

Starting from 2014, Zheng and co-workers conducted a series of experiments to measure the photoelectron spectra of singly and doubly metal doped germanium clusters, such as $[CoGe_n]^-$ (N = 2−11),[532] $[VGe_n]^-$ (N = 3−12),[533] $[RuGe_n]^-$ (n = 3−12),[534] $[AuGe_n]^-$ (N = 2−12),[535] $[TiGe_n]^-$ (N = 7−12),[536] $[FeGe_n]^-$ (n = 3−12),[537] $[Fe_2Ge_n]^-$ (n = 3−12),[538] and $[Cr_2Ge_n]^-$ (n = 3−14).[539] As a representative, Figure 50 shows the photoelectron spectra of $[AuGe_n]^-$ clusters (n = 2−12). One can see remarkable differences in the spectral features of $[AuGe_{12}]^-$ and other clusters.[535] The broad peak centered at 3.60 eV implies a highly symmetric structure for $[AuGe_{12}]^-$, which is further supported by DFT calculations according to which it has an icosahedral structure.

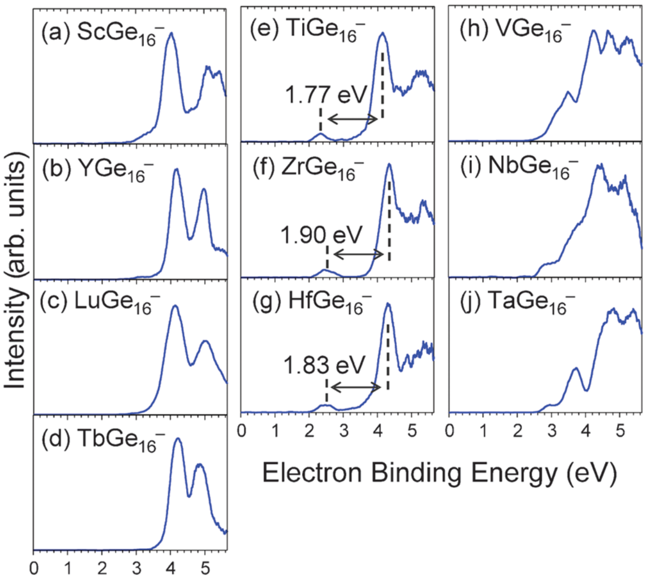

Figure 49. Photoelectron spectra of $[M@Ge_{16}]^-$ (M = Sc, Y, Lu, Tb, Ti, Zr, Hf, V, Nb, Ta) at 213 nm. For the doping of group 4 metal atoms Ti, Zr, and Hf, the photoelectron spectra are similar unlike for the silicon case and there is a large HOMO−LUMO gap of 1.77−1.9 eV. On the other hand, the photoelectron spectra of trivalent dopants are similar and correspond to a closed electronic shell configuration. However, anions of clusters with pentavalent metal atoms do not show occurrence of a large HOMO−LUMO gap. Reproduced with permission from ref 531. Copyright 2012 Royal Society of Chemistry.

In the literature, many *ab initio* calculations have been reported on the atomic structures, energetic stabilities, and electronic properties of endohedrally doped M@Ge$_n$ clusters in both neutral and charged states,[53,58,67,91,95,448,473,528,529,532−590] which are summarized in Table 10. Generally speaking, the smallest cage that can accommodate a metal atom is Ge$_8$. Most theoretical studies focused on the Ge$_n$ cage sizes at n = 10, 12, and the largest endohedrally doped germanium clusters explored is Th@Ge$_{20}$. Due to the diverse theoretical results on endohedral germanium clusters using different functionals and basis sets, herein we performed systematic PBE0/6-311+G(d), SDD calculations on the atomic structures, energetic stability, and electronic and magnetic properties of these endohedral M@Ge$_n$ cages of different sizes (n = 10, 11, 12, 13, 14, 15, 16). In the following subsections, we discuss the doped germanium caged clusters of different sizes one by one, based on our own calculations and the previously reported results.

6.1.1. Endohedrally Doped Ge$_8$ and Ge$_9$ Cages.

Intuitively, the Ge$_8$ cage is too small to accommodate a transition metal or rare earth metal atom. In a pioneering study, Kumar and Kawazoe[67] considered a possible endohedral cubic cage of Be@Ge$_8$ and obtained a HOMO−LUMO gap of 1.75 eV and an embedding energy of 3.22 eV from planewave pseudopotential calculations with the PW91 functional. Later, using DFT calculations at the B3LYP/6-31G(d) level of theory, Uta and King[569] explored the lowest-energy structures of $[Be@Ge_8]^q$ clusters with different charge states: q = −4, −2, 0, +2. They found that the lowest-energy structures of these clusters are all eight-vertex polyhedra with a centered Be atom, i.e., a D$_{4d}$ square antiprism for $[Be@Ge_8]^{4-}$, a D$_{2d}$ bisdisphenoid for $[Be@Ge_8]^{2-}$, an ideal O$_h$ cube for Be@Ge$_8$ as also obtained by Kumar and Kawazoe,[67] and a C$_{2v}$ distorted cube for $[Be@Ge_8]^{2+}$. The dependence of cluster geometry on the charge state can be rationalized by the Wade−Mingos rules according

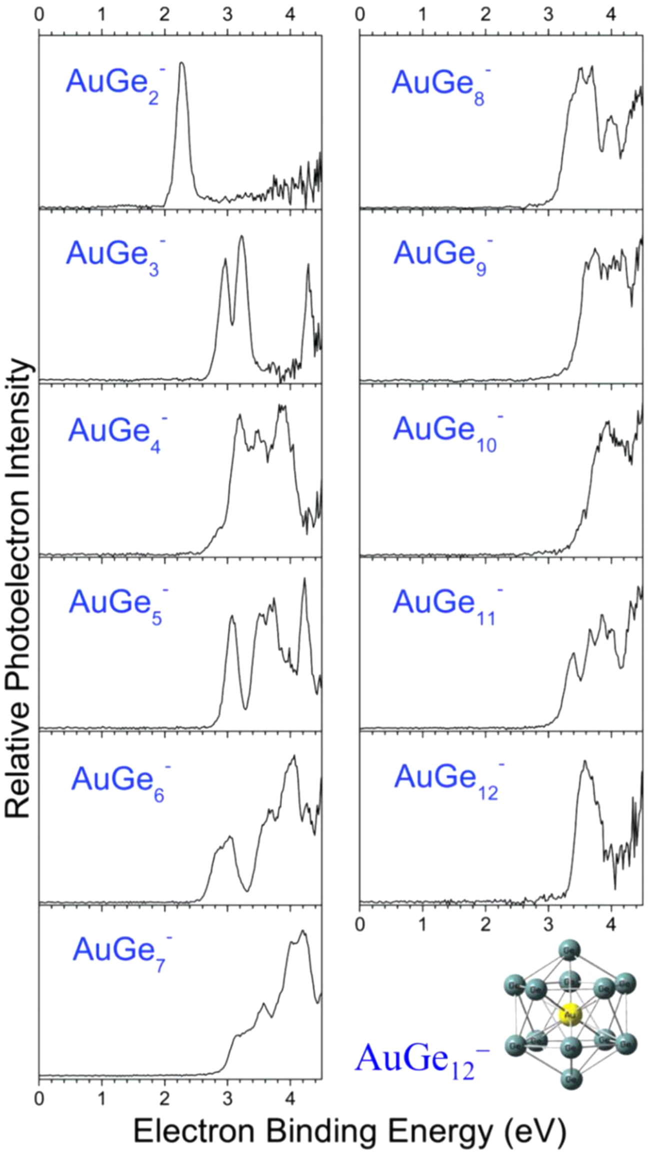

Figure 50. Photoelectron spectra of [AuGe$_n$]$^-$ (n = 2−12) clusters recorded with 266 nm photons. The molecular structure of [AuGe$_{12}$]$^-$ is also shown which is a perfect icosahedron with Au atom inside. Reproduced with permission from ref 535. Copyright 2016 Royal Society of Chemistry.

to which a D_{4d} square antiprism as an *arachno*-deltahedron, is favored for [Be@Ge$_8$]$^{4-}$ because it has $4n_v + 6 = 38$ valence electrons. On the other hand for the neutral Be@Ge$_8$ cluster with 34 electrons, an 8-vertex deltahedron (D_{2d} bisdisphenoid) should be favored. However, the size consideration of the endohedral Be atom favors a 3-connected cube with higher internal volume. Note that 34 electrons also correspond to a 1F subshell closure in a jellium model. But the lack of *f* valence electrons in endohedral Be atom leads to relatively small HOMO−LUMO gap.

Hung *et al.*[571] optimized a few isomeric structures of BeGe$_8$ and explored their isomeric conversion paths. They also obtained a perfect cube using a 6-31G(d) basis set with B3LYP functional. However, a distorted cube (C_{2v}) was found to be lower in energy than the perfect O_h cube at the B3LYP/6-311++G(3df) level of theory. Uta and King[569] also showed that the cluster buildup reaction Be@Ge$_8{}^q$ + Ge$_2$ → Be@Ge$_{10}{}^q$ is highly exothermic and that could be a reason for the lack of observation of such eight-vertex endohedral clusters.

In experiment, the smallest endohedral Zintl anion is [Ni@Ge$_9$]$^{3-}$, which adopts a tricapped trigonal prism structure.[91] There have also been some theoretical explorations on the endohedral M@Ge$_9$ cage clusters. Bandyopadhyay and Sen[559] investigated the structural evolution of NiGe$_n$ clusters with n = 1−20 and found that the smallest cage to completely enclose a Ni atom is Ge$_9$. At the B3PW91/LanL2DZ level, Ni@Ge$_9$ prefers an endohedral irregular cage (C_1 symmetry), having a large HOMO−LUMO gap of about 2 eV and a substantial embedding energy of about 5 eV. This structure distinctly differs from the reported Zintl anion of [Ni@Ge$_9$]$^{3-}$,[91] indicating that the addition of three extra electrons has significant impact on the cluster geometry. Using GA combined with first-principles calculations and considering a series of dopants (Si, Li, Mg, Al, Fe, Mn, Pb, Au, Ag, Yb, Pm, and Dy), Qin *et al.*[582] found that the neutral and cationic FeGe$_9$ and MnGe$_9$ clusters form endohedral cages. In fact both neutral (cationic) Fe@Ge$_9$ and Mn@Ge$_9$ clusters share the same ground state structure. However, the lowest-energy configurations for neutral and cationic clusters are different. The HOMO−LUMO gaps (using PBE functional) for both endohedral clusters are only moderate, i.e., 0.586 eV for Fe@Ge$_9$ and 0.665 eV for Mn@Ge$_9$, respectively.

6.1.2. Endohedrally Doped Ge$_{10}$ Cages.

Earlier theoretical studies have explored a number of endohedral guest atoms or ions, such as Be,[67,565] Mg,[568] Ti,[536,572] V,[533] Cr,[579] Mn,[551,566,581] Fe,[537,553] Co,[532,544,550,566,567] Ni,[58,547,556,557,566,574] Cu,[546,556,563,564,573,587] Zn,[549,556] Zr,[572] Nb,[588] Mo,[576] Ru,[534] Pd,[58,557] Ag,[563,564] Hf,[572] W,[548] Pt,[58,557] and Au.[473,558,563,564,575] We have performed PBE0 calculations by considering six structural isomers for the endohedral M@Ge$_{10}$ cages for a variety of M atoms as schematically shown in Figure 51. According to our geometry optimizations, Ti-, Cr-, V-, Mn-, Zr-, Nb-, Mo-, Ag-, Hf-, W-, and Au-doped Ge$_{10}$ clusters prefer open-cage structures, which is supported by the threshold sizes for the formation of an endohedral cage deduced by the measured adsorption reactivity toward H_2O vapor,[531] i.e., n = 11 for V, n = 12 for Ti and Nb, and n = 13 for Hf. Thus these clusters will not be discussed further.

For the remaining stable M@Ge$_{10}$ endohedral cages (M = Be, Mg, Fe, Co, Ni, Cu, Zn, Ru, Pd, Pt), our *ab initio* results are summarized in Table S13. Among them, only Fe@Ge$_{10}$ does not adopt the lowest spin state, showing a total magnetic spin moment of 2 μ_B. Except for the divalent metal dopants (Mg and Zn), the embedding energies for most M@Ge$_{10}$ systems exceed 4.0 eV, with the largest value being 9.319 eV for Ru@Ge$_{10}$. According to the NBO analysis, the transition metal atom gains 1.9−4.2 electrons from the Ge$_{10}$ cage, in line with some previous calculations.[532,537,547,551,566] In contrast, the encapsulated Be or Mg atom donates about one electron to the Ge$_{10}$ framework.

Be@Ge$_{10}$ adopts a bicapped tetragonal antiprism configuration with D_{4d} symmetry (Figure 51a).[67,565] This 10-vertex deltahedron satisfies the Wade−Mingos rules with $4n_v + 2 = 42$ electrons. A similar squashed capped tetragonal antiprism structure (D_{4d}, Figure 51b) with elongated Ge−Ge bonds is found for Mg@Ge$_{10}$, Ni@Ge$_{10}$, Cu@Ge$_{10}$, Zn@Ge$_{10}$, and Pd@Ge$_{10}$, consistent with previous theoretical reports.[58,546,549,556,557,563,568,573,574] A capped tetragonal−pentagonal antiprism (Figure 51c) was predicted for Ni@Ge$_{10}$[547,556,566] and Pd@Ge$_{10}$,[58] which lies, however, slightly higher in energy than our

Table 10. Summary of Previous Theoretical Studies on Doped Germanium Clusters $[M_xGe_n]^{q}$[a]

Method	System
BP86/DZP	$[Co_2@Ge_{16}]^q$ ($q = -4, -3, -2, -1, 0$) [95]
BP86/TZP	$[Co_2@Ge_{16}]^q$ ($q = -4, -3, -2, -1, 0$) [95]; $M@Ge_{12}$ (M = Sc, Ti, V, Cr, Mn, Fe, Co, Ni, Cu, Zn, Zr, Nb, Mo, Tc, Ru, Rh, Pd, Ag, Cd) [448]
PW91/planewave	$Zn@Ge_{12}$ [528]; MGe_n (n = 14, 15, 16; M = Ti, Zr, Hf, Pb, Cr, Mo, W, Fe, Ru, Os) [53]; MGe_n (n = 8, 9, 10, 12, 14; M = Be, Mg, Zn, Mn) [67]; $M@Ge_{10}$ (M = Ni, Pd, Pt) [58]; $Th@Ge_n$ (n = 16, 18, 20) [529]; MGe_n (n = 1–13; M = Mn, Co, Ni) [566]; MGe_n (n = 9, 10; M = Si, Li, Mg, Al, Fe, Mn, Pb, Au, Ag, Yb, Pm, Dy) [582]; $[ZrGe_n]^{-/0}$ (n = 1–21) [583];
PW91/DNP	$CoGe_n$ (n = 1–13) [550]; $FeGe_n$ (n = 9–16) [553]; $MnGe_n$ (n = 2–16) [555]
PW91/LanL2DZ	$[RuGe_n]^-$ (n = 3–12) [534]
MPW91PW91/6-311+G	$CoGe_n$ (n = 1–13) [550]
BPW91/LanL2DZ	$M@Ge_{12}$ (M = Mn, Tc, Re, Zn, Cd, Hg) [590]
B3PW91/LanL2DZ	$NiGe_n$ (n = 1–20) [559]; $[M@Ge_n]^q$ (n = 14–20; M = Sc, Ti, V; $q = -1, 0, +1$) [561]; $CuGe_n$ (n = 1–20) [573];
B3PW91/6-311+G(d)	MGe_n (n = 1–20; M = Ti, Zr, Hf) [572]; $[CoGe_n]^{-/0}$ (n = 2–11) [532]; $[VGe_n]^{-/0}$ (n = 3–12) [533]; $[FeGe_n]^{-/0}$ (n = 3–12) [537]
PBE/DNP	$MnGe_n$ (n = 1–13) [551]; MGe_n (n = 9, 10; M = Si, Li, Mg, Al, Fe, Mn, Pb, Au, Ag, Yb, Pm, Dy) [582]; $[Fe_2Ge_n]^{-/0}$ (n = 3–12) [538]
PBE/DZ	VGe_n (n = 1–19) [584]
PBE/DZP	$CrGe_n$ (n = 1–13) [570]; VGe_n (n = 1–19) [584]; MGe_n (n = 1–19; M = Cu, Ag, Au) [587]
PBE/LanL2DZ, cc-pVTZ	MGe_n (n = 1–19; M = Cu, Ag, Au) [587]
PBE/LanL2DZdp, 6-311G	$CrGe_n$ (n = 1–17) [579]
PBE/6-311+G(d)	$[Cr_2Ge_n]^{-/0}$ (n = 3–14) [539]
PBE0/LanL2DZ	$[RuGe_n]^{2-/3-}$ (n = 2–12) [589]
BLYP/DNP	$M@Ge_{12}$ (M = Sc, Ti, V, Cr, Mn, Fe, Co, Ni) [562]
B3LYP/LanL2DZ	$[CoGe_{10}]^-$ [544]; MGe_{12} (M = Hf, W, Os, Ni, Zn) [545]; $CuGe_n$ (n = 2–13) [546]; $NiGe_n$ (n = 1–13) [547]; WGe_n (n = 1–17) [548]; Mo_2Ge_n (n = 9–15) [552]; $HfGe_n$ (n = 9–24) [554]; $[M@Ge_{10}]^q$ ($q = -4, -2, 0$; M = Ni, Pd, Pt) [557]; $AuGe_n$ (n = 2–13) [558]; $[MGe_{10}]^{-1/0}$ (M = Cu, Ag, Au) [563]; $[MGe_{10}]^+$ (M = Cu, Ag, Au) [564]; $NiGe_n$ (n = 1–20) [574]; $[AuGe_n]^-$ (n = 1–13) [575]; $MoGe_n$ (n = 1–20) [576]; $M@Ge_n$ (n = 10, 12, 14; M = Ag, Au) [473]; $NbGe_n$ (n = 7–18) [588]
B3LYP/DGDZVP	$[NbGe_n]^-$ (n = 8–20) [585]; $[ZrGe_n]^-$ (n = 8–20) [586]
B3LYP/SDD	$[TaGe_n]^-$ (n = 8–17) [577]; $[HfGe_n]^-$ (n = 6–21) [580]; $[AuGe_n]^-$ (n = 2–12) [535]
B3LYP/6-31G	$ZnGe_n$ (n = 1–13) [549]
B3LYP/6-31G(d)	$[M@Ge_{10}]^q$ ($q = -6, -5, -4, -3, -2, -1, 0, +1, +2$; M = Ni, Cu, Zn) [556]; $[Be@Ge_{10}]^q$ ($q = -2, 0, +2, +4$) [565]; $[Co@Ge_{10}]^q$ ($q = -5, -4, -3, -2, -1, 0, +1$) [567]; $[Be@Ge_{10}]^q$ ($q = -4, -2, 0, +2$) [568]; $[Be@Ge_n]^q$ (n = 6, 7, 8; $q = -4, -2, 0, +2$) [569]; $Be@Ge_8$[571]; $[Mn@Ge_{10}]^q$ ($q = -5, -4, -3, -2, -1, 0, +1$) [581]
B3LYP/6-311+G(d)	MGe_{12} (M = Li^-, Na^-, Be, Mg, B^+, Al^+)[560]; $[ScGe_n]^-$ (n = 6–16) [578]; $[AuGe_n]^-$ (n = 2–12) [535]; $[TiGe_n]^-$ (n = 7–12) [536]; $[NbGe_n]^-$ (n = 8–20) [585]; $[ZrGe_n]^-$ (n = 8–20) [586]
B3LYP/6-311++G(3df)	$Be@Ge_8$ [571]

[a] Here M denotes the endohedral atom, x is the number of M atoms, n is the number of Ge atoms, and q is the charge on the cluster.

calculated ground state geometry (Figure 51b) by 0.032 and 0.019 eV, respectively.

Most of the previous calculations as well as our present calculations revealed that a capped tetragonal−pentagonal antiprism (Figure 51c) is favored by $Fe@Ge_{10}$,[537] $Co@Ge_{10}$,[532,544,566,567] and $Pt@Ge_{10}$.[58] In comparison, the dimer-capped square antiprism (C_{2v}, Figure 51d) earlier predicted for $Co@Ge_{10}$[550] is found to lie 1.658 eV higher in energy, while an Fe-centered pentagonal prism (Figure 51e) earlier obtained for $Fe@Ge_{10}$[553] lies about 2 eV higher in energy.[557] However, the bicapped tetragonal antiprism configuration (D_{4d}, Figure 51b) obtained for $Pt@Ge_{10}$[557] is nearly isoenergetic with a tiny energy difference of 0.004 eV. An endohedral fullerene-like cage with C_s symmetry (Figure 51f) reported by Zheng and co-workers[534] is also obtained as the ground state for $Ru@Ge_{10}$ in our calculations.

King and co-workers[556,557,565,567,568] have interpreted the most stable structures of a series of endohedral $M@Ge_{10}$ clusters in various charge states based on the Wade−Mingos rules. For example, $Be@Ge_{10}$, $Mg@Ge_{10}$, and $Zn@Ge_{10}$ have 22 skeletal electrons, and their preferred bicapped square antiprismatic structure is analogous to the well-known $[B_{10}H_{10}]^{2-}$ molecule in borane chemistry.[591] On the other hand, $Ni@Ge_{10}$, $[Cu@Ge_{10}]^+$, and $[Co@Ge_{10}]^-$ (and also undoped Ge_{10}) clusters have a total of 40 effective valence electrons which is a magic number within the spherical jellium model, if not counting the pseudo-noble $3d^{10}$ shell from the central transition metal atom. Indeed, *ab initio* calculations using the B3LYP functional yield rather large HOMO−LUMO gaps for these cluster species, i.e., 2.4 eV for $[Cu@Ge_{10}]^+$,[564] 2.975 eV (Table S13) or 2.553 eV[547] for $Ni@Ge_{10}$, and 2.49 eV for $[Co@Ge_{10}]^-$.[544] A detailed analysis of the shape and energy levels of molecular orbitals of $[Cu@Ge_{10}]^+$ (D_{4d}) in Figure 52 indicates that its 40 valence electrons are distributed following the electronic shell pattern, namely, $1S^21P^61D^{10}1F^22S^21F^{12}2P^6$.[547] The large embedding energy as well as increased binding energy after doping such as with Ni (Table S13) show that doping can enhance the stability of the magic cluster Ge_{10}. Furthermore, size-dependences of the binding energy and second order difference of energy revealed that $Ni@Ge_{10}$ is the most stable one among $Ni@Ge_n$ clusters (n = 2−13),[547,566] consistent with early experimental observation of the isoelectronic counterpart $[Co@Ge_{10}]^-$ as a prominent peak in the mass spectrum.[530]

6.1.3. Endohedrally Doped Ge_{11} Cages.

In the literature, many 3*d* transition metal elements (Ti, V, Cr, Mn, Fe, Co, Ni) and a few 4*d* elements (Mo, Ru) have been considered as the dopants to fit into the Ge_{11} cage (see Table 10). As schematically depicted in Figure 53, we considered six structural isomers for these endohedral $M@Ge_{11}$ cages, and the results from our PBE0 calculations are presented in Table S14. The embedding energies lie in the range of 3.486 eV (for Cr) to 9.561 eV (for Mo). It should be noticed that $Cr@Ge_{11}$,

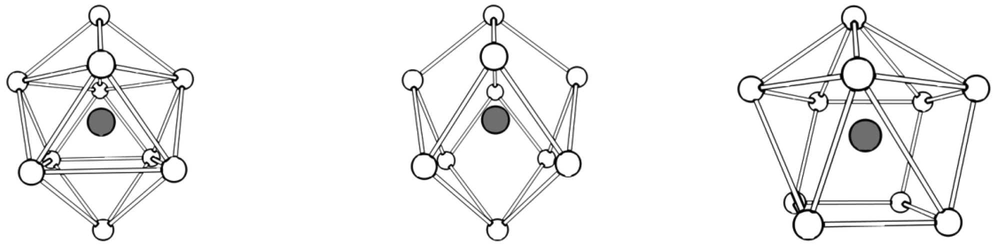

(a) Standard Bicapped Tetragonal Antiprism (D_{4d}) (b) Squashed Bicapped Tetragonal Antiprism (D_{4d}) (c) Capped Tetragonal-pentagonal Antiprism (C_{2v})

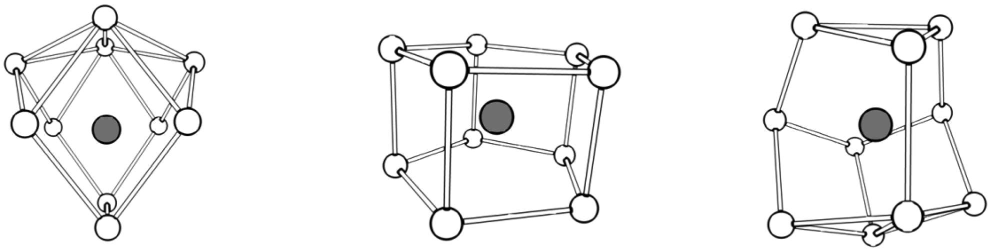

(d) Dimer Capped Tetragonal Antiprism (C_{2v}) (e) Pentagonal Prism (D_{5h}) (f) Fullerene-like cage (C_s)

Figure 51. Schematic structures of several isomers for M@Ge_{10} cage clusters with M the endohedral dopant as given in Table S13. The symmetry is given in parentheses. M (Ge) atom is shown by dark (empty) circle.

Mn@Ge_{11}, and Fe@Ge_{11} clusters are magnetic with the total spin moments of 4 μ_B, 3 μ_B, and 4 μ_B, respectively.

Generally speaking, the most stable geometries for M@Ge_{11} cluster from the present PBE0 calculations coincide well with the earlier theoretical studies, that is, a tricapped tetragonal antiprism (Figure 53a) for Ti@Ge_{11},[572] Co@Ge_{11},[550,566] Ni@Ge_{11},[574] and Ru@Ge_{11},[534] a capped pentagonal antiprism or incomplete icosahedron (Figure 53b) for V@Ge_{11}, Mn@Ge_{11},[551] and Fe@Ge_{11},[537,553] a basket-like structure (Figure 53c) for Mo@Ge_{11},[576] and a distorted side-capped tetragonal prism (Figure 53d) for Cr@Ge_{11}.[579] Previously, the isomeric structure in Figure 53a was predicted as the ground state for Mn@Ge_{11},[555] but it is higher in energy by 0.317 eV than our predicted ground state structure. Analogous to Ti@Ge_{11}, endohedral cages of Zr@Ge_{11} and Hf@Ge_{11} (isomer a)[572] were also considered in our calculations. However, these cage structures were broken upon optimization.

6.1.4. Endohedrally Doped Ge_{12} Cages.

In the case of endohedrally doped Ge_{12} clusters, many germanium cage frameworks are possible (see Figure 54) and numerous dopant atoms have been considered in earlier theoretical studies (Table 10). First, our geometry optimization at the PBE0/6-311+G(d), SDD level of theory demonstrated that Hf@Ge_{12} and Au@Ge_{12} prefer open-half-cage structures and Ni@Ge_{12} prefers capped pentagonal antiprism structure, in agreement with experimental observation of the formation of endohedral germanium cage until $HfGe_{13}^-$,[531] even though endohedral cages were predicted for them in the literature.[448,473,545,547,554,558,559,574,587] Our computational results on the stable M@Ge_{12} cage clusters are summarized in Table S15. Roughly speaking, all transition metal atoms can be stably encapsulated in a Ge_{12} cage with appreciable embedding energies of 3.7 eV to 11.6 eV, except for Cd having closed 3*d* and 4*s* shells and therefore a smaller embedding energy of 3.073 eV. Among the M@Ge_{12} cage clusters in Table S15, Mn@Ge_{12} possesses a markedly large magnetic moment of 5 μ_B,[67,562] while Cr@Ge_{12} and Fe@Ge_{12} both have a magnetic moment of 2 μ_B.[537,553]

Figure 52. continued

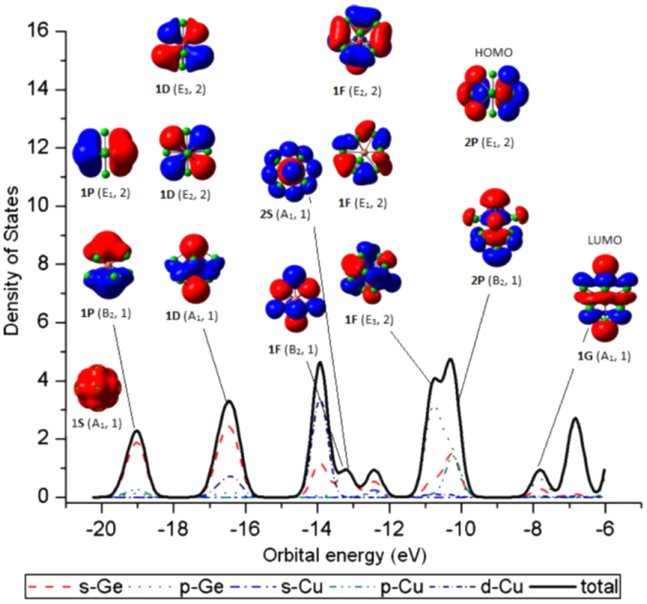

Figure 52. Gaussian broadened total and angular momentum decomposed DOS of the global minimum energy isomer of $[Cu@Ge_{10}]^+$ (D_{4d}) using the B3LYP/LanL2DZ level of theory. The molecular orbitals with dominant angular momentum character are also shown and labeled following the spherical shell model. The peak

A perfect icosahedral structure with a dopant atom in the center of the Ge_{12} cage is obtained for Be@Ge_{12},[67,560] B@Ge_{12},[560] Mg@Ge_{12},[67,560] Mn@Ge_{12},[67,448,551,561] Zn@Ge_{12},[67,448,528,545,549] and Cd@Ge_{12}.[448] If we do not count the half-filled $3d^5$ shell (Mn) and the fully filled $3d^{10}$ (Zn) or $4d^{10}$ (Cd) shell from the encapsulated transition metal atom,

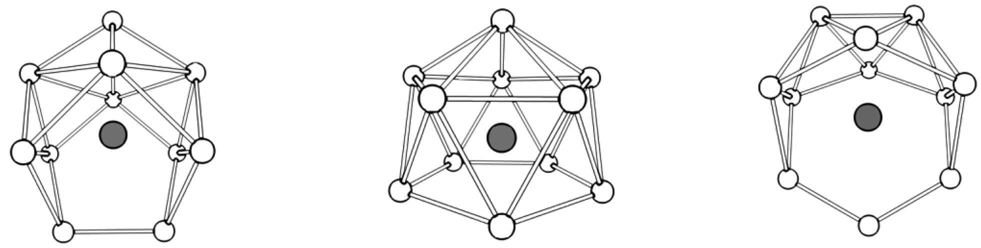

(a) Tricapped Tetragonal Antiprism (C_{2v}, C_s, C_1)

(b) Capped Pentagonal Antiprism (C_{5v}, C_1)

(c) Basket-like Prism (C_{2v}, C_1)

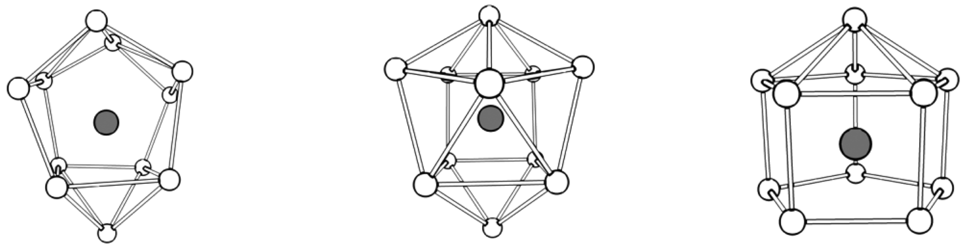

(d) Distorted Side Capped Tetragonal Prism (C_2)

(e) Bicapped Tetragonal-pentagonal Prism (C_s)

(f) Capped Pentagonal Prism (C_s)

Figure 53. Schematic structures of several isomers for M@Ge$_{11}$ cage clusters with M the endohedral dopant as given in Table S14. Other details are as in Figure 51.

all these clusters (except for B@Ge$_{12}$) effectively have 50 valence electrons. Under icosahedral symmetry, the high-momentum 1G^{18} molecular orbital splits into two well-separated subsets: 1G^{10} and 1G^{8}. The former is fully occupied as HOMO and the latter is empty as LUMO. Hence, the 50 valence electrons of these clusters fill the superatomic orbitals 1S^{2}1P^{6}1D^{10}2S^{2}1F^{14}2P^{6}1G^{10} within the shell model (see Figure 55 taking [Li@Ge$_{12}$]$^-$ as a representative).[560] Meanwhile, according to the Wade−Mingos rules, icosahedron as a 12-vertex *closo*-deltahedron requires a total of $4n_v + 2 = 50$ valence electrons (here the enclosed metal atom either does not have *d* electron or the metal *d* electrons do not contribute to the electron count[448]). As a consequence of the closed electronic shell conforming both shell model and Wade−Mingos rules, we obtained large HOMO−LUMO gaps (using PBE0 functional) for these clusters, namely, 3.321 eV for Be@Ge$_{12}$, 3.385 eV for Mg@Ge$_{12}$, 2.864 eV for Mn@Ge$_{12}$, 3.290 eV for Zn@Ge$_{12}$, and 3.240 eV for Cd@Ge$_{12}$, which are comparable to the previously reported values, e.g., 2.5 eV (PW91)[67] and 3.13 eV (B3LYP)[560] for Be@Ge$_{12}$, 3.27 eV (B3LYP) for Mg@Ge$_{12}$,[560] 2.212 eV (PW91),[67528] and 3.160 eV (B3LYP)[549] for Zn@Ge$_{12}$. Moreover, the size-dependent binding energy exhibits maximum at $n = 12$ for MnGe$_n$ ($n = 1-15$)[551] and ZnGe$_n$ ($n = 3-13$),[549] whereas Zn@Ge$_{12}$ cluster also shows a peak in the size-dependent fragmentation energy, both demonstrating the relatively high thermodynamic stability of these two clusters. Among these clusters, Mn@Ge$_{12}$ with perfect icosahedral geometry, sizeable HOMO−LUMO gap (2.504 eV by B3LYP functional), and large magnetic moment (5 μ_B) stands out and was suggested as a magnetic superatom,[67] providing an ideal building block for novel magnetic nanomaterials and spintronics.

Furthermore, icosahedra with reduced symmetry of D_{5d} (Figure 54b) have been obtained for neutral clusters of Li@Ge$_{12}$, Na@Ge$_{12}$, Cu@Ge$_{12}$, and Ag@Ge$_{12}$,[448,587] all with one electron less compared with the aforementioned 50-electron closed-shell systems, while Sc@Ge$_{12}$ with one electron excess has D_{3d} reduced symmetry.[448] Previous DFT calculations also predicted a perfect icosahedron as the ground state configuration for Ni@Ge$_{12}$,[562,574] but it is indeed energetically less favorable than the capped pentagon antiprism structure by 0.130 eV from our PBE0 calculation. Experimentally, an elongated icosahedron with D_{5d} symmetry was observed for [Co@Ge$_{12}$]$^{3-}$ in a Zintl compound crystal.[592] Although [Co@Ge$_{12}$]$^{3-}$ anion is isoelectronic to Zn@Ge$_{12}$ discussed above, the elongation of the nearly spherical Ge$_{12}$ shell by about 0.3 Å is a consequence of the fact that the hollow I_h-[Ge$_{12}$]$^{2-}$ cage with the diameter of 5.2 Å is too small to accommodate a Co atom.

Another common structural motif for M@Ge$_{12}$ is the hexagonal prism with different extents of distortion. Perfect hexagonal prism (D_{6h}) configuration (Figure 54d) was found to be the ground state for Mo@Ge$_{12}$[576] and W@Ge$_{12}$,[548] while a distorted hexagonal prism (Figure 54e) has been obtained for Os@Ge$_{12}$.[545] On the other hand, a puckered hexagonal prism (Figure 54f) is most favorable for V@Ge$_{12}$,[448] Cr@Ge$_{12}$,[579] Fe@Ge$_{12}$,[537,553] and Ru@Ge$_{12}$.[448] Similar to the highly stable Mo@Si$_{12}$ and W@Si$_{12}$ clusters discussed in Section 5.3.3, Mo@Ge$_{12}$ and W@Ge$_{12}$ also possess sizeable HOMO−LUMO gap of 2.801 and 2.932 eV as well as large embedding energy of 9.394 and 11.648 eV, respectively. A hexagonal antiprism with D_{6d} symmetry (Figure 54g) is obtained for Nb@Ge$_{12}$ by our present calculations and also in earlier studies.[448,588] This cluster geometry can be interpreted by the Wade−Mingos rules for a 12-vertex *arachno*-deltahedron, which requires $4n_v + 6 = 54$ valence electrons and leaves one electron deficiency to have a magnetic moment of 1 μ_B.

The lowest-energy structure of Co@Ge$_{12}$ and Zr@Ge$_{12}$ is a capped hexagonal−pentagonal antiprism with C_s symmetry (Figure 54c). The same structure was also reported for Co@Ge$_{12}$ by Jing *et al.*,[550] while a perfect icosahedron (Figure 54a)[562] and a distorted bicapped pentagonal prism (Figure 54h)[448] are higher in energy by 0.142 and 0.828 eV, respectively, according to our PBE0 calculations. As for Zr@Ge$_{12}$, the puckered hexagonal prism (Figure 54f) reported in ref 572 and the hexagonal antiprism (Figure 54g) proposed by Goicoechea and McGrady[448]

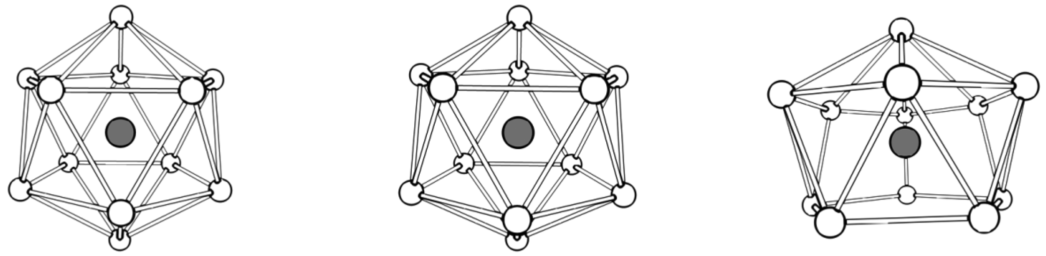
(a) Perfect Icosahedron (I_h)

(b) Distorted Icosahedron (D_{5d}, D_{3d})

(c) Capped Hexagonal-pentagonal Antiprism (C_s)

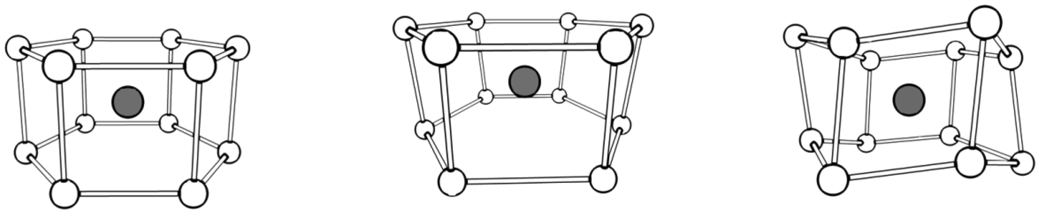
(d) Hexagonal Prism (D_{6h})

(e) Distorted Hexagonal Prism (D_3, C_{2h}, C_2)

(f) Puckered Hexagonal Prism (D_{3d}, C_{2h}, C_i , C_1)

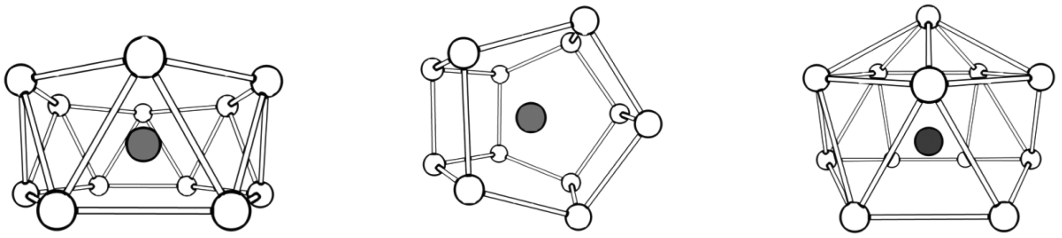
(g) Hexagonal Antiprism (D_{6d})

(h) Distorted Bicapped Pentagonal Prism (D_{2d} , C_2)

(i) Capped Pentagonal-hexagonal Antiprism (C_s)

Figure 54. Schematic structures of several isomers for M@Ge_{12} cage clusters with M the endohedral dopant as given in Table S15. Other details are as in Figure 51.

is less stable than the ground state configuration in Figure 54c by 0.284 and 0.421 eV, respectively. Similarly, a capped pentagonal–hexagonal antiprism with C_s symmetry (Figure 54i) has been found for Ti@Ge_{12}.[536] It energetically prevails the puckered hexagonal prism (Figure 54f)[448] and perfect icosahedron (Figure 54a)[562] by 0.256 and 1.132 eV, respectively.

A distorted bicapped pentagonal prism with D_{2d} (or C_2) symmetry (Figure 54h) is obtained to be the most stable structure for Ge_{12} cage encapsulating a late 4*d* transition metal atom, in accord with the previous theoretical results for Rh@Ge_{12}[448] and Pd@Ge_{12}.[448] Such endohedral D_{2d} cage was experimentally observed for $[Ru@Ge_{12}]^{3-}$ anion in the crystalline Zintl compound.[543] According to the Wade–Mingos rules, this D_{2d} (or C_2) cage is a 12-vertex three-connected polyhedron and requires 60 electrons, while the total number of valence electrons is 57 and 58 for Rh@Ge_{12} and Pd@Ge_{12}, respectively.

6.1.5. Endohedrally Doped Ge_{13} Cages.

For endohedral doping in Ge_{13}, our calculations revealed that many transition metal atoms, such as Cr, Fe, Co, Ni, Cu, and W, tend to form Ge-capped M@Ge_{12} cage structures instead of M@Ge_{13} cages. Hence, here we only discuss a few transition metal dopants (M = Ti, V, Mn, Zr, Nb, Mo, Hf) that can reside in the Ge_{13} host cage with six possible geometries, as shown in Figure 56, and the results from PBE0 calculations are summarized in Table S16. Roughly speaking, most of the lowest-energy structures of the explored M@Ge_{13} clusters can be constructed by capping on hexagonal prism or antiprism. Specifically, Ti@Ge_{13}, Zr@Ge_{13}, Nb@Ge_{13}, and Hf@Ge_{13} prefer a capped hexagonal antiprism (Figure 56a), in agreement with the previous study.[572] A capped hexagonal prism with C_{6v} symmetry (Figure 56b) is found as the ground state geometry for V@Ge_{13}.[584] Similarly, a capped puckered hexagonal prism structure (Figure 56c) is obtained for Mo@Ge_{13}.[576] As an exception of the hexagonal prism/antiprism motif, a fullerene-like cage (Figure 56d) composed of five triangles and five pentagons capped by an additional Ge atom is obtained for Mn@Ge_{13}.[551]

In addition to the singly doped Ge clusters, combining DFT calculations and anionic photoelectron spectroscopy, X. Q. Liang *et al.* have explored the lowest-energy structures, electronic states, and magnetic behavior of dual transition metal atoms doped Ge_n clusters in neutral and anionic states, i.e., $[Fe_2Ge_n]^{-1/0}$ (n = 3−12)[538] and $[Cr_2Ge_n]^{-1/0}$ (n = 3−14).[539] Endohedral Ge cages with one transition metal atom at the cage center and the other one on the surface were found for neutral Fe_2Ge_n clusters (n = 10−12) and anionic $[Cr_2Ge_{10}]^-$ cluster. Furthermore, a recent theoretical study by S. Zhou *et al.*[593] revealed that the most stable structure of neutral Cr_2Fe_{12} is a Cr-centered hexagonal antiprism with one of the hexagonal faces capped by the other Cr atom, while M_2Ge_{12} clusters (M = Mn, Fe, Co, Ni) adopt an endohedral 13-vertex cage with one interior metal atom and one surface metal atom as the ground state. Interestingly, these M_2Ge_{12} clusters are able to catalyze CO oxidation under the Eley–Rideal mechanism (see Figure 57). The reaction barrier is linearly related

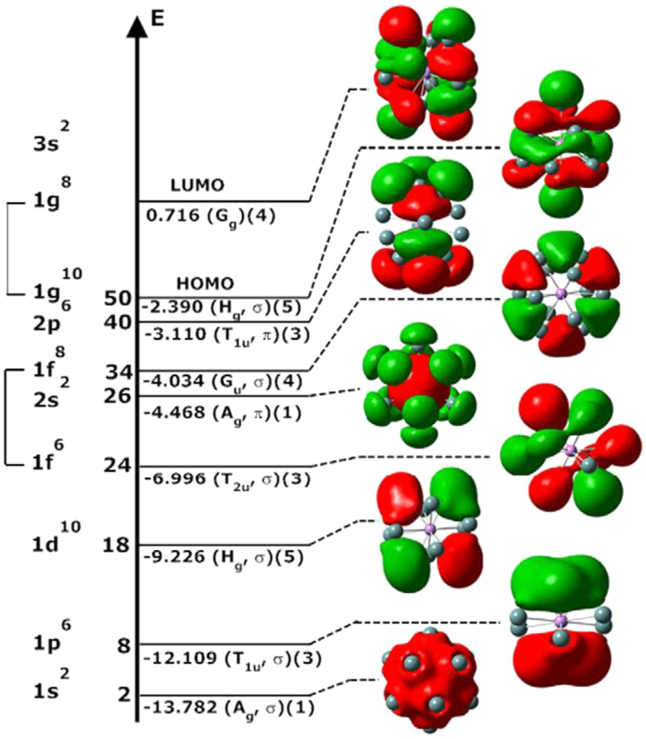

Figure 55. Energy levels (eV) and molecular orbitals of icosahedral (I_h) $[Li@Ge_{12}]^-$ from B3LYP/6-311+G(d) calculations. The orbital character, symmetry, and number of electrons are also given. Note that here the angular momentum is denoted by lower case letters in contrast to upper case letters used in the rest of the paper. Reproduced with permission from ref 560. Copyright 2010 Elsevier B.V.

to the O_2 binding strength on the cluster, which in turn is correlated to the *d* orbital center of the two metal dopants. Among the four doped clusters explored, Ni_2Ge_{12} exhibits the lowest barrier of 0.35 eV and has good thermal stability and high resistance to agglomeration. Thus, it is a promising catalyst for low-temperature CO oxidation.[593]

6.1.6. Endohedrally Doped Ge_{14} Cages.

There have been a number of theoretical studies on $M@Ge_{14}$ cage clusters for different M atoms (see Table 10). We have performed geometry optimization with the PBE0/6-311+G(d), SDD method by considering many systems. Capped endohedral cage structures are found for $Ti@Ge_{14}$, $Cr@Ge_{14}$, $Mn@Ge_{14}$, $Ni@Ge_{14}$, and $Ag@Ge_{14}$. Therefore, they are not further discussed here. Following the literature, we considered nine cage configurations of Ge_{14} and 12 metal dopants, as presented in Figure 58 and Table S17. All these doped clusters possess reasonable embedding energies in the range of 3.686 eV to 12.552 eV. Among them, $Fe@Ge_{14}$ possesses a total magnetic spin moment of 2 μ_B.[53]

The 14-vertex cubic cage structures with different degrees of distortion (Figure 58b, c) are obtained for several $M@Ge_{14}$ clusters, and the results are given in Table S17. A symmetric cubic structure (O_h) is obtained for $Mg@Ge_{14}$.[67] It has 58 valence electrons (a magic number within the spherical shell model) and a large HOMO−LUMO gap of 2.718 eV. Lower symmetry cubic structures are obtained for $V@Ge_{14}$,[584] $Fe@Ge_{14}$,[553] $Cu@Ge_{14}$,[587] and $Au@Ge_{14}$.[587] In a theoretical study of $V@Ge_n$ clusters (n = 1−19),[584] $V@Ge_{14}$ was found to exhibit peculiar electronic stability, showing a prominent peak on the size-dependent HOMO−LUMO gap and chemical hardness (defined as the energy difference between VIP and VEA). In this cluster, the valence electrons of V and Ge atoms are delocalized and fill the shell orbitals $1S^21P^61D^{10}2S^21F^{14}3S^22P^61G^{15}2D^4$ associated with the quasi-spherical geometry.[584] With odd number of electrons (and thus 1 μ_B magnetic moment), the HOMO−LUMO gap is 1.716 eV with PBE functional.

For $Zr@Ge_{14}$ and $Hf@Ge_{14}$, a bicapped distorted hexagonal antiprism (Figure 58f) is the lowest-energy structure.[572] In an earlier study, isomeric structure in Figure 58e was reported as

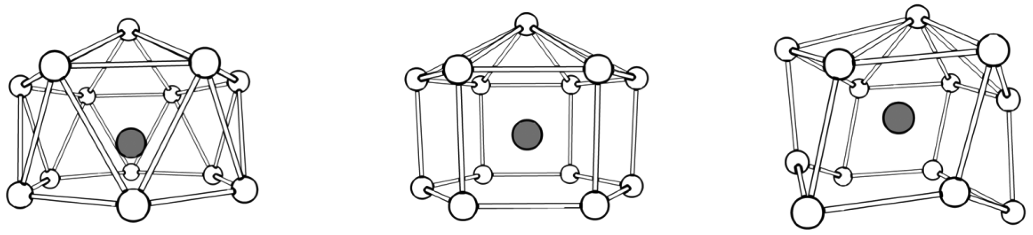

(a) Capped Hexagonal Antiprism (C_{6v}, C_{2v}, C_2)

(b) Capped Hexagonal Prism (C_{6v})

(c) Capped Puckered Hexagonal Prism (C_{3v})

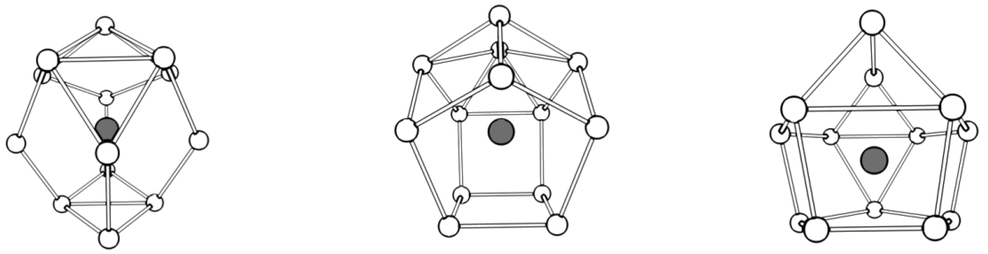

(d) Capped Fullerene-like Cage (C_s)

(e) Capped Fullerene-like Cage (C_s)

(f) Dimer Capped Pentagonal-hexagonal Prism (C_1)

Figure 56. Schematic structures of several isomers for $M@Ge_{13}$ cage clusters with M the endohedral dopant as given in Table S16. Other details are as in Figure 51.

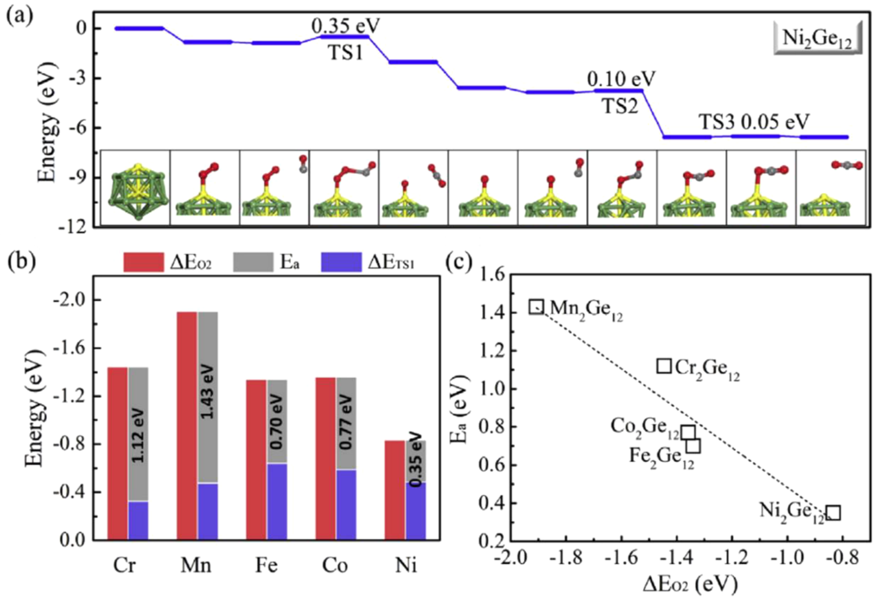

Figure 57. (a) Energy diagrams of CO oxidation on a Ni_2Ge_{12} cluster, and the corresponding structures of elementary steps. Transition states and kinetic barriers are indicated. (b) Adsorption energies of an O_2 molecule on the M_2Ge_{12} clusters (ΔE_{O2}) and the $^*O_2$−CO intermediate in the TS (ΔE_{TS1}), the difference between which gives the kinetic barrier of CO oxidation (E_a). (c) Kinetic barrier of CO oxidation as a function of O_2 adsorption energy. The C, O, Ge, and Ni atoms are shown in grey, red, green, and yellow, respectively. Reproduced with permission from ref 593. Copyright 2019 Elsevier B.V.

the ground state for Zr@Ge_{14},[583] but it is slightly less stable by 0.003 eV than the present one at the PBE0/6-311+G(d), SDD level. Also a fullerene-like cage (Figure 58a) was predicted for Hf@Ge_{14},[554] but it lies higher in energy by 1.216 eV compared with the ground state configuration in Figure 58f by our PBE0 calculations.

Both Ru@Ge_{14} and Os@Ge_{14} adopt a tetracapped pentagonal prism structure with C_{2v} symmetry (Figure 58h) as their lowest-energy configuration.[53] Also note that these two clusters have large embedding energies (10.941 eV for Ru@Ge_{14}, 12.552 eV for Os@Ge_{14}) and sizeable HOMO−LUMO gaps, i.e., 2.691 eV (PBE0) or 1.565 eV (PW91) for Ru@Ge_{14} and 2.796 eV (PBE0) or 1.610 eV (PW91) for Ru@Ge_{14}.

From our calculations, a cage-like configuration, named as tetracapped Ge_{10} boat by Yang *et al.*[460] (Figure 58d), is most favorable for Nb@Ge_{14}, Mo@Ge_{14}, and W@Ge_{14}, while the previously reported structures for these clusters[548,576,588] are all higher in energy by at least 1 eV. It is also noteworthy that the "tetracapped Ge_{10} structure" previously proposed for Mo@Ge_{14} and W@Ge_{14}[53] would transform into the present ground state structure upon relaxation. From Table S17, the HOMO−LUMO gap (with PBE0) for both Mo@Ge_{14} and W@Ge_{14} is as large as 2.778 and 2.891 eV, respectively. Also, the embedding energies are quite large (10.141 and 12.420 eV, respectively), suggesting high stability of these species.

6.1.7. Endohedrally Doped Ge_{15} and Ge_{16} Cages.

In an early study, Kumar and Kawazoe[53] pointed out that Ge_{15} and Ge_{16} cages are ideal hosts for enclosing a variety of transition metal atoms, such as Ti, Zr, Hf, Cr, Mo, W, Fe, Ru, and Os. Afterward, there have been many theoretical studies on M@Ge_{15} and M@Ge_{16} cage clusters (see Table 10). According to our PBE0 calculations, Ti-, Mn-, Fe-, or Nb-doped Ge_{15} clusters prefer capped cage structures; thus, these clusters will not be further discussed. In Table S18, we present our theoretical results on nine M@Ge_{15} clusters, and the corresponding isomeric structures are given in Figure 59. Except for Cr@Ge_{15}, all the considered M@Ge_{15} clusters possess considerable embedding energies of 8.143−13.121 eV.

A nearly spherical cage structure, namely, pentacapped pentagonal prism with C_{2v} symmetry (Figure 59a) is obtained as the lowest-energy configuration for Sc@Ge_{15},[561] Zr@Ge_{15},[53,572,583] and Hf@Ge_{15}.[53,572] A similar cage structure with C_s symmetry shown in Figure 59b is most favorable for V@Ge_{15}.[584] It is interesting to note that Sc@Ge_{15} and V@Ge_{15} clusters are possible 18-electron and 20-electron systems,[561] but both of them have doublet spin multiplicity and moderate HOMO−LUMO gap of 1.403 and 1.751 eV (using PBE0 functional), respectively. This again indicates the limitation of the 18- or 20-electron rule in doped germanium clusters.

The ground state structure (Figure 59d) of Ru@Ge_{15} and Os@Ge_{15} is a FK-like cage (C_s), which can also be obtained by capping three Ge atoms on the D_{2d} Ge_{12} cage in Figure 54h. A similar FK-like cage also with C_s symmetry (Figure 59e) is obtained for Mo@Ge_{15} and W@Ge_{15}, and another FK-like polyhedron (Figure 59c) is obtained for Cr@Ge_{15}. The same FK-like cages were previously found for these M@Ge_{15} clusters (M = Ru, Os, Mo, W),[53] except that the isomer in Figure 59e was predicted for Cr@Ge_{15}; but it would transform into the structure in Figure 59c upon relaxation during our DFT calculation. Interestingly, M@Ge_{15} clusters with M = Ru and Os have 68 valence electrons, which corresponds to the electronic shell closing under a spherical potential, and this also explains their large HOMO−LUMO gaps of over 2 eV.

As cluster size further increases, Ge_{16} is a bit too large to encapsulate a transition metal or actinide metal atom for many elements. Indeed, our geometry optimization yields capped cage structures for Mn@Ge_{16} and W@Ge_{16} clusters. Here, we consider three isomers for the Ge_{16} cage (Figure 59g−i) and six metal dopants (M = Ti, Cr, Zr, Nb, Hf, Th), and our theoretical results are summarized in Table S19.

Experiments by Nakajima and co-workers found that neutral Ti@Ge_{16}, Zr@Ge_{16}, and Hf@Ge_{16} are magic clusters showing

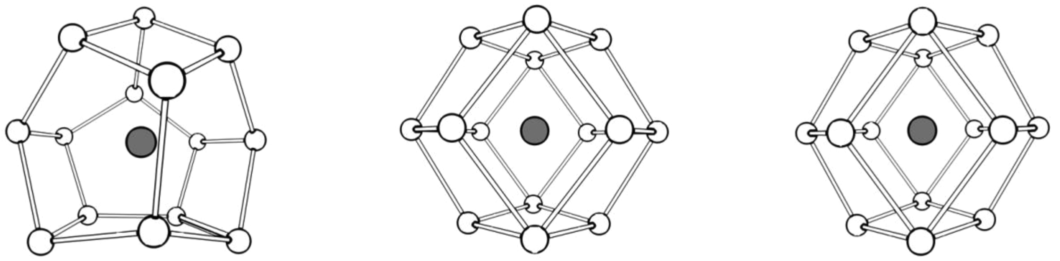
(a) Fullerene-like Cage (C_2)
(b) Cubic Cage (O_h, D_{4h}, D_{3d}, D_{2h})
(c) Distorted Cubic Cage (C_i)

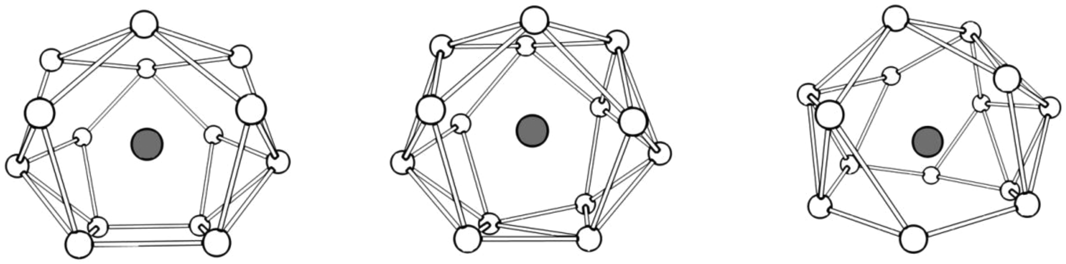
(d) Arachno Architecture (C_{2v}, C_2)
(e) Distorted Arachno Architecture (C_2)
(f) Distorted Bicapped Hexagonal Antiprism (C_1)

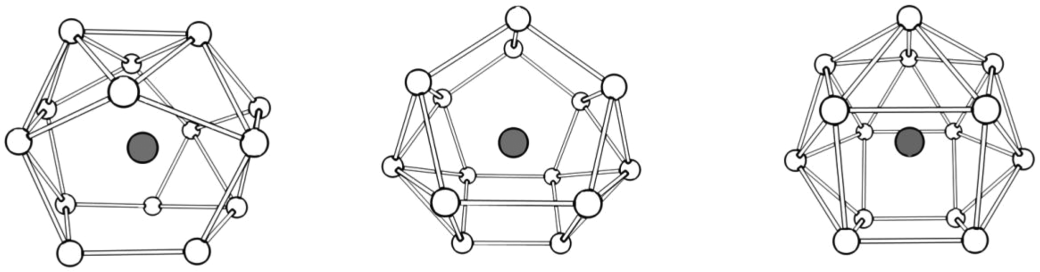
(g) Tetracapped Ge_{10} Boat (C_1)
(h) Tetracapped Pentagonal Prism (C_{2v})
(i) Tetracapped Pentagonal Prism (C_{2v})

Figure 58. Schematic structures of several isomers for M@Ge_{14} cage clusters with M the endohedral dopant as given in Table S17. Other details are as in Figure 51.

prominent peaks in the mass spectra and large HOMO−LUMO gaps.[531] From the present and previous DFT calculations,[53,561,583] all these clusters adopt a highly symmetric FK cage (T_d), as shown in Figure 59h, and their embedding energies are rather large (between 9.988 and 13.780 eV). It is also noteworthy that a FK-like polyhedron (Figure 59i) was previously proposed for these clusters,[572] but the corresponding energies are slightly higher by 0.147 eV for Ti@Ge_{16}, 0.092 eV for Zr@Ge_{16}, and 0.095 eV for Hf@Ge_{16}, respectively. For Ti@Ge_{16}, Zr@Ge_{16}, and Hf@Ge_{16} clusters, the theoretical HOMO−LUMO gaps computed by the PBE0 functional are 3.189, 3.346, and 3.092 eV, respectively, and those by the PW91 functional are 1.790, 1.955, and 1.979 eV, respectively.[53] It is well known that PW91 underestimates the HOMO−LUMO gap. The theoretical PW91 gaps are, however, closer to the experimental values of 1.77, 1.90, and 1.83 eV, respectively, measured from photoelectron spectra of the anionic clusters. But this coincidence is accidental, since for cluster anions, the symmetry is generally lowered compared to these neutral clusters and the HOMO−LUMO gap of the anionic clusters is expected to be smaller. In the previous theoretical studies of M@Ge_n (M = Ti, Zr, Hf; n = 1−20[572]) and Zr@Ge_n clusters (n = 1−21),[583] the maximum peaks at n = 16 on the size-dependent curves of the binding energy, embedding energy, and HOMO−LUMO gap as well as local minima on that of the electron affinity were found, indicating that Ge_{16} clusters doped with the group 4 elements are very stable species. Ti@Ge_{16}, Zr@Ge_{16}, and Hf@Ge_{16}, like their silicon counterparts discussed in Section 5.3.7, have totally 68 valence electrons that is a magic number within the spherical shell model. Therefore, these clusters with symmetric cage structure and closed electronic shell might be potential building blocks for cluster-assembled materials.[53] It is noteworthy that some of these clusters are chemically reactive,[80,488] which makes it challenging to integrate them without causing aggregation or collapse of the individual cage structures.

The same FK cage with T_d symmetry is also found as the ground state structure for Cr@Ge_{16},[53] which carries a total magnetic moment of 2 μ_B. A distorted FK cage with C_s symmetry is obtained for Nb@Ge_{16}, which is more stable than the previously reported structural isomer of the fullerene-like cage (Figure 59g)[588] by 1.373 eV from our PBE0 calculations. Indeed, this fullerene-like cage with D_{4d} symmetry is the lowest-energy structure for Th@Ge_{16}.[529] Thorium is also tetravalent and bigger than Zr. Accordingly, it fits well in the Ge_{16} fullerene cage similar to Zr@Si_{16}. The HOMO−LUMO

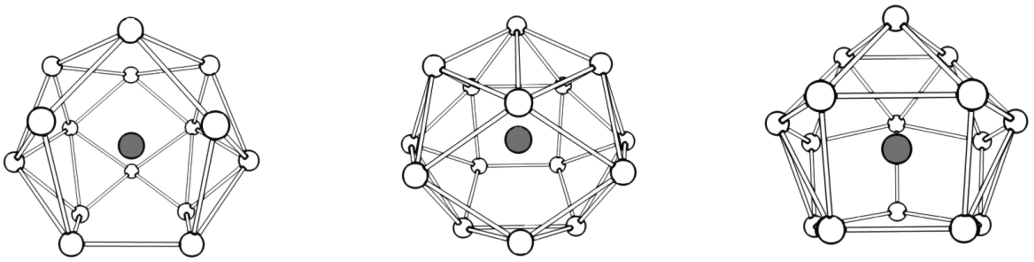

(a) Pentacapped Pentagonal Prism (C_{2v}, C_1) (b) Pentacapped Pentagonal Prism (C_s) (c) Frank-Kasper-like Polyhedron (C_s)

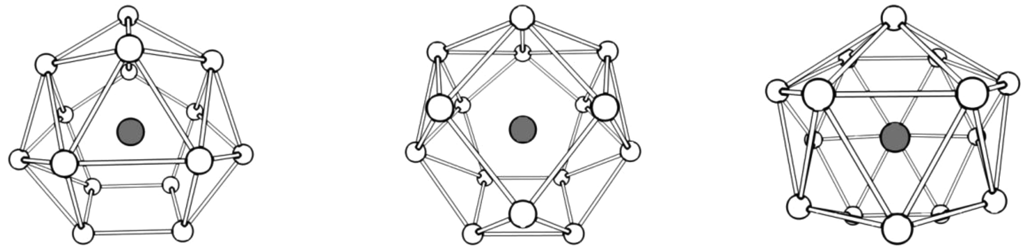

(d) Pentacapped Pentagonal Prism (C_s) (e) Pentacapped Pentagonal Prism (C_s) (f) Frank-Kasper Polyhedron (C_s)

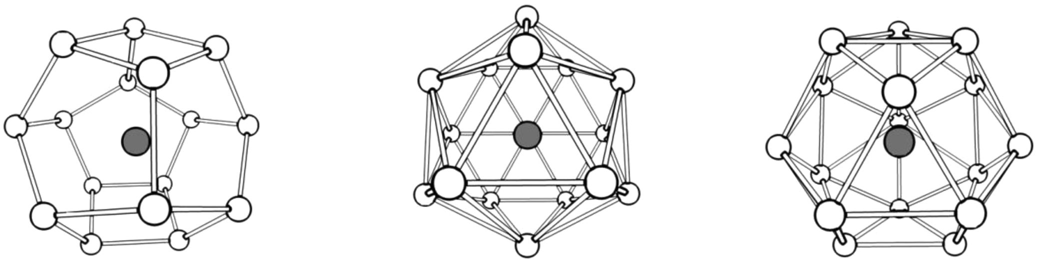

(g) Fullerene-like Cage (D_{4d}) (h) Frank-Kasper Polyhedron (T_d, C_2, C_s) (i) Frank-Kasper-like Polyhedron (C_{3v})

Figure 59. Schematic structures of several isomers for M@Ge_{15} (a−f) and M@Ge_{16} (g−i) cage clusters with M the endohedral dopant as given in Tables S18 and S19, respectively. Other details are as in Figure 51.

gap of 2.124 eV is, however, smaller compared with the values of 3.092−3.346 eV for the doping of group 4 elements (Table S19) at the same level of theory.

6.1.8. Endohedrally Doped Ge_{18} and Ge_{20} Cages.

Beyond n = 16, only a few endohedrally doped germanium cages have been explored in the literature, that is, Zr@Ge_{18},[583] Th@Ge_{18}, and Th@Ge_{20}.[529] It was argued that Th@Ge_{20} is the largest germanium cage cluster that can be stabilized by doping a single metal atom. However, unlike Th@Si_{20} cluster with dodecahedral structure discussed in Section 5.3.8, the most stable structure of Th@Ge_{20} is a FK deltahedron cage (Figure 41d) having a modest HOMO−LUMO gap of 1.11 eV (PW91) and an appreciable embedding energy of 13 eV. The gap is relatively small, as there is no shell closing with 84 valence electrons. The striking difference in structures of Si and Ge cages indicates that the slight difference in atomic size and bonding nature between Si and Ge may result in rather distinct behaviors for the metal encapsulated Si and Ge clusters. Furthermore, charge density analysis of Th@Ge_{16}, Th@Ge_{18}, and Th@Ge_{20} revealed the charge accumulation between the Th atom and the Ge cage, suggesting a covalent bonding character.[529]

6.2. Doped Tin Cages

Among the group 14 elements, bulk crystals of Si and Ge in diamond structure are semiconductors, while Sn exists in two phases, α-Sn and β-Sn. The former has diamond structure and is semi-metallic, while the latter (white tin) exists in BCT structure and is metallic. Going down further in the column, the metallic character increases and thus solid Pb is a metal with FCC lattice. Therefore, it is intriguing to explore how the atomic and electronic structures of tin clusters differ from those of silicon and germanium. The neutral, cationic and anionic tin clusters have been extensively investigated by Knudsen cell mass spectrometry,[594] electric deflection,[595] ion mobility spectrometry,[596,597] trapped ion electron diffraction,[596,598,599] collision induced dissociation,[596,599] photoelectron spectroscopy,[600] and DFT calculations.[601,602] The photoelectron spectra of small $[Sn_n]^-$ clusters ($n \leq 13$) are similar to those of $[Ge_n]^-$, and the medium-sized $[Sn_n]^-$ and Sn_n clusters follow the "face-sharing-pearl" or "pearl-chain" growth mode by face-sharing or stacking TTP or (bi)capped square antiprism as the basic units. A noticeable exception is $[Sn_{12}]^-$ with a slightly distorted hollow icosahedron,[596] which is related to a unique $[Sn_{12}]^{2-}$ cluster (named as stannaspherene[603]) with a perfect icosahedral structure and closed-shell electronic configuration (HOMO−LUMO gap being 2.77 eV at the B3LYP/aug-cc-pVDZ-PP level[604]). The high-symmetry structure and unusual stability of $[Sn_{12}]^{2-}$ can be related to its 50 valence electrons, obeying the $2(N + 1)^2$ electron count rule for spherical aromaticity[133] and the Wade−Mingos $4n_v + 2$ rule

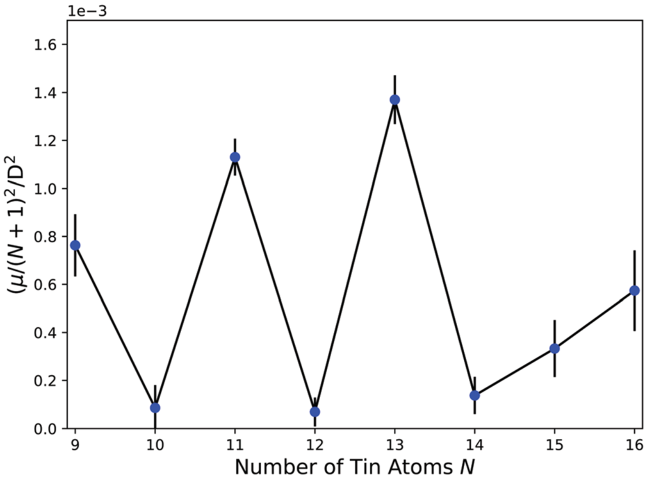

Figure 60. Measured squared electric dipole moment per atom $(\mu/(N + 1))^2$ in D^2 (squared Debye) of Sn_NCu (N = 9−16 is the number of Sn atoms), as extracted from electric field deflection via first order perturbation theory at a nozzle temperature of 20 K. The error bars represent the respective standard deviation and have been taken over at least five different beam profiles. Reproduced with permission from ref 613. Copyright 2019 Royal Society of Chemistry.

for 12-vertex *closo*-deltahedron with $2n_v + 2$ electrons for the skeletal bonding molecular orbitals, simultaneously.

Experimental studies on gas-phase doped tin clusters mainly focused on their geometries, stabilities, electronic and magnetic properties using mass spectrometry, anionic photoelectron spectroscopy, molecular beam electric deflection, and Stern-Gerlach magnetic deflection techniques.[57,68,69,483,531,605−613] From the mass spectrometric measurement by Neukermans *et al.*,[483] the particularly abundant species among M@Sn_n clusters (M = Cr, Mn, Cu, Zn; $n \leq 20$) are $CrSn_{10}$, $[CrSn_{15}]^+$, $[CrSn_{16}]^+$, $[MnSn_{13}]^+$, $[MnSn_{16}]^+$, $[MnSn_{12}]^{+,0}$, $[CuSn_{10}]^{+,0}$, $ZnSn_{10}$, and $ZnSn_{12}$ (see Table 8). In the experiment by Breaux *et al.*,[605] copper doped tin clusters were initially produced by laser vaporization and annealed at high temperature. These copper doped tin clusters were then converted into more stable copper-rich binary clusters in a narrow range of compositions: $[CuSn_{10-15}]^+$, $[Cu_2Sn_{12-18}]^+$, $[Cu_3Sn_{15-21}]^+$, $[Cu_4Sn_{18-24}]^+$, and $[Cu_5Sn_{21-27}]^+$, suggesting that they may adopt core-shell geometries.

Recently, Gleditzsch and co-workers[612,613] have investigated the dielectric properties and structural evolution of neutral Sn_nAu (n = 6−16) and Sn_nCu (n = 9−16) clusters using molecular beam electric deflection at different temperatures (T = 20 K, 40 K, 60 K). The measured cluster beam profiles were compared with classical rotational dynamic simulations using the cluster geometries from DFT-based GA global search. Generally speaking, Sn_nAu and Sn_nCu clusters exhibit similar size-dependent variation of dipole moment. Figure 60 plots the electric dipole moment measured for Sn_nCu clusters. Combined with DFT-GA calculations, it was found that at least nine Sn atoms are necessary to encapsulate a coinage metal (Cu or Au) atom and form an endohedral cage. Two highly symmetric structures, i.e., bicapped square antiprism and icosahedron, are found at n = 10 and 12, respectively, corresponding to nearly vanishing electric dipole moment measured in experiment (see Figure 60). Then, capped cage structure emerges from n = 13, gradually evolving into a double cage configuration at n = 16.

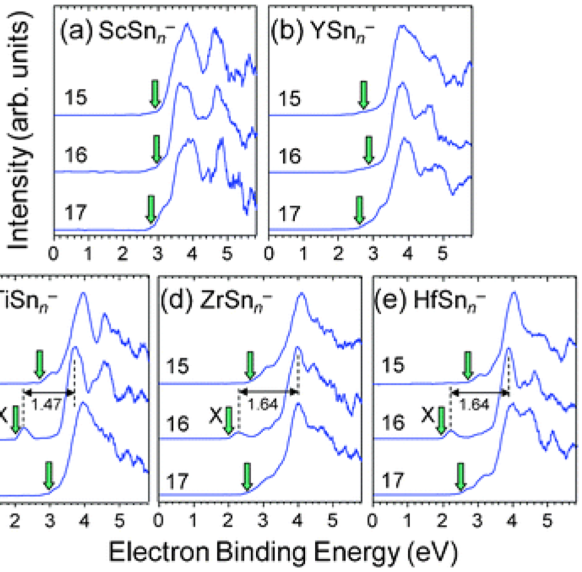

Figure 61. Photoelectron spectra of (a) $[ScSn_n]^-$, (b) $[YSn_n]^-$, (c) $[TiSn_n]^-$, (d) $[ZrSn_n]^-$, and (e) $[HfSn_n]^-$ (n = 15−17) at 213 nm. For the group 4 metals, namely Ti, Zr, and Hf, a HOMO−LUMO gap of 1.4−1.6 eV is observed for the anionic clusters with n = 16. Reproduced with permission from ref 531. Copyright 2012 Royal Society of Chemistry.

Nakajima's group[57,531] measured the photoelectron spectra of $[MSn_n]^-$ anions (n = 15−17; M = Sc, Y, Ti, Zr, Hf), as shown in Figure 61. Similar to the transition metal doped silicon and germanium clusters discussed before, the spectra of anionic tin clusters doped with group 4 elements show a small bump at around 2.0 eV (labeled as X), followed by a large energy separation of around 1.5 eV and more discrete transitions at higher binding energies. Accordingly, the neutral Ti@Sn_{16}, Zr@Sn_{16}, and Hf@Sn_{16} clusters have closed electronic shell with HOMO−LUMO gap of 1.47, 1.64, and 1.64 eV, respectively. The simulated photoelectron spectrum of $[Ti@Sn_{16}]^-$ with a slightly deformed FK cage structure using TD-B3PW91 calculations reasonably reproduces the first and second peaks of the measured spectrum, yielding a HOMO−LUMO gap of 1.22 eV.

Following the discovery of stannaspherene, Cui *et al.*[606] reported that the icosahedral Sn_{12} cage can trap a transition metal or rare earth metal atom to form a new class of endohedral clusters. A series of $[M@Sn_{12}]^-$ cage clusters (M = Ti, V, Cr, Fe, Co, Ni, Cu, Y, Nb, Gd, Hf, Ta, Pt, Au) were produced by laser vaporization and characterized by photoelectron spectroscopy. Figure 62 shows the spectra of selected $[M@Sn_{12}]^-$ clusters. In general, the spectra of $[M@Sn_{12}]^-$ become more complicated as the dopant varies from Cu to the early transition metals with open d shell. A characteristic doublet feature near 5 eV (labeled as g_u) emerges as the common feature for all the $[M@Sn_{12}]^-$ clusters. More details about the atomic and electronic structures of these M@Sn_{12} clusters will be discussed in Section 6.2.2.

Rohrmann *et al.* carried out a series of Stern−Gerlach and Stark experiments to measure the electric and magnetic molecular beam deflection of neutral $MnSn_n$ (n = 6−18) and Fe@Sn_{12} clusters.[68,69,607,608] The measured beam profiles of $MnSn_n$ clusters in the size range of n = 9−18 are presented in Figure 63. The electric and magnetic dipole moments of $MnSn_n$ clusters determined from these deflection data are plotted in Figures 64 and 65, respectively. One can see that both magnetic and electric dipole moments are temperature

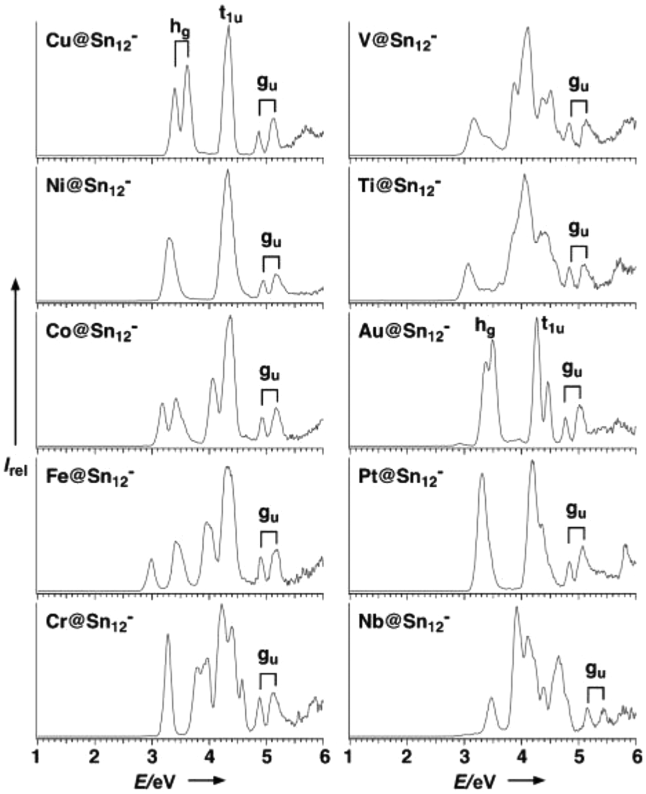

Figure 62. Photoelectron spectra of selected $[M@Sn_{12}]^-$ (M = Ti, V, Cr, Fe, Co, Ni, Cu, Nb, Pt, Au) clusters at 193 nm (6.424 eV). Reproduced with permission from ref 606. Copyright 2007 WILEY-VCH Verlag GmbH & Co. KGaA, Weinheim.

dependent and exhibit size dependent variation. Except for Sn_9, the electric dipole moments of the doped $MnSn_n$ clusters are reduced with regard to the pure Sn_n clusters, suggesting the Mn-centered endohedral cage structures with higher symmetry. All these $MnSn_n$ clusters possess magnetic moments mostly in the range of 4–6 μ_B. Temperature dependent experiments further revealed that molecular vibrations contribute crucially to the spin dynamics of $Mn@Sn_{12}$. The $Mn@Sn_{12}$ cluster in its vibrational ground state behaves like a superparamagnetic atom in a sextet spin state. It should be noted that Kumar and Kawazoe[67] predicted $Mn@Sn_{12}$ to be a magnetic superatom with 5 μ_B magnetic moment in a high-symmetry icosahedral structure. This is also consistent with the almost zero electric dipole moments measured on this cluster. However, magnetization of the molecular beam was observed when the $Mn@Sn_{12}$ clusters were vibrationally excited. Recently, Fuchs and Schäfer[609] conducted magnetic double deflection experiments on cold $Mn@Sn_{12}$ clusters. The spin dynamics were probed by introducing magnetic-flux density variations along the molecular-beam path. Similar to $Mn@Sn_{12}$, the magnetic response of $Fe@Sn_{12}$ cluster was investigated by the Stern–Gerlach magnetic beam deflection experiments,[608] and the total magnetic moment was determined to be 6.0 ± 0.2 μ_B. In particular, there is a substantial contribution from the electronic orbital angular momentum of about 1.1 μ_B. This might lead to a new opportunity in tailoring the magnetic anisotropy energy in the doped atomic clusters.

Compared to the extensive *ab initio* studies of doped silicon and germanium clusters, less theoretical efforts have been devoted to the endohedral tin cage clusters. In the following subsections, we will discuss the theoretical results of endohedral $M@Sn_n$ clusters with $n = 10$ and 12.

6.2.1. Endohedrally Doped Sn_{10} Cages.

In line with the experimental synthesis of endohedral Zintl anions of $[Rh@Sn_{10}]^{3-}$,[614] *ab initio* calculations confirmed that most gas-phase $M@Sn_{10}$ clusters adopt a bicapped square antiprism with D_{4d} point group symmetry. Table 11 summarizes the essential results from previous theoretical calculations.[58,563,564,615,616] Except for $Li@Sn_{10}$ and $Zn@Sn_{10}$, most endohedral clusters possess appreciable embedding energies between 3.37 and 5.80 eV. Among the systems explored, $[Cu@Sn_{10}]^-$, $[Ag@Sn_{10}]^-$, $[Au@Sn_{10}]^-$, $Be@Sn_{10}$, and $Zn@Sn_{10}$ with totally 42 valence electrons are closed-shell species with sizeable HOMO–LUMO gaps in the range of 2.07 eV to 2.71 eV. This was interpreted by the picture of spherical aromaticity of π-electrons.[564] Specifically, the valence orbitals of $[Cu@Sn_{10}]^-$ can be divided into two subsets: (i) $1S^2 1P^6 1D^{10} 1F^2 1F^8 1F^4 1G^2$ shells occupied by 34 σ electrons; (ii) $2S^2 2P^2 2P^4$ shells occupied by 8 π electrons. The latter fulfills the $2(N+1)^2$ electron count rule with $N = 1$.[133] On the other hand, the bicapped square antiprism is a 10-vertex *closo*-deltahedron, which requires a total of 42 valence electrons according to the Wade–Mingos rules. The coincidence of spherical aromaticity and closed shell in these 42 skeleton electron systems can explain why most $M@Sn_{10}$ clusters adopt bicapped square antiprism structure.

6.2.2. Endohedrally Doped Sn_{12} Cages.

So far, most previous theoretical studies focused on endohedrally doped $M@Sn_{12}$ cage clusters,[67,590,615,617–622] and the main results are summarized in Table 12. All these $M@Sn_{12}$ clusters prefer a nearly perfect icosahedral cage configuration with only small distortion, while the other possible cage isomers such as cuboctahedron are less stable.[620] This is consistent with the experimental observation of endohedral Zintl anions of $[Rh@Sn_{12}]^{3-}$[614] and $[Ir@Sn_{12}]^{3-}$[623] with distorted icosahedral configuration, which will be discussed in Section 6.4 later. For the icosahedral $M@Sn_{12}$ cages, most of the M–Sn distances are around 3 Å, while the atoms/cations of heavy elements (Pu, Hg, Lr^+, Lu^+, La^+, Ac^+) form slightly longer M–Sn bonds of about 3.2–3.3 Å. The $M@Sn_{12}$ cage clusters with 50 valence electrons (e.g., $Be@Sn_{12}$, $Mg@Sn_{12}$, $Ca@Sn_{12}$) attain closed electronic shells and exhibit a sizeable HOMO–LUMO gap of about 2 eV, which can be understood by the high stability of their isoelectronic counterpart, i.e., stannaspherene $[Sn_{12}]^{2-}$ discussed above (if one assumes the two *s* valence electrons are completely transferred from the metal dopant to the Sn_{12} cage).

Doping open-shell transition metal elements such as Ti, V, Cr, Mn, Fe, Co, and Cr induces a magnetic spin moment of 2–5 μ_B in the endohedral $M@Sn_{12}$ cage, which is identical to the magnetic moment of the free atom (except for Cr). Therefore, it is possible to adjust the magnetic spin moment of $M@Sn_{12}$ cluster by the choice of the transition metal dopant, providing a family of magnetic superatoms with tunable magnetic moment. In particular, all the theoretical studies predicted that $Mn@Sn_{12}$ possesses a large magnetic moment of 5 μ_B[67,528,590,618–620], which was confirmed by experiment (5.3 ± 1.2 μ_B).[607] Note that $Mn@Sn_{12}$ also has a moderate HOMO–LUMO gap of about 1.1 eV and a reasonable embedding energy (up to 6.89 eV),[590] making it a stable magnetic superatom[67] as a building block of spintronic devices and magnetic nanomaterials.

To understand the superatomic characteristics, charge density isosurfaces and energy levels for the molecular orbitals

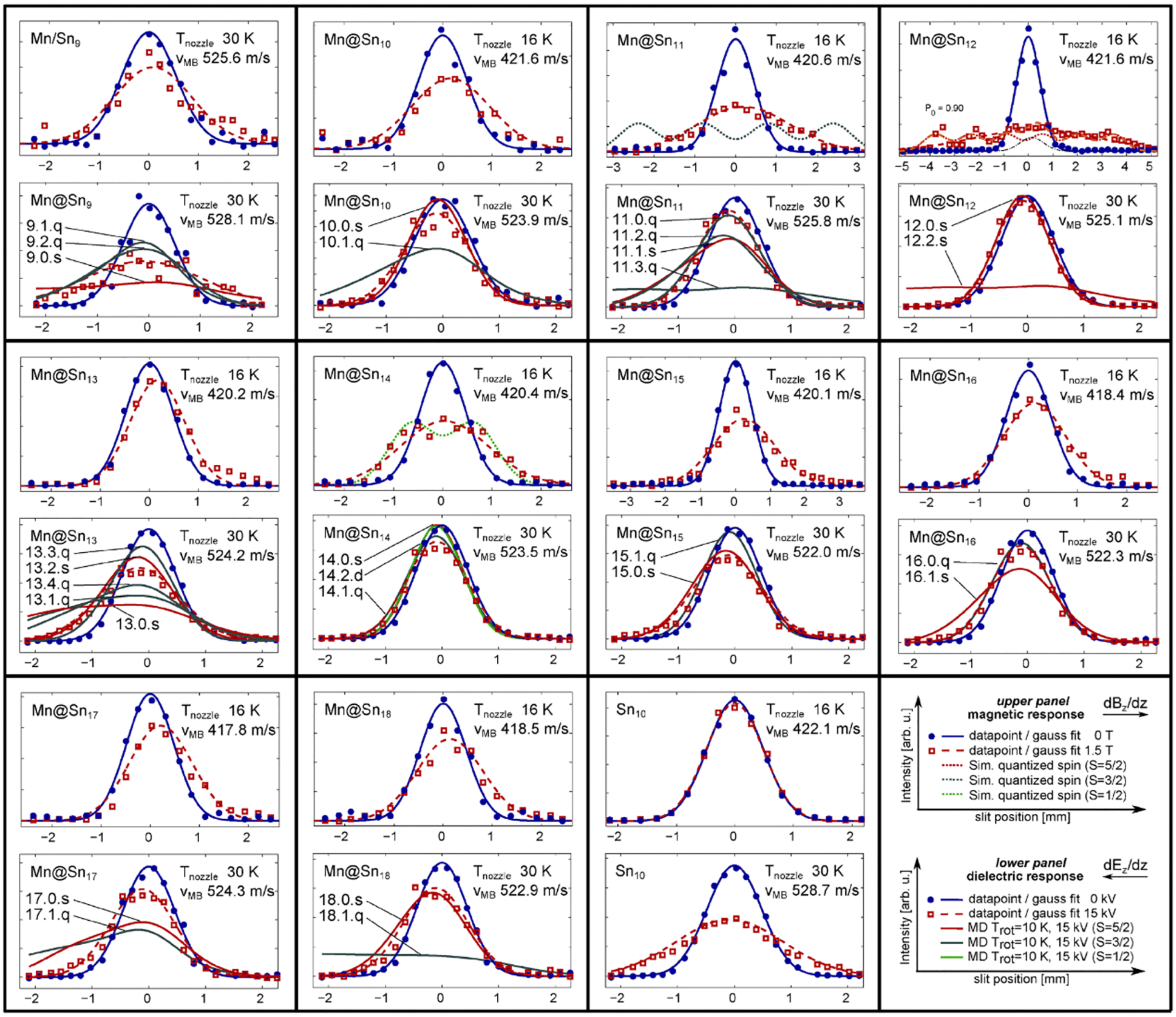

Figure 63. Beam profiles of $MnSn_n$ clusters with $n = 9-18$ and Sn_{10} measured with an inhomogeneous magnetic field (upper panel, $B_z = 1.5$ T) and electric field (lower panel, deflection voltage $U_{defl} = 15$ kV). In order to analyze the measured beam profiles (blue dots without and red square with an applied field) by first order perturbation theory, Gaussian functions are fitted to the data points (solid blue line and dashed red line). Upper panels show the beam profiles for $Mn@Sn_{11}$, $Mn@Sn_{12}$, and $Mn@Sn_{14}$ according to quasi-atomic paramagnetic response for $S = 3/2$ (grey dotted line), $S = 5/2$ (red dotted line), and $S = 1/2$ (green dotted line), respectively. For $Mn@Sn_{12}$, a two-component fit is shown (dashed orange line), corresponding to $T_{vib} = 28$ K. Lower panels show the dielectric response of the isomers obtained by MD simulation, with solid green, grey, and red lines for $S = 1/2$, $S = 3/2$, and $S = 5/2$ spin-isomers. Additionally the labels corresponding to Figure 1 of ref 69 are included. Reproduced with permission from ref 69. Copyright 2014 Royal Society of Chemistry.

of $Zn@Sn_{12}$ and $Mn@Sn_{12}$ clusters[590] are shown in Figure 66. For $Zn@Sn_{12}$, the lowest-energy level corresponds to the localized Zn-3d^{10} atomic orbitals. The other orbitals are mostly diffused over the Sn_{12} cage and mainly contributed by Sn-5*s* and 5*p* electrons. Due to the icosahedral ligand field, $1F^{14}$ molecular orbitals split into $1F^6$ and $1F^8$ submolecular orbitals, and $1G^{18}$ molecular orbitals split into occupied $1G^{10}$ and unoccupied $1G^8$ submolecular orbitals. The filling of 25 occupied superatomic orbitals is given by the energy sequence of $1S^2(a_g)1P^6(t_{1u})1D^{10}(h_g)1F^6(t_{2u})2S^2(a_g)1F^8(g_u)2P^6(t_{1u})1G^{10}(h_g)$. The half-filled *d* orbitals (unpaired 3d^5 spin-up electrons) of Mn atom do not contribute to the superatomic orbitals, even though the energy levels lie in between the occupied superatomic orbitals. Thus, the filling of the remaining 50 electrons follows the energy sequence of $1S_\alpha^1 1S_\beta^1 1P_\alpha^3 1P_\beta^3 1D_\alpha^5 1D_\beta^5 1F_\alpha^3 1F_\beta^3 2S_\alpha^1 2S_\beta^1 1F_\alpha^4 1F_\beta^4 2P_\alpha^3 2P_\beta^3 1G_\alpha^5 1G_\beta^5$ (here α and β denote the spin-up and spin-down states, respectively).

Replacing two Sn atoms in Sn_{12} by Bi with one more valence electron leads to a $Sn_{10}Bi_2$ alloy cage that is isoelectronic and isostructural to stannaspherene $[Sn_{12}]^{2-}$.[617] Further doping a Pd or Pt atom inside this cage results in stable endohedral complexes with large HOMO−LUMO gaps of 2.25−2.29 eV and appreciable embedding energies of 4.22−5.95 eV, which are comparable to those calculated for $[Pt@Sn_{12}]^{2-}$ and $[Pd@Sn_{12}]^{2-}$.

6.3. Doped Lead Cages

Among group 14 elements (C, Si, Ge, Sn, Pb), lead is the heaviest one and exhibits the most pronounced metallic

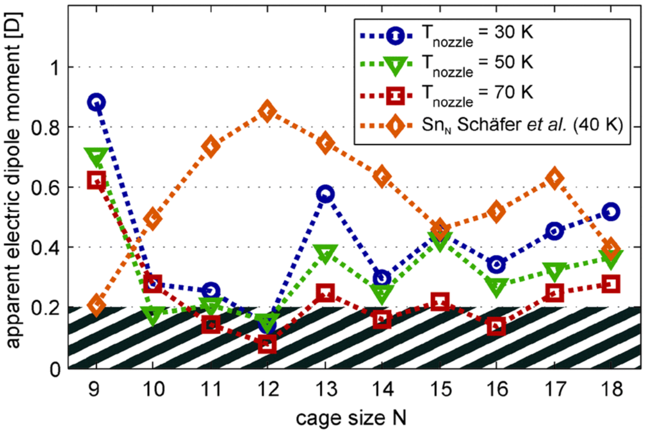

Figure 64. Apparent magnitude $\mu_{el,0}$ of the electric dipole moments of $MnSn_N$ clusters produced at nozzle temperatures T_{nozzle} = 30 K (blue circles), 50 K (green triangles), and 70 K (red squares). The orange diamonds correspond to the measured electric dipole moment of the pure Sn_N clusters. Data points are connected by a dotted line with corresponding color as a guide to the eye. The electric dipole moments are extracted from the variance of Gaussian functions fitted to the molecular beam profiles without and with an applied electric field (deflection voltage U_{defl} = 15 kV). The shaded gray area reflects the experimental uncertainties in Stark deflection. Here N is the number of Sn atoms. Notice the dip at N = 12. Reproduced with permission from ref 69. Copyright 2014 Royal Society of Chemistry.

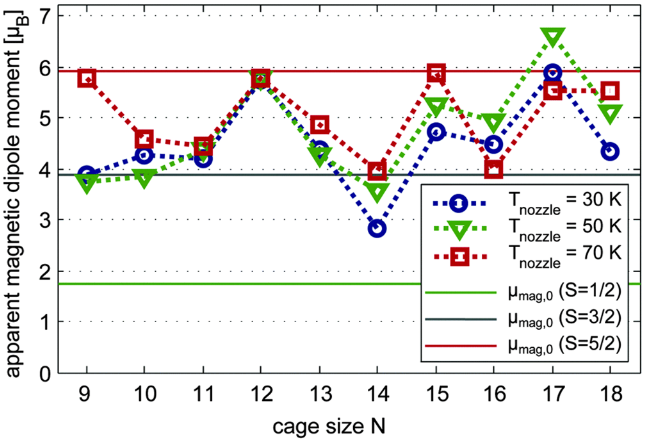

Figure 65. Apparent magnitude $\mu_{mag,0}$ of the magnetic dipole moments of $MnSn_N$ clusters produced at nozzle temperatures T_{nozzle} = 30 K (blue circles), 50 K (green triangles), and 70 K (red squares). As a guide to the eye the data points are connected by a dotted line with corresponding color. The magnetic dipole moments are extracted from the shift of gauss functions fitted to the molecular beam profiles without and with an applied magnetic field (B_z = 1.53 T, $\partial B/\partial z$ = 335 T m^{-1}). The straight solid line represent the magnitude of the magnetic dipole moment resulting from S = 1/2 (green), S = 3/2 (grey), and S = 5/2 (red) with a spin-only Landé factor g = 2. Reproduced with permission from ref 69. Copyright 2014 Royal Society of Chemistry.

character. Thus, the structures and properties of lead clusters are expected to be different from those of germanium and tin clusters. The evolution of atomic and electronic structures of pure lead clusters with cluster size has been studied using ion mobility measurement,[624] core-hole photoelectron spectroscopy,[625] molecular beam electric deflection,[626,627] and DFT calculations.[628] In the medium-size range (n = 13−22), two structural growth patterns, i.e., layered stacking structures and more-spherical atom-centered compact structures, coexist and compete with each other. As the cluster size n grows, a non-metal to metal transition has been found to occur at around n = 20 both theoretically and experimentally. An analogue of stannaspherene ($[Sn_{12}]^{2-}$), $[Pb_{12}]^{2-}$ cluster (named as "plumbaspherene") was also proposed by Cui *et al.* based on the photoelectron spectra of Pb_{12}^- and KPb_{12}^- anions.[629] The ground state structure of $[Pb_{12}]^{2-}$ is a perfect icosahedral cage with a large HOMO−LUMO gap (2.78 eV at the B3LYP/aug-cc-pVDZ-PP level).[604] However, different from $[Sn_{12}]^{2-}$, which is only weakly aromatic (NICS value: −5.0 ppm), $[Pb_{12}]^{2-}$ is strongly aromatic with a NICS value of −20.7 ppm at the cage center,[604] meaning it should be even more stable than $[Sn_{12}]^{2-}$.

So far, there have been a few experiments on the doped lead clusters from different aspects, such as mass spectrometry[57,59,483,630−633], photodissociation,[634] molecular beam electric deflection,[632] and photoelectron spectroscopy.[57,633,635] In an early mass spectrometry experiment, X. Zhang *et al.*[630] produced binary Pb−Co alloy clusters and observed two abundant peaks at $[Co@Pb_{10}]^-$ and $[Co@Pb_{12}]^-$, which were assumed to be an endohedral bicapped square antiprism and a Co-centered icosahedron, respectively. Later, the same group generated and analyzed M-Pb cluster anions (M = Cu, Ag, Au)[631] with many binary compositions. Among them, $[MPb_n]^-$ clusters show relatively intense peaks or sharp turning points at n = 5, 10, and 12 in the mass spectra. Furthermore, in a mass spectrometric measurement on Cr, Mn, Cu, and Zn doped Pb clusters by Neukermans *et al.*,[483] particularly abundant clusters were found to be $[CrPb_{10}]^{+,0}$, $[CrPb_{12}]^{+,0}$, $[MnPb_{12}]^{+,0}$, $[CuPb_{10}]^{+,0}$, $[CuPb_{12}]^{+,0}$, and $ZnPb_{12}$ (see Table 8). Neukermans *et al.* also reported mass spectrometric characterization of the gas-phase Al doped $[Pb_n]^+$ clusters.[59] In the mass abundance spectrum of mixed $[AlPb_n]^+$ clusters, the first and second prominent peaks were observed at $[AlPb_{12}]^+$ and $[AlPb_{10}]^+$, respectively (see Figure 67). Later, the same group reported the fragmentation pathways and dissociation energies of $[AlPb_n]^+$ (n = 7−16) clusters.[634] Consistent with the mass spectral observation, $[AlPb_{10}]^+$ and $[AlPb_{12}]^+$ are the dominant products in the photon induced decay chain of most larger $[AlPb_n]^+$ clusters (n > 10), demonstrating their high stability. Furthermore, the dissociation energy of $[AlPb_{12}]^+$ (2.33−2.98 eV) is higher than that of the neighboring-size clusters, again confirming its high stability.

Nakajima and co-workers[57] carried out a comparative study of $[MSi_{16}]^-$, $[MGe_{16}]^-$, $[MSn_{16}]^-$, and $[MPb_{16}]^-$ (M = Ti, Zr, Hf) clusters using time-of-flight mass spectrometry and anion photoelectron spectroscopy. Different from the prominent abundant peak at $Ti@Ge_{16}$ or $Ti@Si_{16}$, the mass spectrum of neutral $TiPb_n$ clusters does not show a peak at $TiPb_{16}$; instead the spectrum resembles that of pure Pb_n clusters. Moreover, the HOMO−LUMO gaps measured from the anion photoelectron spectra are 0.85 eV for $TiPb_{16}$, 0.86 eV for $ZrPb_{16}$, and 0.93 eV for $HfPb_{16}$. Therefore, MPb_{16} (M = Ti, Zr, Hf) clusters are electronically not very stable, which can be associated with the relatively lower stability of the $[Pb_{16}]^{4-}$ cage. Indeed, the computed NICS value at the cage center is −65.9 ppm for $[Si_{16}]^{4-}$, −30.5 ppm for $[Ge_{16}]^{4-}$, −12.3 ppm for $[Sn_{16}]^{4-}$, and 8.2 ppm for $[Pb_{16}]^{4-}$, suggesting that only $[Pb_{16}]^{4-}$ is antiaromatic among these four 16-vertex cages of group 14 elements.

Grubisic *et al.*[633] prepared $[PtPb_n]^-$ cluster anions from "preassembled" clusters generated from crystalline $[K2,2,2\text{-crypt}]_2[Pt@Pb_{12}]$ that were brought into the gas phase using an infrared desorption/photoemission anion source. The

Table 11. Summary of Previous Theoretical Resultson Endohedrally Doped M@Sn_{10} Cages: Distance between MAtom and Sn Atom (R), HOMO−LUMO Gap (E_{HL}), Embedding Energy (E_{em}), and Vertical IonizationPotential (VIP)[a]

Cluster	Method	R (Å)	E_{HL} (eV)	E_b (eV)	E_{em} (eV)	VIP (eV)
Ni@Sn_{10} [58]	PW91/planewave		1.24	3.15		
Pd@Sn_{10} [58]	PW91/planewave		1.17	3.06		
Pt@Sn_{10} [58]	PW91/planewave		1.30	3.24		
Cu@Sn_{10} [563]	B3LYP/LanL2DZ	2.795, 2.977		2.68	3.76	6.14
Ag@Sn_{10} [563]	B3LYP/LanL2DZ	2.880, 3.015		2.68	3.76	6.14
Au@Sn_{10} [563]	B3LYP/LanL2DZ	2.883, 3.019		2.68	3.76	6.14
$[Cu@Sn_{10}]^-$ [563]	B3LYP/LanL2DZ	2.753, 3.204	2.39	2.87	5.80	3.11
$[Ag@Sn_{10}]^-$ [563]	B3LYP/LanL2DZ	2.845, 3.218	2.16	2.71	4.01	2.99
$[Au@Sn_{10}]^-$ [563]	B3LYP/LanL2DZ	2.848, 3.236	2.07	2.71	4.06	2.90
$[Cu@Sn_{10}]^+$ [564]	B3LYP/LanL2DZ	2.841, 2.784	2.0	2.43		
$[Ag@Sn_{10}]^+$ [564]	B3LYP/LanL2DZ	2.917, 2.861	1.9	2.29		
$[Au@Sn_{10}]^+$ [564]	B3LYP/LanL2DZ	2.915, 2.871	2.0	2.55		
Zn@Sn_{10} [615]	B3LYP/LanL2DZ		2.35	2.44	1.00	
Li@Sn_{10} [616]	B3LYP/cc-pVTZ(-PP)		1.05	3.27	1.62	6.37
Be@Sn_{10} [616]	B3LYP/cc-pVTZ(-PP)	2.674, 3.164	2.71	3.43	3.37	6.62
B@Sn_{10} [616]	B3LYP/cc-pVTZ(-PP)		1.15	3.45	3.59	5.49

[a] All clustersadopt D_{4d} point group symmetry, except for B@Sn_{10} which has onlyC_1 symmetry. For M−Sn bond lengths, the first R value is between M and Sn atoms of Sn_8 squareantiprism and the second R value is between M andcapped Sn atoms along the C_4 axis.

Table 12. Summary of Previous Theoretical Results on Endohedrally Doped M@Sn_{12} Cages: M−Sn Distance (R), HOMO−LUMO Gap (E_{HL}), Binding Energy per Atom (E_b), Embedding Energy (E_{em}), and Total Magnetic Spin Moment (μ_t)[a]

Cluster	Method	R (Å)	E_{HL} (eV)	E_b (eV)	E_{em} (eV)	μ_t (μ_B)
Be@Sn_{12} [67]	PW91/planewave	2.98	1.97	2.98	4.62	0
Mg@Sn_{12} [67]	PW91/planewave	3.05	2.00	2.86	3.05	0
Ca@Sn_{12} [67]	PW91/planewave	3.13	1.92	2.81	2.38	0
Mn@Sn_{12} [67]	PW91/planewave	3.01	1.15	2.96	4.36	5
Zn@Sn_{12} [67]	PW91/planewave	3.02	1.96	2.82	2.57	0
Cd@Sn_{12} [67]	PW91/planewave	3.06	1.94	2.77	1.87	0
$[Pd@Sn_{12}]^{2-}$ [617]	B3LYP/def-TZVPP		2.49		4.07	0
$[Pt@Sn_{12}]^{2-}$ [617]	B3LYP/def-TZVPP		2.43		5.76	0
Pd@Bi_2Sn_{10} [617]	B3LYP/def-TZVPP		2.29		4.22	0
Pt@Bi_2Sn_{10} [617]	B3LYP/def-TZVPP		2.25		5.95	0
Mn@Sn_{12} [618]	MPWB1K/SKBJ	3.03				5
Mn@Sn_{12} [619]	PW91/planewave	3.05	1.12			5
Ti@Sn_{12} [620]	BLYP/DNP		0.57	2.55	4.47	2
V@Sn_{12} [620]	BLYP/DNP		0.58	2.57	4.78	3
Cr@Sn_{12} [620]	BLYP/DNP		0.05	2.41	3.35	4
Mn@Sn_{12} [620]	BLYP/DNP		1.08	2.43	3.59	5
Fe@Sn_{12} [620]	BLYP/DNP		0.20	2.52	4.01	4
Co@Sn_{12} [620]	BLYP/DNP		0.43	2.58	4.35	3
Ni@Sn_{12} [620]	BLYP/DNP		0.22	2.59	4.11	2
Pu@Sn_{12} [621]	B3LYP/TZVP	3.22	1.97	2.01		0
Zn@Sn_{12} [615]	B3LYP/LanL2DZ		2.74	2.50	2.12	0
Mn@Sn_{12} [590]	BPW91/LanL2DZ	3.08	1.08	2.64	6.89	5
Tc@Sn_{12} [590]	BPW91/LanL2DZ	3.05	0.54	2.75	9.17	5
Re@Sn_{12} [590]	BPW91/LanL2DZ	3.04	0.52	2.76	8.16	5
Zn@Sn_{12} [590]	BPW91/LanL2DZ	3.10	1.97	2.40	3.94	0
Cd@Sn_{12} [590]	BPW91/LanL2DZ	3.16	1.95	2.34	3.01	0
Hg@Sn_{12} [590]	BPW91/LanL2DZ	3.18	1.93	2.26	1.85	0
$[Lr@Sn_{12}]^+$ [622]	PBE/def-TZVP	3.21	1.62	2.79		0
$[Lu@Sn_{12}]^+$ [622]	PBE/def-TZVP	3.18	1.70	2.95		0
$[La@Sn_{12}]^+$ [622]	PBE/def-TZVP	3.29	1.06	2.31		0
$[Ac@Sn_{12}]^+$ [622]	PBE/def-TZVP	3.34	1.02	2.11		0

[a] Most clusters adopt I_h point group symmetry except for Pd@Bi_2Sn_{10} and Pt@Bi_2Sn_{10}.

resulting mass spectra are given in Figure 68a, showing the coexistence of $[Pb_n]^-$, $[PtPb_n]^-$, $[KPb_n]^-$, and $[KPtPb_n]^-$ clusters. For $n \geq 10$, two prominent peaks corresponding to $[PtPb_{10}]^-$ and $[PtPb_{12}]^-$ clusters are observed, while the $[PtPb_n]^-$ series abruptly ends at $n = 12$. The anion photoelectron spectra of $[PtPb_{10}]^-$ and $[PtPb_{12}]^-$ clusters from experiments and DFT simulations are shown in Figure 68b, along with those of pure $[Pb_{10}]^-$ and $[Pb_{12}]^-$ clusters. For both $n = 10$ and $n = 12$, the photoelectron spectra for the pure and Pt doped $[Pb_n]^-$ clusters are similar in terms of both their

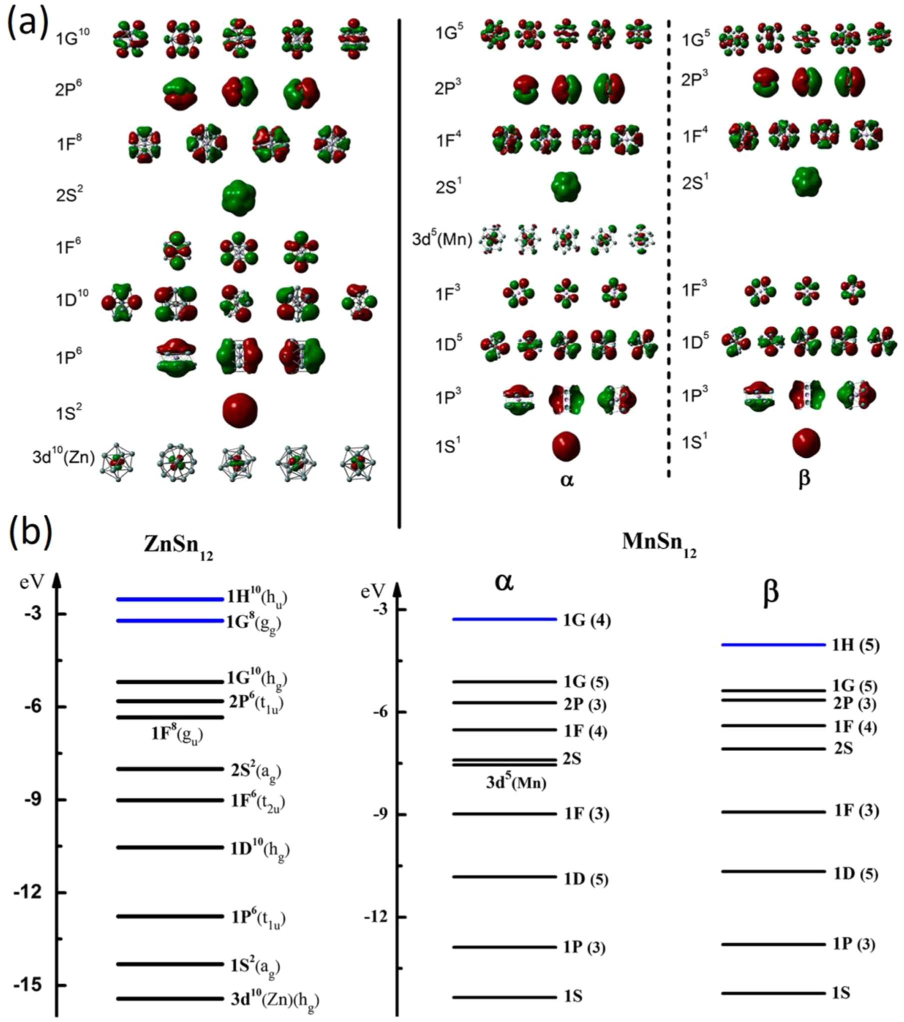

Figure 66. (a) Molecular orbital isosurfaces for Zn@Sn_{12} and Mn@Sn_{12}, where α and β represent spin-up and spin-down, respectively. (b) Molecular orbital energy levels (in eV) of Zn@Sn_{12} and Mn@Sn_{12}, where the superatomic orbitals corresponding to different spherical harmonics (angular momentum) have been indicated. Black lines and blue lines represent the occupied levels and the unoccupied levels, respectively. For each level, the angular (using upper-case letter), total electrons (using superscript), and degenerated states (using parentheses) are marked. The 3*d* states of Zn and Mn atoms are also shown. Reproduced with permission from ref 590. Copyright 2016 AIP Publishing LLC.

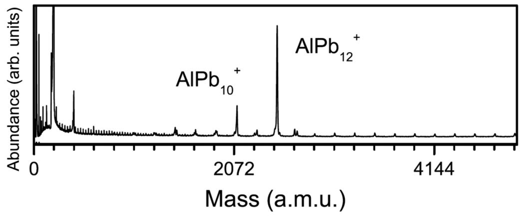

Figure 67. Mass abundance spectrum of mixed $[AlPb_n]^+$ clusters, showing the enhanced stability of $[AlPb_{10}]^+$ and $[AlPb_{12}]^+$. Reproduced with permission from ref 59. Copyright 2004 American Physical Society.

electron binding energies and their complexities, implying that their electronic structures are mainly lead based. DFT geometry optimization and comparison between experimental and simulated photoelectron spectra demonstrated that $[PtPb_{10}]^-$ and $[PtPb_{12}]^-$ clusters adopt an endohedral bicapped square antiprism and Pt-centered icosahedron, respectively. According to the NMR and photoelectron spectroscopic features, electronic stability of the icosahedral $[PtPb_{12}]^-$ cluster is superior to that of $[PtPb_{10}]^-$ due to the effect of aromaticity.

H. Xie *et al.*[635] investigated $[AgPb_n]^-$ clusters (n = 5−12) using photoelectron velocity-map imaging spectroscopy and *ab initio* calculations at the BHLYP/def2-TZVP level for geometry optimization and the RI-MP2/aug-cc-pVTZ-PP level for more accurate single-point energy calculation. By comparing the experimental photoelectron spectra and VDE with the simulated ones, the most probable structures of $[Ag@Pb_n]^-$ clusters have been determined. They found that Ag atom prefers to stay outside the smaller $[AgPb_n]^-$ clusters with $n \leq 6$ and intends to be encapsulated in the larger Pb_n clusters with $n > 6$. The completely endohedral cage configuration starts from $[Ag@Pb_{10}]^-$. The most probable structures of $[Ag@Pb_{10}]^-$, $[Ag@Pb_{11}]^-$, and $[Ag@Pb_{12}]^-$ are an endohedral bicapped square antiprism, an endohedral cage structure bearing the square and pentagonal pyramids simultaneously, and a Ag-centered bicapped pentagonal prismatic cage, respectively.

Schäfer *et al.*[632] reported the TOF mass spectra of pure and Mg doped Pb_n clusters (n = 8−18). The experiments with different Pb/Mg target compositions revealed that a Pb_n cluster with more than ten Pb atoms is necessary to attach a single Mg atom, and Pb_n clusters with $n \geq 15$ start to uptake two Mg atoms. They further utilized the electric deflection of the molecular beam

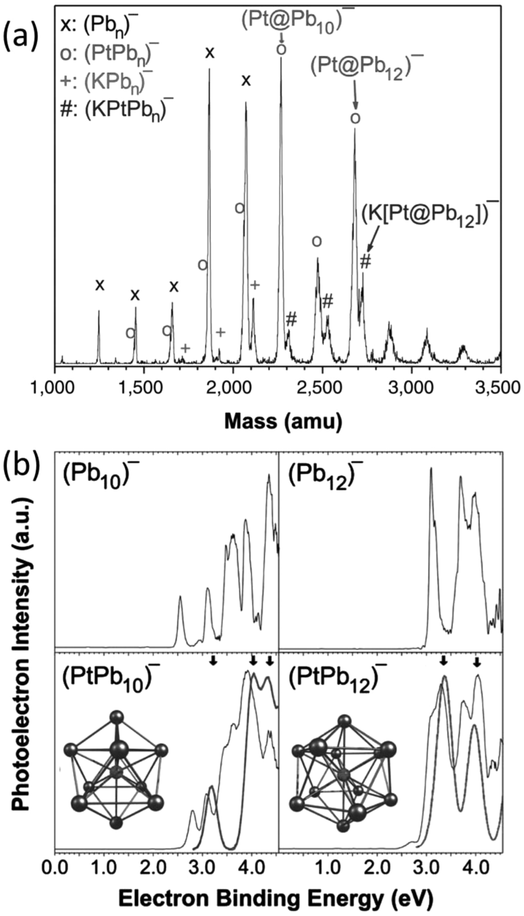

Figure 68. (a) Anion mass spectrum of $[K2,2,2\text{-crypt}]_2[Pt@Pb_{12}]$ sample obtained by employing the infrared desorption/photoemission anion source. (b) Photoelectron spectra of $[PtPb_{10}]^-$ and $[PtPb_{12}]^-$ (lower) as well as $[Pb_{10}]^-$ and $[Pb_{12}]^-$ (upper) recorded with 266 nm photons. The calculated structures of the Pt-containing clusters along with the predicted photoelectron transitions (arrows) are also shown. Simulated photoelectron spectra (dark lines) are obtained by convoluting the predicted transitions with Gaussians whose widths correspond to the experimental resolution. Reproduced with permission from ref 633. Copyright 2011 National Academy of Sciences.

to measure the polarizabilities and electric dipole moments of pure and doped Pb_n clusters. In the size range $n = 10{-}16$, $MgPb_n$ clusters (especially $MgPb_{12}$ and $MgPb_{14}$) exhibit low polarizabilities and nearly vanishing dipole moments, suggesting that the Mg atom is encapsulated in a highly symmetric lead cage.

There are many *ab initio* calculations focused on the endohedral $M@Pb_{10}$ and $M@Pb_{12}$ cages, which will be discussed in the following. Beyond these two commonly studied sizes, the smallest endohedral Pb cluster is $C@Pb_8$,[636] which adopts a distorted tetragonal antiprism configuration with the C dopant occupying the endohedral site. The calculated embedding energy of 4.59 eV and the HOMO−LUMO gap of 0.74 eV (using PBE functional) for $C@Pb_8$ signify its moderate stability. The neutral $Al@Pb_9$ cluster was also found to possess an endohedral geometry, namely, capped square antiprism, whereas the most stable structure of cationic $[Al@Pb_9]^+$ is still an open cage.[637] On the other hand, larger endohedral $M@Pb_{14}$ cages were proposed for M = C, Al, In, Mg, and Sr as the lowest-energy structure.[636] Their embedding energies are in the range of 2.45 eV to 4.0 eV and their HOMO−LUMO gaps are around 1.0 eV (with PBE functional), except for $Al@Pb_{14}$ and $In@Pb_{14}$ clusters which have odd number of electrons.

6.3.1. Endohedrally Doped Pb_{10} Cages.

As for endohedral $M@Pb_{10}$ cages, many dopant elements such as M = C, Mg, Al, Fe, Co, Ni, Cu, Ag, Au, and Pt[563,564,636−638] have been studied. The main theoretical results are summarized in Table 13. All these clusters share the same structure, namely, a bicapped square antiprism of Pb_{10} enclosing an M dopant or ion (see Figure 68b). According to the computed embedding energies which vary from 2.47 to 5.54 eV, all these dopants can be stably encapsulated in the Pb_{10} cage. Most of these endohedral complexes are nonmagnetic, while the total magnetic spin moments of $Fe@Pb_{10}$, $Co@Pb_{10}$, and $Ni@Pb_{10}$ clusters reported by X. Chen *et al.* are 2 μ_B, 1 μ_B, and 2 μ_B, respectively.[638] Using the B3LYP functional, exceptionally large HOMO−LUMO gaps of over 2.2 eV have been found for the 42-electron systems, such as $[Cu@Pb_{10}]^-$, $[Ag@Pb_{10}]^-$, $[Au@Pb_{10}]^-$, $Mg@Pb_{10}$, and $[Al@Pb_{10}]^+$.[59,563,636,637] The high stability of $[Al@Pb_{10}]^+$ from DFT calculations coincides well with the experimental observations using mass spectrometry (Figure 67) and photodissociation methods[59,633,634]. As we have already discussed in Section 6.2.1, the 42-electron closed-shell systems can be rationalized by the crystal-field splitting of the 1G shell in the spherical potential model, which leads to the occupation of molecular orbitals by 34 σ electrons $(1S^21P^61D^{10}1F^21F^81F^41G^2)$ and 8 π electrons $(2S^22P^22P^4)$ with spherical aromatic characters.[59,563] It is also interesting to point out that, another 42-electron system, the Zintl anion $[Pb_{10}]^{2-}$, has been experimentally synthesized in a Zintl compound.[639] Both the hollow $[Pb_{10}]^{2-}$ cage and the filled $M@Pb_{10}$ cages with 42 valence electrons conform to the Wade−Mingos rules for a *closo*-deltahedron with 10 vertices.

6.3.2. Endohedrally Doped Pb_{12} Cages.

Mass spectrometry and photodissociation experiments on metal doped Pb_n clusters usually show $M@Pb_{12}$ as highly stable species in different charge states (cationic, neutral, anionic).[59,483,622,630,631,633,634] Accordingly, several calculations have been performed on $[M@Pb_{12}]^{+/0}$ clusters,[120,132,621,636,637,640−644] and the resulting geometric and electronic properties are summarized in Table 14. Generally speaking, the most stable $[M@Pb_{12}]^{+/0}$ clusters are either perfect icosahedron or slightly distorted icosahedron due to the Jahn−Teller effect. For instance, neutral $Al@Pb_{12}$ and $In@Pb_{12}$ clusters have T_h point group symmetry instead of I_h. It is also worth mentioning that the specific values of binding and embedding energies in Tables 11−14 may vary substantially with the computational scheme, namely, the exchange-correlation functional and basis set.

Table 14 shows that the studied $[M@Pb_{12}]^{+/0}$ clusters with 50 valence electrons are closed-shell species with a sizeable HOMO−LUMO gap in the range of 2.06 eV to 3.13 eV. In order to understand the stability of the “50-electron species”, we present the energies, symmetries, and symmetry patterns of the molecular orbital of $[AlPb_{12}]^+$ in Figure 69. The high (I_h) symmetry of this cluster leads to the molecular orbitals that exhibit the character of spherical harmonics. As a consequence, 42 electrons $(1S^2{+}1P^6{+}1D^{10}{+}1F^{14}{+}1G^{10})$ from the first spherical set and 8 electrons $(2S^2{+}2P^6)$ from the second set constitute the total 50 valence electrons of $[AlPb_{12}]^+$.[59] Therefore, the shell closure with 50 electrons actually originates from the crystal-field splitting of the molecular orbitals with high angular momentum. Specifically, the splitting of $1G^{18}$ orbitals into $1G^{10}$ and $1G^8$ subsets leads to a large HOMO−LUMO gap

Table 13. Summary of the Theoretical Results on Endohedrally Doped M@Pb_{10} Cages: Distance between M Atom and Pb Atom (R), HOMO−LUMO Gap (E_{HL}), Binding Energy per Atom (E_b), Embedding Energy (E_{em}), and Vertical Ionization Potential (VIP)[a]

Cluster	Method	R (Å)	E_{HL} (eV)	E_b (eV)	E_{em} (eV)	VIP (eV)
Cu@Pb_{10} [563]	B3LYP/LanL2DZ	2.864, 3.093		2.43	3.56	5.93
Ag@Pb_{10} [563]	B3LYP/LanL2DZ	2.931, 3.117		2.33	2.47	5.84
Au@Pb_{10} [563]	B3LYP/LanL2DZ	2.948, 3.131		2.43	3.53	5.72
$[Cu@Pb_{10}]^-$ [563]	B3LYP/LanL2DZ	2.819, 3.314	2.58	2.61	5.53	2.97
$[Ag@Pb_{10}]^-$ [563]	B3LYP/LanL2DZ	2.892, 3.320	2.39	2.49	4.19	2.85
$[Au@Pb_{10}]^-$ [563]	B3LYP/LanL2DZ	2.908, 3.346	2.26	2.49	4.17	2.75
$[Cu@Pb_{10}]^+$ [564]	B3LYP/LanL2DZ	2.899, 2.914	1.80	2.36		
$[Ag@Pb_{10}]^+$ [564]	B3LYP/LanL2DZ	2.969, 2.984	1.70	2.25		
$[Au@Pb_{10}]^+$ [564]	B3LYP/LanL2DZ	2.985, 2.983	1.80	2.50		
$[Al@Pb_{10}]^+$ [637]	B3LYP/aug-cc-pVDZ(-PP)		2.74		4.94	
Al@Pb_{10} [637]	B3LYP/aug-cc-pVDZ(-PP)		1.55		4.03	5.09
C@Pb_{10} [636]	PBE/planewave	2.75	0.88	2.04		
Al@Pb_{10} [636]	PBE/planewave	2.97	0.18	1.90		
Mg@Pb_{10} [636]	PBE/planewave	2.90	1.79	1.77		
Fe@Pb_{10} [638]	PBE/DNP		0.76		4.31	
Co@Pb_{10} [638]	PBE/DNP		0.79		4.48	
Ni@Pb_{10} [638]	PBE/DNP		0.83		5.54	

[a] All the clusters adopt D_{4d} point group symmetry. For M−Pb bond lengths, the first R value is between M and Pb atoms of Pb_8 square antiprism while the second R value is between M and capped Pb atoms along the C_4 axis.

of 3.1 eV for $[AlPb_{12}]^+$. Moreover, by adding one extra electron to the closed-shell 50-electron systems, one can achieve a cluster with super alkali metal character. Note that the VIPs of neutral B@Pb_{12}, Al@Pb_{12}, Ga@Pb_{12}, In@Pb_{12}, and Tl@Pb_{12} clusters are 5.03, 4.36, 4.43, 4.45, and 4.81 eV, respectively,[644] all of which are smaller than those of alkali metal atoms (i.e., 5.39 eV for Li, 5.14 eV for Na).

Using relativistic DFT calculations at the PBE/DNP level, X. Chen *et al.*[642] have demonstrated tunable magnetic properties of the endohedral M@Pb_{12} clusters (M = Sc, Ti, V, Cr, Mn, Fe, Co, Ni). The calculated total magnetic spin moments of the whole cluster are 1 μ_B (Sc), 2 μ_B (Ti), 3 μ_B (V), 4 μ_B (Cr), 5 μ_B (Mn), 4 μ_B (Fe), 3 μ_B (Co), and 2 μ_B (Ni), respectively. Among them, Mn@Pb_{12} is of particular interest due to its highest magnetic moment (5 μ_B) and the largest HOMO−LUMO gap (1.25 eV), showing great potential as a building block of cluster-assembled magnetic materials. Note that Mn@Ge_{12} and Mn@Sn_{12} are also stable magnetic superatoms with the same value of magnetic spin moment (5 μ_B), as we have already discussed above.

T. Li *et al.*[120] further investigated the effect of spin-orbit coupling (SOC) on the symmetry and magnetism of M@Pb_{12} clusters (M = 3*d* and 4*d* elements). SOC was found to enhance the symmetry of some cluster geometries (e.g., Sc@Pb_{12}, Ni@Pb_{12}, and Pd@Pb_{12}), owing to the increasing number of delocalized electrons after inclusion of SOC. However, the SOC has only weak influence on the local spin magnetic moments of 3*d* atoms, but it remarkably reduces the spin moments of most 4*d* dopant atoms due to the strong coupling between M-4*d* and Pb-6*p* states. After considering SOC, substantial orbital magnetic moments are obtained, especially for Ti, V, Co, and Ru dopants with the magnitude of the orbital moments larger than 0.8 μ_B. The variation of the orbital moments for different transition metal dopants can be well explained by Hund's rule. Guennic and Autschbach[643] have investigated the contributions of SOC to NMR parameters in $[Pt@Pb_{12}]^{2-}$, which is entirely composed of heavy atoms and should be considered as a "strongly relativistic" system. The Pt−Pb spin−spin coupling constant was predicted to be negative, and its magnitude reasonably coincided with experiment. The NMR parameters are sensitive to the theoretical approximations, and the inclusion of SOC is crucial to achieve reliable results.

Recently, Joshi *et al.*[622] considered encapsulation of Lr^+, Lu^+, La^+, and Ac^+ cations into icosahedral Sn_{12} and Pb_{12} cages and demonstrated that the resulting $[M@Pb_{12}]^+$ and $[M@Sn_{12}]^+$ clusters (M = Lr, Lu, La, Ac) all belong to the stable 18-electron species with sizeable HOMO−LUMO gap (1.0−1.9 eV with PBE) and large binding energy. Using the ZORA approach, they further found that the SOC does not have significant effect on the structural and electronic properties of these endohedral cages, while the most visible impact is the reduction of the HOMO−LUMO gap by about 0.3 eV.

Using *ab initio* calculations at the B3LYP/TZVP level of theory, Dognon *et al.*[132,621] doped a Pu^{2+} ion into the icosahedral plumbaspherene $[Pb_{12}]^{2-}$ cage. The resulting neutral Pu@Pb_{12} cluster is actually the first example of the 32-electron rule with an appreciable HOMO−LUMO gap of 1.93 eV. Comparison of the molecular orbitals of Pu@Pb_{12} and $[Pb_{12}]^{2-}$ with the same I_h symmetry revealed participation of the central Pu atom orbitals in the a_g, g_u, h_g, t_{1u}, and t_{2u} valence molecular orbitals (see Figure 70a). Furthermore, the radial Pu−Pb bonding is clearly revealed by the electron localization function in Figure 70b, showing noticeable deformation of the density around each Pb atom in the direction of the central Pu atom. One can consider that the central Pu atom contributes its two 7*s* electrons to the skeletal bonding orbital of the $[Pb_{12}]^{2-}$ cage, fulfilling the requirement of the Wade−Mingos rules for a 12-vertex *closo*-deltahedron. The 5*f* orbitals of the central Pu atom occupied with six electrons strongly hybridize with the valence molecular orbitals of the $[Pb_{12}]^{2-}$ cage, achieving a 32-electron system. An isoelectronic counterpart, $[Am@Pb_{12}]^+$ cation, is also magic and possesses an even larger HOMO−LUMO gap of 2.45 eV.

6.4. Endohedral Zintl Clusters in Crystalline Phases

Apart from the gas-phase clusters discussed above, group 14 elements (except C and Si) are able to form ligand-free

Table 14. Summary of Theoretical Results on Endohedrally Doped M@Pb$_{12}$ Cages: M−Pb Distance (R), HOMO−LUMO Gap (E_{HL}), Binding Energy per Atom (E_b), Embedding Energy (E_{em}), and Vertical Ionization Potential (VIP)[a]

Cluster	Method	R (Å)	E_{HL} (eV)	E_b (eV)	E_{em} (eV)	VIP (eV)
$[B@Pb_{12}]^+$ [644]	B3LYP/aug-cc-pVDZ(-PP)	3.13	2.06		6.70	
$[Al@Pb_{12}]^+$[644]	B3LYP/aug-cc-pVDZ(-PP)	3.19	3.13		6.59	
$[Ga@Pb_{12}]^+$[644]	B3LYP/aug-cc-pVDZ(-PP)	3.19	2.69		6.03	
$[In@Pb_{12}]^+$ [644]	B3LYP/aug-cc-pVDZ(-PP)	3.24	3.04		5.54	
$[Tl@Pb_{12}]^+$ [644]	B3LYP/aug-cc-pVDZ(-PP)	3.25	2.59		4.74	
$[Al@Pb_{12}]^+$ [637]	B3LYP/aug-cc-pVDZ(-PP)		3.13		5.97	
$Al@Pb_{12}$ [637]	B3LYP/aug-cc-pVDZ(-PP)		1.06		4.26	4.32
$Pu@Pb_{12}$ [621]	B3LYP/TZVP	3.33	1.93	2.06		
$Yb@Pb_{12}$ [132]	PBE/TZ2P	3.28	0.80	1.54		
$[Am@Pb_{12}]^+$ [132]	PBE/TZ2P	3.35	2.45	3.01		
$C@Pb_{12}$ [641]	PBE/planewave	3.07	2.00	2.04	5.29	
$Mg@Pb_{12}$ [641]	PBE/planewave	3.16	2.30	1.89	3.33	
$Al@Pb_{12}$ [641]	PBE/planewave	3.00	0.37	1.93	3.77	
$In@Pb_{12}$ [636]	PBE/planewave	3.20	0.40	1.89	3.27	
$Sc@Pb_{12}$ [642]	PBE/DNP		0.24	2.68	5.97	
$Ti@Pb_{12}$ [642]	PBE/DNP		0.63	2.79	6.11	
$V@Pb_{12}$ [642]	PBE/DNP		0.53	2.82	5.86	
$Cr@Pb_{12}$ [642]	PBE/DNP		0.06	2.62	4.73	
$Mn@Pb_{12}$ [642]	PBE/DNP		1.25	2.68	5.43	
$Fe@Pb_{12}$ [642]	PBE/DNP		0.20	2.74	5.33	
$Co@Pb_{12}$ [642]	PBE/DNP		0.52	2.80	6.14	
$Ni@Pb_{12}$ [642]	PBE/DNP		0.31	2.81	5.77	
$[Lr@Pb_{12}]^+$ [622]	PBE/def-TZVP	3.30	1.81	2.86		0
$[Lu@Pb_{12}]^+$ [622]	PBE/def-TZVP	3.28	1.87	2.92		0
$[La@Pb_{12}]^+$ [622]	PBE/def-TZVP	3.38	1.26	2.41		0
$[Ac@Pb_{12}]^+$ [622]	PBE/def-TZVP	3.43	1.22	2.22		0

[a] All clusters adopt an icosahedral structure, either symmetric or possibly with Jahn−Teller distortion.

cage clusters enclosing one or a few transition metal atoms, which are discrete building units of the crystalline Zintl compounds.[81−87] As a representative, Figure 71 depicts the crystal structure of $K_{5-x}Co_{1-x}Sn_9$ (x = 0.21) ternary compound, which contains four crystallographically independent isolated $Co_{1-x}@Sn_9$ clusters per unit cell. The $[Co_{1-x}@Sn_9]^{(5-x)-}$ anions are well separated with a minimum vertex-to-vertex distance of 4.172 Å and surrounded by a large number of K^+ cations. To date, there have been more than 30 endohedral Zintl anions of group 14 elements synthesized in the laboratory, which are summarized in Table 15 with their cage geometries plotted in Figure 71. Generally speaking, all these endohedral Zintl clusters with one endohedral atom, given in Table 15, can be represented as $[M@E_n]^{q-}$ (M = transition metal; E = Ge, Sn, Pb; n = 9, 10, 12; q = 2, 3, 4, 5).

In Zintl compounds of group 14 elements, the smallest cages that can encapsulate a metal atom have 9 vertices, such as D_{3h} tricapped trigonal prism (Figure 74a) for $[Co@Ge_9]^{5-}$,[645] $[Ni@Ge_9]^{3-}$,[91] $[Co@Sn_9]^{5-}$,[92,93,645] $[Ni@Sn_9]^{4-}$,[93] $[Cu@Sn_9]^{3-}$,[94] and $[Cu@Pb_9]^{3-}$,[94] and C_{4v} capped square antiprism (Figure 74b) for $[Co@Sn_9]^{5-}$,[92,93,646] $[Ni@Sn_9]^{4-}$,[93,647,648] and $[Cu@Sn_9]^{3-}$.[649] As a representative, Figure 72 shows the molecular structure and NMR spectrum of $[Cu@Sn_9]^{3-}$ anion in $[K(2,2,2\text{-crypt})]_3[Cu@Sn_9](dmf)_2$ compound.[94] The observed resonance frequency of ^{63}Cu suggested that the Cu atom has the formal oxidation state +1; therefore, the $[Cu@Sn_9]^{3-}$ anion can be formulated as $Cu^+@[Sn_9]^{4-}$. The molecular orbital interaction diagram in Figure 72c further revealed that the main interactions between the endohedral Cu^+ ion and the $[Sn_9]^{4-}$ cage involve Cu-d, -s, and -p orbital contributions.

In the case of 10-vertex cages, there are three isomeric structures, that is, D_{5h} pentagonal prism structure (Figure 74c) for $[Fe@Ge_{10}]^{3-}$[541] and $[Co@Ge_{10}]^{3-}$,[542] D_{4d} bicapped square antiprism (Figure 74e) for $[Rh@Sn_{10}]^{3-}$[614] and $[Ni@Pb_{10}]^{2-}$,[650,651] and C_{2v} cage (Figure 74d, which can be viewed as an intermediate between the former two structures) for $[Fe@Sn_{10}]^{3-}$.[652] In addition, hollow cage $[Pb_{10}]^{2-}$ with bicapped square antiprism configuration was also reported in $[\{K(2.2.2\text{-crypt})\}_2Pb_{10}]$ compound,[639] suggesting that an endohedral metal atom (like in the case of $[Ni@Pb_{10}]^{2-}$) is not necessary for the formation of a stable Pb_{10} cage in crystalline environment.

Although icosahedral $[Sn_{12}]^{2-}$ and $[Pb_{12}]^{2-}$ clusters are remarkably stable, these polyanions have not been isolated in crystalline form yet.[84] For isolation, it requires endohedral doping. Most reported 12-vertex Zintl cages are based on icosahedron with different extents of distortion, including $[Co@Ge_{12}]^{3-}$ (D_{5d} with prominent elongation),[592] $[Rh@Sn_{12}]^{3-}$,[614] $[Ir@Sn_{12}]^{3-}$,[623] $[M@Pb_{12}]^{2-}$ (M = Ni, Pd, Pt),[651,653] $[Rh@Pb_{12}]^{3-}$,[654] $[Mn@Pb_{12}]^{3-}$ (D_{2h}),[655] and $[Au@Pb_{12}]^{3-}$ (D_{3d}).[656] Similar to those found for $Rh@Ge_{12}$ and $Pd@Ge_{12}$ clusters of gas phase,[448] $[Ru@Ge_{12}]^{3-}$ has a unique D_{2d} cage structure.[543] As shown in Figure 73a, the elemental composition of this Zintl cluster anion was confirmed by electrospray ionization mass spectrometry studies on DMF solutions of the crystalline $[K(2,2,2\text{-crypt})]_3[Ru@Ge_{12}]$-$(py)_4$.[543] Furthermore, EPR measurements (Figure 73b) confirm the paramagnetic character of the anion, and the endohedral Cu shows strong hyperfine coupling to 8 of the 12 Ge nuclei and much weaker coupling to the other four. The molecular orbital diagram of $[Ru@Ge_{12}]^{3-}$ is presented in

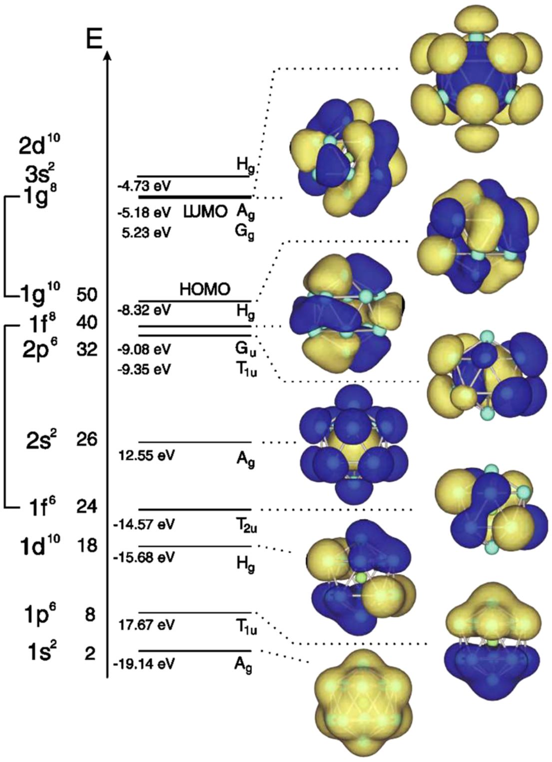

Figure 69. Energy level scheme and molecular orbitals (one for each set) for the $[AlPb_{12}]^+$ ground state (I_h) at the B3LYP/LanL2DZ level. Reproduced with permission from ref 59. Copyright 2004 American Physical Society. Note that in the main text we have used capital letters to denote the angular character for the molecular orbital to be consistent.

Figure 73c, revealing that singly occupied molecular orbital ($2a_2$) is localized entirely on the Ge_{12} cage.

Beyond the above spherical-like endohedral cages with single dopant atom, it is possible to encapsulate two metal atoms in a prolate Zintl cage with 16 to 18 vertex atoms. For example, two isomeric cages have been found to co-exist in a $[K(2,2,2\text{-crypt})]_4[Co_2@Ge_{16}](en)$ compound (1) α-$[Co_2@Ge_{16}]^{4-}$ with D_{2h} symmetry structure based on two pentagonal prisms sharing a square face (Figure 74h)[95,96] (2) β-$[Co_2@Ge_{16}]^{4-}$ with quasi-C_{2h}-symmetric endohedral cage based on two distorted *arachno* $Co@Ge_{10}$ units sharing a square face (Figure 74i).[96] A quasi-D_{3d}-symmetric 18-vertex deltahedral cage (Figure 74k) was obtained for both $[Pd_2@Ge_{18}]^{4-}$[540] and $[Pd_2@Sn_{18}]^{4-}$[97,98]. In between 16- and 18-vertex cages, $[Pt_2@Sn_{17}]^{4-}$ with a C_2 capsule-like structure (Figure 74j) was obtained.[657] This structure can be viewed as two $Pt@Sn_9$ subunits sharing a common Sn vertex. Very recently, a C_{3v} multi-cage structure (Figure 74l) has been obtained for $[Rh_3@Sn_{24}]^{5-}$,[614] which is composed of three fused $Rh@Sn_{10}$ units arranged in three-fold symmetry.

The geometric structures and numbers of valence electrons for most of the aforementioned endohedral Zintl clusters can be explained by the Wade–Mingos rules, as presented in Table 16, from which we can summarize several general regulations. For those *closo*- or *nido*-deltahedra with 9, 10, and 12 vertices, the late transition metal atom (Co, Ni, Cu, Rh, Pd, Pt) encapsulated in a cage tends to form closed d^{10} shell configuration (leaving an empty s^0 valence shell), except for Au which attains $5d^{10}6s^2$ closed-shell configuration. For 3-connect polyhedral cage with 10 or 12 vertices, the $5n_v$ electrons required by Wades–Mingos rules can be roughly satisfied if all *s* and *d* valence electrons of the endohedral transition metal atom are taken into account for the electron count, for example, $[Fe@Ge_{10}]^{3-}$ with 51 electrons (one electron excess), $[Co@Ge_{10}]^{3-}$ with 52 electrons (two electrons excess), and $[Ru@Ge_{12}]^{3-}$ with 59 electrons (one electron deficiency). In the case of Zintl anions encapsulating dual transition metal atoms, Wade–Mingos rules are still applicable, but they require more careful analysis. For instance, the 18-vertex deltahedral cage of $[Pd_2@Ge_{18}]^{4-}$ or $[Pd_2@Sn_{18}]^{4-}$ has two radial bonding orbitals pointing at the two Pd atoms, thus requiring $4n_v + 4$ electrons instead of $4n_v + 2$ ($n = 18$).[540] As for α-$[Co_2@Ge_{16}]^{4-}$ anion, there are 8 Ge–Ge bonding orbitals simultaneously contributing to skeletal bonding of the Ge_{16} cage and the 4*s*, 4*p*, 3*d* manifold of the Co atoms; thereby, both the 80-electron count for the 3-connect cage with the 16 vertex and the 18-electron count at each metal atom are satisfied.[95]

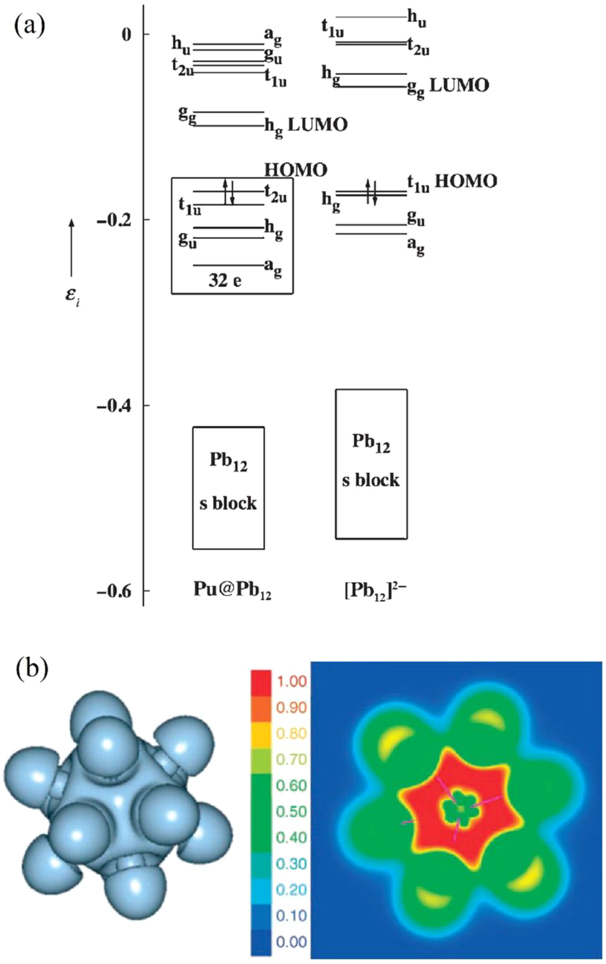

Figure 70. (a) Orbital energies (in unit of Hartree) of $Pu@Pb_{12}$ and $[Pb_{12}]^{2-}$. The latter have been shifted to make the HOMOs equal. (b) Isosurface (left) and cross section (right) of electron localization function for $Pu@Pb_{12}$. Reproduced with permission from ref 132. Copyright 2007 Wiley-VCH Verlag GmbH & Co. KGaA, Weinheim.

According to the "pseudo-atom" concept developed by Klemm,[88] the negatively charged atom would behave structurally similar to the corresponding isoelectronic neutral element of a group on its right. Hence, the highly charged Zintl clusters observed in crystalline compounds can be correlated with the isoelectronic gas-phase clusters in neutral or singly charged state. As for the 10-vertex cages with bicapped square antiprism

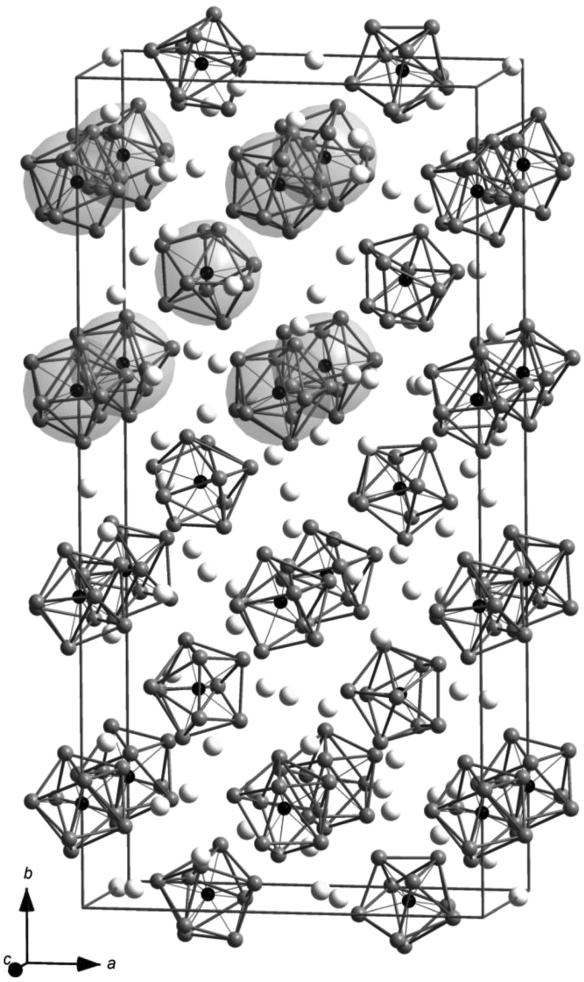

Figure 71. Structure of $K_{5-x}Co_{1-x}Sn_9$ containing the $Co_{1-x}@Sn_9$ clusters (gray spheres) in a BCC-analogous packing. K, Co, and Sn atoms are drawn in white, black, and gray spheres, respectively. Reproduced with permission from ref 92. Copyright 2012 Wiley-VCH Verlag GmbH&Co. KGaA, Weinheim.

(Figure 74e, D_{4d}) and 42 valence electrons (if we do not count the filled d^{10} shell of transition metal atom), $[Rh@Sn_{10}]^{3-}$[614] is isoelectronic to $[Cu@Sn_{10}]^-$, $[Ag@Sn_{10}]^-$, $[Au@Sn_{10}]^-$, $Be@Sn_{10}$, and $Zn@Sn_{10}$ discussed in Section 6.2.1, and $[Ni@Pb_{10}]^{2-}$[650,651] is isoelectronic to $[Cu@Pb_{10}]^-$, $[Ag@Pb_{10}]^-$, $[Au@Pb_{10}]^-$, $Mg@Pb_{10}$, and $[Al@Pb_{10}]^+$ discussed in Section 6.3.1. In the case of 12-vertex icosahedra with 50 valence electrons, $[Rh@Sn_{12}]^{3-}$[614] and $[Ir@Sn_{12}]^{3-}$[623] are isoelectronic to $Be@Sn_{12}$, $Mg@Sn_{12}$, $Ca@Sn_{12}$, $Zn@Sn_{12}$, $Cd@Sn_{12}$, and $Hg@Sn_{12}$ discussed in Section 6.2.2, while $[M@Pb_{12}]^{2-}$ (M = Ni, Pd, Pt)[651,653] and $[Rh@Pb_{12}]^{3-}$[654] are isoelectronic to $[B@Pb_{12}]^+$, $[Al@Pb_{12}]^+$, $[Ga@Pb_{12}]^+$, $[In@Pb_{12}]^+$, $[Tl@Pb_{12}]^+$, and $Mg@Pb_{12}$ discussed in Section 6.3.2.

However, the extra multiple charge on the cluster may result in distinct geometric difference between a Zintl anion cluster and its isoelectronic counterpart in gas phase. For example, endohedral clusters $[Fe@Ge_{10}]^{3-}$ and $[Co@Ge_{10}]^{3-}$ in the Zintl phase compounds prefer pentagonal prism structure[541,542], while their isoelectronic counterparts $Cu@Ge_{10}$ and $Zn@Ge_{10}$ in gas phase adopt D_{4d} bicapped tetragonal antiprism. DFT calculations at the B3LYP/cc-pVTZ(-NR) level on the D_{5h} symmetric $[Co@Ge_{10}]^{3-}$ cluster predicted a HOMO−LUMO gap of 2.27 eV and a natural charge of −1.05 electrons on the central Co atom, suggesting a d^{10} configuration.[542] In contrast, bicapped tetragonal antiprism isomer for $[Co@Ge_{10}]^{3-}$ is a stationary state with imaginary frequencies.

McGrady and co-workers[448,449,456,543,652,655] developed a model of bonding based on valence-electron count to rationalize the structure and bonding in endohedral caged clusters of group 14 elements with 10-, 12-, and 14-vertices and a transition metal dopant, aiming to bridge the neutral gas-phase clusters of silicon and Zintl anions of the heavier tetrels. More details can be found in their recent review.[658]

To summarize this section, endohedral doping of Ge, Sn, and Pb clusters has also attracted much interest, and plenty of experimental and theoretical studies have been done following the developments on doped silicon clusters. As reported in the first paper on these systems by Kumar and Kawazoe,[53] the small difference in the atomic size of these atoms leads to different behavior compared with silicon. Among these, the 16 Ge atom FK polyhedron such as $Zr@Ge_{16}$ stands out similar to FK $Ti@Si_{16}$ while $Th@Ge_{16}$ forms a fullerene-like structure similar to $Zr@Si_{16}$, all with 68 valence electrons. But interestingly, a 16-atom cage of Pb is not so favorable. Other interesting cases are FK $Ru@Ge_{15}$ cage with 68 valence electrons and doping of divalent atom in Ge_{14} making it a 58-valence electron cluster, all belonging to magic number in a spherical potential model. These results amply demonstrate the power and possibilities of endohedral doping. Unlike for Si, a 10-atom polyhedral cluster as well as the highest symmetry 12-atom icosahedron is favored by all the three elements, i.e., Ge, Sn, and Pb, and even a magnetic superatom was predicted for the first time by doping of Mn in Ge_{12} and Sn_{12}.[67] Most importantly, assemblies of some of them in the crystalline form such as the Zintl phases already exist. Therefore, these systems are excellent candidates of cluster assembled materials and provide a nice opportunity to study the properties of the cluster assemblies. Furthermore, clusters of Pb, a heavy element, and their doping with rare earth atoms can provide interesting possibilities for magnetic materials. It is also hoped that some of the developments on crystalline structures may be carried over to other cases. Lastly, some clusters doped with more than one metal atom are already known in these cases and they can be helpful to extend the scope of endohedrally doped cage clusters of group 14.

7. ENDOHEDRALLY DOPED CAGES OF GROUP 11 ELEMENTS

7.1. Doped Au Cages

Owing to the unusual catalytic behavior of Au nanoclusters,[659] tremendous attention has been paid to study their atomic and electronic structure during the past 30 years. The relativistic effects[660,661] in Au_n clusters lead to some surprising atomic structures that are distinct from the other coinage metal clusters like Cu_n and Ag_n. For example, the most stable geometries of anionic $[Au_n]^-$ clusters remain planar up to $n = 12$[64,65,662], and a tetrahedral pyramid structure with T_d symmetry was discovered for Au_{20}.[663] Impressively, hollow cages have been reported for $[Au_{16}]^-$, $[Au_{17}]^-$, and $[Au_{18}]^-$ from a combined study of photoelectron spectroscopy and *ab initio* search of global minimum structures[664] as well as trapped ion electron diffraction experiment.[665] A larger Au_{32} cluster was also theoretically predicted to adopt a rhombic triacontahedron with I_h symmetry (named as "golden fullerene") as its ground state configuration at zero temperature.[666,667] Intuitively, the

Table 15. Interatomic Distances and Structures (Struc.) as in Figure 74 of the Reported Endohedral Cluster Anions in Zintl Compounds ([a])

Cluster	Compound	M−E (Å)	E−E (Å)	Struc.	Ref.
$[Co@Ge_9]^{5-}$	$K_5Co_{1.2}Ge_9$	2.331−2.374	2.683−2.811	(a)	645
$[Ni@Ge_9]^{3-}$	$[K(2,2,2\text{-crypt})]_3\{[Ni@(Ge_9Ni\text{-en})]_{0.735}([Ni@Ge_9]\cdot en)_{0.265}\}(en)$			(a)	91
$[Fe@Ge_{10}]^{3-}$	$[K(2,2,2\text{-crypt})]_3[Fe@Ge_{10}](en)_2$	2.509−2.535	2.526−2.622	(c)	541
$[Co@Ge_{10}]^{3-}$	$[K(2,2,2\text{-crypt})]_4[Co@Ge_{10}][Co(C_8H_{12})_2](tol)$	2.479−2.523	2.502−2.622	(c)	542
$[Ru@Ge_{12}]^{3-}$	$[K(2,2,2\text{-crypt})]_3[Ru@Ge_{12}](py)_4$	2.651−2.771	2.442−2.601	(g)	543
$[Co@Ge_{12}]^{3-}$	$[K(2,2,2\text{-crypt})]_3[CoGe_{12}]_{0.76}[CoGe_{10}]_{0.24}(en)$	2.479−2.781	2.569−3.022	(f)	592
$\alpha\text{-}[Co_2@Ge_{16}]^{4-}$	$[K(2,2,2\text{-crypt})]_4[Co_2@Ge_{16}](en)^b$	2.519−2.627	2.445−2.592	(h)	96
$\beta\text{-}[Co_2@Ge_{16}]^{4-}$	$[K(2,2,2\text{-crypt})]_4[Co_2@Ge_{16}](en)^b$	2.480−2.654	2.556−3.210	(i)	96
$[Pd_2@Ge_{18}]^{4-}$	$[K(2,2,2\text{-crypt})]_4[Pd_2@Ge_{18}](tol)_2$	2.605−2.646	2.657−2.965	(k)	540
$[Co@Sn_9]^{5-}$	$K_4Ru_3Sn_7$	2.641−2.700	3.051−3.141	(a)	645
$[Co@Sn_9]^{5-}$	$K_{12.92}Co_{0.95}Sn_{17}$	2.563−2.670	2.943−3.743	(a)	93
$[Co@Sn_9]^{5-}$	$K_{12.92}Co_{0.95}Sn_{17}$	2.581−2.680	2.943−3.743	(b)	93
$[Co@Sn_9]^{5-}$	$K_{13}CoSn_{16.9}$	2.583−2.680	2.963−3.079	(b)	646
$[Co@Sn_9]^{5-}$	$K_{4.79}Co_{0.79}Sn_9$	2.518−2.702	2.957−3.750	(b)	92
$[Ni@Sn_9]^{4-}$	$K_{12.92}Co_{0.95}Sn_{17}$	2.563−2.755	2.943−3.743	(a)	93
$[Ni@Sn_9]^{4-}$	$K_{12.92}Co_{0.95}Sn_{17}$	2.563−2.755	2.943−3.743	(b)	93
$[Ni@Sn_9]^{4-}$	$[K(2,2,2\text{-crypt})]_6[Ni@Sn_9]_2(en)_3(tol)$	2.562−2.743	2.915−3.451	(a)	647
$[Ni@Sn_9]^{4-}$	$K[K(18\text{-crown-}6)]_3[Ni@Sn_9](benzene)_3$	2.521−2.738	2.953−3.436	(a)	648
$[Cu@Sn_9]^{3-}$	$[K(2,2,2\text{-crypt})]_3[Cu@Sn_9](dmf)_2$	2.611−2.700	3.052−3.097	(a)	94
$[Cu@Sn_9]^{3-}$	$[K([18]crown\text{-}6)]_2[K([18]crown\text{-}6)(MesH)(NH_3)][Cu@Sn_9](thf)$	2.599−2.697	3.021−3.143	(b)	649
$[Fe@Sn_{10}]^{3-}$	$[K(2,2,2\text{-crypt})]_3[Fe@Sn_{10}](py)_4$	2.578−2.808	2.703−3.282	(d)	652
$[Rh@Sn_{10}]^{3-}$	$[K(2,2,2\text{-crypt})]_3[Rh@Sn_{10}](en)_2$	2.670−2.887	2.712−3.342	(e)	614
$[Rh@Sn_{12}]^{3-}$	$[K(2,2,2\text{-crypt})]_3[Rh@Sn_{12}](tol)_2$	2.878−2.950	3.041−3.129	(f)	614
$[Ir@Sn_{12}]^{3-}$	$[K(2,2,2\text{-crypt})]_3[Ir@Sn_{12}](tol)$	2.883−2.941	3.025−3.100	(f)	623
$[Pt_2@Sn_{17}]^{4-}$	$[K(2,2,2\text{-crypt})]_3[Pt_2@Sn_{17}](en)_3$	2.672−2.815	2.958−3.460	(j)	657
$[Pd_2@Sn_{18}]^{4-}$	$[K(2,2,2\text{-crypt})]_4[Pd_2@Sn_{18}](en)_3$	2.857−2.917	3.012−3.145	(k)	97
$[Pd_2@Sn_{18}]^{4-}$	$[K(2,2,2\text{-crypt})]_4[Pd_2@Sn_{18}](en)_3$	2.849−2.883	3.003−3.393	(k)	98
$[Rh_3@Sn_{24}]^{5-}$	$[K(2,2,2\text{-crypt})]_5[Rh_3@Sn_{24}](dmf)_2(tol)$	2.657−3.059	2.967−3.190	(l)	614
$[Cu@Pb_9]^{3-}$	$[K(2,2,2\text{-crypt})]_3[Cu@Pb_9](dmf)_2$	2.710−2.802	3.163−3.224	(a)	94
$[Ni@Pb_{10}]^{2-}$	$[K(2,2,2\text{-crypt})]_2[Ni@Pb_{10}]$	2.722, 3.210	3.094−3.405	(e)	650
$[Ni@Pb_{10}]^{2-}$	$[K(2,2,2\text{-crypt})]_2[Ni@Pb_{10}]$	2.716−3.210	3.103−3.445	(e)	651
$[Ni@Pb_{12}]^{2-}$	$[K(2,2,2\text{-crypt})]_2[Ni@Pb_{12}](en)$	2.889−3.113	2.864−3.292	(f)	651
$[Pd@Pb_{12}]^{2-}$	$[K(2,2,2\text{-crypt})]_2[Pd@Pb_{12}](en)$	2.921−3.145	3.109−3.269	(f)	651
$[Pt@Pb_{12}]^{2-}$	$[K(2,2,2\text{-crypt})]_2[Pt@Pb_{12}]$	3.055−3.061	3.188−3.244	(f)	651
$[Pt@Pb_{12}]^{2-}$	$[K(2,2,2\text{-crypt})]_2[Pt@Pb_{12}]$	3.205−3.223	3.058	(f)	653
$[Mn@Pb_{12}]^{3-}$	$[K(2,2,2\text{-crypt})]_3[Mn@Pb_{12}](en)_{1.5}$	2.869−3.308	3.078−3.426	(f)	655
$[Rh@Pb_{12}]^{3-}$	$[K([18]crown\text{-}6)]_3[Rh@Pb_{12}](en)_2$	2.984−3.028	3.133−3.199	(f)	654
$[Au@Pb_{12}]^{3-}$	$[K(2,2,2\text{-crypt})]_3[Au@Pb_{12}](py)_2$	2.840−3.093	3.108−3.257	(f)	656

[a] M = transition metal; E = Ge, Sn, Pb; 2,2,2-crypt = 4,7,13,16,21,24-hexaoxa-1,10-diazabicyclo[8.8.8]hexacosane; en = ethylenediamine; py = pyridine; tol = toluene; dmf = dimethylformamide; 18-Crown-6 = 1,4,7,10,13,16-hexaoxacyclooctadecane; MesH = mesitylene; thf = tetrahydrofuran. [b] In this compound, $\alpha\text{-}[Co_2@Ge_{16}]^{4-}$ and $\beta\text{-}[Co_2@Ge_{16}]^{4-}$ clusters coexist with 10% occupancy and 90% occupancy, respectively.

existence of Au_n cage clusters implies a rich class of novel endohedral golden cages, as we will discuss below. Figure 75 shows the atomic structures of typical endohedral $M@Au_n$ cage clusters that have been investigated in the literature. To present an overview of the endohedral $M@Au_n$ cage clusters, Table S20 summarizes their geometric parameters and key electronic properties from our own DFT calculations at the PBE0/SDD level of theory. One can see that these $M@Au_n$ clusters possess high thermodynamic stability as manifested by the appreciable embedding energies in the range of 4.233 eV to 14.283 eV, and large HOMO−LUMO gaps of 2.201 eV to 3.397 eV, except for the magnetic $Mn@Au_{12}$ having a gap of 1.705 eV.

7.1.1. Endohedrally Doped Au_{12} Cages.

Analogous to the I_h $[Au_{13}]^{5+}$ cage discussed by Mingos[668] using the extended Hückel theory, Pyykkö and Runeberg[61] predicted theoretically an icosahedral $W@Au_{12}$ cluster (or its isoelectronic anion $[Ta@Au_{12}]^-$ and cation $[Re@Au_{12}]^+$), as shown in Figure 75a, which is stabilized by aurophilic attraction and relativistic effects. The 12 6*s* valence electrons from the Au_{12} icosahedron together with the six valence electrons from the central W atom fill the hybridized 1S, 1P, and 1D molecular orbitals in perfect accordance with the 18-electron rule. As a consequence of the electronic shell closure, B3LYP/LANL1DZ calculations demonstrated high stability of this $W@Au_{12}$ cluster, as all vibrational frequencies were real positive in the range of 30−190 cm^{-1} and the HOMO−-LUMO gap was 3.0 eV. Later, Sato *et al.*[669] presented a picture of the bonding and orbital interactions in $W@Au_{12}$. As shown in Figure 76, the frontier 6*s* orbitals of the 12 Au atoms span the irreducible representations of the I_h point group: $a_g + t_{1u} + h_g + t_{2u}$. The resulting orbitals of the Au_{12} cage are ordered in shells in accordance with their spherical parentage as $a_{1g}(s) < t_{1u}(p) < h_g(d) \ll t_{2u}(f)$. Owing to the hybridization between the $h_g(d)$ molecular orbital on Au and the 5*d* orbitals on W, the h_g HOMO of the neutral $W@Au_{12}$ cluster is fully occupied by ten electrons with dominant Au-6*s* character, whereas the $h_g{}^*$ LUMO is mainly of W-5*d* character.

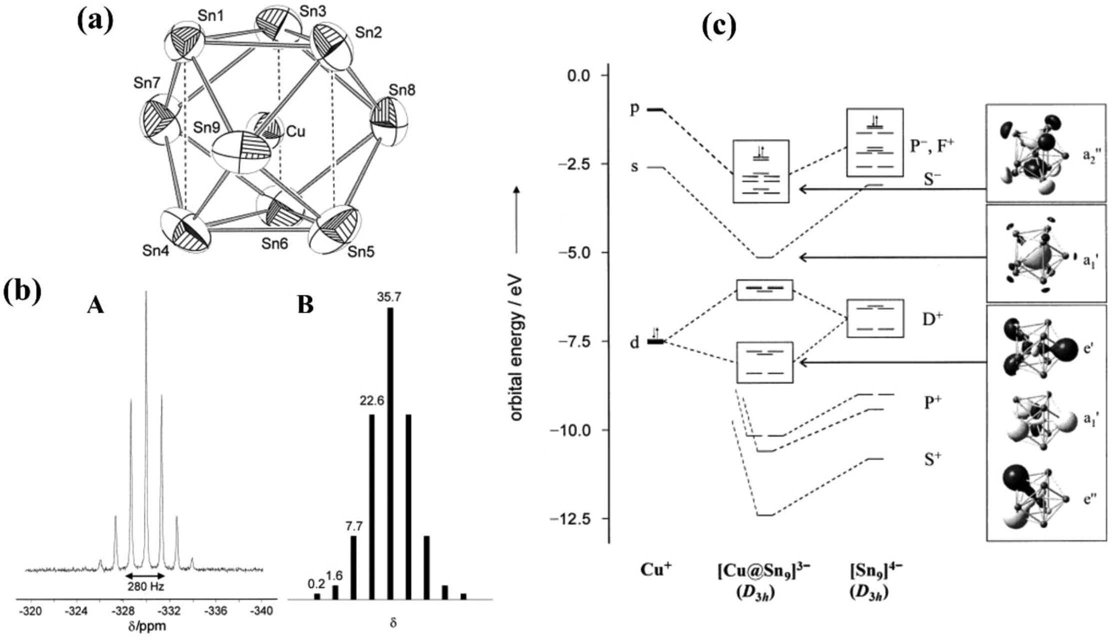

Figure 72. (a) Structure of the $[Cu@Sn_9]^{3-}$ anion. (b) ^{63}Cu NMR spectrum of $[K(2,2,2\text{-crypt})]_3[Cu@Sn_9](dmf)_2$: A is the measured spectrum in acetonitrile at room temperature, and B is the simulated spectrum for $[Cu@^{117/119}Sn_xSn_{(9-x)}]^{3-}$ (with x = 0, 1, ..., 4). (c) Molecular orbital interaction diagram of $[Cu@Sn_9]^{3-}$ in fragments of Cu^+ and D_{3h}-$[Sn_9]^{4-}$ calculated at the B3LYP level using the aug-cc-pVTZ-PP basis set. Important contributions are indicated by dashed lines, and relevant molecular orbitals of $[Cu@Sn_9]^{3-}$ are shown on the right. Reproduced with permission from ref 94. Copyright 2008 Wiley-VCH Verlag GmbH&Co. KGaA, Weinheim.

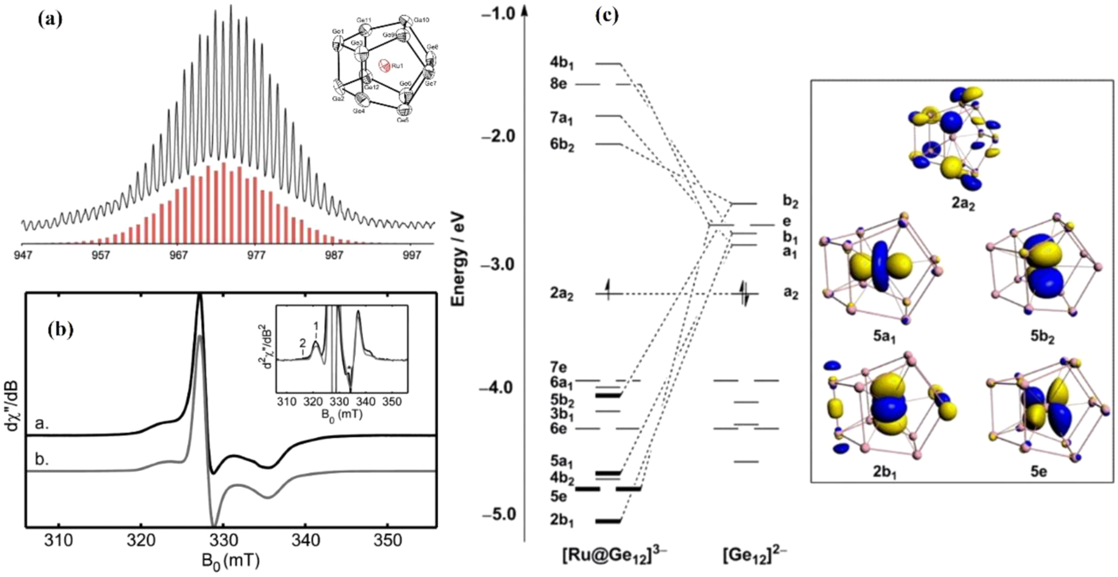

Figure 73. (a) Negative ion-mode electrospray mass-envelope corresponding to $[Ru@Ge_{12}]^{3-}$. Recorded experimental data are given in black with the calculated isotopic distribution in red. Inset is the fullerene-like molecular structure (Figure 54(h)) of this anionic cluster. (b) Experimental (a, black) and simulated (b, gray) EPR spectra for $[Ru@Ge_{12}]^{3-}$. (c) Frontier Kohn−Sham orbitals for D_{2d}-symmetric $[Ru@Ge_{12}]^{3-}$ computed at BP86/TZ2P level. Orbitals with dominant Ru contribution are shown in bold. Reproduced with permission from ref 543. Copyright 2013 American Chemical Society.

Soon after the theoretical prediction, L. S. Wang's group[62] produced the anionic $[W@Au_{12}]^-$ cluster and its 4*d* analog $[Mo@Au_{12}]^-$ in gas phase. The measured photoelectron spectra, as shown in Figure 77, exhibit similar features. The HOMO−LUMO gaps of the neutral clusters deduced from the spectra are 1.68 eV for $W@Au_{12}$ and 1.48 eV for $Mo@Au_{12}$, respectively, in qualitative agreement with the large gap predicted by Pyykkö and Runeberg. DFT calculations by L. S. Wang and coworkers on $Mo@Au_{12}$ and $W@Au_{12}$ clusters showed the icosahedral (I_h) configuration to be the ground state. For $Mo@Au_{12}$ ($W@Au_{12}$), it is more stable than the isomers with O_h (Figure 75b) and D_{5h} (Figure 75c) symmetry by 9.8 (0.3) kJ/mol and 20.4 (18.4) kJ/mol, respectively. Furthermore, the simulated spectra for the I_h isomers are in excellent agreement with the experimental results (see Figure 77), confirming that the observed species were indeed the endohedrally doped Au_{12} icosahedron for both $[W@Au_{12}]^-$ and $[Mo@Au_{12}]^-$. Later, using combined anion photoelectron

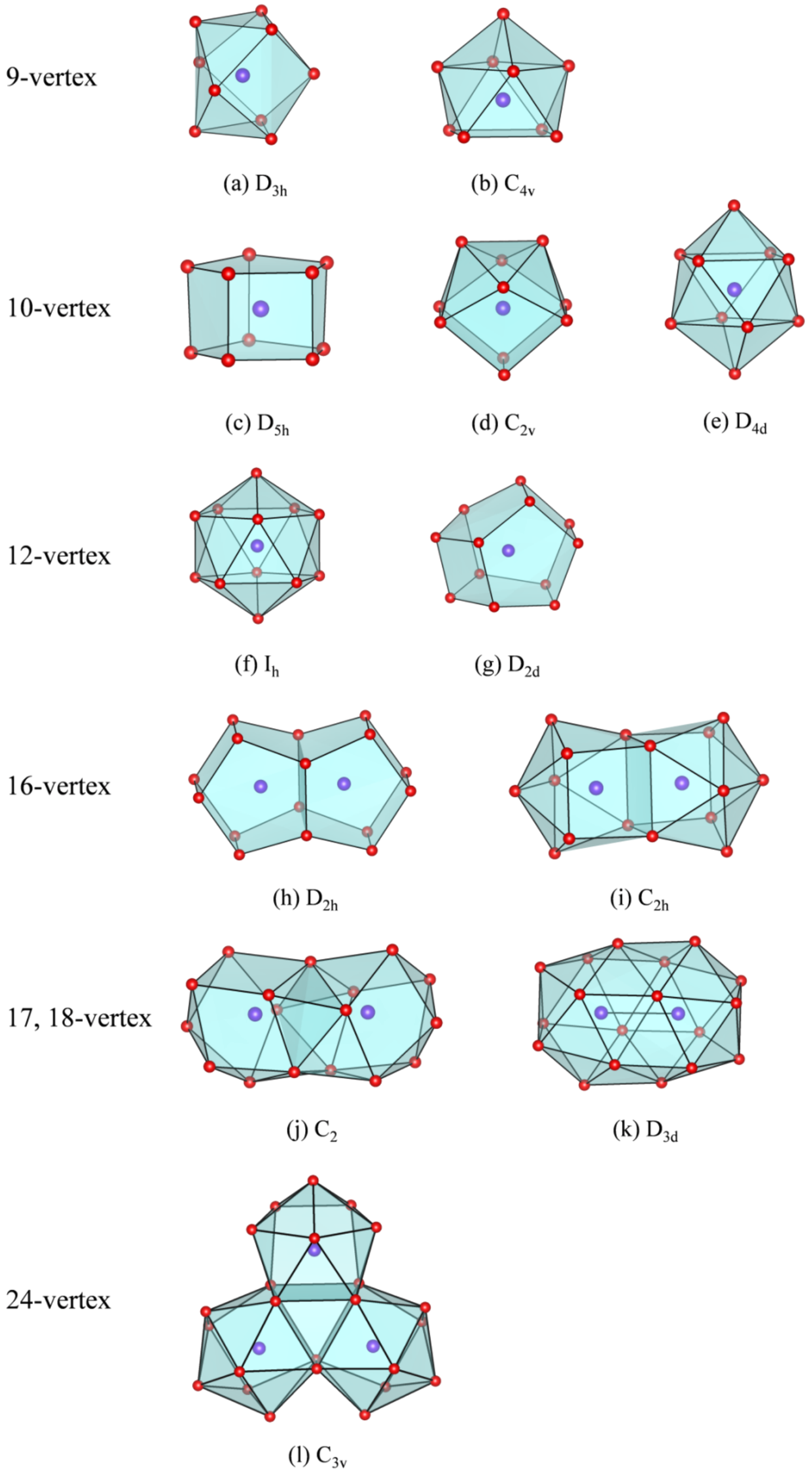

(a) D_{3h} (b) C_{4v}

(c) D_{5h} (d) C_{2v} (e) D_{4d}

(f) I_h (g) D_{2d}

(h) D_{2h} (i) C_{2h}

(j) C_2 (k) D_{3d}

(l) C_{3v}

Figure 74. Schematic structures of the reported endohedral Zintl cages of group 14 elements. For each cage, the highest symmetry without distortion is given, while the actual cage symmetry in Zintl compounds could be reduced.

spectroscopy and DFT calculations, L. S. Wang's group[670] reported the observation and characterization of icosahedral gold cage clusters encapsulating a central atom from group 5 transition metals: $[M@Au_{12}]^-$ (M = V, Nb, Ta). These 18-valence-electron anionic clusters are isoelectronic to the neutral $W@Au_{12}$ species and have closed electronic shells. The measured ADE and VDE values are high, i.e., 3.70 and 3.79 eV for $[V@Au_{12}]^-$, 3.77 and 3.88 eV for $[Nb@Au_{12}]^-$, and 3.76 and 3.90 eV for $[Ta@Au_{12}]^-$, respectively. Again, the endohedral icosahedral (I_h) configuration was confirmed as the ground state for these anionic clusters from

Table 16. Summary of Reported $[M@E_n]^{q-}$ Zintl Clusters (E = Ge, Sn, Pb) Obeying the Wade−Mingos Rules[a]

n	Skeleton geometry	TVE	Zintl cluster
9	capped square antiprism (*nido*-deltahedron)	4 × 9 + 4 = 40	$[Co@Sn_9]^{5-}$ [92-93,646], $[Ni@Sn_9]^{4-}$ [93], $[Cu@Sn_9]^{3-}$ [649]
10	bicapped square antiprism (*closo*-deltahedron)	4 × 10 + 2 = 42	$[Rh@Sn_{10}]^{3-}$ [614], $[Ni@Pb_{10}]^{2-}$ [650-651]
10	pentagonal prism structure (3-connect polyhedron)	5 × 10 = 50	$[Fe@Ge_{10}]^{3-}$ [541], $[Co@Ge_{10}]^{3-}$ [542]
12	icosahedron (*closo*-deltahedron)	4 × 12 + 2 = 50	$[Co@Ge_{12}]^{3-}$ [592], $[Rh@Sn_{12}]^{3-}$ [614], $[Ir@Sn_{12}]^{3-}$ [623], $[Ni@Pb_{12}]^{2-}$ [650-651], $[Pd@Pb_{12}]^{2-}$ [651], $[Pt@Pb_{12}]^{2-}$ [651-653], $[Rh@Pb_{12}]^{3-}$ [654], $[Au@Pb_{12}]^{3-}$ [656]
12	D_{2h} cage (3-connect polyhedron)	5 × 12 = 60	$[Ru@Ge_{12}]^{3-}$ [543]
16	D_{2h} prolate cage (3-connect polyhedron)	5 × 16 = 80	$[Co_2@Ge_{16}]^{4-}$ [95-96]
18	D_{3d} prolate cage (*closo*-deltahedron)	4 × 18 + 4 = 76	$[Pd_2@Ge_{18}]^{4-}$ [540], $[Pd_2@Sn_{18}]^{4-}$ [97-98]

[a] Here *n* is the number of E atoms, skeleton geometry is only for E atoms (polyhedral type is given in the parentheses), TVE gives the total number of valence electrons calculated by the Wade−Mingos rules.

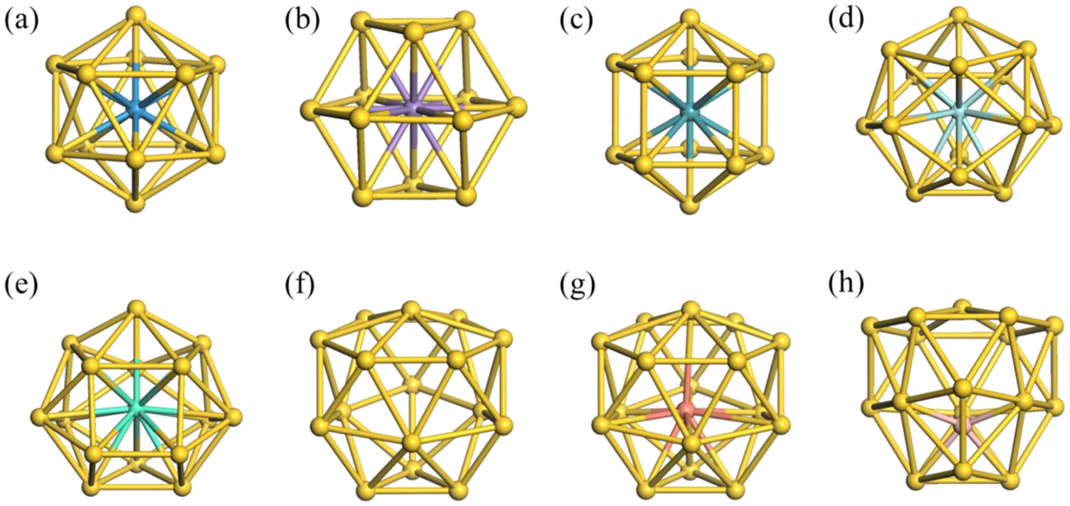

Figure 75. Atomic structures of (a) $W@Au_{12}$ (I_h symmetry) (also for $Mo@Au_{12}$, $[V@Au_{12}]^-$, $[Nb@Au_{12}]^-$, $[Ta@Al_{12}]^-$, and $[Au@Au_{12}]^{5+}$), (b) $Mn@Au_{12}$ (O_h symmetry), (c) $M@Au_{12}$ (D_{5h} symmetry), (d) $Zr@Au_{14}$ (D_{2d} symmetry) (also for $Ti@Au_{14}$ and $Hf@Au_{14}$), (e) $Gd@Au_{15}$ (C_s symmetry), (f) $[Au_{16}]^{2-}$ (T_d symmetry), (g) $[Cu@Au_{16}]^-$ (C_s symmetry) (also for $[Sc@Au_{16}]^+$, $[Y@Au_{16}]^+$, and $Eu@Au_{16}$) clusters, and (h) $[B@Au_{16}]^-$ (C_{3v} symmetry) obtained from PBE0/SDD calculations.

DFT calculations by considering O_h and D_{5h} isomers as well as by comparing the simulated photoelectron spectra of the I_h isomers with the measured ones.

After the discovery of the $W@Au_{12}$ cage and its isoelectronic analogs, numerous theoretical efforts have been made to investigate their bonding characteristics and electronic properties, as well as to explore other possible $M@Au_{12}$ cage clusters.[121,671−690] Following the pioneering theoretical prediction, Autschbach *et al.* have performed a series of DFT calculations on the physical properties and thermal behavior of $W@Au_{12}$ with the BP86 and B3LYP functional as well as high-level MP2 and coupled-cluster calculations. They obtained the vibrational spectra, NMR chemical shifts, spin−spin coupling constants and quadrupole coupling constants as well as optical spectra at the level of single and double excitations of the neutral $W@Au_{12}$ cluster with the icosahedral configuration.[671] Further, the finite-temperature behaviors of $W@Au_{12}$ at selected temperatures of 224, 366, 512, 602, and 857 K have been simulated using AIMD.[672] Between 366 and 512 K, a surface melting behavior was observed, that is, Au atoms diffuse on the "surface shell" of the cluster, while they are strongly attracted by the central W atom similar to the behavior found for the doping of Ti in Si_{16}.[396] Interestingly, the thermally averaged electronic DOS of $W@Au_{12}$ at finite temperature was in good agreement with the experimental PES of $[W@Au_{12}]^-$. Furthermore, it was predicted that $W@Au_{12}$ can be fully coated by 12 carbonyl groups with favorable binding energy of 1.02 eV per carbonyl, as computed at the TPSSh/def2-QZVPP level of theory.[673] The resulting carbonyl compound $W@Au_{12}(CO)_{12}$ retains I_h symmetry and possesses a HOMO−LUMO gap of 2.68 eV, slightly larger than that of bare $W@Au_{12}$ cluster (2.55 eV).

Endohedral $M@Au_{12}$ cage clusters with M = 3*d*, 4*d*, and 5*d* elements have been theoretically explored by many groups[121,674−679,688,689]. Using PW91 functional and DNP basis set, S. Y. Wang *et al.*[674] investigated the energetics and magnetic moment of a single 3*d* (Sc−Ni) or 4*d* (Y−Pd) impurity enclosed in an icosahedral Au_{12} cage. Strong coupling between the *d* orbitals of the M atom (3*d* or 4*d* element) and the 6*s* orbitals of Au atoms leads to relatively large embedding energies compared with the doping of Au atom in Au_{12} icosahedral cage, from E_{em} = 2.186 eV for Pd to E_{em} = 7.791 eV for Zr. Meanwhile, large local spin moments ranging from 0.758 μ_B to 3.512 μ_B were found for some 3*d* or 4*d* atoms, including Cr, Mn, Fe, Co, Ni, Tc, Ru, and Rh. Later, relativistic

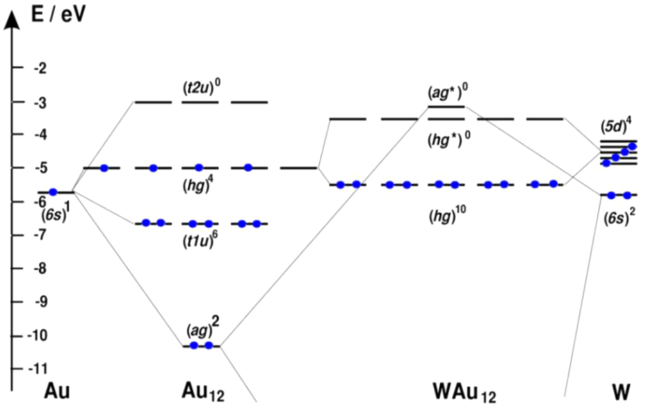

Figure 76. Orbital interactions in the neutral W@Au$_{12}$ cluster within the relativistic ZORA. The 1S type bonding orbital $(a_g)^2$ lies deeper (not seen in the figure), while the 1P type $(t_{1u})^6$ orbitals of Au$_{12}$ interact weakly with the atomic orbitals of W and are not shown for WAu$_{12}$. Reproduced with permission from ref 669. Copyright 2014 American Chemical Society.

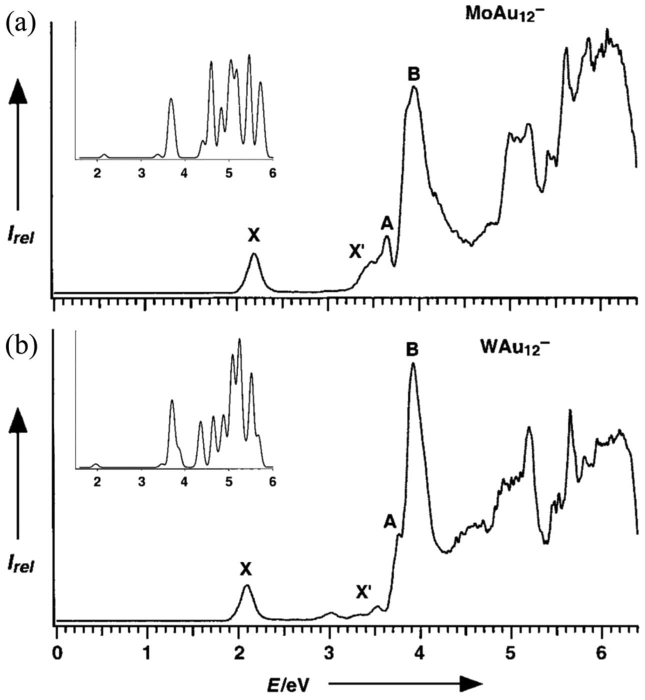

Figure 77. Photoelectron spectra of (a) [Mo@Au$_{12}$]$^-$ and (b) [W@Au$_{12}$]$^-$ at 193 nm (6.424 eV). Insets show the simulated photoelectron spectra of these two clusters with the icosahedral configuration. Reproduced with permission from ref 62. Copyright 2002 WILEY-VCH Verlag GmbH & Co. KGaA, Weinheim.

DFT calculations with PBE functional were performed on M@Au$_{12}$ (M = 3*d* elements)[121] and large local magnetic moments of over 2 μ_B were found for M = Mn, Fe, and Co. It was argued that the orbital magnetism of these 3*d* doped icosahedral clusters (up to about 0.65 μ_B, aligned either antiparallel or parallel to the magnetic spin moment) can be rationalized by the relativistic effects together with a superatom picture. Yarzhemsky and co-workers[679] performed B3LYP/LanL2DZ calculations on a series of 18-electron M@Au$_{12}$ clusters with M = Zr^{2-}, Nb$^-$, Mo, Tc$^+$, Ru^{2+}, Hf^{2-}, Ta$^-$, W, Re$^+$, and Os^{2+}. Most of them prefer high symmetry icosahedral (I$_h$) configurations, except for Tc$^+$@Au$_{12}$, which adopts a cuboctahedral (O$_h$) structure. Indeed, the energetic stability of M@Au$_{12}$ icosahedral cages (I$_h$) has been compared with those of the (distorted) cuboctahedral cages with O$_h$, D$_{4h}$, D$_{2h}$, D$_{3d}$, and D$_{3h}$ symmetries considering all 3*d*, 4*d*, and 5*d* endohedral atoms.[677] Among them, only Mo@Au$_{12}$, Tc@Au$_{12}$, and W@Au$_{12}$ and Au@Au$_{12}$ prefer a high symmetry icosahedral cage. Computed at the PW91/QZ4P level of theory, neutral Mn@Au$_{12}$ cluster favors the O$_h$ structure (Figure 75b) rather than the I$_h$ one, with a large magnetic moment of 5 μ_B and a moderate HOMO−LUMO gap of 0.36 eV.[678] Note that this cluster does not correspond to completion of an electronic shell and effectively there are 14 delocalized electrons, while the five *d* electrons are more localized on Mn. Accordingly, the HOMO−LUMO gap is small. Using B3PW91/LanL2DZ calculations, the transition from planar to 3D cage configurations in 18-electron M@Au$_{12}$ clusters (M = V$^-$, Nb$^-$, Ta$^-$, Cr, Mo, W, Mn$^+$, Tc$^+$, Re$^+$) has been explored by Nijamudheen *et al.*.[676] From the above mentioned studies, there remain some controversies about the most stable geometries of M@Au$_{12}$ clusters. For those clusters not corresponding to 18-electron systems, the high-symmetry cage configurations (I$_h$ or O$_h$) are not necessarily the ground states. Thus, *ab initio* based global search is desirable to determine the lowest-energy configurations and to further unveil the interplay between geometric and electronic effects in the M@Au$_{12}$ clusters.

Besides the above discussed M@Au$_{12}$ clusters, there are also reports of other Au$_{12}$ based endohedral cage clusters. For example, Sg is the heavier homologue of W in the periodic table. In this regard, Cao, Schwarz, and Li[680] investigated the geometric and electronic structures of Sg@Au$_{12}$ cluster using DFT, MP2, and CCSD(T) calculations. The lowest-energy isomer of Sg@Au$_{12}$ has the icosahedral symmetry with strong Sg(6*d*)−Au(6*s*) covalent-metallic interaction. Starting from the icosahedral W@Au$_{12}$ cluster, Muñoz-Castro[682] has designed two novel trimetallic superatoms by including an electron-excess (electron-deficient) element on the cage along with an electron-deficient (electron-excess) element as the endohedral atom. As a consequence, Re@Au$_{11}$Pt and Ta@Au$_{11}$Hg were demonstrated as two isostructural and isoelectronic counterparts to the W@Au$_{12}$ cluster, both possessing a closed-shell electronic configuration of 1S^{2}1P^{6}1D^{10}. Muñoz-Castro[681] further extended the scope of endohedral atoms to the *p* block elements (*E*) and considered a series of $[E@Au_{12}]^{q-}$ (q = 1−5) clusters. Interestingly, these $[E@Au_{12}]^{q-}$ clusters (except for *E* = N, O, F, Cl, Br) follow a 20 valence electron rule instead of the 18-electron one (each Au atom contributes one 6*s* electron), giving rise to a stable icosahedral geometry with a 1S^{2}1P^{6}2S^{2}1D^{10} electronic configuration. For example, at the PBE/TZ2P level of theory, [B@Au$_{12}$]$^{5-}$, [Sn@Au$_{12}$]$^{4-}$, [Bi@Au$_{12}$]$^{3-}$, [Te@Au$_{12}$]$^{2-}$, and [I@Au$_{12}$]$^-$ clusters with the same endohedral cage of I$_h$ symmetry were shown to possess a HOMO−LUMO gap of 1.80, 1.85, 1.77, 0.99, and 0.23 eV, respectively.

Since Au is a heavy element, spin-orbit coupling effects on the electronic structures and spectroscopic properties of M@Au$_{12}$ cage clusters have also been explored by several groups.[683−686] Using TD-DFT calculations within the zeroth order regular approximation at the scalar relativistic level, Stener *et al.*[683] discussed the SOC effects on the excitation spectra (i.e., description of the photoabsorption process) of W@Au$_{12}$ and Mo@Au$_{12}$ clusters. In the low-energy region (up to 6 eV), the inclusion of SOC is necessary since the discrete excitations are well separated from each other. In contrast, when the discrete levels become much denser at higher energy, the convoluted intensity can be properly described already at the scalar relativistic level. Using the same theoretical approach, Stener *et al.* further considered three isoelectronic clusters, i.e., $[M@Au_{12}]^-$ (M = V, Nb, Ta).[684] A comparison of all the five endohedral cage clusters revealed that the photoabsorption spectrum can be tuned by properly selecting the encapsulated metal atom. Ju and Yang[685] investigated the influence of SOC on the electronic structure of $M@Au_{12}$ (M = 3*d*, 4*d*, and 5*d* elements) by DFT calculations. It was found that SOC stabilizes the Au cage clusters. Generally speaking, SOC can disperse much the frontier orbitals of $M@Au_{12}$ clusters, especially those with heavy transition metal dopants in each series, and thus result in reduced HOMO−LUMO gaps. After the inclusion of SOC, the hybridization between M *d* states and Au 6*s*, 5*d* states is enhanced, which leads to the increase of spin and orbital magnetic moments as well as increase in cluster binding energies by about 5%.

As for the smaller-sized $M@Au_n$ clusters with $n < 12$, Hossain *et al.*[687] extended the scope of $M@Au_n$ cage clusters down to $n = 10$ with endohedral bicapped tetragonal antiprism or prism structure and related distorted cage configurations, or a pentagonal antiprism structure using LanL2DZ basis set and different exchange-correlation functionals. They found that an M atom (M = W, Mo, Ru, Co) can be encapsulated in Au_{10} cage with appreciable binding energies and moderate HOMO−LUMO gaps. Especially, $W@Au_{10}$ and $Mo@Au_{10}$ clusters have large AEA of 3.28 and 4.36 eV, respectively, at the B3LYP/LanL2DZ level, and might exhibit superhalogen-like behavior. Recently, Carey and Muñoz-Castro[691] discovered an endohedral $Re@Au_{11}$ cluster with D_{3h} symmetry, which is isoelectronic to $W@Au_{12}$ cluster and possesses the same $1S^21P^61D^{10}$ electronic configuration as a close-shell superatom with a HOMO−LUMO gap of 1.30 eV at the PBE/ZORA level.

7.1.2. Endohedrally Doped Au_{14} and Au_{15} Cages.

In 2005, Zeng's group[692] reported a new series of isoelectronic caged clusters i.e., $M@Au_{14}$ (M = Zr, Hf) and $[M@Au_{14}]^-$ (M = Sc, Y), in which 14 Au atoms form a D_{2d} cage encapsulating the M atom (Figure 75d). DFT calculations at the BP86/SDD+Au(2*f*) level showed the HOMO−LUMO gap of $Zr@Au_{14}$ and $Hf@Au_{14}$ to be 2.33 and 2.05 eV, respectively, somewhat higher than that of $W@Au_{12}$ (1.8 eV computed with the same method). Furthermore, the calculated electron affinity of anionic $Sc@Au_{14}$ is as high as 4.13 eV, which is even higher than the EA value of Al_{13} (about 3.6 eV), signifying a prominent superhalogen behavior. Starting from the above discussed four $M@Au_{14}$ cage clusters, J. R. H. Xie *et al.*[693] proposed a way to tune their optical excitation and emission over a broad wavelength region from near infrared to green by doping other transition metal atoms (e.g., V, Ti, Nb, and Ta) and adjusting the total number of electrons accordingly.

Toprek and Koteski[694] have performed a global search for the lowest-energy structures of titanium doped gold clusters, i.e., Au_nTi with $n = 1−32$ using DFT-based simulated annealing. They found $Ti@Au_{14}$ to stand out due to its symmetric endohedral cage geometry, high stability (maxima on the plots of the binding energy, second-order energy difference, and ionization potential), and large HOMO−LUMO gap (1.4 eV with PBE functional), which can be easily understood by the 18-electron rule. The same conclusion was drawn by Chen and Yan[695] in an earlier study of the Au_nTi cluster ($n = 2−16$), where an endohedral D_{2d} cage with high stability was reported for $Ti@Au_{14}$. Nhat and Nguyen[688] have studied the neutral $V@Au_{14}$ cluster that has a similar structure as the D_{2d} of $M@Au_{14}$ (M = Zr, Hf, Ti) and another nearly degenerate C_{2v} isomer. The anionic $V@Au_{14}$ cluster was also found to have a D_{2d} type structure as for the neutral one. However, the lowest-energy configuration of $Mn@Au_{14}$ is a C_1 cage with Mn atom inside the cage and carrying a spin magnetic moment of 3 μ_B,[696] which can be understood from 21 valence electrons on this cluster, that is 3 electrons more than the shell closing at 18 electrons.

Z. Wang's group[697−700] extended the family of endohedral $M@Au_{14}$ clusters to actinides (M = U, Th, Ac, Pa, Np, Pu) and lanthanide (M = Ce). Using the BP86 or PBE functional combined with the TZP or TP2P basis set, they found partially occupied 5*f* levels in the encapsulated actinide atoms to be preferentially excited to 6*d* shells to satisfy the 18-electron principle, while the remaining 5*f* electrons remained unpaired and contributed to the magnetic moments on these clusters. Specifically, neutral $An@Au_{14}$ (An = Th, Pa, U, Np, Pu) clusters are superatoms with electronic shell configurations of $1S^21P^61D^{10}1F^0$, $1S^21P^61D^{10}1F^1$, $1S^21P^61D^{10}1F^2$, $1S^21P^61D^{10}1F^3$, and $1S^21P^61D^{10}1F^4$ and spin magnetic moments of 0, 1, 2, 3, and 4 μ_B, respectively. In addition, the endohedral $Gd@Au_{14}$ cage cluster has been investigated, which possesses a C_s symmetry and a large spin moment of 6 μ_B.[701]

Following the 18-electron rule, Zeng's group[640] further considered endohedral doping of a Sc or Y atom into a neutral Au_{15} cage. Although the global minimum configurations of both $Sc@Au_{15}$ and $Y@Au_{15}$ are endohedral cages without any point group symmetry (C_1), an appreciable HOMO−LUMO gap of 1.74 eV (using BP86 functional) was found for both clusters, indicating that they are closed electronic shell species. Besides, M. Zhang *et al.*[696] have found an endohedral cage with C_{2v} symmetry as the lowest-energy structure for $Mn@Au_{15}$. It possesses a large magnetic moment of 4 μ_B and a small HOMO−LUMO gap of 0.116 eV (with the PBE functional).

In 2010, Yadav and Kumar[702] reported an endohedral $Gd@Au_{15}$ cage cluster having an appreciable HOMO−LUMO gap of 1.31 eV (PW91 functional) and a reasonable binding energy of 2.641 eV/atom, which is substantially larger than that of the planar Au_{15} cluster (2.222 eV/atom). This unique FK-like cage of Au_{15} with C_s symmetry is composed of six quadrangles and 14 triangles (Figure 75e). Since the electronic configuration of Gd is $4f^75d^16s^2$, its three 5*d* and 6*s* valence electrons together with 15 6*s* valence electrons from Au atoms contribute to the cage stability by satisfying the 18-electron rule, while the seven 4*f* electrons on the Gd atom remain unpaired and result in a large spin magnetic moment of 7 μ_B. This magnetic superatom cage cluster is potentially useful for phototherapy of cancer cells and magnetic resonance imaging. Later, Kumar's group[703] systematically explored the evolution of atomic and electronic structures of small Au_n ($n = 1−16$) clusters doped by a Gd atom. They found that the doping of a Gd atom can effectively transform the planar Au_n clusters into an endohedral cage starting from $n = 10$. Among all these $Gd@Au_n$ clusters, $Gd@Au_{15}$ stands out. In particular, the embedding energy gained by doping a Gd atom in a Au_{15} cage is as high as 9.5 eV.

7.1.3. Endohedrally Doped Au_{16-18} Cages.

In 2006, Bulusu *et al.* reported the experimental and theoretical evidences of $[Au_n]^-$ ($n = 16−18$) hollow cage clusters.[664] These hollow golden cages with an average diameter > 5.5 Å can easily accommodate one guest atom inside, offering versatile possibilities of endohedral doping. Later, they carried out joint DFT and photoelectron spectroscopic studies to explore endohedral $[Au_n]^-$ cages (n = 16−18)[704−707]. They produced $[Cu@Au_{16}]^-$ and $[Cu@Au_{17}]^-$ clusters with a cluster beam apparatus.[704] As shown in Figure 78, there is remarkable similarity between the PES spectra of $[Cu@Au_n]^-$ and $[Au_n]^-$ species. This suggests that the Cu dopant sits inside the cage and does not disturb the atomic and electronic structures of the parent $[Au_n]^-$ cage significantly, which was further supported by DFT calculations. A careful comparison between DFT-simulated PES and experimental ones revealed that $[Cu@Au_{16}]^-$ shown in Figure 75g is an endohedral cage with C_s symmetry (distorted from the parent $[Au_{16}]^{2-}$ cage with T_d symmetry in Figure 75f), in which the Cu atom is displaced from the center, whereas the Cu atom in the center of the $[Au_{17}]^-$ cage might be fluxional, leading to coexistence of C_{2v} and C_s structures for $[Cu@Au_{17}]^-$. For $[Cu@Au_{16}]^-$, the additional charge on cluster anion and the 4*s* valence electron from Cu atom make it an 18-electron cluster with closed electronic shell configuration. In other words, $[Cu@Au_{16}]^-$ can be viewed as $Cu^+@[Au_{16}]^{2-}$.

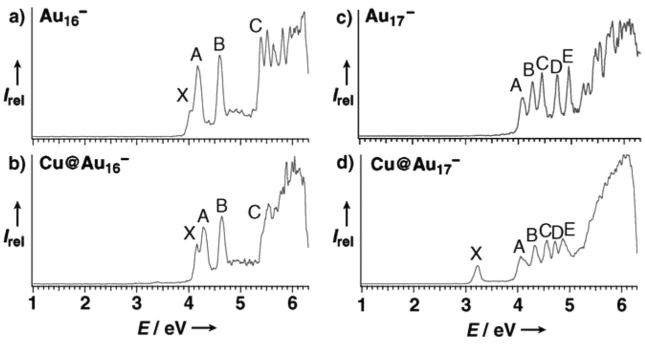

Figure 78. Photoelectron spectra of the $[Cu@Au_{16}]^-$ and $[Cu@Au_{17}]^-$ anion clusters, compared to $[Au_{16}]^-$ and $[Au_{17}]^-$. Reproduced with permission from ref 704. Copyright 2007 Wiley-VCH Verlag GmbH & Co. KGaA, Weinheim.

In a subsequent study,[706] similar results were obtained for the $[Au_{16}]^-$ cage doped by M atoms with different number of valence electrons (M = Ag, Zn, In). In these three cases, the M dopant atom with closed *d* shell does not alter significantly the electronic and atomic structures of $[Au_{16}]^-$, except for donating its valence electrons to the gold cage. As a consequence, the $[M@Au_{16}]^-$ clusters prefer the endohedral cage structures with nearly perfect T_d symmetry and can be formally viewed as $Ag^+@[Au_{16}]^{2-}$, $Zn^{2+}@[Au_{16}]^{3-}$, and $In^{3+}@[Au_{16}]^{4-}$ with totally 18, 19, and 20 valence electrons (if not counting the filled d^{10} shell), respectively. When a transition metal atom with open *d* shell (M = Fe, Co, Ni) is doped into the $[Au_{16}]^-$ cage, the parent $[Au_{16}]^-$ cage is substantially distorted and has much lower point group symmetry, i.e., C_2 for $[Fe@Au_{16}]^-$ and $[Co@Au_{16}]^-$ and C_1 for $[Ni@Au_{16}]^-$.[707] These cluster geometries were further supported by the electron diffraction experiments. Detailed theoretical analysis showed that the Fe, Co, and Ni dopants donate two, two, and one electrons to the cage, respectively, and the remaining 3*d* electrons induce atomic-like spin moments on the encapsulated transition metal atoms.

In contrast to group 4 transition metals, when a group 14 atom E (E = Si, Ge, Sn) is doped into the $[Au_{16}]^-$ cage, the lowest-energy configuration of $[E@Au_{16}]^-$ cluster is no longer an endohedral cage,[705] as evidenced by photoelectron spectroscopy and DFT-based global search using the basin hopping algorithm. Instead, the dopant atom either stays exohedrally on the cage (Ge, Sn) or becomes a part of the cage (Si). In the latter case, Si atom is attached to a dangling Au atom. A similar configuration was actually found for $[Si@Au_{16}]^-$ by Sun and co-workers[708] using DFT-based global optimization with a simulated annealing method. The ground state structure with an on-surface Si atom and a dangling Au atom atop Si was found to be more stable than the endohedral cage with an off-center Si atom by 0.457 eV, whereas the latter was predicted as the ground state configuration for $[Si@Au_{16}]^-$ by Walter and Häkkinen in an earlier study.[709] Covalent bonding between Au−Au and Au−Si was found to dominate the stability of the Si doped Au clusters.

Photoabsorption spectroscopy experiments on gas-phase pure $[Au_n]^+$ and doped $[Au_{n-1}Pd]^+$ ($13 \leq n \leq 20$) clusters[710] have shown that the Pd dopant strongly reduces the optical absorption cross section in the size range of n = 14−16, which may be related to the dopant induced structural changes such as the formation of Pd-centered endohedral caged structures. However, further theoretical efforts are needed to confirm this speculation.

Photofragmentation experiments on $[Au_nX]^+$ (X = Y, Sc, Ti, V, Cr, Mn, Fe, Co, Ni) clusters by Lievens' group[711,712] showed pronounced intensity drops in the mass abundance for $[Sc@Au_{16}]^+$, $[Y@Au_{16}]^+$, $[Ti@Au_{15}]^+$, $[Cr@Au_{17}]^+$, $[Mn@Au_{17}]^+$, $[Fe@Au_{17}]^+$, $[Co@Au_{17}]^+$, and $[Ni@Au_{18}]^+$ (see the results for $[Au_nY]^+$ in Figure 79 as an example). All these magic numbers can be associated with the closed electronic shell at 18 electrons, assuming that Y/Sc, Ti, Cr/Mn/Fe/Co, and Ni dopants contribute three, four, two, and one itinerant electrons, respectively. Also note that a computational study predicted stable endohedral fullerene-like structures for $Au_{15}Y$ and $Au_{15}Sc$ clusters with 18 valence electrons,[640] which are isoelectronic with $[Au_{16}Y]^+$ and $[Au_{16}Sc]^+$, respectively. Nevertheless, further calculations are needed to determine

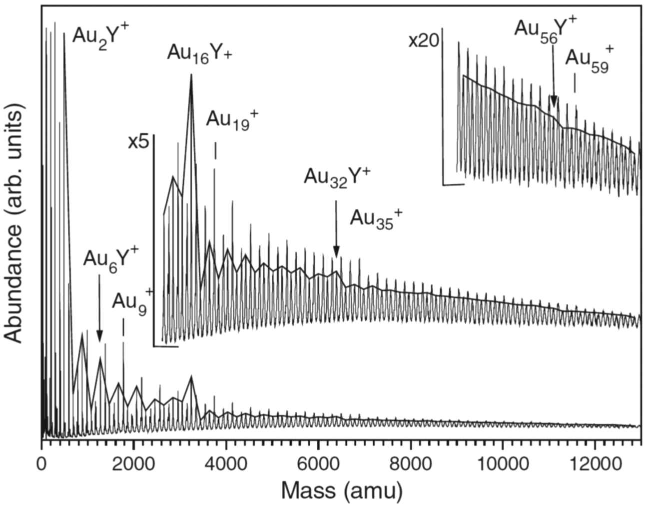

Figure 79. Mass-abundance spectrum of cationic $[Au_n]^+$ and $[Au_nY_m]^+$ clusters after photofragmentation. The solid line connects the $[Au_nY]^+$ species. Steps in abundance are observed at n = 2, 6, 16, 32, and 56. The pronounced pattern results from cooling by fragmentation and can be explained by the enhanced stability related to electronic shell closings for 2, 8, 18, 34, and 58 delocalized valence electrons and similarly for the pure gold clusters. Reproduced with permission from ref 712. Copyright 1999 Elsevier Science B.V.

their most stable geometries and illuminate the electron counting rule in these doped gold cluster cations.

Parallel to the aforementioned experimental efforts, many *ab initio* calculations have been carried out to explore neutral or ionic endohedral Au_n cages (n = 16−18) with various guest atoms.[640,703,708,709,713−722] These theoretical results are summarized in Table 17. So far, most theoretical studies focused on endohedral Au_{16} cages. It was found that a variety of guest M atoms (M = Cu, Li, Na, B, Al, Ga, In, Sc, Ti, V, Cr, Mn, Mo, Tc, Rh, Gd, Eu) can be encapsulated stably inside the neutral or charged Au_{16} cages. However, for some elements (M = C, Si, K, Ag), the M atom prefers the exohedral site outside the Au_{16} cage as also discussed above for Si, possibly due to either the smaller size of the M atom and strong Au−M interaction or larger radius of the M atom. Among these $[M@Au_{16}]^q$ endohedral cages, $[Li@Au_{16}]^-$, $[Na@Au_{16}]^-$, $[B@Au_{16}]^-$, and $[Ga@Au_{16}]^-$ exhibit extraordinarily large HOMO−LUMO gap beyond 1.5 eV (using PBE or PW91 functional), rendering them potential building blocks with reasonable chemical stability for cluster-assembled materials. The $[B@Au_{16}]^-$ cluster with C_{3v} symmetry is shown in Figure 75h. On the other hand, as discussed before, some neutral endohedral species with transition metal or rare earth metal dopant possess appreciable magnetic moment (e.g., 4 μ_B for $Cr@Au_{16}$, 5 μ_B for $Mn@Au_{16}$, 6 μ_B for $Gd@Au_{16}$, and 7 μ_B for $Eu@Au_{16}$)[696,703,715], which can be correlated with electronic shell closing with 18 electrons. These are potentially useful for magnetic nanomaterials and spintronics. Moreover, the transition metal dopant usually induces a large distortion of the parent Au_{16} cage due to the strong dopant−cage interaction.

Table 17. Summary of Theoretical Studies on Endohedrally Doped $[M@Au_n]^q$ Cages[a]

System	Method	Author (year)
$M@Au_{16}$ (M = Mg, Ca, Sr)	BP86/SDD+2*f*, LanL2DZ	Gao *et al.* (2006)[640]
$M@Au_{17}$ (M = Na, K)	BP86/SDD+2*f*, LanL2DZ	Gao *et al.* (2006)[640]
$M@Au_{16}$ (M = Si, Al)	PBE/planewave	Walter *et al.* (2006)[709]
$[M@Au_{16}]^-$ (M = Cu, Ag, Li, Na, K)	PBE/DNP	Fa *et al.* (2008)[713]
$[C@Au_{16}]^-$	PW91/DNP	Fa *et al.* (2008)[714]
$[Cu@Au_n]^-$ (n = 16, 17)	PBE/LanL2DZ	Zorriasatein *et al.* (2008)[722]
$Mn@Au_{16}$	PW91/DNP	M. Zhang *et al.* (2012)[696]
$[Gd@Au_{16}]^{0/+}$	PW91/planewave	Shinde *et al.* (2012)[703]
$Eu@Au_{16}$	PW91/planewave	Shinde *et al.* (2012)[703]
$[M@Au_{16}]^{-/0}$ (M = Cr, Mn)	PBE/SDD+2*f*, 6-311+G(*d*)	H. Q. Wang *et al.* (2013)[715]
$[M@Au_{16}]^-$ (M = B, Al, Ga, In)	PBE/DNP	Tang *et al.* (2013)[716]
$[M@Au_{16}]^{-/0}$ (M = Sc, Ti, V)	PBE/LanL2DZ	H. F. Li *et al.* (2014)[717]
$M@Au_{17}$ (M = Cu, Ag, Li, Na, K)	PBE/DNP	Tang *et al.* (2014)[720]
$M@Au_{18}$ (M = Na, K, Mg, Ca, Al, Ga)	PBE/LanL2DZ	Manzoor *et al.* (2016)[721]
$[Rh@Au_{16}]^{-/0}$	PBE/planewave	J. X. Liu *et al.* (2017)[718]
$[M@Au_{16}]^{-/0}$ (M = Mo, Tc)	PBE/SDD+2*f*, ECP28MWB	H. F. Li *et al.* (2018)[719]

[a] Here M denotes the endohedral atom, n is the number of Au atoms, and q is the charge on the cluster.

There were also a few investigations on Au_{17} and Au_{18} cages encapsulating a metal atom.[640,720−722] In particular, neutral $M@Au_{17}$ (M = Cu, Ag, Li, Na) cage clusters are closed electronic shell 18-electron systems and exhibit enhanced stability, as demonstrated by their large embedding energy (5.45−6.72 eV) and substantial HOMO−LUMO gap (1.14−1.62 eV using the PBE functional).[720]

7.1.4. Endohedrally Doped Au_{32} Cages. Among the larger Au clusters, a hollow cage with I_h symmetry was found as the global minimum structure for Au_{32},[666,667] which is an excellent example satisfying the spherical aromaticity rule. It can be regarded as a gold counterpart of carbon fullerene, and thereby, it was termed as "golden fullerene". Analogous to the widely studied endohedral carbon fullerenes, the Au_{32} cage with 9 Å radius can host a variety of endohedral dopants. Using DFT calculations, Ghanty and co-workers[723,724] have explored the atomic structure and stability of endohedrally doped golden fullerenes $X@Au_{32}$ (X = Li^+, Na^+, K^+, Rb^+, Cs^+, Zn, Cd, Hg). They found that alkali metal cation dopants can be stably encapsulated in the Au_{32} cage, and the off-center site is energetically more favorable than the central position, especially for the cations with smaller radius like Li^+ and Na^+,[723] suggesting the electrophilicity of these alkali metal cations. For the neutral divalent metal dopants, only $Hg@Au_{32}$ prefers perfect endohedral cage structure with I_h symmetry, whereas Cd atom stays in the endohedral off-center position (C_{5v}) and Zn atom locates on the cage.[724] In contrast to the negligible charge transfer between Hg dopant and the I_h-Ag_{32} cage, the encapsulated Zn and Cd atom donates about 0.75 and 0.14 electrons to the Au_{32} cage, respectively; thus, the Au_{32} cluster becomes closer to its anionic form which prefers low-symmetry distorted structure.

In addition to the pure Au_{32} cage cluster, Kumar[725] proposed an all-metal compound fullerene $Al_{12}Au_{20}$, in which 12 Al atoms cap the pentagonal faces of a dodecahedral Au_{20} cage. The $Al_{12}Au_{20}$ cage has a binding energy of 3.017 eV/atom, substantially higher than that of Au_{32} fullerene (2.457 eV/atom). The hollow $Al_{12}Au_{20}$ cage with I_h symmetry can be further stabilized by an endohedral Al^- anion, and the resulting $[Al@Al_{12}Au_{20}]^-$ cluster has a moderate HOMO−LUMO gap of 0.55 eV (with PW91 functional). On the other hand, if an Au^- anion is doped inside the cage, the $[Au@Al_{12}Au_{20}]^-$ cluster becomes a 58-valence-electron species with a larger gap of 0.99 eV. In the same year, Q. Wang *et al.*[726] proposed an interesting $Mn_4@Al_{12}Au_{20}$ endohedral complex, which exhibits magnetic bistability with 0 μ_B and 14 μ_B configurations being energetically nearly degenerate (the antiferromagnetic state of 0 μ_B is lower in energy than the ferromagnetic state of 14 μ_B by only 0.09 eV). In contrast, isolated Mn_4 cluster is ferromagnetic with a larger magnetic moment of 20 μ_B. Such a change in the magnetic behavior of the encaged Mn_4 cluster suggests its substantial interaction with the $Al_{12}Au_{20}$ cage, as demonstrated by the embedding energy of 5.74 eV.

7.2. Doped Ag Cages

Unlike small Au_n clusters which favor planar structures for sizes up to about n = 12,[64,65] silver clusters adopt 3D configurations starting from a rather small size, i.e., n = 7 for neutral Ag_n[727] and n = 5 for cationic $[Ag_n]^+$.[728] Hence, it might be possible to obtain endohedrally doped silver cages with relatively smaller sizes. Janssens et al.[729−731] reported the production of singly doped $[Ag_nX]^+$ (X = Sc, Ti, V, Cr, Mn, Fe, Co, Ni, Cu) clusters and their mass spectra after laser fragmentation. Their results showed enhanced stability of clusters with either 8 valence electrons ($[Sc@Ag_6]^+$) or 18 valence electrons ($[Sc@Ag_{16}]^+$, $[Ti@Ag_{15}]^+$, $[V@Ag_{14}]^+$, $[Fe@Ag_{11}]^+$, $[Co@Ag_{10}]^+$, and $[Ni@Ag_9]^+$), as shown in Figure 80. This is similar to the Y doped cation gold clusters discussed above. DFT calculations on $[Co@Ag_{10}]^+$ at the BP86/TZ2P level revealed its lowest-energy structure to be a symmetric Ag_{10} cage (slightly distorted from D_{4d} to C_s symmetry) encapsulating a Co atom. Strong hybridization of the Ag-5*s* orbitals with the Co-3*d* orbitals leads to the formation of a series of delocalized $1S^21P^61D^{10}$ superatomic orbitals. As a consequence of the filled 18-electron shell, the magnetic moment on the Co atom is completely quenched. Similar to $[Co@Ag_{10}]^+$, $[Co@Ag_8]^-$ is also a closed-shell 18-electron species with a singlet spin state and a sizeable HOMO−LUMO gap of about 1 eV found by using photoelectron spectroscopy and DFT calculations with the PB86 functional.[732] In contrast, $[Co@Ag_6]^-$ and $[Co@Ag_7]^-$ clusters with open-shell electronic configurations carry 2 μ_B and 1 μ_B spin magnetic moment, respectively. Intriguingly, all the three $[Co@Ag_n]^-$ clusters form Co-centered endohedral cages with the point group symmetry of D_{2h} ($n = 6$), C_{2v} ($n = 7$), and D_{2d} ($n = 8$). Similarly, an endohedral cage structure with C_{2v} symmetry was found for $Co@Ag_9$ with 18 valence electrons, in which the local magnetic moment of the encapsulated Co atom is completely quenched by the Ag_9 host cluster.[733]

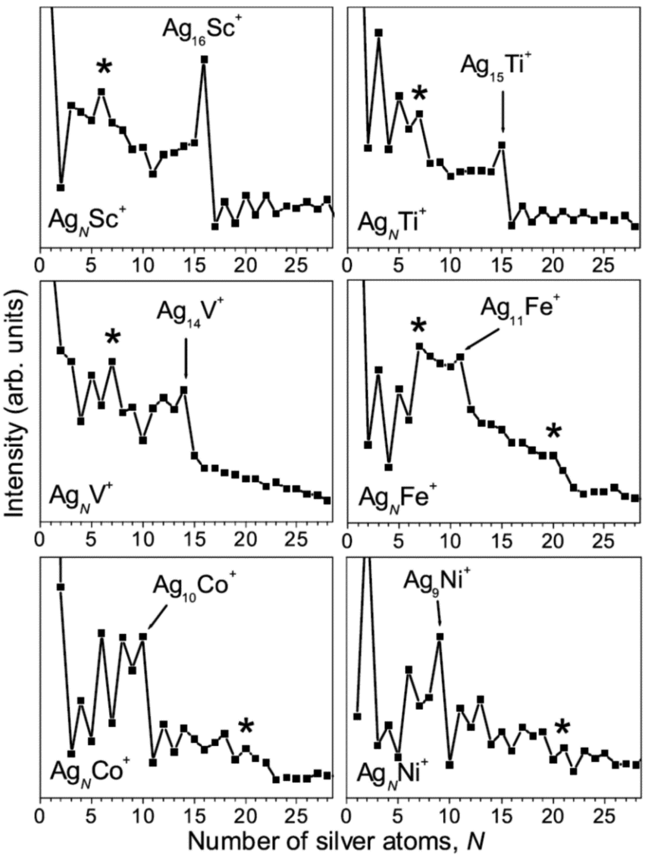

Figure 80. Measured cluster intensities after photofragmentation as a function of size for $[Ag_nX]^+$ (X = Sc, Ti, V, Fe, Co, Ni; $n < 30$). The most pronounced features in these graphs are steps in intensity after the $[Ag_{16}Sc]^+$, $[Ag_{15}Ti]^+$, $[Ag_{14}V]^+$, $[Ag_{11}Fe]^+$, $[Ag_{10}Co]^+$, and $[Ag_9Ni]^+$ clusters that correlate with a magic number of 18 delocalized valence electrons. Other smaller intensity drops can be identified with the magic behavior at 8 and 20 valence electrons, and these are marked with an asterisk. Reproduced with permission from ref 729. Copyright 2005 American Physical Society.

Analogous to the icosahedral $M@Au_{12}$ clusters discussed previously in Section 7.1.1, there are some theoretical studies on the possible silver counterparts, i.e., $M@Ag_{12}$ clusters with the endohedral icosahedral cage.[689,734−737] M. Zhang *et al.*[734] systematically explored the geometries as well as electronic and magnetic properties of such clusters with M = 3*d*, 4*d*, and 5*d* elements using DFT calculations with the PW91 functional and DNP basis set. They showed that the M-centered icosahedral cage with I_h symmetry was more stable than a cuboctahedral configuration. All the doped $M@Ag_{12}$ clusters possess larger binding energies than the pure icosahedral Ag_{13} cluster, indicating that all the transition metal atoms with open *d* shell stabilize the Ag_{12} cage. Later, Gong *et al.*[735] investigated the effect of SOC on the magnetic behavior of icosahedral $M@Ag_{12}$ clusters (M = 3*d* and 4*d* elements) using the PBE functional and planewave basis set. They obtained the total magnetic moments of the $M@Ag_{12}$ clusters to vary from 0 to 5 μ_B (3*d* series) or 6 μ_B (4*d* series). It was found that the total and local spin magnetic moments of $M@Ag_{12}$ clusters were hardly affected by the inclusion of SOC except for Tc, Ru, Rh, and Pd cases. The spin and orbital magnetic moments from DFT calculations with SOC can be understood by the Hund's rule for a superatom.[121] In particular, $Mo@Ag_{12}$ is found to be a closed-shell 18-electron system, quenching both spin and orbital magnetic moments.

Medel *et al.*[738] have explored the size-dependent evolution of the atomic structure, bonding character, stability, and magnetic moment of neutral and cationic Ag_nV clusters with $4 \leq n \leq 15$ using DFT calculations at the PW86/DZVP level. Starting from $n = 7$, $[Ag_nV]^{0/+}$ clusters favor a 3D cage-like geometry with the V atom gradually encapsulated in the cage. $[V@Ag_{12}]^{0/+}$ is the smallest cluster where the V atom gets completely encapsulated. The neutral $V@Ag_{12}$ cluster is a highly deformed icosahedron, but the lowest-energy configuration of $[V@Ag_{12}]^+$ is a cuboctahedron (O_h symmetry), similar to the theoretical finding by Blades *et al.*[689] A gyro-enlongated hexagonal bipyramidal structure has been predicted for $[V@Ag_{14}]^{0/+}$. In particular, $[V@Ag_{14}]^+$ has a total of 18 valence electrons (leaving the 4*d* electrons on Ag atoms) and it behaves as a closed-shell species with high stability (HOMO−LUMO gap as large as ∼1.2 eV), in line with the mass spectrometric observation by Janssens *et al.*[729,730] as shown in Figure 80. The filling of $1S^21P^61D^{10}$ superatomic orbitals in $[V@Ag_{14}]^+$ leads to complete quenching of the spin moment of V. With two electrons deficiency to the closure of the superatomic orbital, $[V@Ag_{12}]^+$ has a total spin moment of 2 μ_B. Similar results were obtained by Xiong *et al.*[739] for neutral Ag_nV clusters with $4 \leq n \leq 12$. It was found that the Ag_nV clusters follow a pentagonal pyramid based growth pattern starting from $n = 7$. They also found a V-centered distorted icosahedron with D_{3d} symmetry for $V@Ag_{12}$, with 1 μ_B magnetic moment similar to the results by Medel *et al.*.[738]

The size-dependent evolution of atomic structures and electronic properties of other transition metal doped silver clusters such as Ag_nFe ($n \leq 15$),[740] Ag_nRh ($n \leq 15$),[741] and Ag_nSc ($n \leq 16$)[742] have been theoretically explored by several groups using DFT calculations. It was found that Fe dopant prefers to stay inside the Ag_n host cluster starting from $n = 8$. Afterward, the $Fe@Ag_n$ clusters carry a total magnetic moment

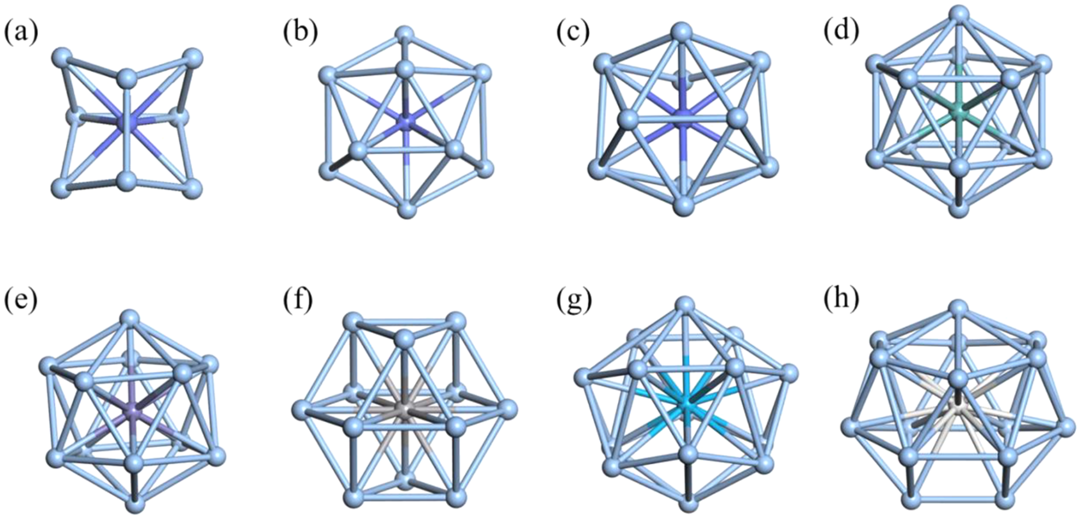

Figure 81. Atomic structures of (a) $[Co@Ag_8]^-$ (D_{2d} symmetry), (b) $Co@Ag_9$ (C_s symmetry), (c) $[Co@Ag_{10}]^+$ (C_{3v} symmetry) (also for $Fe@Ag_{10}$), (d) $Mo@Ag_{12}$ (I_h symmetry), (e) $Fe@Ag_{12}$ (C_i symmetry), (f) $[V@Ag_{12}]^+$ (O_h symmetry), (g) $Th@Ag_{14}$ (D_{2d} symmetry), and (h) $Sc@Ag_{15}$ (C_{2v} symmetry) clusters obtained from PBE0/SDD calculations.

of 1 μ_B or 2 μ_B.[740] The only exception is $Fe@Ag_{10}$, which has a closed electronic shell with 18 valence electrons and is relatively stable according to the second-order difference of energies. The most stable configuration of $Fe@Ag_{12}$ is a Fe-centered icosahedron, beyond which additional Ag atoms cap on the Ag_{12} icosahedron. Starting from $n = 9$, $Rh@Ag_n$ clusters adopt an endohedral cage structure with the Rh atom at the center. As an exception, the lowest-energy geometry of $Rh@Ag_{12}$ is not an endohedral icosahedron, but a capped incomplete icosahedron.[741] Similarly, $Sc@Ag_{12}$ cluster prefers a capped pentagonal bipyramid structure instead of endohedral icosahedron.[742] Endohedral cages with an interior Sc atom were found for $Sc@Ag_{14}$ and $Sc@Ag_{15}$. The latter one behaves as a superatom having the highest vertical ionization energy of 6.23 eV and the largest HOMO−LUMO gap (1.58 eV using PW91 functional) among the considered $Sc@Ag_n$ clusters.

Beyond transition metal dopants, 18-electron superatom with $1S^21P^61D^{10}$ configuration is also found for Ag_{14} clusters doped with a 5*f*-element atom, i.e., $An@Ag_{14}$ (An = Ac^-, Th, Pa^+).[743] The bonding interaction between the endohedral actinide atom and the host cage primarily involves the 6*d* and 7*s* atomic orbitals of the actinide atom and the superatomic orbitals of Ag_{14}. Their potential applications for SERS will be discussed in Section 7.4.

Figure 81 and Table S21 summarize the atomic structures, geometry parameters, and key electronic properties of some representative endohedral $M@Ag_n$ cage clusters computed at the PBE0/SDD level of theory. Most of these doped silver clusters carry a finite magnetic moment of 2 μ_B, whereas $[Co@Ag_{10}]^+$, $Mo@Ag_{12}$, and $Sc@Ag_{15}$ having a total of 18 valence electrons are nonmagnetic closed electronic shell species and exhibit sizeable HOMO−LUMO gap of 2.962, 3.121, and 2.471 eV, respectively. Even with much smaller cage size (down to $n = 8$) in comparison with the endohedral gold cages, the embedding energy between the silver host cage and the transition metal dopant lies in the range of 3.361 to 9.345 eV, which is sufficient to stabilize the endohedral complex.

7.3. Doped Cu Cages

As known, Ag and Au atoms have comparable radius, whereas Cu atom has smaller size. Therefore, the structural pattern and relative stability of doped copper cage clusters are expected to be different from their silver and gold counterparts. So far, much less theoretical or experimental efforts have been devoted to the endohedrally doped copper cages.

In a pioneering DFT study in 1996, Sun and co-workers[744] have systematically studied the local magnetic properties and electronic structures of $M@Cu_{12}$ clusters with I_h and O_h symmetries (M = Sc, Ti, V, Cr, Mn, Fe, Co, Ni, Y, Zr, Nb, Mo, Tc, Ru, Rh, Pd, Ag). For all these $M@Cu_{12}$ clusters, the icosahedral configuration (I_h) was found to be more stable than the octahedral one (O_h). Except for Ag and Pd dopants, all 3*d* and 4*d* impurities enhance the binding energy of the doped Cu clusters by up to about 8 eV compared with the value for pure Cu_{13} cluster. Similar to $Cr@Ag_{12}$ and $Mo@Au_{12}$ discussed above, $Cr@Cu_{12}$ and $Mo@Cu_{12}$ possess closed-shell electronic configurations and are nonmagnetic, whereas all other 3*d* or 4*d* impurities in the Cu_{12} host cluster induce a local magnetic moment up to ∼1.7 μ_B.

A series of combined experimental and computational studies on $[Cu_nSc]^{0/+}$ clusters have been conducted by Lievens, Nguyen, and their co-workers.[63,745,746] In the mass abundance spectrum of $[Cu_nSc]^+$ (n = 1−30) clusters (see Figure 82), $[Sc@Cu_{16}]^+$ corresponds to the magic number at 18 valence electrons and has electronic shell closing ($1S^21P^61D^{10}$). Accordingly, it stands out with exceptional stability. Geometry optimization at the BP86/LanL2DZ level of theory revealed that it is a Sc-centered FK tetrahedron (T_d symmetry) with a large HOMO−LUMO gap of 2.05 eV. Interestingly, the NICS value at the center of the $[Cu_{16}]^{2-}$ cage (which is an isoelectronic system of $[Sc@Cu_{16}]^+$) was computed to be −65.5 ppm, indicating its spherical aromaticity. On the other hand, the neutral $Sc@Cu_{16}$ cluster involving 19 valence electrons possesses rather low adiabatic ionization energy of 5.03 eV comparable to that of lithium atom (5.14 eV) and moderate electron affinity of 1.95 eV, suggesting its superatomic behavior is chemically similar to the alkali metal atoms. In the mass spectra of $[Cu_nTi]^+$ and $[Cu_nV]^+$ clusters recorded by Hirabayashi and Ichihashi,[747] a stepwise reduction of the abundance was observed beyond n = 15 and 14, respectively, which can also be associated with the total of 18 valence electrons for both cluster species.

Later, Pham *et al.*[748] conducted DFT calculations on neutral $Cr@Cu_n$ (n = 9−16) clusters using the BP86 functional with

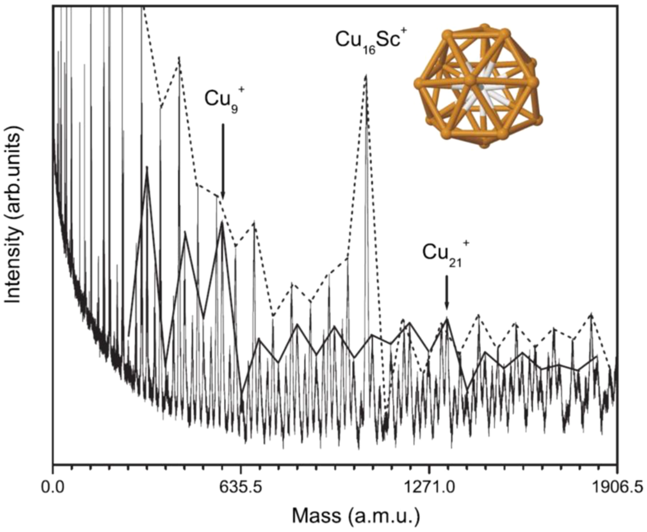

Figure 82. Mass abundance spectrum of scandium doped copper clusters $[Cu_nSc]^+$, n = 1−30 recorded with the cluster source operating at liquid nitrogen temperature and following high fluence irradiation with an ArF excimer. The mass peaks connected with a solid line correspond to pure $[Cu_n]^+$ clusters. Singly doped species are connected by a dashed line. The inset shows the most stable structure of $[Cu_{16}Sc]^+$ with the Sc atom indicated by the light gray sphere. $[Cu_9]^+$, $[Cu_{16}Sc]^+$, and $[Cu_{21}]^+$ clusters with 8, 18, and 20 valence electrons are marked. Reproduced with permission from ref 63. Copyright 2007 American Physical Society.

the SDD basis set for Cu and the aug-cc-pVTZ basis set for Cr, respectively. During the geometry evolution as the cluster size increases, the highly stable Cr@Cu$_{12}$ icosahedron acts as the central architecture; that is, the smaller clusters with n = 9−11 are partially completed icosahedra, while the structures of larger-sized clusters are obtained by adding Cu atoms to the Cr@Cu$_{12}$ core. Except for Cr@Cu$_{12}$ with effectively 18 valence electron closed shell, the other Cr@Cu$_n$ clusters possess total magnetic spin moments in the range of 1−4 μ_B. In a recent theoretical study, $[V@Cu_{12}]^+$ was found to have a T$_h$ structure that is distorted from a perfect icosahedron (I$_h$), and its total magnetic spin moment is 2 μ_B.[689]

Figure 83 and Table S22 summarize the atomic structures, geometry parameters, and key electronic properties of selected endohedral M@Cu$_n$ cage clusters from our own PBE0 calculations, in comparison with those of the hollow $[Cu_{16}]^{2-}$ cage. All these clusters belong to the 18-electron species, thus having sizeable HOMO−LUMO gap in the range of 1.835 to 3.238 eV. The embedding energy gained by encapsulating a Cr (Mo) atom in the Cu$_{12}$ cage and a Sc$^+$ cation in the Cu$_{16}$ cage is 4.485 (9.565) eV and 12.131 eV, respectively.

7.4. Reactivity and SERS of Endohedral Coinage Metal Cages

The endohedrally doped coinage metal cages with high stability as well as tunable physicochemical properties endow them many potential applications, such as gas sensor, catalysis, and SERS. So far, most relevant studies have been carried out from a theoretical point of view, whereas there are only limited experiments on the gas adsorption behavior of doped copper clusters. Using a guided ion beam tandem mass spectrometer combined with DFT calculations, the gas-phase reactions of $[Cu_nTi]^+$ (n = 4−15) and $[Cu_nV]^+$ (n = 5−14, 16) clusters with NO and O$_2$ have been investigated.[747] For both kinds of clusters, the total cross sections for the reaction with NO increase gradually in a small size range up to n = 11 and drop rapidly at n = 12 (see Figure 84), which can be associated with a structural transition from the dopant-exposed structure to the dopant-encapsulated one at n = 12 (as revealed by DFT calculations for $[Cu_nTi]^+$ clusters). Similar reduction of reactivity with O$_2$ was also observed for both $[Ti@Cu_n]^+$ and $[V@Cu_n]^+$ around n = 12, but the total cross sections for the reaction with O$_2$ vary insignificantly in the small size range (n = 4−11).[749]

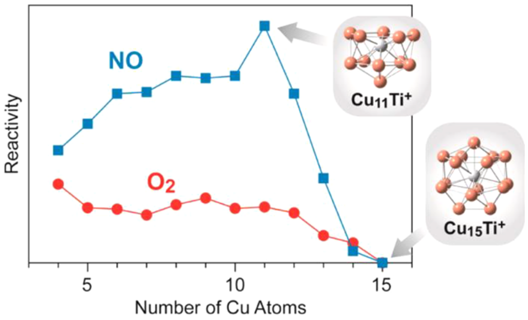

Figure 84. Total cross sections for the reactions of $[Cu_nTi]^+$ (n = 4−15) with NO and O$_2$ as a function of the number of Cu atoms in the cluster at the collision energy of 0.2 eV. Insets are the most stable structures of $[Ti@Cu_{11}]^+$ and $[Ti@Cu_{15}]^+$ clusters. Reproduced with permission from ref 747. Copyright 2016 American Chemical Society.

Many *ab initio* calculations on the gas adsorption of endohedrally doped coinage metal cages focused on their catalytic behavior for CO oxidization.[721,750−754] An early DFT calculation using PW91 functional and planewave basis set predicted that $[V@Au_{12}]^-$ cluster is able to bind 12 CO molecules on top of each Au atom of the icosahedral cage with an appreciable adsorption energy of about 1 eV.[750] The adsorption mechanism was interpreted by a charge donation from CO to $[V@Au_{12}]^-$ and a back donation from the cluster to the antibonding π* orbitals of CO. Using DFT calculations

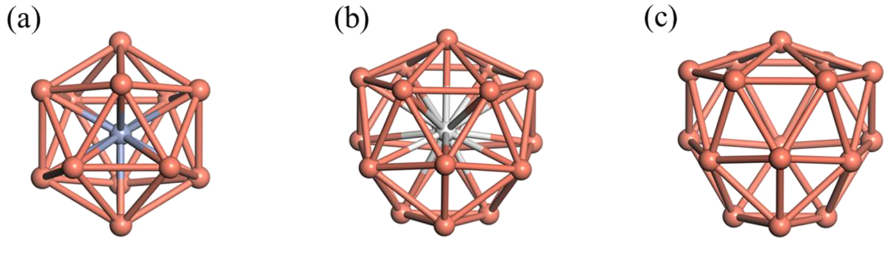

Figure 83. Atomic structures of (a) Cr@Cu$_{12}$ (I$_h$ symmetry) (also for $[V@Cu_{12}]^+$, Mo@Cu$_{12}$), (b) $[Sc@Cu_{16}]^+$ (T$_d$ symmetry), and (c) $[Cu_{16}]^{2-}$ (T$_d$ symmetry) clusters obtained from PBE0/SDD calculations.

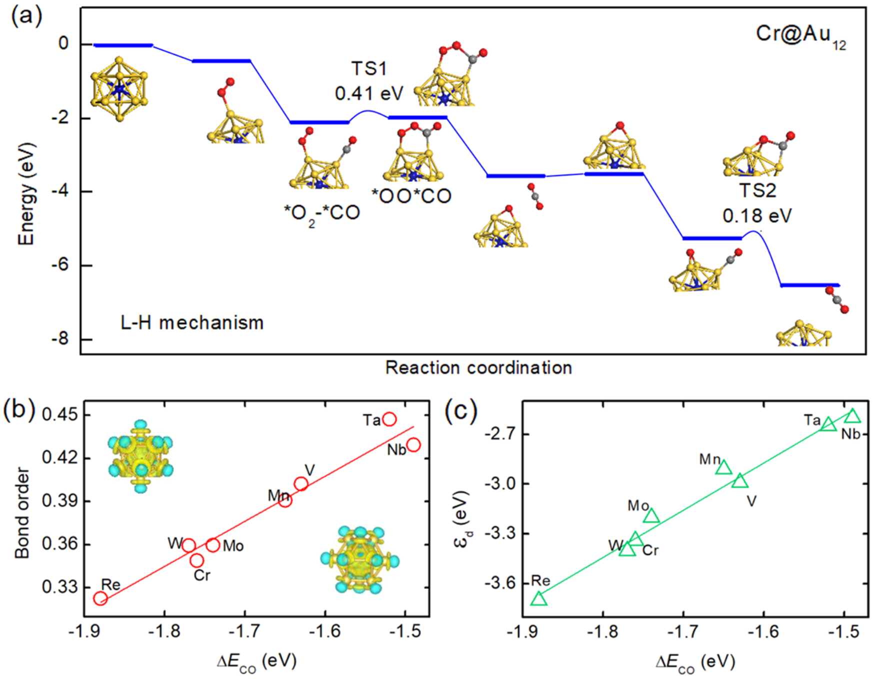

Figure 85. (a) Reaction pathways of CO oxidation on the Cr@Au$_{12}$ cluster under the L-H mechanism. The insets show the structures of the corresponding reaction intermediates and TS. The numbers indicate the kinetic barriers. The C, O, Cr, and Au atoms are shown in grey, red, blue, and yellow, respectively. (b) M−Au bond order and (c) *d* orbital center as a function of CO adsorption energy for various M@Au$_{12}$ clusters. The insets in (b) show the differential charge density distributions of Cr@Au$_{12}$ (I_h) and Ta@Au$_{12}$ (O_h). The yellow and cyan colors represent the electron accumulation and depletation regions with isosurface value of 0.015 e/Å^3, respectively. Reproduced with permission from ref 754. Copyright 2019 Royal Society of Chemistry.

with PBE functional and relativistic ECP combined with DNP basis set, Gao *et al.*[751] investigated CO oxidation on six endohedral cage clusters, namely, W@Au$_{12}$, Nb@Au$_{13}$, Zr@Au$_{14}$, Sc@Au$_{15}$, Ca@Au$_{16}$, and Na@Au$_{17}$. All these endohedral clusters can strongly attach CO molecule with adsorption energies in the range of 0.82 eV to 1.39 eV. Among them, three clusters (Nb@Au$_{13}$, Zr@Au$_{14}$, and Sc@Au$_{15}$) were found to be promising catalysts for CO oxidation with reaction barriers of 0.22−0.27 eV, even lower than those on bare gold clusters. Their high activity was attributed to the low coordination number (3−6) of the Au atoms, charge transfer from the dopant to the gold cage, as well as the geometry fluxionality of the endohedral cage. Manzoor *et al.*[721] theoretically investigated O_2 activation and CO oxidation on Au$_{18}$ and M@Au$_{18}$ (M = Na, K, Mg, Ca, Al, Ga) cage clusters using PBE functional combined with LanL2DZ (for Au) and TZVP (for O, C, M) basis sets. They revealed that endohedral doping leads to a significant enhancement in the O_2 adsorption energy, e.g., from 0.14 eV on Au$_{18}$ to 0.84 eV on Al@Au$_{18}$. Compared to bare Au$_{18}$, O_2 adsorbed on the doped M@Au$_{18}$ cages is activated, as demonstrated by the reduced Au−O bond length, elongated O−O bond length, and enhanced charge transfer to the O_2 molecule. As a result, these M@Au$_{18}$ clusters show rather low barriers for CO oxidation reaction with regard to the pristine Au$_{18}$ cage.

Very recently, S. Zhou *et al.* performed DFT calculations using all-electron relativistic potential, PBE functional, and DNP basis set to elucidate the effect of doping on the activity of M@Au$_{12}$ (M = V, Cr, Mn, Nb, Mo, Ta, W, Re) clusters for catalytic CO oxidation.[754] It was shown that the central dopant atom has substantial impact on the electronic and catalytic properties of the entire cluster. As depicted in Figure 85, the adsorption strength of CO, O_2, and intermediate species is linearly correlated to the M−Au bond order and *d* orbital level of the M@Au$_{12}$ cluster. Cr@Au$_{12}$ and Mn@Au$_{12}$ possessing suitable binding capability have the lowest barriers of 0.41 eV for CO oxidation under the L-H mechanism. These endohedrally doped clusters have prominent charge densities on the gold cage surface, which are related to the electronic states near the HOMO and responsible for the chemical reactivity. This explicit activity−electronic structure relation would help modulation of the catalytic behavior of doped gold clusters with atomic precision.

Kim *et al.* examined the catalytic properties of icosahedral (I_h) Ag$_{13}$ clusters with the central Ag atom substituted by a Ni, Cu, Pd, Pt, or Au atom for CO oxidation.[752] DFT calculations with RPBE functional, semi-core pseudopotentials, and DNP basis set revealed that the endohedral doping provides structural robustness to the I_h structure by lowering the surface electron density of the silver cage. In contrast, the pure Ag$_{13}$ cluster transforms to an amorphous state after the reaction. Among these M@Ag$_{12}$ clusters, Pd@Ag$_{12}$ was predicted to be most active for CO oxidation with a reaction barrier of 0.45 eV. A subsequent study further clarified the reaction mechanism of CO oxidation on M@Ag$_{12}$ clusters.[753] It showed that the association mechanism operates for the clusters with strong interaction with both CO and O_2 molecules, while the carbonate-mediated mechanism dominates when CO interacts weakly with the cluster. Therefore, the reaction mechanism can be mediated by charging the clusters to adjust the adsorption energies of reactant molecules.

In addition to CO, adsorption of other molecules or radicals on endohedrally doped gold or silver cage clusters has been studied by DFT calculations.[701,742,755,756] Fu *et al.*[755] have investigated the interaction between W@Au$_{12}$ and a series of isoelectronic ligands (AE = NO$^+$, CO, BF, CN$^-$, BO$^-$) using

PW91 functional and polarized STO basis set of triple-ξ quality. The top site was found to be the most favorable and the AE−W@Au_{12} bond energy is 3.82, 1.27, 2.24, 3.30, and 3.97 eV for NO^+, CO, BF, CN^-, and BO^-, respectively, with the bond length in the range of 1.94−2.05 Å. However, the H_2 adsorption energies on Sc@Ag_{15} and Sc@Ag_{16} clusters computed at the PW91/LanL2DZ level of theory are rather small (about 0.07 eV), and the cluster geometries remain almost unchanged.[742] This is interesting for the hydrogen storage. Yong *et al.*[701] examined adsorption of CO, NO, NO_2, O_2, CO_2, N_2, and H_2O molecules on Gd@Au_{14} and Gd@Au_{15} clusters. Interestingly, the toxic molecules (CO, NO, and NO_2) are chemisorbed on Gd@Au_n clusters with strong binding energy (in the range of 0.5 to 1.5 eV) and noticeable charge transfer, while the common molecules (O_2, CO_2, N_2, and H_2O) are physisorbed on Gd@Au_n clusters with the exception of O_2 on Gd@Au_{14}. These theoretical results suggest potential application of these Gd@Au_n clusters as sensors for toxic gas detection.

Z. Wang and co-workers carried out a series of DFT studies on the SERS of pyridine adsorbed on the endohedrally doped gold and silver cages, including M@Au_{12} and M@Ag_{12} (M = Mo, W),[757] M@Au_{12} (M = V^-, Nb^-, Ta^-, Cr, Mo, W, Mn^+, Tc^+, Re^+),[758] M@Ag_{12} (M = V, Nb, Ta, Cr, Mo, W, Mn^+, Tc^+, Re^+),[759] and Th@Au_{14}.[698,743] The calculated SERS enhancement for these pyridine-cluster complexes up to the order of 10^4 is mainly caused by the strong charge transfer transition excitations from the metal clusters to pyridine, which is modulated by the interaction between the central dopant atom and the silver/gold atoms on the cages. Furthermore, the magnitude of nonresonant enhancement is associated with the charge state of the doped metal clusters, i.e., pyridine on anionic clusters exhibits stronger nonresonant enhancement than that on neutral and cationic clusters. Therefore, these theoretical studies provide a basis for the design and synthesis of binary alloy SERS substrate nanomaterials.

To summarize this section, among the coinage metal clusters, gold clusters have attracted long-lasting attention from both experimental and theoretical points of view because of their tendency to form planar and cage structures as well as their superior catalytic and optical properties. Indeed, gold is the only example among metals to be able to form an empty cage structure of elemental clusters with as large as 32 atoms. There have been lots of studies on the doping of gold clusters with metal atoms, which transforms planar clusters into endohedral structures. W@Au_{12} and Mo@Au_{12} are typical examples which have perfect icosahedral structures. This has led to many studies on endohedral gold clusters with 14, 15, and 16 atoms to have high symmetry cage structures doped with transition metal and rare earth metal atoms following the 18-electron rule. These doped systems have also opened up great possibilities to tailor their properties for catalytic applications and to design magnetic superatoms. Endohedral cage clusters of other coinage metals, silver and copper, have been studied to a lesser extent; but both these metals also form similar cages, though the difference in the atomic size of Cu affects its behavior. All these systems with electronic shell closing have good stability, have sizeable HOMO−LUMO gap, and show potential to make assemblies, for which there has also been some progress particularly for gold clusters that will be discussed in Section 10. These systems are also promising for spintronics as well as biological systems. We hope that further studies would be carried out particularly on Ag and Cu based systems as well as their applications.

8. ENDOHEDRALLY DOPED CAGES OF COMPOUNDS

In addition to the elemental cages discussed in the above sections, there are many possibilities to achieve hollow cage structures of compound clusters,[357] especially those with equiatomic stoichiometry. Among these, cages of BN are well known similar to the carbon fullerenes, although BN cages are made of even membered rings such as 8-, 6-, and 4-membered rings compared with 6-membered and 5-membered rings for carbon fullerenes. Intuitively, the spherical hollow clusters provide the cavity for hosting dopant atoms or molecules. To date, endohedral doping of cage clusters of various compounds (BN, SiC, GaN, GaAs, InSb, ZnS, ZnSe, ZnTe, CdS, BeO, MgO, ZnO) has been extensively explored by *ab initio* calculations, but experimental evidences have been reported only on M-encapsulated B_nN_n cages with M = Fe, Y, La; n = 36, 48. It should be noted that the undoped empty cages may not be stable or as ground states for many of the compound clusters mentioned above such as CdS, ZnS, and ZnSe, but endohedral doping may facilitate cage formation. Otherwise, even in many cases where core-shell structures are known to exist, there are possibilities to tailor such structures to vary their properties such as photoluminescence by engineering the HOMO−LUMO gap.

8.1. Endohedral BN Cages

Analogous to carbon fullerenes, BN cages composed of squares, hexagons, and octagons with alternate B−N arrangement were theoretically predicted by semiempirical and *ab initio* calculations.[760−763] In 1998, Bando's group[764,765] reported experimental observation of single layered and nested BN fullerenes with rectangle-like shapes from HREM images. The smallest and most observed BN cages fall in a diameter range of 0.4 nm to 0.7 nm, corresponding to the $B_{12}N_{12}$, $B_{16}N_{16}$, and $B_{28}N_{28}$ octahedral polyhedra from theoretical predictions. These stable subnanometer BN cages naturally serve as ideal hosts for endohedral doping with guest atoms, just like carbon fullerenes.

Since 2001, Oku and co-workers[766−769] carried out a series of experiments to synthesize endohedral boron nitride metallofullerenes and characterized them by mass spectrometry and HREM. Briefly speaking, B_nN_n nanocages (n = 24−60) were synthesized by the arc-melting method in a N_2 or Ar−N_2 mixed gas atmosphere using boron-based alloy or mixture powders (LaB_6, YB_6, B/FeO_x) as the starting material. The BN samples were analyzed by LD-TOF mass spectrometry. As a representative, Figure 86 displays the LD-TOF mass spectrum for BN clusters in pyridine solution, showing the presence of pristine B_nN_n (n = 24−60) clusters with strong peaks at n = 24, 34, 36, 37, 46, 48, ... as well as a few Y-doped B_nN_n clusters with n = 36, 37, and 48.[769] Similar mass spectrometric evidence of $B_{36}N_{36}$ and Y-doped $B_{36}N_{36}$ clusters was also reported in ref 768. HREM observations of the as-prepared endohedral M@B_nN_n clusters were performed by a 300 kV electron microscope with a point-to-point resolution of 0.17 nm. Figures 87(a, b) depict typical HREM images of the BN clusters. The diameters of the BN clusters were in the range of 0.7−0.9 nm, which coincide with the size of $B_{36}N_{36}$ that consists of 6 four-membered rings and 32 six-membered rings. Dark contrast was observed near the center of the BN clusters, suggesting the existence of an encapsulated Y atom in

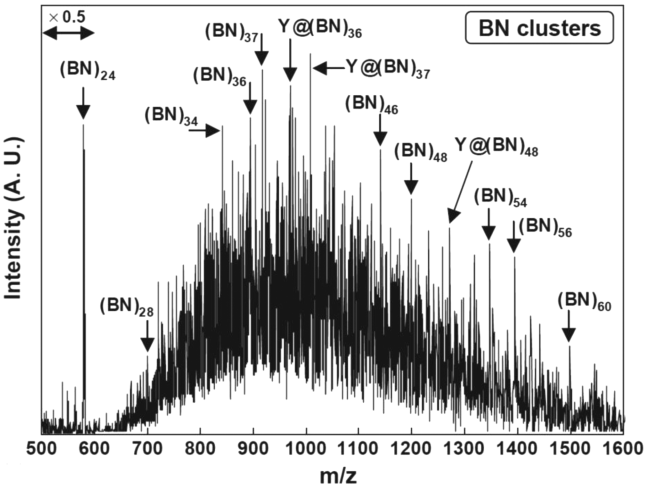

Figure 86. Mass spectrum of pure BN and Y doped BN clusters. The measurements were carried out by LD-TOF mass spectrometry with a pyridine matrix. Reproduced with permission from ref 769. Copyright 2004 Elsevier B.V.

the $B_{36}N_{36}$ cavity. The structural models and simulated images along different orientations are shown in Figures 87(c–f). One can see that the experimental HREM images are reproduced by the simulated HREM images calculated at a defocus value of −40 nm, confirming the observation of $Y@B_{36}N_{36}$ cluster.

Inspired by the experimental success, endohedral doping of a single atom or very small clusters (up to tetramers) in different B_nN_n (n = 12, 16, 20, 24, 28, 36, 48) cages has been explored by numerous *ab initio* calculations.[770−788] The geometries of these BN cages are depicted in Figure 88. Intuitively, the smallest possible BN cage to contain a dopant atom is $B_{12}N_{12}$ consisting of 6 tetragonal and 8 hexagonal BN rings with T_h symmetry (Figure 88a). However, according to the B3LYP/6-311G(d,p) calculations by Beheshtian *et al.*,[770] encapsulation of divalent alkaline earth metal cations in this cage is endothermic with positive enthalpy change (ΔH) or Gibbs free energy change (ΔG). Specifically, the calculated ΔG values are 4.40, 9.02, and 15.32 eV for the encapsulation of a Be^{2+}, Mg^{2+}, or Ca^{2+} cation in the $B_{12}N_{12}$ cage, respectively. Similarly, B3LYP/6-311+G(d) calculations by Z. Liu *et al.*[771] also revealed that the endohedral $X@B_{12}N_{12}$ cluster is less stable than the exohedral isomer by 1.56, 4.74, and 8.68 eV for X = F, Cl, and Br, respectively. Despite the metastable nature, it is interesting to note that the $F@B_{12}N_{12}$ cluster with an exceptionally high electron affinity of 5.36 eV behaves as a novel superhalogen that can serve as the building block for lithium salts and hyperhalogens.[771]

For the larger encapsulated BN cages beyond $M@B_{12}N_{12}$, Feng *et al.*[772] examined the energetic stability, electronic properties, and vibrational spectra of endohedral $Ca@B_nN_n$ (n = 16, 20, 24, 28, 36) and $Zn@B_nN_n$ (n = 16, 20, 24) clusters at the B3LYP/6-31G(d) level of theory. Except for $Zn@B_{28}N_{28}$ (S_8 symmetry), endohedral doping of Ca or Zn atom in all other considered systems is endothermic. The evolution of heat of formation (which is actually the negative value of embedding energy for an endohedral cage) of $M@B_nN_n$ clusters (M = 3*d* and 4*d* transition metal elements; n = 12, 16, 20, 24, 28) has been calculated by J. Wang *et al.* at the PBE/DNP level.[773] As shown in Figure 89, the heats of formation of both $M@B_{12}N_{12}$ and $M@B_{16}N_{16}$ are positive, meaning that the endohedral doping in these cages is endothermic. At n = 20, however, some endohedral $M@B_{20}N_{20}$ clusters (M = Ti, Ni, Zr, Mo, Tc, Ru, Rh) exhibit negative heat of formation, but for Ti and Zr, the heats of formation are quite small. The doping of Ni is favorable, but the heat of formation is slightly positive for Pd. Similarly, while the doping of Ru and Rh leads to a significant gain in energy, the 3*d* elements Fe and Co are unfavorable. These results suggest a

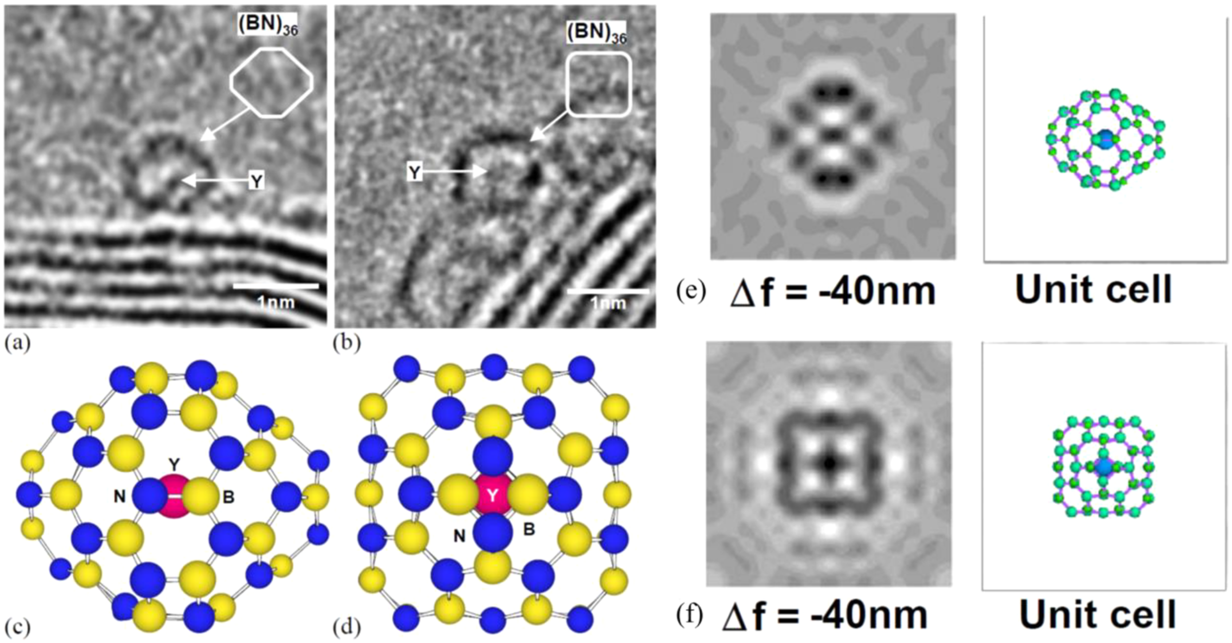

Figure 87. (a) and (b) show the HREM images of $Y@B_{36}N_{36}$ clusters, while (c) and (d) are the corresponding structural models of the clusters in images (a) and (b), respectively. The structural model (d) is viewed in a direction perpendicular to the direction of observation of (c). (e) and (f) are the calculated HREM images (left panels) of the $Y@B_{36}N_{36}$ cluster at a defocus value of −40 nm along different directions and the atomic structure (right panels). Reproduced with permission from ref 769. Copyright 2004 Elsevier B.V.

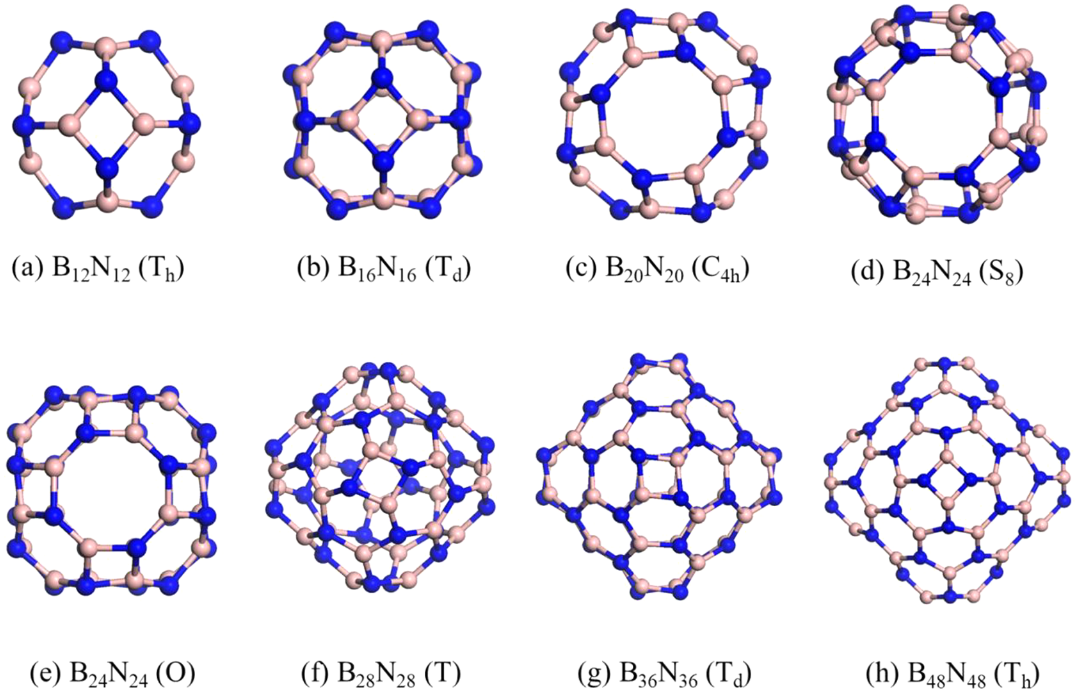

Figure 88. Cage structures for (a) $B_{12}N_{12}$, (b) $B_{16}N_{16}$, (c) $B_{20}N_{20}$, (d) $B_{24}N_{24}$ (S_8 isomer), (e) $B_{24}N_{24}$ (O isomer), (f) $B_{28}N_{28}$, (g) $B_{36}N_{36}$, and (h) $B_{48}N_{48}$ clusters. The symmetries of the clusters are given in parentheses.

crucial role of the size of the endohedral atom as well as coupling of the dopant atomic orbitals with the molecular orbitals of the BN cage. As the cluster size increases further to $n = 24$, the heats of formation for most of the endohedral complexes become negative except for Ti, Zr, Ag, and Cd doped cages. However, continuing further with larger cages, it is found that the heat of formation of $M@B_{28}N_{28}$ becomes positive for most of the endohedral clusters with the exception of M = Sc, Fe, Co, Ni, Cu, Ru, Rh.

Note that the HOMO−LUMO gap of some of the BN cages is quite large and this would affect the interaction of the dopant with the cage. Generally speaking, the interior spaces for $B_{12}N_{12}$, $B_{16}N_{16}$, and $B_{20}N_{20}$ cages are insufficient for incorporating a guest atom or ion. It was argued that the $B_{24}N_{24}$ cage with S_8 symmetry is energetically optimal for encapsulating a 3*d* or 4*d* transitional metal atom among the B_nN_n cages ($n = 12$−28). Based on this consideration, J. Wang *et al.*[773] explored the electronic and magnetic properties of $M@B_{24}N_{24}$ in detail by examining the heat of formation, HOMO−LUMO gap, local magnetic moments on M atoms, average B−N bond length, and cage symmetry. These results are summarized in Table 18. Compared to the pristine $B_{24}N_{24}$ cage with B−N bond length of 1.463 Å, the cage structures of $M@B_{24}N_{24}$ are slightly expanded, and about half of them retain the original S_8 point group symmetry. Most of the encaged 3*d* and 4*d* transition metal atoms in $B_{24}N_{24}$ remain magnetic as in the case of the free atom, but generally the magnetic moment on the M atom is reduced due to interaction with the cage. The reduction is more pronounced for the 4*d* atoms. The overall behavior is similar to what has been found for the doping of V, Cr, Mn, and Fe atoms in hydrogenated cages of Si such as $Si_{16}H_{16}$.[789,790] The interaction of the dopant in these cages is generally weak due to the large HOMO−LUMO gap. The largest magnetic moment of 4.54 μ_B on the M atom has been obtained for $Mn@B_{24}N_{24}$. Note that a total magnetic moment of 5 μ_B was also reported for the $Mn@Si_{16}H_{16}$ cluster with the Mn atom at the center of the cage. On the other hand, there is zero magnetic moment in the case of Ni doping for both $B_{24}N_{24}$ and hydrogenated Si cages. Mulliken population analysis revealed that there is about 0.4−1.1 electrons charge transfer from the $B_{24}N_{24}$ cage to the M dopant. The charge transfer is stronger for the 4*d* atoms due to more extended nature of their valence orbitals with regard to the 3*d* atoms, which make better overlap with the molecular orbitals of the cage. The electronic states of the M atom generally lie in the HOMO−LUMO gap of the cage. Furthermore, encapsulation of Co_2 or Rh_2 dimer in the $B_{24}N_{24}$ (S_8) cage leads to negative heat of formation (−4.648 eV for $Co_2@B_{24}N_{24}$ and −3.532 eV for $Rh_2@B_{24}N_{24}$), suggesting that the formation of both endohedral complexes of transition metal dimer is exothermic.[773] Interestingly, the spins on Co_2 dimer inside $B_{24}N_{24}$ are ferromagnetically aligned with a total spin moment of 3.906 μ_B, with the two Co atoms having 2.224 μ_B and 1.682 μ_B magnetic moments. In contrast, the magnetic moments on the two encapsulated Rh atoms are completely quenched due to strong interaction with N atoms.

Besides the 3*d* and 4*d* transition metal atoms, encapsulation of alkali metal atoms, namely Li, Na, and K in the $B_{24}N_{24}$ cage, has been computationally studied.[774−776] Oliaey *et al.*[774] performed spin-polarized calculations for $B_{24}N_{24}$ and its endohedrally doped derivatives ($M@B_{24}N_{24}$ with M = Li, Na, K). They found that the alkali atoms have remarkable impact on the characteristics of the natural bond orbitals of the $B_{24}N_{24}$ cage by establishing new orbital interactions within the cluster structure. In a further study using the semi-empirical PM5 method, Koi *et al.*[775] examined the effects of endohedral doping of an alkali metal atom on the hydrogenation of $B_{24}N_{24}$ clusters. They found that full hydrogenation of $Li@B_{24}N_{24}$ on the N sites is more favorable than on B sites and that among the alkali atoms, Li encapsulation leads to more negative heat of formation for the hydrogenated cage compared with Na- or

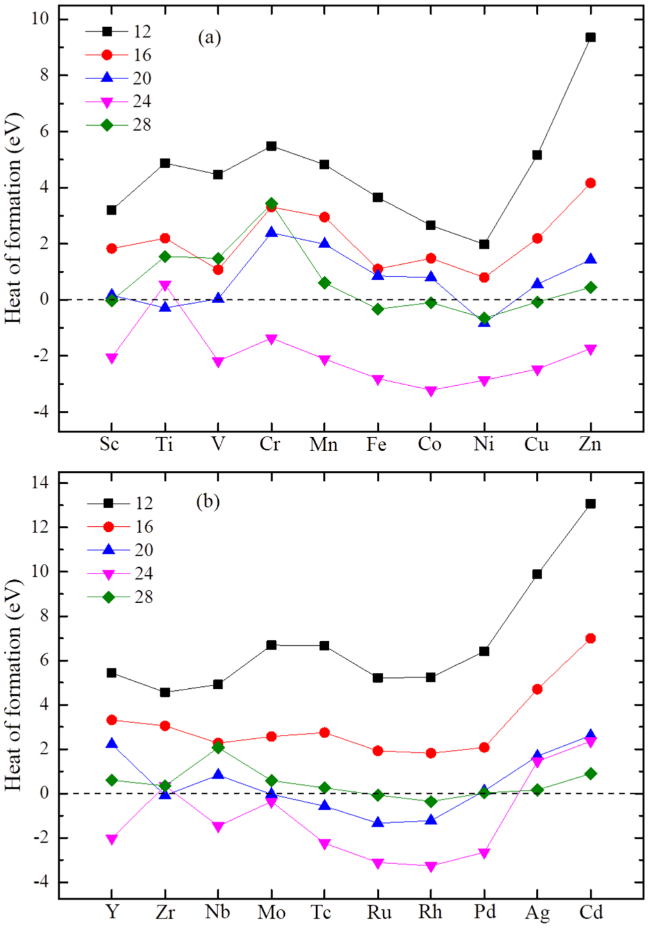

Figure 89. Heats of formation of the equilibrium structures for (a) 3*d* and (b) 4*d* transition metal atoms in B_nN_n (n = 12, 16, 20, 24, and 28) cages. Reproduced with permission from ref 773. Copyright 2008 American Institute of Physics.

K-doped cages, giving rise to a hydrogen storage capacity of 3.84 wt %.

Karachi *et al.*[776] have calculated the HOMO−LUMO gap, VIP, VEA, chemical hardness η = VIP − VEA, chemical potential $\mu = -(\mathrm{VIP} + \mathrm{VEA})/2$, electronegativity $\chi = -\mu$ following Mulliken's method, and the global electrophilicity index ω (I,A) = $\mu^2/2\eta$ of $B_{24}N_{24}$ and its derivatives $M@B_{24}N_{24}$ (M = Li, Na, K) in order to probe the changes in reactivity descriptors due to doping of an M atom. The electrophilicity index measures the stabilization in energy when a system gains additional charge from the environment. Using B3LYP/6-311++G(d,p) calculations, they found that after endohedral doping of alkali metal atoms, all other reactivity descriptors of $B_{24}N_{24}$ nanocage such as IP, E_{HL}, μ, and η reduce significantly but electrophilicity does not change much. All these results showed that by endohedral doping, the chemical properties of the $B_{24}N_{24}$ cage can be modified significantly.

Su *et al.*[777] have studied encapsulation of polynitrogen clusters in $B_{24}N_{24}$ cages with both S_8 and O symmetries (Figure 88d, e) as prospective nanoscale high energy materials. Polynitrogen molecules can release a large amount of energy when decomposed into N_2 molecules, but these are not stable in free space. BN cages could be used to trap such molecules. Using the xB97X-D level of theory with the 6-31G(d) basis set, it has been shown that $B_{24}N_{24}$ (S_8) and $B_{24}N_{24}$ (O) cages can accommodate up to nine and ten nitrogen atoms, respectively.

Table 18. Heat of Formation (H_f), HOMO−LUMO Gap (E_{HL}), Magnetic Moment on M Atom (μ_M), Charge Transfer (Q) to the M Atom, Average B−N Bond Length, and Symmetry of the $M@B_{24}N_{24}$ Cages (M = 3*d* and 4*d* Atoms) from PBE/DND Calculations[773]

Cluster	H_f (eV)	E_{HL} (eV)	μ_M (μ_B)	Q (e)	B−N bond length (Å)	Symmetry
$Sc@B_{24}N_{24}$	−2.047	0.573	1.034	0.663	1.471	S_8
$Ti@B_{24}N_{24}$	0.544	1.181	2.161	0.871	1.445	C_4
$V@B_{24}N_{24}$	−2.183	0.359	3.069	0.822	1.470	S_8
$Cr@B_{24}N_{24}$	−1.364	1.564	3.886	0.647	1.465	S_8
$Mn@B_{24}N_{24}$	−2.015	0.784	4.540	0.403	1.470	S_8
$Fe@B_{24}N_{24}$	−2.807	1.168	2.937	0.611	1.465	C_1
$Co@B_{24}N_{24}$	−3.218	0.990	1.432	0.685	1.466	S_8
$Ni@B_{24}N_{24}$	−2.861	0.433	0.000	0.701	1.469	S_8
$Cu@B_{24}N_{24}$	−2.469	0.694	0.000	0.787	1.470	S_8
$Zn@B_{24}N_{24}$	−1.737	3.551	0.000	0.851	1.469	S_8
$Y@B_{24}N_{24}$	−2.019	0.404	0.700	0.968	1.473	C_1
$Zr@B_{24}N_{24}$	0.354	0.891	0.000	1.092	1.447	C_4
$Nb@B_{24}N_{24}$	−1.467	0.901	1.006	1.010	1.470	C_4
$Mo@B_{24}N_{24}$	−0.359	0.475	1.899	0.843	1.470	S_8
$Tc@B_{24}N_{24}$	−2.236	0.810	2.966	0.611	1.470	S_8
$Ru@B_{24}N_{24}$	−3.112	1.225	1.994	0.850	1.471	C_4
$Rh@B_{24}N_{24}$	−3.264	0.426	0.962	0.834	1.469	C_4
$Pd@B_{24}N_{24}$	−2.648	2.554	0.000	0.886	1.469	S_8
$Ag@B_{24}N_{24}$	1.452	0.597	0.000	0.929	1.444	C_4
$Cd@B_{24}N_{24}$	2.362	3.214	0.000	0.962	1.453	C_4

Therefore, the $B_{24}N_{24}$ cage can provide the confinement space to stabilize polynitrogen clusters, suggesting a novel nanoscale high-density energetic material.

Experiments by Oku *et al.* showed[766−769] that $B_{36}N_{36}$ is the most frequently observed cage incorporating a guest metal atom. Therefore, encapsulation of various dopant atoms in the $B_{36}N_{36}$ cage has been extensively studied by many groups.[778−786] Soon after the experimental observation of $La@B_{36}N_{36}$, Q. Wang *et al.*[778] performed spin-polarized calculations using a planewave basis and PW91 functional. They found that the endohedral La atom stays at an off-center position (1.18 Å from the cage center) and interacts weakly with the BN cage having an exothermic embedding energy of 0.89 eV. The entire cluster carries a small magnetic moment of 1 μ_B and its HOMO-LUMO gap is significantly reduced to 0.37 eV compared with 4.93 eV for the pristine $B_{36}N_{36}$ cage. Nishiwaki and co-workers[779] have studied the atomic and electronic structures of endohedral $M@B_{36}N_{36}$ clusters with a large variety of dopants by semiempirical molecular orbital calculations using the AM1 method. Comparing the heat of formation of the bare $B_{36}N_{36}$ cage with that of the endohedrally doped cage, it was reported that the doping of K, Ga, and Mg is exothermic. Boshra *et al.*[780] also performed DFT calculations on $K@B_{36}N_{36}$ using the B3LYP functional combined with the 6-31G(d) basis set and reported the endohedral doping of K to be exothermic. The NBO analysis revealed about 0.18 electron charge transfer to the cage from the confined K atom. Oliaey and Boshra[781] have carried out B3LYP/6-31G(d) calculations of the atomic structure, vibrational stability, thermochemistry of inclusion reactions, and global reactivity indexes of $[Fe@B_{36}N_{36}]^{2+}$ and $[Fe@B_{36}N_{36}]^{3+}$. The Fe ion drifts to an off-center position in the cage. According to the NBO analysis, the encaged Fe^{2+} ion forms a stable endohedral complex with three N atoms of the BN cage, while Fe^{3+} does not. Encapsulation of both Fe^{2+} and Fe^{3+} ions substantially affects the π-bonding structure of the natural bond orbitals of the $B_{36}N_{36}$ cluster and significantly reduces the HOMO−LUMO gap.

Batista and co-workers[782] have performed DFT calculations on the interaction of transition metal atoms (Fe, Co, and W) or FeO molecule encapsulated in the $B_{36}N_{36}$ fullerene cage. As a metal boride is often used to form the BN cages, there is a possibility of encapsulation of metal atom or a metal oxide molecule inside the cage. It was found that the encapsulation of a Fe atom at the center as well as adsorption outside the cage lead to the same interacting energy of 1.25 eV, while Co doping is more favorable inside the cage with the embedding energy of 1.81 eV. The Mulliken population analysis disclosed a reduction in the *s* orbital occupation on the M atom due to confinement in the cage. The doping of W is favorable at the center of the cage with an embedding energy of 1.19 eV. However, the FeO molecule breaks the cage.

A systematic study of the atomic and electronic structures as well as the magnetic properties of a series of endohedral $M@B_{36}N_{36}$ and $M_4@B_{36}N_{36}$ clusters (M = Ti, V, Cr, Mn, Fe, Co, Ni, Cu) has been conducted by Majumder and coworkers[783−785] using a planewave basis and PBE functional. The calculated embedding energy and magnetic moment of the encapsulated M atoms and M_4 clusters in the $B_{36}N_{36}$ cage are summarized in Table 19. Inside the $B_{36}N_{36}$ cage, the dopant atom prefers to occupy either the cage center (Cr, Mn, Cu) or the off-center site close to the hexagonal ring of the cage (Ti, V, Fe, Co, Ni), depending on the strength of the embedding energy (i.e., weak E_{em} for cage center vs strong E_{em} for the off-center site). The doping of Mn is slightly endothermic presumably due to its $3d^5 4s^2$ electronic configuration as well as the large HOMO−LUMO gap of the $B_{36}N_{36}$ cage. For the singly doped systems, the magnetic moments of the enclosed transition metal atoms follow the same trend as that for the free atoms, except for the quenching of the magnetic moment on the encaged Ni atom. This behavior is again similar to the one found for the other BN cages as well as the hydrogenated silicon cages. In contrast, the magnetic moments of M_4 clusters in the $B_{36}N_{36}$ cage are modified due to the dopant-cage interactions (see Table 19). Generally speaking, the stronger the embedding energy E_{em} is, the larger is the change in the magnetic moments; for example, there is a reduction from 20 μ_B for free Mn_4 to 10 μ_B for $Mn_4@B_{36}N_{36}$ with E_{em} = 2.68 eV. Note that the embedding energy for Mn_4 becomes exothermic. However, in the case of the Cr_4 cluster, the magnetic moment in the cage is increased to 8 μ_B while for the free cluster it is 0 μ_B due to antiferromagnetic coupling. Nevertheless, the $B_{36}N_{36}$ nanocage with the diameter of about 0.8 nm can provide a physical coating to the magnetic nanoclusters by retaining their magnetic character to a certain extent, which might be useful for biological applications and spintronics devices.

Table 19. Magnetic Moments and Embedding Energy of $M@B_{36}N_{36}$ and $M_4@B_{36}N_{36}$ Clusters from PBE Calculations with PAW Potentials[785a]

	$M@B_{36}N_{36}$		$M_4@B_{36}N_{36}$	
M	Magnetic Moment (μ_B)	Embedding energy (eV)	Magnetic Moment (μ_B)	Embedding energy (eV)
Ti	4 (4)	1.02	2 (4)	0.31
V	5 (5)	0.40	0 (0)	0.51
Cr	6 (6)	0.06	8 (0)	3.79
Mn	5 (5)	−0.10	10 (20)	2.68
Fe	4 (4)	0.20	10 (14)	1.12
Co	3 (3)	0.64	6 (10)	1.57
Ni	0 (2)	0.78	2 (4)	1.73
Cu	1 (1)	0.12	0 (0)	−0.59

[a] The numbers in parentheses are magnetic moments of free M atom or M_4 cluster.

Further calculations for CO oxidation reaction on $Fe@B_{36}N_{36}$ and $Fe_4@B_{36}N_{36}$ clusters illuminated the effect of endohedral impurity on the chemical reactivity of the BN cage.[784] First of all, the incorporation of Fe atom or cluster inside a $B_{36}N_{36}$ cage introduces localized states in the HOMO−LUMO gap region of $B_{36}N_{36}$ as also found for other dopants. These impurity states effectively activate the BN cage, which is otherwise inert due to its large HOMO−LUMO gap. As a consequence, an O_2 molecule adsorbs on the endohedral BN cage with elongated O−O bond length of 1.47 Å on $Fe@B_{36}N_{36}$ and 1.52 Å on $Fe_4@B_{36}N_{36}$. CO oxidation can proceed via the Elay−Rideal mechanism, in which two incoming CO molecules react one after another with the chemisorbed O_2 molecule to form two CO_2 molecules, as illustrated in Figure 90. There is a small barrier of 0.51 eV on $Fe@B_{36}N_{36}$ for the formation of the second CO_2 molecule, while for $Fe_4@B_{36}N_{36}$ both reaction steps occur spontaneously.

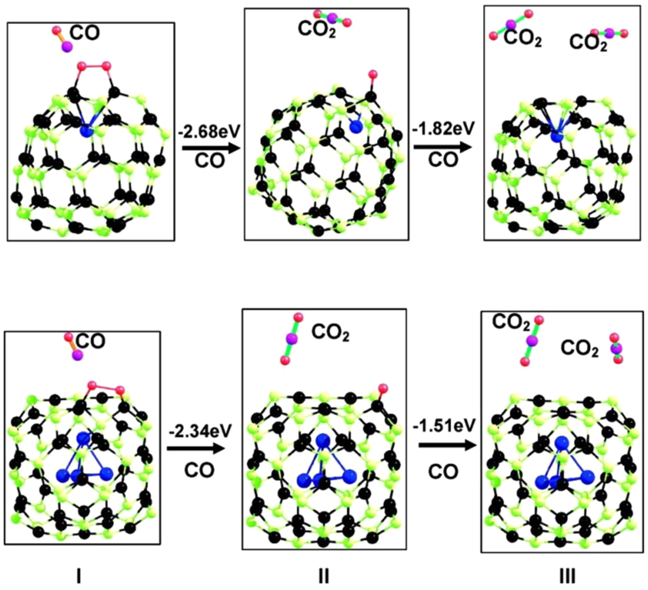

Figure 90. Step by step illustration of the CO oxidation process on the $Fe@(BN)_{36}O_2$ and $Fe_4(BN)_{36}O_2$ clusters: (I) Interaction of CO with $Fe(BN)_{36}O_2$ or $Fe_4@(BN)_{36}O_2$ cluster; (II) formation of the first CO_2 molecule, and (III) formation of the second CO_2 molecule. It may be noted that for $Fe@(BN)_{36}O_2$, the second CO_2 formation occurs via an activation barrier of 0.13 eV. Reproduced with permission from ref 784. Copyright 2008 American Chemical Society.

Using planewave PAW calculations with the PW91 functional, Wen *et al.*[786] have studied a series of endohedral BN metallofullerene $M@B_{36}N_{36}$ complexes with M = Li, Na, Be, Mg, and Ti, to explore their potential application as hydrogen storage materials. There has been much interest in exploring hydrogen storage on carbon fullerenes and nanotubes by adding some metal atoms such as Sr and Ti,[791,792] owing to their large surface area and light weight. In a similar way, BN cages with large HOMO−LUMO gap could be interesting candidates, because the properties of BN cages can be modified by metal doping. Although there is little charge transfer between the metal atom and the BN cage, the metal-induced electronic states lie in the HOMO−LUMO gap, which would in turn affect the electronic properties. It has been shown that the chemisorption energy of an H atom on the BN cage can be effectively enhanced by the encapsulated metal atom, e.g., from −0.61 eV on the B site for bare $B_{36}N_{36}$ cage to about −3.8 eV for Ti@$B_{36}N_{36}$. Chemisorption on B sites was found to be energetically much more favorable than on N sites while the difference in chemisorption energy on tetragonal or hexagonal rings is quite small. This result is different from the result of H adsorption on Li@$B_{24}N_{24}$ for which H was reported to be more favorable on N site.[775] These results point to a dependence of the H interaction on the cage size/curvature. There is much electrostatic contribution to the interactions between B, N, or H atom and the endohedral metal atom, which donates some charge and becomes positively charged. This leads to a repulsive interaction between the metal atom and B atoms, while attractive interaction between the metal atom and N atoms that have excess electronic charge. This results in a reduction in sp^3 character of bonding at the N site when H is attached and weaker bonding of H with N. Li and Ti atoms lie close to the cage and have stronger interaction, while Na, Be, and Mg are close to the center of the cage and have weak interaction with the cage. Accordingly, the chemisorption energy of H is significantly higher for Li and Ti doping. Further study of a H_2 molecule insertion in the cage showed that it is favorable only in the case of Ti with a binding energy of 0.32 eV. It forms two Ti−H bonds. Another four H_2 molecules can be inserted through hexagons in the cage forming a Kubas complex of $Ti(H_2)_5$ with a total binding energy of 0.17 eV without significant expansion of the cage. Further chemisorption of H on (outside) the cage with the Kubas complex inside showed an increase in the chemisorption energy on B and N sites (2.35 eV on average per H atom compared with 2.13 eV on pristine $B_{36}N_{36}$) for both tetragons and hexagons. Finally, a total of 32 H atoms could be added on this cage, corresponding to a high hydrogen content of 8 wt % for Ti@$B_{36}N_{36}$.

Beyond $B_{36}N_{36}$, W. Liang *et al.*[787,788,793] have explored encapsulation of a variety of transition metal atoms and small clusters in the $B_{48}N_{48}$ cage, including single M atoms and Mo−M dimers (M = Sc, Ti, V, Cr, Mn, Fe, Co, Ni, Cu), M−Cr dimers, and M_2Cr trimers (M = Fe, Co, Ni), and M_{2-4} clusters (M = Fe, Co, Ni). Generally speaking, their *ab initio* calculations at the BPW91/LanL2DZ level of theory revealed that these magnetic atoms and clusters interact strongly with the $B_{48}N_{48}$ cage and prefer the off-center positions near the hexagonal ring of the cage. In many situations among the above systems, the $B_{48}N_{48}$ cage was found to enhance the stability of these small magnetic clusters due to interactions with the cage and simultaneously protect their magnetic nature as also found in the case of smaller BN cages, thus paving the way for novel applications in magnetic nanomaterials, spintronic devices, and magnetic sensors.

8.2. Endohedral Doping of Cages of II−VI Semiconductors

Clusters of group 12 chalcogenides (II−VI semiconductors), such as ZnS, ZnSe, ZnTe, CdS, and CdSe, have been extensively studied. Burnin and BelBruno[794] produced cationic clusters of ZnS by laser ablation and found $[Zn_{13}S_{13}]^+$ and $[Zn_{34}S_{34}]^+$ to have much greater intensity in the mass abundance spectrum than other clusters with 1:1 stoichiometric composition in their respective mass range. Later, Kasuya *et al.*[795,796] studied clusters of CdSe, CdS, ZnS, and ZnSe and found high abundances for clusters with 13, 33, and 34 II−VI molecules and weak abundance at 19. Following the discovery of endohedral silicon fullerenes, they predicted novel core-shell cage clusters with 13, 33, and 34 molecules using DFT calculations, such that one CdSe molecule is encapsulated inside a $(CdSe)_{12}$ cage (isostructural to $B_{12}N_{12}$), $(CdSe)_5$, and $(CdSe)_6$ cluster in a $(CdSe)_{28}$ cage (isostructural to $B_{28}N_{28}$), respectively. The $(CdSe)_{13}$ cluster converged to a Se@$Cd_{13}Se_{12}$ configuration with a buckled cage of $Cd_{13}Se_{12}$ and a Se atom inside, as shown in Figure 91. Similar structures were obtained for clusters of other compounds in this family. These theoretical results supported experimental findings of magic clusters of II−VI semiconductors, which are indeed endohedral species with an atom or a group of atoms inside a buckled cage. Kukreja *et al.*[797] produced ZnSe and ZnO clusters from UV laser ablation and found elevated intensities at sizes of 6, 13, 19, 23, and 33 ZnSe molecules, but ZnO clusters did not exhibit any magic behavior or high intensity at a particular size as what indeed was found by Burnin and BelBruno.[794]

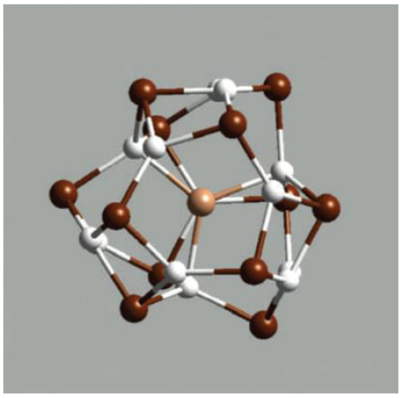

Figure 91. Atomic structure of Se@$Cd_{13}Se_{12}$ cluster. 12 Se (dark brown) atoms and 13 Cd (white) atoms form a buckled cage around an endohedral Se (light brown) atom, which is connected to 4 Cd atom on the cage. Reproduced with permission from ref 795. Copyright 2004, Nature Publishing Group, U.K.

Some research groups[794,798] have suggested hollow polyhedral structures of group 12 chalcogenide clusters (e.g., ZnS clusters), though they did not explain the magic nature of clusters with 13, 33, or 34 molecules. Note that some of the II−VI compound clusters can have hollow cage configurations at particular sizes (e.g., n = 12 and 16) that are able to host some endohedral species including metal atoms. Accordingly, many *ab initio* calculations have been carried out, and the results have been summarized in Table 20. In these calculations, Zn_4S_4 has been considered as the smallest cage cluster for endohedral doping. However, it is too small to accommodate even a Li atom or cation and the corresponding negative (endothermic) embedding energy is −0.88 eV for Li atom and −2.10 eV for Li^+ cation, respectively.[799] The next smallest size considered for endohedral doping in Zn_nS_n cage was n = 6. DFT calculations at the PBE/TZ2P level of theory revealed that incorporation of a Ti or V atom inside the cavity of Zn_6S_6 cluster is indeed exothermic with energy gain of about 0.40 or 0.65 eV, respectively, while inclusion of the other 3d atoms (e.g., Cr, Mn, Fe, Co, Ni) is endothermic.[800] For Zn_9S_9,

Table 20. Summary of Theoretical Studies on Endohedrally Doped $M@X_nY_n$ Cages (X = Zn, Cd; Y = S, Se, Te)[a]

M	XY	n	Method	Author (year)
Li	ZnS	4	B3LYP/6-311+G(d)	Matxain *et al.* (2007)[799]
Na, K, Na^+, K^+	ZnS	9, 12, 13, 15, 16	B3LYP/6-311+G(d)	Matxain *et al.* (2007)[799]
Cl, Br, Cl^-, Br^-	ZnS	9, 12, 15, 16	B3LYP/6-311+G(d)	Matxain *et al.* (2007)[799]
Sc, Ti, V, Cr, Mn, Fe, Co, Ni, Cu	ZnS	12, 16	B3LYP/SKBJ	Matxain *et al.* (2008)[801]
Cr	ZnS	12	PBE/DNP	Chen *et al.* (2010)[804]
Mn	ZnS	12	PBE/DNP	Chen *et al.* (2010)[805]
Fe, Co, Ni	ZnS	12	PBE/DNP	Chen *et al.* (2011)[806]
Sc, Ti, V, Cr, Mn, Fe, Co, Ni, Cu	ZnS	12, 16	B3LYP/SKBJ	Jimenez-Izal *et al.* (2011)[802]
Y, Zr, Nb, Mo, Tc, Ru, Rh, Pd, Ag, Cd	ZnS	12, 16	B3LYP/SKBJ	Jimenez-Izal *et al.* (2013)[803]
Ti, V, Cr, Mn, Fe, Co, Ni	ZnS	6, 12	PBE/TZ2P	Poggio *et al.* (2015)[800]
Mn	ZnSe	6, 7, 8, 9, 10, 11, 12, 13	BLYP/DNP	D. Zhang *et al.* (2011)[807]
Cr	ZnTe	12	PBE/planewave	Yadav *et al.* (2009)[808]
Cr	CdS	12	BLYP/DNP	Ghosh *et al.* (2010)[809]
K, K^+, Cl, Br, Cl^-, Br^-	CdS	9, 12, 15, 16	B3LYP/6-311+G(d)	Jimenez-Izal *et al.* (2010)[810]
Ti, V, Cr, Mn, Fe, Co, Ni	CdS	6, 12	PBE/TZ2P	Poggio *et al.* (2015)[811]

[a] Here M denotes the endohedral atom or ion while n is the number of X or Y atoms.

encapsulation is endothermic for alkali metal atoms or cations (i.e., Na, Na^+, K, K^+) but becomes exothermic for neutral Cl atom (E_{em} = −0.39 eV) or Cl^- anion (E_{em} = −1.40 eV).

Many theoretical studies have focused on endohedral doping of $Zn_{12}S_{12}$ cage (Figure 92), and a variety of guest atoms or ions have been considered (see Table 20).[799−806] Briefly speaking, most 3*d* and 4*d* transition metal atoms (except for Sc, Zn, Ag, and Cd) can be exothermically encapsulated in the $Zn_{12}S_{12}$ cage.[801,803] However, a comparison of the energies of exohedrally and substitutionally doped derivatives showed that most transition metal dopants (e.g., Ti, V, Cr, Mn, Fe, Co, Ni, Cu, Y, Zr, Nb, Mo, Ru, Rh) favor either to replace one Zn atom on the cage framework[800,804−806] or to adsorb on the outer surface of the $Zn_{12}S_{12}$ cage,[802,803] rather than doping inside the cage. The former phenomenon reflects the stronger bonding of S with transition metal atoms than with Zn atom. Although exohedrally doped configurations (see Figure 92) are thermodynamically more stable than endohedral isomers, large enough energy barriers would prevent endohedral compounds from rearranging into the exohedral ones.[803] Beside transition metal dopants, inclusion of an alkali metal atom or cation (Na, Na^+, K, and K^+) inside the $Zn_{12}S_{12}$ cage is still thermodynamically unfavorable, whereas endohedral complex by trapping a halogen atom or anion (Cl, Cl^-, Br, and Br^-) inside $Zn_{12}S_{12}$ is exothermic.[799]

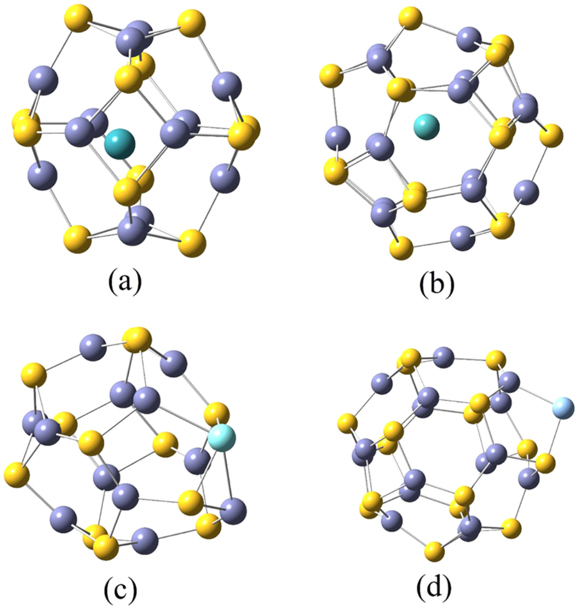
(a) (b) (c) (d)

Figure 92. $M@Zn_{12}S_{12}$ (a) and $M@Zn_{16}S_{16}$ (b) endohedral clusters and $M\&Zn_{12}S_{12}$ (c) and $M\&Zn_{16}S_{16}$ (d) exohedral clusters (also called as surface-doped structures). M stands for the second-row transition-metals from Y to Cd. S atoms are drawn in yellow, Zn atoms in violet, and M in blue. Reproduced with permission from ref 803. Copyright 2013 MDPI, Basel, Switzerland.

To date, the largest ZnS cage explored for endohedral doping is $Zn_{16}S_{16}$ (Figure 91), but the intermediate-sized cages, i.e., $Zn_{13}S_{13}$ and $Zn_{15}S_{15}$, have also been considered. It has been found that Na, Na^+, Cl^-, and Br^- can be incorporated inside these larger Zn_nS_n cages (n = 13, 15, 16) with favorable embedding energies, especially for Cl^- and Br^- (up to 3.38 eV for $Cl^-@Zn_{15}S_{15}$).[799] However, $Zn_{13}S_{13}$ itself is a magic cluster with $S@Zn_{13}S_{12}$ structure (similar to Figure 91) and it is unclear if such endohedral clusters can be realized. Nevertheless, it could be possible that halogen anions X^- = Cl^-, Br^-, I^- act as a nucleation center and form $X^-@Zn_{12}S_{12}$ cages as it was also the case of hydrogenated silicon fullerenes.[506,507] Indeed, $X^-@Zn_{12}S_{12}$ and $S@Zn_{13}S_{12}$ are electronically equivalent, suggesting that such endohedral species are very likely to be formed. One can further generalize that suitable ions could be templates for cages of different sizes. Interestingly as discussed above, encapsulation of a halogen (Cl or Br) atom shows a large gain in energy for n = 12 and also for n = 15 and 16 cages. In fact, these neutral clusters are superhalogen as they have extraordinarily large electron affinity, e.g., 4.73 eV for $Cl@Zn_9S_9$, 5.27 eV for $Cl@Zn_{12}S_{12}$, and 5.28 eV for $Br@Zn_{12}S_{12}$.[799] Studies on 3*d* or 4*d* transition metal atom doping in $Zn_{16}S_{16}$ (i.e., an endohedral or exohedral form) have shown their energetic preference to be generally the same as that for $Zn_{12}S_{12}$ described above, except that Sc and Zn atoms are able to be encapsulated in the $Zn_{16}S_{16}$ cage.[801−803] In both $Zn_{12}S_{12}$ and $Zn_{16}S_{16}$ cages, most of the encapsulated transition metal atoms prefer to stay at off-center position instead of cage center, while the off-center distance (0.71−1.10 Å) in $Zn_{12}S_{12}$ is generally smaller than that in $Zn_{16}S_{16}$ (0.83−1.66 Å).[801]

According to Poggio's calculations at the PBE/TZ2P level, the HOMO−LUMO gap of the $M@Zn_nS_n$ cluster complex significantly drops upon incorporation of a 3*d* transition metal atom M, for example, from 3.36 eV for pristine $Zn_{12}S_{12}$ to 2.167 eV for Cr@$Zn_{12}S_{12}$ and further to 0.602 eV for Co@$Zn_{12}S_{12}$. A similar trend of gap reduction was found by H. Chen *et al.* using PBE/DNP calculations.[804−806] As in the other cases, most 3*d* transition metal atoms (except for Co@$Zn_{16}S_{16}$) enclosed inside a $Zn_{12}S_{12}$ or $Zn_{16}S_{16}$ cage favor atomic-like high-spin state, due to the weak guest−host interaction and little charge transfer from the transition metal atom to the host cage.[801] In contrast, almost all 4*d* transition metal dopants encapsulated in $Zn_{12}S_{12}$ or $Zn_{16}S_{16}$ cage adopt a low-spin state, with the exception of Y@$Zn_{12}S_{12}$.[803]

Similar to ZnS cages, Mn doping into Zn_nSe_n cages (n = 6−13) and Cr doping into $Zn_{12}Te_{12}$ cage have also been theoretically explored.[807,808] In both cases, from an energetic point of view, Mn/Cr atom prefers to substitute a Zn atom instead of being encapsulated in the cage. Especially, for Zn_nSe_n cages of small sizes, i.e., n = 6−11, endohedral doping a Mn atom is rather energetically unfavorable.

There also have been some theoretical reports on endohedrally doped Cd_nS_n cages of selected sizes (n = 6, 9, 12, 15, 16).[809−811] Again, for all 3*d* transition metal dopants, substitutional doping always prevails over endohedral doping energetically, while the encapsulated metal dopants usually retain the atom-like high-spin state. It was, however, found that K atom as well as Cl/Br atom or anion can be exothermically trapped in those Cd_nS_n cages. Similar to the ZnS counterpart, Cd_nS_n cages (n = 9, 12, 15, 16) endohedrally doped by a Cl or Br atom are superhalogen clusters with exceptionally large electron affinities in the range of 4.66 eV to 5.31 eV, making them suitable building blocks for ionic cluster-assembled materials.[810]

8.3. Endohedrally Doped Group 13 and Group 15 (III−V Semiconductors) Compound Cages

Clusters of group 13−15 compounds (III−V semiconductors) such as GaN, GaP, GaAs, AlN, AlP, AlAs, InAs, InP, and InSb have been studied extensively because of the technological importance of these materials. Shevlin *et al.*[812] have studied the AlN, GaN, and InN clusters having up to 196 formula units with specific sizes and showed that these clusters have the same nanocage structures as BN clusters, namely cages with T_d symmetry for n = 16, 36, 64, 100, 144, and 196, with T_h symmetry for n = 12, 48, 60, 108, and 192, with S_8 symmetry for n = 24, and with S_6 symmetry for n = 18 and 36. Kaur *et al.*[813] have studied small clusters with n = 13, 32, and 34 molecules and showed that $(AlN)_n$ and $(GaN)_n$ clusters favor empty cage structures, while $(AlP)_{13}$ favors a filled cage structure similar to $(CdSe)_{13}$ and is magic. $(GaP)_{32}$ was also predicted to be a magic cluster consisting of a $(GaP)_{28}$ cage and a $(GaP)_4$ molecule inside. For $(InN)_{32}$, however, a rocksalt structure was found to be favorable,[814] as also for $(PbS)_{32}$ cluster.[815] Bulk AlN, GaN, and InN crystals are known to undergo a structural transition from wurtzite to rocksalt under pressure.[816,817] However, in nanocluster form, $(InN)_{32}$ was found to favor rocksalt structure without applying external pressure. These results suggest that while large clusters show different behaviors, small clusters of many compound semiconductors have cage structures with alternate cation−anion bonds and may be potential hosts to endohedrally accommodate one or more transition metal or other impurity atoms.

There have been several theoretical explorations on such systems, which are summarized in Table 21. Starting from pristine Ga_nAs_n (n = 7−12) nanocages, J. Wang *et al.*[818] systematically considered substitutional, endohedral, and exohedral doping of one Mn or Fe atom. With increasing size of the GaAs cage, the most favorable Mn doping site gradually moves from the surface to interior sites, and a stable endohedral cage of Mn@$Ga_{12}As_{12}$ is formed. For Fe, endohedral doping is most favorable for n = 8, 10, and 12. The ground state structures of Mn- and Fe-doped Ga_nAs_n cages carry spin moments of 5 μ_B and 2 μ_B, respectively, except for Fe@$Ga_{12}As_{12}$ which has a magnetic moment of 4 μ_B like in free Fe atom. Similarly, P. Lu *et al.*[819,820] calculated Mn- and Fe-doped $Ga_{12}N_{12}$ cages by comparing a variety of substitutional, exohedral, and endohedral configurations. They found that substitutional doping is most favorable for Mn atom, while Fe atom prefers exohedral doping. Compared to the HOMO−LUMO gap of 1.529 eV (using PBE functional) for pure $Ga_{12}N_{12}$ cage, the HOMO−LUMO gap for the endohedrally doped Mn@$Ga_{12}N_{12}$ and Fe@$Ga_{12}N_{12}$ clusters as metastable states reduces to almost half, i.e., 0.83 and 0.78 eV, and their total magnetic moments are 5.426 μ_B and 5.316 μ_B, respectively. These results show that in many cases of these clusters, substitutional doping is most favorable in contrast to BN cages, because the size of the cations in these cages becomes comparable to that of the dopant atom/ion.

Using DFT calculations with PBE functional and triple-ζ doubly polarized basis set, Longo *et al.*[821] have explored a number of transition metal doped In_nP_n cage clusters (see Table 21 for the cluster species). Generally speaking, the encapsulated transition metal atoms (Ti, Cr, Mn, Fe, and Co) preserve their atomic spin moments, except for some smaller systems like Ti@In_7P_7 and Ti@In_8P_8. Among the Ti@In_nP_n (n = 7−12) endohedral complexes, Ti@$In_{11}P_{11}$ shows relatively high stability with a peak in the second-order finite difference of the total energy, which can be related to a 92-electron closed shell system within the spherical jellium model. Later, Ding *et al.*[822] have investigated the geometric, electronic, and magnetic properties of Mn-, Fe-, and Co-doped In_nSb_n clusters (n = 7−12, 14, 16) using PBE/DNP calculations. Among these systems, endohedral doping configurations are most favorable only for Fe@In_8Sb_8, Co@$In_{11}Sb_{11}$, Mn@$In_{12}Sb_{12}$, and Fe@$In_{14}Sb_{14}$, which have a small HOMO−LUMO gap of 0.218, 0.394, 0.605, and 0.783 eV and a total magnetic moment of about 2.47 μ_B, 1 μ_B, 5 μ_B, and 2 μ_B, respectively. These results show that there is a reduction in the magnetic moment of the

Table 21. Summary of Theoretical Studies on Endohedrally Doped M@X_nY_n Cages[a]

M	XY	n	Method	Author (year)
Mn, Fe	GaAs	7, 8, 9, 10, 11, 12	PBE/DNP	J. Wang *et al.* (2008)[818]
Mn	GaN	12	PBE/DNP	Lu *et al.* (2013)[819]
Fe	GaN	12	PBE/DNP	Lu *et al.* (2013)[820]
Ti	InP	7, 8, 9, 10, 11, 12	PBE/TZ2P	Longo *et al.* (2009)[821]
Cr, Mn, Fe, Co	InP	10	PBE/TZ2P	Longo *et al.* (2009)[821]
Mn, Fe, Co	InSb	7, 8, 9, 10, 11, 12, 14, 16	PBE/DNP	Ding *et al.* (2011)[822]

[a] Here XY represents a compound of groups 13 and 15 (III−V compound semiconductor), M denotes the endohedral atom, and n is the number of X or Y atoms.

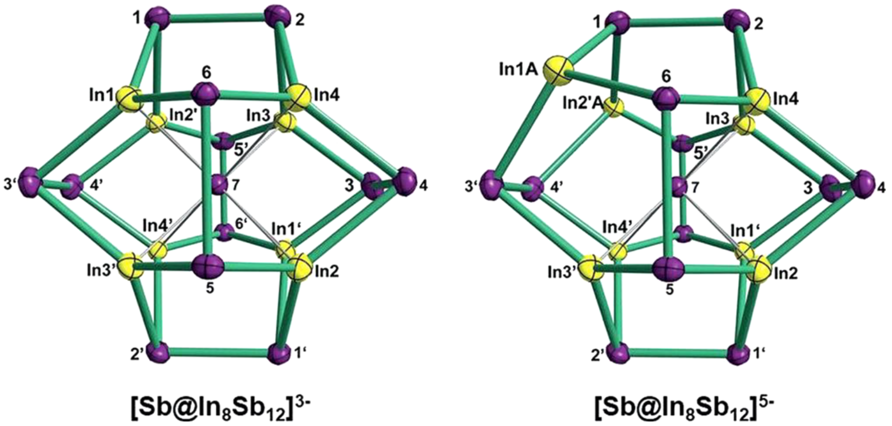

$[Sb@In_8Sb_{12}]^{3-}$ $[Sb@In_8Sb_{12}]^{5-}$

Figure 93. Structures of the $[Sb@In_8Sb_{12}]^{q-}$ core in the two components of the anionic cluster in $[K([2.2.2]crypt)]_4[In_8Sb_{13}]$ compound. Reproduced with permission from ref 823. Copyright 2019 Wiley-VCH Verlag GmbH & Co. KGaA, Weinheim.

M atom except for the Mn case. On the other hand, the reduction in the HOMO−LUMO gap is similar to what has been found for the doped BN cages.

Recently, C. Liu *et al.*[823] have reported a Zintl phase $[K([2.2.2]crypt)]_4[In_8Sb_{13}]$, which contains a 1:1 mixture of $[Sb@In_8Sb_{12}]^{3-}$ and $[Sb@In_8Sb_{12}]^{5-}$ anions. As shown in Figure 93, the former anion with 92 electrons is a symmetric T_h In_8Sb_{12} cage accommodating an endohedral Sb atom, while the latter one has a similar structure with substantial distortion (C_s symmetry) due to the additional two electrons. Bonding analysis of $[Sb@In_8Sb_{12}]^{3-}$ revealed that it contains eight $[In]^{3+}$ centers arranged in a cube and 12 Sb atoms in an icosahedral structure, while the electron deficiency is partially alleviated by interaction with the *s* and *p* orbitals of the endohedral $[Sb]^{3-}$ center. On the other hand, $[Sb@In_8Sb_{12}]^{5-}$ anion might be highly fluxional, as evidenced by its complex potential energy surface featuring eight equivalent minima with a single displaced In^+ center linked by low-lying transition states.

8.4. Endohedral Metal Oxide Cages

Clusters of many oxides have been studied. Among them, zinc oxide is an important semiconducting and piezoelectric material, and its clusters have attracted significant attention. In the size range of $n = 9-18$, cage and tube structures have been shown to be dominant global minimum structures for $(ZnO)_n$ clusters.[824] The cage structures are similar to those of BN. Among them, the $Zn_{12}O_{12}$ cage with T_h symmetry has been found to be a magic cluster with particularly high stability, as evidenced by the maximum peaks in the HOMO−LUMO gap and second-order difference of the total energy when plotted as a function of cluster size. Therefore, the highly symmetric and stable $Zn_{12}O_{12}$ cage provides a promising host for endohedral doping. To this end, several metal dopants, such as Mn,[825] Cr,[826] Li, Na, K, and Rb[827] have been explored by DFT calculations. However, it has been shown that the binding energy of an endohedrally doped $Mn@Zn_{12}O_{12}$ cluster is less than that of substitutional isomer and exohedral isomer by 2.38 and 2.25 eV, respectively.[825] As for the Cr dopant, it prefers an exohedral configuration in the $Zn_{12}O_{12}$ cage, followed by substitutional and endohedral isomers.[826] In both the cases, the Mn and Cr atoms encapsulated in the metastable endohedral cage retain atomic-like spin moments of 5 μ_B and 6 μ_B, respectively. It is worth mentioning that Nanavati *et al.*[828] have shown a nonstoichiometric Mn doped cluster $Zn_{11}MnSe_{13}$ to be magic with a total magnetic moment of 3 μ_B predominantly localized on the Mn atom, while the magnetic moment on a Mn doped stoichiometric cluster $Zn_{11}MnSe_{12}$ is 5 μ_B. The Mn atom in $Zn_{11}MnSe_{13}$ locates on the cage and can interact with more Se atoms.

The embedding energies (E_{em}) and Gibbs free energy changes (ΔG) for alkali metal doped $Zn_{12}O_{12}$ cage have been computed at the B3LYP/LANL2DZ level by Baei *et al.*.[827] Encapsulation of smaller alkali metal atoms in $Zn_{12}O_{12}$ is thermodynamically favorable, i.e., E_{em} = 1.32 eV for $Li@Zn_{12}O_{12}$ and 0.69 eV for $Na@Zn_{12}O_{12}$. As atomic size increases, encapsulation reaction for K or Rb dopant becomes endothermic. It is noteworthy that alkali metal doping can effectively modulate the electronic properties of the $Zn_{12}O_{12}$ cage cluster, e.g., the ionization potential reduces from 8.23 eV for bare $Zn_{12}O_{12}$ to 5.13 eV for $Na@Zn_{12}O_{12}$. Besides the $Zn_{12}O_{12}$ cage, encapsulation of Li, Na, and K atoms in $Be_{12}O_{12}$ and $Mg_{12}O_{12}$ has been computationally explored by Shakerzdeh *et al.*.[829] Among the six endohedral derivatives, only the formation of $Li@Mg_{12}O_{12}$ is exothermic, which is however still higher in energy than the exohedral isomer by 1.3 eV. Nevertheless, encapsulation of Li atom in $Mg_{12}O_{12}$ leads to large hyperpolarizability (2860 a.u.), suggesting its potential applications as a nonlinear optical material. Table 22 summarizes the theoretical studies on metal doped $X_{12}O_{12}$ (X = Zn, Be, Mg).

Table 22. Summary of Theoretical Studies on Endohedrally Doped $M@X_{12}O_{12}$ (X = Zn, Be, Mg) Cages[a]

M	Cage cluster	Method	Author (year)
Mn	$Zn_{12}O_{12}$	PW91/DNP	H. Liu *et al.* (2006)[825]
Cr	$Zn_{12}O_{12}$	PBE/planewave	H. Liu *et al.* (2018)[826]
Li, Na, K, Rb	$Zn_{12}O_{12}$	B3LYP/LANL2DZ	Baei *et al.* (2013)[827]
Li, Na, K	$Be_{12}O_{12}$	B3LYP/6-311+G(d)	Shakerzdeh *et al.* (2015)[829]
Li, Na, K	$Mg_{12}O_{12}$	B3LYP/6-311+G(d)	Shakerzdeh *et al.* (2015)[829]

[a] Here M denotes the endohedral atom.

8.5. Endohedral Cages of Group 14-15 and 14-14 Compounds

Analogous to the endohedral Zintl anions of metal filled group 14 homocages discussed in Section 6.4, some endohedral

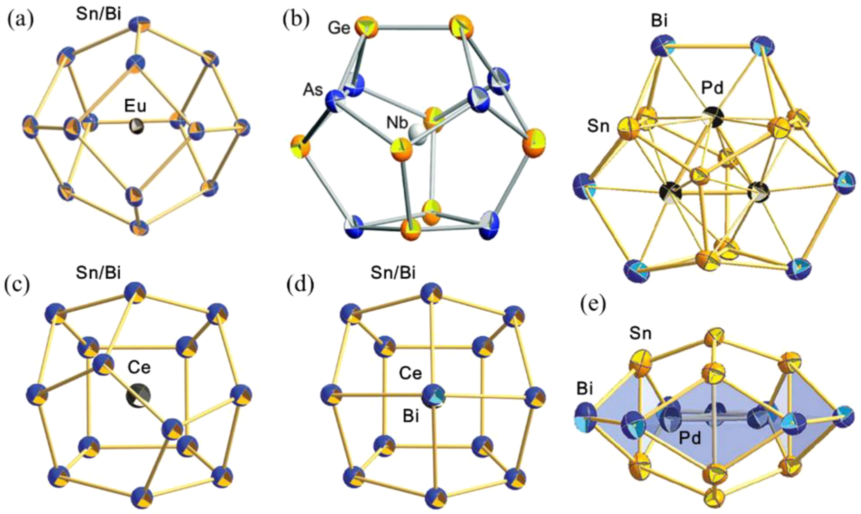

Figure 94. Structures of the cluster anions: (a) $[Eu@Sn_6Bi_8]^{4-}$[836] (Reproduced with permission from ref 836. Copyright 2011 Wiley-VCH Verlag GmbH & Co. KGaA, Weinheim.), (b) $[Nb@Ge_8As_6]^{3-}$[839] (Reproduced with permission from ref 839. Copyright 2015 Royal Society of Chemistry.), (c) $[Ce@Sn_7Bi_7]^{4-}$,[837] (d) $[Ce@Sn_4Bi_9]^{4-}$,[837] and (e) $[Pd_3Sn_8Bi_6]^{4-}$ (upper and lower panels for top and side views, respectively)[843] (Reproduced with permission from refs 837 and 843. Copyright 2011, 2012 American Chemical Society.) The label Sn/Bi in panels (a), (c), and (d) means that this position should be occupied by either a Sn or a Bi atom.

homocages of group 15 elements such as Bi have been obtained in crystalline phase. These include $[Rh@Bi_9]^{4+}$,[830] $[Pd@Bi_{10}]^{4+}$,[831,832] $[Pt@Bi_{10}]^{4+}$,[833] $[Au@Bi_{10}]^{5+}$,[834] and $[U@Bi_{12}]^{3-}$.[835] Further, combining elements from these two groups (14 and 15) of nonmetal or metalloids, a number of heteropolyatomic Zintl anion compounds encapsulated by a transition metal or lanthanide atom have been synthesized in the laboratory, such as $[Eu@Sn_6Bi_8]^{4-}$,[836] $[Ln@Sn_7Bi_7]^{4-}$, and $[Ln@Sn_4Bi_9]^{4-}$ (Ln = La, Ce),[837] $[Ln@Pb_6Bi_8]^{3-}$, $[Ln@Pb_3Bi_{10}]^{3-}$, $[Ln@Pb_7Bi_7]^{4-}$, and $[Ln@Pb_4Bi_9]^{4-}$ (Ln = La, Ce, Nd, Gd, Sm, Tb),[838] $[V@Ge_8As_4]^{3-}$ and $[Nb@Ge_8As_6]^{3-}$,[839] and $[Ta@Ge_8As_4]^{3-}$, $[Ta@Ge_8As_6]^{3-}$, and $[Ta@Ge_8As_6]^{3-}$.[840] In some cases, even two or three transition metal atoms can be encapsulated in the cavity of Zintl anions of tubular or ellipsoidal shape, including $[Ni_2@Sn_7Bi_5]^{3-}$,[841] $[Co@Sn_6Sb_6]^{3-}$, $[Co_2@Sn_5Sb_7]^{3-}$, $[Ni_2@Sn_7Sb_5]^{3-}$,[842] and $[Pd_3@Sn_8Bi_6]^{4-}$.[843] Figure 94 shows the molecular structures of a few of these endohedral Zintl anions as representatives. Usually, the compound cages are nearly spherical polyhedra with 12-, 13-, or 14-vertices, enclosing a metal atom. It is noteworthy that the Wade−Mingos rules are still applicable for some 12- and 14-vertices endohedral cages (which requires $5n_v$ = 60 and 70 valence electrons for a 3-connected n_v-vertex polyhedron, respectively), for example, $[V@Ge_8As_4]^{3-}$,[839] $[Nb@Ge_8As_6]^{3-}$,[839] $[Ta@Ge_8As_4]^{3-}$, and $[Ta@Ge_8As_6]^{3-}$[840] (V/Nb/Ta contributes all the five *s* and *d* valence electrons to the skeletal bonding of the cage), $[Eu@Sn_6Bi_8]^{4-}$ (Eu donates two 6*s* electrons to the skeletal bonding of the cage and keeps seven unpaired 4*f* electrons to form a half-filled shell),[836] and $[La@Sn_7Bi_7]^{4-}$ (La contributes two 6*s* electrons and one 4*f* electron to the skeletal bonding of the cage).[837] In the cages with 12- and 14-vertices, each group 14 atom (Ge or Sn) gains one electron and behaves as a pseudo group 15 atom like As or Bi. Particularly, Eu^{2+} cation inside $[Eu@Sn_6Bi_8]^{4-}$ adopts a high-spin state (S = 7/2) according to magnetic measurement as well as DFT calculations.[836] It is also interesting to point out that a 14-vertex fullerene-like endohedral cage similar to the structure in Figure 94b has been theoretically predicted for $M@Si_{14}$ clusters (M = V, W, Ta), but none of them satisfy the electron count required by Wade−Mingos rules, as discussed in Section 5.3.5.

Analogous to the synthesized intermetalloid anions of $[V@Ge_8As_4]^{3-}$ and $[Nb@Ge_8As_6]^{3-}$, Pham and Nguyen[844] theoretically proposed a series of endohedral compound cages $M@A_8E_6$ (A = Si, Ge; E = P, As; M = Cr, Mo, W) with structure similar to the one in Figure 94b. The 68 valence electrons in each of these endohedral clusters occupy the superatomic orbitals $1S^21P^61D^{10}1F^{14}1G^{18}2S^22P^62D^{10}$ (see Figure 95), leading to closed electronic shells. Meanwhile, the A_8E_6 cages donate about four electrons to the central transition metal dopant, thereby attaining a full d^{10} configuration for the metal atom. The simultaneous closure of both superatomic orbital of $M@A_8E_6$ and central *d* orbital of dopant M results in high D_{3h} symmetry and singlet spin state, signifying enhanced stability of these ternary intermetalloid clusters. Similarly, Tam et al.[845] proposed an endohedral cage $Cr@Si_8N_6$ and its isoelectronic cluster ions, $[V@Si_8N_6]^-$ and $[Mn@Si_8N_6]^+$. Their B3P86/LanL2DZ calculations and chemical bonding analysis revealed the vital role of doped metal atom/ion in stabilizing the Si_8N_6 cage. As a result, $[V@Si_8N_6]^-$ and $Cr@Si_8N_6$ cages (C_{2v} symmetry) adopt a singlet spin state and possess a sizeable HOMO−LUMO gap of 2.22 and 1.88 eV, respectively.

Besides the above discussed systems, we should point out that there are in principle many other possible compound cage clusters for endohedral doping. For example, encapsulation of 3*d* and 4*d* transition metal atoms in Si_nC_n (n = 7−10) cage-like clusters has been considered by Song *et al.*.[846] According to their DFT calculations at the PBE/DNP level, most of the 3*d* and 4*d* transition metal atoms (except Cu, Zn, Pd, Ag, and Cd) can be encapsulated in the Si_nC_n cage. Within the considered size range, the Si_8C_8 cage is the energetically optimal cage for encapsulating a metal atom. The total magnetic moments of the resulting $M@Si_8C_8$ clusters oscillate from 0 to 1 μ_B across the periodic table, and their HOMO−LUMO gaps are in the range of 0.28−1.06 eV. Recently, Pham *et al.*[847] constructed a $Si_8B_3N_3$ heterocage by substituting Si sites of the rhombus face in the Si_{14} cage with B and N atoms and then endohedrally

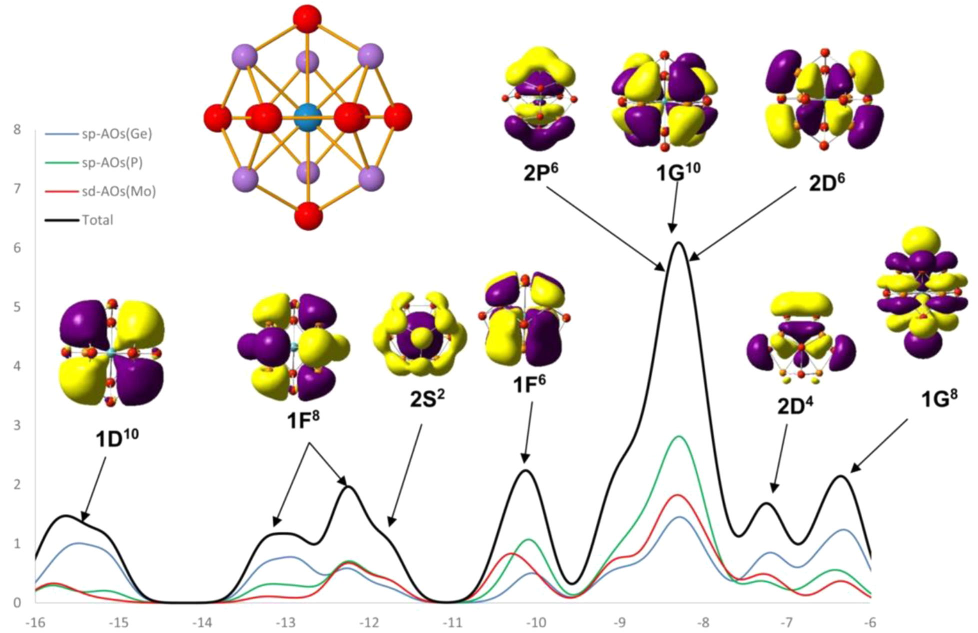

Figure 95. Gaussian broadened partial DOS and total DOS maps of the Mo@Ge_8P_6 heterofullerene. Inset shows the cluster geometry. Reproduced with permission from ref 844. Copyright 2017 American Chemical Society.

doped a Mn^+ cation inside the cage. According to their BP86/6-311+G(d) calculations, the valence electrons in the resulting $[Mn@Si_8B_3N_3]^+$ cage (C_s symmetry) occupy an electronic shell configuration of $1S^21P^61D^{10}1F^{14}1G^{12}2S^22P^62D^{10}$, and the high spin moment of the Mn^+ cation is completely quenched by the hetero-silicon fullerene.

To summarize, clusters of many compounds such as II−VI and III−V have attracted very wide attention because of their interesting electronic and optical properties. Some of them form cage structures similar to carbon fullerenes and have a large HOMO−LUMO gap while in some other cases, novel endohedral core-shell structures are formed. Some studies have been done to dope these cages with a variety of atoms. This helps modify their properties since some electronic states fall in the HOMO−LUMO gap, thus changing the reactivity of the cages all together. On the other hand, transition metal atoms generally occupy the cation site and if endohedrally doped, they keep their magnetic moments to a large extent as in the case of hydrogenated silicon fullerenes. Experimental studies on these systems are very limited and further work would be certainly helpful to develop the endohedrally doped clusters of these compounds, which offer interesting possibility to design their optical, magnetic, and catalytic properties. However, there is significant progress on II−VI discrete-size clusters with 13, 33, and 34 molecules, which have been formed in relatively large quantities using solution route and their doping has also been achieved with e.g. Mn atoms. Furthermore, use of halogen anions could be interesting to form cages in many cases. Noticeably, there already exist some Zintl phases in which endohedral cage clusters are closely packed such as in a FCC lattice. These are very intriguing systems for developing various cluster-assembled materials and exploring their properties.

9. MULTILAYER MATRYOSHKA CAGES AND CORE-SHELL STRUCTURES

Most of the endohedral clusters discussed above have one atom inside a cage. These can also be viewed as core-shell clusters with the core made of just one atom. One can then generalize the concept of endohedral doping and consider a group of endohedral atoms to form a broader category of core-shell clusters and also multilayer (onion-like) clusters. In this regard, a fascinating family of doped cage clusters called Matryoshka clusters, with multilayer high symmetry core-shell structure, have been discovered in experiments and extensively studied in theory.

In a pioneering study in 2003, Moses *et al.*[99] reported the synthesis and characterization of the $[As@Ni_{12}@As_{20}]^{3-}$ Zintl anion in the crystalline compound of $[P(C_4H_9)_4]_3[As@Ni_{12}@As_{20}](en)_{1.5}$ salt, which is a monoclinic crystal with space group P21/n. The $[As@Ni_{12}@As_{20}]^{3-}$ anion with nearly perfect I_h symmetry discretely resides on a general position in the crystal lattice without any crystallographically imposed symmetry. The $[As@Ni_{12}@As_{20}]^{3-}$ complex was further characterized by the LDI-TOF MS. As shown in Figure 96, a distinctive mass envelope for the oxidized molecular ion, $[As@Ni_{12}@As_{20}]^-$, can be seen. As displayed in Figure 97, the $[As@Ni_{12}@As_{20}]^{3-}$ cluster comprises an icosahedral $[As@Ni_{12}]^{3-}$ fragment residing at the center of an As_{20} dodecahedral cage to form an onionskin-like structure. Later, this unique 33-atom multilayer structure with icosahedral point group symmetry was nicknamed as “Matryoshka nesting doll” by King and Zhao.[848]

Soon after its discovery, several groups carried out subsequent DFT calculations to illuminate the bonding character and electronic properties of $[As@Ni_{12}@As_{20}]^{3-}$ cluster[850−853]. This icosahedral Matryoshka cluster was found to be vibrationally stable, with the harmonic frequencies ranging between 49 and 302 cm^{-1}. The formation of the Matryoshka $[As@Ni_{12}@As_{20}]^{3-}$ cluster from its subunits of $[As@Ni_{12}]^{3-}$ icosahedron and As_{20} dodecahedral cage gains about 26−28 eV in energy,[850−852] reflecting relatively strong bonding between these two subunits. With three extra electrons, the $[As@Ni_{12}@As_{20}]^{3-}$ cluster achieves a close-shell electronic configuration with a HOMO−LUMO gap of about 1.45 eV using the PBE functional. Both the HOMO and LUMO are fivefold-degenerate

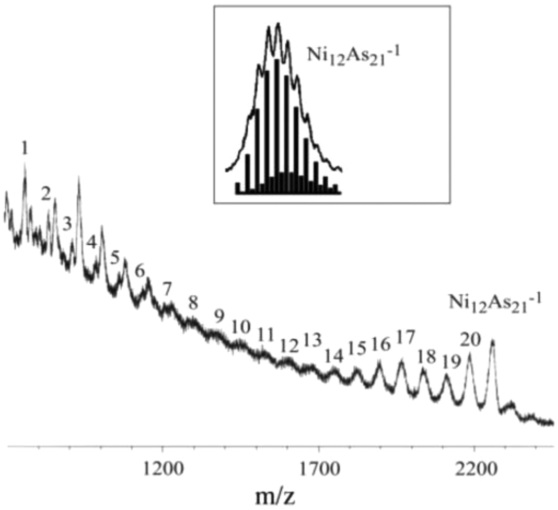

Figure 96. LDI-TOF mass spectrum of the $[PBu_4]_3[As@Ni_{12}@As_{20}]\cdot1.5en$ salt. The numbers denote the clusters of the $[Ni_{12}As_n]^-$ series, where $n = 21$ to 0 inclusively. (Inset) Enlarged view of the observed and calculated mass envelope of the $[Ni_{12}As_{21}]^-$ ion. Reproduced with permission from ref 99. Copyright 2003 American Association for the Advancement of Science.

with h_u and h_g symmetries, and they are delocalized on the Ni atoms and the surface As atoms, respectively.

Inspired by the icosahedral Matryoshka $[As@Ni_{12}@As_{20}]^{3-}$ cluster with an unusual atomic structure and peculiar electronic properties, there have been some theoretical attempts to explore its possible analogues, including $[Sb@Pd_{12}@Sb_{20}]^{3-}$,[852] $Kr@Ni_{12}@As_{20}$, $Kr@Ni_{12}@Sb_{20}$, $Kr@Ni_{12}@Bi_{20}$, $Kr@Pd_{12}@Sb_{20}$, $Kr@Pd_{12}@Bi_{20}$, $Xe@Ni_{12}@As_{20}$, $[Br@Ni_{12}@As_{20}]^-$,[853] $Ge@Zn_{12}@Ge_{20}$, and $As@Zn_{12}@Ge_{20}$.[854] But no experimental breakthrough could be made until Stegmaier and Fässler[100] reported a completely analogous $[Sn@Cu_{12}@Sn_{20}]^{12-}$ icosahedral Matryoshka doll anion in $A_{12}Cu_{12}Sn_{21}$ intermetallics (A = Na, K) in 2011. Their synthesized Zintl compounds $Na_{12}Cu_{12}Sn_{21}$ and $K_{12}Cu_{12}Sn_{21}$ crystallized in an FCC lattice with space group $Pn\bar{3}m$, in which the discrete $[Sn@Cu_{12}@Sn_{20}]$ clusters with D_{3d} point symmetry (deviated from I_h) occupy the vertices and face centers of an FCC lattice and are separated from each other by the alkali metal atoms (see Figure 98). Using the atomic coordinates from the single-crystal XRD data and assuming a complete charge transfer from the alkali metal atoms to the $Sn@Cu_{12}@Sn_{20}$ clusters, they performed *ab initio* single-point calculation of $[Sn@Cu_{12}@Sn_{20}]^{12-}$ cluster anion at the B3LYP/(PP-)Def2-TZVP level and obtained a HOMO−LUMO gap of 1.34 eV, which is comparable to that of $[As@Ni_{12}@As_{20}]^{3-}$. The molecular orbital analysis demonstrated that the $[Sn@Cu_{12}@Sn_{20}]^{12-}$ cluster can be considered as an entity with delocalized bonding within and between the structural subshells. Further band structure calculations revealed that the $A_{12}Cu_{12}Sn_{21}$ solids are semiconductors with moderate band gap (0.3 eV for $Na_{12}Cu_{12}Sn_{21}$ and 0.8 eV for $K_{12}Cu_{12}Sn_{21}$) and can be considered as salt-like compounds just like the Zintl phases.

Based on the knowledge that icosahedral Matryoshka clusters of $[As@Ni_{12}@As_{20}]^{3-}$ and $[Sn@Cu_{12}@Sn_{20}]^{12-}$ have 108 valence electrons without counting the filled d^{10} shells for As, Ni, Sn, and Cu, Huang *et al.*[855] proposed a generic 108-electron rule and further designed a series of Matryoshka clusters of $E@M_{12}@E_{20}$ (E = Sn, Pb; M = Mg, Zn, Cd) with large HOMO−LUMO gaps (1.29−1.54 eV using PW91 functional) and low formation energies (0.06−0.21 eV/atom). By DFT-based GA global search of the potential energy surface, they proved that icosahedral Matryoshka structures are indeed the ground state configurations of these $E_{21}M_{12}$ clusters. As a representative, Figure 99 depicts the energy levels and spatial distribution of the molecular orbitals of $Sn@Mg_{12}@Sn_{20}$. From the energy level distribution and the nodal shape of the orbitals, one can identify a series of occupied superatomic orbitals in the sequence of 1S, 1P, 2S, 1D, 1F, 1G, 2P, 3S, 2D, 1H, 2F, 3P, and 1I corresponding to the 54 lowest-lying valence molecular orbitals. Among them, 1S, 1P, 2S, 1D, 1F, 1G, 2P, 3S, 2D, and 3P orbitals are completely filled and account for 76 electrons. The 2F, 1H, and 1I superatomic orbitals split into two, three, and four components, respectively, due to the icosahedral ligand field[856] as shown in Figure 99 and are only partially filled accommodating 36 electrons. In other words, the "magic number" of 108 electrons of these icosahedral Matryoshka clusters originates from the high I_h symmetry and consequently the splitting of superatomic orbitals of high angular momentum. The universal arrangement of molecular orbitals has been observed in four icosahedral Matryoshka clusters considered, i.e., $[As@Ni_{12}@As_{20}]^{3-}$, $[Sn@Cu_{12}@Sn_{20}]^{12-}$, $Sn@Mg_{12}@Sn_{20}$, and $Sn@Zn_{12}@Sn_{20}$, indicating the existence of a family of Matryoshka clusters with similar geometries and electronic properties.

Further replacing the Zn or Cd atoms with a filled d^{10} shell by Mn atoms having a half-filled d^5 shell leads to two new icosahedral Matryoshka clusters with a giant magnetic moment (28 μ_B), that is, $Sn@Mn_{12}@Sn_{20}$ and $Pb@Mn_{12}@Pb_{20}$. DFT calculations at the PW91/DNP level by Huang *et al.*[855] showed

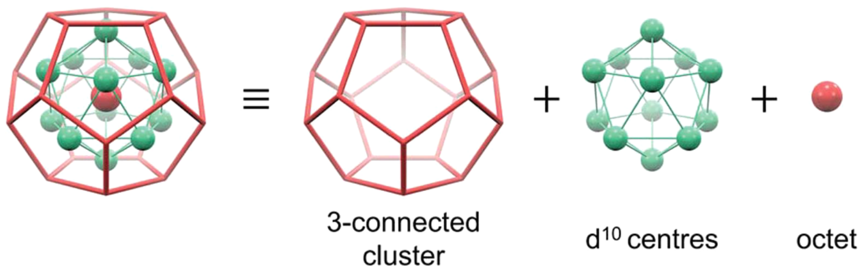

Figure 97. Chemical bonding model for understanding the icosahedral Matryoshka clusters by taking $[As@Ni_{12}@As_{20}]^{3-}$ as an example. The outer 3-connected polyhedron (red dodecahedron) is based on the electron precise clusters (5 valence electrons for each vertex); the transition metal centers (green spheres) in the middle layer have a d^{10} electronic configuration; and the core atom (red sphere) is assigned with an octet electronic configuration. There is no classical bonding interactions between these d^{10} centers, and they are held together merely by d^{10}-d^{10} interactions (thin green bonds). Reproduced with permission from ref 849. Copyright 2015 Royal Society of Chemistry.

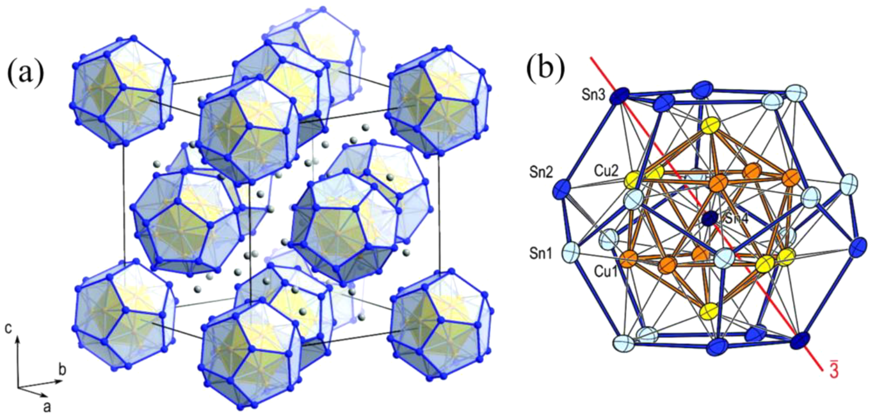

Figure 98. (a) Representation of the unit cell of the $A_{12}Cu_{12}Sn_{21}$ phase. The $Sn@Cu_{12}@Sn_{20}$ clusters adopt an FCC arrangement. Sn atoms are represented with blue, Cu atoms with orange, and A atoms with gray color. (b) Representation of the $Sn@Cu_{12}@Sn_{20}$ cluster units in $A_{12}Cu_{12}Sn_{21}$. Different color shades are used to distinguish the Wyckoff positions. The crystallographic 3-fold inversion axis 3 is drawn as a red line. Thermal ellipsoids (atomic displacement parameters) are shown with 70% probability level for $K_{12}Cu_{12}Sn_{21}$. Reproduced with permission from ref 100. Copyright 2011 American Chemical Society.

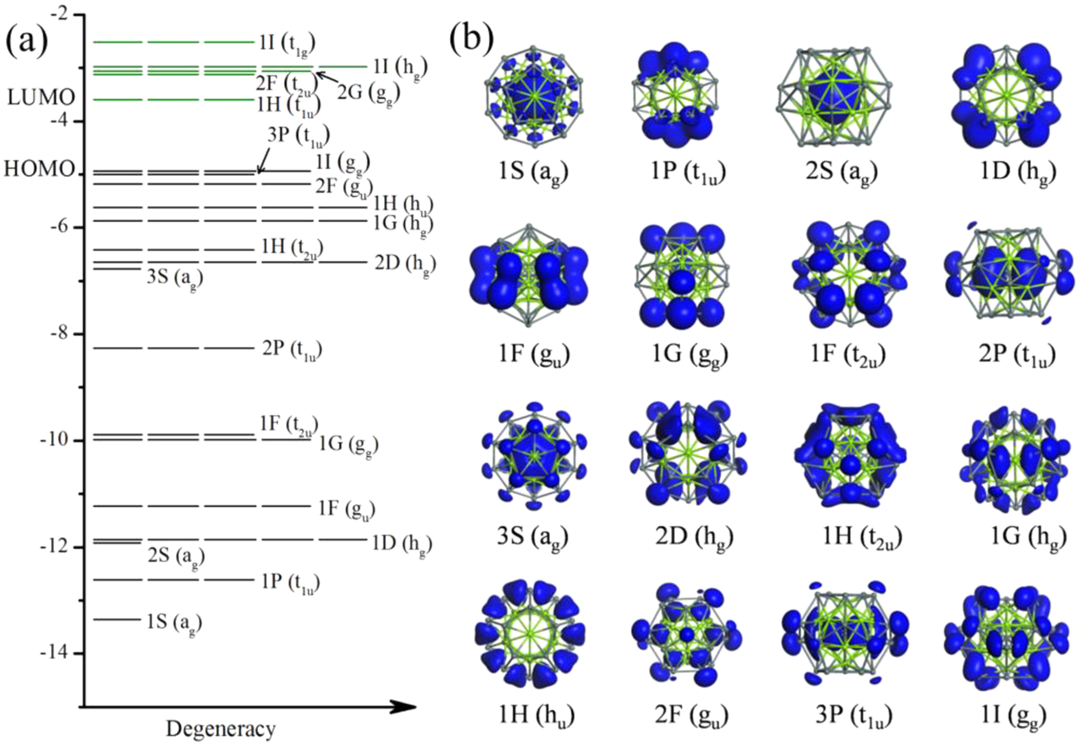

Figure 99. (a) Energy levels (in eV) for the molecular orbitals of the $Sn@Mg_{12}@Sn_{20}$ cluster, which can be assigned to a series of superatomic orbitals corresponding to the indicated spherical harmonics. A few unoccupied levels are also shown and highlighted in green color. (b) Isosurfaces for the spatial distribution of the occupied superatomic orbitals of $Sn@Mg_{12}@Sn_{20}$ cluster. Reproduced with permission from ref 855. Copyright 2014 Springer Nature.

that these two magnetic superatoms exhibit moderate HOMO−LUMO gaps of 0.382 and 0.614 eV, and low formation energies of 0.346 and 0.507 eV/atom (by taking the energy of each elemental solid as reference), respectively. More importantly, these two clusters can keep their identities and retain their magnetic moments in the cluster assemblies due to weak inter-cluster interactions (binding energies of 0.359 and 0.291 eV for $[Sn@Mn_{12}@Sn_{20}]_2$ and $[Pb@Mn_{12}@Pb_{20}]_2$, respectively). The spin-polarized electronic structure and transport properties of the icosahedral Matryoshka cluster $Pb@Mn_{12}@Pb_{20}$ were further examined by L. Zhang *et al.* using a nonequilibrium Green's function technique combined with DFT.[857] As shown in Figure 100, the spin-resolved transmission spectra of the molecular junctions formed by sandwiching a $Pb@Mn_{12}@Pb_{20}$ cluster between two Au(100) electrodes exhibit a robust spin filtering efficiency of 83.2%, and the conductance under the small bias voltage is mainly contributed by the spin-up electrons. Further calculations demonstrated that such spin filtering effect is not sensitive to the anchoring Au−Pb distance and the adopted electrode materials, e.g., Li(100) and Cu(100) electrodes. Therefore, this unique magnetic icosahedral Matryoshka cluster with huge magnetic moment is a promising building block for the spin-filtering device in molecular spintronics.

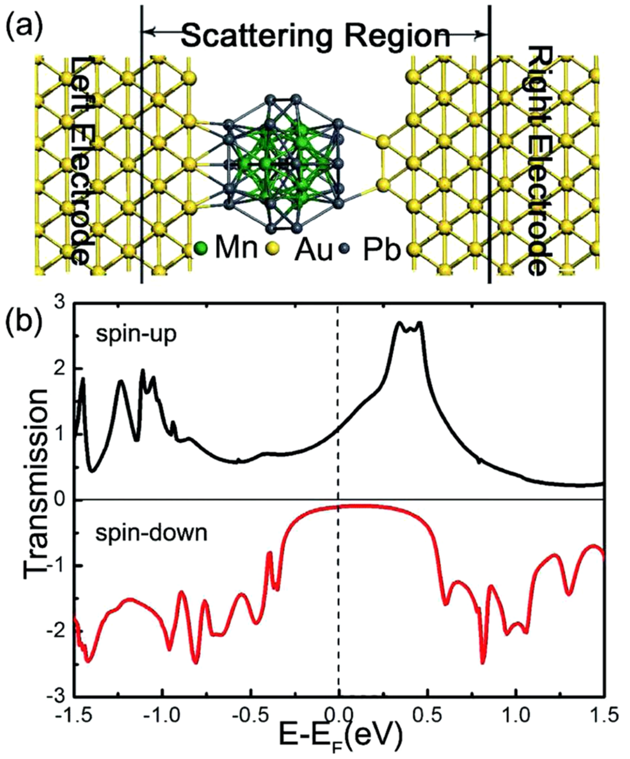

Figure 100. (a) Proposed molecular junction, in which a Pb@Mn_{12}@Pb_{20} cluster is sandwiched between two Au(100) electrodes. (b) Zero-bias energy dependent spin-resolved transmission spectra. Reproduced with permission from ref 857. Copyright 2017 Royal Society of Chemistry.

The SOC effects in the icosahedral Matryoshka clusters, E@M_{12}@E_{20} (E = Ge, M = Zn; E = Sn, M = Mg, Mn, Zn, Cd; E = Pb, M = Mg, Mn, Cd, Hg) have been systematically investigated by Long *et al.*[858] using the PAW potentials with a SOC term added to the scalar relativistic DFT Hamiltonian. For the Matryoshka superatoms containing heavy elements like Pb, SOC was found to play a substantial role in reducing the atomization energy and the HOMO−LUMO gap to a certain extent.

King and Zhao[848] proposed a chemical bonding model to interpret the high stability of $[As@Ni_{12}@As_{20}]^{3-}$ cluster. First, the central trivalent As^{3-} anion is isoelectronic to noble element Kr. In the intermediate icosahedral layer, Ni atom has a filled d^{10} shell and can be considered as pseudo noble gas. Then, the outer As_{20} dodecahedral shell has a total of 100 valence electrons. Among them, 60 electrons are required for two-center two-electron (2c−2e) bonds along the 30 edges of the dodecahedron and the rest of the 40 electrons contribute to the lone pair on each of the 20 As atoms. The overlap between the As_{20} dodecahedral and Ni_{12} icosahedral layers generates 20 tetrahedral $AsNi_3$ cavities, providing the location of 4c−2e bonds to accommodate the 40 lone-pair electrons. In short, the Ni_{12} icosahedron is well positioned to attain 40 skeletal electrons, corresponding to a magic number of a jellium cluster analogous to the well-known $[Al_{13}]^-$ superatom.[149] Later, the $[\{As@Ni_{12}\}^{3-}@\{As_{20}\}^0]$ form of $[As@Ni_{12}@As_{20}]^{3-}$ was confirmed by Carey *et al.*,[859] while the same group proposed that $[Sn@Cu_{12}@Sn_{20}]^{12-}$ can be regarded formally as $[\{Sn@Cu_{12}\}^{4-}@\{Sn_{20}\}^{8-}]$ with the inner-core having close-shell $1S^21P^62S^21D^{10}$ superatomic orbitals.[860]

Sheong *et al.*[849] proposed a revised electron counting model by dividing each of the icosahedral Matryoshka clusters in a layer-by-layer manner and allowing each layer to follow a simple electron-filling rule. As illustrated in Figure 97, the octet electron rule is applicable to the core atom; each of the atoms in the middle layer should have a stable d^{10} configuration; the exterior dodecahedron as 3-connected polyhedron obeys Mingos' polyhedral skeletal electron pair theory and thus requires totally 100 valence electrons.[139] For $[As@Ni_{12}@As_{20}]^{3-}$ cluster, Sheong's model is actually the same as that by King and Zhao;[848] whereas $[Sn@Cu_{12}@Sn_{20}]^{12-}$ should be regarded formally as $[\{Sn\}^{4-}@\{Cu_{12}\}^{12+}@\{Sn_{20}\}^{20-}]$.

Recently, Y. Wang *et al.*[101] synthesized $[Sb@Ni_{12}@Sb_{20}]^{-/+}$ and $[Sb@Pd_{12}@Sb_{20}]^q$ (q = +1, −1, −3, −4) clusters in the laboratory, fulfilling the earlier theoretical hypothesis by Zhao and Xie.[852] In particular, in the monoclinic crystalline phases of $[Sb@Pd_{12}@Sb_{20}]^{q-}/PBu_4$ (q = 3, 4) salts, $[Sb@Pd_{12}@Sb_{20}]^{q-}$ clusters in the two charge states are structurally identical, both having icosahedral Matryoshka geometry with nearly perfect I_h point group symmetry. All-electron DFT calculations using an analytic density functional on the gas-phase clusters revealed a large HOMO−LUMO gap of 1.33 eV in $[Sb@Pd_{12}@Sb_{20}]^{3-}$, which keeps I_h point group symmetry. In contrast, due to the extra unpaired electron, the $[Sb@Pd_{12}@Sb_{20}]^{4-}$ cluster undergoes a Jahn−Teller distortion from I_h to D_{3d} symmetry and possesses a small gap of 0.1 eV only. Moreover, gas-phase clusters of $[Sb@M_{12}@Sb_{20}]^{-/+}$ (M = Ni, Pd) were detected in the LDI-TOF MS. In another recent experiment by Li *et al.*,[102] the Matryoshka $[Sb@Pd_{12}@Sb_{20}]^{3-}$ clusters were isolated as $[K(2,2,2\text{-cryptand})]^+$ salt in hexagonal lattice with space group $R\overline{3}c$, while the electron-rich $[Sb@Pd_{12}@Sb_{20}]^{4-}$ clusters were isolated as $[K(18\text{-crown-}6)]^+$ salt in cubic lattice with space group $Pa\overline{3}$.

Table 23 summarizes key structural parameters, HOMO−LUMO gap, and binding energy of the above discussed icosahedral Matryoshka clusters $[E@M_{12}@E_{20}]^{q-}$ with 108 valence electrons from experimental measurements and theoretical calculations. Using conventional exchange-correlation functionals like PBE, PW91, and BP86, most of these Matryoshka clusters have an appreciable HOMO−LUMO gap of around 1.3−1.5 eV, except the two magnetic species ($Sn@Mn_{12}@Sn_{20}$ and $Pb@Mn_{12}@Pb_{20}$) and $[Br@Ni_{12}@As_{20}]^-$. The theoretical binding energies are in the range 2.01−5.21 eV.

Besides the icosahedral Matryoshka clusters following the 108 electron rule, any bimetallic cluster can possibly form the 33-atom onionskin structure if the atomic sizes of the two elements match each other (e.g. $Ni_{13}@Mg_{20}$,[861] $Pt_{13}Ag_{20}$, and $Pt_{13}Pd_{20}$[862]). In an earlier study, J. L. Wang *et al.*[863] proposed an interesting $[Mn_{13}@Au_{20}]^-$ cluster, which has a slightly distorted icosahedral Matryoshka structure with a giant magnetic moment of 44 μ_B. A recent study by Bai *et al.*[864] considered a variety of Matryoshka $M@Mn_{12}@Au_{20}$ clusters, and the total magnetic moments from planewave PBE calculations were 52 μ_B, 17 μ_B, 0 μ_B, 34 μ_B, 35 μ_B, 16 μ_B, and 16 μ_B for M = Fe, Co, Ni, Ru, Rh, Pd, and Pt, respectively. Kou *et al.*[865] explored the energetic stability and electronic and magnetic properties of 20 $[M_{13}@Bi_{20}]^-$ clusters (M = 3*d* and 4*d* elements) with the icosahedral Matryoshka configuration at the PW91/DND level of theory. They found that a large portion of M_{13} clusters can be favorably encapsulated into the Bi_{20} cage with appreciable core-shell bonding energy of over 20 eV. Among them, $[Mn_{13}@Bi_{20}]^-$ cluster with a modest HOMO−LUMO gap of 0.37 eV and a large magnetic moment of 36 μ_B was identified as a magnetic superatom with the half-filled subshell.

Table 23. Key Structural Parameters and Electronic Properties of 108-Electron Icosahedral Matryoshka Clusters $[E@M_{12}@E_{20}]^{q-}$ from Experimental XRD Measurement and DFT Calculations: Average $E-M_{12}$ Distance (R_1) and $M_{12}-E_{20}$ Distance (R_2), HOMO−LUMO gap (E_{HL}), and Binding Energy per Atom (E_b)[a]

Cluster	Method	R_1 (Å)	R_2 (Å)	E_{HL} (eV)	E_b (eV)
$[As@Ni_{12}@As_{20}]^{3-}$[99]	XRD	2.558	2.396		
$[As@Ni_{12}@As_{20}]^{3-}$[850,851]	PBE/Gaussian basis	2.59	2.44	1.45	
$[As@Ni_{12}@As_{20}]^{3-}$[852]	PW91/Planewave	2.65	2.43	1.44	5.21
$[As@Ni_{12}@As_{20}]^{3-}$[853,854]	BP86/LANL2DZ	2.579	2.488	1.41	3.45
$[As@Ni_{12}@As_{20}]^{3-}$[859]	PBE/TZ2P	2.591	2.418		
$[Br@Ni_{12}@As_{20}]^{-}$[853]	BP86/LANL2DZ	2.656	2.792	1.07	3.37
$[Sb@Pd_{12}@Sb_{20}]^{3-}$[101]	XRD, analytic density functional/DZVP	2.856	2.713	1.33	
$[Sb@Pd_{12}@Sb_{20}]^{3-}$[102]	XRD, B3LYP	2.850	2.709	2.24	
$[Sb@Pd_{12}@Sb_{20}]^{3-}$[852]	PW91/Planewave	3.87	2.69	1.41	4.49
$[Sn@Cu_{12}@Sn_{20}]^{12-}$ (Na)[100]	XRD	2.631	2.766		
$[Sn@Cu_{12}@Sn_{20}]^{12-}$ (K)[100]	XRD, B3LYP/(PP-)Def2-TZVP	2.625	2.760	1.34	
$[Sn@Cu_{12}@Sn_{20}]^{12-}$[859,860]	PBE/TZ2P	2.697	2.865		
$Ge@Zn_{12}@Ge_{20}$[854]	BP86/LANL2DZ	2.802	2.813	1.39	2.01
$Sn@Mg_{12}@Sn_{20}$[855]	PW91/DND	2.996	3.029	1.38	2.79
$Sn@Zn_{12}@Sn_{20}$[855]	PW91/DND	2.827	2.907	1.47	3.43
$Sn@Cd_{12}@Sn_{20}$[855]	PW91/DND	3.128	3.034	1.29	2.60
$Sn@Mn_{12}@Sn_{20}$[855]	PW91/DND	2.569	2.870	0.38	
$Pb@Mg_{12}@Pb_{20}$[855]	PW91/DND	3.073	3.140	1.50	2.52
$Pb@Zn_{12}@Pb_{20}$[855]	PW91/DND	2.919	3.033	1.54	2.97
$Pb@Cd_{12}@Pb_{20}$[855]	PW91/DND	3.187	3.147	1.27	2.28
$Pb@Mn_{12}@Pb_{20}$[855]	PW91/DND	2.629	3.016	0.61	

[a] For some cases, DFT single-point calculations were performed using cluster structure from experimental XRD data.

It is noteworthy that there are many other possibilities to achieve clusters with the Matryoshka nesting doll structure beyond the 33-atom onionskin configuration. For instance, J. T. Wang *et al.*[299] proposed an onion-like $B@Co_{12}@B_{80}$ cluster with strong core-shell bonding of ∼30 eV and a sizeable HOMO−LUMO gap of 0.96 eV (using the PBE functional). Starting from the synthesized $[Na_{12}@[(UO_2)(O_2)_{1.5}]_{20}]^{8-}$ clusters,[866] Hu and Kaltsoyannis[867] computationally designed a series of Matryoshka actinide clusters, $[E@Na_{12}@[(UO_2)(O_2)_{1.5}]_{20}]^{10-}$, $[E@Ag_{12}@[(UO_2)(O_2)_{1.5}]_{20}]^{10-}$, and $[E@Mg_{12}@[(UO_2)(O_2)_{1.5}]_{20}]^{2+}$ (E = S, Se, Te, Po). Further replacing Mg with Mn and U with Np or Pu leads to some stable Matryoshka clusters with very high spin ground states. Among them, $[E@Mn_{12}@[(PuO_2)(O_2)_{1.5}]_{20}]^{2+}$ possesses the highest spin value yet reported for a molecular cluster (S = 100/2). Meanwhile, the closed-shell central S^{2-} anion plays an essential role in stabilizing the highest spin electronic configurations. Beyond I_h symmetry, a novel $[Ln_4@Ln_4]$ (Ln = Eu, Gd, Dy) Matryoshka tetrahedron was developed for building 3D metal organic frameworks (MOFs).[868]

To briefly summarize this section, $[As@Ni_{12}@As_{20}]^{3-}$ Zintl anion together with many of its isoelectronic and isostructural clusters such as $[Sn@Cu_{12}@Sn_{20}]^{12-}$, $[Sb@Pd_{12}@Sb_{20}]^{3-}$, and $Sn@Mg_{12}@Sn_{20}$, constitute a fantastic family of Matryoshka clusters with high I_h symmetry, unified pattern of molecular orbitals, and large HOMO−LUMO gap. Besides them, there are also many possibilities to achieve other kinds of Matryoshka clusters with high stability and desired properties. In the future, we expect experimental synthesis of more Matryoshka clusters with either icosahedral or other symmetry. More importantly, it is imperative to study the physical and chemical properties of these clusters in both gas phase and crystalline Zintl phase and explore their potential applications, such as the prototype spin filter proposed for $Pb@Mn_{12}@Pb_{20}$.

10. ASSEMBLIES OF ENDOHEDRALLY DOPED CAGE CLUSTERS

In a pioneering paper in 1992, Khanna and Jena[152] suggested that the stability of a cluster can be significantly enhanced by changing its size and/or composition to achieve a closed electronic shell as well as a closed atomic shell. Intuitively, such clusters with both electronic and geometric shells closed would interact weakly with each other when they are soft landed on a non-interacting substrate. Thus, it can be expected that materials assembled from such clusters can retain the properties of individual clusters. Taking Mg_4 cluster with closed electronic shell of $1S^2 1P^6$ and perfect tetrahedron geometry as a prototype, *ab initio* calculations demonstrated that, when two Mg_4 clusters are brought close to each other, the individual clusters keep their structural and electronic integrity. Khanna and Jena further suggested that $C@Al_{12}$ and $Si@Al_{12}$ clusters with perfect icosahedron geometry and 40 electrons (which is a magic number for electronic shell closure within the spherical jellium model) should also hold the potential for cluster assemblies.

Actually, many of the endohedrally doped cage clusters discussed in previous sections may satisfy the above criteria of closed atomic and electronic shells and thus provide versatile building blocks for novel cluster-assembled materials.[10−12] In the following, we present an overview of the relevant cluster assemblies of different dimensions, from 0D dimers or aggregates, to 1D nanotubes and 2D monolayers, and finally to 3D crystals.

10.1. Dimers and Aggregates of Endohedrally Doped Cages

We start from the dimers of endohedrally doped cage clusters, where the key issue is the cluster−cluster interaction. From the point of view of cluster assembly, ideally, when two clusters form a dimer, the interaction between them should not be too strong such that each of them can maintain its structural and electronic identity to a large extent. However, owing to the high surface activity and low coordination number, the two clusters would tend to interact with each other and coalesce into a bigger cluster in most situations to lower the energy. In this regard, endohedrally doped cage clusters with near spherical geometry and high stability offer opportunities to reduce the cluster−cluster interaction and retain the identity of individual clusters.

In the literature, many *ab initio* calculations have been conducted to explore dimers of various endohedrally doped cage clusters, including $[Si@Al_{12}]_2$,[869] $[B@Al_{12}][P@Al_{12}]$,[869] $[Al@Al_{12}-P@Al_{12}]$,[869] $[Zr@Si_{16}]_2$,[48] $[Ti@Ge_{16}]_2$,[53] $[Ta@Si_{16}F]_2$,[426] $[W@Si_{12}]_2$,[870] $[Cr@Si_{12}]_2$,[871] $[Ti@Si_{16}]_2$,[48,872] $[Sc@Si_{16}K]_2$ and $[V@Si_{16}F]_2$,[872] $[Sc@Si_{16}-V@Si_{16}]$,[873] $[Ta@Si_{16}]_2$,[874] $[V_2Si_{20}]_2$,[442] $[Mn@Sn_{12}]_2$,[618,619] $[MPb_{10}]_2$ (M = Fe, Co, Ni),[638] $[Ti@Au_{14}]_2$,[695] $[Mo@Au_{12}]_2$,[875] $[W@Au_{12}]_2$,[875] $[M@Cd_nS_n]_2$ (M = Y, Zr, Nb, Mo, Tc, Ru, Rh, Rh, Pd, Ag, Cd; n = 12, 16),[803] and $[A@X_{12}@A_{20}]_2$ (A = Sn, Pb; X = Mg, Zn, Cd, Mn).[855] However, it turns out that most of the aforementioned doped clusters with cage-like structures and closed electronic shells, such as $Si@Al_{12}$, $W@Si_{12}$, $Zr@Si_{16}$, $Ti@Au_{14}$, $Mo@Au_{12}$, and $W@Au_{12}$, still interact strongly with each other by forming chemical bonds (with intercluster binding energy larger than 1 eV).[695,869,870,872,875] Consequently, the structural identity and unique electronic properties of each of these clusters cannot be well retained in the cluster dimers.

In an early paper by Kumar and Kawazoe,[48] the intercluster interaction in two dimers of doped Si_{16} cluster were comparatively studied using the PW91 functional and planewave basis set, and the optimized structures of $[Zr@Si_{16}]_2$ and $[Ti@Si_{16}]_2$ are shown in Figure 101. For the $Zr@Si_{16}$ cluster with fullerene-like cage structure, the interaction between two clusters is relatively strong, as evidenced by the binding energy of 1.345 eV and intercluster covalent Si−Si bond of 2.52 Å. Accordingly, the HOMO−LUMO gap reduces from 1.58 eV for $Zr@Si_{16}$ monomer to 0.673 eV for $[Zr@Si_{16}]_2$ dimer. In contrast, the intercluster interaction between two $Ti@Si_{16}$ FK polyhedra was rather weak, and it did not change significantly the atomic structure of the individual clusters. The calculated intercluster binding energy, intercage Si−Si distance, and HOMO−LUMO gap of $[Ti@Si_{16}]_2$ dimer are 0.048 eV, 4.04 Å, and 2.211 eV (2.238 eV for monomer), respectively. Similar results were obtained in $[Ti@Ge_{16}]_2$ dimer in a subsequent study by Kumar and Kawazoe.[53] The calculated intercluster binding energy, inte-cage Ge−Ge distance, and HOMO−LUMO gap of $[Ti@Ge_{16}]_2$ dimer are 0.047 eV, 4.50 Å, and 1.729 eV (1.790 eV for monomer), respectively. Therefore, the $Ti@Si_{16}$ and $Ti@Ge_{16}$ clusters with symmetric FK cage and closed electronic shell (see Sections 5.3.6 and 6.1.7 for details) satisfy the criteria for building blocks of cluster-assembled materials proposed by Khanna and Jena[152] and call for further explorations from both experimental and theoretical aspects. Accordingly, assemblies of such clusters as well as other molecular dimers with features of a p−n junction such as $[Sc@Si_{16}][Ta@Si_{16}]$ and $[YSi_{16}][Nb@Si_{16}]$ were explored soon after their discoveries.[369,876,877] It was also pointed out that for $[Ti@Si_{16}]_2$ the fullerene type isomer becomes of lower energy due to stronger intercage interaction between the fullerenes.[872] Accordingly, the atomic structure of such aggregates may depend on the method of preparation.

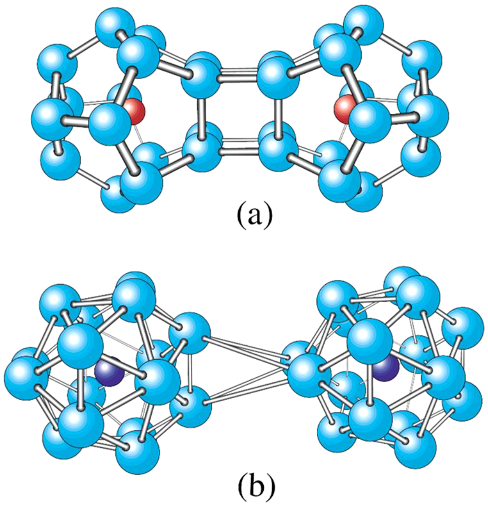
(a)

(b)

Figure 101. Optimized structures of dimers of (a) $Zr@Si_{16}$ with fullerene-like structure and (b) $Ti@Si_{16}$ with FK structure. Reproduced with permission from ref 48. Copyright 2001 American Physical Society.

Another notable building block of cluster assemblies is the magnetic superatom $Mn@Sn_{12}$. DFT calculations using MPWB1K and PW91 functionals predicted an intercage Sn−Sn bond length of 3.7 Å[618] and 3.26 Å,[619] as well as an intercluster binding energy of 0.028 eV[618] and 0.73 eV,[619] respectively. Antiferromagnetic coupling was found between the on-site spin moments of the two Mn atoms (±4.04 μ_B reported in ref 619). With PW91 functional, the HOMO−LUMO gap of $[Mn@Sn_{12}]$ monomer and $[Mn@Sn_{12}]_2$ dimer is 1.12 and 0.88 eV, respectively.[619] Moreover, AIMD simulation showed that $[Mn@Sn_{12}]_2$ dimer remains stable at room temperature after 1 ps, that is, the two cages do not collapse and each monomer maintains its cage skeleton.[619] The moderate intercluster interaction in $[Mn@Sn_{12}]_2$ dimer as well as the fascinating electronic and magnetic properties of $[Mn@Sn_{12}]$ monomer described in Section 6.2 make this magnetic superatom a promising building block for novel magnetic nanomaterials and spintronic devices.

Chen *et al.*[638] have investigated the geometric and magnetic properties of $[MPb_{10}]_2$ (M = Fe, Co, Ni) dimers using PBE functional and DND basis sets. Each individual cluster adopts a bicapped tetragonal antiprism structure with pseudo-D_{4d} symmetry, which is well retained in the cluster dimers. Similar to the case of $[Mn@Sn_{12}]_2$, the strength of intercluster interaction is moderate for $[MPb_{10}]_2$, with the binding energy in the range of 0.63−0.84 eV and intercluster Pb−Pb distance of about 3.4 Å. Accordingly, the HOMO−LUMO gap also reduces by half, i.e., from 0.76−0.83 eV for monomers to 0.31−0.49 eV for dimers. It is interesting to find that the transition metal atoms are ferromagnetically coupled in $[FePb_{10}]_2$ and $[CoPb_{10}]_2$, leading to a total magnetic spin moment of 4 μ_B for these cluster dimers. However, $[NiPb_{10}]_2$ exhibits antiferromagnetic order with on-site spin moment of 0.41 μ_B on Ni atoms.

Beyond cluster dimers, there have been some theoretical studies on the microscopic aggregates or complexes of endohedrally doped clusters, such as $[Al_{13}Na_3O]_m$ and $[Al_{13}K_3O]_m$ (m = 2−6),[878] $[Cu@Al_{12}(K_3O)_n]$ (n = 1−4),[879] $[Cu@Al_{12}(Crypt)_3]_m$ (m = 1−4),[879] $[Ta@Si_{16}F]_m$ (m = 1−8),[426] $[WSi_{12}]_3$,[880] $[Ti@Si_{16}]_m$ (m = 2−9),[872,881] $[Sc@Si_{16}K]_m$ (m = 2−9),[872,881] $[V@Si_{16}F]_m$ (m = 2−9),[872,881] $[Sc@Si_{16}-Ti@$

Si_{16}−V@Si_{16}],[873] and [V_2Si_{20}]$_m$ (m = 2−4).[442] Generally speaking, the component clusters in these aggregates are usually bound by strong covalent bonds. As a consequence, the electronic properties of the building clusters would be largely disturbed. Nevertheless, these finite aggregates can be considered as embryo of the infinite 1D, 2D, and 3D systems, which will be discussed in the following contents.

10.2. From Endohedrally Doped Clusters to Metal Filled One-Dimensional Nanotubes or Nanowires

As discussed in Sections 5.3.1 and 5.3.3, metal doped silicon clusters can adopt short tubular structures, e.g., pentagonal prism for M@Si_{10} and hexagonal prism (or antiprism) for M@Si_{12} with an encapsulated metal atom M. Singh *et al.*[882] found that an initially hexagonal prism Be@Si_{12} cluster deformed to a chair-shaped cluster upon optimization. However, when two such chair-shaped clusters were stacked on top of each other, each Si_6 hexagon became flat with sp^2 bonding due to interaction between Si atoms of the two clusters. Such $Si_{24}Be_2$ tubular clusters could be stacked further to form long nanotubes, also by putting more Be atoms in between the Be@Si_{12} pieces. Subsequently, several tubular clusters with M = Sc, Ti, V, Cr, Mn, Fe, Co, Ni, Cu, Zn, Mo, W, and Eu have been theoretically explored by different groups.[379,402,883−892] Although most of these finite-size Si nanotubes with metal encapsulation are hypothetical, it was reported that the ground state structure of Mo_2Si_{15} is indeed a tubular structure with the Mo_2 dimer inserted in parallel in the three-layer pentagonal Si_{15} prism.[402] A similar tubular structure was found for Mn_2Si_{15} cluster as the most stable isomer, in which the Mn_2 dimer is inserted along the main axis of a (3 × 5) Si_{15} antiprism with D_{5h} symmetry.[886] Also, $Si_{18}W_2$ clusters were reported to be free of hydrogen atom in experiments by Hiura *et al.*[47] and these were shown to have tubular structure with three hexagons of Si in prism framework and two W atoms in between the hexagons.[360]

Inspired by the stability of the endohedrally doped tubular clusters, one can naturally extend from such 0D to 1D infinite nanotube structures. Soon after the developments of endohedrally doped silicon clusters, two groups independently predicted such kind of metal-encapsulated infinite silicon nanotubes.[882−885,893,894] Then, a variety of combinations of nanotube morphologies and endohedral atoms have been explored by DFT calculations, and their 1D electronic band structures and magnetic properties have been intensively investigated. Figure 102 summarizes the schematic structures of 11 kinds of metal-filled silicon nanotubes reported in the literature.

A pentagonal nanotube with stoichiometry of MSi_5 shown in Figure 102a has been predicted for M = Fe[889,890] or Ni[883,885]. It can be viewed as an infinite extension of a metal-centered pentagonal prism, which is the ground state for Mn@Si_{10} and Fe@Si_{10} (see Section 5.3.1). According to DFT calculations, both $NiSi_5$ and $FeSi_5$ nanotubes are nonmagnetic and metallic.[885,890] With the same metal-to-silicon ratio (M : Si = 1 : 5), a metal-encapsulated Si pentagonal antiprism tube (Figure 102b) was reported for the infinite Ni−Si nanotube complex, which also exhibits metallic behavior.[883] It is noteworthy that the term "metallic" is used here in its traditional condensed matter definition, i.e., a material without a gap between the conduction and valence bands.

Among the doped silicon nanotubes, hexagonal nanotubes with stoichiometry of MSi_6 have attracted particular attention.[882,889,890,893−895] Figures 102c and d show two possible configurations of these MSi_6 nanotubes, which differ by the relative position of the Si_6 hexagons to the central M atom. Specifically, M dopant sits in between two Si_6 hexagons (possibly with a small drift) in the structure of Figure 102c, while M dopant is located at the center of each Si_6 hexagon in the structure of Figure 102d. The former structure is favorable for infinite Si nanotubes doped with Cr,[895] Mn[882,893,895], Fe,[889,890] and Be,[882] while the latter one is preferred for Ni- and Co- (with a small drift of 0.27 Å) filled Si nanotubes.[894] All these metal-filled silicon nanotubes are found to be metallic. From the energetic point of view, for a metal dopant it might be more favorable to optimize interaction with one ring rather than to stay in between the successive rings because the Si atoms in successive rings cannot be brought closer beyond a certain distance and that may not be optimal.

As representatives, Figures 103(a, b) show the atomic structures and spin-polarized 1D band structures of Fe_4Si_{24} and Mn_4Si_{24} nanotubes. The Fe-doped hexagonal Si nanotube is ferromagnetic with 2.4 μ_B[894] or 2.18 μ_B[890] magnetic moment on each Fe atom, which is comparable to the value of bulk Fe solid. The hexagonal Si nanotube encapsulated by a Cr atomic chain is also ferromagnetic with a small magnetic moment of 0.34 μ_B per $CrSi_6$ unit.[895] It should be mentioned that a hexagonal prism Cr@Si_{12} cluster has no magnetic moment, but interaction between Si atoms of successive such clusters reduces the interaction of Si atoms with the M atom and leads to finite magnetic moments on the M atoms. Further addition of M atoms between two successive Si_6 hexagons without M atom in between leads to interesting magnetic behavior. Accordingly, for a Mn_4Si_{24} nanotube, an interesting antiferromagnetic state was found, that is, pairs of ferromagnetically coupled Mn atoms are antiferromagnetically coupled with their neighboring pairs (see Figure 103c).[894] The ferromagnetic state for the Mn_4Si_{24} nanotube is metastable and lies only 0.03 eV per Mn_4Si_{24} unit higher in energy. Such small energy difference suggests that transformation from the antiferromagnetic to ferromagnetic state may be achieved by applying a weak magnetic field; thus spin-polarized current flow could be controlled in this way. On the other hand, the Co- and Ni-doped infinite nanotubes are nonmagnetic, but alternatively replacing half of the Mn atoms in the $MnSi_6$ nanotube by Co atoms results in a half-metal hexagonal silicon nanotube encapsulated by a hybrid Mn−Co chain. In the spin-polarized 1D band structure, the Fermi level intersects only in the spin-up band, whereas the spin-down states exhibit semiconducting characteristics. In an earlier study, an infinite $BeSi_{12}$ nanotube was predicted.[882] Starting from Figure 102c, one can remove half of the M dopants periodically and derive this hexagonal nanotube with MSi_{12} stoichiometry (Figure 102f). This has been further considered for finite-length M-doped Si nanotubes (M = Fe, Ni, Co, Ti, V, Cu, Nb, Pd, Mo, Ta, W, Pt).[891]

Huang *et al.*[443] constructed a V-centered Si nanotube (Figure 102e) using the hexagonal antiprism of V_3Si_{12} cluster (which has been discussed in Section 5.3.4) as a building block. In this case, the two V atoms in the unit cell have nonequivalent coordination environments due to the Peierls instability in 1D systems; that is, one V atom forms shorter V−Si bonds (2.678 Å) with 12 neighboring Si atoms, while the other makes longer V−Si bonds (2.784 Å) with 12 surrounding Si atoms. As a consequence, the entire V_2Si_{12} nanotube exhibits a ferrimagnetic behavior with on-site magnetic moments

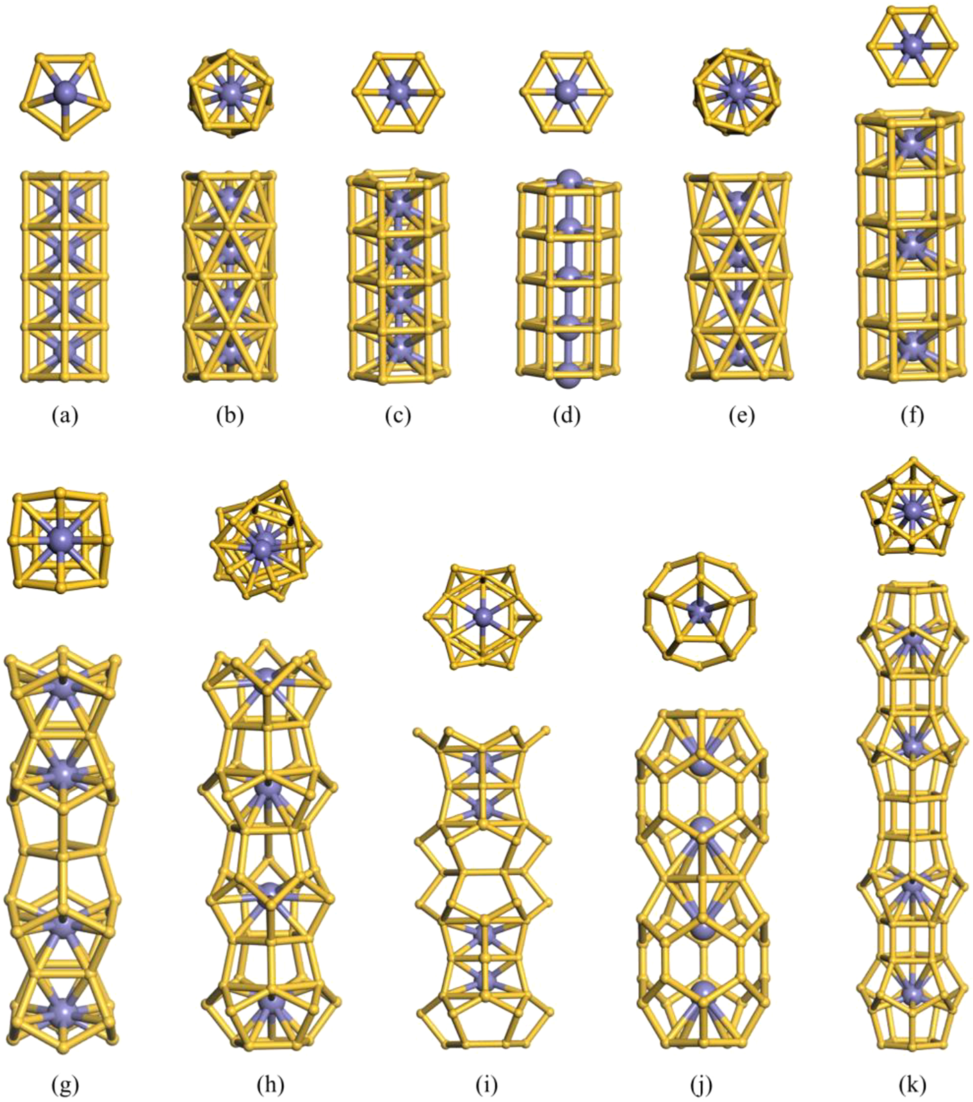

Figure 102. Atomic structures of metal (M) doped silicon nanotubes reported in the literature[443,882,883,885,889−891,893−898] with the following formula per unit cell: (a) MSi_5, (b) M_2Si_{10}, (c) MSi_6, (d) MSi_6, (e) M_2Si_{12}, (f) MSi_{12}, (g) M_2Si_{24}, (h) M_2Si_{30}, (i) M_2Si_{36}, (j) M_2Si_{25}, and (k) M_2Si_{40}. To display the 1D structure, two to five unit cells are plotted. For each structure, top view (upper) and side view (lower) are provided. See the text for detailed discussion of these structures.

of 1.076 μ_B on one V atom and −0.181 μ_B on the other V atom, respectively.

Silicon cage clusters encapsulated by one or two metal atoms can also be utilized as building blocks to construct pearl necklace like nanowires that resemble silicon clathrate.[895−898] The possible fullerene-like Si cages as the elementary building units include Si_{16} (Figure 102g) and Si_{20} (Figure 102h, k) with one M atom in the cage or Si_{24} (Figure 102i) and Si_{30} (Figure 102j) with two M atoms in a cage. The difference between the structures shown in Figures 102h and k is the way the adjacent Si_{20} units are arranged. In the former, a Si_5 pentagon is shared by two cages while in the latter it is not. Early calculations using the planewave and PW91 functional on a nanowire of $Zr@Si_{16}$ found it to be semiconducting.[877] Other nanowires with Cr, Fe, Mn, and Eu doping were theoretically studied.[895−898] Metallic behavior was found for a Cr_2Si_{30} nanowire with the structure in Figure 102i. But semimetallic behavior was obtained for Cr_2Si_{24} and Fe_2Si_{24} nanowires (Figure 102g) as well as the Fe_2Si_{36} nanowire (Figure 102i). Mn_2Si_{24} with the structure in Figure 102g is a semiconductor. Cr_2Si_{30}, Mn_2Si_{30}, and Fe_2Si_{30} nanowires with the structure in Figure 102h as well as Mn_2Si_{36} with the structure in Figure 102i belong to half-metal. All these nine 1D systems except Cr_2Si_{24} are magnetic. However, silicon nanowires based on Si_{16}, Si_{20}, and Si_{24} cages (Figure 102g, h, i) doped with Cr, Fe, and Mn[895] may not be realized, as for these endohedral atoms, cages with less number of silicon atoms are more favored.

Based on the fullerene-like Si_{20} and Si_{30} cages, Y. Liu and co-workers[896,897] proposed two hollow silicon nanowire structures and doped them with Eu atoms, as shown in Figure 102j and k. The infinite Eu_2Si_{25} nanowire (Figure 102j) was found to be ferromagnetic with a total spin moment of 13 μ_B per unit cell. Furthermore, the Eu_2Si_{40} nanowire (Figure 102k) is a semiconductor with a direct band gap of 0.42 eV using the PW91 functional and each Eu atom having a large spin moment of about 7 μ_B.

Sirichantaropass *et al.*[898] investigated the electronic properties of Si nanowires with structures in Figures 102h and i doped with a variety of alkali and alkaline earth atoms (M = Na, K, Rb, Cs, Ca, Sr, Ba). Almost all M_2Si_{30} structures are semiconductors

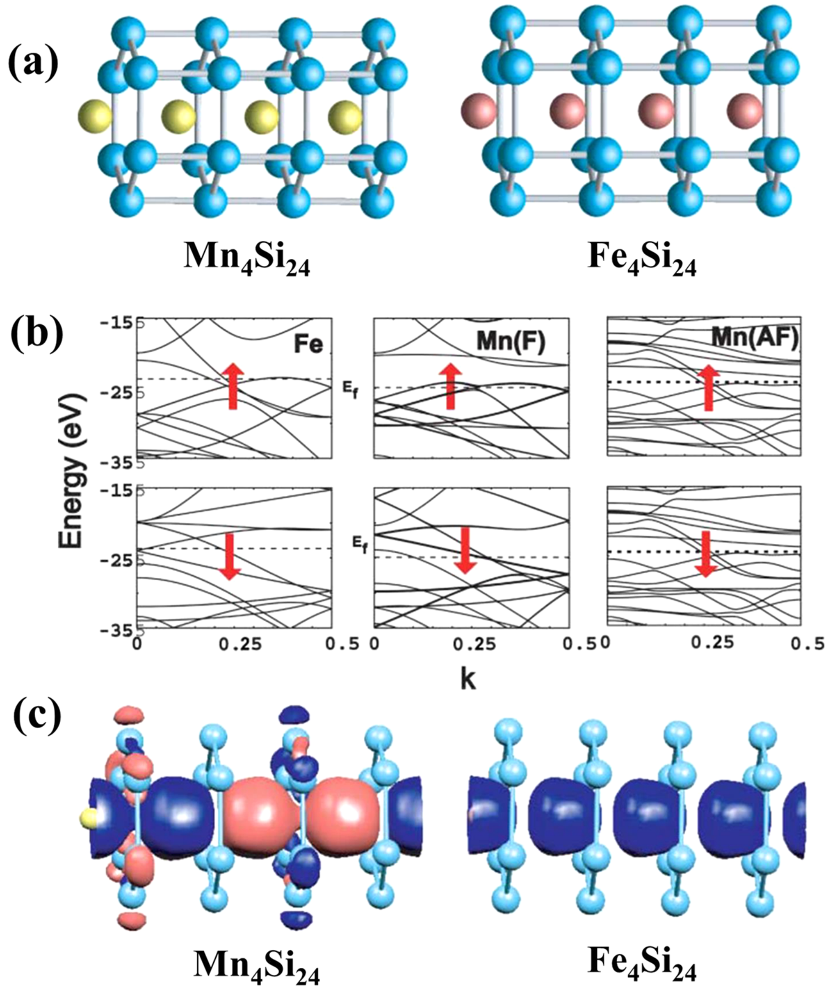

Figure 103. (a) Atomic structures of infinite Fe_4Si_{24} and Mn_4Si_{24} hexagonal nanotubes. Note the shift in the positions of the metal atoms. (b) Band structures of infinite ferromagnetic (F) Fe_4Si_{24} and F as well as antiferromagnetic (AF) Mn_4Si_{24} nanotubes along the nanotube axis. Both the spin-up and spin-down band structures are shown. The Fermi energy is represented by a dashed line. (c) Spin density isosurfaces of AF Mn_4Si_{24} and F Fe_4Si_{24} nanotubes. Blue/red isosurfaces show spin-up/down densities. Reproduced with permission from ref 893. Copyright 2004 Royal Society of Chemistry.

with direct band gap of up to 0.6 eV (within LDA), while all M_2Si_{36} structures are metallic. Therefore, the 1D band structures of these M-intercalated silicon nanowires can be switched from metallic to semiconducting state by varying the type of M dopant and the structure of the silicon cage as building block.

Similar to the aforementioned silicon nanotubes with metal encapsulation, a series of metal doped germanium nanotubes have also been investigated by Singh *et al.*[899−901] Pentagonal and hexagonal antiprism nanotubes of germanium doped with Mn atoms were proposed, i.e., pentagonal Mn_4Ge_{20} nanotube with the structure in Figure 102b and hexagonal Mn_4Ge_{24} nanotube with the structure in Figure 102e, both having a ferromagnetic spin state with average magnetic moment of 2.40 μ_B and 3.06 μ_B on each Mn atom, respectively.[899] Moreover, uniaxial compression of the 1D lattice of the pentagonal antiprism nanotube of Mn_4Ge_{20} by about 3% leads to a transition from the ferromagnetic to ferrimagnetic state along with an abrupt reduction in the magnetic moments, suggesting the possible 1D piezomagnets using these Mn doped Ge nanotubes. Singh *et al.* further considered V, Nb, Mo, and W doping in the Ge nanotubes with atomic structures based on an alternate prism and antiprism stacking of hexagonal Ge_6 rings[900,901]. With a stoichiometry of MGe_6 (indeed M_4Ge_{24} per unit cell), V and Nb doped systems are metallic, while Mo and W doped Ge nanotubes are semiconductors with a direct band gap of 0.38 and 0.50 eV (using PW91 functional), respectively. Moreover, V_4Ge_{24} nanotube is magnetic with a total spin moment of 2.13 μ_B per unit cell.

Besides the silicon and germanium based 1D nanostructures inspired by the endohedrally doped cage clusters, there have been a few theoretical designs of 1D nanotubes or nanowires based on doped Au_{12} cage clusters. Using Mg[Ti@Au_{12}] clusters that fulfill the 18-electron rule as building blocks, J. Zhou *et al.*[902] proposed a 1D periodic Zintl-like phase of Mg[Ti@Au_{12}], which is a ferromagnetic metal with each Ti atom carrying a magnetic moment of 2.13 μ_B. Recently, Yong *et al.*[903] have constructed an ultrathin W−Au alloy nanowire by assembling icosahedral W@Au_{12} clusters (which have been discussed in Section 7.1.1), as shown in Figure 104. The resulting W@Au_{12} based nanowire is a semiconductor with a direct band gap of 0.685 eV calculated by the PBE functional. The dynamic stability of this nanowire is further assessed by frequency analysis and AIMD simulations at 300 K. Further, the adsorption behaviors and electronic properties of NO, CO_2, CH_4, O_2, H_2, N_2, and H_2O molecules on the W@Au_{12} based nanowire have been investigated. Most of the above gaseous molecules interact only weakly with the

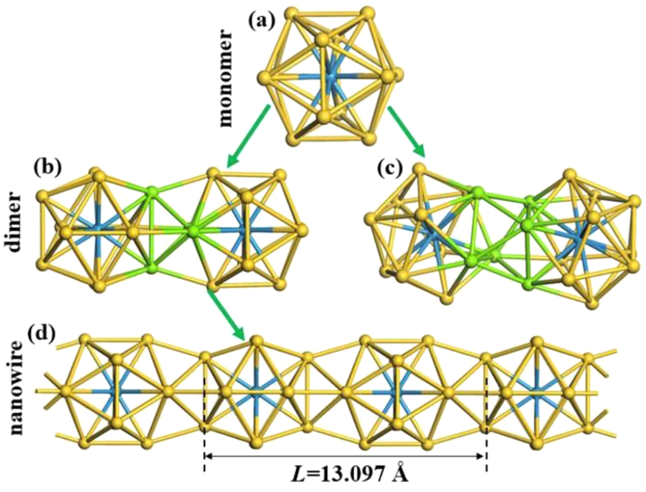

Figure 104. Optimized configurations of W@Au_{12} based nanostructures: (a) W@Au_{12} monomer; (b) and (c) the two most stable structures of W@Au_{12} dimers; (d) W@Au_{12} based nanowire. Yellow and green balls are Au atoms, and light-blue balls are W atoms. L in (d) is the length of the translational periodicity for the nanowire. The interaction region between two monomers is labeled in green. Reproduced with permission from ref 903. Copyright 2018 Elsevier Ltd.

nanowire with adsorption energy smaller than 0.3 eV. However, the electronic properties of the W@Au_{12} based nanowire are dramatically changed upon adsorption of NO molecule, showing a transition from semiconducting to conducting behavior. This suggests the potential usage as a sensor for NO gas detection, whereas the estimated recovery time for such a nanowire-based sensor is about 12 s at 300 K.

Very recently, Li and Yang[904] have designed a series of transition metal embedded stannaspherene nanowires using endohedrally doped M@Sn_{12} (M = Ti−Ni) caged clusters as building units. In these novel nanowire structures, the M@Sn_{12} cages are connected by additional M atoms as bridges, forming an infinite 1D chain of caged clusters. Hence these nanowires could be synthesized by molecular assembly of endohedral stannaspherenes in a confined direction. Interestingly, for M = V, Cr, and Fe, the resulting $[M_2(Sn_{12})]_\infty$ nanowires are robust 1D ferromagnetic semiconductors with moderate direct or quasidirect band gaps of about 1 eV and sizeable magnetic anisotropy energy (about 1 meV per transition metal atom). Moreover, $[Cr_2(Sn_{12})]_\infty$ and $[Fe_2(Sn_{12})]_\infty$ are bipolar magnetic semiconductors with valence and conduction band edges spin polarized in the opposite directions; in contrast, $[V_2(Sn_{12})]_\infty$ is a half-semiconductor[905] having a band gap of 0.96 eV (PBE) with both the valence band maximum and the conduction band minimum fully spin-polarized in the same spin channel. The former systems are promising for switching carriers' spin orientation by electrical gating, and the latter one can be used for spin-polarized carrier generation.

According to the above discussions, tunable and fascinating magnetic properties, such as ferromagnetic, antiferromagnetic, ferrimagnetic, half-metallic, and piezomagnetic effects, can be achieved in the doped silicon, germanium, tin, and gold nanotubes or nanowires. Undoubtedly, these studies lay the ground for 1D spintronics and other nanodevice applications.

Despite the aforementioned theoretical predictions, only a few endohedrally doped 1D nanotubes have been synthesized in the laboratory. Following the predictions of Be doped silicon nanotubes,[882] Saranin *et al.*[906] deposited Be atoms onto the Si(111) 7 × 7 surface under ultrahigh vacuum conditions and observed highly ordered honeycomb-like nanostructure arrays. Figure 105a shows the STM image of a 140 × 200 nm^2 surface area with two patches of nanostructure arrays, where the interior of the patches exhibits an ordered honeycomb-like structure. The high-resolution STM image (Figure 105b) shows that the nanostructure array is arranged by stacking hexagons in four different types, labeled as A, B, C, and D in Figure 105c. Figure 105e shows the scan of the filled and empty states for the region shown in d, while f shows model structures as the building blocks of the nanostructure arrays, which resemble the short Be-encapsulated hexagonal Si nanotubes (e.g., $Si_{24}Be_2$) from theoretical predictions.[882]

As a 1D counterpart of the icosahedral Matryoshka cluster Sn@Cu_{12}@Sn_{20}[100] discussed in Section 9, Stegmaier and Fässler[907] synthesized a ternary crystalline alloy of $Na_{2.8}Cu_5Sn_{5.6}$, which features discrete 1D double-walled nanorods of $Sn_{0:6}$@Cu_5@Sn_5 with pseudo-fivefold symmetry as shown in Figure 106. In the orthorhombic crystal structure of $Na_{2.8}Cu_5Sn_{5.6}$, $Sn_{0:6}$@Cu_5@Sn_5 nanorods are aligned in parallel in a hexagonal packing and separated by interstitial Na atoms. Each $Sn_{0:6}$@Cu_5@Sn_5 nanowire is composed of an outer shell of Sn atoms, an inner tube of Cu atoms, and a central chain of Sn atoms with disorder. Furthermore, the fragment of pentagonal anti-prismatic Sn@Cu_{10}@Sn_{10} cluster (highlighted in Figure 106e) clearly resembles the segment of $Sn_{0:6}$@Cu_5@Sn_5 nanorod in Figure 106d.

10.3. Two-Dimensional Assemblies of Endohedrally Doped Cage Clusters

One of the ultimate goals of cluster science is to fabricate 2D arrays of selected size and composition of clusters in a desired manner on a properly selected substrate, which is still a challenging task from the point of view of nanofabrication,[908] but very encouraging progress has been made in recent years. One feasible technique is to spontaneously assemble magic clusters on a solid surface such as Si(111)-7×7 with suitable periodicity arising from surface-mediated interactions.[909] A recently developed approach for preparing superatomic 2D semiconductors is mechanical exfoliation of the van der Waals crystals (e.g., $Re_6Se_8Cl_2$).[910] All these experimental advances encourage further theoretical design and experimental synthesis of the 2D periodic structures using endohedrally doped clusters as building blocks due to their versatility.

Few theoretical and experimental efforts have been devoted to 2D assemblies of endohedrally doped cage clusters. One of the challenges is the production of identical clusters in large quantity. Conventional gas-phase synthesis of clusters such as using the laser vaporization method is not suitable for real life applications. In an early theoretical attempt, Miyazaki and Kanayama[911] constructed a 2D network by assembling Zr@Si_{12} clusters with hexagonal prism structure by making covalent Si−Si bonds between the clusters as shown in Figure 107. The binding energy of this layered material relative to the isolated Zr@Si_{12} clusters is 6.12 eV per $ZrSi_{12}$ unit. Band structure calculation with PBE functional indicated that the Zr@Si_{12} based monolayer is a semiconductor with an indirect band gap of 0.3 eV, which may be a prototype candidate material for thin film channels of ultimately scaled metal-oxide-semiconductor transistors.

Taking the V@Si_{12} cluster as a building block, Z. Liu *et al.*[912] proposed two types of 2D assemblies that exhibit hexagonal porous and honeycomb-like framework (Figures 108a−d). The stabilities of these two V@Si_{12} based 2D sheets have been

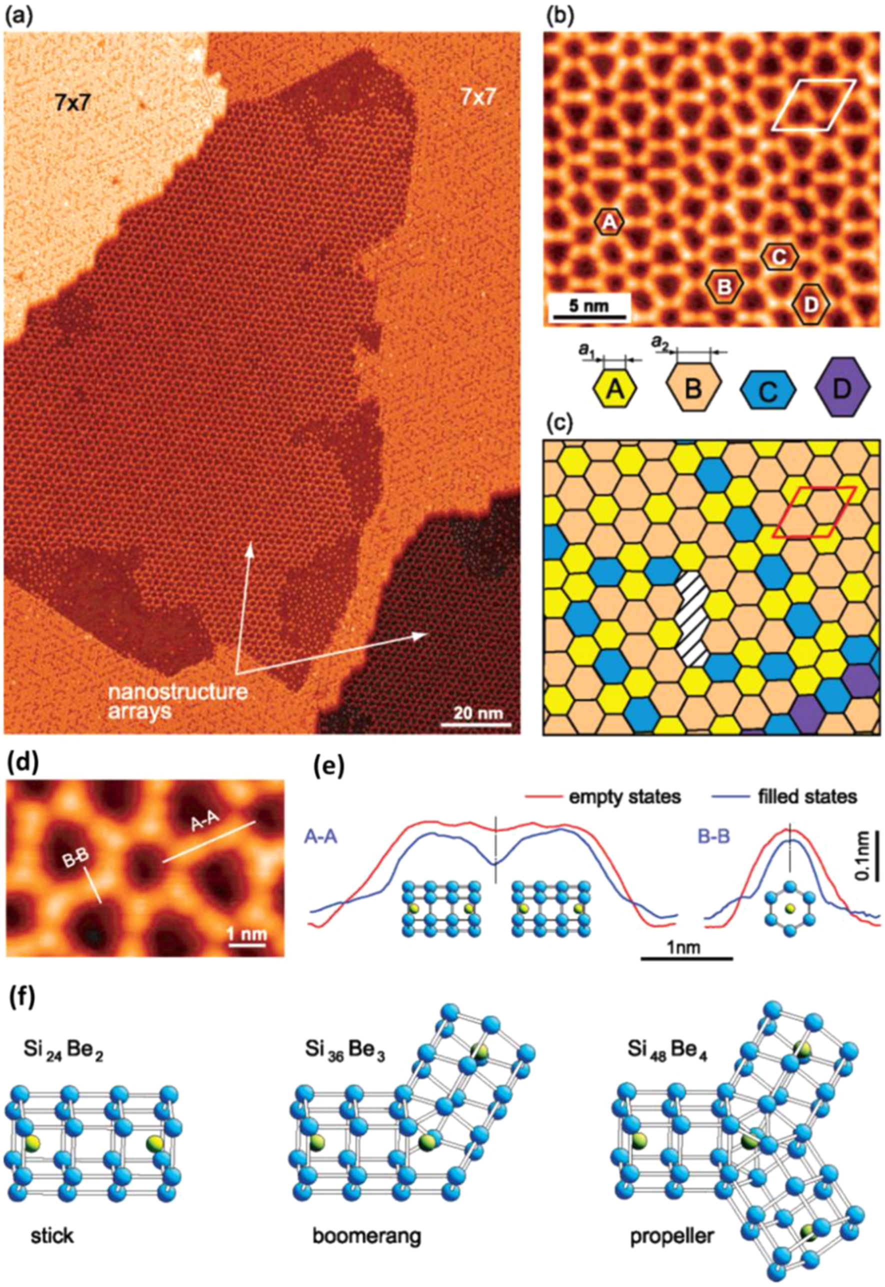

Figure 105. (a) Large-scale STM image of two nanostructure arrays developed at the neighboring atomic terraces, showing that ordered nanostructure arrays are formed upon Be deposition onto the Si(111) surface. (b) High-resolution empty-state STM image of the nanostructure array. Array is built of four types of hexagons labeled A, B, C, and D. The sides of hexagons are $a_1 \approx 1.08$ nm and $a_2 \approx 1.66$ nm. (c) Sketch of the array shown in (b). The defected area is hatched. The ideal array structure is built of A-type and B-type hexagons (the corresponding unit cell is outlined), the anti-phase domain walls of A-type, C-type, and D-type hexagons. (d) Fragment of the nanostructure array from STM image. Line profiles along (A−A) and perpendicular to (B−B) stick elements are indicated in (e). Red line for the empty states and blue line for the filled states. (g) Schematic diagram showing the model atomic structure of the array building blocks: $Si_{24}Be_2$ for stick, $Si_{36}Be_3$ for boomerang, and $Si_{48}Be_4$ for propeller. Reproduced with permission from ref 906. Copyright 2004 American Chemical Society.

confirmed by the analysis of binding energies with respect to the individual V@Si_{12} clusters as well as the phonon spectrum. Remarkably, the ground states of these 2D sheets have been shown to be ferromagnetic (Figures 108e, f) due to the free-electron mediated mechanism. The large magnetic moments (3.5 μ_B per building unit) are mainly on the V atoms and there is stable ferromagnetic coupling at room temperature. Accordingly, the V@Si_{12} based hexagonal porous sheet would have promising applications in spintronics. Subsequently, the electronic and magnetic properties of M@Si_{12} (M = 3*d* transition metal) assembled 2D sheets were further investigated by Nie et al.,[913] together with two other lattice structures (square lattice and central rectangular lattice). The honeycomb and hexagonal porous structures were shown to be thermodynamically stable at room temperature from AIMD simulations, and the honeycomb structure was further shown to be more stable than the porous structure. Almost in all cases of the 2D structures of TM@Si_{12}, there is a certain degree of magnetic ordering. Ti-, V-, and Fe-doped 2D assemblies were shown to be ferromagnetic, while Mn- and Co-doped 2D structures were

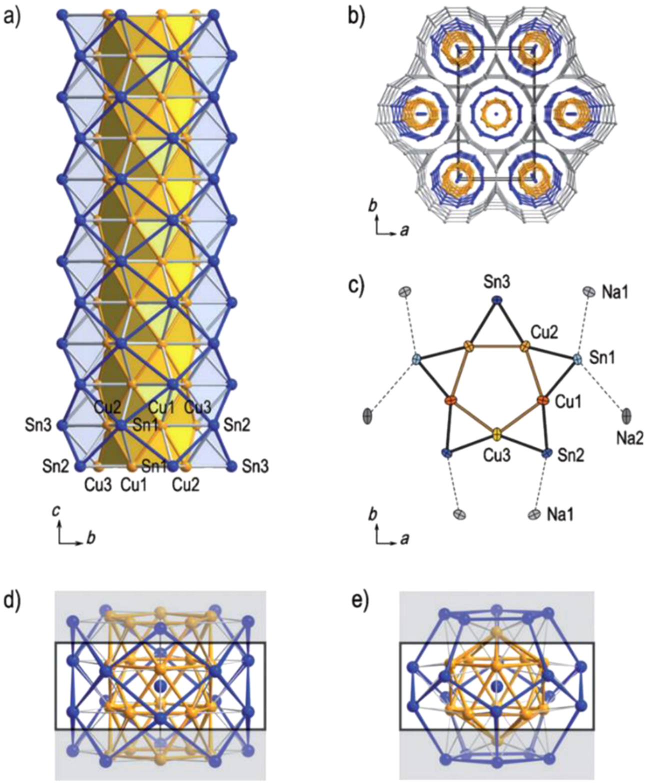

Figure 106. (a) Double-walled Cu−Sn nanotube. (b) Cu−Sn columns separated by Na atoms in Na$_{2.8}$Cu$_5$Sn$_{5.6}$. Contacts between Cu (orange) and Sn (blue) atoms are not shown for clarity. Gray lines illustrate the Na substructure. (c) Coplanar Cu$_5$Sn$_5$ unit with surrounding Na sites. Thermal ellipsoids are at 70% probability level. (d) Sn$_{0.6}$@Cu$_5$@Sn$_5$ column in Na$_{2.8}$Cu$_5$Sn$_{5.6}$. Only one Sn$_4$ site in the column center is shown. (e) Sn@Cu$_{12}$@Sn$_{20}$ cluster in A$_{12}$Cu$_{12}$Sn$_{21}$ (A = Na, K, Rb, Cs).[100] Reproduced with permission from ref 907. Copyright 2012 Wiley-VCH.

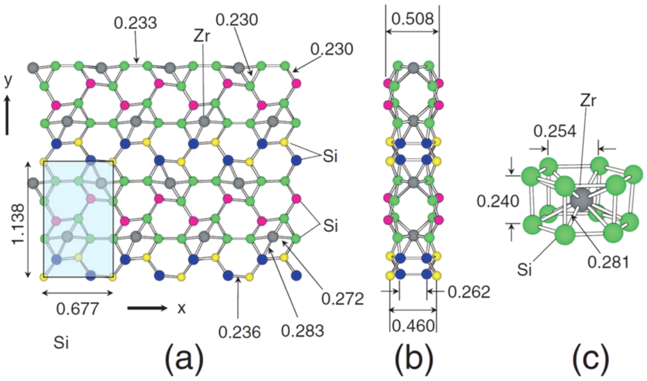

Figure 107. Panels (a) and (b) show the optimized atomic structure of layered semiconductor made of Zr@Si$_{12}$ clusters: (a) View from the direction normal to the layer and (b) view from the direction parallel to the layer. In these panels, red, blue, yellow, and green dots are Si atoms. Grey dots represent Zr atoms. As shown in panel (b), the thickness of this layered material is measured to be 0.508 nm at the maximum (the distance between Si atoms denoted by red circles) and 0.262 nm at the minimum (the distance between Si atoms denoted by blue circles). In panel (a), the thin blue rectangle at the left bottom corner is the unit cell that contains two Zr@Si$_{12}$ building blocks. (c) Optimized atomic structure of an isolated Zr@Si$_{12}$ cluster. In all the panels, the bars connecting Si with Si and Zr atoms are drawn if the Si−Si and Si−Zr distances are less than 0.27 and 0.29 nm, respectively. The numbers in each panel are the Si−Si and Si−Zr distances in nm. Reproduced with permission from ref 911. Copyright 2007 Japan Society of Applied Physics.

found to favor antiferromagnetic coupling. In the case of Cr@Si$_{12}$ and Ni@Si$_{12}$, the honeycomb 2D structure is ferromagnetic, while the porous structure is antiferromagnetic for Cr@Si$_{12}$ and nonmagnetic for Ni@Si$_{12}$. These insights pave a new way to achieve 2D silicon-based spintronic materials.

Following the 18-electron rule and using Na$_2$[Ti@Au$_{12}$] clusters as building blocks, J. Zhou *et al.*[902] designed a 2D periodic Zintl-like phase of Na$_2$[Ti@Au$_{12}$] (Figure 109a), which is a semiconductor with an indirect band gap of 0.55 eV using PBE functional as can be seen from the band structure shown in Figure 109b. Bader charge analysis revealed that each Na atom donates about 0.77 electrons to the Ti@Au$_{12}$ moiety, confirming its Zintl-like character. Their results on 1D and 2D Zintl-like phases open a route to design and synthesize a new class of Zintl-like ions and compounds with potential applications in solution chemistry and thermoelectric materials.

Starting from 2014, Nakajima's group[80,488,489,914−916] has made great progress on producing size-selected doped silicon clusters and depositing them onto carefully chosen substrates to form stable 2D monolayer assemblies. In their series of experiments, [Ta@Si$_{16}$]$^+$ caged clusters behaving as rare-gas-like superatoms were generated in the gas phase, mass selected, and deposited on several C$_{60}$ terminated conductive surfaces, including HOPG, Si(111)-7×7, and Si(111)-$\sqrt{3}\times\sqrt{3}$R30°-Ag. STM/STS measurements have demonstrated that Ta@Si$_{16}$ cations are densely immobilized onto these C$_{60}$-terminated surfaces,[914,916] forming stable monolayers of Ta@Si$_{16}$ cations retaining their fullerene cage shape and positive charge, as shown in Figure 110. The chemical states and stability of the Ta@Si$_{16}$/C$_{60}$ film on HOPG were further evaluated by XPS and UPS.[488,915] Analysis of XPS spectra revealed that each Ta@Si$_{16}$ cluster combines with C$_{60}$ to form a one-to-one superatomic charge transfer complex, namely, [Ta@Si$_{16}$]$^+$[C$_{60}$]$^-$. This superatomic charge-transfer complex showed excellent thermal and chemical robustness, as evidenced by the XPS and UPS measurements conducted before and after heat treatment up to 720 K and oxygen exposure.

Following the experimental progress on 2D assemblies of Ta@Si$_{16}$, J. Liu *et al.*[874] recently designed two kinds of self-assembled 2D hexagonal crystals of Ta@Si$_{16}$ superatoms, i.e., compact simple lattice and honeycomb complex lattice, which usually can maintain their structural stability at room temperature. The 2D assemblies are semiconductors with band gap in the range of 0.43−1.32 eV (using PBE functional) and could be potential photocatalysts. More interestingly, the line-contact Ta@Si$_{16}$/C$_{60}$ structure is an intrinsic ferromagnet with a Curie temperature of 294 K.

10.4. Three-Dimensional Crystals Assembled from Endohedrally Doped Cage Clusters

Soon after the proposal of Khanna and Jena[152] to assemble crystals from X@Al$_{12}$ (X = C, Si, Al, ...) clusters, there have been some theoretical explorations on the possible 3D crystals built from X@Al$_{12}$.[161,167,917−922] Typically, two kinds of X@Al$_{12}$ based crystals have been considered: (i) direct assembling Si@Al$_{12}$ or C@Al$_{12}$ with closed electronic shell into a compact solid and (ii) combining Al$_{13}$ or B@Al$_{12}$ as superhalogen with alkali metal to form an "ionic crystal". The main results from these theoretical studies are summarized in Table 24.

Khanna and Jena[167] calculated the electronic band structure of a FCC crystal with lattice constant equal to 11.7 Å and each lattice site occupied by a jellium sphere to mimic the C@A$_{12}$

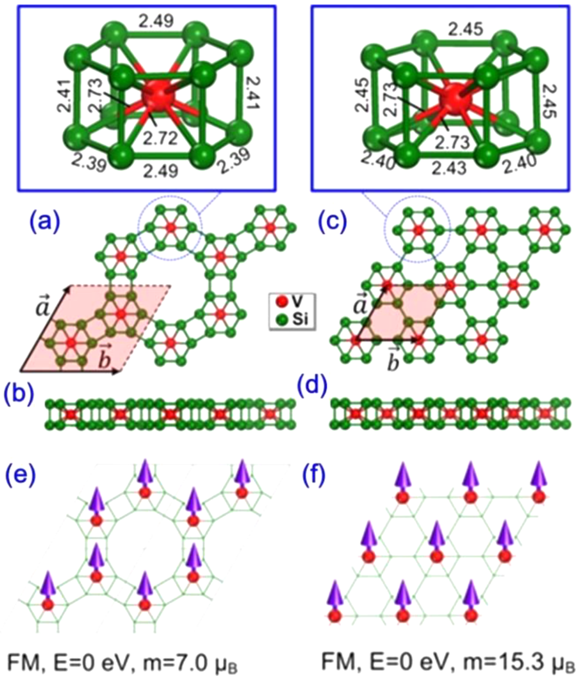

Figure 108. (a) Top and (b) side view of the hexagonal porous sheet (P6/mmm); (c) top and (d) side view of the honeycomb-like sheet (P6/mmm). Dashed rhombus with Bravais lattice vectors *a* and *b* (|**a**| = |**b**|) marks the primitive unit cell for the corresponding sheet. (e) and (f) show the ferromagnetic (FM) coupling for the porous sheet and the honeycomb-like sheet, respectively. The arrows represent spin directions of the encapsulated V atoms. The relative energies (E) and magnetic moments (m) for (1 × 1) unit cell of the porous sheet and (2 × 2) supercell of the honeycomb-like sheet are also given. Reproduced with permission from ref 912. Copyright 2015 American Chemical Society.

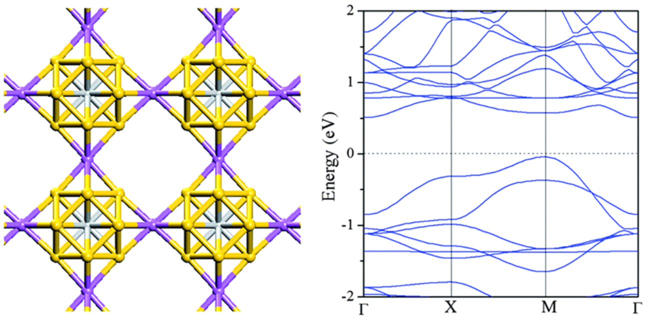

(a) (b)

Figure 109. (a) Relaxed geometry (belonging to the P4/mm plane symmetry group) and (b) band structure of 2D $Na_2[Ti@Au_{12}]$ along high symmetry directions: Γ(0,0,0) to X(1/2,0,0), then to M(1/2,1/2,0), and finally to Γ. Reproduced with permission from ref 902. Copyright 2014 Royal Society of Chemistry.

cluster. The model system is a semiconductor with a narrow band gap of 0.5 eV (LDA). However, using the Car-Parrinello method within LDA, Seitsonen *et al.*[161,917] showed that the hypothetical FCC crystal assembled from $C@Al_{12}$ or $Si@Al_{12}$ clusters is unstable upon relaxation; that is, the clusters will coalesce to a bulk Al metal with substitutional C or Si impurities. By considering the relative orientation of clusters, Gong[920] proposed a cubic crystal structure for the cluster-assembled solid based on $C@Al_{12}$ or $Si@Al_{12}$ with eight clusters per unit cell, in which each building cluster is rotated by 90° with respect to all its nearest neighbors. The resulting $C@Al_{12}$ ($Si@Al_{12}$) assembled crystal has an equilibrium lattice constant of 16.3 (17.2) Å and is a semiconductor with a band gap of 1.52 (1.41) eV within LDA. The very small cohesive

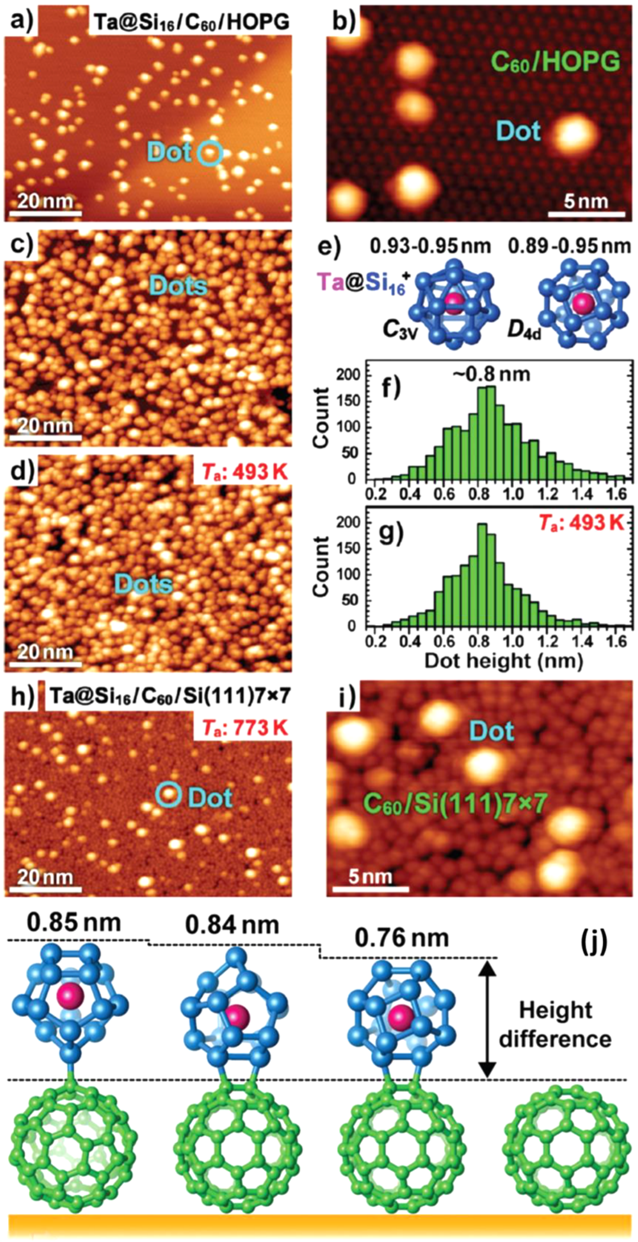

Figure 110. Stable immobilization of $Ta@Si_{16}$ nanoclusters onto a C_{60}-terminated surface. (a−d) STM images of a C_{60}/HOPG surface obtained after depositing $Ta@Si_{16}$ cations. (a) Wide- and (b) molecular-scale images obtained after the initial deposition. (c) and (d) show the surfaces densely covered with dots before and after annealing at 493 K, respectively. (e) Geometrical models and sizes of C_{3v} (deformed FK polyhedron) and D_{4d} (fullerene) isomers of $Ta@Si_{16}$ cations. (f) and (g) show histograms of the dot heights measured in (c) and (d), respectively. (h) Wide- and (i) molecular-scale STM images of the $[Ta@Si_{16}]^+$-deposited C_{60}/Si(111)7×7 surface obtained after annealing at 773 K. The imaging conditions (V_{tip} and I_t) are −2.3 V and 2 pA for (a−d), 2.2 V and 5 pA for (h), and 1.8 V and 5 pA for (i). (j) Examples of theoretical motifs of neutral $Ta@Si_{16}$ fullerene-C_{60} complexes with the fullerene in different orientations on C_{60} and the height differences. Reproduced with permission from ref 914. Copyright 2014 Royal Society of Chemistry.

Table 24. Chemical Formula, Type of Crystal Structure (Str.), Number of Formula per Unit Cell (N_c), Lattice Constant (a), Type of Electronic Band Structure (M Denotes Metal, S Denotes Semiconductor), and Band Gap (E_g) of the Crystalline Solids Assembled from X@Al_{12} (X = C, B, Si, Al) Clusters

Formula	Str.	N_c	a (Å)	Type	E_g (eV)	Author (year)
[C@Al_{12}]	Cubic	8	16.30	S	1.52	Gong[920] (1997)
[Si@Al_{12}]	Cubic	8	17.20	S	1.41	Gong[920] (1997)
[Al@Al_{12}]K	CsCl	1	6.52	M		F. Liu *et al.*[918] (1996)
[B@Al_{12}]Cs	CsCl	1	6.42	M		Ashman *et al.*[919] (1997)
[B@Al_{12}]Li	CsCl	1	6.28	M		Zhu *et al.*[921] (1998)

energy (about 0.55 eV per cluster) and the small overlap of charge density between C@Al_{12} (Si@Al_{12}) clusters suggested the intercluster interaction to be of van der Waals type. Moreover, the icosahedral structure of the C@Al_{12} cluster remains unchanged during AIMD simulation at low temperature (20 K).

As we have discussed in Section 3.1, Al_{13} or B@Al_{12} cluster with 39 valence electrons (one short of the complete electronic shell) and large electron affinity can be viewed as a superhalogen. Intuitively, an ionic crystal can be formed by assembling Al_{13} or B@Al_{12} superhalogen clusters with alkali metal atoms. Owing to the large size mismatch between the Al_{13} or B@Al_{12} cluster and alkali metal atoms, CsCl type structure should be more favorable than NaCl type for an ionic crystal, which has been proven by DFT calculations.[918,919,921] Due to crystal field effects, the Al_{13} or B@Al_{12} cluster in the solid phase prefers the cuboctahedral structure to the ground state icosahedral structure for the gas phase. However, different from the ionic crystals which are usually insulators, all these cubic compound crystals made of Al_{13} or B@Al_{12} and alkali metals are metallic, which can be considered as an aluminum-like metal with B and alkali metal atoms as impurities.[921] It is also worth pointing out that K and Al are immiscible elements over the entire composition range.[923] Therefore, the theoretical prediction of [Al@Al_{12}]K crystal demonstrates that one might be able to make solid state alloys from two immiscible elements by confining one of them into clusters first, which provides a new opportunity to form artificial crystals.

The endohedrally doped silicon cage clusters such as M@Si_{16} (M = Ti, Zr, Hf) superatoms with closed-shell electronic configuration, near spherical geometry, large HOMO−LUMO gap, and possibly weak intercluster interactions (as discussed in Sections 10.1 and 5.3.7), are promising building blocks for cluster-assembled solids and have been theoretically explored by two independent groups. Reis *et al.*[421,924,925] predicted some stable molecular solids made of the robust M@Si_{16} (M = Ti, Zr, Hf) clusters using PBE calculations with planewave basis. Taking the M@Si_{16} clusters with the FK cage structure as the elementary building units (though this is not of the lowest energy in all cases as discussed in Section 5), it was argued that the HCP crystalline structure is more stable than the other considered phases, namely SC, diamond-type, BCC, and FCC. The atomic structures of an individual M@Si_{16} cluster and its assembled HCP crystal are shown in Figure 111.

The structural and physical properties of the M@Si_{16} (M = Ti, Zr, Hf) assembled solids in the HCP phase are summarized in Table 25. All the three cages crystallize in HCP structure with the maximum deviation of the c/a ratio of the lattice parameters by 1.8% from that of the ideal packing. Fully unconstrained QLMD simulations of these crystal structures confirmed their stability at room temperature and ambient pressure. These crystalline materials exhibit phase stability under hydrostatic compression up to about 1 GPa. Their theoretical bulk modulus is about 1 GPa, which is very soft even as molecular solids. The weak intercluster interactions in these solids are also manifested by the small cohesive energies which lie in the range of 0.14 eV to 0.20 eV per cage. All the three M@Si_{16} based crystals are indirect band gap semiconductors, whereas their band gap (1.3 eV for Ti@Si_{16}, 1.6 eV for Zr@Si_{16} and Hf@Si_{16}, respectively) is lower than that of the individual clusters by about 0.8 to 1.0 eV. More interestingly, the HCP crystals of M@Si_{16} clusters doped with electron donor atoms in the interstitial space possess superconducting transition temperature of over 80 K from theoretical estimation,[421] similar to the superconductivity in fullerides.[926] This opens an avenue for nanoscale design of novel superconducting alloys based on the semiconducting elements such as Si and Ge.

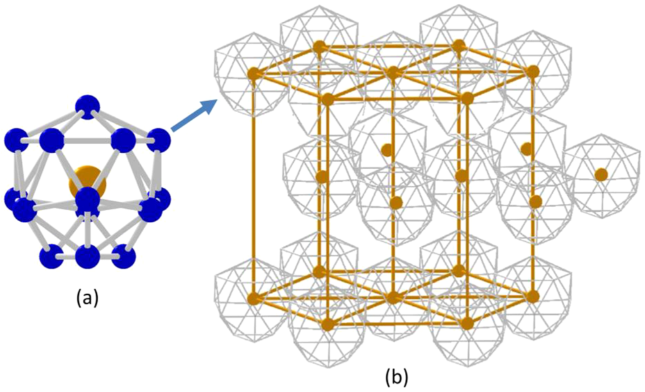

Figure 111. (a) FK cage structure of M@Si_{16} (M = Ti, Zr, Hf) clusters, which are used as the building blocks of molecular solids. This highly symmetric structure exhibits several C_3 symmetry axes. (b) Equilibrium structure of bulk M@Si_{16} crystal. Each cage occupies the site of a HCP lattice. Reproduced with permission from ref 924. Copyright 2007 American Physical Society.

Table 25. Lattice Parameters (a, c), Intercluster Cohesive Energy per Superatom (E_c), Bulk Modulus (B), Band Gap (E_g) for the FK M@Si_{16} (M = Ti, Zr, Hf) Molecular Solids with HCP Lattice Structure, as well as HOMO−LUMO Gap (E_{HL}) for Each Individual Cluster from DFT-PBE Calculations[925]

	a (Å)	c (Å)	E_c (eV)	B (GPa)	E_g (eV)	E_{HL} (eV)
Ti@Si_{16}	8.75	14.36	0.20	1.25	1.3	2.3
Zr@Si_{16}	9.05	14.79	0.14	0.90	1.6	2.4
Hf@Si_{16}	8.96	14.89	0.15	0.97	1.6	2.5

Using DFT calculations with the DZP basis set and PBE functional, Torres and co-workers[881,927] investigated FCC, BCC, and SC crystalline phases having the Ti@Si_{16} cluster as the basic unit. Among them, the BCC crystal of the D_{4d} fullerene-like cage of Ti@Si_{16} (Figure 39a) with a lattice constant of 8.75 Å and a cohesive energy of 5.72 eV is most stable, in which the neighboring Ti@Si_{16} cages are connected via covalent bonds. It should be noted that free Ti@Si_{16} cluster has a FK polyhedral structure. They also considered cubic NaCl and CsCl bulk structures of [Sc@Si_{16}]K and [V@Si_{16}]F supermolecules, both of which possess large cohesive energy of 5.58 and 4.51 eV per unit cell, respectively; and [V@Si_{16}]F crystal exhibits a metallic character.

In contrast to the aforementioned M@Si_{16} assembled systems, Pacheco *et al.*[928] investigated the possibility of synthesizing a crystalline phase using W@Si_{12} or Nb@Si_{12} clusters with a hexagonal prism structure as elementary building blocks but found that the M@Si_{12} cage structures in the solid phase are not retained during QLMD simulation. The chemical bonds between Si atoms of the neighboring clusters lead to severe rearrangement for each cluster and drive the crystalline solid into an amorphous one. This finding clearly supports the design principle of building clusters for assembling crystals, which require both closed electronic shell and closed atomic packing. Although W@Si_{12} has a substantial HOMO−LUMO gap (as discussed in Section 5.3.3), its tubular geometry is far more open than the above M@Si_{16} cages (M = Ti, Zr, Hf).

The above simulation results by Pacheco *et al.*[928] were partly supported by a series of experiments conducted by Uchida *et al.*,[929] who deposited hydrogenated transition-metal-encapsulated Si clusters (MSi_nH_x: M = Nb or Mo; n = 1−16) onto a silica substrate, followed by annealing at 500 °C for dehydrogenation. The deposited films with thickness of 10−20 nm were actually amorphous assembled by random arrangements of MSi_n clusters rather than crystalline solid. For $n \geq 7$, the MSi_n based films are semiconductors with measured optical gap in the range of 0.6−1.0 eV and relatively high mobility.

In addition to doped aluminum and silicon cages, other possible building blocks of cluster-assembled solids reported in the literature are endohedrally doped X(Y)@$Zn_{12}S_{12}$,[930] X(Y)@$Cd_{12}S_{12}$, and X(Y)@$Cd_{16}S_{16}$[931] (X = Na, K; Y = Cl, Br) clusters. To assemble crystals, the ZnS (CdS) nanocages could be either empty (without dopant) or pairwise encapsulated by alkali metal (Na, K) and halogen (Cl, Br) atoms together. Then, the empty or filled ZnS (CdS) cages are interconnected by Zn−S (Cd−S) covalent bonds to form zeolite-like nanoporous 3D crystals, including the known zeolite phases of FAU, LTA, and SOD.[931] Among these three phases, SOD structure is the most stable for CdS based crystals and it is also the most compact one. The $Zn_{12}S_{12}$ based solids are semiconductors with FCC crystal structure, with a lattice parameter of around 13.8 Å and a band gap of 2.2 eV (for bare solid) or about 1.8 eV (for doped solids) using RPBE functional.[930] Most $Cd_{12}S_{12}$ and $Cd_{16}S_{16}$ based solids except SOD-[K@$Cd_{16}S_{16}$]-[Cl@$Cd_{16}S_{16}$] are semiconductors, with band gaps in the range of 1.06 eV to 1.76 eV. All these cluster-assembled solids were found to be thermodynamically stable with reasonable cohesive energy and thermally stable at room temperature from QLMD simulations.

Lastly we would like to point out that, instead of "bottom-up" assembling endohedral clusters into 3D solids, the rapidly growing family of Zintl compounds provides an alternative opportunity of producing crystalline cluster-assembled materials in macroscopic quantities. As the two examples show in Figure 71 ($K_{5-x}Co_{1-x}Sn_9$) and Figure 98 ($Na_{12}Cu_{12}Sn_{21}$ and $K_{12}Cu_{12}Sn_{21}$), discrete endohedral cages with multiple negative charges (namely, Zintl anions) are closely packed to form crystalline Zintl compounds, but there are many metal cations in between the Zintl anion cages. It is thus imperative to explore the difference between isolated Zintl anion (or its isoelectronic neutral cluster) and the corresponding Zintl crystal in terms of electronic structures and physical and chemical properties.

10.5. Self-Assembled Crystals of Ligated Endohedrally Metal-Atom-Doped Nanoclusters

In the past decade or so, great progress has been made[932−946] in the synthesis of discrete size atomically precise ligand protected nanoclusters of coinage metals, particularly Au and Ag such as $Au_{25}(SR)_{18}$, $Au_{38}(SR)_{24}$, $Au_{102}(SR)_{44}$, $Ag_{25}(SR)_{18}$, and their self-assembled crystals. Here SR is thiolate but other types of ligands namely weakly interacting phosphines (PR_3) and halides (X) have also been used. Michael Faraday[947] reported synthesis of gold nanoparticles and their color in 1857, but identification of the precise number of atoms and their structure has been a challenge for a long time. Among the large number of nanoclusters that have been studied and synthesized, $Au_{25}(SR)_{18}$ nanoclusters and their crystals have attracted the widest attention. The unit cell of the single crystal of $Au_{25}(SCH_2CH_2Ph)_{18}$ nanoclusters contains one nanocluster and its associated TOA+ (tetraoctylammonium) counterion[948,949]. The development of crystals made it possible to completely determine the atomic structure of the nanocluster as well as the ligands using the well-established X-ray crystallography method. The thiolate protected gold nanoparticles have high stability due to the affinity of sulfur to bind with Au atoms. As shown in Figure 112, there is a central 13-atom icosahedral core of gold in these thiolated gold clusters. This is protected by six $Au_2(SR)_3$ oligomers such that 12 Au atoms occupy sites in an octahedral arrangement of dimers around the Au_{13} icosahedron, and 18 sulfur atoms of the thiol molecule connect the Au atoms such that each sulfur atom is connected to two Au atoms. It is to be noted that pure Au_{13} cluster tends to have a planar structure while around the size of 32 Au atoms, cage structures become favorable, as discussed in Section 7.1. Accordingly, ligands such as thiols affect the structure of gold clusters very significantly. The stability of these clusters has been associated[950] with the filling of the electronic shells in a spherical potential model discussed in Section 2, according to which $[Au_{25}(SR)_{18}]^-$ nanocluster has a $1S^21P^6$ closed electronic shell configuration with eight 6*s* delocalized valence electrons predominantly on the icosahedral core.[951] Here we have considered that 5*d* orbitals of Au atoms remain more or less completely filled and the 6*s* orbital of each Au atom contributes one electron. Further, each SR molecule takes one electron in bonding with the Au nanocluster and the remaining 8 electrons including the extra one due to charge contribute to the bonding between Au atoms. A large HOMO−LUMO gap also makes these clusters behave like a noble gas superatom.

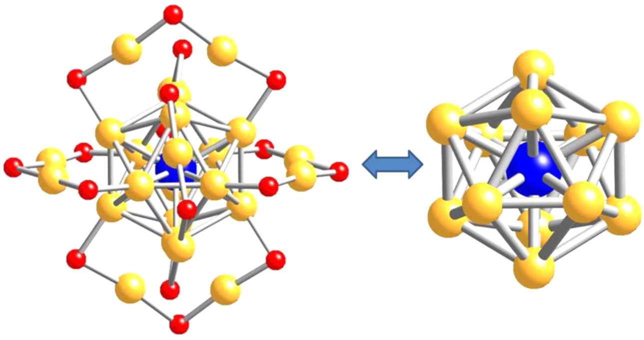

Figure 112. Molecular structure of the $Au_{25}(SR)_{18}$ nanocluster. On the right is the Au_{13} icosahedral cluster in which the central Au atom can be substituted by another metal atom such as Pt and Pd (shown by a blue ball). This icosahedron is capped by six Au_2S_3 units as shown on the left side. Yellow balls show the Au atoms while red balls show S atoms. For clarity, R is not shown. In a crystal, there are also counterions (not shown here). Reproduced with permission from ref 946. Copyright 2012 American Chemical Society.

These developments are exciting and are in the direction of fulfilling the dream of assembling clusters to make crystals. Crystals of $Au_{36}(SR)_{24}$ have also been obtained in a FCC structure.[952]

Interestingly, it is possible to dope one to a few isoelectronic heteroatoms such as Ag and Cu in $Au_{25}(SR)_{18}$[953] and also for some other cluster sizes. The alloyed nanoclusters can be formed with the same number of metal atoms as the thiolated pure gold nanoclusters. Strikingly, it has been shown that one Cu atom occupies the center of the Au_{13} icosahedron presumably due to its smaller size even though DFT calculations showed substitutional doping on a shell site of the icosahedron to be more favorable.[954] As discussed earlier, in an icosahedron, the center to vertex distance is about 5% shorter than the vertex to vertex distance and therefore a smaller endohedral atom is favorable at the center. But Cu atom is much smaller (atomic radius: 1.28 Å) than Au atom (atomic radius: 1.44 Å). Therefore, the doping of Cu leads to distortion and lower stability of the thiolated gold clusters $Cu_nAu_{25\text{-}n}(SC_2H_4Ph)_{18}$ (n = 1−5) in solution which were prepared with high purity.[953] This contrasts from the fact that bulk Cu−Au alloys are ordered systems, meaning the Cu−Au bond is stronger compared with the Au−Au bond. On the other hand, Ag and Au atoms have nearly the same radius and the doping of one Ag atom occurs at the surface of the Au_{13} icosahedron, and Ag concentration can be modulated continuously.[955] Up to 11 silver atoms could be doped in $Au_{25}(SR)_{18}$ (R = $C_{12}H_{25}$ or C_2H_4Ph). Excessive doping destabilizes the nanoclusters due to weaker S−Ag bond. However, the formation of $Ag_{25}(SR)_{18}$[933] as well as doping in silver nanoclusters[956] has been reported and is discussed later. In both the cases of Cu and Ag doping in Au nanoclusters, the optical properties of the gold nanoclusters are affected. Most interestingly, one Pt[946] or Pd[957,958] atom could be incorporated at the center of the Au_{12} icosahedron of $Au_{25}(SR)_{18}$. Much progress has been made in the synthesis of these systems as well as understanding their properties in recent years. Here we discuss some of the interesting developments as these systems fall in the category of endohedrally doped nanoclusters and their assemblies, which is the focus of this review.

Jiang and Dai[959] have performed *ab initio* calculations on $[M@Au_{24}(SR)_{18}]^q$ clusters with M = Ni, Pd, and Pt, and $q = -2$; Cu, Ag, and alkali atoms with $q = -1$; divalent atoms with $d^{10}s^2$ or s^2 electronic configuration such as Zn, Cd, Hg, Be, ... and $q = 0$; trivalent atoms with s^2p^1 configuration namely B, Al, Ga, In, and Tl with $q = 1$; and tetravalent atoms C, Si, Ge, Sn, and Pb with $q = 2$. It was shown that the doping of an Ag or Cu atom at the center leads to a smaller HOMO−LUMO gap compared with that having the center occupied with Au atom, but the doping of Pt leads to the largest HOMO−LUMO gap and largest gain in energy as shown in Figure 113. Christensen *et al.*[946] synthesized $Pt@Au_{24}(SR)_{18}$ nanoclusters and observed contraction in metal−thiolate and metal−metal bond distances using EXAFS and XPS as well as enhancement in the stability of the thiolated gold nanocluster by Pt doping. Qian *et al.*[960] also produced $Au_{24}Pt(SC_2H_4Ph)_{18}$. A similar result has been obtained by Fields-Zinna *et al.*[961] on Pd doping and they showed the formation of $Au_{24}Pd(SC_2H_4Ph)_{18}$ regardless of the ratio of Au to Pd in the synthesis of the nanoclusters. Negishi *et al.*[957] isolated Pd doped dodecanethiolate-protected gold cluster $Pd_1Au_{24}(SC_{12}H_{25})_{18}$ in high purity by solvent fractionation and high performance liquid chromatography. It has similar structure as $Au_{25}(SR)_{18}$, and the Pd atom was shown to occupy the center of the Au_{12} icosahedron. Also, experiments showed $Pd_1Au_{24}(SC_{12}H_{25})_{18}$ to be more stable than $Au_{25}(SC_{12}H_{25})_{18}$ against degradation in solution and laser dissociation. Kacprzak *et al.*[958] have performed DFT calculations on methylthiolate protected $PdAu_{24}(SR)_{18}$ (R = Me) nanoclusters in different charge states. The optimized atomic structure showed the structure of gold nanocluster to be robust when a Pd atom replaces the Au atom. The Pd atom remains close to the zero-valent $4d^{10}5s^0$ configuration and it does not contribute to the delocalized electron charge density in the gold icosahedron. But the calculated optical absorption and HOMO−LUMO gap depend sensitively on the site of the doping Pd atom. This was suggested to be useful for assigning the structure of $PdAu_{24}(SR)_{18}$ from experimental data. Tofanelli *et al.*[962] studied the atomic structure of the single crystal of $PdAu_{24}(PET)_{18}$ (PET = phenylethanethiol) from X-ray diffraction and confirmed that Pd occupies the core of icosahedron and that the Pd−Au bond length is shorter than Au−Au. Also there is a blue shift in the UV/vis spectrum. The nanoclusters crystallize in a triclinic structure. They further analyzed the electrochemical/spectroscopic data and assigned the solved structure to have $1S^21P^4$ superatom electronic configuration, suggesting that the Pd atom does not donate any electrons to the superatom electronic structure as also supported from other studies. Also, linear absorption spectroscopy and electrochemical measurements suggested that the $PdAu_{24}(PET)_{18}$ nanocluster is isoelectronic with the $[Au_{25}(SR)_{18}]^+$ nanocluster. These results show that such endohedral doping can not only enhance the stability of these clusters but also allow manipulation of the properties of the nanoclusters and assembling into the solids, as discussed in other sections. Doping of two Pd atoms has been achieved[963] in $Au_{38}(SC_2H_4Ph)_{24}$, leading to the formation of $Pd_2Au_{36}(SC_2H_4Ph)_{24}$ with higher stability than the parent nanocluster.

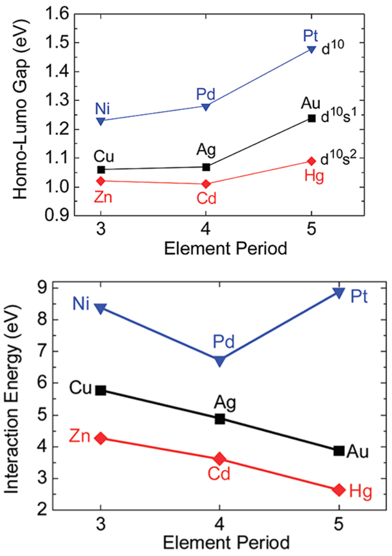

Figure 113. (Above) HOMO−LUMO gap of $[M@Au_{24}(SR)_{18}]^q$ for M being a transition metal (Ni, Pd, and Pt with $q = -2$); coinage metal atom with $q = -1$, and divalent ($q = 0$) atom. (Below) Interaction energy between M and the $[Au_{24}(SR)_{18}]^q$ frame for different M atoms. Reproduced with permission from ref 959. Copyright 2009 American Chemical Society.

X. Liu *et al.*[964] have studied crystal and solution photoluminescence of $MAg_{24}(SR)_{18}$ (M = Ag, Pd, Pt, and Au) in a way similar to the gold nanoclusters, while doped thiolated silver $[MAg_{24}(SR)_{18}]^{2-}$ (M = Pd, Pt) nanoclusters have been studied by Yan *et al.*,[965] who performed calculations to determine the structure and also analyzed the electronic structure of these doped thiolated silver nanoclusters. They suggested that Pd and Pt atoms occupy the center of the Ag_{13} icosahedron, very similar to the case of the Au nanoclusters. Bootharaju *et al.*[966,967] synthesized Au doped thiolated silver nanoclusters $[Ag_{24}Au(SR)_{18}]^-$ using $Ag_{25}(SR)_{18}$ as template. While up to 8 Au atoms could be doped, mass spectrometry and single crystal X-ray analysis of $[Ag_{24}Au(SR)_{18}]^-$ revealed the formation of Au centered thiolated nanoclusters $[Ag_{24}Au(SPhMe_2)_{18}]^-$, as shown in Figure 114. The detailed molecular structure of the $[Ag_{24}Au(SPhMe_2)_{18}]^-$ is depicted in Figure 115. The doping increased stability of the nanocluster as well as changed the electronic and optical properties with 25-fold enhancement in the photoluminescence compared with $[Ag_{25}(SPhMe_2)_{18}]^-$. Recently, $[Ag_{29}(LA)_{12}]^{3-}$ nanoclusters capped with lipoic acid (LA) have been doped with a single gold atom to obtain $[AuAg_{28}(LA)_{12}]^{3-}$ species.[968] Using EXAFS, XANES, and electronic structure calculations, it was shown that Au atom occupies the center of the cluster. The doped cluster has enhanced stability against heat and UV light as well as has increased luminescence efficiency. The optical properties changed with a blue shift in the absorption and emission spectra. Khatun *et al.*[969] have used a mixture of thiol/phosphine protected red luminescent silver nanoclusters $[Ag_{29}(BDT)_{12}(PPh_3)_4]^{3-}$ (BDT = 1,3-benzenedithiol), $[Au_xAg_{29-x}(BDT)_{12}(PPh_3)_4]^{3-}$ ($x = 1-4$), and $Ag_{29}(LA)_{12}$ as one of the fluorophores together with blue luminescent Si nanoparticles and green luminescent fluorescein isothiocyanate to obtain white light emission. The mixture produced white light with emission coordinates near to that of pure white light emission. Mishra *et al.*[970] have reported about six-fold enhancement in the photoluminescence of $AuAg_{28}(DHLA)_{12}$ compared with $Ag_{29}(DHLA)_{12}$, while Soldan *et al.*[971] have reported 26-fold enhancement in the luminescence quantum yield of Au doped silver nanoclusters. Kang *et al.*[972] and Bootharaju *et al.*[973] have studied doping of Pt in ligated silver nanoclusters $PtAg_{28}(SR)_{18}(PPh_3)_4$ and $[PtAg_{28}(BDT)_{12}(TPP)_4]^{4-}$, (BDT = benzenedithiolate, TPP = triphenylphosphine), respectively. The crystal structure of the tetrahedral shaped $PtAg_{28}(SR)_{18}(PPh_3)_4$ nanoclusters was determined by X-ray crystallography. The metal framework $PtAg_{24}$ of the nanocluster was shown to have FCC structure in contrast to generally icosahedral structure such as for $PtAu_{24}$. Also there is large enhancement in photoluminescence at ∼672 nm. $[PtAg_{28}(BDT)_{12}(TPP)_4]^{4-}$ nanoclusters were characterized by optical and photoelectron spectroscopy, mass spectrometry, total electron count, and TD-DFT calculations.[973] The Pt dopant was shown to occupy the center of the $PtAg_{28}$ nanocluster and modulate its electronic structure that enhances the photoluminescence intensity and excited-state lifetime. There is much less work on larger clusters and on other dopants, but the above achievements give much hope for future progress. Divalent dopants such as Cd and Hg have been studied[974−976], for example, $Au_{24}Hg(PET)_{18}$ (PET = phenylethanethiolate) with high resolution ESI-MS together with XPS and TGA.[975] X-ray single-crystal diffraction showed that the structure of $Au_{24}Hg_1(PET)_{18}$ has the structural framework of $Au_{25}(PET)_{18}$ with one of the outer-shell gold atoms replaced by one Hg atom. This has been supported by theoretical calculations as well. But Cd reconstructs the surface of the gold nanocluster.[974] An earlier study on doping of divalent metal ions such as Cd and Hg in thiolated Au_{25} nanocluster also showed that Cd tends to occupy one of the core sites while Hg occupies the outer Au site.[976]

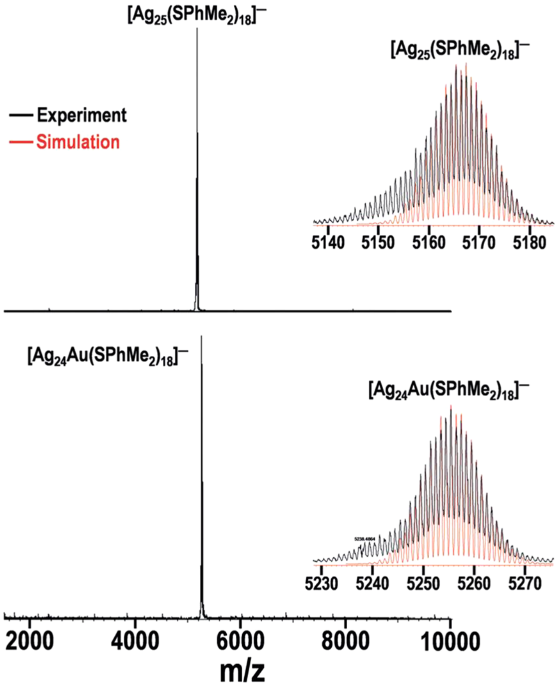

Figure 114. Negative-mode ESI MS of $[Ag_{25}(SPhMe_2)_{18}]^-$ and its galvanic exchange product with Au^+, namely the $[Ag_{24}Au(SPhMe_2)_{18}]^-$ nanocluster. Insets: experimental and simulated mass spectra of corresponding clusters. Reproduced with permission from ref 966. Copyright 2016 Wiley-VCH Verlag GmbH & Co. KGaA, Weinheim.

Atomically discrete clusters/nanoparticles of II−VI compound semiconductors and their assemblies have attracted much attention after the report of the formation of macroscopic quantities of ultrastable $Cd_{33}Se_{33}$ and $Cd_{34}Se_{34}$ nanoparticles with weaker abundance of $Cd_{13}Se_{13}$.[795] This development led to great interest in the isolation and assemblies of these systems as has been the case of C_{60}. These nanoparticles show strong quantum confinement effect with a strong absorption peak at 415 nm from $Cd_{33}Se_{33}$ and $Cd_{34}Se_{34}$ nanoparticles and a peak at 352 nm from $Cd_{13}Se_{13}$. These are considerably blue shifted from the bulk value of 680 nm. As discussed earlier, the structures of these endohedral Se@$Cd_{13}Se_{12}$, $(CdSe)_5$@$(CdSe)_{28}$, and $(CdSe)_6$@$(CdSe)_{28}$ nanoparticles have been obtained from *ab initio* calculations,[795] which showed the diameter of the largest nanoparticle to be 1.45 nm in excellent agreement with the experimental value of 1.5 nm. These developments opened up excellent opportunities for their applications in bio-labelling, imaging, photovoltaics, light emitting diodes, and other nanotechnologies, because most device applications require control of size and size distribution of such colloidal nanoparticles with narrow absorption and emission peaks. The abundances of these magic nanoparticles depend on the growth conditions including temperature as well as the ligands and can be controlled. Y. Wang *et al.*[977] later reported the isolation of $(CdSe)_{13}$(n-octylamine)$_{13}$ bundles from the lamellar structures that spontaneously form from the reaction of cadmium acetate dihydrate $[Cd(OAc)_2(H_2O)_2]$ with selenourea $[H_2NC(Se)NH_2]$ in

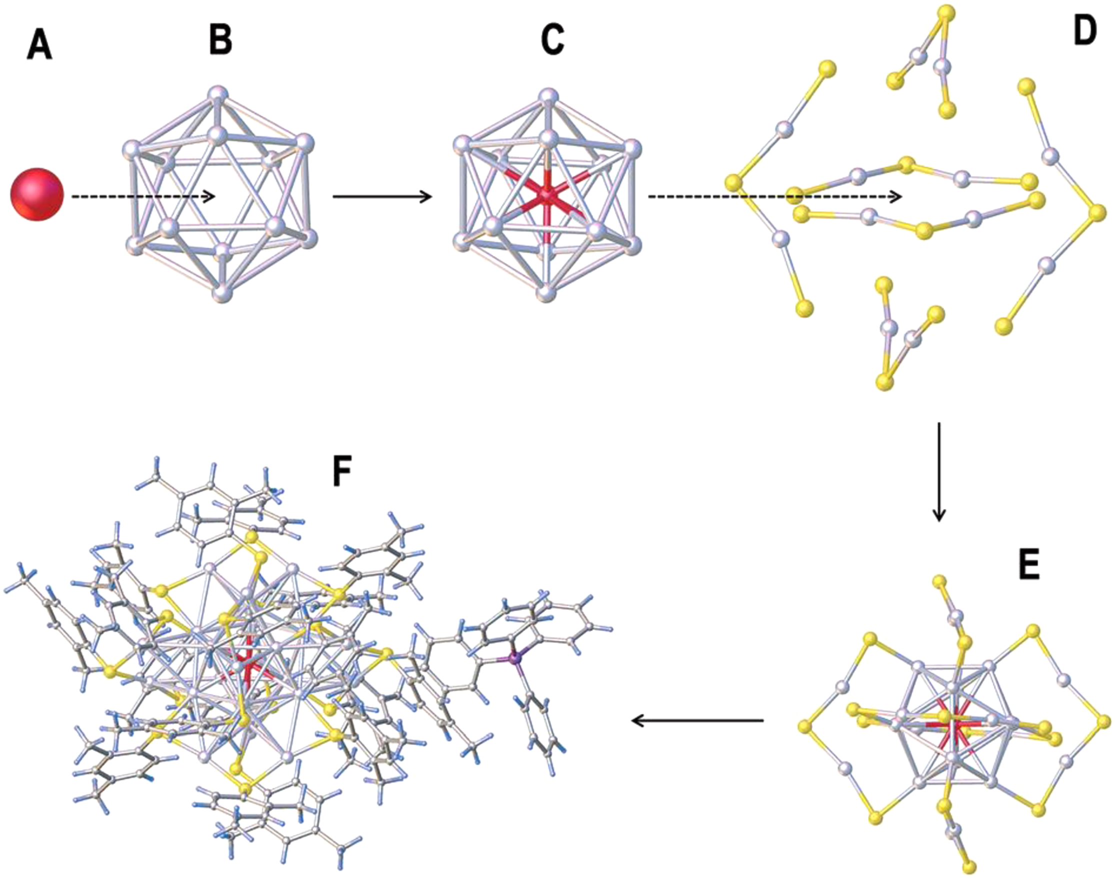

Figure 115. X-ray structure of $[Ag_{24}Au(SPhMe_2)_{18}]^-PPh_4^+$. (A) Au atom; (B) Ag_{12} icosahedron; (C) Ag_{12} with central Au forming $Ag_{12}Au$ core; (D) six V shaped Ag_2S_3 units; (E) capping $Ag_{12}Au$ core with six Ag_2S_3 units; and (F) the total structure of $[Ag_{24}Au(SPhMe_2)_{18}]^-PPh_4^+$ with counterion PPh_4. Balls show the atoms (Au: red, Ag: silver white, S: yellow, P: purple, C: gray). Reproduced with permission from ref 966. Copyright 2016 Wiley-VCH Verlag GmbH & Co. KGaA, Weinheim.

n-octylamine solvent at room temperature. The laser desorption ionization mass spectrometry of these bundles showed a strong peak of $(CdSe)_{13}$(*n*-octylamine)$_{13}$ while the abundances of other sizes were very small. Also, the UV/Vis spectra of these nanoclusters showed a strong peak at 350 nm. Further sonication of the mixtures of $[(CdSe)_{13}$(*n*-octylamine)$_{13}]$ in toluene with an excess of oleylamine resulted in the dissolution of $[(CdSe)_{13}$(n-octylamine)$_{13}]$ and the formation of free $[(CdSe)_{13}$(oleylamine)$_{13}]$ nanoparticles into the solution. It was also reported that the $(CdSe)_{13}$ bundles, sheets, and free nanoclusters were stable at room temperature in the solid state, in dispersion, or in solution for at least six months. Liu *et al.*[978] also reported a similar formation of lamellar assembly of $(CdSe)_{13}$ nanoclusters in n-octylamine solvent that transformed to CdSe quantum belts upon heating. Hsieh *et al.*[979] reported the formation of pairs of magic size $(CdSe)_{13}$ nanoclusters.

Doping of transition metals in semiconductors has been an area of much interest for spintronics, but doping in precisely controlled nanoclusters is difficult to achieve. In 2009, Yu *et al.*[980] reported doping of up to about 10% Mn in CdSe quantum nanoribbons using a nucleation-controlled doping process. It was shown that the doping of Mn is highly efficient at the Cd sites in $(CdSe)_{13}$ and that it is not favorable in $(CdSe)_{34}$ nanoparticles. Up to two Mn atoms could be doped in $(CdSe)_{13}$. The doping of Mn in nanoribbons of such magic nanoparticles resulted in giant exciton Zeeman splitting with an effective g-factor of 600, which is the largest value reported in diluted magnetic semiconductor nanocrystals. Yang *et al.*[981] also reported large-scale production of Mn doped $(CdSe)_{13}$ nanoparticles, where one or two Cd atoms were replaced by Mn leading to the formation of $Cd_{13}Se_{13}$, $Cd_{12}MnSe_{13}$, and $Cd_{11}Mn_2Se_{13}$ nanoparticles. Other magic nanoparticles namely $(CdSe)_{34}$ or $(CdSe)_{19}$ were not detected, confirming the high purity of the products. The optical absorption spectra of these nanoparticles showed a strong peak at 350 nm. Also, the photoluminescence spectra showed an intense emission around 600 nm which was attributed to the internal $(^4T_1\text{-}^6A_1)$ Mn^{2+} transition. A pronounced magnetic circular dichroism signal was observed for the Mn^{2+} doped clusters, which indicated a strong coupling between the charge carriers of the host material and the Mn^{2+}-dopants, suggesting that these materials belong to the family of dilute magnetic semiconductor nanostructures. Muckle *et al.*[982] have shown that in such Mn^{2+} bidoped $(CdSe)_{13}$ nanoparticles the spins on Mn sites were antiferromagnetically coupled and were magneto-optically passive. There has been a great amount of work and progress in these systems, and we refer the reader a recent perspective article[983] on the future of these colloidal magic nanoparticles.

To conclude this section, we shall emphasize that endohedral doping is a general concept to intentionally design caged clusters with high stability (usually also with high symmetry) and desired physical and chemical properties. Using these endohedrally doped cage clusters as building blocks, many possible cluster-assemblies from 0D to 1D, 2D, and 3D can be obtained, and some other low-dimensional nanostructures (e.g., metal-filled Si or Ge nanotubes) can be inspired. While there have been many theoretical studies, several interesting experimental realizations and new developments have taken place such as Be-encapsulated short Si nanotube arrays on Si(111) surface,[906] monolayer of Ta@Si_{16} nanoclusters on C_{60}-terminated HOPG surface,[914] assemblies of ligated gold and silver clusters as well as clusters of compound semiconductors, crystals of Zintl clusters, and Matryoshka clusters. We believe that, with the state-of-the-art techniques for synthesis of Zintl compounds and the continuous advance in cluster-beam with mass selection and deposition, more endohedral cluster assembled materials would be precisely designed and mass-produced in the near future.

11. PERSPECTIVE

The results presented in this review firmly demonstrate that endohedral doping is a very effective and novel strategy to create new ground state structures of nanomaterials, different from the corresponding undoped ones and with quite distinct properties in general. Most importantly, there is enhanced stability of the doped cluster as well as size selectivity that leads to high abundance in the mass spectrum, which is desirable to make cluster-assembled materials. Selection of suitable dopant and host material can tailor the fundamental properties of an atomic cluster. Furthermore, charged endohedral clusters are soluble and available in weighable amounts in synthetic chemistry. Therefore, endohedral doping provides many new opportunities to design novel clusters with desired functions as building blocks of cluster-assembled materials for different applications.

Since the theoretical prediction of the endohedrally doped Ti@Si_{16} FK polyhedron, Zr@Si_{16} silicon fullerene cage, and other structures in 2001, and their subsequent realization in the laboratory, great experimental and theoretical progress has been made not only in endohedral silicon clusters but also in a variety of other materials including group 14 elements C, Ge, Sn, and Pb, group 13 elements predominantly Al, B, and Ga, coinage metals, compound semiconductors, and some other cases. Research on endohedrally doped aluminum clusters has been particularly exciting in developing atom-like behavior of clusters (so called "*superatom*"), and further work on other clusters would be interesting to develop a 3D periodic table. There have also been interesting developments on Russian doll-like multishell Matryoshka clusters. In fact, the field of endohedral clusters has grown rapidly in the past decade or so, leading to the discovery of a rich variety of new clusters mostly having cage structures. In this review, we have made an effort to cover these exciting developments, and some of the prominent endohedral clusters can be mentioned here, namely Si@Al_{12} as well as W@Au_{12} and related systems, Ti@Si_{16}, Zr@Si_{16}, Ta@Si_{16} and related 68 valence electron clusters, magnetic superatoms Mn@Sn_{12}, Gd@Au_{15}, Eu@Si_{20}, and rare earth metal doped small carbon fullerenes, Mo@B_{24} and related systems, As@Ni_{12}@As_{20} and other Matryoshka clusters, ligated doped clusters such as those of gold, silver, and II−VI, as well as Zintl clusters. Most of these mentioned clusters have a large HOMO−LUMO gap and substantial embedding energy.

However, compared to the extensive and long-time studies on atoms, molecules, and solids, the history of research on generating size-selected gas phase clusters and characterizing them with spectroscopic approaches is of only about 40 years, while the developments on endohedrally doped clusters have been in the past less than 20 years only (if not counting the earlier efforts on X@Al_{12} which in fact did not focus on the endohedral aspect for designing novel clusters). Therefore, there is still a large untouched realm of endohedrally doped clusters such as those of transition metals because of the weak magic nature of such clusters, weakly interacting materials including organic ones though *organometallic* materials constitute a big subject, and a large variety of alloys/compounds as well as many other elements not well studied so far. A few noteworthy examples are Cr@Zn_{17} with D_{5h} symmetry and 6 μ_B magnetic moment,[984] Mo@Nb_{14} cluster, and its isoelectronic counterparts (such as W@Nb_{14}, Mo@Ta_{14}, and W@Ta_{14}) with moderate HOMO−LUMO gap of about 0.8 eV[985] within GGA. Moreover, the numbers of theoretical and experimental papers in this field are largely unbalanced with many theoretical predictions still awaiting experimental validation.

A further extension of the endohedrally doped systems would be atomically well-designed core-shell clusters/nanoparticles with the core having more than one atom such as $(CdSe)_6$@$(CdSe)_{28}$. Though a large body of research has been carried out on a variety of nanoparticles and core-shell clusters, more efforts would be desirable to develop these systems in an atomically controlled manner. We believe that there would be great opportunities to discover many other novel systems and find their applications.

So far most developments are on gas-phase clusters. In order to establish a complete understanding of the structures and properties of endohedrally doped clusters and to eventually utilize them for practical applications, it is very important to be able to produce such clusters in large quantity at low cost. The recent work by Nakajima's group on Ti@Si_{16} and Ta@Si_{16} clusters, which could be produced in about 100 mg quantity using dry-chemistry methods, is very encouraging. This has made it possible to use traditional methods to study the structure and properties of these systems. We expect that the production of these species may be increased in the near future and that the technique could be extended to produce other kinds of clusters in large quantity. There is another way of producing clusters by a wet chemistry method. In this direction, significant progress has been made such as production of Ni@Pb_{10} clusters, halogen-ion templated hydrogenated silicon clusters, synthesis of crystalline Zintl compounds based on endohedral cage clusters, which is an alternative way to achieve bulk amount of precisely controlled clusters in ordered crystalline form as well as other aggregates, and ligated coinage metal clusters such as those of Au and Ag doped with other coinage metal atoms or transition metal atoms, e.g. Pd and Pt. Even solids of some of these doped clusters have been formed, and this has been one of the objectives in cluster science to produce assemblies of clusters. Therefore, the progress in recent years is commendable, and we hope that such methods would be used more widely to produce nanoclusters of a variety of materials and their assemblies in different dimensions. An area that also needs attention is the study of properties of cluster assembled solids, though the progress on coinage metals is very encouraging. We believe that this will open up new possibilities of cluster-based materials, both at the nano and macroscopic scale. There are also well-known cluster compounds such as those based on Mo_6S_8 cluster. This wide knowledge of already known nano and cluster-based bulk materials as well as the progress in experimental methods would further help in making new materials.

We think that the following directions would be interesting to explore in future studies:

(1) Despite many endohedrally doped clusters already discovered, as mentioned above, there are still numerous possibilities to search for such clusters with high stability and exotic physical and chemical properties that are awaiting exploration, considering that a very large number of combinations of elements and spatial arrangements of atoms are possible. In this regard, global search methods based on *ab initio* calculations could be an exciting tool in theoretical design of novel endohedrally doped clusters.

(2) While already quite a few interesting endohedrally doped clusters with high stability have been predicted from theory, only a small number of them have been generated and well characterized in the laboratory. Although this progress on some clusters is very encouraging, there are many interesting systems such as metal doped boron cages Mo@B_{24} awaiting realization. Also, many small carbon fullerenes with endohedral doping have been predicted, and it would be interesting to carry out experiments on these systems as there could be a good possibility for assembling them. In general, in order to realize new materials and device applications, one must be able to produce clusters with a specific size and composition in macroscopic amount. A good example is the mass production of C_{60} fullerene using electric arc evaporation of graphite that fueled much progress, and we hope for interesting developments for the large-scale production of a variety of endohedral clusters in the future.

(3) The current theoretical and experimental studies mainly focus on the fundamental properties, and much less efforts have been devoted to the potential applications of endohedrally doped clusters by exploiting their advantageous characteristics. As an example, there is an upsurge in single atom catalysis, and it would be interesting to explore how to utilize the endohedrally doped clusters such as those of transition metals and coinage metals with tunable surface activity to develop highly efficient catalysts. With proper selection of dopant atoms and host caged clusters, novel nonmetal catalysts based on endohedrally doped clusters may also be designed. Furthermore, the endohedral clusters may have novel temperature-dependent properties, which are still largely unexplored.

(4) There have been a few successful examples of magnetic superatoms with large magnetic moments, moderate HOMO−LUMO gap, and high stability, such as Mn@Ge_{12}, Mn@Sn_{12}, Eu@Si_{20}, and Gd@Au_{15}. These clusters may offer possibilities to develop new magnetic materials. More such species are sought after, and further research would be desirable. Moreover, the endohedrally doped clusters have tunable electronic gap, and for many of them the gap amplitudes are in the visible light range, allowing them to harvest the majority of the spectrum of the sunlight. These features should be taken advantage of for optoelectronic applications. Another question is if such clusters could be candidates for the ultimate molecular level devices. Experimental exploration of cluster-based devices is still in its embryonic stage, although there have been a few theoretical designs of cluster-based devices for spintronic, nanoelectronics, and optoelectronics. Certainly, further work on cluster-based devices from both theoretical and experimental sides is needed.

(5) In practical applications, the size-selected gas phase clusters have to be deposited on a substrate. For such supported clusters, the cluster−substrate interaction would be a crucial topic that would be worth further investigation. A carefully chosen substrate should not only support and anchor the clusters, but also avoid their aggregation and further growth, and result in optimal functional properties by making use of the synergic effect. Recent work on 2D assemblies of Ta@Si_{16} fullerene clusters on C_{60} covered TiO_2 support is promising, and further work is expected in the future so that we could have guidelines for 1D, 2D, and 3D assemblies. For this, as we have discussed in Section 10, cluster−cluster interaction in dimers of many endohedral cage clusters is still rather strong (binding energy larger than 1.0 eV), but there are a few exceptions such as FK polyhedral clusters of Ti@Si_{16} and Ti@Ge_{16}. More such clusters with weak intercluster interaction should be searched and explored for the development of cluster-assembled systems in different dimensions, similar to solid C_{60} and its compounds. Besides, there would be tremendous opportunities for making crystals of ligated clusters.

In closing this review, we feel that this field will grow rapidly in the near future and we believe that the topics on endohedral doping covered in the review will provide an excellent reference for researchers to enter the field as well as to know what has been achieved.

ASSOCIATED CONTENT

Supporting Information

The Supporting Information is available free of charge at https://pubs.acs.org/doi/10.1021/acs.chemrev.9b00651.

Comparison between the calculated (PBE0/6-311+G(d)) and experimental bond lengths as well as Raman and infrared frequencies of C_{60} fullerene (Table S1); comparison between the theoretical (PBE0/PAW) and experimental equilibrium lattice constant, cohesive energy, and bulk modulus of B, C, Si, Ge, Al, Au, Ag, Cu crystals (Table S2). Tables S3−S22 give the geometric and electronic properties of endohedral cage clusters from PBE0/6-311+G(d), SDD calculations for M@C_{28}, M@B_n (n = 18−24), M@Si_{10}, M@Si_{11}, M@Si_{12}, M@Si_{13}, M@Si_{14}, M@Si_{15}, M@Si_{16}, M@$Si_{18, 20}$, M@Ge_{10}, M@Ge_{11}, M@Ge_{12}, M@Ge_{13}, M@Ge_{14}, M@Ge_{15}, M@Ge_{16}, M@Au_n (n = 12−17), M@Ag_n (n = 8−15), and M@Cu_n (n = 12, 16). (PDF)

AUTHOR INFORMATION

Corresponding Authors

Si Zhou − *Key Laboratory of Materials Modification by Laser, Ion and Electron Beams, (Dalian University of Technology), Ministry of Education, Dalian 116024, China;* orcid.org/0000-0002-0842-1075; Email: sizhou@dlut.edu.cn

Vijay Kumar − *Center for Informatics, School of Natural Sciences, Shiv Nadar University, Tehsil Dadri 201314, India; Dr. Vijay Kumar Foundation, Gurgaon 122001, Haryana,*

India; orcid.org/0000-0002-5283-5443;
Email: vijay.kumar@snu.edu.in

Authors

Jijun Zhao − *Key Laboratory of Materials Modification by Laser, Ion and Electron Beams, (Dalian University of Technology), Ministry of Education, Dalian 116024, China;* orcid.org/0000-0002-3263-7159

Qiuying Du − *Key Laboratory of Materials Modification by Laser, Ion and Electron Beams, (Dalian University of Technology), Ministry of Education, Dalian 116024, China*

Complete contact information is available at:
https://pubs.acs.org/10.1021/acs.chemrev.9b00651

Notes

The authors declare no competing financial interest.

Biographies

Jijun Zhao received his Ph.D in condensed matter physics from Nanjing University (China) in 1996 and became a professor in Dalian University of Technology (China) in 2006. Since 2018, he has been awarded the Changjiang distinguished professorship. He is now dean of school of physics in Dalian University of Technology and director of the key laboratory of materials modification by laser, ion, and electron beams (Ministry of Education). He serves as editorial board member of *Advances in Physics X*, *Computational Condensed Matter*, *Molecular Simulation*, *Journal of Cluster Science*, and *Scientific Reports*. His major research field is computational materials science with special interest in clusters and low-dimensional nanostructures. He has contributed more than 500 refereed journal papers in *Science Advances*, *Nature Communications*, *JACS*, *PRL*, *Advanced Materials*, *Progress in Materials Science*, *ACS Nano*, etc., which have been cited by over 18000 times. His current H-index is 69.

Qiuying Du is currently a Ph.D. candidate working with Jijun Zhao in Dalian University of Technology (China). She obtained her B.S. from Inner Mongolia University in 2016. Her research interests focus on the structures and electronic properties of metal clusters.

Si Zhou received her Ph.D. in condensed matter physics from Georgia Institute of Technology in USA in 2014 and became a professor in Dalian University of Technology in 2019. Her major research field is computational materials science with special interests in low-dimensional materials from clusters, nanotube, and nanowires, two-dimensional materials, to their heterostructures. Her iconic work includes the structure prediction of graphene oxide and design of nonmetal catalysts for energy and environmental applications. She has over 70 refereed journal papers in *Nat. Mater.*, *Acc. Chem. Res.*, *J. Am. Chem. Soc.*, *Adv. Mater.*, *Angew. Chem. Int. Ed.*, *Nano Lett.*, *Adv. Energy Mater.*, *Nano Energy*, *J. Mater. Chem. A*, etc., which have been cited by over 2300 times. Her current H-index is 24.

Vijay Kumar did his M.Sc. (1972) and Ph.D. (1977) from the University of Roorkee, now known as Indian Institute of Technology, Roorkee. He was a Humboldt Fellow (1979−80) and then Wissenschaftlermitarbeiter at the Institute for Theoretische Physik, Freie Universität Berlin (1980−85). He served at the Indira Gandhi Center for Atomic Research, Kalpakkam (1985−1999) and was invited by the International Center for Theoretical Physics (ICTP), Trieste to Coordinate the Diploma Course in Condensed Matter Physics (1991−93) where he also directed several activities. He was Visiting Scientist/Professor at the Cavendish Laboratory; International School of Advanced Studies, Trieste; Laboratoire Aime Cotton, CNRS, Orsay; Institute for Materials Research/International Frontier Center for Advanced Materials/Center for Interdisciplinary Research, Tohoku University, Japan; Invited Researcher at the Hokkaido University/Research Institute for Computational Science (RICS), AIST, Tuskuba; and Institute for Mathematical Sciences, Chennai. He was Junior Associate and later Associate of the ICTP, Trieste, and received Gold Medal in M.Sc., the Materials Research Society of India (MRSI) Medal in 1996, and the Asian Consortium for Computational Materials Science (ACCMS) Award in 2004. He was the Chairman of the Subject Group "Computer Aided Design of Materials" and Member of the Council of MRSI. He is currently Research Professor at the Center for Informatics, Shiv Nadar University, and Founder President, Dr. Vijay Kumar Foundation.

ACKNOWLEDGMENTS

JZ and SZ would like to acknowledge support by the National Natural Science Foundation of China (91961204, 11974068, 11574040), the Fundamental Research Funds for the Central Universities of China (DUT20LAB110), and the Supercomputing Center of Dalian University of Technology. VK would like to thank all his collaborators for fruitful cooperation that has helped in the development of many ideas and results presented in this review. In particular, he is grateful to Y. Kawazoe and many students and visitors at the Institute for Materials Research at the Tohoku University where many interesting papers were written and all the computational resources of the Center for Computational Materials Science that were so important to carry out the work. VK is also thankful to the Asian Office of the Aerospace Research and Development (AOARD) and International Technology Center-Pacific (ITC-PAC) for their support on different projects that helped to continue to make progress on these systems and all collaborators at the Foundation and Shiv Nadar University (SNU). VK is grateful to N. Sukumar for all the help and cooperation at the SNU. VK also acknowledges the computational resources from the Center for the Development of Advanced Computing (CDAC), Pune and the MAGUS resources at the SNU where some of the work has been carried out. Finally we sincerely thank the reviewers for their great efforts and constructive suggestions that helped us to improve the presentation.

LIST OF ABBREVIATIONS

ADE	adiabatic detachment energies
AEA	adiabatic electron affinity
AIMD	*ab initio* molecular dynamics
AIP	adiabatic ionization potential
amu	atomic mass unit
BCC	body centered cubic
BCT	body centered tetragonal
BN	boron nitride
CC	coupled cluster
DFT	density functional theory
DOS	density of state
ECP	effective core potential
ESI-MS	electrospray ionization mass spectrometry
EPR	electron paramagnetic resonance
FCC	face centered cubic
FK	Frank−Kasper
FT-ICR	Fourier transform−ion cyclotron resonance
GA	genetic algorithm
GGA	generalized gradient approximation
HCP	hexagonal close packed

HF	Hartree−Fock
HOMO	highest occupied molecular orbital
HREM	high-resolution electron microscopy
LUMO	lowest unoccupied molecular orbital
HOPG	highly oriented pyrolytic graphite
IR-MPD	infrared multiple photon dissociation
IR-UV2CI	infrared−ultraviolet two-color ionization
LDA	local density approximation
LDI-TOF	laser desorption−ionization time-of-flight
LD-TOF	laser desorption time-of-flight
MD	molecular dynamics
L-H	Langmuir−Hinshelwood
MS	mass spectrometry
NBO	natural bond orbital
NICS	nucleus-independent chemical shift
NMR	nuclear magnetic resonance
PAW	projector augmented wave
PEG-DME	poly(ethylene glycol) dimethyl ether
PES	photoelectron spectrum
QLMD	quantum Langevin molecular dynamics
RPA	random-phase approximation
SC	simple cubic
SERS	surface-enhanced Raman spectroscopy
SOC	spin-orbital coupling
STM/STS	scanning tunneling microscopy and spectroscopy
TD-DFT	time-dependent density functional theory
TGA	thermogravimetric analysis
TS	transition states
TTP	tricapped-trigonal-prism
UPS	ultraviolet photoelectron spectroscopy
VEA	vertical electron affinity
VIP	vertical ionization potential
XPS	X-ray photoelectron spectroscopy
XMCD	X-ray magnetic circular dichroism
ZORA	zeroth-order approximation
0D	zero-dimensional
1D	one-dimensional
2D	two-dimensional
3D	three-dimensional

REFERENCES

(1) De Heer, W. A. The physics of simple metal clusters: experimental aspects and simple models. *Rev. Mod. Phys.* **1993**, *65*, 611−676.

(2) Castleman, A.; Bowen, K. Clusters: Structure, energetics, and dynamics of intermediate states of matter. *J. Phys. Chem.* **1996**, *100*, 12911−12944.

(3) Alonso, J. Electronic and atomic structure, and magnetism of transition-metal clusters. *Chem. Rev.* **2000**, *100*, 637−678.

(4) Janssens, E.; Neukermans, S.; Lievens, P. Shells of electrons in metal doped simple metal clusters. *Curr. Opin. Solid State Mater. Sci.* **2004**, *8*, 185−193.

(5) Baletto, F.; Ferrando, R. Structural properties of nanoclusters: Energetic, thermodynamic, and kinetic effects. *Rev. Mod. Phys.* **2005**, *77*, 371−423.

(6) Ferrando, R.; Jellinek, J.; Johnston, R. L. Nanoalloys: from theory to applications of alloy clusters and nanoparticles. *Chem. Rev.* **2008**, *108*, 845−910.

(7) Jena, P.; Castleman, A., Jr Mass spectrometry and its role in advancing cluster science. *Int. J. Mass Spectrom.* **2015**, *377*, 235−247.

(8) Zhao, J.; Huang, X.; Jin, P.; Chen, Z. Magnetic properties of atomic clusters and endohedral metallofullerenes. *Coord. Chem. Rev.* **2015**, *289*, 315−340.

(9) Luo, Z.; Castleman, A., Jr; Khanna, S. N. Reactivity of metal clusters. *Chem. Rev.* **2016**, *116*, 14456−14492.

(10) Claridge, S. A.; Castleman, A., Jr; Khanna, S. N.; Murray, C. B.; Sen, A.; Weiss, P. S. Cluster-assembled materials. *ACS Nano* **2009**, *3*, 244−255.

(11) Mandal, S.; Reber, A. C.; Qian, M.; Weiss, P. S.; Khanna, S. N.; Sen, A. Controlling the band gap energy of cluster-assembled materials. *Acc. Chem. Res.* **2013**, *46*, 2385−2395.

(12) Jena, P.; Sun, Q. Super atomic clusters: design rules and potential for building blocks of materials. *Chem. Rev.* **2018**, *118*, 5755−5870.

(13) Kumar, V. In *Handbook of Nanophysics*; CRC Press, 2010; pp 65−87.

(14) Zhao, J.; Huang, X.; Shi, R.; Tang, L.; Su, Y.; Sai, L. Ab initio global optimization of clusters. *Chemical Modelling* **2015**, *12*, 249−292.

(15) Kumar, V.; Esfarjani, K.; Kawazoe, Y. In *Clusters and nanomaterials*; Springer, 2002; pp 9−88.

(16) Knight, W.; Clemenger, K.; de Heer, W. A.; Saunders, W. A.; Chou, M.; Cohen, M. L. Electronic shell structure and abundances of sodium clusters. *Phys. Rev. Lett.* **1984**, *52*, 2141−2143.

(17) Frauendorf, S. G.; Guet, C. Atomic clusters as a branch of nuclear physics. *Annu. Rev. Nucl. Part. Sci.* **2001**, *51*, 219−259.

(18) Brack, M. The physics of simple metal clusters: self-consistent jellium model and semiclassical approaches. *Rev. Mod. Phys.* **1993**, *65*, 677−732.

(19) Itoh, M.; Kumar, V.; Adschiri, T.; Kawazoe, Y. Comprehensive study of sodium, copper, and silver clusters over a wide range of sizes $2 \leq N \leq 75$. *J. Chem. Phys.* **2009**, *131*, 174510.

(20) Martin, T.; Bergmann, T.; Göhlich, H.; Lange, T. Observation of electronic shells and shells of atoms in large Na clusters. *Chem. Phys. Lett.* **1990**, *172*, 209−213.

(21) Echt, O.; Sattler, K.; Recknagel, E. Magic numbers for sphere packings: experimental verification in free xenon clusters. *Phys. Rev. Lett.* **1981**, *47*, 1121−1124.

(22) Leuchtner, R.; Harms, A.; Castleman, A., Jr Thermal metal cluster anion reactions: Behavior of aluminum clusters with oxygen. *J. Chem. Phys.* **1989**, *91*, 2753−2754.

(23) Leuchtner, R.; Harms, A.; Castleman, A., Jr Aluminum cluster reactions. *J. Chem. Phys.* **1991**, *94*, 1093−1101.

(24) Gong, X.; Kumar, V. Enhanced stability of magic clusters: A case study of icosahedral $Al_{12}X$, X = B, Al, Ga, C, Si, Ge, Ti, As. *Phys. Rev. Lett.* **1993**, *70*, 2078−2081.

(25) Wang, L.; Zhao, J.; Zhou, Z.; Zhang, S.; Chen, Z. First-principles study of molecular hydrogen dissociation on doped $Al_{12}X$ (X = B, Al, C, Si, P, Mg, and Ca) clusters. *J. Comput. Chem.* **2009**, *30*, 2509−2514.

(26) Castleman, A., Jr; Khanna, S. Clusters, superatoms, and building blocks of new materials. *J. Phys. Chem. C* **2009**, *113*, 2664−2675.

(27) Castleman, A., Jr From elements to clusters: The periodic table revisited. *J. Phys. Chem. Lett.* **2011**, *2*, 1062−1069.

(28) Luo, Z.; Castleman, A. W. Special and general superatoms. *Acc. Chem. Res.* **2014**, *47*, 2931−2940.

(29) Jena, P. Beyond the periodic table of elements: The role of superatoms. *J. Phys. Chem. Lett.* **2013**, *4*, 1432−1442.

(30) Kroto, H. W.; Heath, J. R.; O'Brien, S. C.; Curl, R. F.; Smalley, R. E. C_{60}: Buckminsterfullerene. *Nature* **1985**, *318*, 162−163.

(31) Krätschmer, W.; Lamb, L. D.; Fostiropoulos, K.; Huffman, D. R. Solid C_{60}: a new form of carbon. *Nature* **1990**, *347*, 354−358.

(32) Hebard, A. F.; Rosseinsky, M. J.; Haddon, R. C.; Murphy, D. W.; Glarum, S. H.; Palstra, T. T. M.; Ramirez, A. P.; Kortan, A. R. Superconductivity at 18 K in Potassium-doped C_{60}. *Nature* **1991**, *350*, 600−601.

(33) Canham, L. T. Silicon quantum wire array fabrication by electrochemical and chemical dissolution of wafers. *Appl. Phys. Lett.* **1990**, *57*, 1046−1048.

(34) Uhlir, A., Jr Electrolytic shaping of germanium and silicon. *Bell Syst. Tech. J.* **1956**, *35*, 333−347.

(35) Bisi, O.; Ossicini, S.; Pavesi, L. Porous silicon: a quantum sponge structure for silicon based optoelectronics. *Surf. Sci. Rep.* **2000**, *38*, 1−126.

(36) Beck, S. M. Studies of silicon cluster−metal atom compound formation in a supersonic molecular beam. *J. Chem. Phys.* **1987**, *87*, 4233−4234.

(37) Beck, S. M. Mixed metal−silicon clusters formed by chemical reaction in a supersonic molecular beam: implications for reactions at the metal/silicon interface. *J. Chem. Phys.* **1989**, *90*, 6306−6312.

(38) Heath, J.; O'brien, S.; Zhang, Q.; Liu, Y.; Curl, R.; Tittel, F.; Smalley, R. Lanthanum complexes of spheroidal carbon shells. *J. Am. Chem. Soc.* **1985**, *107*, 7779−7780.

(39) Lu, X.; Chen, Z. Curved pi-conjugation, aromaticity, and the related chemistry of small fullerenes (< C_{60}) and single-walled carbon nanotubes. *Chem. Rev.* **2005**, *105*, 3643−3696.

(40) Rodríguez-Fortea, A.; Balch, A. L.; Poblet, J. M. Endohedral metallofullerenes: a unique host−guest association. *Chem. Soc. Rev.* **2011**, *40*, 3551−3563.

(41) Lu, X.; Feng, L.; Akasaka, T.; Nagase, S. Current status and future developments of endohedral metallofullerenes. *Chem. Soc. Rev.* **2012**, *41*, 7723−7760.

(42) Popov, A. A.; Yang, S.; Dunsch, L. Endohedral fullerenes. *Chem. Rev.* **2013**, *113*, 5989−6113.

(43) Garcia-Borras, M.; Osuna, S.; Luis, J. M.; Swart, M.; Solà, M. The role of aromaticity in determining the molecular structure and reactivity of (endohedral metallo) fullerenes. *Chem. Soc. Rev.* **2014**, *43*, 5089−5105.

(44) Yang, S.; Wei, T.; Jin, F. When metal clusters meet carbon cages: endohedral clusterfullerenes. *Chem. Soc. Rev.* **2017**, *46*, 5005−5058.

(45) Guo, T.; Diener, M. D.; Chai, Y.; Alford, M. J.; Haufler, R. E.; McClure, S. M.; Ohno, T.; Weaver, J. H.; Scuseria, G. E.; Smalley, R. E. Uranium stabilization of C_{28}: a tetravalent fullerene. *Science* **1992**, *257*, 1661−1664.

(46) Jackson, K.; Nellermoe, B. Zr@Si_{20}: a strongly bound Si endohedral system. *Chem. Phys. Lett.* **1996**, *254*, 249−256.

(47) Hiura, H.; Miyazaki, T.; Kanayama, T. Formation of metal-encapsulating Si cage clusters. *Phys. Rev. Lett.* **2001**, *86*, 1733−1736.

(48) Kumar, V.; Kawazoe, Y. Metal-encapsulated fullerenelike and cubic caged clusters of silicon. *Phys. Rev. Lett.* **2001**, *87*, 045503.

(49) Kumar, V.; Kawazoe, Y. Erratum: Metal-Encapsulated Fullerenelike and Cubic Caged Clusters of Silicon [Phys. Rev. Lett. 87, 045503 (2001)]. *Phys. Rev. Lett.* **2003**, *91*, 199901.

(50) O'brien, S.; Heath, J.; Curl, R.; Smalley, R. Photophysics of buckminsterfullerene and other carbon cluster ions. *J. Chem. Phys.* **1988**, *88*, 220−230.

(51) Zhu, X.; Zeng, X. C.; Lei, Y.; Pan, B. Structures and stability of medium silicon clusters. II. Ab initio molecular orbital calculations of Si_{12}−Si_{20}. *J. Chem. Phys.* **2004**, *120*, 8985−8995.

(52) Yoo, S.; Zeng, X. C. Structures and stability of medium-sized silicon clusters. III. Reexamination of motif transition in growth pattern from Si_{15} to Si_{20}. *J. Chem. Phys.* **2005**, *123*, 164303.

(53) Kumar, V.; Kawazoe, Y. Metal-encapsulated caged clusters of germanium with large gaps and different growth behavior than silicon. *Phys. Rev. Lett.* **2002**, *88*, 235504.

(54) Ohara, M.; Koyasu, K.; Nakajima, A.; Kaya, K. Geometric and electronic structures of metal (M)-doped silicon clusters (M = Ti, Hf, Mo and W). *Chem. Phys. Lett.* **2003**, *371*, 490−497.

(55) Koyasu, K.; Akutsu, M.; Mitsui, M.; Nakajima, A. Selective formation of MSi_{16} (M = Sc, Ti, and V). *J. Am. Chem. Soc.* **2005**, *127*, 4998−4999.

(56) Lau, J.; Hirsch, K.; Klar, P.; Langenberg, A.; Lofink, F.; Richter, R.; Rittmann, J.; Vogel, M.; Zamudio-Bayer, V.; Möller, T. X-ray spectroscopy reveals high symmetry and electronic shell structure of transition-metal-doped silicon clusters. *Phys. Rev. A: At., Mol., Opt. Phys.* **2009**, *79*, 053201.

(57) Furuse, S.; Koyasu, K.; Atobe, J.; Nakajima, A. Experimental and theoretical characterization of MSi_{16}^{-}, MGe_{16}^{-}, MSn_{16}^{-}, and MPb_{16}^{-} (M = Ti, Zr, and Hf): The role of cage aromaticity. *J. Chem. Phys.* **2008**, *129*, 064311.

(58) Kumar, V.; Singh, A. K.; Kawazoe, Y. Smallest magic caged clusters of Si, Ge, Sn, and Pb by encapsulation of transition metal atom. *Nano Lett.* **2004**, *4*, 677−681.

(59) Neukermans, S.; Janssens, E.; Chen, Z.; Silverans, R.; Schleyer, P. v. R.; Lievens, P. Extremely stable metal-encapsulated $AlPb_{10}^{+}$ and $AlPb_{12}^{+}$ clusters: Mass-Spectrometric discovery and density functional theory study. *Phys. Rev. Lett.* **2004**, *92*, 163401.

(60) Lv, J.; Wang, Y.; Zhang, L.; Lin, H.; Zhao, J.; Ma, Y. Stabilization of fullerene-like boron cages by transition metal encapsulation. *Nanoscale* **2015**, *7*, 10482−10489.

(61) Pyykkö, P.; Runeberg, N. Icosahedral WAu_{12}: A predicted closed-shell species, stabilized by aurophilic attraction and relativity and in accord with the 18-electron rule. *Angew. Chem., Int. Ed.* **2002**, *41*, 2174−2176.

(62) Li, X.; Kiran, B.; Li, J.; Zhai, H. J.; Wang, L. S. Experimental observation and confirmation of icosahedral W@Au_{12} and Mo@Au_{12} molecules. *Angew. Chem., Int. Ed.* **2002**, *41*, 4786−4789.

(63) Veldeman, N.; Höltzl, T.; Neukermans, S.; Veszprémi, T.; Nguyen, M. T.; Lievens, P. Experimental observation and computational identification of Sc@Cu_{16}^{+}, a stable dopant-encapsulated copper cage. *Phys. Rev. A: At., Mol., Opt. Phys.* **2007**, *76*, 011201.

(64) Hakkinen, H.; Yoon, B.; Landman, U.; Li, X.; Zhai, H. J.; Wang, L. S. On the electronic and atomic structures of small Au_N^- (N=4-14) clusters: A photoelectron spectroscopy and density-functional study. *J. Phys. Chem. A* **2003**, *107*, 6168−6175.

(65) Huang, W.; Wang, L.-S. Probing the 2D to 3D structural transition in gold cluster anions using argon tagging. *Phys. Rev. Lett.* **2009**, *102*, 153401.

(66) Jian, T.; Chen, X.; Li, S.-D.; Boldyrev, A. I.; Li, J.; Wang, L.-S. Probing the structures and bonding of size-selected boron and doped-boron clusters. *Chem. Soc. Rev.* **2019**, *48*, 3550−3591.

(67) Kumar, V.; Kawazoe, Y. Metal-doped magic clusters of Si, Ge, and Sn: The finding of a magnetic superatom. *Appl. Phys. Lett.* **2003**, *83*, 2677−2679.

(68) Rohrmann, U.; Schäfer, R. Stern-Gerlach experiments on Mn@Sn_{12}: Identification of a paramagnetic superatom and vibrationally induced spin orientation. *Phys. Rev. Lett.* **2013**, *111*, 133401.

(69) Rohrmann, U.; Schwerdtfeger, P.; Schäfer, R. Atomic domain magnetic nanoalloys: interplay between molecular structure and temperature dependent magnetic and dielectric properties in manganese doped tin clusters. *Phys. Chem. Chem. Phys.* **2014**, *16*, 23952−23966.

(70) Zhang, M.; Zhang, J.; Feng, X.; Zhang, H.; Zhao, L.; Luo, Y.; Cao, W. Magnetic superatoms in VLi_n (n = 1−13) clusters: A first-principles prediction. *J. Phys. Chem. A* **2013**, *117*, 13025−13036.

(71) Reveles, J. U.; Clayborne, P. A.; Reber, A. C.; Khanna, S. N.; Pradhan, K.; Sen, P.; Pederson, M. R. Designer magnetic superatoms. *Nat. Chem.* **2009**, *1*, 310−315.

(72) Medel, V. M.; Reveles, J. U.; Khanna, S. N.; Chauhan, V.; Sen, P.; Castleman, A. W. Hund's rule in superatoms with transition metal impurities. *Proc. Natl. Acad. Sci. U. S. A.* **2011**, *108*, 10062−10066.

(73) Ge, G.-X.; Han, Y.; Wan, J.-G.; Zhao, J.-J.; Wang, G.-H. First-principles prediction of magnetic superatoms in 4d-transition-metal-doped magnesium clusters. *J. Chem. Phys.* **2013**, *139*, 174309.

(74) Chauhan, V.; Medel, V. M.; Reveles, J. U.; Khanna, S. N.; Sen, P. Shell magnetism in transition metal doped calcium superatom. *Chem. Phys. Lett.* **2012**, *528*, 39−43.

(75) Medel, V. M.; Reveles, J. U.; Islam, M. F.; Khanna, S. N. Robust magnetic moments on impurities in metallic clusters: Localized magnetic states in superatoms. *J. Phys. Chem. A* **2013**, *117*, 4297−4303.

(76) Medel, V.; Reveles, J. U.; Khanna, S. N. Magnetism of electrons in atoms and superatoms. *J. Appl. Phys.* **2012**, *112*, 064313.

(77) Pradhan, K.; Reveles, J. U.; Sen, P.; Khanna, S. Enhanced magnetic moments of alkali metal coated Sc clusters: New magnetic superatoms. *J. Chem. Phys.* **2010**, *132*, 124302.

(78) González-Ramírez, H.; Ulises Reveles, J.; Gómez-Sandoval, Z. High magnetic moments on binary yttrium-alkali superatoms. *Chem. Phys. Lett.* **2013**, *583*, 97−102.

(79) Zhang, X.; Wang, Y.; Wang, H.; Lim, A.; Gantefoer, G.; Bowen, K. H.; Reveles, J. U.; Khanna, S. N. On the existence of designer magnetic superatoms. *J. Am. Chem. Soc.* **2013**, *135*, 4856−4861.

(80) Tsunoyama, H.; Akatsuka, H.; Shibuta, M.; Iwasa, T.; Mizuhata, Y.; Tokitoh, N.; Nakajima, A. Development of integrated Dry−Wet synthesis method for metal encapsulating silicon cage superatoms of $M@Si_{16}$ (M = Ti and Ta). *J. Phys. Chem. C* **2017**, *121*, 20507−20516.

(81) Weinert, B.; Dehnen, S. *Clusters−Contemporary Insight in Structure and Bonding*; Springer, 2016; pp 99−134.

(82) Mayer, K.; Weßing, J.; Fässler, T. F.; Fischer, R. A. Intermetalloid clusters: molecules and solids in a dialogue. *Angew. Chem., Int. Ed.* **2018**, *57*, 14372−14393.

(83) Wilson, R. J.; Weinert, B.; Dehnen, S. Recent developments in Zintl cluster chemistry. *Dalton Trans.* **2018**, *47*, 14861−14869.

(84) Scharfe, S.; Kraus, F.; Stegmaier, S.; Schier, A.; Faessler, T. F. Zintl ions, cage compounds, and intermetalloid clusters of group 14 and group 15 elements. *Angew. Chem., Int. Ed.* **2011**, *50*, 3630−3670.

(85) Fässler, T. F.; Hoffmann, S. D. Endohedral Zintl ions: intermetalloid clusters. *Angew. Chem., Int. Ed.* **2004**, *43*, 6242−6247.

(86) Liu, C.; Sun, Z.-M. Recent advances in structural chemistry of Group 14 Zintl ions. *Coord. Chem. Rev.* **2019**, *382*, 32−56.

(87) Wilson, R. J.; Lichtenberger, N.; Weinert, B.; Dehnen, S. Intermetalloid and Heterometallic Clusters Combining p-Block (Semi) Metals with d-or f-Block Metals. *Chem. Rev.* **2019**, *119*, 8506−8554.

(88) Klemm, W. Metalloids and their compounds with the alkali metals. *P. Chem. Soc.* **1958**, 329−364.

(89) Guloy, A. M.; Ramlau, R.; Tang, Z.; Schnelle, W.; Baitinger, M.; Grin, Y. A guest-free germanium clathrate. *Nature* **2006**, *443*, 320−323.

(90) Bentlohner, M. M.; Waibel, M.; Zeller, P.; Sarkar, K.; Müller-Buschbaum, P.; Fattakhova-Rohlfing, D.; Fässler, T. F. Zintl clusters as wet-chemical precursors for germanium nanomorphologies with tunable composition. *Angew. Chem., Int. Ed.* **2016**, *55*, 2441−2445.

(91) Goicoechea, J. M.; Sevov, S. C. Deltahedral germanium clusters: Insertion of transition-metal atoms and addition of organometallic fragments. *J. Am. Chem. Soc.* **2006**, *128*, 4155−4161.

(92) Hlukhyy, V.; He, H.; Jantke, L. A.; Fässler, T. F. The neat ternary solid $K_{5-x}Co_{1-x}Sn_9$ with endohedral $[Co@Sn_9]^{5-}$ cluster units: a precursor for soluble intermetalloid $[Co2@Sn_{17}]^{5-}$ clusters. *Chem. - Eur. J.* **2012**, *18*, 12000−12007.

(93) Hlukhyy, V.; Stegmaier, S.; van Wüllen, L.; Fässler, T. F. Endohedrally filled $[Ni@Sn_9]^{4-}$ and $[Co@Sn_9]^{5-}$ clusters in the neat solids $Na_{12}Ni_{1-x}Sn_{17}$ and $K_{13-x}Co_{1-x}Sn_{17}$: Crystal structure and ^{119}Sn solid-state NMR spectroscopy. *Chem. - Eur. J.* **2014**, *20*, 12157−12164.

(94) Scharfe, S.; Fässler, T. F.; Stegmaier, S.; Hoffmann, S. D.; Ruhland, K. $[Cu@Sn_9]^{3-}$ and $[Cu@Pb_9]^{3-}$: Intermetalloid clusters with endohedral Cu atoms in spherical environments. *Chem. - Eur. J.* **2008**, *14*, 4479−4483.

(95) Jin, X.; Espinoza-Quintero, G.; Below, B.; Arcisauskaite, V.; Goicoechea, J. M.; McGrady, J. E. Structure and bonding in a bimetallic endohedral cage, $[Co_2@Ge_{16}]^{z-}$. *J. Organomet. Chem.* **2015**, *792*, 149−153.

(96) Liu, C.; Popov, I. $[Co_2@Ge_{16}]^{4-}$: Localized versus delocalized bonding in two isomeric intermetalloid clusters. *Chem. - Eur. J.* **2018**, *24*, 699.

(97) Sun, Z.-M.; Xiao, H.; Li, J.; Wang, L.-S. $Pd_2@Sn_{18}{}^{4-}$: Fusion of two endohedral stannaspherenes. *J. Am. Chem. Soc.* **2007**, *129*, 9560−9561.

(98) Kocak, F. S.; Zavalij, P.; Lam, Y.-F.; Eichhorn, B. W. Solution dynamics and gas-phase chemistry of $Pd_2@Sn_{18}{}^{4-}$. *Inorg. Chem.* **2008**, *47*, 3515−3520.

(99) Moses, M. J.; Fettinger, J. C.; Eichhorn, B. W. Interpenetrating As_{20} fullerene and Ni_{12} icosahedra in the onion-skin $[As@Ni_{12}@As_{20}]^{3-}$ ion. *Science* **2003**, *300*, 778−780.

(100) Stegmaier, S.; Fassler, T. F. A bronze matryoshka: the discrete intermetalloid cluster $[Sn@Cu_{12}@Sn_{20}]^{12-}$ in the ternary phases $A_{12}Cu_{12}Sn_{21}$ (A = Na, K). *J. Am. Chem. Soc.* **2011**, *133*, 19758−19768.

(101) Wang, Y.; Moses-DeBusk, M.; Stevens, L.; Hu, J.; Zavalij, P.; Bowen, K.; Dunlap, B. I.; Glaser, E. R.; Eichhorn, B. $Sb@Ni_{12}@Sb_{20}{}^{-/+}$ and $Sb@Pd_{12}@Sb_{20}{}^{n}$ cluster anions, where n = +1, -1, -3, -4: Multi-oxidation-state clusters of interpenetrating platonic solids. *J. Am. Chem. Soc.* **2017**, *139*, 619−622.

(102) Li, Z.; Ruan, H.; Wang, L.; Liu, C.; Xu, L. Counterion-induced crystallization of intermetalloid Matryoshka clusters $[Sb@Pd_{12}@Sb_{20}]^{3-},{}^{4-}$. *Dalton Trans.* **2017**, *46*, 3453−3456.

(103) Adamo, C.; Barone, V. Toward reliable density functional methods without adjustable parameters: The PBE0 model. *J. Chem. Phys.* **1999**, *110*, 6158−6170.

(104) Bruna, P. J.; Wright, J. S. Theoretical study of the ionization potentials of boron dimer. *J. Phys. Chem.* **1990**, *94*, 1774−1781.

(105) Rohlfing, C. M.; Martin, R. L. A theoretical study of the isovalent diatomics carbon dimer, silicon dimer, and silicon monocarbide. *J. Phys. Chem.* **1986**, *90*, 2043−2046.

(106) Bauschlicher, C. W., Jr; Barnes, L. A.; Taylor, P. R. Lowest ionization potentials of aluminum dimer. *J. Phys. Chem.* **1989**, *93*, 2932−2935.

(107) Huber, K.-P.; Herzberg, G. *Constants of diatomic molecules*; Van Nostrand Reinhold Company: New York, 1979.

(108) Pacchioni, G. On the ground-state properties of the germanium dimer. *Chem. Phys. Lett.* **1984**, *107*, 70−71.

(109) Ho, J.; Polak, M. L.; Ervin, K. M.; Lineberger, W. C. Photoelectron spectroscopy of nickel group dimers: Ni_2, Pd_2, and Pt_2. *J. Chem. Phys.* **1993**, *99*, 8542−8551.

(110) Ghosh, A.; Chaudhuri, R. K.; Chattopadhyay, S. Relativistic state-specific multireference coupled cluster theory description for bond-breaking energy surfaces. *J. Chem. Phys.* **2016**, *145*, 124303.

(111) Suzumura, T.; Nakajima, T.; Hirao, K. Ground-stale properties of MH, MCl, and M_2 (M = Cu, Ag, and Au) calculated by a scalar relativistic density functional theory. *Int. J. Quantum Chem.* **1999**, *75*, 757−766.

(112) Miralrio, A.; Sansores, L. E. On the search of stable, aromatic and ionic endohedral compounds of C_{28}: A theoretical study. *Comput. Theor. Chem.* **2016**, *1083*, 53−63.

(113) Chase, B.; Herron, N.; Holler, E. Vibrational spectroscopy of fullerenes (C_{60} and C_{70}). Temperature dependant studies. *J. Phys. Chem.* **1992**, *96*, 4262−4266.

(114) Wu, X.; Liang, X.; Du, Q.; Zhao, J.; Chen, M.; Lin, M.; Wang, J.; Yin, G.; Ma, L.; King, R. B. Medium-sized (n = 14−20) clusters: a combined study of photoelectron spectroscopy and DFT calculations. *J. Phys.: Condens. Matter* **2018**, *30*, 354002.

(115) Zhao, J.; Huang, X.; Shi, R.; Liu, H.; Su, Y.; King, R. B. B_{28}: The smallest all-boron cage from an ab initio global search. *Nanoscale* **2015**, *7*, 15086−15090.

(116) Li, F.; Jin, P.; Jiang, D.-e.; Wang, L.; Zhang, S. B.; Zhao, J.; Chen, Z. B_{80} and $B_{101-103}$ clusters: Remarkable stability of the core-shell structures established by validated density functionals. *J. Chem. Phys.* **2012**, *136*, 074302.

(117) Olejniczak, A.; Cichy, B.; Stręk, W. DFT calculations of metal-organic I-III-VI semiconductor clusters: Benchmark of exchange-correlation functionals and localized basis sets. *Comput. Mater. Sci.* **2019**, *163*, 186−195.

(118) Lousada, C. M.; Johansson, A. J.; Brinck, T.; Jonsson, M. Reactivity of metal oxide clusters with hydrogen peroxide and water−a DFT study evaluating the performance of different exchange−correlation functionals. *Phys. Chem. Chem. Phys.* **2013**, *15*, 5539−5552.

(119) Guo, L.; Zheng, X.; Zeng, Z.; Zhang, C. Spin orbital effect in lanthanides doped silicon cage clusters. *Chem. Phys. Lett.* **2012**, *550*, 134−137.

(120) Li, T.; Feng, Z.; Jing, C.; Hong, F.; Cao, S.; Zhang, J. Importance of spin−orbit coupling in M@Pb_{12} clusters (M = 3d and 4d atoms). *Chem. Phys. Lett.* **2012**, *543*, 106−110.

(121) Sargolzaei, M.; Lotfizadeh, N. Spin and orbital magnetism of a single 3d transition-metal atom doped into icosahedral coinage-metal clusters X_{12} (X = Cu, Ag, Au). *Phys. Rev. B: Condens. Matter Mater. Phys.* **2011**, *83*, 155404.

(122) Wales, D. J.; Doye, J. P. Global optimization by basin-hopping and the lowest energy structures of Lennard-Jones clusters containing up to 110 atoms. *J. Phys. Chem. A* **1997**, *101*, 5111−5116.

(123) Goedecker, S. Minima hopping: An efficient search method for the global minimum of the potential energy surface of complex molecular systems. *J. Chem. Phys.* **2004**, *120*, 9911−9917.

(124) Heiles, S.; Johnston, R. L. Global optimization of clusters using electronic structure methods. *Int. J. Quantum Chem.* **2013**, *113*, 2091−2109.

(125) Lyakhov, A. O.; Oganov, A. R.; Stokes, H. T.; Zhu, Q. New developments in evolutionary structure prediction algorithm USPEX. *Comput. Phys. Commun.* **2013**, *184*, 1172−1182.

(126) Zhao, J. J.; Shi, R. L.; Sai, L. W.; Huang, X. M.; Su, Y. Comprehensive genetic algorithm for ab initio global optimisation of clusters. *Mol. Simul.* **2016**, *42*, 809−819.

(127) Shang, C.; Liu, Z.-P. Stochastic surface walking method for structure prediction and pathway searching. *J. Chem. Theory Comput.* **2013**, *9*, 1838−1845.

(128) Lv, J.; Wang, Y.; Zhu, L.; Ma, Y. Particle-swarm structure prediction on clusters. *J. Chem. Phys.* **2012**, *137*, 084104.

(129) Lewis, G. N. The atom and the molecule. *J. Am. Chem. Soc.* **1916**, *38*, 762−785.

(130) Langmuir, I. Types of valence. *Science* **1921**, *54*, 59−67.

(131) Pyykkö, P. Understanding the eighteen-electron rule. *J. Organomet. Chem.* **2006**, *691*, 4336−4340.

(132) Dognon, J. P.; Clavaguéra, C.; Pyykkö, P. Towards a 32-electron principle: Pu@Pb_{12} and related systems. *Angew. Chem., Int. Ed.* **2007**, *46*, 1427−1430.

(133) Hirsch, A.; Chen, Z.; Jiao, H. Spherical aromaticity in I_h symmetrical fullerenes: The $2(N+1)^2$ rule. *Angew. Chem., Int. Ed.* **2000**, *39*, 3915−3917.

(134) Chen, Z.; Jiao, H.; Hirsch, A.; Thiel, W. The $2(N+1)^2$ rule for spherical aromaticity: further validation. *J. Mol. Model.* **2001**, *7*, 161−163.

(135) Hückel, E. Quantentheoretische beiträge zum benzolproblem. *Eur. Phys. J. A* **1931**, *70*, 204−286.

(136) Chen, Z.; Wannere, C. S.; Corminboeuf, C.; Puchta, R.; Schleyer, P. V. R. Nucleus-independent chemical shifts (NICS) as an aromaticity criterion. *Chem. Rev.* **2005**, *105*, 3842−3888.

(137) Hirsch, A.; Chen, Z.; Jiao, H. Spherical aromaticity of inorganic cage molecules. *Angew. Chem., Int. Ed.* **2001**, *40*, 2834−2838.

(138) Clemenger, K. Ellipsoidal shell structure in free-electron metal clusters. *Phys. Rev. B: Condens. Matter Mater. Phys.* **1985**, *32*, 1359−1362.

(139) Wade, K. The structural significance of the number of skeletal bonding electron-pairs in carboranes, the higher boranes and borane anions, and various transition-metal carbonyl cluster compounds. *J. Chem. Soc. D* **1971**, 792−793.

(140) Mingos, D. M. P. Polyhedral Skeletal Electron Pair Approach. *Acc. Chem. Res.* **1984**, *17*, 311−319.

(141) Mingos, D. M. P.; Slee, T.; Zhenyang, L. Bonding models for ligated and bare clusters. *Chem. Rev.* **1990**, *90*, 383−402.

(142) Duncan, M. A. Invited review article: laser vaporization cluster sources. *Rev. Sci. Instrum.* **2012**, *83*, 041101.

(143) Cox, D.; Trevor, D.; Whetten, R.; Rohlfing, E.; Kaldor, A. Aluminum clusters: Magnetic properties. *J. Chem. Phys.* **1986**, *84*, 4651−4656.

(144) Kumar, V. Structure and electronic properties of Al_{14} and $Al_{13}Na$ clusters. *Phys. Rev. B: Condens. Matter Mater. Phys.* **1998**, *57*, 8827−8829.

(145) Jarrold, M. F.; Bower, J. E. The reactions of mass selected aluminum cluster ions, Al^{+n} (n = 4−25), with oxygen. *J. Chem. Phys.* **1986**, *85*, 5373−5375.

(146) Thomas, O. C.; Zheng, W.; Bowen, K. H., Jr Magic numbers in copper-doped aluminum cluster anions. *J. Chem. Phys.* **2001**, *114*, 5514−5519.

(147) Taylor, K.; Pettiette, C.; Craycraft, M.; Chesnovsky, O.; Smalley, R. Ups of negative aluminum clusters. *Chem. Phys. Lett.* **1988**, *152*, 347−352.

(148) Ma, L.; v. Issendorff, B.; Aguado, A. Photoelectron spectroscopy of cold aluminum cluster anions: Comparison with density functional theory results. *J. Chem. Phys.* **2010**, *132*, 104303.

(149) Bergeron, D. E.; Castleman, A. W.; Morisato, T.; Khanna, S. N. Formation of $Al_{13}I^-$: Evidence for the superhalogen character of Al_{13}. *Science* **2004**, *304*, 84−87.

(150) Kambe, T.; Haruta, N.; Imaoka, T.; Yamamoto, K. Solution-phase synthesis of Al_{13}^- using a dendrimer template. *Nat. Commun.* **2017**, *8*, 2046.

(151) Ko, Y. J.; Shakya, A.; Wang, H.; Grubisic, A.; Zheng, W.; Götz, M.; Ganteför, G.; Bowen, K. H.; Jena, P.; Kiran, B. Electronic structure and properties of isoelectronic magic clusters: $Al_{13}X$ (X = H, Au, Li, Na, K, Rb, Cs). *J. Chem. Phys.* **2010**, *133*, 124308.

(152) Khanna, S.; Jena, P. Assembling crystals from clusters. *Phys. Rev. Lett.* **1992**, *69*, 1664−1667.

(153) Nakajima, A.; Kishi, T.; Sugioka, T.; Kaya, K. Electronic and geometric structures of aluminum-boron negative cluster ions (Al_nB^{-m}). *Chem. Phys. Lett.* **1991**, *187*, 239−244.

(154) Smith, J. C.; Reber, A. C.; Khanna, S. N.; Castleman, A., Jr Boron substitution in aluminum cluster anions: Magic clusters and reactivity with oxygen. *J. Phys. Chem. A* **2014**, *118*, 8485−8492.

(155) Pal, R.; Cui, L.-F.; Bulusu, S.; Zhai, H.-J.; Wang, L.-S.; Zeng, X. C. Probing the electronic and structural properties of doped aluminum clusters: MAl_{12}^- (M = Li, Cu, and Au). *J. Chem. Phys.* **2008**, *128*, 024305.

(156) Kawamata, H.; Negishi, Y.; Nakajima, A.; Kaya, K. Electronic properties of substituted aluminum clusters by boron and carbon atoms ($Al_nB_m^-/Al_nC_m^-$); new insights into s−p hybridization and perturbed shell structures. *Chem. Phys. Lett.* **2001**, *337*, 255−262.

(157) Lang, S. M.; Claes, P.; Neukermans, S.; Janssens, E. Cage structure formation of singly doped aluminum cluster cations Al_nTM^+(TM= Ti, V, Cr). *J. Am. Soc. Mass Spectrom.* **2011**, *22*, 1508.

(158) Akutsu, M.; Koyasu, K.; Atobe, J.; Miyajima, K.; Mitsui, M.; Tsunoyama, H.; Nakajima, A. Geometric and electronic properties of Si-atom doped Al clusters: robustness of binary superatoms against charging. *Phys. Chem. Chem. Phys.* **2017**, *19*, 20401−20411.

(159) Akutsu, M.; Koyasu, K.; Atobe, J.; Hosoya, N.; Miyajima, K.; Mitsui, M.; Nakajima, A. Experimental and theoretical characterization of aluminum-based binary superatoms of $Al_{12}X$ and their cluster salts. *J. Phys. Chem. A* **2006**, *110*, 12073−12076.

(160) Li, X.; Wang, L.-S. Experimental search and characterization of icosahedral clusters: $Al_{12}X^-$ (X = C, Ge, Sn, Pb). *Phys. Rev. B: Condens. Matter Mater. Phys.* **2002**, *65*, 153404.

(161) Seitsonen, A. P.; Laasonen, K.; Nieminen, R. M.; Klein, M. L. Structure of CAl_{12}. *J. Chem. Phys.* **1995**, *103*, 8075−8080.

(162) Li, S.; Gong, X. Neutral and negatively charged $Al_{12}X$ (X = Si, Ge, Sn, Pb) clusters studied from first principles. *Phys. Rev. B: Condens. Matter Mater. Phys.* **2006**, *74*, 045432.

(163) Kumar, V.; Sundararajan, V. Ab initio molecular-dynamics studies of doped magic clusters and their interaction with atoms. *Phys. Rev. B: Condens. Matter Mater. Phys.* **1998**, *57*, 4939−4942.

(164) Kumar, V.; Bhattacharjee, S.; Kawazoe, Y. Silicon-doped icosahedral, cuboctahedral, and decahedral clusters of aluminum. *Phys. Rev. B: Condens. Matter Mater. Phys.* **2000**, *61*, 8541−8547.

(165) Kumar, V.; Kawazoe, Y. Hund's rule in metal clusters: Prediction of high magnetic moment state of $Al_{12}Cu$ from first-principles calculations. *Phys. Rev. B: Condens. Matter Mater. Phys.* **2001**, *64*, 115405.

(166) Chen, G.; Kawazoe, Y. Structural and electronic properties of $Al_{12}X^+$ (X = C, Si, Ge, Sn, and Pb) clusters. *J. Chem. Phys.* **2007**, *126*, 014703.

(167) Khanna, S.; Jena, P. Atomic clusters: Building blocks for a class of solids. *Phys. Rev. B: Condens. Matter Mater. Phys.* **1995**, *51*, 13705−13716.

(168) Kumar, V. $Al_{10}Li_8$: A magic compound cluster. *Phys. Rev. B: Condens. Matter Mater. Phys.* **1999**, *60*, 2916−2920.

(169) Thomas, O.; Zheng, W.-J.; Lippa, T.; Xu, S.-J.; Lyapustina, S.; Bowen, K., Jr In search of theoretically predicted magic clusters: Lithium-doped aluminum cluster anions. *J. Chem. Phys.* **2001**, *114*, 9895−9900.

(170) Rao, B.; Jena, P. Energetics and electronic structure of carbon doped aluminum clusters. *J. Chem. Phys.* **2001**, *115*, 778−783.

(171) Khanna, S.; Ashman, C.; Rao, B.; Jena, P. Geometry, electronic structure, and energetics of copper-doped aluminum clusters. *J. Chem. Phys.* **2001**, *114*, 9792−9796.

(172) Rao, B.; Khanna, S.; Jena, P. Isomers of Al_{13} clusters and their interaction with alkali atoms. *Phys. Rev. B: Condens. Matter Mater. Phys.* **2000**, *62*, 4666−4671.

(173) Majumder, C.; Das, G.; Kulshrestha, S.; Shah, V.; Kanhere, D. Ground state geometries and energetics of AL_nLi (n = 1, 13) clusters using ab initio density-based molecular dynamics. *Chem. Phys. Lett.* **1996**, *261*, 515−520.

(174) Vichare, A.; Kanhere, D. Surface coverage studies of the icosahedron by Li using density based molecular dynamics. *Eur. Phys. J. D* **1998**, *4*, 89−94.

(175) Chandrachud, P.; Joshi, K.; Kanhere, D. Thermodynamics of carbon-doped Al and Ga clusters: Ab initio molecular dynamics simulations. *Phys. Rev. B: Condens. Matter Mater. Phys.* **2007**, *76*, 235423.

(176) Charkin, O.; Charkin, D.; Klimenko, N.; Mebel, A. A theoretical study of isomerism in doped aluminum XAl_{12} clusters (X = B, Al, Ga, C, Si, Ge) with 40 valence electrons. *Chem. Phys. Lett.* **2002**, *365*, 494−504.

(177) Wu, C.; Lu, P.; Yu, Z.; Ding, L.; Liu, Y.; Han, L. Structural and electronic properties of neutral clusters $Al_{12}X$ (X = P, As, Sb, and Bi) and their cations. *J. Comput. Theor. Nanosci.* **2013**, *10*, 1055−1060.

(178) Xie, R.-H.; Bryant, G. W.; Zhao, J.; Kar, T.; Smith, V. H., Jr Tunable optical properties of icosahedral, dodecahedral, and tetrahedral clusters. *Phys. Rev. B: Condens. Matter Mater. Phys.* **2005**, *71*, 125422.

(179) Li, S.; Gong, X. Charge-induced structural changes in $Al_{12}C$ clusters. *Phys. Rev. B: Condens. Matter Mater. Phys.* **2004**, *70*, 075404.

(180) Sun, Q.; Wang, Q.; Yu, J.; Kumar, V.; Kawazoe, Y. Real-space representation of electron localization and shell structure in jelliumlike clusters. *Phys. Rev. B: Condens. Matter Mater. Phys.* **2001**, *63*, 193408.

(181) Wang, B.; Zhao, J.; Shi, D.; Chen, X.; Wang, G. Density-functional study of structural and electronic properties of Al_nN (n = 2−12) clusters. *Phys. Rev. A: At., Mol., Opt. Phys.* **2005**, *72*, 023204.

(182) Molina, B.; Soto, J. R.; Castro, J. J. Stability and nonadiabatic effects of the endohedral clusters $X@Al_{12}$ (X = B, C, N, Al, Si, P) with 39, 40, and 41 valence electrons. *J. Phys. Chem. C* **2012**, *116*, 9290−9299.

(183) Jimenez-Izal, E.; Moreno, D.; Mercero, J. M.; Matxain, J. M.; Audiffred, M.; Merino, G.; Ugalde, J. M. Doped aluminum cluster anions: size matters. *J. Phys. Chem. A* **2014**, *118*, 4309−4314.

(184) Lu, Q.; Jalbout, A.; Luo, Q.; Wan, J.; Wang, G. Theoretical study of hydrogenated Mg, $Ca@Al_{12}$ clusters. *J. Chem. Phys.* **2008**, *128*, 224707.

(185) Charkin, O.; Klimenko, N.; Charkin, D.; Mebel, A. Isomerism of Doped Aluminum Clusters with the Icosahedral $[Al_{12}]$ Cage. *Russ. J. Inorg. Chem.* **2005**, *50*, S17.

(186) Charkin, O. P.; Charkin, D. O.; Klimenko, N. M.; Mebel, A. M. A theoretical study of isomerism in doped aluminum MAl_{12} and $MAl_{12}X_{12}$ clusters with 40 and 50 valence electrons. *Faraday Discuss.* **2003**, *124*, 215−237.

(187) Lei, X.-L. Geometrical and electronic properties of neutral and anionic Al_nB_m (n + m = 13) clusters. *J. Cluster Sci.* **2011**, *22*, 159−172.

(188) Sun, W.-M.; Wu, D.; Li, X.-H.; Li, Y.; Chen, J.-H.; Li, C.-Y.; Liu, J.-Y.; Li, Z.-R. Quasi-Chalcogen characteristics of $Al_{12}Be$: A new member of the three-dimensional periodic table. *J. Phys. Chem. C* **2016**, *120*, 2464−2471.

(189) Ouyang, Y.; Wang, P.; Xiang, P.; Chen, H.; Du, Y. Density-functional theory study of Al_n and $Al_{n-1}Mg$ (n = 2−17) clusters. *Comput. Theor. Chem.* **2012**, *984*, 68−75.

(190) Zhang, J.; Sun, J.; Liu, Y.; Li, J.; Liang, X.; Duan, H. The first-principles study of $Al_{12}X$ (X = Sc-Zn) clusters and their adsorption of H, O and N. *AIP Adv.* **2016**, *6*, 075312.

(191) Castro, J.; Soto, J.; Molina, B. Jahn-Teller analysis of the electronic properties of the endohedral clusters $M@Al_{12}$ (M = B, Al, Ga) and their anions. *AIP Conf. Proc.* **2011**, *1420*, 145−150.

(192) Zhao, J.; Liu, B.; Zhai, H.; Zhou, R.; Ni, G.; Xu, Z. Mass spectrometric and first principles study of Al_nC^- clusters. *Solid State Commun.* **2002**, *122*, 543−547.

(193) Kumar, V. Ab initio molecular dynamics studies of metal clusters. *Bull. Mater. Sci.* **1997**, *20*, 745−754.

(194) Kumar, V. Icosahedral symmetry in clusters. *Prog. Cryst. Growth Charact. Mater.* **1997**, *34*, 95−131.

(195) Frisch, M. J.; Trucks, G.; Schlegel, H.; Scuseria, G.; Robb, M.; Cheeseman, J.; Scalmani, G.; Barone, V.; Mennucci, B.; Petersson, G. Gaussian 09, Revision D. 01. *Gaussian. Inc.: Wallingford, CT* **2009**, *2*, 4.

(196) Li, X.; Wu, H.; Wang, X.-B.; Wang, L.-S. S-p hybridization and electron shell structures in aluminum clusters: A photoelectron spectroscopy study. *Phys. Rev. Lett.* **1998**, *81*, 1909−1912.

(197) Tsunoyama, H.; Akutsu, M.; Koyasu, K.; Nakajima, A. The stability of binary $Al_{12}X$ nanoclusters (X = Sc and Ti): Superatom or Wade's polyhedron. *J. Phys.: Condens. Matter* **2018**, *30*, 494004.

(198) Kresse, G.; Joubert, D. From ultrasoft pseudopotentials to the projector augmented-wave method. *Phys. Rev. B: Condens. Matter Mater. Phys.* **1999**, *59*, 1758−1775.

(199) Kresse, G.; Furthermuller, J. Effect of Er doping on the electronic structure optical properties of ZnO. *Phys. Rev. B* **1996**, *54*, 11169−11186.

(200) Leskiw, B. D.; Castleman, A. W. The interplay between the electronic structure and reactivity of aluminum clusters: Model systems as building blocks for cluster assembled materials. *Chem. Phys. Lett.* **2000**, *316*, 31−36.

(201) Sun, Q.; Wang, Q.; Gong, X. G.; Kumar, V.; Kawazoe, Y. Structures and stability of Al_7C and Al_7N clusters. *Eur. Phys. J. D* **2002**, *18*, 77−81.

(202) Bai, Q.; Song, B.; Hou, J.; He, P. First principles study of structural and electronic properties of Al_nN (N = 1−19) clusters. *Phys. Lett. A* **2008**, *372*, 4545−4552.

(203) Averkiev, B. B.; Call, S.; Boldyrev, A. I.; Wang, L.-M.; Huang, W.; Wang, L.-S. Photoelectron spectroscopy and Ab initio study of the structure and bonding of Al_7N^- and Al_7N. *J. Phys. Chem. A* **2008**, *112*, 1873−1879.

(204) Kumar, V. Chemical compositions at alloy surfaces. *Phys. Rev. B: Condens. Matter Mater. Phys.* **1981**, *23*, 3756−3764.

(205) Kumar, V. Segregation at alloy surfaces. *Surf. Sci.* **1979**, *84*, L231−L234.

(206) Guerra, C. F.; Snijders, J.; te Velde, G. t.; Baerends, E. Towards an order-N DFT method. *Theor. Chem. Acc.* **1998**, *99*, 391−403.

(207) Te Velde, G. t.; Bickelhaupt, F. M.; Baerends, E. J.; Fonseca Guerra, C.; van Gisbergen, S. J.; Snijders, J. G.; Ziegler, T. Chemistry with ADF. *J. Comput. Chem.* **2001**, *22*, 931−967.

(208) Sharma, H.; Garg, I.; Dharamvir, K.; Jindal, V. Ab Initio Study of Structural and Electronic Properties of Al_nN (n = 1−22) Clusters. *J. Comput. Theor. Nanosci.* **2010**, *7*, 2297−2307.

(209) Parr, R. G.; Zhou, Z. Absolute hardness: Unifying concept for identifying shells and subshells in nuclei, atoms, molecules, and metallic clusters. *Acc. Chem. Res.* **1993**, *26*, 256−258.

(210) Reveles, J. U.; Khanna, S.; Roach, P.; Castleman, A. Multiple valence superatoms. *Proc. Natl. Acad. Sci. U. S. A.* **2006**, *103*, 18405−18410.

(211) Chauhan, V.; Singh, A.; Majumder, C.; Sen, P. Structural, electronic and magnetic properties of binary transition metal aluminum clusters: Absence of electronic shell structure. *J. Phys.: Condens. Matter* **2014**, *26*, 015006.

(212) Tam, N. M.; Van Duong, L.; Cuong, N. T.; Nguyen, M. T. Structure, stability, absorption spectra and aromaticity of the singly and doubly silicon doped aluminum clusters $Al_nSi_m^{0/+}$ with n = 3−16 and m = 1, 2. *RSC Adv.* **2019**, *9*, 27208−27223.

(213) Lu, Q.; Wan, J. Sc-coated Si@Al_{12} as high-capacity hydrogen storage medium. *J. Chem. Phys.* **2010**, *132*, 224308.

(214) Lochan, R. C.; Head-Gordon, M. Computational studies of molecular hydrogen binding affinities: The role of dispersion forces, electrostatics, and orbital interactions. *Phys. Chem. Chem. Phys.* **2006**, *8*, 1357−1370.

(215) Gong, X. G.; Kumar, V. Metallic coverings of calcium on C_{60}. *Chem. Phys. Lett.* **2001**, *334*, 238−244.

(216) Yoon, M.; Yang, S.; Hicke, C.; Wang, E.; Geohegan, D.; Zhang, Z. Calcium as the superior coating metal in functionalization of carbon fullerenes for high-capacity hydrogen storage. *Phys. Rev. Lett.* **2008**, *100*, 206806.

(217) Reyhani, A.; Mortazavi, S.; Mirershadi, S.; Moshfegh, A.; Parvin, P.; Golikand, A. N. Hydrogen storage in decorated multiwalled carbon nanotubes by Ca, Co, Fe, Ni, and Pd nanoparticles under ambient conditions. *J. Phys. Chem. C* **2011**, *115*, 6994−7001.

(218) Sun, Q.; Wang, Q.; Jena, P.; Kawazoe, Y. Clustering of Ti on a C_{60} surface and its effect on hydrogen storage. *J. Am. Chem. Soc.* **2005**, *127*, 14582−14583.

(219) Delley, B. An all-electron numerical method for solving the local density functional for polyatomic molecules. *J. Chem. Phys.* **1990**, *92*, 508−517.

(220) Gong, X.; Kumar, V. Electronic structure and relative stability of icosahedral Al−transition-metal clusters. *Phys. Rev. B: Condens. Matter Mater. Phys.* **1994**, *50*, 17701−17704.

(221) Pearson, W. B. *The crystal chemistry and physics of metals and alloys*; Wiley-Interscience: New York, 1972.

(222) Lu, Q. L.; Chen, L. L.; Wan, J. G.; Wang, G. H. First principles studies on the interaction of O_2 with X@Al_{12} (X = Al^-, P^+, C, Si) clusters. *J. Comput. Chem.* **2010**, *31*, 2804−2809.

(223) Zhao, J.-Y.; Zhao, F.-Q.; Xu, S.-Y.; Ju, X.-H. DFT studies on doping effect of $Al_{12}X$: adsorption and dissociation of H_2O on $Al_{12}X$ clusters. *J. Phys. Chem. A* **2013**, *117*, 2213−2222.

(224) Zhao, J.-Y.; Zhao, F.-Q.; Xu, S.-Y.; Ju, X.-H. Theoretical study of the geometries and decomposition energies of CO_2 on $Al_{12}X$: Doping effect of $Al_{12}X$. *J. Mol. Graphics Modell.* **2014**, *48*, 9−17.

(225) Zhao, J.-Y.; Zhang, Y.; Zhao, F.-Q.; Ju, X.-H. Adsorption of carbon dioxide on $Al_{12}X$ clusters studied by density functional theory: Effect of charge and doping. *J. Phys. Chem. A* **2013**, *117*, 12519−12528.

(226) Jin, P.; Chen, Y.; Zhang, S. B.; Chen, Z. Interactions between $Al_{12}X$ (X = Al, C, N and P) nanoparticles and DNA nucleobases/base pairs: Implications for nanotoxicity. *J. Mol. Model.* **2012**, *18*, 559−568.

(227) Gong, X.; Chiarotti, G. L.; Parrinello, M.; Tosatti, E. α-gallium: A metallic molecular crystal. *Phys. Rev. B: Condens. Matter Mater. Phys.* **1991**, *43*, 14277−14280.

(228) Chacko, S.; Joshi, K.; Kanhere, D.; Blundell, S. Why do gallium clusters have a higher melting point than the bulk? *Phys. Rev. Lett.* **2004**, *92*, 135506.

(229) Henry, D. J. Structures and stability of doped gallium nanoclusters. *J. Phys. Chem. C* **2012**, *116*, 24814−24823.

(230) Guo, L. Computational investigation of Ga_nAl (n = 1−15) clusters by the density-functional theory. *Comput. Mater. Sci.* **2009**, *45*, 951−958.

(231) Yuan, G.; Lu, P.; Han, L.; Yu, Z.; Shen, Y.; Zhao, L.; Liu, Y. Structural and electronic properties of neutral clusters $Ga_{12}X$ (X = C, Si, Ge, Sn, and Pb) and their anions from first principles. *Phys. B* **2011**, *406*, 3498−3501.

(232) Song, B.; Yao, C.-H.; Cao, P.-L. Density-functional study of structural and electronic properties of Ga_nN (n = 1−19) clusters. *Phys. Rev. B: Condens. Matter Mater. Phys.* **2006**, *74*, 035306.

(233) Akutsu, M.; Koyasu, K.; Atobe, J.; Miyajima, K.; Mitsui, M.; Nakajima, A. Electronic properties of Si and Ge atoms doped in clusters: In_nSi m and In_nGe_m. *J. Phys. Chem. A* **2007**, *111*, 573−577.

(234) Nakajima, A.; Hoshino, K.; Sugioka, T.; Naganuma, T.; Taguwa, T.; Yamada, Y.; Watanabe, K.; Kaya, K. Electronic shell structure of indium-sodium (In_nNa_m) bimetallic clusters examined by their ionization potentials and mass distributions. *J. Phys. Chem.* **1993**, *97*, 86−90.

(235) Liu, Y.; Deng, K.; Yuan, Y.; Chen, X.; Wu, H.; Wang, X. Structural and electronic properties of neutral clusters $In_{12}X$ (X = C, Si, Ge, and Sn) and their anions from first principles. *Chem. Phys. Lett.* **2009**, *469*, 321−324.

(236) Henning, R. W.; Corbett, J. D. Formation of isolated nickel-centered gallium clusters in $Na_{10}Ga_{10}Ni$ and a 2-D network of gallium octahedra in K_2Ga_3. *Inorg. Chem.* **1999**, *38*, 3883−3888.

(237) Sevov, S. C.; Corbett, J. D. Potassium indium zinc compound $K_8In_{10}Zn$: Interstitially-stabilized analogs of early-transition-metal halide clusters. *Inorg. Chem.* **1993**, *32*, 1059−1061.

(238) Sevov, S. C.; Corbett, J. D. $K_{10}In_{10}Z$ (Z = Ni, Pd, Pt): Zintl phases containing isolated decaindium clusters centered by transition elements. *J. Am. Chem. Soc.* **1993**, *115*, 9089−9094.

(239) Handschuh, H.; Ganteför, G.; Kessler, B.; Bechthold, P. S.; Eberhardt, W. Stable configurations of carbon clusters: Chains, rings, and fullerenes. *Phys. Rev. Lett.* **1995**, *74*, 1095−1098.

(240) Martin, J. M. C_{28}: The smallest stable fullerene? *Chem. Phys. Lett.* **1996**, *255*, 1−6.

(241) Kroto, H. W. The stability of the fullerenes C_n, with n = 24, 28, 32, 36, 50, 60 and 70. *Nature* **1987**, *329*, 529−531.

(242) Chen, Z.; Jiao, H.; Bühl, M.; Hirsch, A.; Thiel, W. Theoretical investigation into structures and magnetic properties of smaller fullerenes and their heteroanalogues. *Theor. Chem. Acc.* **2001**, *106*, 352−363.

(243) Diener, M. D.; Smith, C. A.; Veirs, D. K. Anaerobic preparation and solvent-free separation of uranium endohedral metallofullerenes. *Chem. Mater.* **1997**, *9*, 1773−1777.

(244) Akiyama, K.; Zhao, Y.; Sueki, K.; Tsukada, K.; Haba, H.; Nagame, Y.; Kodama, T.; Suzuki, S.; Ohtsuki, T.; Sakaguchi, M. Isolation and characterization of light actinide metallofullerenes. *J. Am. Chem. Soc.* **2001**, *123*, 181−182.

(245) Dunk, P. W.; Kaiser, N. K.; Mulet-Gas, M.; Rodríguez-Fortea, A.; Poblet, J. M.; Shinohara, H.; Hendrickson, C. L.; Marshall, A. G.; Kroto, H. W. The smallest stable fullerene, M@C_{28} (M = Ti, Zr, U): Stabilization and growth from carbon vapor. *J. Am. Chem. Soc.* **2012**, *134*, 9380−9389.

(246) Makurin, Y. N.; Sofronov, A. A.; Gusev, A. I.; Ivanovsky, A. L. Electronic structure and chemical stabilization of C_{28} fullerene. *Chem. Phys.* **2001**, *270*, 293−308.

(247) Pederson, M. R.; Laouini, N. Covalent container compound: Empty, endohedral, and exohedral C_{28} complexes. *Phys. Rev. B: Condens. Matter Mater. Phys.* **1993**, *48*, 2733−2737.

(248) Jackson, K.; Kaxiras, E.; Pederson, M. R. Electronic states of group-IV endohedral atoms in C_{28}. *Phys. Rev. B: Condens. Matter Mater. Phys.* **1993**, *48*, 17556−17561.

(249) Guo, T.; Smalley, R. E.; Scuseria, G. E. Ab initio theoretical predictions of C_{28}, $C_{28}H_4$, $C_{28}F_4$,(Ti@C_{28})H_4, and M@C_{28} (M = Mg, Al, Si, S, Ca, Sc, Ti, Ge, Zr, and Sn). *J. Chem. Phys.* **1993**, *99*, 352−359.

(250) Jackson, K.; Kaxiras, E.; Pederson, M. R. Bonding of endohedral atoms in small carbon fullerenes. *J. Phys. Chem.* **1994**, *98*, 7805−7810.

(251) Ryzhkov, M. V.; Medvedeva, N. I.; Delley, B. Electronic structures of endohedral fullerenes with scandium, titanium and iron atoms and metal-carbon clusters. *Polyhedron* **2017**, *134*, 376−384.

(252) Dunlap, B. I.; Haeberlen, O. D.; Roesch, N. Asymmetric localization of titanium in carbon molecule (C_{28}). *J. Phys. Chem.* **1992**, *96*, 9095−9097.
(253) Skwara, B.; Góra, R. W.; Zalesny, R.; Lipkowski, P.; Bartkowiak, W.; Reis, H.; Papadopoulos, M. G.; Luis, J. M.; Kirtman, B. Electronic structure, bonding, spectra, and linear and nonlinear electric properties of Ti@C_{28}. *J. Phys. Chem. A* **2011**, *115*, 10370−10381.
(254) Muñoz-Castro, A.; King, R. B. Formation of spherical aromatic endohedral metallic fullerenes. Evaluation of magnetic properties of M@C_{28} (M = Ti, Zr, and Hf) from DFT calculations. *Inorg. Chem.* **2017**, *56*, 15251−15258.
(255) Garg, I.; Sharma, H.; Kapila, N.; Dharamvir, K.; Jindal, V. K. Transition metal induced magnetism in smaller fullerenes (C_n for $n \leq 36$). *Nanoscale* **2011**, *3*, 217−224.
(256) Mulet-Gas, M.; Abella, L.; Dunk, P. W.; Rodríguez-Fortea, A.; Kroto, H. W.; Poblet, J. M. Small endohedral metallofullerenes: Exploration of the structure and growth mechanism in the Ti@C_{2n} (2n = 26−50) family. *Chem. Sci.* **2015**, *6*, 675−686.
(257) Muñoz-Castro, A.; Bruce King, R. Evaluation of bonding, electron affinity, and optical properties of M@C_{28} (M = Zr, Hf, Th, and U): Role of d-and f-orbitals in endohedral fullerenes from relativistic DFT calculations. *J. Comput. Chem.* **2017**, *38*, 44−50.
(258) Tuan, D. F.-T.; Pitzer, R. M. Electronic Structure of Hf@C_{28} and Its Ions. 2. CI Calculations. *J. Phys. Chem.* **1995**, *99*, 15069−15073.
(259) Zhao, K.; Pitzer, R. M. Electronic structure of C_{28}, Pa@C_{28}, and U@C_{28}. *J. Phys. Chem.* **1996**, *100*, 4798−4802.
(260) Dai, X.; Gao, Y.; Jiang, W.; Lei, Y.; Wang, Z. U@C_{28}: The electronic structure induced by the 32-electron principle. *Phys. Chem. Chem. Phys.* **2015**, *17*, 23308−23311.
(261) Rösch, N.; Häberlen, O. D.; Dunlap, B. I. Bonding in endohedral metal−fullerene complexes: F-orbital covalency in Ce@C_{28}. *Angew. Chem., Int. Ed. Engl.* **1993**, *32*, 108−110.
(262) Dognon, J.-P.; Clavaguéra, C.; Pyykkö, P. A predicted organometallic series following a 32-electron principle: An@C_{28} (An = Th, Pa^+, U^{2+}, Pu^{4+}). *J. Am. Chem. Soc.* **2009**, *131*, 238−243.
(263) Ryzhkov, M. V.; Ivanovskii, A. L.; Delley, B. Electronic structure of endohedral fullerenes An@C_{28} (An = Th−Md). *Comput. Theor. Chem.* **2012**, *985*, 46−52.
(264) Manna, D.; Ghanty, T. K. Prediction of a new series of thermodynamically stable actinide encapsulated fullerene systems fulfilling the 32-electron principle. *J. Phys. Chem. C* **2012**, *116*, 25630−25641.
(265) Manna, D.; Sirohiwal, A.; Ghanty, T. K. Pu@C_{24}: A new example satisfying the 32-electron principle. *J. Phys. Chem. C* **2014**, *118*, 7211−7221.
(266) Peng, S.; Zhang, Y.; Li, X. J.; Ren, Y.; Zhang, D. X. DFT calculations on the structural stability and infrared spectroscopy of endohedral metallofullerenes. *Spectrochim. Acta, Part A* **2009**, *74*, 553−557.
(267) Sun, Z.; Li, X.; Tian, M.; Zhao, G.; Li, J.; Ma, B. Comparative study on metal-encapsulated TM@C_{24} and TM@$C_{24}H_{12}$ (TM = Ti, Zr and Hf). *J. Mol. Struct.: THEOCHEM* **2009**, *913*, 265−269.
(268) Zhang, Y.; Peng, S.; Li, X. J.; Zhang, D. X. Structural stability, electronegativity and electronic property of endohedral TM@C_{24} and exohedral TMC_{24} (TM = Sc, Y and La) metallofullerene complexes: Density-functional theory investigations. *J. Mol. Struct.: THEOCHEM* **2010**, *947*, 16−21.
(269) Wu, J.; Sun, Z.; Li, X.; Chen, L.; Tian, M. Molecular geometries, electronic properties, and vibrational spectroscopic studies of endohedral metallofullerenes TM@C_{24} and TM@$C_{24}H_{12}$ (TM = Cr, Mo, and W). *Struct. Chem.* **2010**, *21*, 673−680.
(270) Yue, Y.; Li, X. J. Density functional investigations of endohedral metallofullerenes TM@C_{24} (TM = Mn, Fe, Co, Ni, Cu, and Zn. *Int. J. Quantum Chem.* **2011**, *111*, 96−102.
(271) Erkoç, Ş. Metal atom endohedrally doped C_{20} cage structure: (X@C_{20}; X = Ni, Fe, Co. *Int. J. Mod. Phys. C* **2005**, *16*, 1553−1560.
(272) Poklonski, N. A.; Kislyakov, E. F.; Vyrko, S. A.; Hieu, N. N.; Bubel, O. N.; Siahlo, A. I.; Lebedeva, I. V.; Knizhnik, A. A.; Popov, A. M.; Lozovik, Y. E. Magnetically operated nanorelay based on two single-walled carbon nanotubes filled with endofullerenes Fe@C_{20}. *J. Nanophotonics* **2010**, *4*, 041675.
(273) Samah, M.; Boughiden, B. Structures, electronic and magnetic properties of C_{20} fullerenes doped transition metal atoms M@C_{20} (M = Fe, Co, Ti, V). *Int. J. Mod. Phys. C* **2010**, *21*, 1469−1477.
(274) Baei, M. T.; Soltani, A.; Torabi, P.; Hosseini, F. Formation and electronic structure of C_{20} fullerene transition metal clusters. *Monatsh. Chem.* **2014**, *145*, 1401−1405.
(275) An, Y.-P.; Yang, C.-L.; Wang, M.-S.; Ma, X.-G.; Wang, D.-H. Ab initio investigations of the charge transport properties of endohedral M@C_{20} (M = Na and K) metallofullerenes. *Chin. Phys. B* **2010**, *19*, 113402.
(276) An, Y.-P.; Yang, C.-L.; Wang, M.-S.; Ma, X.-G.; Wang, D.-H. Geometrical and electronic properties of the clusters of C_{20} cage doped with alkali metal atoms. *J. Cluster Sci.* **2011**, *22*, 31−39.
(277) Wu, J.; Sun, Z.; Li, X.; Ma, B.; Tian, M.; Li, S. Theoretical study on the smallest endohedral metallofullerenes: TM@C_{20} (TM = Ce and Gd). *Int. J. Quantum Chem.* **2010**, *111*, 3786−3792.
(278) Manna, D.; Ghanty, T. K. Theoretical prediction of icosahedral U@C_{20} and analogous systems with high HOMO−LUMO gap. *J. Phys. Chem. C* **2012**, *116*, 16716−16725.
(279) Meng, F.; Zhou, Z.; Zhang, P.; Jiang, M.; Xu, X.; Wang, Y.; Gou, J.; Hui, D.; Die, D. Encapsulation of an f-block metal atom/ion to enhance the stability of C_{20} with the I_h symmetry. *Phys. Chem. Chem. Phys.* **2015**, *17*, 4328−4336.
(280) Muñoz-Castro, A.; King, R. B. On the formation of smaller p-block endohedral fullerenes: Bonding analysis in the E@C_{20} (E = Si, Ge, Sn, Pb) series from relativistic DFT calculations. *J. Comput. Chem.* **2017**, *38*, 1661−1667.
(281) Gonzalez, M.; Lujan, S.; Beran, K. A. Investigation into the molecular structure, electronic properties, and energetic stability of endohedral (TM@C_{20}) and exohedral (TM-C_{20}) metallofullerene derivatives of C_{20}: TM = Group 11 and 12 transition metal atoms/ions. *Comput. Theor. Chem.* **2017**, *1119*, 32−44.
(282) Szwacki, N. G.; Sadrzadeh, A.; Yakobson, B. I. B_{80} fullerene: An ab initio prediction of geometry, stability, and electronic structure. *Phys. Rev. Lett.* **2007**, *98*, 166804.
(283) Szwacki, N. G.; Sadrzadeh, A.; Yakobson, B. I. Erratum: B_{80} Fullerene: An ab initio prediction of geometry, stability, and electronic structure [Phys. Rev. Lett. 98, 166804 (2007)]. *Phys. Rev. Lett.* **2008**, *100*, 159901.
(284) Zhao, J.; Wang, L.; Li, F.; Chen, Z. B_{80} and other medium-sized boron clusters: Core−shell structures, not hollow cages. *J. Phys. Chem. A* **2010**, *114*, 9969−9972.
(285) De, S.; Willand, A.; Amsler, M.; Pochet, P.; Genovese, L.; Goedecker, S. Energy landscape of fullerene materials: A comparison of boron to boron nitride and carbon. *Phys. Rev. Lett.* **2011**, *106*, 225502.
(286) Rahane, A. B.; Kumar, V. B_{84}: A quasi-planar boron cluster stabilized with hexagonal holes. *Nanoscale* **2015**, *7*, 4055−4062.
(287) Xu, S.-G.; Zhao, Y.-J.; Yang, X.-B.; Xu, H. A practical criterion for screening stable boron nanostructures. *J. Phys. Chem. C* **2017**, *121*, 11950−11955.
(288) Pochet, P.; Genovese, L.; De, S.; Goedecker, S.; Caliste, D.; Ghasemi, S. A.; Bao, K.; Deutsch, T. Low-energy boron fullerenes: Role of disorder and potential synthesis pathways. *Phys. Rev. B: Condens. Matter Mater. Phys.* **2011**, *83*, 081403.
(289) Li, J. L.; Yang, G. W. Iron endohedral-doped boron fullerene: A potential single molecular device with tunable electronic and magnetic properties. *J. Phys. Chem. C* **2009**, *113*, 18292−18295.
(290) Li, J. L.; Yang, G. W. Tuning electronic and magnetic properties of endohedral Co@B_{80} and exohedral Co-B_{80} metallofullerenes by positioning Co atom. *J. Appl. Phys.* **2010**, *107*, 113702.
(291) Li, J. L.; Yang, G. W. Ni@B_{80}: A single molecular magnetic switch. *Appl. Phys. Lett.* **2009**, *95*, 133115.

(292) Li, C.; Liu, J.; Lefkidis, G.; Hübner, W. Reversible ultrafast spin switching on Ni@B_{80} endohedral fullerene. *Phys. Chem. Chem. Phys.* **2017**, *19*, 673−680.

(293) Mahdavifar, Z.; Poulad, M. Theoretical prediction of ozone sensing using pristine and endohedral metalloboron B_{80} fullerenes. *Sens. Actuators, B* **2014**, *205*, 26−38.

(294) Jin, P.; Hao, C.; Gao, Z.; Zhang, S. B.; Chen, Z. Endohedral metalloborofullerenes $La_2@B_{80}$ and $Sc_3N@B_{80}$: A density functional theory prediction. *J. Phys. Chem. A* **2009**, *113*, 11613−11618.

(295) Liu, C.; Yang, L.; Jin, P.; Hou, Q.; Li, L. Computational prediction of endohedral dimetalloborofullerenes $M_2@B_{80}$ (M = Sc, Y). *Chem. Phys. Lett.* **2017**, *676*, 89−94.

(296) Jin, P.; Liu, C.; Hou, Q.; Li, L.; Tang, C.; Chen, Z. Scandium carbides/cyanides in the boron cage: Computational prediction of X@B_{80} (X = Sc_2C_2, Sc_3C_2, Sc_3CN and Sc_3C_2CN). *Phys. Chem. Chem. Phys.* **2016**, *18*, 21398−21411.

(297) Mahdavifar, Z.; Ershadifar, M.; Farrokhnia, A. Electro-optical properties and structural stability perspectives of M_3N and M_2C_2 (M = Sc, La) clusters encapsulated in B_{80} fullerene: A density functional theory study. *J. Electron. Mater.* **2018**, *47*, 550−565.

(298) Muya, J. T.; Lijnen, E.; Nguyen, M. T.; Ceulemans, A. Encapsulation of small base molecules and tetrahedral/cubane-like clusters of group V atoms in the boron buckyball: A density functional theory study. *J. Phys. Chem. A* **2011**, *115*, 2268−2280.

(299) Wang, J.-T.; Chen, C.; Wang, E. G.; Wang, D.-S.; Mizuseki, H.; Kawazoe, Y. Highly stable and symmetric boron caged B@Co_{12}@B_{80} core-shell cluster. *Appl. Phys. Lett.* **2009**, *94*, 133102.

(300) Zhai, H.-J.; Zhao, Y.-F.; Li, W.-L.; Chen, Q.; Bai, H.; Hu, H.-S.; Piazza, Z. A.; Tian, W.-J.; Lu, H.-G.; Wu, Y.-B. Observation of an all-boron fullerene. *Nat. Chem.* **2014**, *6*, 727−731.

(301) Chen, Q.; Li, W.-L.; Zhao, Y.-F.; Zhang, S.-Y.; Hu, H.-S.; Bai, H.; Li, H.-R.; Tian, W.-J.; Lu, H.-G.; Zhai, H.-J. Experimental and theoretical evidence of an axially chiral borospherene. *ACS Nano* **2015**, *9*, 754−760.

(302) Wang, Y.-J.; Zhao, Y.-F.; Li, W.-L.; Jian, T.; Chen, Q.; You, X.-R.; Ou, T.; Zhao, X.-Y.; Zhai, H.-J.; Li, S.-D. Observation and characterization of the smallest borospherene, B_{28}^- and B_{28}. *J. Chem. Phys.* **2016**, *144*, 064307.

(303) Lv, J.; Wang, Y.; Zhu, L.; Ma, Y. B_{38}: An all-boron fullerene analogue. *Nanoscale* **2014**, *6*, 11692−11696.

(304) BaáTai, T.; ThoáNguyen, M. A new chiral boron cluster B_{44} containing nonagonal holes. *Chem. Commun.* **2016**, *52*, 1653−1656.

(305) Xu, Q.; Liu, C.; Yang, L.; Jin, P.; Tang, C.; Chen, Z. Computational investigation on MB_n (M = Li-Cs, Be-Ba, Sc-La and Ti; n = 28 and 38). *J. Mol. Model.* **2016**, *22*, 184.

(306) Bai, H.; Chen, Q.; Zhai, H. J.; Li, S. D. Endohedral and exohedral metalloborospheres: M@B_{40} (M = Ca, Sr) and M&B_{40} (M = Be, Mg). *Angew. Chem., Int. Ed.* **2015**, *54*, 941−945.

(307) Jin, P.; Hou, Q.; Tang, C.; Chen, Z. Computational investigation on the endohedral borofullerenes M@B_{40} (M = Sc, Y, La). *Theor. Chem. Acc.* **2015**, *134*, 13.

(308) Fa, W.; Chen, S.; Pande, S.; Zeng, X. C. Stability of metal-encapsulating boron fullerene B_{40}. *J. Phys. Chem. A* **2015**, *119*, 11208−11214.

(309) Shah, E. V.; Roy, D. R. Sc_3N and Sc_2C_2 encapsulated B_{40}: Smarter than its carbon analogue. *Phys. E* **2016**, *84*, 354−360.

(310) Shakerzadeh, E.; Biglari, Z.; Tahmasebi, E. M@B_{40} (M = Li, Na, K) serving as a potential promising novel NLO nanomaterial. *Chem. Phys. Lett.* **2016**, *654*, 76−80.

(311) Li, S.-X.; Zhang, Z.-P.; Long, Z.-W.; Qin, S.-J. Structures, stabilities and spectral properties of metalloborospherenes $MB^{0/-40}$ (M = Cu, Ag, and Au). *RSC Adv.* **2017**, *7*, 38526−38537.

(312) Jin, P.; Yang, L.; Liu, C.; Hou, Q.; Li, L. Computational prediction of the endohedral metalloborofullerenes $Ti_n@B_{40}$ (n = 1, 2). *Theor. Chem. Acc.* **2017**, *136*, 56.

(313) Xi, C.; Yang, L.; Liu, C.; You, P.; Li, L.; Jin, P. Lanthanide metals in the boron cages: Computational prediction of M@B_n (M = Eu, Gd; n = 38, 40). *Int. J. Quantum Chem.* **2018**, *118*, No. e25576.

(314) Yong, Y.; Su, X.; Kuang, Y.; Li, X.; Lu, Z. B_{40} and M@B_{40} (M = Li and Ba) fullerenes as potential molecular sensors for acetone detection A first-principles study. *J. Mol. Liq.* **2018**, *264*, 1−8.

(315) Yu, T.; Gao, Y.; Xu, D.; Wang, Z. Actinide endohedral boron clusters: A closed-shell electronic structure of U@B_{40}. *Nano Res.* **2018**, *11*, 354−359.

(316) Chojecki, M.; Yourdkhani, S.; Rutkowska-Zbik, D.; Korona, T. Stability of endo-and exohedral complexes of all-boron fullerene B_{40}. *Comput. Theor. Chem.* **2018**, *1133*, 7−17.

(317) Maniei, Z.; Shakerzadeh, E.; Mahdavifar, Z. Theoretical approach into potential possibility of efficient NO_2 detection via B_{40} and Li@B_{40} fullerenes. *Chem. Phys. Lett.* **2018**, *691*, 360−365.

(318) An, Y.; Zhang, M.; Wu, D.; Fu, Z.; Wang, T.; Xia, C. Electronic transport properties of the first all-boron fullerene B_{40} and its metallofullerene Sr@B_{40}. *Phys. Chem. Chem. Phys.* **2016**, *18*, 12024−12028.

(319) Wang, W.; Guo, Y.-D.; Yan, X.-H. The spin-dependent transport of transition metal encapsulated B_{40} fullerene. *RSC Adv.* **2016**, *6*, 40155−40161.

(320) Mahdavifar, Z.; Poulad, M. Stability prediction of pristine and metal endohedral borofullerenes: Computational approach. *J. Mol. Liq.* **2016**, *219*, 1144−1156.

(321) Wang, C.-Z.; Bo, T.; Lan, J.-H.; Wu, Q.-Y.; Chai, Z.-F.; Gibson, J. K.; Shi, W.-Q. Ultrastable actinide endohedral borospherenes. *Chem. Commun.* **2018**, *54*, 2248−2251.

(322) Chen, Q.; Li, H.-R.; Tian, W.-J.; Lu, H.-G.; Zhai, H.-J.; Li, S.-D. Endohedral charge-transfer complex Ca@B_{37}^-: Stabilization of a B_{37}^{3-} borospherene trianion by metal-encapsulation. *Phys. Chem. Chem. Phys.* **2016**, *18*, 14186−14190.

(323) Lu, Q. L.; Luo, Q. Q.; De Li, Y.; Huang, S. G. DFT study on endohedral and exohedral B_{38} fullerenes: M@B_{38} (M = Sc, Y, Ti) and M&B_{38} (M = Nb, Fe, Co, Ni). *Phys. Chem. Chem. Phys.* **2015**, *17*, 20897−20902.

(324) Chen, Q.; Li, H.-R.; Miao, C.-Q.; Wang, Y.-J.; Lu, H.-G.; Mu, Y.-W.; Ren, G.-M.; Zhai, H.-J.; Li, S.-D. Endohedral Ca@B_{38}: Stabilization of a B_{38}^{2-} borospherene dianion by metal encapsulation. *Phys. Chem. Chem. Phys.* **2016**, *18*, 11610−11615.

(325) Chen, Q.; Gao, T.; Tian, W.-J.; Bai, H.; Zhang, S.-Y.; Li, H.-R.; Miao, C.-Q.; Mu, Y.-W.; Lu, H.-G.; Zhai, H.-J. Endohedral C_3Ca@B_{39}^+ and C_2Ca@B_{39}^+: Axially chiral metalloborospheres based on B_{39}^-. *Phys. Chem. Chem. Phys.* **2015**, *17*, 19690−19694.

(326) Stasyuk, A. J.; Solà, M. Does the endohedral borospherene supersalt $FLi_2@B_{39}$ maintain the "super" properties of its subunits? *Phys. Chem. Chem. Phys.* **2017**, *19*, 21276−21281.

(327) Yang, L.; Jin, P.; Hou, Q.; Li, L. Endohedral metalloborofullerenes M@B_{44} (M = Ca, Sr, Ba): A computational investigation. *J. Mol. Model.* **2016**, *22*, 297.

(328) Zhao, R.-N.; Yuan, Y.-H.; Han, J.-G.; Duan, Y. Geometries, stabilities, and electronic properties of tungsten encapsulated nanosize irregular B_n (n = 20, 24, 28, and 32) fullerenes: A density functional investigation. *Chem. Phys. Lett.* **2016**, *648*, 41−46.

(329) Liu, L.; Osorio, E.; Heine, T. The importance of dynamics studies on the design of sandwich structures: A CrB_{24} case. *Phys. Chem. Chem. Phys.* **2016**, *18*, 18336−18341.

(330) Li, H.-R.; Liu, H.; Tian, X.-X.; Zan, W.-Y.; Mu, Y.-W.; Lu, H.-G.; Li, J.; Wang, Y.-K.; Li, S.-D. Structural transition in metal-centered boron clusters: From tubular molecular rotors Ta@B_{21} and Ta@B_{22}^+ to cage-like endohedral metalloborospherene Ta@B_{22}^-. *Phys. Chem. Chem. Phys.* **2017**, *19*, 27025−27030.

(331) Li, H.-R.; Liu, H.; Lu, X.-Q.; Zan, W.-Y.; Tian, X.-X.; Lu, H.-G.; Wu, Y.-B.; Mu, Y.-W.; Li, S.-D. Cage-like Ta@B^{qn} complexes (n = 23−28, q = −1 − + 3) in 18-electron configurations with the highest coordination number of twenty-eight. *Nanoscale* **2018**, *10*, 7451−7456.

(332) Rahane, A. B.; Saha, P.; Sukumar, N.; Kumar, V. Smallest Fullerene-like Structures of Boron with Cr, Mo, and W Encapsulation. *arXiv:1907.12611* **2019**.

(333) Minh Tam, N.; Tan Pham, H.; Van Duong, L.; Phuong Pham-Ho, M.; Tho Nguyen, M. Fullerene-like boron clusters stabilized by

an endohedrally doped iron atom: B_nFe with n = 14, 16, 18 and 20. *Phys. Chem. Chem. Phys.* **2015**, *17*, 3000−3003.

(334) Zhao, L.; Qu, X.; Wang, Y.; Lv, J.; Zhang, L.; Hu, Z.; Gu, G.; Ma, Y. Effects of manganese doping on the structure evolution of small-sized boron clusters. *J. Phys.: Condens. Matter* **2017**, *29*, 265401.

(335) Wang, Y.; Wu, X.; Zhao, J. Structural evolution and superatoms in molybdenum atom stabilized boron clusters: MoB_n (n = 10−24). *J. Cluster Sci.* **2018**, *29*, 847−852.

(336) Chen, B.; Sun, W.; Kuang, X.; Lu, C.; Xia, X.; Shi, H.; Gutsev, G. L. Insights into the effects produced by doping of medium-sized boron clusters with ruthenium. *Phys. Chem. Chem. Phys.* **2018**, *20*, 30376−30383.

(337) Shao, X.; Qu, X.; Liu, S.; Yang, L.; Yang, J.; Liu, X.; Zhong, X.; Sun, S.; Vaitheeswaran, G.; Lv, J. Structure evolution of chromium-doped boron clusters: Toward the formation of endohedral boron cages. *RSC Adv.* **2019**, *9*, 2870−2876.

(338) Chen, B. L.; Sun, W. G.; Kuang, X. Y.; Lu, C.; Xia, X. X.; Shi, H. X.; Maroulis, G. Structural stability and evolution of medium-sized tantalum-doped boron clusters: A half-sandwich-structured TaB_{12}^- cluster. *Inorg. Chem.* **2018**, *57*, 343−350.

(339) Saha, P.; Rahane, A. B.; Kumar, V.; Sukumar, N. Electronic origin of the stability of transition-metal-doped B_{14} drum-shaped boron clusters and their assembly into a nanotube. *J. Phys. Chem. C* **2017**, *121*, 10728−10742.

(340) Saha, P.; Rahane, A.; Kumar, V.; Sukumar, N. Analysis of the electron density features of small boron clusters and the effects of doping with C, P, Al, Si, and Zn: Magic B_7P and B_8Si clusters. *Phys. Scr.* **2016**, *91*, 053005.

(341) Popov, I. A.; Jian, T.; Lopez, G. V.; Boldyrev, A. I.; Wang, L.-S. Cobalt-centred boron molecular drums with the highest coordination number in the CoB_{16}^- cluster. *Nat. Commun.* **2015**, *6*, 8654.

(342) Jian, T.; Li, W.-L.; Popov, I. A.; Lopez, G. V.; Chen, X.; Boldyrev, A. I.; Li, J.; Wang, L.-S. Manganese-centered tubular boron cluster−MnB_{16}^-: A new class of transition-metal molecules. *J. Chem. Phys.* **2016**, *144*, 154310.

(343) Li, W.; Jian, T.; Chen, X.; Li, H.; Chen, T.; Luo, X.; Li, S.; Li, J.; Wang, L. Observation of a metal-centered B_2-Ta@B_{18}^- tubular molecular rotor and a perfect Ta@B_{20}^- boron drum with the record coordination number of twenty. *Chem. Commun.* **2017**, *53*, 1587−1590.

(344) Li, W.-L.; Chen, X.; Jian, T.; Chen, T.-T.; Li, J.; Wang, L.-S. From planar boron clusters to borophenes and metalloborophenes. *Nat. Rev. Chem.* **2017**, *1*, 0071.

(345) Romanescu, C.; Galeev, T. R.; Li, W.-L.; Boldyrev, A. I.; Wang, L.-S. Transition-metal-centered monocyclic boron wheel clusters (M@B_n): A new class of aromatic borometallic compounds. *Acc. Chem. Res.* **2013**, *46*, 350−358.

(346) Zhai, H. J.; Alexandrova, A. N.; Birch, K. A.; Boldyrev, A. I.; Wang, L. S. Hepta-and octacoordinate boron in molecular wheels of eight-and nine-atom boron clusters: Observation and confirmation. *Angew. Chem., Int. Ed.* **2003**, *42*, 6004−6008.

(347) Ito, K.; Pu, Z.; Li, Q.-S.; Schleyer, P. V. R. Cyclic boron clusters enclosing planar hypercoordinate cobalt, iron, and nickel. *Inorg. Chem.* **2008**, *47*, 10906−10910.

(348) Chen, T.-T.; Li, W.-L.; Bai, H.; Chen, W.-J.; Dong, X.-R.; Li, J.; Wang, L.-S. Re@B_8^- and Re@B_9^-: New members of the transition-metal-centered borometallic molecular wheel family. *J. Phys. Chem. A* **2019**, *123*, 5317−5324.

(349) Galeev, T. R.; Romanescu, C.; Li, W.-L.; Wang, L.-S.; Boldyrev, A. I. Observation of the highest coordination number in planar species: Decacoordinated Ta@B_{10}^- and Nb@B_{10}^- anions. *Angew. Chem., Int. Ed.* **2012**, *51*, 2101−2105.

(350) Li, W.-L.; Ivanov, A. S.; Federic, J.; Romanescu, C.; Cernusak, I.; Boldyrev, A. I.; Wang, L.-S. On the way to the highest coordination number in the planar metal-centred aromatic Ta@B_{10}^- cluster: Evolution of the structures of TaB_n^- (n = 3-8). *J. Chem. Phys.* **2013**, *139*, 104312.

(351) Pu, Z.; Ito, K.; Schleyer, P. v. R.; Li, Q.-S. Planar hepta-, octa-, nona-, and decacoordinate first row d-block metals enclosed by boron rings. *Inorg. Chem.* **2009**, *48*, 10679−10686.

(352) Romanescu, C.; Galeev, T. R.; Li, W.-L.; Boldyrev, A. I.; Wang, L.-S. Aromatic metal-centered monocyclic boron rings: Co@B_8^- and Ru@B_9^-. *Angew. Chem., Int. Ed.* **2011**, *50*, 9334−9337.

(353) Li, W.-L.; Romanescu, C.; Galeev, T. R.; Piazza, Z. A.; Boldyrev, A. I.; Wang, L.-S. Transition-metal-centered nine-membered boron rings: M@B_9 and M@B_9^- (M = Rh, Ir). *J. Am. Chem. Soc.* **2012**, *134*, 165−168.

(354) Kumar, V. *Nanosilicon*; Elsevier: Amsterdam, 2008.

(355) Zhu, X.; Zeng, X. C. Structures and stabilities of small silicon clusters: Ab initio molecular-orbital calculations of Si_7−Si_{11}. *J. Chem. Phys.* **2003**, *118*, 3558−3570.

(356) Götz, D.; Heiles, S.; Johnston, R.; Schäfer, R. Note: Gas phase structures of bare Si_8 and Si_{11} clusters from molecular beam electric deflection experiments. *J. Chem. Phys.* **2012**, *136*, 186101.

(357) Zhao, J.; Ma, L.; Tian, D.; Xie, R. Fullerene-like cage clusters from non-carbon elements. *J. Comput. Theor. Nanosci.* **2008**, *5*, 7−22.

(358) Kumar, V.; Kawazoe, Y. Magic behavior of $Si_{15}M$ and $Si_{16}M$ (M = Cr, Mo, and W) clusters. *Phys. Rev. B: Condens. Matter Mater. Phys.* **2002**, *65*, 073404.

(359) Kumar, V.; Majumder, C.; Kawazoe, Y. M@Si_{16}, M = Ti, Zr, Hf: π conjugation, ionization potentials and electron affinities. *Chem. Phys. Lett.* **2002**, *363*, 319−322.

(360) Kumar, V.; Kawazoe, Y. Hydrogenated silicon fullerenes: Effects of H on the stability of metal-encapsulated silicon clusters. *Phys. Rev. Lett.* **2003**, *90*, 055502.

(361) Kumar, V.; Briere, T. M.; Kawazoe, Y. Ab initio calculations of electronic structures, polarizabilities, Raman and infrared spectra, optical gaps, and absorption spectra of M@Si_{16} (M = Ti and Zr) clusters. *Phys. Rev. B: Condens. Matter Mater. Phys.* **2003**, *68*, 155412.

(362) Kawamura, H.; Kumar, V.; Kawazoe, Y. Growth, magic behavior, and electronic and vibrational properties of Cr-doped Si clusters. *Phys. Rev. B: Condens. Matter Mater. Phys.* **2004**, *70*, 245433.

(363) Sun, Q.; Wang, Q.; Briere, T.; Kumar, V.; Kawazoe, Y.; Jena, P. First-principles calculations of metal stabilized Si_{20} cages. *Phys. Rev. B: Condens. Matter Mater. Phys.* **2002**, *65*, 235417.

(364) Kawamura, H.; Kumar, V.; Kawazoe, Y. Growth and magic behavior of metal encapsulated silicon clusters. *Mater. Trans.* **2004**, *45*, 1429−1432.

(365) Kawamura, H.; Kumar, V.; Kawazoe, Y. Growth behavior of metal-doped silicon clusters Si_nM (M = Ti, Zr, Hf; n = 8−16). *Phys. Rev. B: Condens. Matter Mater. Phys.* **2005**, *71*, 075423.

(366) Singh, A. K.; Kumar, V.; Kawazoe, Y. Stabilizing the silicon fullerene Si_{20} by thorium encapsulation. *Phys. Rev. B: Condens. Matter Mater. Phys.* **2005**, *71*, 115429.

(367) Kumar, V.; Singh, A. K.; Kawazoe, Y. Charged and magnetic fullerenes of silicon by metal encapsulation: Predictions from ab initio calculations. *Phys. Rev. B: Condens. Matter Mater. Phys.* **2006**, *74*, 125411.

(368) Hongo, K.; Kumar, V.; Kawazoe, Y.; Yasuhara, H. Quantum monte carlo study of electron correlation in chromium-doped silicon cluster Cr@Si_{12}. *Mater. Trans.* **2006**, *47*, 2617−2619.

(369) Kumar, V. Alchemy at the nanoscale: Magic heteroatom clusters and assemblies. *Comput. Mater. Sci.* **2006**, *36*, 1−11.

(370) Jaiswal, S.; Babar, V. P.; Kumar, V. Growth behavior, electronic structure, and vibrational properties of Si_nY anion clusters (n = 4−20): Metal atom as linker and endohedral dopant. *Phys. Rev. B: Condens. Matter Mater. Phys.* **2013**, *88*, 085412.

(371) Khanna, S.; Rao, B.; Jena, P. Magic numbers in metallo-inorganic clusters: Chromium encapsulated in silicon cages. *Phys. Rev. Lett.* **2002**, *89*, 016803.

(372) Xiao, C.; Hagelberg, F.; Lester, W. A., Jr Geometric, energetic, and bonding properties of neutral and charged copper-doped silicon clusters. *Phys. Rev. B: Condens. Matter Mater. Phys.* **2002**, *66*, 075425.

(373) Han, J.-G.; Xiao, C.; Hagelberg, F. Geometric and electronic structure of WSi_N (N = 1−6, 12) clusters. *Struct. Chem.* **2002**, *13*, 173−191.

(374) Miyazaki, T.; Hiura, H.; Kanayama, T. Topology and energetics of metal-encapsulating Si fullerenelike cage clusters. *Phys. Rev. B: Condens. Matter Mater. Phys.* **2002**, *66*, 121403.

(375) Gueorguiev, G.; Pacheco, J. Silicon and metal nanotemplates: Size and species dependence of structural and electronic properties. *J. Chem. Phys.* **2003**, *119*, 10313−10317.

(376) Lu, J.; Nagase, S. Structural and electronic properties of metal-encapsulated silicon clusters in a large size range. *Phys. Rev. Lett.* **2003**, *90*, 115506.

(377) Khanna, S.; Rao, B.; Jena, P.; Nayak, S. Stability and magnetic properties of iron atoms encapsulated in Si clusters. *Chem. Phys. Lett.* **2003**, *373*, 433−438.

(378) Miyazaki, T.; Hiura, H.; Kanayama, T. Electronic properties of transition-metal-atom doped Si cage clusters. *Eur. Phys. J. D* **2003**, *24*, 241−244.

(379) Hagelberg, F.; Xiao, C.; Lester, W. A., Jr Cagelike Si_{12} clusters with endohedral Cu, Mo, and W metal atom impurities. *Phys. Rev. B: Condens. Matter Mater. Phys.* **2003**, *67*, 035426.

(380) Mpourmpakis, G.; Froudakis, G. E.; Andriotis, A. N.; Menon, M. Fe encapsulation by silicon clusters: Ab initio electronic structure calculations. *Phys. Rev. B: Condens. Matter Mater. Phys.* **2003**, *68*, 125407.

(381) Sen, P.; Mitas, L. Electronic structure and ground states of transition metals encapsulated in a Si_{12} hexagonal prism cage. *Phys. Rev. B: Condens. Matter Mater. Phys.* **2003**, *68*, 155404.

(382) Guo, P.; Ren, Z.-Y.; Wang, F.; Bian, J.; Han, J.-G.; Wang, G.-H. Structural and electronic properties of $TaSi_n$ (n = 1−13) clusters: A relativistic density functional investigation. *J. Chem. Phys.* **2004**, *121*, 12265−12275.

(383) Andriotis, A. N.; Mpourmpakis, G.; Froudakis, G. E.; Menon, M. Magnetic enhancement and magnetic reduction in binary clusters of transition metal atoms. *J. Chem. Phys.* **2004**, *120*, 11901−11904.

(384) Han, J.-G.; Ren, Z.-Y.; Lu, B.-Z. Geometries and stabilities of Re-doped Si_n (n = 1− 12) clusters: A density functional investigation. *J. Phys. Chem. A* **2004**, *108*, 5100−5110.

(385) Reveles, J. U.; Khanna, S. N. Nearly-free-electron gas in a silicon cage. *Phys. Rev. B: Condens. Matter Mater. Phys.* **2005**, *72*, 165413.

(386) Wang, J.; Han, J.-G. Geometries, stabilities, and electronic properties of different-sized $ZrSi_n$ (n = 1−16) clusters: A density-functional investigation. *J. Chem. Phys.* **2005**, *123*, 064306.

(387) Ma, L.; Zhao, J.; Wang, J.; Lu, Q.; Zhu, L.; Wang, G. Structure and electronic properties of cobalt atoms encapsulated in Si_n (n = 1−13) clusters. *Chem. Phys. Lett.* **2005**, *411*, 279−284.

(388) Guo, P.; Ren, Z.-Y.; Yang, A.-P.; Han, J.-G.; Bian, J.; Wang, G.-H. Relativistic computational investigation: The geometries and electronic properties of $TaSi_n^+$ (n = 1−13, 16) clusters. *J. Phys. Chem. A* **2006**, *110*, 7453−7460.

(389) Ma, L.; Zhao, J.; Wang, J.; Wang, B.; Lu, Q.; Wang, G. Growth behavior and magnetic properties of Si_nFe (n = 2−14) clusters. *Phys. Rev. B: Condens. Matter Mater. Phys.* **2006**, *73*, 125439.

(390) Uchida, N.; Miyazaki, T.; Kanayama, T. Stabilization mechanism of Si_{12} cage clusters by encapsulation of a transition-metal atom: A density-functional theory study. *Phys. Rev. B: Condens. Matter Mater. Phys.* **2006**, *74*, 205427.

(391) Reveles, J. U.; Khanna, S. N. Electronic counting rules for the stability of metal-silicon clusters. *Phys. Rev. B: Condens. Matter Mater. Phys.* **2006**, *74*, 035435.

(392) Chen, Z.; Neukermans, S.; Wang, X.; Janssens, E.; Zhou, Z.; Silverans, R. E.; King, R. B.; Schleyer, P. v. R.; Lievens, P. To achieve stable spherical clusters: General principles and experimental confirmations. *J. Am. Chem. Soc.* **2006**, *128*, 12829−12834.

(393) Koukaras, E. N.; Garoufalis, C. S.; Zdetsis, A. D. Structure and properties of the Ni@Si_{12} cluster from all-electron ab initio calculations. *Phys. Rev. B: Condens. Matter Mater. Phys.* **2006**, *73*, 235417.

(394) Gueorguiev, G. K.; Pacheco, J.; Stafström, S.; Hultman, L. Silicon−metal clusters: Nano-templates for cluster assembled materials. *Thin Solid Films* **2006**, *515*, 1192−1196.

(395) Kumar, V. Novel metal-encapsulated caged clusters of silicon and germanium. *Eur. Phys. J. D* **2003**, *24*, 227−232.

(396) Zorriasatein, S.; Joshi, K.; Kanhere, D. Dopant-induced stabilization of silicon clusters at finite temperature. *Phys. Rev. B: Condens. Matter Mater. Phys.* **2007**, *75*, 045117.

(397) Zdetsis, A. D. Bonding and structural characteristics of Zn-, Cu-, and Ni-encapsulated Si clusters: Density-functional theory calculations. *Phys. Rev. B: Condens. Matter Mater. Phys.* **2007**, *75*, 085409.

(398) Wang, J.; Ma, Q.-M.; Xie, Z.; Liu, Y.; Li, Y.-C. From Si_nNi to Ni@Si_n: An investigation of configurations and electronic structure. *Phys. Rev. B: Condens. Matter Mater. Phys.* **2007**, *76*, 035406.

(399) Wang, J.; Zhao, J.; Ma, L.; Wang, B.; Wang, G. Structure and magnetic properties of cobalt doped Si_n (n = 2−14) clusters. *Phys. Lett. A* **2007**, *367*, 335−344.

(400) Torres, M.; Balbás, L. Relative stability of Si_n and Si_nSc^- clusters in the range n = 14−18). *Eur. Phys. J. D* **2007**, *43*, 217−220.

(401) Torres, M.; Fernández, E.; Balbás, L. Theoretical study of isoelectronic Si_nM clusters (M = Sc^-, Ti, V^+; n = 14−18. *Phys. Rev. B: Condens. Matter Mater. Phys.* **2007**, *75*, 205425.

(402) Han, J.-G.; Zhao, R.-N.; Duan, Y. Geometries, stabilities, and growth patterns of the bimetal Mo_2-doped Si_n (n = 9−16) clusters: A density functional investigation. *J. Phys. Chem. A* **2007**, *111*, 2148−2155.

(403) Guo, L.-J.; Liu, X.; Zhao, G.-F.; Luo, Y.-H. Computational investigation of $TiSi_n$ (n = 2−15) clusters by the density-functional theory. *J. Chem. Phys.* **2007**, *126*, 234704.

(404) Chuang, F.-C.; Hsieh, Y.-Y.; Hsu, C.-C.; Albao, M. A. Geometries and stabilities of Ag-doped Si_n (n = 1−13) clusters: A first-principles study. *J. Chem. Phys.* **2007**, *127*, 144313.

(405) Guo, L.-j.; Zhao, G.-f.; Gu, Y.-z.; Liu, X.; Zeng, Z. Density-functional investigation of metal-silicon cage clusters MSi_n (M = Sc, Ti, V, Cr, Mn, Fe, Co, Ni, Cu, Zn; n = 8−16). *Phys. Rev. B: Condens. Matter Mater. Phys.* **2008**, *77*, 195417.

(406) Hossain, D.; Pittman, C. U., Jr; Gwaltney, S. R. Structures and stabilities of copper encapsulated within silicon nano-clusters: Cu@Si_n (n = 9−15). *Chem. Phys. Lett.* **2008**, *451*, 93−97.

(407) Yang, A.-P.; Ren, Z.-Y.; Guo, P.; Wang, G.-H. Geometries, stabilities, and electronic properties of Y-doped Si_n (n = 1−16) clusters: A relativistic density functional investigation. *J. Mol. Struct.: THEOCHEM* **2008**, *856*, 88−95.

(408) Peng, Q.; Shen, J. Growth behavior of La@Si_n (n = 1−21) metal-encapsulated clusters. *J. Chem. Phys.* **2008**, *128*, 084711.

(409) Wang, J.; Liu, J. H. Investigation of size-selective Zr_2@Si_n (n = 16−24) caged clusters. *J. Phys. Chem. A* **2008**, *112*, 4562−4567.

(410) Bandyopadhyay, D. A density functional theory−based study of the electronic structures and properties of cage like metal doped silicon clusters. *J. Appl. Phys.* **2008**, *104*, 084308.

(411) Bandyopadhyay, D.; Kumar, M. The electronic structures and properties of transition metal-doped silicon nanoclusters: A density functional investigation. *Chem. Phys.* **2008**, *353*, 170−176.

(412) Bandyopadhyay, D. The study of the electronic structures and properties of pure and transition metal-doped silicon nanoclusters: A density functional theory approach. *Mol. Simul.* **2009**, *35*, 381−394.

(413) Zhao, G.-f.; Sun, J.-m.; Gu, Y.-z.; Wang, Y.-x. Density-functional study of structural, electronic, and magnetic properties of the $EuSi_n$ (n = 1−13) clusters. *J. Chem. Phys.* **2009**, *131*, 114312.

(414) Lan, Y.-Z.; Feng, Y.-L. Comparative study on the geometric and energetic properties, absorption spectra, and polarizabilities of charged and neutral Cu@Si_n clusters (n = 9−14). *Phys. Rev. A: At., Mol., Opt. Phys.* **2009**, *79*, 033201.

(415) Wang, J.; Liu, J. H. Novel bi-transition metallic encapsulated naphthalene-like Si_{20} prismatic cage: A DFT investigation. *J. Comput. Chem.* **2009**, *30*, 1103−1110.

(416) Li, J.-r.; Yao, C.-h.; Mu, Y.-w.; Wan, J.-g.; Han, M. Structures and magnetic properties of Si_nNi (n = 1−17) clusters. *J. Mol. Struct.: THEOCHEM* **2009**, *916*, 139−146.

(417) He, J.; Wu, K.; Liu, C.; Sa, R. Stabilities of 3d transition-metal doped Si_{14} clusters. *Chem. Phys. Lett.* **2009**, *483*, 30−34.

(418) Wang, J.; Ma, Q.-M.; Xu, R.-P.; Liu, Y.; Li, Y.-C. 3d transition metals: Which is the ideal guest for Si_n (n = 15, 16) cages? *Phys. Lett. A* **2009**, *373*, 2869−2875.

(419) Zdetsis, A.; Koukaras, E.; Garoufalis, C. A parallel study of $Ni@Si_{12}$ and $Cu@Si_{12}$ nanoclusters. *J. Math. Chem.* **2009**, *46*, 971−980.

(420) Li, J.-r.; Wang, G.-h.; Yao, C.-h.; Mu, Y.-w.; Wan, J.-g.; Han, M. Structures and magnetic properties of Si_nMn (n = 1−15) clusters. *J. Chem. Phys.* **2009**, *130*, 164514.

(421) Reis, C.; Pacheco, J. Vibrational spectra of silicon cage clusters doped with Ti, Zr, or Hf. *Phys. Rev. B: Condens. Matter Mater. Phys.* **2010**, *82*, 155440.

(422) Wang, J.; Liu, Y.; Li, Y.-C. Magnetic silicon fullerene. *Phys. Chem. Chem. Phys.* **2010**, *12*, 11428−11431.

(423) Wang, J.; Liu, Y.; Li, Y.-C. $Au@Si_n$: Growth behavior, stability and electronic structure. *Phys. Lett. A* **2010**, *374*, 2736−2742.

(424) Willand, A.; Gramzow, M.; Ghasemi, S. A.; Genovese, L.; Deutsch, T.; Reuter, K.; Goedecker, S. Structural metastability of endohedral silicon fullerenes. *Phys. Rev. B: Condens. Matter Mater. Phys.* **2010**, *81*, 201405.

(425) Palagin, D.; Gramzow, M.; Reuter, K. On the stability of "non-magic" endohedrally doped Si clusters: A first-principles sampling study of MSi_{16}^+ (M = Ti, V, Cr). *J. Chem. Phys.* **2011**, *134*, 244705.

(426) Cantera-López, H.; Balbás, L.; Borstel, G. First-principles calculations of structural and electronic properties of Ta-doped Si clusters, wires, and bulk systems. *Phys. Rev. B: Condens. Matter Mater. Phys.* **2011**, *83*, 075434.

(427) Oña, O. B.; Ferraro, M. B.; Facelli, J. C. Transition from exo to endo Cu absorption in $CuSi_n$ clusters: A genetic algorithms density functional theory study. *Mol. Simul.* **2011**, *37*, 678−688.

(428) Liu, T.-g.; Zhao, G.-f.; Wang, Y.-x. Structural, electronic and magnetic properties of $GdSi_n$ (n = 1−17) clusters: A density functional study. *Phys. Lett. A* **2011**, *375*, 1120−1127.

(429) Ziella, D. H.; Caputo, M. C.; Provasi, P. F. Study of geometries and electronic properties of $AgSi_n$ clusters using DFT/TB. *Int. J. Quantum Chem.* **2011**, *111*, 1680−1693.

(430) Dognon, J.-P.; Clavaguéra, C.; Pyykkö, P. A new, centered 32-electron system: The predicted $[U@Si_{20}]^{6-}$-like isoelectronic series. *Chem. Sci.* **2012**, *3*, 2843−2848.

(431) Xu, H.-G.; Wu, M. M.; Zhang, Z.-G.; Yuan, J.; Sun, Q.; Zheng, W. Photoelectron spectroscopy and density functional calculations of $CuSi_n^-$ (n = 4−18) clusters. *J. Chem. Phys.* **2012**, *136*, 104308.

(432) Kong, X.; Xu, H.-G.; Zheng, W. Structures and magnetic properties of $CrSi_n^-$ (n = 3−12) clusters: Photoelectron spectroscopy and density functional calculations. *J. Chem. Phys.* **2012**, *137*, 064307.

(433) Kong, X.-Y.; Deng, X.-J.; Xu, H.-G.; Yang, Z.; Xu, X.-L.; Zheng, W.-J. Photoelectron spectroscopy and density functional calculations of $AgSi_n^-$ (n = 3−12) clusters. *J. Chem. Phys.* **2013**, *138*, 244312.

(434) Ma, L.; Wang, J.; Wang, G. Site-specific analysis of dipole polarizabilities of heterogeneous systems: Iron-doped Si_n (n = 1−14) clusters. *J. Chem. Phys.* **2013**, *138*, 094304.

(435) Oliveira, M.; Rivelino, R.; de Brito Mota, F.; Gueorguiev, G. K. Optical properties and quasiparticle band gaps of transition-metal atoms encapsulated by silicon cages. *J. Phys. Chem. C* **2014**, *118*, 5501−5509.

(436) Oliveira, M. J.; Medeiros, P. V.; Sousa, J. R.; Nogueira, F.; Gueorguiev, G. K. Optical and magnetic excitations of metal-encapsulating Si cages: A systematic study by time-dependent density functional theory. *J. Phys. Chem. C* **2014**, *118*, 11377−11384.

(437) Liu, T.-G.; Zhang, W.-Q.; Li, Y.-L. First-principles study on the structure, electronic and magnetic properties of $HoSi_n$ (n = 1−12, 20) clusters. *Front. Phys.* **2014**, *9*, 210−218.

(438) Zhao, R.-N.; Han, J.-G.; Duan, Y. Density functional theory investigations on the geometrical and electronic properties and growth patterns of Si_n (n = 10−20) clusters with bimetal Pd_2 impurities. *Thin Solid Films* **2014**, *556*, 571−579.

(439) Borshch, N.; Kurganskii, S. Geometric structure, electron-energy spectrum, and growth of anionic scandium-silicon clusters $ScSi_n^-$ (n = 6−20). *J. Appl. Phys.* **2014**, *116*, 124302.

(440) Abreu, M. B.; Reber, A. C.; Khanna, S. N. Does the 18-electron rule apply to $CrSi_{12}$? *J. Phys. Chem. Lett.* **2014**, *5*, 3492−3496.

(441) Zhao, R.-N.; Han, J.-G. Geometrical stabilities and electronic properties of Si_n (n = 12−20) clusters with rare earth holmium impurity: A density functional investigation. *RSC Adv.* **2014**, *4*, 64410−64418.

(442) Xu, H.-G.; Kong, X.-Y.; Deng, X.-J.; Zhang, Z.-G.; Zheng, W.-J. Smallest fullerene-like silicon cage stabilized by a V_2 unit. *J. Chem. Phys.* **2014**, *140*, 024308.

(443) Huang, X.; Xu, H.-G.; Lu, S.; Su, Y.; King, R.; Zhao, J.; Zheng, W. Discovery of a silicon-based ferrimagnetic wheel structure in $V_xSi_{12}^-$ (x = 1−3) clusters: Photoelectron spectroscopy and density functional theory investigation. *Nanoscale* **2014**, *6*, 14617−14621.

(444) Huang, X.; Lu, S.-J.; Liang, X.; Su, Y.; Sai, L.; Zhang, Z.-G.; Zhao, J.; Xu, H.-G.; Zheng, W. Structures and electronic properties of $V_3Si_n^-$ (n = 3−14) clusters: A combined ab Initio and experimental study. *J. Phys. Chem. C* **2015**, *119*, 10987−10994.

(445) Lin, L.; Yang, J. Small copper-doped silicon clusters $CuSi_n$ (n = 4−10) and their anions: Structures, thermochemistry, and electron affinities. *J. Mol. Model.* **2015**, *21*, 155.

(446) Abreu, M. B.; Reber, A. C.; Khanna, S. N. Making sense of the conflicting magic numbers in WSi_n clusters. *J. Chem. Phys.* **2015**, *143*, 074310.

(447) Chauhan, V.; Abreu, M. B.; Reber, A. C.; Khanna, S. N. Geometry controls the stability of $FeSi_{14}$. *Phys. Chem. Chem. Phys.* **2015**, *17*, 15718−15724.

(448) Goicoechea, J. M.; McGrady, J. E. On the structural landscape in endohedral silicon and germanium clusters, $M@Si_{12}$ and $M@Ge_{12}$. *Dalton Trans.* **2015**, *44*, 6755−6766.

(449) Arcisauskaite, V.; Fijan, D.; Spivak, M.; de Graaf, C.; McGrady, J. E. Biradical character in the ground state of $[Mn@Si_{12}]^+$: A DFT and CASPT2 study. *Phys. Chem. Chem. Phys.* **2016**, *18*, 24006−24014.

(450) Xia, X. X.; Hermann, A.; Kuang, X. Y.; Jin, Y. Y.; Lu, C.; Xing, X. D. Study of the structural and electronic properties of neutral and charged niobium-doped silicon clusters: Niobium encapsulated in silicon cages. *J. Phys. Chem. C* **2016**, *120*, 677−684.

(451) Phi, N. D.; Trung, N. T.; Janssens, E.; Ngan, V. T. Electron counting rules for transition metal-doped Si_{12} clusters. *Chem. Phys. Lett.* **2016**, *643*, 103−108.

(452) Hou, L.; Yang, J.; Liu, Y. Reexamination of structures, stabilities, and electronic properties of holmium-doped silicon clusters $HoSi_n$ (n = 12−20). *J. Mol. Model.* **2016**, *22*, 193.

(453) Lu, S.-J.; Cao, G.-J.; Xu, X.-L.; Xu, H.-G.; Zheng, W.-J. The structural and electronic properties of $NbSi_n^{-/0}$ (n = 3−12) clusters: Anion photoelectron spectroscopy and ab initio calculations. *Nanoscale* **2016**, *8*, 19769−19778.

(454) Lu, S.-J.; Xu, X.-L.; Feng, G.; Xu, H.-G.; Zheng, W.-J. Structural and electronic properties of $AuSi_n^-$ (n = 4−12) clusters: Photoelectron spectroscopy and ab initio calculations. *J. Phys. Chem. C* **2016**, *120*, 25628−25637.

(455) Feng, Y.; Yang, J. Stability and electronic properties of praseodymium-doped silicon clusters $PrSi_n$ (n = 12−21). *J. Mol. Model.* **2017**, *23*, 180.

(456) Jin, X.; Arcisauskaite, V.; McGrady, J. E. The structural landscape in 14-vertex clusters of silicon, $M@Si_{14}$: When two bonding paradigms collide. *Dalton Trans.* **2017**, *46*, 11636−11644.

(457) Zhao, R.-N.; Chen, R.; Lu, Z.-C.; Han, J.-G. Geometrical and electronic properties of nanosize semiconductor Pt_2Si_n (n = 10−20) material: A density functional theory investigation. *Mater. Sci. Eng., B* **2017**, *226*, 151−157.

(458) Liu, Y.; Yang, J.; Cheng, L. Structural stability and evolution of scandium-doped silicon clusters: Evolution of linked to encapsulated structures and its influence on the prediction of electron affinities for $ScSi_n$ (n = 4−16) clusters. *Inorg. Chem.* **2018**, *57*, 12934−12940.

(459) Bista, D.; Reber, A. C.; Chauhan, V.; Khanna, S. N. Electronic and magnetic properties of Fe_2Si_n $(1 \le n \le 12)^{+/0/-}$ clusters. *Chem. Phys. Lett.* **2018**, *706*, 113−119.

(460) Yang, B.; Xu, H.; Xu, X.; Zheng, W. Photoelectron spectroscopy and theoretical study of $Cr_nSi_{15-n}^-$ (n = 1−3): Effects of doping Cr atoms on the structural and magnetic properties. *J. Phys. Chem. A* **2018**, *122*, 9886−9893.

(461) Wu, X.; Zhou, S.; Huang, X.; Chen, M.; Bruce King, R.; Zhao, J. Revisit of large-gap Si_{16} clusters encapsulating group-IV metal atoms (Ti, Zr, Hf). *J. Comput. Chem.* **2018**, *39*, 2268−2272.

(462) Lu, S.-J.; Wu, L.-S.; Lin, F. Probing the structures and properties of $Ti_2Si_{20}^{-/0}$ clusters by density functional theory calculations. *Chem. Phys. Lett.* **2018**, *707*, 108−112.

(463) Lu, S.-J. Exploring the structural evolution and electronic properties of medium-sized $Nb_2Si_n^{-/0}$ (n= 13−20) clusters by density functional theory calculations. *Chem. Phys. Lett.* **2018**, *713*, 58−64.

(464) Lu, S.-J.; Wu, L.-S.; Lin, F. Probing the geometric structures and bonding properties in $Nb_2Si_{20}^{-/0}$ clusters by density functional theory calculations. *Chem. Phys. Lett.* **2018**, *709*, 60−64.

(465) Lu, S.-J. Exploring the structural and electronic properties of double-Fe atom-doped Si_{20} cluster by quantum chemical calculations. *Theor. Chem. Acc.* **2019**, *138*, 48.

(466) Yang, B.; Xu, X.-L.; Xu, H.-G.; Farooq, U.; Zheng, W.-J. Structural evolution and electronic properties of $CoSi_n^-$ (n = 3−12) clusters: Mass-selected anion photoelectron spectroscopy and quantum chemistry calculations. *Phys. Chem. Chem. Phys.* **2019**, *21*, 6207−6215.

(467) Majumder, C.; Kulshreshtha, S. Impurity-doped Si_{10} cluster: Understanding the structural and electronic properties from first-principles calculations. *Phys. Rev. B: Condens. Matter Mater. Phys.* **2004**, *70*, 245426.

(468) Sporea, C.; Rabilloud, F. Stability of alkali-encapsulating silicon cage clusters. *J. Chem. Phys.* **2007**, *127*, 164306.

(469) Hossain, D.; Hagelberg, F.; Pittman, C. U.; Saebo, S. Structures and stabilities of clusters of Si_{12}, Si_{18}, and Si_{20} containing endohedral charged and neutral atomic species. *J. Phys. Chem. C* **2007**, *111*, 13864−13871.

(470) Avaltroni, F.; Steinmann, S. N.; Corminboeuf, C. How are small endohedral silicon clusters stabilized? *Phys. Chem. Chem. Phys.* **2012**, *14*, 14842−14849.

(471) Lu, S.-J.; Xu, X.-L.; Cao, G.-J.; Xu, H.-G.; Zheng, W.-J. Structural evolution of $B_2Si_n^{-/0}$ (n = 3−12) clusters: Size-selected anion photoelectron spectroscopy and theoretical calculations. *J. Phys. Chem. C* **2018**, *122*, 2391−2401.

(472) Borshch, N.; Berestnev, K.; Pereslavtseva, N.; Kurganskii, S. Geometric structure and electron spectrum of YSi_n^- clusters (n = 6−17). *Phys. Solid State* **2014**, *56*, 1276−1281.

(473) Trivedi, R.; Bandyopadhyay, D. Evolution of electronic and vibrational properties of $M@X_n$ (M = Ag, Au, X = Ge, Si, n = 10, 12, 14) clusters: A density functional modeling. *J. Mater. Sci.* **2018**, *53*, 8263−8273.

(474) Ngan, V. T.; Pierloot, K.; Nguyen, M. T. $Mn@Si_{14}^+$: A singlet fullerene-like endohedrally doped silicon cluster. *Phys. Chem. Chem. Phys.* **2013**, *15*, 5493−5498.

(475) Li, Y.; Tam, N. M.; Woodham, A. P.; Lyon, J. T.; Li, Z.; Lievens, P.; Fielicke, A.; Nguyen, M. T.; Janssens, E. Structure dependent magnetic coupling in cobalt-doped silicon clusters. *J. Phys. Chem. C* **2016**, *120*, 19454−19460.

(476) Gao, Y.; Zeng, X. C. $M_4@Si_{28}$ (M = Al, Ga): Metal-encapsulated tetrahedral silicon fullerene. *J. Chem. Phys.* **2005**, *123*, 204325.

(477) Hagelberg, F.; Yanov, I.; Leszczynski, J. Theoretical investigations on closed-shell silicon clusters doped with Cu atoms. *J. Mol. Struct.: THEOCHEM* **1999**, *487*, 183−192.

(478) Pederson, M. R.; Jackson, K. A. Variational mesh for quantum-mechanical simulations. *Phys. Rev. B: Condens. Matter Mater. Phys.* **1990**, *41*, 7453−7461.

(479) Porezag, D.; Pederson, M. R. Optimization of Gaussian basis sets for density-functional calculations. *Phys. Rev. A: At., Mol., Opt. Phys.* **1999**, *60*, 2840−2847.

(480) Jaeger, J.; Jaeger, T.; Duncan, M. Photodissociation of metal−silicon clusters: Encapsulated versus surface-bound metal. *J. Phys. Chem. A* **2006**, *110*, 9310−9314.

(481) Negishi, A.; Kariya, N.; Sugawara, K.-i.; Arai, I.; Hiura, H.; Kanayama, T. Size-selective formation of tungsten cluster-containing silicon cages by the reactions of W_n^+ (n = 1−5) with SiH_4. *Chem. Phys. Lett.* **2004**, *388*, 463−467.

(482) Kaneko, T.; Takaya, H.; Hatakeyama, R. Generation of argon-ion mixed silicon plasmas forming argon encapsulated silicon clusters. *Appl. Phys. Lett.* **2006**, *89*, 241501.

(483) Neukermans, S.; Wang, X.; Veldeman, N.; Janssens, E.; Silverans, R.; Lievens, P. Mass spectrometric stability study of binary MS_n clusters (S = Si, Ge, Sn, Pb, and M = Cr, Mn, Cu, Zn). *Int. J. Mass Spectrom.* **2006**, *252*, 145−150.

(484) Janssens, E.; Gruene, P.; Meijer, G.; Wöste, L.; Lievens, P.; Fielicke, A. Argon physisorption as structural probe for endohedrally doped silicon clusters. *Phys. Rev. Lett.* **2007**, *99*, 063401.

(485) Ohara, M.; Miyajima, K.; Pramann, A.; Nakajima, A.; Kaya, K. Geometric and electronic structures of terbium−silicon mixed clusters ($TbSi_n$; $6 \le n \le 16$). *J. Phys. Chem. A* **2002**, *106*, 3702−3705.

(486) Koyasu, K.; Atobe, J.; Akutsu, M.; Mitsui, M.; Nakajima, A. Electronic and geometric stabilities of clusters with transition metal encapsulated by silicon. *J. Phys. Chem. A* **2007**, *111*, 42−49.

(487) Koyasu, K.; Atobe, J.; Furuse, S.; Nakajima, A. Anion photoelectron spectroscopy of transition metal-and lanthanide metal-silicon clusters: MSi_n^- (n= 6−20). *J. Chem. Phys.* **2008**, *129*, 214301.

(488) Shibuta, M.; Ohta, T.; Nakaya, M.; Tsunoyama, H.; Eguchi, T.; Nakajima, A. Chemical characterization of an alkali-like superatom consisting of a Ta-encapsulating Si_{16} cage. *J. Am. Chem. Soc.* **2015**, *137*, 14015−14018.

(489) Tsunoyama, H.; Shibuta, M.; Nakaya, M.; Eguchi, T.; Nakajima, A. Synthesis and characterization of metal-encapsulating Si_{16} cage superatoms. *Acc. Chem. Res.* **2018**, *51*, 1735−1745.

(490) Zheng, W.; Nilles, J. M.; Radisic, D.; Bowen, K. H., Jr Photoelectron spectroscopy of chromium-doped silicon cluster anions. *J. Chem. Phys.* **2005**, *122*, 071101.

(491) Grubisic, A.; Wang, H.; Ko, Y. J.; Bowen, K. H. Photoelectron spectroscopy of europium-silicon cluster anions, $EuSi_n^-$ $(3 \leqslant n \leqslant 17)$. *J. Chem. Phys.* **2008**, *129*, 054302.

(492) Grubisic, A.; Ko, Y. J.; Wang, H.; Bowen, K. H. Photoelectron spectroscopy of lanthanide−silicon cluster anions $LnSi_n^-$ ($3 \le n \le 13$; Ln = Ho, Gd, Pr, Sm, Eu, Yb): Prospect for magnetic silicon-based clusters. *J. Am. Chem. Soc.* **2009**, *131*, 10783−10790.

(493) Zamudio-Bayer, V.; Leppert, L.; Hirsch, K.; Langenberg, A.; Rittmann, J.; Kossick, M.; Vogel, M.; Richter, R.; Terasaki, A.; Möller, T. Coordination-driven magnetic-to-nonmagnetic transition in manganese-doped silicon clusters. *Phys. Rev. B: Condens. Matter Mater. Phys.* **2013**, *88*, 115425.

(494) Lau, J.; Vogel, M.; Langenberg, A.; Hirsch, K.; Rittmann, J.; Zamudio-Bayer, V.; Möller, T.; Issendorff, B. v. Communication: Highest occupied molecular orbital−lowest unoccupied molecular orbital gaps of doped silicon clusters from core level spectroscopy. *J. Chem. Phys.* **2011**, *134*, 041102.

(495) Ngan, V. T.; Gruene, P.; Claes, P.; Janssens, E.; Fielicke, A.; Nguyen, M. T.; Lievens, P. Disparate effects of Cu and V on structures of exohedral transition metal-doped silicon clusters: A combined far-infrared spectroscopic and computational study. *J. Am. Chem. Soc.* **2010**, *132*, 15589−15602.

(496) Claes, P.; Janssens, E.; Ngan, V.; Gruene, P.; Lyon, J. T.; Harding, D. J.; Fielicke, A.; Nguyen, M.; Lievens, P. Structural identification of caged vanadium doped silicon clusters. *Phys. Rev. Lett.* **2011**, *107*, 173401.

(497) Ngan, V. T.; Janssens, E.; Claes, P.; Lyon, J. T.; Fielicke, A.; Nguyen, M. T.; Lievens, P. High magnetic moments in manganese-doped silicon clusters. *Chem. - Eur. J.* **2012**, *18*, 15788−15793.

(498) Li, X.; Claes, P.; Haertelt, M.; Lievens, P.; Janssens, E.; Fielicke, A. Structural determination of niobium-doped silicon clusters by far-infrared spectroscopy and theory. *Phys. Chem. Chem. Phys.* **2016**, *18*, 6291−6300.

(499) Li, Y.; Tam, N. M.; Claes, P.; Woodham, A. P.; Lyon, J. T.; Ngan, V. T.; Nguyen, M. T.; Lievens, P.; Fielicke, A.; Janssens, E. Structure assignment, electronic properties, and magnetism quenching of endohedrally doped neutral silicon clusters, Si_nCo (n = 10−12). *J. Phys. Chem. A* **2014**, *118*, 8198−8203.

(500) Cheshnovsky, O.; Yang, S.; Pettiette, C.; Craycraft, M.; Liu, Y.; Smalley, R. Ultraviolet photoelectron spectroscopy of semiconductor clusters: Silicon and germanium. *Chem. Phys. Lett.* **1987**, *138*, 119−124.

(501) Hoffmann, M. A.; Wrigge, G.; Issendorff, B. v.; Müller, J.; Ganteför, G.; Haberland, H. Ultraviolet photoelectron spectroscopy of Si_4 to Si_{1000}. *Eur. Phys. J. D* **2001**, *16*, 9−11.

(502) Meloni, G.; Ferguson, M. J.; Sheehan, S. M.; Neumark, D. M. Probing structural transitions of nanosize silicon clusters via anion photoelectron spectroscopy at 7.9 eV. *Chem. Phys. Lett.* **2004**, *399*, 389−391.

(503) Akola, J.; Manninen, M.; Häkkinen, H.; Landman, U.; Li, X.; Wang, L.-S. Photoelectron spectra of aluminum cluster anions: Temperature effects and ab initio simulations. *Phys. Rev. B: Condens. Matter Mater. Phys.* **1999**, *60*, R11297−R11300.

(504) Honea, E.; Ogura, A.; Peale, D.; Felix, C.; Murray, C.; Raghavachari, K.; Sprenger, W.; Jarrold, M.; Brown, W. Structures and coalescence behavior of size-selected silicon nanoclusters studied by surface-plasmon-polariton enhanced Raman spectroscopy. *J. Chem. Phys.* **1999**, *110*, 12161−12172.

(505) Pichierri, F.; Kumar, V.; Kawazoe, Y. Exohedral functionalization of the icosahedral cluster $Si_{20}H_{20}$: A density functional theory study. *Chem. Phys. Lett.* **2004**, *383*, 544−548.

(506) Pichierri, F.; Kumar, V.; Kawazoe, Y. Encapsulation of halide anions in perhydrogenated silicon fullerene: $X^-@Si_{20}H_{20}$ (X= F, Cl, Br, I). *Chem. Phys. Lett.* **2005**, *406*, 341−344.

(507) Tillmann, J.; Wender, J. H.; Bahr, U.; Bolte, M.; Lerner, H. W.; Holthausen, M. C.; Wagner, M. One-Step synthesis of a [20] silafullerane with an endohedral chloride ion. *Angew. Chem., Int. Ed.* **2015**, *54*, 5429−5433.

(508) Wigner, E.; Witmer, E. Über die struktur der zweiatomigen molekelspektren nach der quantenmechanik. *Eur. Phys. J. A* **1928**, *51*, 859−886.

(509) Nolas, G. S. *The physics and chemistry of inorganic clathrates*; Springer: Dordrecht, 2014.

(510) Emsley, J. *The elements*; Oxford University Press: New York, 1991.

(511) He, J.; Wu, K.; Sa, R.; Li, Q.; Wei, Y. (Hyper) polarizabilities and optical absorption spectra of MSi_{12} clusters (M = Sc−Zn): A theoretical study. *Chem. Phys. Lett.* **2010**, *490*, 132−137.

(512) Kong, L.; Chelikowsky, J. R. Transport properties of transition-metal-encapsulated Si cages. *Phys. Rev. B: Condens. Matter Mater. Phys.* **2008**, *77*, 073401.

(513) Kawamura, H.; Kumar, V.; Kawazoe, Y. Water adsorption on Ti-doped silicon clusters. *Phys. Rev. B: Condens. Matter Mater. Phys.* **2004**, *70*, 193402.

(514) Shibuta, M.; Kamoshida, T.; Ohta, T.; Tsunoyama, H.; Nakajima, A. Oxidative reactivity of alkali-like superatoms of group 5 metal-encapsulating Si_{16} cage nanoclusters. *Comm. Chem.* **2018**, *1*, 50.

(515) Shibuta, M.; Niikura, T.; Kamoshida, T.; Tsunoyama, H.; Nakajima, A. Nitric oxide oxidation of a Ta encapsulating Si cage nanocluster superatom ($Ta@Si_{16}$) deposited on an organic substrate; a Si cage collapse indicator. *Phys. Chem. Chem. Phys.* **2018**, *20*, 26273−26279.

(516) Belomoin, G.; Therrien, J.; Smith, A.; Rao, S.; Twesten, R.; Chaieb, S.; Nayfeh, M. H.; Wagner, L.; Mitas, L. Observation of a magic discrete family of ultrabright Si nanoparticles. *Appl. Phys. Lett.* **2002**, *80*, 841−843.

(517) Li, S.; Xue, X.; Zhai, H.; Nie, X.; Wang, F.; Sun, Q.; Jia, Y.; Guo, Z.; Shevlin, S. High inertness of $W@Si_{12}$ cluster toward O2 molecule. *Phys. Lett. A* **2012**, *376*, 1454−1459.

(518) Yong, Y.; Lv, S.; Li, X.; Li, T.; Cui, H. $W@Si_{12}$ cluster as a potential sensor for CO and NO detection. *EPL* **2015**, *111*, 10006.

(519) Zhou, S.; Yang, X.; Pei, W.; Zhao, J.; Du, A. Silicon nanocages for selective carbon dioxide conversion under visible light. *J. Phys. Chem. C* **2019**, *123*, 9973−9980.

(520) Zhou, S.; Yang, X.; Pei, W.; Liu, N.; Zhao, J. Heterostructures of MXenes and N-doped graphene as highly active bifunctional electrocatalysts. *Nanoscale* **2018**, *10*, 10876−10883.

(521) Pei, W.; Zhou, S.; Bai, Y.; Zhao, J. N-doped graphitic carbon materials hybridized with transition metals (compounds) for hydrogen evolution reaction: Understanding the synergistic effect from atomistic level. *Carbon* **2018**, *133*, 260−266.

(522) Hunter, J.; Fye, J.; Jarrold, M.; Bower, J. Structural transitions in size-selected germanium cluster ions. *Phys. Rev. Lett.* **1994**, *73*, 2063−2066.

(523) Burton, G. R.; Xu, C.; Arnold, C. C.; Neumark, D. M. Photoelectron spectroscopy and zero electron kinetic energy spectroscopy of germanium cluster anions. *J. Chem. Phys.* **1996**, *104*, 2757−2764.

(524) Gingerich, K. A.; Schmude, R., Jr; Sai Baba, M.; Meloni, G. Atomization enthalpies and enthalpies of formation of the germanium clusters, Ge_5, Ge_6, Ge_7, and Ge_8 by Knudsen effusion mass spectrometry. *J. Chem. Phys.* **2000**, *112*, 7443−7448.

(525) Schäfer, S.; Schäfer, R. Dielectric response of germanium clusters. *Phys. Rev. B: Condens. Matter Mater. Phys.* **2008**, *77*, 205211.

(526) Wang, J.; Wang, G.; Zhao, J. Structure and electronic properties of Ge_n (n = 2−25) clusters from density-functional theory. *Phys. Rev. B: Condens. Matter Mater. Phys.* **2001**, *64*, 205411.

(527) Bulusu, S.; Yoo, S.; Zeng, X. C. Search for global minimum geometries for medium sized germanium clusters: Ge_{12}−Ge_{20}. *J. Chem. Phys.* **2005**, *122*, 164305.

(528) Kumar, V.; Kawazoe, Y. Metal-encapsulated icosahedral superatoms of germanium and tin with large gaps: $Zn@Ge_{12}$ and $Cd@Sn_{12}$. *Appl. Phys. Lett.* **2002**, *80*, 859−861.

(529) Singh, A. K.; Kumar, V.; Kawazoe, Y. Thorium encapsulated caged clusters of germanium: $Th@Ge_n$, n = 16, 18, and 20. *J. Phys. Chem. B* **2005**, *109*, 15187−15189.

(530) Zhang, X.; Li, G.; Gao, Z. Laser ablation of Co/Ge mixtures: A new type of endohedral structure, a semiconductor cage trapping a metal atom. *Rapid Commun. Mass Spectrom.* **2001**, *15*, 1573−1576.

(531) Atobe, J.; Koyasu, K.; Furuse, S.; Nakajima, A. Anion photoelectron spectroscopy of germanium and tin clusters containing a transition-or lanthanide-metal atom; MGe_n^- (n = 8−20) and MSn_n^- (n = 15−17)(M = Sc−V, Y−Nb, and Lu−Ta). *Phys. Chem. Chem. Phys.* **2012**, *14*, 9403−9410.

(532) Deng, X. J.; Kong, X. Y.; Xu, X. L.; Xu, H. G.; Zheng, W. J. Structural and magnetic properties of $CoGe_n^-$ (n = 2−11) clusters: Photoelectron spectroscopy and density functional calculations. *ChemPhysChem* **2014**, *15*, 3987−3993.

(533) Deng, X.-J.; Kong, X.-Y.; Xu, H.-G.; Xu, X.-L.; Feng, G.; Zheng, W.-J. Photoelectron spectroscopy and density functional calculations of VGe_n^- (n = 3−12) clusters. *J. Phys. Chem. C* **2015**, *119*, 11048−11055.

(534) Jin, Y.; Lu, S.; Hermann, A.; Kuang, X.; Zhang, C.; Lu, C.; Xu, H.; Zheng, W. Probing the structural evolution of ruthenium doped germanium clusters: Photoelectron spectroscopy and density functional theory calculations. *Sci. Rep.* **2016**, *6*, 30116.

(535) Lu, S.-J.; Hu, L.-R.; Xu, X.-L.; Xu, H.-G.; Chen, H.; Zheng, W.-J. Transition from exohedral to endohedral structures of $AuGe_n^-$ (n = 2−12) clusters: Photoelectron spectroscopy and ab initio calculations. *Phys. Chem. Chem. Phys.* **2016**, *18*, 20321−20329.

(536) Deng, X.-j.; Kong, X.-y.; Xu, X.-l.; Xu, H.-g.; Zheng, W.-j. Photoelectron spectroscopy and density functional calculations of $TiGe_n^-$ (n = 7−12) clusters. *Chin. J. Chem. Phys.* **2016**, *29*, 123−128.

(537) Deng, X.-J.; Kong, X.-Y.; Liang, X.; Yang, B.; Xu, H.-G.; Xu, X.-L.; Feng, G.; Zheng, W.-J. Structural and magnetic properties of

$FeGe_n^{-/0}$ (n = 3-12) clusters: Mass-selected anion photoelectron spectroscopy and density functional theory calculations. *J. Chem. Phys.* **2017**, *147*, 234310.

(538) Liang, X.-Q.; Deng, X.-J.; Lu, S.-J.; Huang, X.-M.; Zhao, J.-J.; Xu, H.-G.; Zheng, W.-J.; Zeng, X. C. Probing structural, electronic, and magnetic properties of iron-doped semiconductor clusters $Fe_2Ge_n^{-/0}$ (n = 3−12) via joint photoelectron spectroscopy and density functional study. *J. Phys. Chem. C* **2017**, *121*, 7037−7046.

(539) Liang, X.; Kong, X.; Lu, S.-J.; Huang, Y.; Zhao, J.; Xu, H.-G.; Zheng, W.; Zeng, X. C. Structural evolution and magnetic properties of anionic clusters Cr_2Ge_n (n = 3−14): Photoelectron spectroscopy and density functional theory computation. *J. Phys.: Condens. Matter* **2018**, *30*, 335501.

(540) Goicoechea, J. M.; Sevov, S. C. $[(Pd-Pd)@Ge_{18}]^{4-}$: A palladium dimer inside the largest single-cage deltahedron. *J. Am. Chem. Soc.* **2005**, *127*, 7676−7677.

(541) Zhou, B.; Denning, M. S.; Kays, D. L.; Goicoechea, J. M. Synthesis and isolation of $[Fe@Ge_{10}]^{3-}$: A pentagonal prismatic zintl ion cage encapsulating an interstitial iron atom. *J. Am. Chem. Soc.* **2009**, *131*, 2802−2803.

(542) Wang, J. Q.; Stegmaier, S.; Fässler, T. F. $[Co@Ge_{10}]^{3-}$: An intermetalloid cluster with Archimedean pentagonal prismatic structure. *Angew. Chem., Int. Ed.* **2009**, *48*, 1998−2002.

(543) Espinoza-Quintero, G.; Duckworth, J. C.; Myers, W. K.; McGrady, J. E.; Goicoechea, J. M. Synthesis and characterization of $[Ru@Ge_{12}]^{3-}$: An endohedral 3-connected cluster. *J. Am. Chem. Soc.* **2014**, *136*, 1210−1213.

(544) Li, G.; Zhang, X.; Tang, Z.; Gao, Z. Theoretical studies on the structure of the endohedral $CoGe_{10}^-$ cluster anion. *Chem. Phys. Lett.* **2002**, *359*, 203−212.

(545) Lu, J.; Nagase, S. Metal-doped germanium clusters MGe_ns at the sizes of n = 12 and 10: Divergence of growth patterns from the MSi_n clusters. *Chem. Phys. Lett.* **2003**, *372*, 394−398.

(546) Wang, J.; Han, J.-G. A computational investigation of copper-doped germanium and germanium clusters by the density-functional theory. *J. Chem. Phys.* **2005**, *123*, 244303.

(547) Wang, J.; Han, J.-G. A theoretical study on growth patterns of Ni-doped germanium clusters. *J. Phys. Chem. B* **2006**, *110*, 7820−7827.

(548) Wang, J.; Han, J.-G. Geometries and electronic properties of the tungsten-doped germanium clusters: WGe_n (n = 1−17). *J. Phys. Chem. A* **2006**, *110*, 12670−12677.

(549) Wang, J.; Han, J.-G. The growth behaviors of the Zn-doped different sized germanium clusters: A density functional investigation. *Chem. Phys.* **2007**, *342*, 253−259.

(550) Jing, Q.; Tian, F.-y.; Wang, Y.-x. No quenching of magnetic moment for the Ge_nCo (n = 1−13) clusters: First-principles calculations. *J. Chem. Phys.* **2008**, *128*, 124319.

(551) Wang, J.; Ma, L.; Zhao, J.; Wang, G. Structural growth sequences and electronic properties of manganese-doped germanium clusters: $MnGe_n$ (2−15). *J. Phys.: Condens. Matter* **2008**, *20*, 335223.

(552) Wang, J.; Han, J.-G. Geometries, stabilities, and vibrational properties of bimetallic Mo_2-doped Ge_n (n = 9−15) clusters: A density functional investigation. *J. Phys. Chem. A* **2008**, *112*, 3224−3230.

(553) Zhao, W.-J.; Wang, Y.-X. Geometries, stabilities, and electronic properties of $FeGe_n$ (n = 9−16) clusters: Density-functional theory investigations. *Chem. Phys.* **2008**, *352*, 291−296.

(554) Wang, J.; Chen, X.; Liu, J. H. Investigation of a size-selective single hafnium-encapsulated germanium cage. *J. Phys. Chem. A* **2008**, *112*, 8868−8876.

(555) Zhao, W.-J.; Wang, Y.-X. Geometries, stabilities, and magnetic properties of $MnGe_n$ (n = 2−16) clusters: Density-functional theory investigations. *J. Mol. Struct.: THEOCHEM* **2009**, *901*, 18−23.

(556) King, R. B.; Silaghi-Dumitrescu, I.; Uţă, M. M. Polyhedral structures with three-, four-, and five fold symmetry in metal-centered ten-vertex germanium clusters. *Chem. - Eur. J.* **2008**, *14*, 4542−4550.

(557) King, R.; Silaghi-Dumitrescu, I.; Uta, M. Endohedral nickel, palladium, and platinum atoms in 10-vertex germanium clusters: Competition between bicapped square antiprismatic and pentagonal prismatic structures. *J. Phys. Chem. A* **2009**, *113*, 527−533.

(558) Li, X.-J.; Su, K.-H. Structure, stability and electronic property of the gold-doped germanium clusters: $AuGe_n$ (n = 2−13). *Theor. Chem. Acc.* **2009**, *124*, 345.

(559) Bandyopadhyay, D.; Sen, P. Density functional investigation of structure and stability of Ge_n and Ge_nNi (n = 1−20) clusters: Validity of the electron counting rule. *J. Phys. Chem. A* **2010**, *114*, 1835−1842.

(560) Tai, T. B.; Nguyen, M. T. Lithium atom can be doped at the center of a germanium cage: The stable icosahedral $Ge_{12}Li^-$ cluster and derivatives. *Chem. Phys. Lett.* **2010**, *492*, 290−296.

(561) Bandyopadhyay, D.; Kaur, P.; Sen, P. New insights into applicability of Electron-counting rules in transition metal encapsulating Ge cage clusters. *J. Phys. Chem. A* **2010**, *114*, 12986−12991.

(562) Tang, C.; Liu, M.; Zhu, W.; Deng, K. Probing the geometric, optical, and magnetic properties of 3d transition-metal endohedral $Ge_{12}M$ (M = Sc−Ni) clusters. *Comput. Theor. Chem.* **2011**, *969*, 56−60.

(563) Tai, T. B.; Nguyen, M. T. Enhanced stability by three-dimensional aromaticity of endohedrally doped clusters $X_{10}M^{0/-}$ with X = Ge, Sn, Pb and M = Cu, Ag. *J. Phys. Chem. A* **2011**, *115*, 9993−9999.

(564) Tai, T. B.; Nguyen, H. M. T.; Nguyen, M. T. The group 14 cationic clusters by encapsulation of coinage metals $X_{10}M^+$, with X = Ge, Sn, Pb and M = Cu, Ag, Au: Enhanced stability of 40 valence electron systems. *Chem. Phys. Lett.* **2011**, *502*, 187−193.

(565) King, R.; Silaghi-Dumitrescu, I.; Uta, M. Endohedral beryllium atoms in ten-vertex germanium clusters: Effect of a small interstitial atom on the cluster geometry. *J. Phys. Chem. A* **2011**, *115*, 2847−2852.

(566) Kapila, N.; Jindal, V.; Sharma, H. Structural, electronic and magnetic properties of Mn, Co, Ni in Ge_n for (n = 1−13). *Phys. B* **2011**, *406*, 4612−4619.

(567) Uţă, M.; Cioloboc, D.; King, R. Cobalt-centered ten-vertex germanium clusters: The pentagonal prism as an alternative to polyhedra predicted by the Wade−Mingos rules. *Inorg. Chem.* **2012**, *51*, 3498−3504.

(568) Uţă, M.; Cioloboc, D.; Silaghi-Dumitrescu, I.; King, R. The sphericity of the diverse 10-vertex polyhedra found in bare post-transition metal clusters: Germanium clusters with interstitial magnesium atoms as model systems. *Theor. Chem. Acc.* **2012**, *131*, 1196.

(569) Uţă, M.; King, R. Endohedral beryllium atoms in germanium clusters with eight and fewer vertices: How small can a cluster be and still encapsulate a central atom? *J. Phys. Chem. A* **2012**, *116*, 5227−5234.

(570) Kapila, N.; Garg, I.; Jindal, V.; Sharma, H. First principle investigation into structural growth and magnetic properties in Ge_nCr clusters for n = 1−13. *J. Magn. Magn. Mater.* **2012**, *324*, 2885−2893.

(571) Hung, Y.-M.; Ho, G.-M.; Zhang, Z.-F. Bonding properties and isomeric conversion pathways from exohedral to endohedral $BeGe_8$ clusters. *Comput. Theor. Chem.* **2012**, *999*, 154−161.

(572) Kumar, M.; Bhattacharyya, N.; Bandyopadhyay, D. Architecture, electronic structure and stability of $TM@Ge_n$ (TM = Ti, Zr and Hf; n = 1-20) clusters: A density functional modeling. *J. Mol. Model.* **2012**, *18*, 405−418.

(573) Bandyopadhyay, D. Architectures, electronic structures, and stabilities of Cu-doped Ge_n clusters: Density functional modeling. *J. Mol. Model.* **2012**, *18*, 3887−3902.

(574) Dhaka, K.; Trivedi, R.; Bandyopadhyay, D. Electronic structure and stabilities of Ni-doped germanium nanoclusters: A density functional modeling study. *J. Mol. Model.* **2013**, *19*, 1473−1488.

(575) Li, X.; Su, K.; Yang, X.; Song, L.; Yang, L. Size-selective effects in the geometry and electronic property of bimetallic Au−Ge nanoclusters. *Comput. Theor. Chem.* **2013**, *1010*, 32−37.

(576) Trivedi, R.; Dhaka, K.; Bandyopadhyay, D. Study of electronic properties, stabilities and magnetic quenching of molybdenum-doped

germanium clusters: A density functional investigation. *RSC Adv.* **2014**, *4*, 64825−64834.

(577) Borshch, N.; Pereslavtseva, N.; Kurganskii, S. Spatial and electronic structures of the germanium-tantalum clusters $TaGe_n^-$ (n = 8−17). *Phys. Solid State* **2014**, *56*, 2336−2342.

(578) Borshch, N.; Pereslavtseva, N.; Kurganskii, S. Spatial structure and electron energy spectra of $ScGe_n^-$ (n = 6−16) clusters. *Russ. J. Phys. Chem. B* **2015**, *9*, 9−18.

(579) Dhaka, K.; Bandyopadhyay, D. Study of the electronic structure, stability and magnetic quenching of $CrGe_n$ (n= 1−17) clusters: A density functional investigation. *RSC Adv.* **2015**, *5*, 83004−83012.

(580) Borshch, N.; Kurganskii, S. Spatial structure and electron energy spectrum of $HfGe_n^-$ (n = 6−20) clusters. *Inorg. Mater.* **2015**, *51*, 870−876.

(581) Uţă, M.; King, R. Manganese-centered ten-vertex germanium clusters: The strong field Ge_{10} ligand encapsulating a transition metal. *J. Coord. Chem.* **2015**, *68*, 3485−3497.

(582) Qin, W.; Lu, W.-C.; Xia, L.-H.; Zhao, L.-Z.; Zang, Q.-J.; Wang, C.; Ho, K. Structures and stability of metal-doped Ge_nM (n = 9, 10) clusters. *AIP Adv.* **2015**, *5*, 067159.

(583) Jaiswal, S.; Kumar, V. Growth behavior and electronic structure of neutral and anion $ZrGe_n$ (n = 1−21) clusters. *Comput. Theor. Chem.* **2016**, *1075*, 87−97.

(584) Siouani, C.; Mahtout, S.; Safer, S.; Rabilloud, F. Structure, stability, and electronic and magnetic properties of VGe_n (n = 1−19) clusters. *J. Phys. Chem. A* **2017**, *121*, 3540−3554.

(585) Borshch, N.; Kurganskii, S. Anionic germanium−niobium clusters: atomic structure, mechanisms of cluster formation, and electronic spectra. *Russ. J. Phys. Chem. A* **2018**, *92*, 1720−1726.

(586) Borshch, N.; Kurganskii, S. Atomic structure and electronic properties of anionic germanium−zirconium clusters. *Inorg. Mater.* **2018**, *54*, 1−7.

(587) Mahtout, S.; Siouani, C.; Rabilloud, F. Growth behavior and electronic structure of noble metal-doped germanium clusters. *J. Phys. Chem. A* **2018**, *122*, 662−677.

(588) Triedi, R. K.; Bandyopadhyay, D. Insights of the role of shell closing model and NICS in the stability of $NbGe_n$ (n = 7−18) clusters: A first-principles investigation. *J. Mater. Sci.* **2019**, *54*, 515−528.

(589) Jin, Y.; Tian, Y.; Kuang, X.; Lu, C.; Cabellos, J. L.; Mondal, S.; Merino, G. Structural and electronic properties of ruthenium-doped germanium clusters. *J. Phys. Chem. C* **2016**, *120*, 8399−8404.

(590) Tan, Z.; Zhou, T.; Yang, Y. The role of TM's (M's) d valence electrons in $TM@X_{12}$ and $M@X_{12}$ clusters. *AIP Adv.* **2016**, *6*, 125123.

(591) Middaugh, R.; Muetterties, E. *Boron Hydride Chemistry*; Academic Press: New York, NY, 1975.

(592) Liu, C.; Li, L. J.; Popov, I. A.; Wilson, R. J.; Xu, C. Q.; Li, J.; Boldyrev, A. I.; Sun, Z. M. Symmetry reduction upon size mismatch: The non-Icosahedral intermetalloid cluster $[Co@Ge_{12}]^{3-}$. *Chin. J. Chem.* **2018**, *36*, 1165−1168.

(593) Zhou, S.; Yang, X.; Shen, Y.; King, R. B.; Zhao, J. Dual transition metal doped germanium clusters for catalysis of CO oxidation. *J. Alloys Compd.* **2019**, *806*, 698−704.

(594) Meloni, G.; Schmude, R., Jr; Kingcade, J., Jr; Gingerich, K. A. Thermodynamic stability of Sn_4, Sn_5, Sn_6, and Sn_7 clusters by Knudsen cell mass spectrometry. *J. Chem. Phys.* **2000**, *113*, 1852−1856.

(595) Schäfer, S.; Assadollahzadeh, B.; Mehring, M.; Schwerdtfeger, P.; Schäfer, R. Structure and electric properties of Sn_N clusters (N = 6−20) from combined electric deflection experiments and quantum theoretical studies. *J. Phys. Chem. A* **2008**, *112*, 12312−12319.

(596) Oger, E.; Kelting, R.; Weis, P.; Lechtken, A.; Schooss, D.; Crawford, N. R.; Ahlrichs, R.; Kappes, M. M. Small tin cluster anions: Transition from quasispherical to prolate structures. *J. Chem. Phys.* **2009**, *130*, 124305.

(597) Drebov, N.; Oger, E.; Rapps, T.; Kelting, R.; Schooss, D.; Weis, P.; Kappes, M. M.; Ahlrichs, R. Structures of tin cluster cations Sn_3^+ to Sn_{15}^+. *J. Chem. Phys.* **2010**, *133*, 224302.

(598) Lechtken, A.; Drebov, N.; Ahlrichs, R.; Kappes, M. M.; Schooss, D. Communications: Tin cluster anions (Sn_n^-, n = 18, 20, 23, and 25) comprise dimers of stable subunits. *J. Chem. Phys.* **2010**, *132*, 211102.

(599) Wiesel, A.; Drebov, N.; Rapps, T.; Ahlrichs, R.; Schwarz, U.; Kelting, R.; Weis, P.; Kappes, M. M.; Schooss, D. Structures of medium sized tin cluster anions. *Phys. Chem. Chem. Phys.* **2012**, *14*, 234−245.

(600) Cui, L.-F.; Wang, L.-M.; Wang, L.-S. Evolution of the electronic properties of Sn_n^- clusters (n = 4−45) and the semiconductor-to-metal transition. *J. Chem. Phys.* **2007**, *126*, 064505.

(601) Majumder, C.; Kumar, V.; Mizuseki, H.; Kawazoe, Y. Atomic and electronic structures of neutral and cation Sn_n (n = 2−20) clusters: A comparative theoretical study with different exchange-correlation functionals. *Phys. Rev. B: Condens. Matter Mater. Phys.* **2005**, *71*, 035401.

(602) Wu, D.; Du, Q.; Wu, X.; Shi, R.; Sai, L.; Liang, X.; Huang, X.; Zhao, J. Evolution of atomic structures of Sn_N, and Sn_N^-, and Sn_NCl^- clusters (N = 4-20): Insight from ab initio calculations. *J. Chem. Phys.* **2019**, *150*, 174304.

(603) Cui, L.-F.; Huang, X.; Wang, L.-M.; Zubarev, D. Y.; Boldyrev, A. I.; Li, J.; Wang, L.-S. *J. Am. Chem. Soc.* **2006**, *128*, 8390−8391.

(604) Chen, D.-L.; Tian, W. Q.; Feng, J.-K.; Sun, C.-C. Evidence for d-orbital aromaticity in Sn- and Pb-based clusters: Is Sn_{12}^{2-} aromatic? *J. Phys. Chem. A* **2007**, *111*, 8277−8280.

(605) Breaux, G. A.; Hillman, D. A.; Neal, C. M.; Jarrold, M. F. Stable copper-tin cluster compositions from high-temperature annealing. *J. Phys. Chem. A* **2005**, *109*, 8755−8759.

(606) Cui, L. F.; Huang, X.; Wang, L. M.; Li, J.; Wang, L. S. Endohedral stannaspherenes $M@Sn_{12}^-$: A rich class of stable molecular cage clusters. *Angew. Chem., Int. Ed.* **2007**, *46*, 742−745.

(607) Rohrmann, U.; Schäfer, S.; Schäfer, R. Size- and temperature-dependent magnetic response of molecular cage clusters: Manganese-doped tin clusters. *J. Phys. Chem. A* **2009**, *113*, 12115−12121.

(608) Rohrmann, U.; Schäfer, R. Stern-Gerlach experiments on $Fe@Sn_{12}$: Magnetic response of a Jahn−Teller distorted endohedrally doped molecular cage cluster. *J. Phys. Chem. C* **2015**, *119*, 10958−10961.

(609) Fuchs, T. M.; Schäfer, R. Double Stern-Gerlach experiments on $Mn@Sn_{12}$: Refocusing of a paramagnetic superatom. *Phys. Rev. A: At., Mol., Opt. Phys.* **2018**, *98*, 063411.

(610) Fuchs, T. M.; Schäfer, R. Effect of vibrational excitation and spin-rotation coupling on Stern-Gerlach experiments: A detailed case study on $GdSn_{15}$ as an asymmetric rotor. *Phys. Rev. A: At., Mol., Opt. Phys.* **2019**, *100*, 012512.

(611) Gleditzsch, M.; Fuchs, T. M.; Schäfer, R. N-doping at the sub-nanoscale: Dielectric and magnetic eesponse of neutral phosphorus-doped tin clusters. *J. Phys. Chem. A* **2019**, *123*, 1434−1444.

(612) Gleditzsch, M.; Pašteka, L. F.; Götz, D. A.; Shayeghi, A.; Johnston, R. L.; Schäfer, R. Gold doping of tin clusters: exo-vs. endohedral complexes. *Nanoscale* **2019**, *11*, 12878−12888.

(613) Gleditzsch, M.; Jäger, M.; Pašteka, L. F.; Shayeghi, A.; Schäfer, R. Doping effects on the geometric and electronic structure of tin clusters. *Phys. Chem. Chem. Phys.* **2019**, *21*, 24478−24488.

(614) Liu, C.; Jin, X.; Li, L.; Xu, J.; McGrady, J.; Sun, Z. Synthesis and structure of a family of rhodium polystannide clusters $[Rh@Sn_{10}]^{3-}$, $[Rh@Sn_{12}]^{3-}$, $[Rh_2@Sn_{17}]^{6-}$ and the first triply-fused stannide, $[Rh_3@Sn_{24}]^{5-}$. *Chem. Sci.* **2019**, *10*, 4394−4401.

(615) Tai, T. B.; Tam, N. M.; Nguyen, M. T. Evolution of structures and stabilities of zinc-doped tin clusters Sn_nZn, n = 1−12. Three-dimensional aromaticity of the magic clusters $Sn_{10}Zn$ and $Sn_{12}Zn$. *Chem. Phys.* **2011**, *388*, 1−8.

(616) Bai, Y.-J.; Deng, K.-M.; Shaoa, J.-L.; Xua, N. Structures, stabilities and electronic properties of MSn_{10} (M = Li, Be, B, Ca). *J. At. Mol. Sci.* **2018**, *5*, 217−230.

(617) Zdetsis, A. D. Rationalizing and functionalizing stannaspherene: Very stable stannaspherene "alloys". *J. Chem. Phys.* **2009**, *131*, 224310.

(618) Matxain, J. M.; Piris, M.; Formoso, E.; Mercero, J. M.; Lopez, X.; Ugalde, J. M. Endohedral stannaspherenes Mn@Sn$_{12}$ and its dimer: Ferromagnetic or antiferromagnetic? *ChemPhysChem* **2007**, *8*, 2096−2099.

(619) Kandalam, A. K.; Chen, G.; Jena, P. Unique magnetic coupling between Mn doped stannaspherenes Mn@Sn$_{12}$. *Appl. Phys. Lett.* **2008**, *92*, 143109.

(620) Chen, X.; Deng, K.; Liu, Y.; Tang, C.; Yuan, Y.; Tan, W.; Wang, X. The geometric, optical, and magnetic properties of the endohedral stannaspherenes M@Sn$_{12}$ (M = Ti, V, Cr, Mn, Fe, Co, Ni). *J. Chem. Phys.* **2008**, *129*, 094301.

(621) Dognon, J.-P.; Clavaguéra, C.; Pyykkö, P. Chemical properties of the predicted 32-electron systems Pu@Sn$_{12}$ and Pu@Pb$_{12}$. *C. R. Chim.* **2010**, *13*, 884−888.

(622) Joshi, M.; Chandrasekar, A.; Ghanty, T. K. Theoretical investigation of M@Pb$_{12}^{2-}$ and M@Sn$_{12}^{2-}$ zintl clusters (M = Lr^{n+}, Lu^{n+}, La^{3+}, Ac^{3+} and n = 0, 1, 2, 3). *Phys. Chem. Chem. Phys.* **2018**, *20*, 15253−15272.

(623) Wang, J. Q.; Stegmaier, S.; Wahl, B.; Faessler, T. F. Step-by-step synthesis of the endohedral stannaspherene [Ir@Sn$_{12}$]$^{3-}$ via the capped cluster anion [Sn$_9$Ir(cod)]$^{3-}$. *Chem. - Eur. J.* **2010**, *16*, 1793−1798.

(624) Shvartsburg, A. A.; Jarrold, M. F. Transition from covalent to metallic behavior in group-14 clusters. *Chem. Phys. Lett.* **2000**, *317*, 615−618.

(625) Senz, V.; Fischer, T.; Oelßner, P.; Tiggesbäumker, J.; Stanzel, J.; Bostedt, C.; Thomas, H.; Schöffler, M.; Foucar, L.; Martins, M. Core-hole screening as a probe for a metal-to-nonmetal transition in lead clusters. *Phys. Rev. Lett.* **2009**, *102*, 138303.

(626) Götz, D.; Shayeghi, A.; Johnston, R.; Schwerdtfeger, P.; Schäfer, R. Influence of spin-orbit effects on structures and dielectric properties of neutral lead clusters. *J. Chem. Phys.* **2014**, *140*, 164313.

(627) Götz, D. A.; Shayeghi, A.; Johnston, R. L.; Schwerdtfeger, P.; Schäfer, R. Structural evolution and metallicity of lead clusters. *Nanoscale* **2016**, *8*, 11153−11160.

(628) Wang, B.; Zhao, J.; Chen, X.; Shi, D.; Wang, G. Atomic structures and covalent-to-metallic transition of lead clusters Pb$_n$ (n = 2−22). *Phys. Rev. A: At., Mol., Opt. Phys.* **2005**, *71*, 033201.

(629) Cui, L.-F.; Huang, X.; Wang, L.-M.; Li, J.; Wang, L.-S. *J. Phys. Chem. A* **2006**, *110*, 10169−10172.

(630) Zhang, X.; Li, G.; Xing, X.; Zhao, X.; Tang, Z.; Gao, Z. Formation of binary alloy cluster ions from group-14 elements and cobalt and comparison with solid-state alloys. *Rapid Commun. Mass Spectrom.* **2001**, *15*, 2399−2403.

(631) Xing, X.; Tian, Z.; Liu, H.; Tang, Z. Magic bimetallic cluster anions of M/Pb (M = Au, Ag and Cu) observed and analyzed by laser ablation and time-of-flight mass spectrometry. *Rapid Commun. Mass Spectrom.* **2003**, *17*, 1411−1415.

(632) Schäfer, S.; Schäfer, R. New molecular cage clusters of Pb by encapsulation of Mg. *ChemPhysChem* **2008**, *9*, 1925−1929.

(633) Grubisic, A.; Wang, H.; Li, X.; Ko, Y.-J.; Kocak, F. S.; Pederson, M. R.; Bowen, K. H.; Eichhorn, B. W. Photoelectron spectroscopic and computational studies of the Pt@Pd$_{10}^{-}$ and Pt@Pd$_{12}^{1-/2-}$ anions. *Proc. Natl. Acad. Sci. U. S. A.* **2011**, *108*, 14757−14762.

(634) Bhattacharyya, S.; Nguyen, T. T.; De Haeck, J.; Hansen, K.; Lievens, P.; Janssens, E. Mass-selected photodissociation studies of AlPb$_n^+$ clusters (n = 7−16): Evidence for the extraordinary stability of AlPb$_{10}^+$ and AlPb$_{12}^+$. *Phys. Rev. B: Condens. Matter Mater. Phys.* **2013**, *87*, 054103.

(635) Xie, H.; Qin, Z.; Wu, X.; Tang, Z.; Jiang, L. Photoelectron velocity-map imaging signature of structural evolution of silver-doped lead Zintl anions. *J. Chem. Phys.* **2012**, *137*, 064318.

(636) Rajesh, C.; Majumder, C. Structure and electronic properties of Pb$_n$M (M = C, Al, In, Mg, Sr, Ba, and Pb; n = 8, 10, 12, and 14) clusters: Theoretical investigations based on first principles calculations. *J. Chem. Phys.* **2008**, *128*, 024308.

(637) Chen, D.-L.; Tian, W. Q.; Sun, C.-C. First-principles studies of AlPb$_n$ and AlPb$_n^+$ clusters (n = 1−12): Search for Al-doped clusters with large stabilities. *Phys. Rev. A: At., Mol., Opt. Phys.* **2007**, *75*, 013201.

(638) Chen, X.; Deng, K.; Xiao, C.; Chen, J.; Ellis, D. E. Geometric and magnetic properties of the neutral MPb$_{10}$ and [MPb$_{10}$]^2 clusters (M = Fe, Co, Ni). *Comput. Theor. Chem.* **2011**, *971*, 73−76.

(639) Spiekermann, A.; Hoffmann, S. D.; Fässler, T. F. The Zintl ion [Pb$_{10}$]$^{2-}$: A rare example of a homoatomic closo cluster. *Angew. Chem., Int. Ed.* **2006**, *45*, 3459−3462.

(640) Gao, Y.; Bulusu, S.; Zeng, X. C. A global search of highly stable gold-covered bimetallic clusters M@Au$_n$ (n = 8-17) Endohedral gold clusters. *ChemPhysChem* **2006**, *7*, 2275−2278.

(641) Rajesh, C.; Majumder, C. Energy level reordering and stability of MPb$_{12}$ clusters: An interplay between geometry and electronic structure. *Chem. Phys. Lett.* **2006**, *430*, 101−107.

(642) Chen, X.; Deng, K.; Liu, Y.; Tang, C.; Yuan, Y.; Hu, F.; Wu, H.; Huang, D.; Tan, W.; Wang, X. The geometric and magnetic properties of the endohedral plumbasphere M@Pb$_{12}$ clusters (M = Sc, Ti, V, Cr, Mn, Fe, Co, Ni). *Chem. Phys. Lett.* **2008**, *462*, 275−279.

(643) Le Guennic, B.; Autschbach, J. [Pt@Pb$_{12}$]$^{2-}$—A challenging system for relativistic density functional theory calculations of ^{195}Pt and ^{207}Pb NMR parameters. *Can. J. Chem.* **2011**, *89*, 814−821.

(644) Chen, D.-L.; Tian, W. Q.; Lu, W.-C.; Sun, C.-C. Special stability of cationic MPb$_{12}^+$ clusters and superalkali character of neutral MPb$_{12}$ clusters (M = B, Al, Ga, In, and Tl). *J. Chem. Phys.* **2006**, *124*, 154313.

(645) Witzel, B. J.; Klein, W.; Dums, J. V.; Boyko, M.; Fässler, T. F. Metallocages for metal anions: Highly charged [Co@Ge$_9$]$^{5-}$ and [Ru@Sn$_9$]$^{6-}$ clusters featuring spherically encapsulated Co^{1-} and Ru^{2-} anions. *Angew. Chem., Int. Ed.* **2019**, *58*, 12908−12913.

(646) Yue, C. Y.; Wang, M. F.; Yuan, Z. D.; Zhou, F. X.; Zhang, H. P.; Lei, X. W. K$_{13}$CoSn$_{17-x}$ (x = 0.1): A new ternary phase containing cobalt centered [Sn$_9$] cluster synthesized via high-temperature reaction. *Z. Anorg. Allg. Chem.* **2013**, *639*, 911−917.

(647) Rios, D.; Gillett-Kunnath, M. M.; Taylor, J. D.; Oliver, A. G.; Sevov, S. C. Addition of a thallium vertex to empty and centered nine-atom deltahedral zintl ions of germanium and tin. *Inorg. Chem.* **2011**, *50*, 2373−2377.

(648) Gillett-Kunnath, M. M.; Paik, J. I.; Jensen, S. M.; Taylor, J. D.; Sevov, S. C. Metal-centered deltahedral zintl ions: Synthesis of [Ni@Sn$_9$]$^{4-}$ by direct extraction from intermetallic precursors and of the vertex-fused dimer [{Ni@Sn$_8$(μ-Ge)$_{1/2}$}$_2$]$^{4-}$. *Inorg. Chem.* **2011**, *50*, 11695−11701.

(649) Benda, C. B.; Waibel, M.; Köchner, T.; Fässler, T. F. Reactivity of liquid ammonia solutions of the zintl phase K$_{12}$Sn$_{17}$ towards mesitylcopper (I) and phosphinegold (I) chloride. *Chem. - Eur. J.* **2014**, *20*, 16738−16746.

(650) Esenturk, E. N.; Fettinger, J.; Eichhorn, B. The closo-Pb$_{10}^{2-}$ Zintl ion in the [Ni@Pb$_{10}$]$^{2-}$ cluster. *Chem. Commun.* **2005**, 247−249.

(651) Esenturk, E. N.; Fettinger, J.; Eichhorn, B. The Pb$_{12}^{2-}$ and Pb$_{10}^{2-}$ zintl ions and the M@Pb$_{12}^{2-}$ and M@Pb$_{10}^{2-}$ cluster series where M = Ni, Pd, Pt. *J. Am. Chem. Soc.* **2006**, *128*, 9178−9186.

(652) Krämer, T.; Duckworth, J. C.; Ingram, M. D.; Zhou, B.; McGrady, J. E.; Goicoechea, J. M. Structural trends in ten-vertex endohedral clusters, M@E$_{10}$ and the synthesis of a new member of the family, [Fe@Sn$_{10}$]$^{3-}$. *Dalton Trans.* **2013**, *42*, 12120−12129.

(653) Esenturk, E. N.; Fettinger, J.; Lam, Y. F.; Eichhorn, B. [Pt@Pb$_{12}$]$^{2-}$. *Angew. Chem., Int. Ed.* **2004**, *43*, 2132−2134.

(654) Wang, Y.; Wang, L.-L.; Ruan, H.-P.; Luo, B.-L.; Sang, R.-L.; Xu, L. Synthesis and characterization of the endohedral plumbasphere [Rh@Pb$_{12}$]$^{3-}$. *Chin. J. Struct. Chem.* **2015**, *34*, 1253−1258.

(655) Zhou, B.; Krämer, T.; Thompson, A. L.; McGrady, J. E.; Goicoechea, J. M. A highly distorted open-shell endohedral zintl cluster: [Mn@Pb$_{12}$]$^{3-}$. *Inorg. Chem.* **2011**, *50*, 8028−8037.

(656) Li, L.-J.; Pan, F.-X.; Li, F.-Y.; Chen, Z.-F.; Sun, Z.-M. Synthesis, characterization and electronic properties of an endohedral plumbasphere [Au@Pb$_{12}$]$^{3-}$. *Inorg. Chem. Front.* **2017**, *4*, 1393−1396.

(657) Kesanli, B.; Halsig, J. E.; Zavalij, P.; Fettinger, J. C.; Lam, Y.-F.; Eichhorn, B. W. Cluster growth and fragmentation in the highly fluxional platinum derivatives of Sn_{94}^{-}: Synthesis, characterization, and solution dynamics of $Pt_2@Sn_{17}^{4-}$ and $Pt@Sn_9H^{3-}$. *J. Am. Chem. Soc.* **2007**, *129*, 4567−4574.

(658) Jin, X.; McGrady, J. E. In *Adv. Inorg. Chem.*; Elsevier: Amsterdam, 2019; Vol. 73, pp 265−304.

(659) Valden, M.; Lai, X.; Goodman, D. W. Onset of catalytic activity of gold clusters on titania with the appearance of nonmetallic properties. *Science* **1998**, *281*, 1647−1650.

(660) Pyykkö, P. Theoretical chemistry of gold. *Angew. Chem., Int. Ed.* **2004**, *43*, 4412−4456.

(661) Pyykkö, P. Theoretical chemistry of gold. II. *Inorg. Chim. Acta* **2005**, *358*, 4113−4130.

(662) Schooss, D.; Weis, P.; Hampe, O.; Kappes, M. M. Determining the size-dependent structure of ligand-free gold-cluster ions. *Philos. Trans. R. Soc., A* **2010**, *368*, 1211−1243.

(663) Li, J.; Li, X.; Zhai, H. J.; Wang, L. S. Au_{20}: A tetrahedral cluster. *Science* **2003**, *299*, 864−867.

(664) Bulusu, S.; Li, X.; Wang, L.-S.; Zeng, X. C. Evidence of hollow golden cages. *Proc. Natl. Acad. Sci. U. S. A.* **2006**, *103*, 8326−8330.

(665) Lechtken, A.; Neiss, C.; Kappes, M. M.; Schooss, D. Structure determination of gold clusters by trapped ion electron diffraction: Au_{14}^{-}−Au_{19}^{-}. *Phys. Chem. Chem. Phys.* **2009**, *11*, 4344−4350.

(666) Johansson, M. P.; Sundholm, D.; Vaara, J. Au_{32}: A 24-carat golden fullerene. *Angew. Chem., Int. Ed.* **2004**, *43*, 2678−2681.

(667) Gu, X.; Ji, M.; Wei, S. H.; Gong, X. G. Au_N clusters (N = 32,33,34,35): Cagelike structures of pure metal atoms. *Phys. Rev. B: Condens. Matter Mater. Phys.* **2004**, *70*, 205401.

(668) Mingos, D. M. P. Molecular-orbital calculations on cluster compounds of gold. *J. Chem. Soc., Dalton Trans.* **1976**, 1163−1169.

(669) Sato, T.; Lijnen, E.; Ceulemans, A. Jahn-Teller instability of icosahedral $[W@Au_{12}]^{-}$. *J. Chem. Theory Comput.* **2014**, *10*, 613−622.

(670) Zhai, H. J.; Li, J.; Wang, L. S. Icosahedral gold cage clusters: $M@Au_{12}^{-}$ (M = V, Nb, and Ta. *J. Chem. Phys.* **2004**, *121*, 8369−8374.

(671) Autschbach, J.; Hess, B. A.; Johansson, M. P.; Neugebauer, J.; Patzschke, M.; Pyykkö, P.; Reiher, M.; Sundholm, D. Properties of WAu_{12}. *Phys. Chem. Chem. Phys.* **2004**, *6*, 11−22.

(672) Manninen, K.; Pyykkö, P.; Hakkinen, H. A small spherical liquid: A DFT molecular dynamics study of WAu_{12}. *Phys. Chem. Chem. Phys.* **2005**, *7*, 2208−2211.

(673) Johansson, M. P.; Pyykkö, P. $WAu_{12}(CO)_{12}$? *Chem. Commun.* **2010**, *46*, 3762−3764.

(674) Wang, S. Y.; Yu, J. Z.; Mizuseki, H.; Sun, Q.; Wang, C. Y.; Kawazoe, Y. Energetics and local spin magnetic moment of single 3d, 4d impurities encapsulated in an icosahedral Au_{12} cage. *Phys. Rev. B: Condens. Matter Mater. Phys.* **2004**, *70*, 165413.

(675) Long, J.; Qiu, Y.-X.; Chen, X.-Y.; Wang, S.-G. Stable geometric and electronic structures of gold-coated nanoparticles $M@Au_{12}$ (M = 5d transition metals, from Hf to Hg): I_h or $O_{h?}$ *J. Phys. Chem. C* **2008**, *112*, 12646−12652.

(676) Nijamudheen, A.; Jose, D.; Datta, A. Metal encapsulation mediated planar to three dimensional structural transformation in Au-clusters: The venus flytrap effect. *Comput. Theor. Chem.* **2011**, *966*, 133−136.

(677) Zhang, C.-H.; Cui, H.; Shen, J. The 13-atom encapsulated gold cage clusters. *Chin. Phys. B* **2012**, *21*, 103102.

(678) Raggi, G.; Soto, J. R. Relativistic DFT calculations of magnetic moments of pristine and thiolated $Mn@Au_x$ (x = 6, 12). *Phys. Chem. Chem. Phys.* **2014**, *16*, 21506−21512.

(679) Yarzhemsky, V. G.; Izotov, A. D.; Kazaryan, M. A.; D'Yakov, Y. A. Structure of endohedral clusters $Au_{12}M$. *Dokl. Chem.* **2015**, *462*, 115−117.

(680) Cao, G.-J.; Schwarz, W. H. E.; Li, J. An 18-electron system containing a superheavy element: Theoretical studies of $Sg@Au_{12}$. *Inorg. Chem.* **2015**, *54*, 3695−3701.

(681) Muñoz-Castro, A. Golden endohedral main-group clusters, $[E@Au_{12}]^{q-}$: Theoretical insights into the 20-e principle. *J. Phys. Chem. Lett.* **2013**, *4*, 3363−3366.

(682) Muñoz-Castro, A. Doping the cage. $Re@Au_{11}Pt$ and $Ta@Au_{11}Hg$, as novel 18-ve trimetallic superatoms displaying a doped icosahedral golden cage. *Phys. Chem. Chem. Phys.* **2017**, *19*, 2459−2465.

(683) Stener, M.; Nardelli, A.; Fronzoni, G. Spin-orbit effects in the photoabsorption of WAu_{12} and $MoAu_{12}$: A relativistic time dependent density functional study. *J. Chem. Phys.* **2008**, *128*, 134307.

(684) Stener, M.; Nardelli, A.; Fronzoni, G. Theoretical study on the photoabsorption of MAu_{12}^{-} (M = V, Nb and Ta). *Chem. Phys. Lett.* **2008**, *462*, 358−364.

(685) Ju, W.; Yang, Z. Influence of spin-orbit coupling on electronic structures of $TM@Au_{12}$ (TM = 3d, 4d, and 5d atoms). *Phys. Lett. A* **2012**, *376*, 1300−1305.

(686) Muñoz-Castro, A.; Arratia-Perez, R. Spin-orbit effects on a gold-based superatom: A relativistic Jellium model. *Phys. Chem. Chem. Phys.* **2012**, *14*, 1408−1411.

(687) Hossain, D.; Pittman, C. U., Jr.; Gwaltney, S. R. Structures and stabilities of the metal doped gold nano-clusters: $M@Au_{10}$ (M = W, Mo, Ru, Co). *J. Inorg. Organomet. Polym. Mater.* **2014**, *24*, 241−249.

(688) Nhat, P. V.; Nguyen, M. T. Trends in structural, electronic and energetic properties of bimetallic vanadium-gold clusters Au_nV with n = 1-14. *Phys. Chem. Chem. Phys.* **2011**, *13*, 16254−16264.

(689) Blades, W. H.; Reber, A. C.; Khanna, S. N.; Lopez-Sosa, L.; Calaminici, P.; Koster, A. M. Evolution of the spin magnetic moments and atomic valence of vanadium in VCu_x^{+}, VAg_x^{+}, and VAu_x^{+} clusters (x = 3-14). *J. Phys. Chem. A* **2017**, *121*, 2990−2999.

(690) Du, Q.; Wu, X.; Wang, P.; Wu, D.; Sai, L.; King, R. B.; Park, S. J.; Zhao, J. Structure evolution of transition metal-doped gold clusters $M@Au_{12}$ (M = 3d−5d): Across the periodic table. *J. Phys. Chem. C* **2020**, *124*, 7449−7457.

(691) Carey, D. M.; Muñoz-Castro, A. $Au_{11}Re$: A hollow or endohedral binary cluster? *Chem. Phys. Lett.* **2018**, *701*, 30−33.

(692) Gao, Y.; Bulusu, S.; Zeng, X. C. Gold-caged metal clusters with large HOMO-LUMO gap and high electron affinty. *J. Am. Chem. Soc.* **2005**, *127*, 15680−15681.

(693) Xie, J. R. H.; Cheung, C. F.; Zhao, J. J. Tuning optical absorption and emission of sub-nanometer gold-caged metal systems $M@Au_{14}$ by substitutional doping. *J. Comput. Theor. Nanosci.* **2006**, *3*, 312−314.

(694) Toprek, D.; Koteski, V. Ab initio calculations of the structure, energetics and stability of Au_nTi (n = 1-32) clusters. *Comput. Theor. Chem.* **2016**, *1081*, 9−17.

(695) Chen, M.-X.; Yan, X. A new magic titanium-doped gold cluster and orientation dependent cluster-cluster interaction. *J. Chem. Phys.* **2008**, *128*, 174305.

(696) Zhang, M.; Zhang, H.; Zhao, L.; Li, Y.; Luo, Y. Low-energy isomer identification, structural evolution, and magnetic properties in manganese-doped gold clusters $MnAu_n$ (n = 1-16). *J. Phys. Chem. A* **2012**, *116*, 1493−1502.

(697) Gao, Y.; Dai, X.; Kang, S.-g.; Jimenez-Cruz, C. A.; Xin, M.; Meng, Y.; Han, J.; Wang, Z.; Zhou, R. Structural and electronic properties of uranium-encapsulated Au_{14} cage. *Sci. Rep.* **2015**, *4*, 5862.

(698) Gao, Y.; Wang, B.; Lei, Y.; Teo, B. K.; Wang, Z. Actinide-embedded gold superatom models: Electronic structure, spectroscopic properties, and applications in surface-enhanced Raman scattering. *Nano Res.* **2016**, *9*, 622−632.

(699) Gao, Y.; Liu, X.; Wang, Z. $Ce@Au_{14}$: A bimetallic superatom cluster with 18-electron rule. *J. Electron. Mater.* **2017**, *46*, 3899−3903.

(700) Gao, Y.; Jiang, W.; Xu, D.; Wang, Z. Localization-vs-delocalization of 5f orbitals in superatom systems. *Adv. Theory Simul.* **2018**, *1*, 1700038.

(701) Yong, Y.; Li, X.; Zhou, Q.; Su, X.; Li, T.; Cui, H.; Lv, S. Adsorption of gas molecules on $Gd@Au_n$ (n = 14, 15) clusters and their implication for molecule sensors. *RSC Adv.* **2016**, *6*, 26809−26816.

(702) Yadav, B. D.; Kumar, V. $Gd@Au_{15}$: A magic magnetic gold cluster for cancer therapy and bioimaging. *Appl. Phys. Lett.* **2010**, *97*, 133701.

(703) Shinde, P. P.; Yadav, B. D.; Kumar, V. Evolution of atomic and electronic structure of magnetic Gd-doped gold clusters. *J. Mater. Sci.* **2012**, *47*, 7642−7652.

(704) Wang, L.-M.; Bulusu, S.; Zhai, H.-J.; Zeng, X.-C.; Wang, L.-S. Doping golden buckyballs: Cu@Au$_{16}^-$ and Cu@Au$_{17}^-$ cluster anions. *Angew. Chem., Int. Ed.* **2007**, *46*, 2915−2918.

(705) Wang, L.-M.; Bulusu, S.; Huang, W.; Pal, R.; Wang, L.-S.; Zeng, X. C. Doping the golden cage Au$_{16}^-$ with Si, Ge, and Sn. *J. Am. Chem. Soc.* **2007**, *129*, 15136−15137.

(706) Wang, L.-M.; Pal, R.; Huang, W.; Zeng, X. C.; Wang, L.-S. Tuning the electronic properties of the golden buckyball by endohedral doping: M@Au$_{16}^-$ (M = Ag, Zn, In). *J. Chem. Phys.* **2009**, *130*, 051101.

(707) Wang, L.-M.; Bai, J.; Lechtken, A.; Huang, W.; Schooss, D.; Kappes, M. M.; Zeng, X. C.; Wang, L.-S. Magnetic doping of the golden cage cluster M@Au$_{16}^-$ (M = Fe, Co, Ni). *Phys. Rev. B: Condens. Matter Mater. Phys.* **2009**, *79*, 033413.

(708) Sun, Q.; Wang, Q.; Chen, G.; Jena, P. Structure of SiAu$_{16}$: Can a silicon atom be stabilized in a gold cage? *J. Chem. Phys.* **2007**, *127*, 214706.

(709) Walter, M.; Hakkinen, H. A hollow tetrahedral cage of hexadecagold dianion provides a robust backbone for a tuneable sub-nanometer oxidation and reduction agent via endohedral doping. *Phys. Chem. Chem. Phys.* **2006**, *8*, 5407−5411.

(710) Kaydashev, V. E.; Janssens, E.; Lievens, P. Optical absorption spectra of palladium doped gold cluster cations. *J. Chem. Phys.* **2015**, *142*, 034310.

(711) Neukermans, S.; Janssens, E.; Tanaka, H.; Silverans, R. E.; Lievens, P. Element- and size-dependent electron delocalization in Au$_N$X$^+$ clusters (X = Sc, Ti, V, Cr, Mn, Fe, Co, Ni). *Phys. Rev. Lett.* **2003**, *90*, 033401.

(712) Bouwen, W.; Vanhoutte, F.; Despa, F.; Bouckaert, S.; Neukermans, S.; Kuhn, L. T.; Weidele, H.; Lievens, P.; Silverans, R. E. Stability effects of Au$_n$X$_m^+$ (X = Cu, Al, Y, In) clusters. *Chem. Phys. Lett.* **1999**, *314*, 227−233.

(713) Fa, W.; Dong, J. Structures of MAu$_{16}^-$ (M = Ag, Li, Na, and K): How far is the endohedral doping? *J. Chem. Phys.* **2008**, *128*, 144307.

(714) Fa, W.; Yang, A. Detecting the lowest-energy structures of CAu$_{16}^q$ (q = -1, 0). *Phys. Lett. A* **2008**, *372*, 6392−6395.

(715) Wang, H.-Q.; Li, H.-F.; Zheng, L.-X. Doping golden cage clusters M@Au$_{16}^q$ (M = Cr, Mn; q = 0, -1) with adjustable magnetic properties. *J. Magn. Magn. Mater.* **2013**, *344*, 79−84.

(716) Tang, C.; Zhu, W.; Zhang, A.; Zhang, K.; Liu, M. Endohedrally doping the gold cage Au$_{16}^-$ with an trivalent atom B, Al, Ga, and In: Density functional studies. *Comput. Theor. Chem.* **2013**, *1018*, 1−5.

(717) Li, H.-F.; Wang, H.-Q. Probing the stability of neutral and anionic transition-metal-doped golden cage nanoclusters: M@Au$_{16}$ (M = Sc, Ti, V). *Phys. Chem. Chem. Phys.* **2014**, *16*, 244−254.

(718) Liu, J.-X.; Liu, Z.; Filot, I. A. W.; Su, Y.; Tranca, I.; Hensen, E. J. M. CO oxidation on Rh-doped hexadecagold clusters. *Catal. Sci. Technol.* **2017**, *7*, 75−83.

(719) Li, H.-F.; Wang, H.-Q. Stabilization of golden cages by encapsulation of a single transition metal atom. *R. Soc. Open Sci.* **2018**, *5*, 171019.

(720) Tang, C.; Zhu, W.; Zhang, K.; He, X.; Zhu, F. The density functional studies of the doped gold cages Au$_{17}$M (M = Cu, Ag, Li, Na, K). *Comput. Theor. Chem.* **2014**, *1049*, 62−66.

(721) Manzoor, D.; Krishnamurty, S.; Pal, S. Endohedrally doped gold nanocages: Efficient catalysts for O$_2$ activation and CO oxidation. *Phys. Chem. Chem. Phys.* **2016**, *18*, 7068−7074.

(722) Zorriasatein, S.; Joshi, K.; Kanhere, D. G. Electronic and structural investigations of gold clusters doped with copper: Au$_{n-1}$Cu$^-$ (n = 13-19). *J. Chem. Phys.* **2008**, *128*, 184314.

(723) Jayasekharan, T.; Ghanty, T. K. Endohedrally doped golden fullerenes X@Au$_{32}$ (X = Li$^+$, Na$^+$, K$^+$, Rb$^+$, Cs$^+$). *J. Phys. Chem. C* **2010**, *114*, 8787−8793.

(724) Manna, D.; Jayasekharan, T.; Ghanty, T. K. Structure and stability of Zn, Cd, and Hg atom doped golden fullerene (Au$_{32}$). *J. Phys. Chem. C* **2013**, *117*, 18777−18788.

(725) Kumar, V. Coating of a layer of Au on Al$_{13}$: The findings of icosahedral Al@Al$_{12}$Au$_{20}^-$ and Al$_{12}$Au$_{20}^{2-}$ fullerenes using ab initio pseudopotential calculations. *Phys. Rev. B: Condens. Matter Mater. Phys.* **2009**, *79*, 085423.

(726) Wang, Q.; Sun, Q.; Jena, P. Stabilizing a 22 karat nanogolden cage. *J. Chem. Phys.* **2009**, *131*, 204501.

(727) Tian, D.; Zhang, H.; Zhao, J. Structure and structural evolution of Ag$_n$ (n = 3-22) clusters using a genetic algorithm and density functional theory method. *Solid State Commun.* **2007**, *144*, 174−179.

(728) Weis, P.; Bierweiler, T.; Gilb, S.; Kappes, M. M. Structures of small silver cluster cations (Ag$_n^+$, n < 12): Ion mobility measurements versus density functional and MP2 calculations. *Chem. Phys. Lett.* **2002**, *355*, 355−364.

(729) Janssens, E.; Neukermans, S.; Nguyen, H. M. T.; Nguyen, M. T.; Lievens, P. Quenching of the magnetic moment of a transition metal dopant in silver clusters. *Phys. Rev. Lett.* **2005**, *94*, 113401.

(730) Janssens, E.; Neukermans, S.; Wang, X.; Veldeman, N.; Silverans, R. E.; Lievens, P. Stability patterns of transition metal doped silver clusters: Dopant- and size-dependent electron delocalization. *Eur. Phys. J. D* **2005**, *34*, 23−27.

(731) Janssens, E.; Van Hoof, T.; Veldeman, N.; Neukermans, S.; Hou, M.; Lievens, P. Mass spectrometric and modeling investigations of bimetallic silver-cobalt clusters. *Int. J. Mass Spectrom.* **2006**, *252*, 38−46.

(732) Tono, K.; Terasaki, A.; Ohta, T.; Kondow, T. Photoelectron spectroscopy and density-functional calculations of silver cluster anions doped with a cobalt atom: Size dependent sp-d interaction. *Chem. Phys. Lett.* **2007**, *449*, 276−281.

(733) Rodriguez-Kessler, P. L.; Rodriguez-Dominguez, A. R. Structural, electronic, and magnetic properties of Ag$_n$Co (n = 1-9) clusters: A first-principles study. *Comput. Theor. Chem.* **2015**, *1066*, 55−61.

(734) Zhang, M.; Gu, X.-Y.; Zhang, W.-L.; Zhao, L.-N.; He, L.-M.; Luo, Y.-H. Probing the magnetic and structural properties of the 3d, 4d, 5d impurities encapsulated in an icosahedral Ag$_{12}$ cage. *Phys. B* **2010**, *405*, 642−648.

(735) Gong, X.; Ju, W.; Li, T.; Feng, Z.; Wang, Y. Spin-orbit splitting and magnetism of icosahedral M@Ag$_{12}$ clusters (M = 3d and 4d atoms). *J. Cluster Sci.* **2015**, *26*, 759−773.

(736) Sun, Q.; Wang, Q.; Yu, J. Z.; Li, Z. Q.; Wang, J. T.; Kawazoe, Y. Local magnetism of 3d and 4d impurities in Ag and Pd clusters. *J. Phys. I* **1997**, *7*, 1233−1244.

(737) Harb, M.; Rabilloud, F.; Simon, D. Structural, electronic, magnetic and optical properties of icosahedral silver-nickel nanoclusters. *Phys. Chem. Chem. Phys.* **2010**, *12*, 4246−4254.

(738) Medel, V. M.; Reber, A. C.; Chauhan, V.; Sen, P.; Koester, A. M.; Calaminici, P.; Khanna, S. N. Nature of valence transition and spin moment in Ag$_n$V$^+$ clusters. *J. Am. Chem. Soc.* **2014**, *136*, 8229−8236.

(739) Xiong, R.; Die, D.; Xiao, L.; Xu, Y. G.; Shen, X. Y. Probing the structural, electronic, and magnetic properties of Ag$_n$V (n = 1-12) clusters. *Nanoscale Res. Lett.* **2017**, *12*, 625.

(740) Dong, R.; Chen, X.; Zhao, H.; Wang, X.; Shu, H.; Ding, Z.; Wei, L. Structural, electronic and magnetic properties of Ag$_n$Fe clusters (n ⩽ 15): Local magnetic moment interacting with delocalized electrons. *J. Phys. B: At., Mol. Opt. Phys.* **2011**, *44*, 035102.

(741) Rodríguez-Kessler, P. L.; Pan, S.; Florez, E.; Cabellos, J. L.; Merino, G. Structural evolution of the rhodium-doped silver clusters Ag$_n$Rh (n ≤ 15) and their reactivity toward NO. *J. Phys. Chem. C* **2017**, *121*, 19420−19427.

(742) Xiong, R.; Die, D.; Xu, Y.-G.; Zheng, B.-X.; Fu, Y.-C. Probing the structural, electronic and magnetic properties of Ag$_n$Sc (n = 1-16) clusters. *Phys. Chem. Chem. Phys.* **2018**, *20*, 15824−15834.

(743) Gao, Y.; Jiang, W.; Chen, L.; Wang, J.; Wang, Z. First-principles study on charge transfer in an actinide-containing

superatom from surface-enhanced Raman scattering. *J. Mater. Chem. C* **2017**, *5*, 803−806.

(744) Sun, Q.; Gong, X. G.; Zheng, Q. Q.; Sun, D. Y.; Wang, G. H. Local magnetic properties and electronic structures of 3d and 4d impurities in Cu clusters. *Phys. Rev. B: Condens. Matter Mater. Phys.* **1996**, *54*, 10896−10904.

(745) Holtzl, T.; Veldeman, N.; De Haeck, J.; Veszpremi, T.; Lievens, P.; Nguyen, M. T. Growth mechanism and chemical bonding in scandium-doped copper clusters: Experimental and theoretical study in concert. *Chem. - Eur. J.* **2009**, *15*, 3970−3982.

(746) Janssens, E.; Lievens, P. Growth mechanisms for doped clusters. *Adv. Nat. Sci.: Nanosci. Nanotechnol.* **2011**, *2*, 023001.

(747) Hirabayashi, S.; Ichihashi, M. Reactions of Ti- and V-doped Cu cluster cations with nitric oxide and oxygen: Size dependence and preferential NO adsorption. *J. Phys. Chem. A* **2016**, *120*, 1637−1643.

(748) Pham, H. T.; Cuong, N. T.; Tam, N. M.; Tung, N. T. A systematic investigation on CrCu$_n$ clusters with n = 9-16: Noble gas and tunable magnetic property. *J. Phys. Chem. A* **2016**, *120*, 7335−7343.

(749) Sarugaku, S.; Murakami, R.; Matsumoto, J.; Kawano, T.; Arakawa, M.; Terasaki, A. Size-dependent reactivity of nickel-doped silver cluster cations toward oxygen: Electronic and geometric effects. *Chem. Lett.* **2017**, *46*, 385−388.

(750) Graciani, J.; Oviedo, J.; Sanz, J. F. V@Au$_{12}^-$: An improved novel catalyst for CO oxidation? *J. Phys. Chem. B* **2006**, *110*, 11600−11603.

(751) Gao, Y.; Shao, N.; Bulusu, S.; Zeng, X. C. Effective CO oxidation on endohedral gold-cage nanoclusters. *J. Phys. Chem. C* **2008**, *112*, 8234−8238.

(752) Kim, H. Y.; Kim, D. H.; Ryu, J. H.; Lee, H. M. Design of robust and reactive nanoparticles with atomic precision: 13Ag-Ih and 12Ag-1X (X = Pd, Pt, Au, Ni, or Cu) Core-Shell Nanoparticles. *J. Phys. Chem. C* **2009**, *113*, 15559−15564.

(753) Kim, H. Y.; Han, S. S.; Ryu, J. H.; Lee, H. M. Balance in adsorption energy of reactants steers CO oxidation mechanism of Ag$_{13}$ and Ag$_{12}$Pd$_1$ nanoparticles: Association mechanism versus carbonate-mediated mechanism. *J. Phys. Chem. C* **2010**, *114*, 3156−3160.

(754) Zhou, S.; Pei, W.; Du, Q.; Zhao, J. Foreign atom encapsulated Au$_{12}$ golden cages for catalysis of CO oxidation. *Phys. Chem. Chem. Phys.* **2019**, *21*, 10587−10593.

(755) Fu, Y.; Li, J.; Wang, S.-G. Bonding and electronic structures in W@Au$_{12}$ AE complexes (AE = NO$^+$, CO, BF, CN$^-$, or BO$^-$): Analogies among ligands isoelectronic to carbon monoxide. *J. Mol. Model.* **2010**, *16*, 9−16.

(756) Sinai, H. E.; Avnir, D. Adsorption-induced symmetry distortions in W@Au$_{12}$ nanoclusters, leading to enhanced hyperpolarizabilities. *Isr. J. Chem.* **2016**, *56*, 1076−1081.

(757) Chen, L.; Gao, Y.; Cheng, Y.; Su, Y.; Wang, Z.; Li, Z.; Zhang, R.-Q. Strong core@shell dependence in surface-enhanced raman scattering of pyridine on stable 13-atom silver-caged bimetallic clusters. *J. Phys. Chem. C* **2015**, *119*, 17429−17437.

(758) Chen, L.; Gao, Y.; Cheng, Y.; Li, H.; Wang, Z.; Li, Z.; Zhang, R.-Q. Nonresonant chemical mechanism in surface-enhanced Raman scattering of pyridine on M@Au$_{12}$ clusters. *Nanoscale* **2016**, *8*, 4086−4093.

(759) Chen, L.; Wang, Z.; Li, Z.; Zhang, R.-Q. Chemical coupling SERS properties of pyridine on silver-caged metal clusters M@Ag$_{12}$ (M = V$^-$, Nb$^-$, Ta$^-$, Cr, Mo, W, Mn$^+$, Tc$^+$, Re$^+$). *J. Electron. Mater.* **2017**, *46*, 3904−3909.

(760) Jensen, F.; Toftlund, H. Structure and stability of C$_{24}$ and B$_{12}$N$_{12}$ isomers. *Chem. Phys. Lett.* **1993**, *201*, 89−96.

(761) Silaghi-Dumitrescu, I.; Haiduc, I.; Sowerby, D. B. Fully inorganic (carbon-free) fullerenes? The boron-nitrogen case. *Inorg. Chem.* **1993**, *32*, 3755−3758.

(762) Sun, M.-L.; Slanina, Z.; Lee, S.-L. Square/hexagon route towards the boron-nitrogen clusters. *Chem. Phys. Lett.* **1995**, *233*, 279−283.

(763) Seifert, G.; Fowler, P.; Mitchell, D.; Porezag, D.; Frauenheim, T. Boron-nitrogen analogues of the fullerenes: Electronic and structural properties. *Chem. Phys. Lett.* **1997**, *268*, 352−358.

(764) Stephan, O.; Bando, Y.; Loiseau, A.; Willaime, F.; Shramchenko, N.; Tamiya, T.; Sato, T. Formation of small single-layer and nested BN cages under electron irradiation of nanotubes and bulk material. *Appl. Phys. A: Mater. Sci. Process.* **1998**, *67*, 107−111.

(765) Golberg, D.; Bando, Y.; Stephan, O.; Kurashima, K. Octahedral boron nitride fullerenes formed by electron beam irradiation. *Appl. Phys. Lett.* **1998**, *73*, 2441−2443.

(766) Oku, T.; Kuno, M.; Narita, I. High-resolution electron microscopy and electronic structures of endohedral La@B$_{36}$N$_{36}$ clusters. Diamond Relat. *Diamond Relat. Mater.* **2002**, *11*, 940−944.

(767) Oku, T.; Kuno, M. Synthesis, argon/hydrogen storage and magnetic properties of boron nitride nanotubes and nanocapsules. *Diamond Relat. Mater.* **2003**, *12*, 840−845.

(768) Oku, T.; Narita, I.; Nishiwaki, A. Formation and structures of B$_{36}$N$_{36}$ and Y@B$_{36}$N$_{36}$ clusters studied by high-resolution electron microscopy and mass spectrometry. *J. Phys. Chem. Solids* **2004**, *65*, 369−372.

(769) Oku, T.; Nishiwaki, A.; Narita, I. Formation and atomic structures of B$_n$N$_n$ (n = 24−60) clusters studied by mass spectrometry, high-resolution electron microscopy and molecular orbital calculations. *Phys. B* **2004**, *351*, 184−190.

(770) Beheshtian, J.; Tabar, M. B.; Bagheri, Z.; Peyghan, A. A. Exohedral and endohedral adsorption of alkaline earth cations in BN nanocluster. *J. Mol. Model.* **2013**, *19*, 1445−1450.

(771) Liu, Z.; Liu, X.; Zhao, J. Design of superhalogens using a core−shell structure model. *Nanoscale* **2017**, *9*, 18781−18787.

(772) Feng, L.; Lu, Y.; Kong, J.; Su, Z. Theoretical studies on the structure and properties of BN clusters (BN)$_n$ and endohedral metallo-BN clusters M@(BN)$_n$. *Comput. Theor. Chem.* **2011**, *964*, 56−64.

(773) Wang, J.; Ma, L.; Zhao, J.; Wang, B.; Wang, G. Stability and magnetic properties of transition metal atoms endohedral B$_n$N$_n$ (n = 12−28) cages. *J. Chem. Phys.* **2008**, *128*, 084306.

(774) Oliaey, A. R.; Boshra, A.; Khavary, M. Spin polarized bonding analysis of endohedral boron nitride nanocages: Density functional theory study. *Phys. E* **2010**, *42*, 2314−2318.

(775) Koi, N.; Oku, T.; Suganuma, K. s. Effects of endohedral element in B$_{24}$N$_{24}$ clusters on hydrogenation studied by molecular orbital calculations. *Phys. E* **2005**, *29*, 541−545.

(776) Karachi, N.; Boshra, A.; Jadidi, S. DFT based insights into reactivity descriptors of encapsulated B$_{24}$N$_{24}$ nanocages. *Struct. Chem.* **2011**, *22*, 805−809.

(777) Su, B.; Feng, X.; Guo, X.; Li, N. Polynitrogen clusters encapsulated inside B$_{24}$N$_{24}$ fullerene-like nanocages: Nanoscale high energy materials studied by density functional theory. *Inorg. Chim. Acta* **2017**, *456*, 128−135.

(778) Wang, Q.; Sun, Q.; Oku, T.; Kawazoe, Y. First-principles study of La−B$_{36}$N$_{36}$ cage. *Phys. B* **2003**, *339*, 105−109.

(779) Nishiwaki, A.; Oku, T.; Suganuma, K. Atomic and electronic structures of endohedral B$_{36}$N$_{36}$ clusters with doping elements studied by molecular orbital calculations. *Phys. B* **2004**, *349*, 254−259.

(780) Boshra, A.; Monajjemi, M.; Aghaie, M.; Aghaie, H. Density functional theory investigation of natural bond orbital population analysis and gauge-including atomic orbital NMR tensors of K@B$_{36}$N$_{36}$. *J. Comput. Theor. Nanosci.* **2010**, *7*, 1147−1158.

(781) Oliaey, A. R.; Boshra, A. DFT study of [Fe@B$_{36}$N$_{36}$]$^{n+}$ (n = 2, 3) endohedral nanocages: Chemical reactivity, NBO analysis and thermochemistry. *Phys. E* **2013**, *52*, 136−143.

(782) Batista, R. J.; Mazzoni, M. S.; Chacham, H. Boron nitride fullerene B$_{36}$N$_{36}$ doped with transition metal atoms: First-principles calculations. *Phys. Rev. B: Condens. Matter Mater. Phys.* **2007**, *75*, 035417.

(783) Nigam, S.; Majumder, C. Magnetic needles encapsulated inside (BN)$_{36}$ cage: Prediction of atomic, electronic, and magnetic

structure from first principle calculations. *Appl. Phys. Lett.* **2007**, *91*, 223112.

(784) Nigam, S.; Majumder, C. CO oxidation by BN−fullerene cage: Effect of impurity on the chemical reactivity. *ACS Nano* **2008**, *2*, 1422−1428.

(785) Nigam, S.; Kulshreshtha, S.; Majumder, C. Structural and magnetic isomers of $M(BN)_{36}$ and $M_4(BN)_{36}$ clusters (M = Ti, V, Cr, Mn, Fe, Co, Ni, Cu): An ab initio density functional study. *Phys. Rev. B: Condens. Matter Mater. Phys.* **2008**, *77*, 075438.

(786) Wen, S.-H.; Deng, W.-Q.; Han, K.-L. Endohedral BN metallofullerene $M@B_{36}N_{36}$ complex as promising hydrogen storage materials. *J. Phys. Chem. C* **2008**, *112*, 12195−12200.

(787) Liang, W.; Jia, J.; Lv, J.; Wu, H. Electronic structure, stability and magnetic properties of small M_{1-4} (M = Fe, Co, Ni) clusters encapsulated inside a $(BN)_{48}$ cage. *Chem. Phys. Lett.* **2015**, *622*, 57−62.

(788) Liang, W.; Jia, J.; Lv, J.; Wu, H. Density functional theory study of Mo-doped $M@(BN)_{48}$ (M = Sc, Ti, V, Cr, Mn, Fe, Co, Ni, and Cu) clusters. *J. Mol. Struct.* **2016**, *1108*, 92−95.

(789) Kumar, V.; Kawazoe, Y. Hydrogenated caged clusters of Si, Ge, and Sn and their endohedral doping with atoms: Ab initio calculations. *Phys. Rev. B: Condens. Matter Mater. Phys.* **2007**, *75*, 155425.

(790) Bahramy, M. S.; Kumar, V.; Kawazoe, Y. First-principles calculations of hyperfine structure in M-doped $Si_{16}H_{16}$ fullerene cages (M = Cr, Mn, and Fe). *Phys. Rev. B: Condens. Matter Mater. Phys.* **2009**, *79*, 235443.

(791) Zhao, Y.; Kim, Y.-H.; Dillon, A.; Heben, M.; Zhang, S. Hydrogen storage in novel organometallic buckyballs. *Phys. Rev. Lett.* **2005**, *94*, 155504.

(792) Yildirim, T.; Ciraci, S. Titanium-decorated carbon nanotubes as a potential high-capacity hydrogen storage medium. *Phys. Rev. Lett.* **2005**, *94*, 175501.

(793) Liang, W.; Jia, J.; Lv, J.; Wu, H. Electronic structure, stability and magnetic properties of small $M_{1-2}Cr$ (M= Fe, Co, and Ni) alloy encapsulated inside a $(BN)_{48}$ cage. *Phys. Lett. A* **2015**, *379*, 1715−1721.

(794) Burnin, A.; BelBruno, J. J. $Zn_nS_m^+$ cluster production by laser ablation. *Chem. Phys. Lett.* **2002**, *362*, 341−348.

(795) Kasuya, A.; Sivamohan, R.; Barnakov, Y. A.; Dmitruk, I. M.; Nirasawa, T.; Romanyuk, V. R.; Kumar, V.; Mamykin, S. V.; Tohji, K.; Jeyadevan, B. Ultra-stable nanoparticles of CdSe revealed from mass spectrometry. *Nat. Mater.* **2004**, *3*, 99−102.

(796) Kasuya, A.; Noda, Y.; Dmitruk, I.; Romanyuk, V.; Barnakov, Y.; Tohji, K.; Kumar, V.; Belosludov, R.; Kawazoe, Y.; Ohuchi, N. Stoichiometric and ultra-stable nanoparticles of II-VI compound semiconductors. *Eur. Phys. J. D* **2005**, *34*, 39−41.

(797) Kukreja, L.; Rohlfing, A.; Misra, P.; Hillenkamp, F.; Dreisewerd, K. Cluster formation in UV laser ablation plumes of ZnSe and ZnO studied by time-of-flight mass spectrometry. *Appl. Phys. A: Mater. Sci. Process.* **2004**, *78*, 641−644.

(798) Hamad, S.; Catlow, C. R. A.; Spano, E.; Matxain, J. M.; Ugalde, J. M. Structure and properties of ZnS nanoclusters. *J. Phys. Chem. B* **2005**, *109*, 2703−2709.

(799) Matxain, J. M.; Eriksson, L. A.; Formoso, E.; Piris, M.; Ugalde, J. M. Endohedral $(X@Zn_iS_i)_{i=4\text{-}16}^{0,\pm}$ nanoclusters, X = Li, Na, K, Cl, Br. *J. Phys. Chem. C* **2007**, *111*, 3560−3565.

(800) Poggio, S.; Wang, B.; Gibson, U. J.; BelBruno, J. J. Properties of transition metal substituted zinc sulfide hexamers and dodecamers. *Phys. Chem. Chem. Phys.* **2015**, *17*, 14208−14214.

(801) Matxain, J. M.; Formoso, E.; Mercero, J. M.; Piris, M.; Lopez, X.; Ugalde, J. M. Magnetic endohedral transition-metal-doped semiconducting-nanoclusters. *Chem. - Eur. J.* **2008**, *14*, 8547−8554.

(802) Jimenez-Izal, E.; Matxain, J. M.; Piris, M.; Ugalde, J. M. Thermal stability of endohedral first-row transition-metal $TM@Zn_iS_i$ structures, i = 12, 16. *J. Phys. Chem. C* **2011**, *115*, 7829−7835.

(803) Jimenez-Izal, E.; Matxain, J.; Piris, M.; Ugalde, J. Second-row transition-metal doping of (Zn_iS_i), i = 12, 16 nanoclusters: Structural and magnetic properties. *Computation* **2013**, *1*, 31−45.

(804) Chen, H.; Shi, D.; Qi, J.; Wang, B. Structure, electronic and magnetic properties of Cr-doped $(ZnS)_{12}$ clusters: A first-principles study. *Phys. Lett. A* **2010**, *374*, 4133−4139.

(805) Chen, H.; Shi, D.; Qi, J.; Wang, B. First-principles study on the structure, electronic, and magnetic properties of Mn-doped $(ZnS)_{12}$ clusters. *Phys. E* **2010**, *43*, 117−124.

(806) Chen, H.; Shi, D.; Qi, J.; Wang, B. First-principles study on the magnetic properties of transition-metal atoms doped $(ZnS)_{12}$ cluster. *J. Magn. Magn. Mater.* **2011**, *323*, 781−788.

(807) Zhang, D.; Chen, L.; Zhang, J.; Miao, X. Theoretical investigation of structural and magnetic properties of Zn_nSe_n (n = 6−13) nanoclusters doped with manganese atoms. *J. Am. Ceram. Soc.* **2011**, *94*, 759−764.

(808) Yadav, M. K.; Sanyal, B.; Mookerjee, A. Structural, electronic and magnetic properties of Cr-doped $(ZnTe)_{12}$ clusters. *J. Magn. Magn. Mater.* **2009**, *321*, 235−240.

(809) Ghosh, S.; Sanyal, B.; Das, G. Structural, electronic and magnetic properties of Cr-doped $Cd_{12}S_{12}$ clusters: A density functional investigation. *J. Magn. Magn. Mater.* **2010**, *322*, 734−742.

(810) Jimenez-Izal, E.; Matxain, J. M.; Piris, M.; Ugalde, J. M. Structure and stability of the endohedrally doped $(X@Cd_iS_i)_{i=4,\ 9,\ 12,\ 15,\ 16}^{q=0,\pm1}$, X = Na, K, Cl, Br, nanoclusters. *J. Phys. Chem. C* **2010**, *114*, 2476−2483.

(811) Poggio, S.; King, J.; BelBruno, J. Properties of transition metal doped cadmium sulfide hexamers and dodecamers. *Chem. Phys. Lett.* **2015**, *640*, 106−111.

(812) Shevlin, S.; Guo, Z.; Van Dam, H.; Sherwood, P.; Catlow, C. A.; Sokol, A.; Woodley, S. Structure, optical properties and defects in nitride (III−V) nanoscale cage clusters. *Phys. Chem. Chem. Phys.* **2008**, *10*, 1944−1959.

(813) Kaur, P.; Sekhon, S.; Kumar, V. Empty cage to three-dimensional structural transition in nanoparticles of III-V compound semiconductors: The finding of magic $(AlP)_{13}$ and $(GaP)_{32}$. *Phys. Rev. B: Condens. Matter Mater. Phys.* **2012**, *85*, 085429.

(814) Kaur, P.; Sekhon, S.; Kumar, V. Prediction of rock salt structure of $(InN)_{32}$ nanoparticles from first principles calculations. *J. Chem. Phys.* **2013**, *138*, 114310.

(815) Kiran, B.; Kandalam, A. K.; Rallabandi, R.; Koirala, P.; Li, X.; Tang, X.; Wang, Y.; Fairbrother, H.; Gantefoer, G.; Bowen, K. $(PbS)_{32}$: A baby crystal. *J. Chem. Phys.* **2012**, *136*, 024317.

(816) Ueno, M.; Onodera, A.; Shimomura, O.; Takemura, K. X-ray observation of the structural phase transition of aluminum nitride under high pressure. *Phys. Rev. B: Condens. Matter Mater. Phys.* **1992**, *45*, 10123−10126.

(817) Ueno, M.; Yoshida, M.; Onodera, A.; Shimomura, O.; Takemura, K. Stability of the wurtzite-type structure under high pressure: GaN and InN. *Phys. Rev. B: Condens. Matter Mater. Phys.* **1994**, *49*, 14−21.

(818) Wang, J.; Ma, L.; Zhao, J.; Wang, G.; Chen, X.; Bruce King, R. Electronic and magnetic properties of manganese and iron-doped Ga_nAs_n nanocages (n = 7−12). *J. Chem. Phys.* **2008**, *129*, 044908.

(819) Lu, P.; Wu, C.; Li, Y.; Yu, Z.; Cao, H.; Wang, S. Investigation on structural, electronic, and magnetic properties of Mn-doped $Ga_{12}N_{12}$ clusters. *J. Mater. Sci.* **2013**, *48*, 8552−8558.

(820) Lu, P.; Wu, C.; Cong, Z.; Li, Y.; Zhang, X.; Yu, Z.; Cao, H. Fe-doped $Ga_{12}N_{12}$ clusters: Electronic and magnetic properties. *Mod. Phys. Lett. B* **2013**, *27*, 1350222.

(821) Longo, R.; Carrete, J.; Aguilera-Granja, F.; Vega, A.; Gallego, L. A density-functional study of the structures and electronic properties of neutral, anionic, and endohedrally doped In_xP_x clusters. *J. Chem. Phys.* **2009**, *131*, 074504.

(822) Ding, J.-N.; Yuan, N.-Y.; Li, C.-L.; Wang, X.-Q.; Chen, G.-G.; Chen, X.-S.; Lu, W. Studies on structures, electronic and magnetic properties of TM-doped In_nSb_n (n = 7−12, 14, 16) clusters (TM = Mn, Fe, and Co). *J. Appl. Phys.* **2011**, *109*, 014322.

(823) Liu, C.; Tkachenko, N. V.; Popov, I. A.; Fedik, N.; Min, X.; Xu, C. Q.; Li, J.; McGrady, J. E.; Boldyrev, A. I.; Sun, Z. M. Structure and bonding in $[Sb@In_8Sb_{12}]^{3-}$ and $[Sb@In_8Sb_{12}]^{5-}$. *Angew. Chem., Int. Ed.* **2019**, *58*, 8367−8371.

(824) Wang, B.; Nagase, S.; Zhao, J.; Wang, G. Structural growth sequences and electronic properties of zinc oxide clusters $(ZnO)_n$ (n = 2-18). *J. Phys. Chem. C* **2007**, *111*, 4956−4963.

(825) Liu, H.; Wang, S.; Zhou, G.; Wu, J.; Duan, W. Structural, electronic, and magnetic properties of manganese-doped $Zn_{12}O_{12}$ clusters: A first-principles study. *J. Chem. Phys.* **2006**, *124*, 174705.

(826) Liu, H.; Zhang, J.-M. Investigation on structure, electronic and magnetic properties of Cr doped $(ZnO)_{12}$ clusters: First-principles calculations. *Phys. E* **2018**, *99*, 51−57.

(827) Baei, M. T.; Peyghan, A. A.; Bagheri, Z. First principles study on encapsulation of alkali metals into ZnO nanocage. *Chin. J. Chem. Phys.* **2012**, *25*, 671−675.

(828) Nanavati, S. P.; Sundararajan, V.; Mahamuni, S.; Ghaisas, S.; Kumar, V. Discovery of a nonstoichiometric $Zn_{11}MnSe_{13}$ magnetic magic quantum dot from ab initio calculations. *Phys. Rev. B: Condens. Matter Mater. Phys.* **2011**, *84*, 045306.

(829) Shakerzdeh, E.; Tahmasebi, E.; Shamlouei, H. R. The influence of alkali metals (Li, Na and K) interaction with $Be_{12}O_{12}$ and $Mg_{12}O_{12}$ nanoclusters on their structural, electronic and nonlinear optical properties: A theoretical study. *Synth. Met.* **2015**, *204*, 17−24.

(830) Groh, M. F.; Müller, U.; Isaeva, A.; Ruck, M. Ionothermal syntheses, crystal structures, and chemical bonding of the rhodium-centered clusters $[RhBi_9]^{4+}$ and $[(RhBi_7)I_8]$. *Z. Anorg. Allg. Chem.* **2017**, *643*, 1482−1490.

(831) Ruck, M.; Dubenskyy, V.; Söhnel, T. Structure and bonding of $Pd@[Bi_{10}]^{4+}$ in the subbromide $Bi_{14}PdBr_{16}$. *Angew. Chem., Int. Ed.* **2003**, *42*, 2978−2982.

(832) Dubenskyy, V.; Ruck, M. Das subchlorid $Bi_{16}PdCl_{22}$: $Pd@Bi_{10}{}^{4+}$-polykationen in einem raumnetzwerk aus chlorobismutat(III)-anionen. *Z. Anorg. Allg. Chem.* **2004**, *630*, 2458−2462.

(833) Groh, M. F.; Wolff, A.; Wahl, B.; Rasche, B.; Gebauer, P.; Ruck, M. Pentagonal bismuth antiprisms with endohedral palladium or platinum atoms by low-Temperature syntheses. *Z. Anorg. Allg. Chem.* **2017**, *643*, 69−80.

(834) Wahl, B.; Erbe, M.; Gerisch, A.; Kloo, L.; Ruck, M. Noble-metal centered polycations $[Au@Bi_{10}]^{5+}$ or $[Pd@Bi_{10}]^{4+}$ embedded in halogenido-bismuthate(III)-stannate(II) frameworks. *Z. Anorg. Allg. Chem.* **2009**, *635*, 743−752.

(835) Lichtenberger, N.; Wilson, R. J.; Eulenstein, A. R.; Massa, W.; Clérac, R.; Weigend, F.; Dehnen, S. Main group metal−actinide magnetic coupling and structural response upon U^{4+} inclusion into Bi, Tl/Bi, or Pb/Bi cages. *J. Am. Chem. Soc.* **2016**, *138*, 9033−9036.

(836) Lips, F.; Clérac, R.; Dehnen, S. $[Eu@Sn_6Bi_8]^{4-}$: A mini-fullerane-type zintl anion containing a lanthanide ion. *Angew. Chem., Int. Ed.* **2011**, *50*, 960−964.

(837) Lips, F.; Hołynska, M.łg.; Clerac, R.; Linne, U.; Schellenberg, I.; Pottgen, R.; Weigend, F.; Dehnen, S. Doped semimetal clusters: Ternary, intermetalloid anions $[Ln@Sn_7Bi_7]^{4-}$ and $[Ln@Sn_4Bi_9]^{4-}$ (Ln = La, Ce) with adjustable magnetic properties. *J. Am. Chem. Soc.* **2012**, *134*, 1181−1191.

(838) Ababei, R.; Massa, W.; Weinert, B.; Pollak, P.; Xie, X.; Clérac, R.; Weigend, F.; Dehnen, S. Ionic-radius-driven selection of the main-group-metal cage for intermetalloid clusters $[Ln@Pb_xBi_{14-x}]^{q-}$ and $[Ln@Pb_yBi_{13-y}]^{q-}$ (x/q = 7/4, 6/3; y/q = 4/4, 3/3). *Chem. - Eur. J.* **2015**, *21*, 386−394.

(839) Mitzinger, S.; Broeckaert, L.; Massa, W.; Weigend, F.; Dehnen, S. $[V@Ge_8As_4]^{3-}$ and $[Nb@Ge_8As_6]^{3-}$: Encapsulation of electron-poor transition metal atoms. *Chem. Commun.* **2015**, *51*, 3866−3869.

(840) Mitzinger, S.; Broeckaert, L.; Massa, W.; Weigend, F.; Dehnen, S. Understanding of multimetallic cluster growth. *Nat. Commun.* **2016**, *7*, 10480.

(841) Lips, F.; Dehnen, S. Neither electron-precise nor in accordance with Wade−Mingos rules: The ternary cluster anion $[Ni_2Sn_7Bi_5]^{3-}$. *Angew. Chem., Int. Ed.* **2011**, *50*, 955−959.

(842) Wilson, R. J.; Hastreiter, F.; Reiter, K.; Büschelberger, P.; Wolf, R.; Gschwind, R. M.; Weigend, F.; Dehnen, S. $[Co@Sn_6Sb_6]^{3-}$: An off-center endohedral 12-vertex cluster. *Angew. Chem., Int. Ed.* **2018**, *57*, 15359−15363.

(843) Lips, F.; Clerac, R.; Dehnen, S. $[Pd_3Sn_8Bi_6]^{4-}$: A 14-vertex Sn/Bi cluster embedding a Pd_3 triangle. *J. Am. Chem. Soc.* **2011**, *133*, 14168−14171.

(844) Pham, H. T.; Nguyen, M. T. Theoretical investigation of metallic heterofullerenes of silicon and germanium mixed with phosphorus and arsenic atoms M-A8E6, A = Si, Ge; E = P, As; and M = Cr, Mo, W. *J. Phys. Chem. A* **2017**, *121*, 5056−5066.

(845) Tam, N. M.; Pham, H. T.; Cuong, N. T.; Tung, N. T. A DFT investigation on geometry and chemical bonding of isoelectronic $Si_8N_6V^-$, Si_8N_6Cr, and $Si_8N_6Mn^+$ clusters. *Chem. Phys. Lett.* **2017**, *685*, 410−415.

(846) Song, B.; Zhou, J.; Yong, Y.; He, P. Density functional investigation of transition-metal-encapsulated Si_nC_n (n = 7−10) cagelike clusters. *J. Phys. Chem. C* **2010**, *114*, 10703−10710.

(847) Pham, H. T.; Nguyen, H. T.; Nguyen, M. T. $Mn@B_3N_3Si_8{}^+$: A stable singlet manganese-doped hetero-atom-mixed silicon fullerene. *Struct. Chem.* **2017**, *28*, 1887−1893.

(848) King, R. B.; Zhao, J. The isolable matryoshka nesting doll icosahedral cluster $[As@Ni_{12}@As_{20}]^{3-}$ as a "superatom": Analogy with the jellium cluster $Al_{13}{}^-$ generated in the gas phase by laser vaporization. *Chem. Commun.* **2006**, 4204−4205.

(849) Sheong, F. K.; Chen, W. J.; Kim, H.; Lin, Z. Peeling the onion: A revised model of the electron count for matryoshka clusters. *Dalton Trans.* **2015**, *44*, 7251−7257.

(850) Baruah, T.; Zope, R. R.; Richardson, S. L.; Pederson, M. R. Electronic structure and rebonding in the onionlike $As@Ni_{12}@As_{20}$ cluster. *Phys. Rev. B: Condens. Matter Mater. Phys.* **2003**, *68*, 241404.

(851) Baruah, T.; Zope, R. R.; Richardson, S. L.; Pederson, M. R. Electronic structure, vibrational stability, and predicted infrared-Raman spectra of the As_{20}, $As@Ni_{12}$, and $As@Ni_{12}@As_{20}$ clusters. *J. Chem. Phys.* **2004**, *121*, 11007−11015.

(852) Zhao, J.; Xie, R.-H. Density functional study of onion-skin-like $[As@Ni_{12}As_{20}]^{3-}$ and $[Sb@Pd_{12}Sb_{20}]^{3-}$ cluster ions. *Chem. Phys. Lett.* **2004**, *396*, 161−166.

(853) Chang, C.; Patzer, A. B. C.; Sedlmayr, E.; Sülzle, D. Inorganic cage molecules encapsulating Kr: A computational study. *Phys. Rev. B: Condens. Matter Mater. Phys.* **2005**, *72*, 235402.

(854) Chang, C.; Patzer, A. B. C.; Sedlmayr, E.; Sülzle, D.; Steinke, T. Onion-like inorganic fullerenes of icosahedral symmetry. *Comput. Mater. Sci.* **2006**, *35*, 387−390.

(855) Huang, X.; Zhao, J.; Su, Y.; Chen, Z.; King, R. B. Design of three-shell icosahedral Matryoshka clusters $A@B_{12}@A_{20}$ (A = Sn, Pb; B = Mg, Zn, Cd, Mn). *Sci. Rep.* **2015**, *4*, 6915.

(856) King, R. B. Chemical applications of topology and group theory.31. Atomic orbital graphs and the shapes of the g and h orbitals. *J. Phys. Chem. A* **1997**, *101*, 4653−4656.

(857) Zhang, L.; Huang, J.; Wang, W. Y.; Li, Q. X.; Yang, J. L. Transport properties of a three-shell icosahedral matryoshka cluster: A first-principles study. *RSC Adv.* **2017**, *7*, 12704−12710.

(858) Long, F.; Liu, H.; Li, D.; Yan, J. Spin-orbit coupling effects on ligand-free icosahedral Matryoshka superatoms. *J. Phys. Chem. A* **2017**, *121*, 2420−2428.

(859) MacLeod Carey, D.; Morales-Verdejo, C.; Muñoz-Castro, A. $[As@Ni_{12}@As_{20}]^{3-}$ and $[Sn@Cu_{12}@Sn_{20}]^{12-}$ clusters. Related structures with different construction philosophy. *Chem. Phys. Lett.* **2015**, *638*, 99−102.

(860) Rauhalahti, M.; Munoz-Castro, A. Interaction in multilayer clusters: A theoretical survey of $[Sn@Cu_{12}@Sn_{20}]^{12-}$, a three-layer matryoshka-like intermetalloid. *RSC Adv.* **2015**, *5*, 18782−18787.

(861) Damianos, K.; Solokha, P.; Ferrando, R. Core−shell and matryoshka structures in MgNi nanoalloys: A computational study. *RSC Adv.* **2013**, *3*, 9419−9430.

(862) Borbon-Gonzalez, D. J.; Fortunelli, A.; Barcaro, G.; Sementa, L.; Johnston, R. L.; Posada-Amarillas, A. Global minimum $Pt_{13}M_{20}$ (M = Ag, Au, Cu, Pd) dodecahedral core−shell clusters. *J. Phys. Chem. A* **2013**, *117*, 14261−14266.

(863) Wang, J. L.; Bai, J. L.; Jellinek, J.; Zeng, X. C. Gold-coated transition-metal anion $[Mn_{13}@Au_{20}]^-$ with ultrahigh magnetic moment. *J. Am. Chem. Soc.* **2007**, *129*, 4110−4111.

(864) Bai, X.; Lv, J.; Wu, H.-S. A giant enhancement of magnetic moment in a ternary three-shell icosahedral cluster: Fe@Mn$_{12}$@Au$_{20}$. *Mol. Phys.* **2020**, *118*, 1−7.

(865) Kou, C. Y.; Zhuang, L.; Wang, G. Q.; Cui, H.; Yuan, H. K.; Tian, C. L.; Wang, J. Z.; Chen, H. [TM$_{13}$@Bi$_{20}$]$^{-}$ clusters in three-shell icosahedral matryoshka structure: Being as superatoms. *RSC Adv.* **2015**, *5*, 92134−92143.

(866) Sigmon, G. E.; Ling, J.; Unruh, D. K.; Moore-Shay, L.; Ward, M.; Weaver, B.; Burns, P. C. Uranyl−peroxide interactions favor nanocluster self-assembly. *J. Am. Chem. Soc.* **2009**, *131*, 16648−16649.

(867) Hu, H. S.; Kaltsoyannis, N. High spin ground states in Matryoshka actinide nanoclusters: A computational study. *Chem. - Eur. J.* **2018**, *24*, 347−350.

(868) Zhao, J.; Wang, X.; Zhao, J.; Luo, R.; Shen, X.; Zhu, D.; Jing, S. [Ln$_4$@Ln$_4$] matryoshka tetrahedron: A novel secondary building unit. *CrystEngComm* **2016**, *18*, 863−867.

(869) Iwasa, T.; Nakajima, A. Geometric, electronic, and optical properties of monomer and assembly of endohedral aluminum superatomic clusters. *J. Phys. Chem. C* **2013**, *117*, 21551−21557.

(870) Sun, Q.; Wang, Q.; Briere, T.; Kawazoe, Y. Dimer interactions of magic W@Si$_{12}$ clusters. *J. Phys.: Condens. Matter* **2002**, *14*, 4503−4508.

(871) Robles, R.; Khanna, S. N. Magnetism in assembled and supported silicon endohedral cages: First-principles electronic structure calculations. *Phys. Rev. B: Condens. Matter Mater. Phys.* **2009**, *80*, 115414.

(872) Torres, M.; Fernández, E.; Balbás, L. Study of the structural and electronic properties of [Ti@Si$_{16}$]$_n$, [Sc@Si$_{16}$K]$_n$, and [V@Si$_{16}$F]$_n$ ($n \leq 9$) aggregates from first principles. *J. Phys. Chem. C* **2011**, *115*, 335−350.

(873) Iwasa, T.; Nakajima, A. Geometric, electronic, and optical properties of a superatomic heterodimer and trimer: Sc@Si$_{16}$−V@Si$_{16}$ and Sc@Si$_{16}$−Ti@Si$_{16}$−V@Si$_{16}$. *J. Phys. Chem. C* **2012**, *116*, 14071−14077.

(874) Liu, J.; Guo, P.; Zheng, J.; Zhao, P.; Jiang, Z.; Shen, L. Self-assembly of a two-dimensional sheet with Ta@Si$_{16}$ superatoms and its magnetic and photocatalytic properties. *J. Phys. Chem. C* **2020**, *124*, 6861−6870.

(875) Park, S.; Kim, G.; Kwon, Y.-K. First-principles investigation on dimerization of metal-encapsulated gold nanoclusters. *RSC Adv.* **2014**, *4*, 192−198.

(876) Kumar, V. Predictions of novel nanostructures of silicon by metal encapsulation. *Comput. Mater. Sci.* **2004**, *30*, 260−268.

(877) Kumar, V. Recent theoretical progress on electronic and structural properties of clusters: Permanent electric dipoles, magnetism, novel caged structures, and their assemblies. *Comput. Mater. Sci.* **2006**, *35*, 375−381.

(878) Reber, A. C.; Khanna, S. N.; Castleman, A. W. Superatom compounds, clusters, and assemblies: Ultra alkali motifs and architectures. *J. Am. Chem. Soc.* **2007**, *129*, 10189−10194.

(879) Reveles, J.; Baruah, T.; Zope, R. R. Al$_{12}$Cu Superatom as stable building block of ionic salts. *J. Phys. Chem. C* **2015**, *119*, 5129−5137.

(880) Okada, N.; Uchida, N.; Kanayama, T. Thermal stability of amorphous Si-rich W silicide films composed of W-atom-encapsulated Si clusters. *J. Appl. Phys.* **2017**, *121*, 225308.

(881) Torres, M.; Fernández, E.; Balbás, L. Theoretical study of the structural and electronic properties of aggregates, wires, and bulk phases formed from M@Si$_{16}$ superatoms (M = Sc^{-}, Ti, V^{+}). *Int. J. Quantum Chem.* **2011**, *111*, 444−462.

(882) Singh, A. K.; Kumar, V.; Briere, T. M.; Kawazoe, Y. Cluster assembled metal encapsulated thin nanotubes of silicon. *Nano Lett.* **2002**, *2*, 1243−1248.

(883) Menon, M.; Andriotis, A. N.; Froudakis, G. Structure and stability of Ni-encapsulated Si nanotube. *Nano Lett.* **2002**, *2*, 301−304.

(884) Andriotis, A. N.; Mpourmpakis, G.; Froudakis, G. E.; Menon, M. Stabilization of Si-based cage clusters and nanotubes by encapsulation of transition metal atoms. *New J. Phys.* **2002**, *4*, 78.

(885) Mpourmpakis, G.; Froudakis, G. E.; Andriotis, A. N.; Menon, M. Understanding the structure of metal encapsulated Si cages and nanotubes: Role of symmetry and d-band filling. *J. Chem. Phys.* **2003**, *119*, 7498−7502.

(886) Tan Pham, H.; Minh Tam, N.; Van Duong, L.; Phuong Pham-Ho, M.; Tho Nguyen, M. Mn$_2$@Si$_{15}$: The smallest triple ring tubular silicon cluster. *Phys. Chem. Chem. Phys.* **2015**, *17*, 17566−17570.

(887) Wei-xiao, J.; Chenglin, L. Density-functional investigation of hexagonal prism transition-metal-encapsulated cage M$_2$Si$_{18}$ (M = Sc−Zn) clusters. *Modell. Simul. Mater. Sci. Eng.* **2010**, *18*, 025011.

(888) Ji, W.; Luo, C. Structures, magnetic properties, and electronic counting rule of metals-encapsulated cage-like M$_2$Si$_{18}$ (M = Ti-Zn) clusters. *Int. J. Quantum Chem.* **2012**, *112*, 2525−2531.

(889) Nayak, S.; Gruner, M.; Entel, P. Possible one-dimensional structures obtained from transition metal atom doped silicon nanoclusters. *Phase Transitions* **2006**, *79*, 709−716.

(890) Wang, J.; Zhao, J.; Ma, L.; Wang, G.; King, R. B. Stability and magnetic properties of Fe encapsulating in silicon nanotubes. *Nanotechnology* **2007**, *18*, 235705.

(891) Gueorguiev, G. K.; Stafström, S.; Hultman, L. Nano-wire formation by self-assembly of silicon−metal cage-like molecules. *Chem. Phys. Lett.* **2008**, *458*, 170−174.

(892) Peng, Q.; Shen, J.; Chen, N.-X. Geometry and electronic stability of tungsten encapsulated silicon nanotubes. *J. Chem. Phys.* **2008**, *129*, 034704.

(893) Singh, A. K.; Kumar, V.; Kawazoe, Y. Metal encapsulated nanotubes of silicon and germanium. *J. Mater. Chem.* **2004**, *14*, 555−563.

(894) Singh, A. K.; Briere, T. M.; Kumar, V.; Kawazoe, Y. Magnetism in transition-metal-doped silicon nanotubes. *Phys. Rev. Lett.* **2003**, *91*, 146802.

(895) Dhaka, K.; Bandyopadhyay, D. Magnetism, structures and stabilities of cluster assembled TM@Si nanotubes (TM = Cr, Mn and Fe): A density functional study. *Dalton Trans.* **2016**, *45*, 12432−12443.

(896) Li, J.; Wang, J.; Zhao, H.-Y.; Liu, Y. Magnetic silicon nanotube: Role of encapsulated europium atoms. *J. Phys. Chem. C* **2013**, *117*, 10764−10769.

(897) Wang, J.; Liu, Y. Magnetic silicon fullerenes: Experimental exploration and theoretical insight. *J. Cluster Sci.* **2016**, *27*, 861−873.

(898) Sirichantaropass, S.; García-Suárez, V.; Lambert, C. J. Electronic properties of alkali-and alkaline-earth-intercalated silicon nanowires. *Phys. Rev. B: Condens. Matter Mater. Phys.* **2007**, *75*, 075328.

(899) Singh, A. K.; Kumar, V.; Kawazoe, Y. Surface physics, low-dimensional systems, and related topics-Ferromagnetism and piezomagnetic behavior in Mn-doped germanium nanotubes. *Phys. Rev. B: Condens. Matter Mater. Phys.* **2004**, *69*, 233406.

(900) Singh, A. K.; Kumar, V.; Kawazoe, Y. Design of a very thin direct-band-gap semiconductor nanotube of germanium with metal encapsulation. *Phys. Rev. B: Condens. Matter Mater. Phys.* **2005**, *71*, 075312.

(901) Singh, A. K.; Kumar, V.; Kawazoe, Y. Metal encapsulated nanotubes of germanium with metal dependent electronic properties. *Eur. Phys. J. D* **2005**, *34*, 295−298.

(902) Zhou, J.; Giri, S.; Jena, P. 18-Electron rule inspired Zintl-like ions composed of all transition metals. *Phys. Chem. Chem. Phys.* **2014**, *16*, 20241−20247.

(903) Yong, Y.; Cui, H.; Zhou, Q.; Su, X.; Kuang, Y.; Li, X. Ultrathin nanowire based on icosahedral W@Au$_{12}$ and application as NO gas sensor. *J. Phys. Chem. Solids* **2019**, *127*, 68−75.

(904) Li, X.; Yang, J. Computational design of one-dimensional ferromagnetic semiconductors in transition metal embedded stannaspherene nanowires. *Chin. J. Chem.* **2019**, *37*, 1021−1024.

(905) Rudberg, E.; Sałek, P.; Luo, Y. Nonlocal exchange interaction removes half-metallicity in graphene nanoribbons. *Nano Lett.* **2007**, *7*, 2211−2213.

(906) Saranin, A. A.; Zotov, A. V.; Kotlyar, V. G.; Kasyanova, T. V.; Utas, O. A.; Okado, H.; Katayama, M.; Oura, K. Ordered arrays of Be-

encapsulated Si nanotubes on Si (111) surface. *Nano Lett.* **2004**, *4*, 1469−1473.

(907) Stegmaier, S.; Fässler, T. F. $Na_{2.8}Cu_5Sn_{5.6}$: A crystalline alloy featuring intermetalloid $_\infty{}^1\{Sn_{0.6}@Cu_5@Sn_5\}$ double-walled nanorods with pseudo-five-fold symmetry. *Angew. Chem.* **2012**, *124*, 2701−2704.

(908) Wang, Y.; Saranin, A.; Zotov, A.; Lai, M.; Chang, H. Random and ordered arrays of surface magic clusters. *Int. Rev. Phys. Chem.* **2008**, *27*, 317−360.

(909) Li, J.-L.; Jia, J.-F.; Liang, X.-J.; Liu, X.; Wang, J.-Z.; Xue, Q.-K.; Li, Z.-Q.; John, S. T.; Zhang, Z.; Zhang, S. Spontaneous assembly of perfectly ordered identical-size nanocluster arrays. *Phys. Rev. Lett.* **2002**, *88*, 066101.

(910) Zhong, X.; Lee, K.; Choi, B.; Meggiolaro, D.; Liu, F.; Nuckolls, C.; Pasupathy, A.; De Angelis, F.; Batail, P.; Roy, X. Superatomic two-dimensional semiconductor. *Nano Lett.* **2018**, *18*, 1483−1488.

(911) Miyazaki, T.; Kanayama, T. Ultrathin layered semiconductor: Si-rich transition metal silicide. *Jpn. J. Appl. Phys.* **2007**, *46*, L28−L30.

(912) Liu, Z.; Wang, X.; Cai, J.; Zhu, H. Room-temperature ordered spin structures in cluster-assembled single $V@Si_{12}$ sheets. *J. Phys. Chem. C* **2015**, *119*, 1517−1523.

(913) Nie, Z.; Guo, P.; Zheng, J.; Zhao, P.; Wan, Y.; Jiang, Z. Electronic and magnetic properties of two dimensional cluster-assembled materials based on $TM@Si_{12}$ (TM = 3d transition metal) clusters. *Comput. Mater. Sci.* **2018**, *146*, 134−142.

(914) Nakaya, M.; Iwasa, T.; Tsunoyama, H.; Eguchi, T.; Nakajima, A. Formation of a superatom monolayer using gas-phase-synthesized $Ta@Si_{16}$ nanocluster ions. *Nanoscale* **2014**, *6*, 14702−14707.

(915) Ohta, T.; Shibuta, M.; Tsunoyama, H.; Eguchi, T.; Nakajima, A. Charge transfer complexation of Ta-encapsulating $Ta@Si_{16}$ superatom with C_{60}. *J. Phys. Chem. C* **2016**, *120*, 15265−15271.

(916) Nakaya, M.; Iwasa, T.; Tsunoyama, H.; Eguchi, T.; Nakajima, A. Heterodimerization via the covalent bonding of $Ta@S_{16}$ nanoclusters and C_{60} molecules. *J. Phys. Chem. C* **2015**, *119*, 10962−10968.

(917) Seitsonen, A.; Puska, M. J.; Alatalo, M.; Nieminen, R. M.; Milman, V.; Payne, M. Crystals from metallic clusters: A first-principles calculation. *Phys. Rev. B: Condens. Matter Mater. Phys.* **1993**, *48*, 1981−1983.

(918) Liu, F.; Mostoller, M.; Kaplan, T.; Khanna, S.; Jena, P. Evidence for a new class of solids. First-principles study of $K(Al_{13})$. *Chem. Phys. Lett.* **1996**, *248*, 213−217.

(919) Ashman, C.; Khanna, S.; Liu, F.; Jena, P.; Kaplan, T.; Mostoller, M. $(BAl_{12})Cs$: A cluster-assembled solid. *Phys. Rev. B: Condens. Matter Mater. Phys.* **1997**, *55*, 15868−15873.

(920) Gong, X. Structure and stability of cluster-assembled solid $Al_{12}C(Si)$: A first-principles study. *Phys. Rev. B: Condens. Matter Mater. Phys.* **1997**, *56*, 1091−1094.

(921) Zhu, Z.-z.; Tian, B. Electronic properties of solid $(Al_{12}B)Li$ in the CsCl structure. *Solid State Commun.* **1998**, *108*, 891−894.

(922) Quan, H.-J.; Gong, X.-G. Electronic structure of cluster-assembled $Al_{12}C(Si)$ solid. *Chin. Phys.* **2000**, *9*, 656−660.

(923) Mondolfo, L. F. *Aluminum alloys: structure and properties*; Elsevier: Amsterdam, 2013.

(924) Reis, C.; Martins, J.; Pacheco, J. Stability analysis of a bulk material built from silicon cage clusters: A first-principles approach. *Phys. Rev. B: Condens. Matter Mater. Phys.* **2007**, *76*, 233406.

(925) Reis, C.; Pacheco, J. Bulk materials made of silicon cage clusters doped with Ti, Zr, or Hf. *J. Phys.: Condens. Matter* **2010**, *22*, 035501.

(926) Gunnarsson, O. Superconductivity in fullerides. *Rev. Mod. Phys.* **1997**, *69*, 575−606.

(927) Laurrabaquio, G. L.; Torres, M. B.; Fernández, E. M.; Balbás, L. C. Trends in the formation of aggregates and crystals from $M@Si_{16}$ clusters: A study from first principle calculations. *J. Math. Chem.* **2010**, *48*, 109−117.

(928) Pacheco, J.; Gueorguiev, G.; Martins, J. L. First-principles study of the possibility of condensed phases of endohedral silicon cage clusters. *Phys. Rev. B: Condens. Matter Mater. Phys.* **2002**, *66*, 033401.

(929) Uchida, N.; Kintou, H.; Matsushita, Y.; Tada, T.; Kanayama, T. Synthesis of new amorphous semiconductors assembled from transition-metal-encapsulating Si clusters. *Appl. Phys. Express* **2008**, *1*, 121502.

(930) Matxain, J. M.; Piris, M.; Lopez, X.; Ugalde, J. M. Thermally stable solids based on endohedrally doped ZnS clusters. *Chem. - Eur. J.* **2009**, *15*, 5138−5144.

(931) Jimenez-Izal, E.; Matxain, J. M.; Piris, M.; Ugalde, J. M. Self-assembling endohedrally doped CdS nanoclusters: New porous solid phases of CdS. *Phys. Chem. Chem. Phys.* **2012**, *14*, 9676−9682.

(932) Jadzinsky, P. D.; Calero, G.; Ackerson, C. J.; Bushnell, D. A.; Kornberg, R. D. Structure of a thiol monolayer-protected gold nanoparticle at 1.1 Å resolution. *Science* **2007**, *318*, 430−433.

(933) Joshi, C. P.; Bootharaju, M. S.; Alhilaly, M. J.; Bakr, O. M. $[Ag_{25}(SR)_{18}]^-$: The "golden" silver nanoparticle. *J. Am. Chem. Soc.* **2015**, *137*, 11578−11581.

(934) Aikens, C. M. Electronic and geometric structure, optical properties, and excited state behavior in atomically precise thiolate-stabilized noble metal nanoclusters. *Acc. Chem. Res.* **2018**, *51*, 3065−3073.

(935) Song, Y.; Lambright, K.; Zhou, M.; Kirschbaum, K.; Xiang, J.; Xia, A.; Zhu, M.; Jin, R. Large-scale synthesis, crystal structure, and optical properties of the $Ag_{146}Br_2(SR)_{80}$ nanocluster. *ACS Nano* **2018**, *12*, 9318−9325.

(936) Jin, S.; Du, W.; Wang, S.; Kang, X.; Chen, M.; Hu, D.; Chen, S.; Zou, X.; Sun, G.; Zhu, M. Thiol-induced synthesis of phosphine-protected gold nanoclusters with atomic precision and controlling the structure by ligand/metal engineering. *Inorg. Chem.* **2017**, *56*, 11151−11159.

(937) Chakraborty, I.; Pradeep, T. Atomically precise clusters of noble metals: Emerging link between atoms and nanoparticles. *Chem. Rev.* **2017**, *117*, 8208−8271.

(938) Jin, R.; Zeng, C.; Zhou, M.; Chen, Y. Atomically precise colloidal metal nanoclusters and nanoparticles: Fundamentals and opportunities. *Chem. Rev.* **2016**, *116*, 10346−10413.

(939) Kang, X.; Zhu, M. Tailoring the photoluminescence of atomically precise nanoclusters. *Chem. Soc. Rev.* **2019**, *48*, 2422−2457.

(940) Li, Y.-L.; Wang, Z.-Y.; Ma, X.-H.; Luo, P.; Du, C.-X.; Zang, S.-Q. Distinct photophysical properties in atom-precise silver and copper nanocluster analogues. *Nanoscale* **2019**, *11*, 5151−5157.

(941) Nasaruddin, R. R.; Chen, T.; Yan, N.; Xie, J. Roles of thiolate ligands in the synthesis, properties and catalytic application of gold nanoclusters. *Coord. Chem. Rev.* **2018**, *368*, 60−79.

(942) Liu, X.; Astruc, D. Atomically precise copper nanoclusters and their applications. *Coord. Chem. Rev.* **2018**, *359*, 112−126.

(943) Fang, J.; Zhang, B.; Yao, Q.; Yang, Y.; Xie, J.; Yan, N. Recent advances in the synthesis and catalytic applications of ligand-protected, atomically precise metal nanoclusters. *Coord. Chem. Rev.* **2016**, *322*, 1−29.

(944) Kang, X.; Chong, H.; Zhu, M. $Au_{25}(SR)_{18}$: The captain of the great nanocluster ship. *Nanoscale* **2018**, *10*, 10758−10834.

(945) Yang, J.; Jin, R. New advances in atomically precise silver nanoclusters. *ACS Mater. Lett.* **2019**, *1*, 482−489.

(946) Christensen, S. L.; MacDonald, M. A.; Chatt, A.; Zhang, P.; Qian, H.; Jin, R. Dopant location, local structure, and electronic properties of $Au_{24}Pt(SR)_{18}$ nanoclusters. *J. Phys. Chem. C* **2012**, *116*, 26932−26937.

(947) Faraday, M. X. The Bakerian Lecture.—Experimental relations of gold (and other metals) to light. *Philos. Trans.* **1857**, 145−181.

(948) Heaven, M. W.; Dass, A.; White, P. S.; Holt, K. M.; Murray, R. W. Crystal structure of the gold nanoparticle $[N(C_8H_{17})_4][Au_{25}(SCH_2CH_2Ph)_{18}]$. *J. Am. Chem. Soc.* **2008**, *130*, 3754−3755.

(949) Liu, Z.; Zhu, M.; Meng, X.; Xu, G.; Jin, R. Electron transfer between $[Au_{25}(SC_2H_4Ph)_{18}]^-$ TOA+ and oxoammonium cations. *J. Phys. Chem. Lett.* **2011**, *2*, 2104−2109.

(950) Walter, M.; Akola, J.; Lopez-Acevedo, O.; Jadzinsky, P. D.; Calero, G.; Ackerson, C. J.; Whetten, R. L.; Grönbeck, H.; Häkkinen, H. A unified view of ligand-protected gold clusters as superatom complexes. *Proc. Natl. Acad. Sci. U. S. A.* **2008**, *105*, 9157−9162.

(951) Grönbeck, H. Correspondence: On the bonding in ligand-protected gold clusters. *Nat. Commun.* **2017**, *8*, 1612.

(952) Zeng, C.; Qian, H.; Li, T.; Li, G.; Rosi, N. L.; Yoon, B.; Barnett, R. N.; Whetten, R. L.; Landman, U.; Jin, R. Total structure and electronic properties of the gold nanocrystal $Au_{36}(SR)_{24}$. *Angew. Chem., Int. Ed.* **2012**, *51*, 13114−13118.

(953) Jin, R.; Nobusada, K. Doping and alloying in atomically precise gold nanoparticles. *Nano Res.* **2014**, *7*, 285−300.

(954) Negishi, Y.; Munakata, K.; Ohgake, W.; Nobusada, K. Effect of copper doping on electronic structure, geometric structure, and stability of thiolate-protected Au_{25} nanoclusters. *J. Phys. Chem. Lett.* **2012**, *3*, 2209−2214.

(955) Negishi, Y.; Iwai, T.; Ide, M. Continuous modulation of electronic structure of stable thiolate-protected Au_{25} cluster by Ag doping. *Chem. Commun.* **2010**, *46*, 4713−4715.

(956) Ghosh, A.; Mohammed, O. F.; Bakr, O. M. Atomic-Level Doping of Metal Clusters. *Acc. Chem. Res.* **2018**, *51*, 3094−3103.

(957) Negishi, Y.; Kurashige, W.; Niihori, Y.; Iwasa, T.; Nobusada, K. Isolation, structure, and stability of a dodecanethiolate-protected Pd_1Au_{24} cluster. *Phys. Chem. Chem. Phys.* **2010**, *12*, 6219−6225.

(958) Kacprzak, K. A.; Lehtovaara, L.; Akola, J.; Lopez-Acevedo, O.; Häkkinen, H. A density functional investigation of thiolate-protected bimetal $PdAu_{24}(SR)_{18}{}^{z}$ clusters: Doping the superatom complex. *Phys. Chem. Chem. Phys.* **2009**, *11*, 7123−7129.

(959) Jiang, D.-e.; Dai, S. From superatomic $Au_{25}(SR)_{18}{}^{-}$ to superatomic $M@Au_{24}(SR)_{18}{}^{q}$ core−shell clusters. *Inorg. Chem.* **2009**, *48*, 2720−2722.

(960) Qian, H.; Jiang, D.-e.; Li, G.; Gayathri, C.; Das, A.; Gil, R. R.; Jin, R. Monoplatinum doping of gold nanoclusters and catalytic application. *J. Am. Chem. Soc.* **2012**, *134*, 16159−16162.

(961) Fields-Zinna, C. A.; Crowe, M. C.; Dass, A.; Weaver, J. E.; Murray, R. W. Mass spectrometry of small bimetal monolayer-protected clusters. *Langmuir* **2009**, *25*, 7704−7710.

(962) Tofanelli, M. A.; Ni, T. W.; Phillips, B. D.; Ackerson, C. J. Crystal structure of the $PdAu_{24}(SR)_{180}$ superatom. *Inorg. Chem.* **2016**, *55*, 999−1001.

(963) Negishi, Y.; Igarashi, K.; Munakata, K.; Ohgake, W.; Nobusada, K. Palladium doping of magic gold cluster $Au_{38}(SC_2H_4Ph)_{24}$: Formation of $Pd_2Au_{36}(SC_2H_4Ph)_{24}$ with higher stability than $Au_{38}(SC_2H_4Ph)_{24}$. *Chem. Commun.* **2012**, *48*, 660−662.

(964) Liu, X.; Yuan, J.; Yao, C.; Chen, J.; Li, L.; Bao, X.; Yang, J.; Wu, Z. Crystal and solution photoluminescence of $MAg_{24}(SR)_{18}$ (M = Ag/Pd/Pt/Au) nanoclusters and some implications for the photoluminescence mechanisms. *J. Phys. Chem. C* **2017**, *121*, 13848−13853.

(965) Yan, J.; Su, H.; Yang, H.; Malola, S.; Lin, S.; Häkkinen, H.; Zheng, N. Total structure and electronic structure analysis of doped thiolated silver $[MAg_{24}(SR)_{18}]^{2-}$ (M = Pd, Pt) clusters. *J. Am. Chem. Soc.* **2015**, *137*, 11880−11883.

(966) Bootharaju, M. S.; Joshi, C. P.; Parida, M. R.; Mohammed, O. F.; Bakr, O. M. Templated atom-precise galvanic synthesis and structure elucidation of a $[Ag_{24}Au(SR)_{18}]^{-}$ nanocluster. *Angew. Chem., Int. Ed.* **2016**, *55*, 922−926.

(967) Bootharaju, M. S.; Joshi, C. P.; Parida, M. R.; Mohammed, O. F.; Bakr, O. M. Innentitelbild: Templated atom-precise galvanic synthesis and structure elucidation of a $[Ag_{24}Au(SR)_{18}]^{-}$ nanocluster (Angew. Chem. 3/2016). *Angew. Chem.* **2016**, *128*, 834−834.

(968) Van Der Linden, M.; Van Bunningen, A. J.; Amidani, L.; Bransen, M.; Elnaggar, H.; Glatzel, P.; Meijerink, A.; De Groot, F. M. Single Au atom doping of silver nanoclusters. *ACS Nano* **2018**, *12*, 12751−12760.

(969) Khatun, E.; Bose, S.; Jash, M.; Pradeep, T. Atomically precise cluster-based white light emitters. *J. Chem. Sci.* **2018**, *130*, 147.

(970) Mishra, D.; Lobodin, V.; Zhang, C.; Aldeek, F.; Lochner, E.; Mattoussi, H. Gold-doped silver nanoclusters with enhanced photophysical properties. *Phys. Chem. Chem. Phys.* **2018**, *20*, 12992−13007.

(971) Soldan, G.; Aljuhani, M. A.; Bootharaju, M. S.; AbdulHalim, L. G.; Parida, M. R.; Emwas, A. H.; Mohammed, O. F.; Bakr, O. M. Gold doping of silver nanoclusters: A 26-fold enhancement in the luminescence quantum yield. *Angew. Chem., Int. Ed.* **2016**, *55*, 5749−5753.

(972) Kang, X.; Zhou, M.; Wang, S.; Jin, S.; Sun, G.; Zhu, M.; Jin, R. The tetrahedral structure and luminescence properties of Bi-metallic $Pt_1Ag_{28}(SR)_{18}(PPh_3)_4$ nanocluster. *Chem. Sci.* **2017**, *8*, 2581−2587.

(973) Bootharaju, M. S.; Kozlov, S. M.; Cao, Z.; Harb, M.; Parida, M. R.; Hedhili, M. N.; Mohammed, O. F.; Bakr, O. M.; Cavallo, L.; Basset, J.-M. Direct versus ligand-exchange synthesis of $[PtAg_{28}(BDT)_{12}(TPP)_4]^{4-}$ nanoclusters: Effect of a single-atom dopant on the optoelectronic and chemical properties. *Nanoscale* **2017**, *9*, 9529−9536.

(974) Li, Q.; Lambright, K. J.; Taylor, M. G.; Kirschbaum, K.; Luo, T.-Y.; Zhao, J.; Mpourmpakis, G.; Mokashi-Punekar, S.; Rosi, N. L.; Jin, R. Reconstructing the surface of gold nanoclusters by cadmium doping. *J. Am. Chem. Soc.* **2017**, *139*, 17779−17782.

(975) Liao, L.; Zhou, S.; Dai, Y.; Liu, L.; Yao, C.; Fu, C.; Yang, J.; Wu, Z. Mono-mercury doping of Au_{25} and the HOMO/LUMO energies evaluation employing differential pulse voltammetry. *J. Am. Chem. Soc.* **2015**, *137*, 9511−9514.

(976) Yao, C.; Lin, Y.-j.; Yuan, J.; Liao, L.; Zhu, M.; Weng, L.-h.; Yang, J.; Wu, Z. Mono-cadmium vs mono-mercury doping of Au_{25} nanoclusters. *J. Am. Chem. Soc.* **2015**, *137*, 15350−15353.

(977) Wang, Y.; Liu, Y.-H.; Zhang, Y.; Wang, F.; Kowalski, P. J.; Rohrs, H. W.; Loomis, R. A.; Gross, M. L.; Buhro, W. E. Isolation of the Magic-Size CdSe Nanoclusters $[(CdSe)_{13}(n\text{-octylamine})_{13}]$ and $[(CdSe)_{13}(\text{oleylamine})_{13}]$. *Angew. Chem., Int. Ed.* **2012**, *51*, 6154−6157.

(978) Liu, Y. H.; Wang, F.; Wang, Y.; Gibbons, P. C.; Buhro, W. E. Lamellar assembly of cadmium selenide nanoclusters into quantum belts. *J. Am. Chem. Soc.* **2011**, *133*, 17005−17013.

(979) Hsieh, T.-E.; Yang, T.-W.; Hsieh, C.-Y.; Huang, S.-J.; Yeh, Y.-Q.; Chen, C.-H.; Li, E. Y.; Liu, Y.-H. Unraveling the structure of magic-size $(CdSe)_{13}$ cluster pairs. *Chem. Mater.* **2018**, *30*, 5468−5477.

(980) Yu, J. H.; Liu, X.; Kweon, K. E.; Joo, J.; Park, J.; Ko, K.-T.; Lee, D. W.; Shen, S.; Tivakornsasithorn, K.; Son, J. S.; et al. Giant Zeeman splitting in nucleation-controlled doped $CdSe{:}Mn^{2+}$ quantum nanoribbons. *Nat. Mater.* **2010**, *9*, 47−53.

(981) Yang, J.; Fainblat, R.; Kwon, S. G.; Muckel, F.; Yu, J. H.; Terlinden, H.; Kim, B. H.; Iavarone, D.; Choi, M. K.; Kim, I. Y.; et al. Route to the smallest doped semiconductor: Mn^{2+}-doped $(CdSe)_{13}$ clusters. *J. Am. Chem. Soc.* **2015**, *137*, 12776−12779.

(982) Muckel, F.; Yang, J.; Lorenz, S.; Baek, W.; Chang, H.; Hyeon, T.; Bacher, G.; Fainblat, R. Digital doping in magic-sized CdSe clusters. *ACS Nano* **2016**, *10*, 7135−7141.

(983) Palencia, C.; Yu, K.; Boldt, K. The future of colloidal semiconductor magic-size clusters. *ACS Nano* **2020**, *14*, 1227−1235.

(984) Lebon, A.; Aguado, A.; Vega, A. A new magnetic superatom: *Phys. Chem. Chem. Phys.* **2015**, *17*, 28033−28043.

(985) Kumar, V. High symmetry Nb_n and Ta_n (n = 12, 15, and 17) clusters: High magnetic moments and the finding of superatoms with doping. *Comput. Theor. Chem.* **2013**, *1021*, 149−154.